



# *University of* **HUDDERSFIELD**

## **University of Huddersfield Repository**

Zala, Karina

FLOW CHARACTERISTICS AND DESIGN METHODOLOGY FOR A CENTRIFUGAL COMPRESSOR VOLUTE

### **Original Citation**

Zala, Karina (2019) FLOW CHARACTERISTICS AND DESIGN METHODOLOGY FOR A CENTRIFUGAL COMPRESSOR VOLUTE. Doctoral thesis, University of Huddersfield.

This version is available at <http://eprints.hud.ac.uk/id/eprint/34919/>

The University Repository is a digital collection of the research output of the University, available on Open Access. Copyright and Moral Rights for the items on this site are retained by the individual author and/or other copyright owners. Users may access full items free of charge; copies of full text items generally can be reproduced, displayed or performed and given to third parties in any format or medium for personal research or study, educational or not-for-profit purposes without prior permission or charge, provided:

- The authors, title and full bibliographic details is credited in any copy;
- A hyperlink and/or URL is included for the original metadata page; and
- The content is not changed in any way.

For more information, including our policy and submission procedure, please contact the Repository Team at: [E.mailbox@hud.ac.uk](mailto:E.mailbox@hud.ac.uk).

<http://eprints.hud.ac.uk/>

# FLOW CHARACTERISTICS AND DESIGN METHODOLOGY FOR A CENTRIFUGAL COMPRESSOR VOLUTE

---

A THESIS SUBMITTED IN PARTIAL FULFILMENT OF THE REQUIREMENTS FOR THE  
DEGREE OF DOCTOR OF PHILOSOPHY AT THE UNIVERSITY OF HUDDERSFIELD IN  
COLLABORATION WITH CUMMINS TURBO TECHNOLOGIES

by

Karina Zala  
BEng (Hons) / MEng Mechanical Engineering  
University of Huddersfield, UK, 2013

Professor Rakesh Mishra  
Leader of Energy, Emissions and the Environment Research Group  
Centre for Efficiency and Performance Engineering

School of Computing and Engineering  
University of Huddersfield

UK  
October 2018









*In loving memory of Bobby*

*13-09-2015*

*To my parents, Ashwin and Nayna*

*For all your hardships and endeavours, I will be your legacy...*



# ABSTRACT

---

Throughout the years, many studies have been carried out on engines with every effort to save fuel, reduce emissions and produce more power. Turbochargers have been developed and installed in the exhaust system of an engine to use exhaust emissions for boosting power within an internal combustion engine, which would otherwise be wasted. The turbocharger characteristics are essential to determine its performance. There are three stages in a turbocharger, namely being, the turbine stage where energy is extracted from the exhaust gases; bearing housing where energy is being transferred to the compressor stage; and the compressor stage where ambient air is drawn in and compressed to increase the fluids density and pressure prior to being delivered into the intake system. The compressor stage consists of four main components, namely being, the inducer, impeller, diffuser and volute.

The volute of a turbocharger compressor is the third most important component within the compressor stage and has therefore, not received the attention that is needed. However, manufacturers are continuously seeking to obtain a realistic design methodology where variables exposed in real conditions, such as frictional effects are accounted for to minimise losses during performance. For this reason, it is essential to develop a thorough understanding of the flow phenomena the turbocharger compressor stage experiences under steady and transient conditions from a macroscopic level to a microscopic level. This creates a solid foundation for conducting the presented research.

In this study, a realistic design methodology for a turbocharger compressor volute has been presented. Detailed qualitative and quantitative flow field analyses of the turbocharger compressor stage have been numerically carried out under steady and transient flow conditions using Computational Fluid Dynamics (CFD) based techniques. The numerical investigations carried out in this study allow a clear visualisation of the flow structure within the turbocharger compressor stage volute, which makes it a cost effective method to undertake this research study. Approximations have been presented to design the symmetric and asymmetric type volutes, which have been applied into practice and analysed under steady and transient conditions to validate the presented compressor volute design methodology for turbocharging applications.

# DECLARATION

---

- The author of this thesis (including any appendices and/or schedules to this thesis) owns any copyright in it (the “Copyright”) and she has given The University of Huddersfield the right to use such Copyright for any administrative, promotional, educational and/or teaching purposes.
- Copies of this thesis, either in full or in extracts, may be made only in accordance with the regulations of the University Library. Details of these regulations may be obtained from the Librarian. This page must form part of any such copies made.
- The ownership of any patents, designs, trademarks and any and all other intellectual property rights except for the Copyright (the “Intellectual Property Rights”) and any reproductions of copyright works, for example graphs and tables (“Reproductions”), which may be described in this thesis, may not be owned by the author and may be owned by third parties. Such Intellectual Property Rights and Reproductions cannot and must not be made available for use without the prior written permission of the owner(s) of the relevant Intellectual Property Rights and/or Reproductions.

# ACKNOWLEDGEMENTS

---

First and foremost, I would like to express my most sincere gratitude to Professor Rakesh Mishra for offering me the opportunity to pursue this research, for believing in me, shedding light and expressing his insights and ideas on my project, providing guidance and support throughout my PhD journey. In addition to this, I would like to express my deepest appreciation to Professor Ian Glover for making all this possible for my future. I would like to thank Dr. Belachew Tesfa for introducing me to the sheer satisfaction gained through research during my final year project, which motivated me to pursue my PhD. I would like to share my sincere appreciation to Dr. Paul Baker, Dr. Taimoor Asim at the University of Huddersfield and Dr. Paul Eynon, Dr. Michael Dolton and John Horsley at Cummins Turbo Technologies for their collaboration, support and guidance throughout my PhD journey. I would like to thank and acknowledge Dr. Krzysztof Kubiak, Dr. Naim Mian and Dr. Suman Pradhan for assessing me through my PhD progression. Furthermore, I would like to thank Kuldip Ubbi, Dr. Anthony Johnson, Dr. Violeta Holmes, Dr. Leigh Fleming and Dr. Paul Bills for all their encouragement over the years. I would also like to express my gratitude to Diane McClymont and Heather Lee at the University of Huddersfield for being incredibly supportive; and to Nicola Bagshaw and Samantha McNeely at the University Health Centre whom have been amazing medical practitioners with all my health obstacles I have had to face throughout this journey.

I would like to express my innermost gratitude and acknowledge the following: my parents, Ashwin and Nayna for their encouragement, continuous support and motivation throughout my PhD; my sister, Roxann, for being an inspiration in higher education; Bobby for his patience, uplifting spirit and understanding until his passing; Isuru Sendanayake Achchige and Savith Sendanayake Achchige for being my second family during my PhD and taking me into their hearts and their home. Special thanks to Isuru for consistent motivation and being my light through my dark times throughout this journey.

I would also like to thank and acknowledge my Turbocharger Team, Sree Nirjhor Kaysthaagir and Noukhez Ahmed for their guidance and insights throughout my PhD journey. Additionally, I would like to thank Joshua Higgins, Kristina Zubac, Fajer Mohamed, Ngqabutho Sibanda, Aadil Rafiq and Yiqing Meng for their support. Finally, I would like to thank Peter Wong, Hazel Jones and Jackson Mudaliar for their continuous encouragement, and I would like to acknowledge David Froggett for all the moral support he gave until his passing.

# TABLE OF CONTENTS

---

1.....	1
1.1 Turbochargers.....	2
1.2 Construction of a Turbocharger .....	3
1.3 Operation of a Turbocharger .....	5
1.4 Turbocharger Stages.....	6
1.4.1 Turbocharger Turbine Stage .....	7
1.4.2 Turbocharger Rotor Bearing Stage .....	8
1.4.3 Turbocharger Compressor Stage.....	9
1.5 Fundamental Fluid Principles in a Turbocharger Compressor Stage.....	10
1.6 Turbocharger Compressor Stage Performance Characteristics.....	15
1.7 Centrifugal Compressor Volute Geometry .....	18
1.8 Centrifugal Compressor Volute Loss Mechanisms.....	21
1.9 Volute Design Practices .....	24
1.10 Motivation .....	26
1.11 Research Aim .....	27
1.12 Organisation of Thesis .....	27
2.....	29
2.1 Fluid Flow Characteristics inside a Centrifugal Compressor Volute during Steady Response .....	30
2.2 Fluid Flow Characteristics inside a Centrifugal Compressor Volute during Instantaneous Response .....	34
2.3 Volute Design Methodologies Performance and Losses.....	36
2.4 Scope of Research .....	50
2.5 Research Objectives .....	51
3.....	53



3.1	Numerical Methodology .....	54
3.2	Pre-Processing .....	54
3.2.1	Geometry.....	54
3.2.2	Meshing.....	56
3.3	Solver Execution .....	58
3.3.1	Solver Settings .....	58
3.3.2	Boundary Conditions .....	58
3.3.3	Turbulence Modelling.....	59
3.3.4	Discretization .....	60
3.3.5	Convergence Criteria .....	60
3.4	Post- Processing .....	61
3.4.1	Global Data Extraction Locations through the Centrifugal Compressor Stage.....	61
3.4.2	Local Data Extraction through the Centrifugal Compressor Volute .....	62
3.5	Scope of the Numerical Investigations.....	64
4	.....	65
4.1	Baseline Turbocharger Compressor Stage Numerical Verification against Experimental .....	66
4.2	Turbocharger Compressor Volute Performance .....	68
4.3	Global Static Pressure Distribution around the Centrifugal Compressor during Steady Conditions .....	69
4.4	Local Static Pressure around the Centrifugal Compressor Volute at Low Operating Speed during Steady Conditions.....	76
4.5	Local Static Pressure around the Centrifugal Compressor Volute at High Operating Speed during Steady Conditions.....	87
4.6	Local Speed Comparison of Static Pressure around the Centrifugal Compressor Volute during Steady Conditions.....	97
4.7	Global Velocity Magnitude Distribution around the Centrifugal Compressor during Steady Conditions .....	98

4.8	Local Velocity Magnitude Distribution around the Centrifugal Compressor Volute at Low Operating Speed during Steady Conditions.....	105
4.9	Local Velocity Magnitude around the Centrifugal Compressor Volute at High Operating Speed during Steady Conditions.....	117
4.10	Local Speed Comparison of Velocity Magnitude around the Centrifugal Compressor Volute during Steady Conditions.....	127
4.11	Global Static Temperature Distribution around the Centrifugal Compressor during Steady Conditions .....	128
4.12	Local Static Temperature Distribution around the Centrifugal Compressor Volute at Low Operating Speed during Steady Conditions.....	134
4.13	Local Static Temperature around the Centrifugal Compressor Volute at High Operating Speed during Steady Conditions.....	144
4.14	Local Speed Comparison of Static Temperature around the Centrifugal Compressor Volute during Steady Conditions.....	153
4.15	Summary .....	154
5.....		156
5.1	Turbocharger Compressor Stage Unsteady Performance Comparison.....	157
5.2	Global Static Pressure Distribution at Two Instances during Unsteady Conditions	160
5.3	Local Static Pressure Distribution at Low Speed during Unsteady Conditions.....	163
5.4	Local Asymmetric Ratios of Static Pressure Distribution Profiles along the Radial Direction and Axial Direction at Low Speed during Steady and Unsteady Conditions.....	166
5.5	Local Static Pressure Distribution at High Speed during Unsteady Conditions.....	169
5.6	Local Asymmetric Ratios of Static Pressure Distribution Profiles along the Radial Direction and Axial Direction at High Speed during Steady and Unsteady Conditions .....	172
5.7	Static Pressure Speed Comparison during Unsteady Conditions.....	175
5.8	Global Velocity Magnitude Distribution at Two Instances during Unsteady Conditions.....	176

5.9	Local Velocity Magnitude Distribution at Low Speed during Unsteady Conditions	178
5.10	Local Asymmetric Ratios of Velocity Magnitude Distribution Profiles along the Radial Direction and Axial Direction at Low Speed during Steady and Unsteady Conditions	181
5.11	Local Velocity Magnitude Distribution at High Speed during Unsteady Conditions	184
5.12	Local Asymmetric Ratios of Velocity Magnitude Distribution Profiles along the Radial Direction and Axial Direction at High Speed during Steady and Unsteady Conditions	187
5.13	Velocity Magnitude Speed Comparison during Unsteady Conditions .....	190
5.14	Global Static Temperature Distribution at Two Instances during Unsteady Conditions .....	191
5.15	Local Static Temperature Distribution at Low Speed during Unsteady Conditions	193
5.16	Local Asymmetric Ratios of Static Temperature Distribution Profiles along the Radial Direction and Axial Direction at Low Speed during Steady and Unsteady Conditions	196
5.17	Local Static Temperature Distribution at High Speed during Unsteady Conditions	199
5.18	Local Asymmetric Ratios of Static Temperature Distribution Profiles along the Radial Direction and Axial Direction at High Speed during Steady and Unsteady Conditions	202
5.19	Static Temperature Speed Comparison during Unsteady Conditions .....	204
5.20	Summary .....	205
6.....		209
6.1	Centrifugal Compressor Volute Design Methodology.....	210
6.1.1	Symmetric Volute Design Approximation Neglecting Friction .....	210
6.1.2	Symmetric Volute Design Approximation Incorporating Friction .....	213
6.1.3	Asymmetric Volute Design Approximation .....	217

6.2	Centrifugal Compressor Volute Investigation Details .....	219
6.3	Global Performance Evaluation of the Symmetric Type Volute for Centrifugal Compressor .....	220
6.3.1	Turbocharger Compressor and Volute Performance with Symmetric Type Volutes	220
6.3.2	Global Static Pressure through Symmetric Type Volutes .....	222
6.3.3	Global Velocity Magnitude through Symmetric Type Volutes .....	223
6.3.4	Global Static Temperature through Symmetric Type Volutes .....	225
6.4	Local Performance Evaluation of the Symmetric Type Volute for Centrifugal Compressor .....	226
6.4.1	Local Static Pressure through Symmetric Type Volutes .....	226
6.4.2	Local Velocity Magnitude through Symmetric Type Volutes .....	229
6.4.3	Local Static Temperature through Symmetric Type Volutes .....	231
6.4.4	Head Loss Variation through Symmetric Type Volutes .....	233
6.5	Global Performance Evaluation of the Asymmetric Type Volute for Centrifugal Compressor .....	235
6.5.1	Turbocharger Compressor Performance with Asymmetric Type Volutes .....	235
6.5.2	Turbocharger Compressor Volute Performance with Asymmetric Type Volutes	236
6.5.3	Global Static Pressure through Asymmetric Type Volutes .....	237
6.5.4	Global Velocity Magnitude through Asymmetric Type Volutes .....	238
6.5.5	Global Static Temperature through Asymmetric Type Volutes .....	240
6.6	Local Performance Evaluation of the Asymmetric Type Volute for Centrifugal Compressor .....	241
6.6.1	Local Static Pressure through Asymmetric Type Volutes .....	242
6.6.2	Local Velocity Magnitude through Asymmetric Type Volutes .....	254
6.6.3	Local Static Temperature through Asymmetric Type Volutes .....	266
6.6.4	Head Loss Variation through the Asymmetric Type Volutes .....	278

6.7	Summary .....	282
7.....		285
7.1	Research Problem Synopsis .....	286
7.2	Research Aim and Achievements .....	286
7.3	Thesis Conclusions.....	289
7.4	Thesis Contribution .....	294
7.5	Recommendation for Future Work .....	295
	REFERENCES .....	298
	APPENDICES .....	304
	APPENDIX 1 Computational Fluid Dynamics .....	304
	Working of CFD Codes .....	305
	Numerical Formulation of Fluid Flow.....	308
	Conservation of Mass .....	309
	Conservation of Momentum.....	309
	Conservation of Energy .....	311
	Equation of State .....	312
	APPENDIX 2 Chapter 4 Flow Field Profiles along the Radial Direction and Axial Direction	
	313	
	Static Pressure along the Radial Direction at Low Operating Speed of 58.9rps/ $\sqrt{K}$ .....	314
	Static Pressure along the Axial Direction at Low Operating Speed of 58.9rps/ $\sqrt{K}$ .....	315
	Static Pressure along the Radial Direction at High Operating Speed of 98.2rps/ $\sqrt{K}$ .....	316
	Static Pressure along the Axial Direction at High Operating Speed of 98.2rps/ $\sqrt{K}$ .....	317
	Velocity Magnitude along the Radial Direction at Low Operating Speed of 58.9rps/ $\sqrt{K}$	
	.....	318
	Velocity Magnitude along the Axial Direction at Low Operating Speed of 58.9rps/ $\sqrt{K}$	
	.....	319
	Velocity Magnitude along the Radial Direction at High Operating Speed of 98.2rps/ $\sqrt{K}$	
	.....	320

Velocity Magnitude along the Axial Direction at High Operating Speed of 98.2rps/ $\sqrt{K}$	321
Static Temperature along the Radial Direction at Low Operating Speed of 58.9rps/ $\sqrt{K}$	322
Static Temperature along the Axial Direction at Low Operating Speed of 58.9rps/ $\sqrt{K}$	323
Static Temperature along the Radial Direction at High Operating Speed of 98.2rps/ $\sqrt{K}$	324
Static Temperature along the Axial Direction at High Operating Speed of 98.2rps/ $\sqrt{K}$	325
APPENDIX 3 Chapter 5 Flow Field Profiles along the Radial Direction and Axial Direction	326
Static Pressure along the Radial Direction at Low Operating Speed of 58.9rps/ $\sqrt{K}$ .....	327
Static Pressure along the Axial Direction at Low Operating Speed of 58.9rps/ $\sqrt{K}$ .....	328
Static Pressure along the Radial Direction at High Operating Speed of 98.2rps/ $\sqrt{K}$ .....	329
Static Pressure along the Axial Direction at High Operating Speed of 98.2rps/ $\sqrt{K}$ .....	330
Velocity Magnitude along the Radial Direction at Low Operating Speed of 58.9rps/ $\sqrt{K}$	331
Velocity Magnitude along the Axial Direction at Low Operating Speed of 58.9rps/ $\sqrt{K}$	332
Velocity Magnitude along the Radial Direction at High Operating Speed of 98.2rps/ $\sqrt{K}$	333
Velocity Magnitude along the Axial Direction at High Operating Speed of 98.2rps/ $\sqrt{K}$	334
Static Temperature along the Radial Direction at Low Operating Speed of 58.9rps/ $\sqrt{K}$	335
Static Temperature along the Axial Direction at Low Operating Speed of 58.9rps/ $\sqrt{K}$	336
Static Temperature along the Radial Direction at High Operating Speed of 98.2rps/ $\sqrt{K}$	337
Static Temperature along the Axial Direction at High Operating Speed of 98.2rps/ $\sqrt{K}$	338

APPENDIX 4 Chapter 6 Flow Field Profiles along the Radial Direction and Axial Direction	339
Static Pressure along the Radial Direction .....	340
Static Pressure along the Axial Direction.....	341
Velocity Magnitude along the Radial Direction.....	342
Velocity Magnitude along the Axial Direction .....	343
Static Temperature along the Radial Direction .....	344
Static Temperature along the Axial Direction.....	345
APPENDIX 5 Volute Expression Application .....	346
APPENDIX 6 Volute Models.....	347
APPENDIX 7 Equivalent Length Calculation for Head Loss .....	348
APPENDIX 8 Hydraulic Diameter Calculation for Head Loss.....	348
APPENDIX 9 Wall Shear Stress on Volute Scroll Sections .....	349
APPENDIX 10 Head Loss through Volute Scroll Section.....	350

# LIST OF FIGURES

---

Figure 1.1 Schematic Diagram of an Internal Combustion Engine [6] .....	3
Figure 1.2 Turbocharger [7].....	3
Figure 1.3 Diagram of Turbocharger Operation [8] .....	5
Figure 1.4 Turbocharger Turbine Stage [11] .....	7
Figure 1.5 Turbocharger Bearing System [11] .....	8
Figure 1.6 Turbocharger Compressor Stage [11] .....	9
Figure 1.7 Turbocharger Compressor Map.....	16
Figure 1.8 Turbocharger Efficiency Map .....	17
Figure 1.9 Centrifugal Compressor Volute Layout [20].....	24
Figure 2.1 Volute Cross-Section Shapes[1].....	43
Figure 3.1 Turbocharger Compressor Stage Geometry in ANSYS Design Modeller.....	55
Figure 3.2 Mesh Generation in ANSYS Meshing .....	56
Figure 3.3 Conversion to Polyhedral Mesh in FLUENT .....	57
Figure 3.4 Mesh Independence Study.....	58
Figure 3.5 Centrifugal Compressor Stage Global Analyses Locations .....	61
Figure 3.6 Centrifugal Compressor Volute Local Analyses Locations .....	62
Figure 3.7 Profiles for Data Extraction along the Radial Direction and Axial Direction.....	63
Figure 4.1 Turbocharger Compressor Stage (a) Performance Map (b) Efficiency Map .....	67
Figure 4.2 Turbocharger Compressor Volute Performance (a) Total Pressure Loss Coefficient (b) Static Pressure Recovery Coefficient.....	69
Figure 4.3 Static Pressure Variation in the Turbocharger Compressor Stage during the operating speed of 58.9rps/ $\sqrt{K}$ and 98.2rps/ $\sqrt{K}$ at (a) BEP (b) choke (c) surge .....	74
Figure 4.4 Static pressure difference through each station in the turbocharger compressor stage during (a) 58.9rps/ $\sqrt{K}$ (b) 98.2rps/ $\sqrt{K}$ .....	76
Figure 4.5 Static Pressure around the Compressor Volute during the operating speed of 58.9rps/ $\sqrt{K}$ at (a) BEP (b) choke (c) surge .....	82
Figure 4.6 Static Pressure across each cross-section around the Compressor Volute during the operating speed of 58.9rps/ $\sqrt{K}$ .....	84



Figure 4.7 Asymmetric Ratio of Static Pressure along the Radial Direction on the Profiles around the Centrifugal Compressor Volute at Operating Speed of 58.9rps/ $\sqrt{K}$ during Low Flow Rate, Design Flow Rate and High Flow Rate.....	85
Figure 4.8 Asymmetric Ratio of Static Pressure along the Axial Direction on the Profiles around the Centrifugal Compressor Volute at Operating Speed of 58.9rps/ $\sqrt{K}$ during Low Flow Rate, Design Flow Rate and High Flow Rate.....	87
Figure 4.9 Static Pressure around the Compressor Volute during the operating speed of 98.2rps/ $\sqrt{K}$ at (a) BEP (b) choke (c) surge .....	93
Figure 4.10 Static Pressure across each cross-section around the Compressor Volute during the operating speed of 98.2rps/ $\sqrt{K}$ .....	95
Figure 4.11 Asymmetric Ratio of Static Pressure along the Radial Direction on the Profiles around the Centrifugal Compressor Volute at Operating Speed of 98.2rps/ $\sqrt{K}$ during Low Flow Rate, Design Flow Rate and High Flow Rate.....	96
Figure 4.12 Asymmetric Ratio of Static Pressure along the Axial Direction on the Profiles around the Centrifugal Compressor Volute at Operating Speed of 98.2rps/ $\sqrt{K}$ during Low Flow Rate, Design Flow Rate and High Flow Rate.....	97
Figure 4.13 Velocity Magnitude Variation in the Turbocharger Compressor Stage during the operating speed of 58.9rps/ $\sqrt{K}$ and 98.2rps/ $\sqrt{K}$ at (a) BEP (b) choke (c) surge .....	103
Figure 4.14 Velocity Magnitude difference at the inlet and outlet of each component in the turbocharger compressor stage during (a) 58.9rps/ $\sqrt{K}$ (b) 98.2rps/ $\sqrt{K}$ .....	105
Figure 4.15 Velocity Magnitude around the Compressor Volute during the operating speed of 58.9rps/ $\sqrt{K}$ at (a) BEP (b) choke (c) surge .....	112
Figure 4.16 Velocity Magnitude across each cross-section around the Compressor Volute during the operating speed of 58.9rps/ $\sqrt{K}$ .....	114
Figure 4.17 Asymmetric Ratio of Velocity Magnitude along the Radial Direction on the Profiles around the Centrifugal Compressor Volute at Operating Speed of 58.9rps/ $\sqrt{K}$ during Low Flow Rate, Design Flow Rate and High Flow Rate .....	115
Figure 4.18 Asymmetric Ratio of Velocity Magnitude along the Axial Direction on the Profiles around the Centrifugal Compressor Volute at Operating Speed of 58.9rps/ $\sqrt{K}$ during Low Flow Rate, Design Flow Rate and High Flow Rate .....	116
Figure 4.19 Velocity Magnitude around the Compressor Volute during the operating speed of 98.2rps/ $\sqrt{K}$ at (a) BEP (b) choke (c) surge .....	123
Figure 4.20 Velocity Magnitude across each cross-section around the Compressor Volute during the operating speed of 98.2rps/ $\sqrt{K}$ .....	125

Figure 4.21 Asymmetric Ratio of Velocity Magnitude along the Radial Direction on the Profiles around the Centrifugal Compressor Volute at Operating Speed of 98.2rps/ $\sqrt{K}$ during Low Flow Rate, Design Flow Rate and High Flow Rate .....	126
Figure 4.22 Asymmetric Ratio of Velocity Magnitude along the Axial Direction on the Profiles around the Centrifugal Compressor Volute at Operating Speed of 98.2rps/ $\sqrt{K}$ during Low Flow Rate, Design Flow Rate and High Flow Rate .....	127
Figure 4.23 Static Temperature Variation in the Turbocharger Compressor Stage during the operating speed of 58.9rps/ $\sqrt{K}$ at (a) BEP (b) choke (c) surge .....	132
Figure 4.24 Static Temperature difference at the inlet and outlet of each component in the turbocharger compressor stage during (a) 58.9rps/ $\sqrt{K}$ (b) 98.2rps/ $\sqrt{K}$ .....	134
Figure 4.25 Static Temperature around the Compressor Volute during the operating speed of 58.9rps/ $\sqrt{K}$ at (a) BEP (b) choke (c) surge .....	139
Figure 4.26 Static Temperature across each cross-section around the Compressor Volute during the operating speed of 58.9rps/ $\sqrt{K}$ .....	141
Figure 4.27 Asymmetric Ratio of Static Temperature along the Radial Direction on the Profiles around the Centrifugal Compressor Volute at Operating Speed of 58.9rps/ $\sqrt{K}$ during Low Flow Rate, Design Flow Rate and High Flow Rate .....	142
Figure 4.28 Asymmetric Ratio of Static Temperature along the Axial Direction on the Profiles around the Centrifugal Compressor Volute at Operating Speed of 58.9rps/ $\sqrt{K}$ during Low Flow Rate, Design Flow Rate and High Flow Rate .....	143
Figure 4.29 Static Temperature around the Compressor Volute during the operating speed of 98.2rps/ $\sqrt{K}$ at (a) BEP (b) choke (c) surge .....	149
Figure 4.30 Static Temperature across each cross-section around the Compressor Volute during the operating speed of 98.2rps/ $\sqrt{K}$ .....	151
Figure 4.31 Asymmetric Ratio of Static Temperature along the Radial Direction on the Profiles around the Centrifugal Compressor Volute at Operating Speed of 98.2rps/ $\sqrt{K}$ during Low Flow Rate, Design Flow Rate and High Flow Rate .....	152
Figure 4.32 Asymmetric Ratio of Static Temperature along the Axial Direction on the Profiles around the Centrifugal Compressor Volute at Operating Speed of 98.2rps/ $\sqrt{K}$ during Low Flow Rate, Design Flow Rate and High Flow Rate .....	153
Figure 5.1 Two instances of impeller blade with respect to volute tongue (a) impeller blade aligned with volute tongue (b) volute tongue between two impeller blades .....	157
Figure 5.2 Steady and Revolution Averaged Turbocharger Compressor Performance Comparison of (a) Compressor Map (b) Isentropic Efficiency Map.....	158

Figure 5.3 Steady and Revolution Averaged Turbocharger Compressor Volute Performance Comparison of (a) Static Pressure Recovery Coefficient (b) Total Pressure Loss Coefficient .....	159
Figure 5.4 Static Pressure Variation in the Turbocharger Compressor Stage during the operating speed of 58.9rps/ $\sqrt{K}$ and 98.2rps/ $\sqrt{K}$ at (a) Blade Position 1 (b) Blade Position 2	161
Figure 5.5 Comparison of steady and unsteady response of static pressure difference through each station in the turbocharger compressor stage during (a) 58.9rps/ $\sqrt{K}$ (b) 98.2rps/ $\sqrt{K}$ ....	162
Figure 5.6 Static Pressure around the Compressor Volute during the operating speed of 58.9rps/ $\sqrt{K}$ at (a) Blade Position 1 (b) Blade Position 2.....	164
Figure 5.7 Comparison of steady and unsteady response for static pressure across each cross-section around the compressor volute during the operating speed of 58.9rps/ $\sqrt{K}$ .....	165
Figure 5.8 Asymmetric Ratio of Steady and Unsteady Static Pressure around the Centrifugal Compressor Volute at the operating speed of 58.9rps/ $\sqrt{K}$ along the (a) Radial of the profiles and (b) Axial of the profiles.....	168
Figure 5.9 Static Pressure around the Compressor Volute during the operating speed of 98.2rps/ $\sqrt{K}$ at (a) Blade Position 1 (b) Blade Position 2.....	170
Figure 5.10 Comparison of steady and unsteady response for static pressure across each cross-section around the compressor volute during the operating speed of 98.2rps/ $\sqrt{K}$ .....	171
Figure 5.11 Asymmetric Ratio of Steady and Unsteady Static Pressure around the Centrifugal Compressor Volute at the operating speed of 98.2rps/ $\sqrt{K}$ along the (a) Radial of the profiles and (b) Axial of the profiles.....	174
Figure 5.12 Velocity Magnitude Variation in the Turbocharger Compressor Stage during the operating speed of 58.9rps/ $\sqrt{K}$ and 98.2rps/ $\sqrt{K}$ at (a) Blade Position 1 (b) Blade Position 2	176
Figure 5.13 Comparison of steady and unsteady response of velocity magnitude difference through each station in the turbocharger compressor stage during (a) 58.9rps/ $\sqrt{K}$ (b) 98.2rps/ $\sqrt{K}$ .....	177
Figure 5.14 Velocity Magnitude around the Compressor Volute during the operating speed of 58.9rps/ $\sqrt{K}$ at (a) Blade Position 1 (b) Blade Position 2.....	179
Figure 5.15 Comparison of steady and unsteady response for velocity magnitude across each cross-section around the compressor volute during the operating speed of 58.9rps/ $\sqrt{K}$ .....	180
Figure 5.16 Asymmetric Ratio of Steady and Unsteady Velocity Magnitude around the Centrifugal Compressor Volute at the operating speed of 58.9rps/ $\sqrt{K}$ along the (a) Radial of the profiles and (b) Axial of the profiles.....	183

Figure 5.17 Velocity Magnitude around the Compressor Volute during the operating speed of 98.2rps/ $\sqrt{K}$ at (a) Blade Position 1 (b) Blade Position 2.....	185
Figure 5.18 Comparison of steady and unsteady response for velocity magnitude across each cross-section around the compressor volute during the operating speed of 98.2rps/ $\sqrt{K}$ .....	186
Figure 5.19 Asymmetric Ratio of Steady and Unsteady Velocity Magnitude around the Centrifugal Compressor Volute at the operating speed of 98.2rps/ $\sqrt{K}$ along the (a) Radial of the profiles and (b) Axial of the profiles.....	189
Figure 5.20 Static Temperature Variation in the Turbocharger Compressor Stage during the operating speed of 58.9rps/ $\sqrt{K}$ and 98.2rps/ $\sqrt{K}$ at (a) Blade Position 1 (b) Blade Position 2.....	191
Figure 5.21 Comparison of steady and unsteady response of static temperature difference through each station in the turbocharger compressor stage during (a) 58.9rps/ $\sqrt{K}$ (b) 98.2rps/ $\sqrt{K}$ .....	192
Figure 5.22 Static Temperature around the Compressor Volute during the operating speed of 58.9rps/ $\sqrt{K}$ at (a) Blade Position 1 (b) Blade Position 2.....	194
Figure 5.23 Comparison of steady and unsteady response for static temperature across each cross-section around the compressor volute during the operating speed of 58.9rps/ $\sqrt{K}$ .....	195
Figure 5.24 Asymmetric Ratio of Steady and Unsteady Static Temperature around the Centrifugal Compressor Volute at the operating speed of 58.9rps/ $\sqrt{K}$ along the (a) Radial of the profiles and (b) Axial of the profiles.....	198
Figure 5.25 Static Temperature around the Compressor Volute during the operating speed of 98.2rps/ $\sqrt{K}$ at (a) Blade Position 1 (b) Blade Position 2.....	200
Figure 5.26 Comparison of steady and unsteady response for static temperature across each cross-section around the compressor volute during the operating speed of 98.2rps/ $\sqrt{K}$ .....	201
Figure 5.27 Asymmetric Ratio of Steady and Unsteady Static Temperature around the Centrifugal Compressor Volute at the operating speed of 98.2rps/ $\sqrt{K}$ along the (a) Radial of the profiles and (b) Axial of the profiles.....	204
Figure 6.1 Process chart for the application of Eck's volute design approximation.....	210
Figure 6.2 Volute Design Methodology using Eck's Volute Design Approximation .....	211
Figure 6.3 Symmetric Elliptical Volute Cross-Section where (a) is Elliptical 3:2 and (b) is Elliptical 2:3.....	212
Figure 6.4 Process chart for the application of Baker's volute design approximation.....	212
Figure 6.5 Process Flow Chart for the Application of Symmetric Circular Cross-Section Volute Design Incorporating Friction.....	215

Figure 6.6 Process Flow Chart for the Application of Symmetric Elliptical Cross-Section Volute Design Incorporating Friction.....	216
Figure 6.7 Process Flow Chart for the Application of Asymmetric Circular Cross-Section Volute Design Incorporating Friction.....	218
Figure 6.8 Static pressure at (a) inlet and (b) outlet of each station in the turbocharger compressor stage.....	223
Figure 6.9 Velocity Magnitude at (a) inlet and (b) outlet of each station in the turbocharger compressor stage.....	224
Figure 6.10 Static Temperature at (a) inlet and (b) outlet of each station in the turbocharger compressor stage.....	226
Figure 6.11 Static Pressure through the Symmetric Type Volute .....	228
Figure 6.12 Velocity Magnitude through the Symmetric Type Volute .....	230
Figure 6.13 Static Temperature through the Symmetric Type Volute.....	232
Figure 6.14 Comparison of wall shear stress on the symmetric type centrifugal compressor volute casing .....	234
Figure 6.15 Comparison of head loss through the symmetric type centrifugal compressor volute.....	234
Figure 6.16 Asymmetric Volute and CTT Volute Turbocharger Compressor Performance Comparison of (a) Compressor Map (b) Isentropic Efficiency Map.....	236
Figure 6.17 Asymmetric Volute and CTT Volute Turbocharger Compressor Volute Performance Comparison of (a) Static Pressure Recovery Coefficient (b) Total Pressure Loss Coefficient.....	236
Figure 6.18 Static Pressure Variation in the Turbocharger Compressor Stage with the Asymmetric Volute where (a) static pressure contour (b) inlet static pressure comparison with CTT (c) outlet static pressure comparison with CTT .....	238
Figure 6.19 Velocity Magnitude Variation in the Turbocharger Compressor Stage with the Asymmetric Volute where (a) velocity magnitude contour (b) inlet velocity magnitude comparison with CTT (c) outlet velocity magnitude comparison with CTT.....	239
Figure 6.20 Static Temperature Variation in the Turbocharger Compressor Stage with the Asymmetric Volute where (a) static temperature contour (b) inlet static temperature comparison with CTT (c) outlet static temperature comparison with CTT.....	241
Figure 6.21 Static pressure around the asymmetric type compressor volute.....	243
Figure 6.22 Static pressure across each cross-section around the asymmetric volute and CTT volute.....	244

Figure 6.23 Asymmetric ratio of static pressure around the CTT and asymmetric centrifugal compressor volutes along the (a) radial direction of the profiles and (b) axial direction of the profiles .....	247
Figure 6.24 Percentage difference of static pressure through asymmetric volute at (a) maximum (b) minimum .....	249
Figure 6.25 Percentage difference of static pressure through CTT volute at (a) maximum (b) minimum .....	251
Figure 6.26 Instantaneous static pressure variation through (a) Asymmetric volute and (b) CTT volute .....	253
Figure 6.27 Velocity magnitude around the asymmetric type compressor volute .....	255
Figure 6.28 Velocity magnitude across each cross-section around the asymmetric volute and CTT volute .....	256
Figure 6.29 Asymmetric ratio of velocity magnitude around the CTT and asymmetric centrifugal compressor volutes along the (a) radial direction of the profiles and (b) axial direction of the profiles .....	259
Figure 6.30 Percentage difference of velocity magnitude through asymmetric volute at (a) maximum (b) minimum .....	261
Figure 6.31 Percentage difference of velocity magnitude through CTT volute at (a) maximum (b) minimum .....	263
Figure 6.32 Instantaneous velocity magnitude variation through (a) Asymmetric volute and (b) CTT volute .....	265
Figure 6.33 Static temperature around the asymmetric type compressor volute .....	267
Figure 6.34 Static temperature across each cross-section around the asymmetric volute and CTT volute .....	268
Figure 6.35 Asymmetric ratio of static temperature around the CTT and asymmetric centrifugal compressor volutes along the (a) radial direction of the profiles and (b) axial direction of the profiles .....	271
Figure 6.36 Percentage Difference of Static Temperature through Asymmetric Volute at (a) Maximum (b) Minimum .....	273
Figure 6.37 Percentage Difference of Static Temperature through CTT Volute at (a) Maximum (b) Minimum .....	275
Figure 6.38 Instantaneous static temperature variation through (a) Asymmetric volute and (b) CTT volute .....	277
Figure 6.39 Total Head Loss through the Volute at different flow rates .....	278

Figure 6.40 Head loss variation through (a) CTT volute and (b) Asymmetric volute.....	279
Figure 6.41 Comparison of wall shear stress on the asymmetric type centrifugal compressor volute casing .....	280
Figure 6.42 Comparison of head loss on the asymmetric type centrifugal compressor volute casing .....	280
Figure 6.43 Instantaneous head loss variation through (a) Asymmetric volute and (b) CTT volute.....	282
Figure A.1 Process of the Solver .....	305
Figure A.2 CFD Overview.....	307
Figure A.3 Forces Acting on the Fluid Element [60] .....	310

# LIST OF TABLES

---

Table 1.1 Main Turbocharger Components .....	4
Table 4.1 Global Speed Comparison of Static Pressure Variation .....	74
Table 4.2 Local Speed Comparison of Static Pressure Variation during Steady Response ....	98
Table 4.3 Global Speed Comparison of Velocity Magnitude Variation.....	103
Table 4.4 Local Speed Comparison of Velocity Magnitude Variation during Steady Response .....	128
Table 4.5 Global Speed Comparison of Static Temperature Variation .....	132
Table 4.6 Local Speed Comparison of Static Temperature Variation during Steady Response .....	154
Table 5.1 Turbocharger Compressor Performance Comparison .....	158
Table 5.2 Turbocharger Compressor Volute Performance Comparison .....	160
Table 5.3 Comparison of unsteady and steady response of static pressure variation at the inlet, outlet and through-flow across each station at low speed of 58.9rps/ $\sqrt{K}$ and high speed of 98.2rps/ $\sqrt{K}$ .....	162
Table 5.4 Comparison of steady and unsteady response of plane to plane and outlet to plane static pressure variation at 58.9 rps/ $\sqrt{K}$ .....	166
Table 5.5 Comparison of steady and unsteady response of plane to plane and outlet to plane static pressure variation at 98.2rps/ $\sqrt{K}$ .....	172
Table 5.6 Local Speed Comparison of Static Pressure Variation during Unsteady Response .....	175
Table 5.7 Comparison of steady and unsteady response of velocity magnitude at the inlet, outlet and through-flow across each station at low speed of 58.9rps/ $\sqrt{K}$ and high speed of 98.2rps/ $\sqrt{K}$ .....	178
Table 5.8 Comparison of steady and unsteady response of plane to plane and outlet to plane velocity magnitude variation at 58.9 rps/ $\sqrt{K}$ .....	181
Table 5.9 Comparison of steady and unsteady response of plane to plane and outlet to plane velocity magnitude variation at 98.2 rps/ $\sqrt{K}$ .....	187
Table 5.10 Local Speed Comparison of Velocity Magnitude Variation during Unsteady Response .....	190



Table 5.11 Comparison of steady and unsteady response of static temperature at the inlet, outlet and through-flow across each station at low speed of 58.9rps/ $\sqrt{K}$ and high speed of 98.2rps/ $\sqrt{K}$ .....	193
Table 5.12 Comparison of steady and unsteady response of plane to plane and outlet to plane static temperature variation at 58.9 rps/ $\sqrt{K}$ .....	196
Table 5.13 Comparison of steady and unsteady response of plane to plane and outlet to plane static temperature variation at 98.2rps/ $\sqrt{K}$ .....	202
Table 5.14 Local Speed Comparison of Static Temperature Variation during Unsteady Response .....	205
Table 6.1 Details of the Investigated Centrifugal Compressor Volute Models .....	219
Table 6.2 Compressor and Volute Performance of various Symmetric Cross-Sections Designed to Ideal and Actual Conditions .....	221
Table 6.3 Static Pressure Variation of volute designed to actual conditions against volute designed to ideal conditions.....	223
Table 6.4 Velocity Magnitude Variation of volute designed to actual conditions against volute designed to ideal conditions.....	225
Table 6.5 Static Temperature Variation of volute designed to actual conditions against volute designed to ideal conditions.....	226
Table 6.6 Static Pressure Variation through Symmetric Type Volutes .....	228
Table 6.7 Velocity Magnitude Variation through Symmetric Type Volutes.....	230
Table 6.8 Static Temperature Variation through Symmetric Type Volutes .....	232
Table 6.9 Asymmetric volute comparison with CTT volute of static pressure variation from plane to plane and outlet to plane .....	244
Table 6.10 Asymmetric volute comparison with CTT volute of velocity magnitude variation from plane to plane and outlet to plane.....	256
Table 6.11 Asymmetric volute comparison with CTT volute of static temperature variation from plane to plane and outlet to plane.....	268

# LIST OF EQUATIONS

---

Equation 1.1 Atmospheric Pressure .....	10
Equation 1.2 Bernoulli's Principle .....	10
Equation 1.3 Total Pressure .....	11
Equation 1.4 Total Temperature .....	11
Equation 1.5 Total Pressure for Compressible Flow .....	11
Equation 1.6 Mach number.....	11
Equation 1.7 Mass Flow Rate .....	12
Equation 1.8 Ideal Gas.....	12
Equation 1.9 Mach Number.....	12
Equation 1.10 Corrected Mass Flow Rate .....	13
Equation 1.11 Flow Parameter.....	13
Equation 1.12 Speed Parameter .....	13
Equation 1.13 Entropy .....	14
Equation 1.14 Change in Entropy.....	14
Equation 1.15 Enthalpy.....	14
Equation 1.16 Change in Enthalpy .....	15
Equation 1.17 Total-to Total Compressor Isentropic Efficiency.....	18
Equation 1.18 Total –to-Total Pressure Ratio.....	18
Equation 1.19 Meridional velocity dump loss .....	21
Equation 1.20 Skin friction loss.....	22
Equation 1.21 Average path length of flow .....	22
Equation 1.22 Hydraulic diameter .....	22
Equation 1.23 Exit cone loss.....	22
Equation 1.24 Tangential velocity dump loss.....	23
Equation 1.25 Sizing Parameter.....	23
Equation 1.26 Total head loss of volute.....	23
Equation 1.27 Head Loss .....	23
Equation 1.28 Pressure Loss .....	24
Equation 1.29 Darcy's Friction Factor .....	24
Equation 3.1 Extension Length Approximation .....	55

Equation 4.1 Total Pressure Loss Coefficient.....	68
Equation 4.2 Static Pressure Recovery Coefficient .....	68
Equation 6.1 Eck’s Frictionless Symmetric Circular Volute Design Approximation .....	210
Equation 6.2 Baker's Elliptical Volute Design Approximation.....	211
Equation 6.3 Elliptical Ratio.....	211
Equation 6.4 Volute Design Principle of Continuity .....	213
Equation 6.5 Volute Design Principle of Energy Equation .....	213
Equation 6.6 Volute Design Principle of Friction Head Loss .....	214
Equation 6.7 Volute Design Principle of Head Loss .....	214
Equation 6.8 Symmetric Circular Cross-Section Volute Design Expression Incorporating Friction.....	214
Equation 6.9 Symmetric Elliptical Cross-Section Volute Design Expression Incorporating Friction.....	215
Equation 6.10 Baker's Asymmetric Volute Design Approximation.....	217
Equation 6.11 Baker's Asymmetric Volute Design Approximation Constant Parameter .....	217
Equation A.1 Conservation of Mass .....	309
Equation A.2: Conservation of Momentum.....	311
Equation A.3 Conservation of Energy .....	312

# NOMENCLATURE

---

$\dot{m}$  = mass flow rate [kg/s]

$m$  = mass [kg]

$v$  = velocity [m/s]

$C$  = absolute velocity [m/s]

$A$  = cross sectional area [m<sup>2</sup>]

$g$  = gravity [9.81m/s]

$h$  = head [m] (m of air)

$p$  = Absolute Pressure = Gauge Pressure + Atmospheric Pressure [Pa]

$p_{\text{atm}}$  = atmospheric pressure

$p_{\text{abs}}$  = absolute pressure

$p_{\text{gauge}}$  = gauge pressure

$p_T$  = Absolute total pressure [atm]

$p_s$  = Absolute static pressure [atm]

$p_{\text{Tin}}$  = Absolute Total Inlet Pressure [atm]

$p_{\text{Sout}}$  = Absolute Static Outlet Pressure [atm]

$PR$  = Pressure Ratio (compressor side)

$ER$  = Expansion Ratio (turbine side)

$\rho$  = Density [kg/m<sup>3</sup>]

$C_p$  = Specific heat at constant pressure [J/kg K]

$C_v$  = Specific heat at constant volume [J/kg K]

$\gamma$  = specific heat ratio, given by ( $C_p/C_v$ ) (dependent on the air/fuel ratio and temperature: 1.4 for compressor stage; 1.3 for turbine stage)

$T$  = Absolute Temperature [K]

$\Delta T_T$  = difference in absolute total temperature at inlet and outlet

$M$  = Mach Number

$c$  = speed of sound [m/s] given by ( $\sqrt{\gamma RT}$ )

$R$  = gas constant (dependent on the particular gas and is related to the molecular weight of the gas)

$N_{\text{physical}}$  = Shaft Speed [rps/]

$W$  = Work [J]

$W_{\text{ACTUAL}}$  = actual work done by the gas flowing through the turbine

$W_{\text{TS,IDEAL}}$  = total-to-static work done that could be extracted from the gas by an isentropic expansion of the pressure ratio across the turbine

$W_{\text{ideal}}$  = ideal work that would be needed to compress the air isentropically (adiabatic and without friction loss) through the pressure ratio across the compressor

$W_{\text{actual}}$  = actual work done on the air flowing through the compressor to reach the same amount of increase in total pressure.

$K_p$  = total pressure loss coefficient

$C_p$  = static pressure recovery coefficient

$\eta$  = Efficiency [%]

$U$  = blade tip velocity [m/s]

$\zeta$  = spouting velocity [m/s]

$d$  = diameter [m]

$S$  = entropy [J/K]

$Q$  = heat [J] ( $\Delta Q$  is positive when heat is absorbed; negative when heat is expelled)

$t$  = time [s]

$F$  = Force [Nm]

$a$  = acceleration [ $\text{m/s}^2$ ]

$H$  = Enthalpy [J/kg]

$V$  = Volume [ $\text{m}^3$ ]

$\Delta$  = change (difference)

$k_B$  = Boltzmann constant ( $1.3804 \times 10^{-23}$ ) [J/K]

$\Omega$  = number of microstates

$\ln$  =  $\log_e$

$\theta$  = azimuth angle [ $^\circ$ ]

$c_f$  = Coefficient of friction

$c_{ec}$  = Exit cone coefficient

$D_h$  = Hydraulic diameter [m]

$\lambda$  = swirl parameter ( $C_u / C_r$ )

$r$  = radius [m]

$L$  = average path length of flow [m]

$SP$  = sizing parameter

$K$  = Loss Coefficient

$\alpha$  = diffuser inclination

$\alpha^\circ$  = diffuser inclination angle

$q_v$  = volume flow rate

$r_c$  = radius centroid (defined by  $r_4 + r$ )

$b$  = interface width

Other subscripts:

(1) = initial

(2) = final

0 = Impeller Eye

1 = Impeller Entry

2 = Impeller Tip Condition

3 = Impeller Exit / Diffuser Entry

4 = Diffuser Exit / Volute Entry

5 = Volute Exit

th = throat

in = inlet

out = outlet

is = isentropic

t = turbine

c = compressor

T = total

S = Static

dl = dump loss

ecl = exit cone loss

sfl = skin friction loss

$m$  = meridional velocity [m/s]

$u$  = tangential velocity [m/s]

$r$  = radial velocity [m/s]

$a$  = axial velocity [m/s]

$av$  = average





# CHAPTER 1

## INTRODUCTION

---

Turbochargers are primarily used for engine downsizing, which means that instead of having a larger capacity engine to boost power, a turbocharger is fitted on the same size engine to generate the same amount of power as a larger capacity engine. This research project focuses on the compressor side of the turbocharger, more specifically, its volute. In order to gain a clear understanding and a solid foundation of turbochargers and their flow characteristics, this chapter explores the turbocharger, its compressor stage and its volute.

## 1.1 Turbochargers

The turbocharger was first developed by an engineer from Switzerland, Alfred Büchi, between the years of 1902 to 1912; however the work of the turbocharger was not established until 1925 [4, 5]. Figure 1.1 provides a graphical representation of a standard internal combustion engine depicting its standard components, more specifically, identifying the location of the turbocharger. The turbine side of the turbocharger is mounted between the exhaust manifold and the tail pipe of the exhaust system while the compressor side of the turbocharger is mounted between the air cleaner and the intake manifold of the engine. The purpose of a turbocharger is to generate more output power for higher engine efficiency and performance by using a forced-induction process to increase the air density and force more air into the combustion chamber. Turbocharging is used for numerous reasons, such as:

- To improve thermal efficiency by recovering the energy generated from the exhaust that would otherwise been lost.
- To generate more power from the engine by increase the density of the air for a much more rapid air intake, resulting in improved engine performance.
- Engine downsizing in that instead to having a higher-capacity engine which is of higher weight bearing, the same size or lower-capacity engine can be used boosting the same amount of power as the bigger engine.
- Reduces fuel consumption of up to 40% for diesel engines; and up to 20% for petrol engines.
- Optimises boost, power and performance to the system improving fuel efficiency, which in turn reduces total cost.

In order to understand this research based study, it is important to understand the entire process of what a turbocharger is, how it operates and what is its prime purpose. Since turbocharging was developed to enhance engine performance through generating more power, the fundamentals of how an engine operates is elaborated to provide a base for employing a device as superior as a turbocharger.

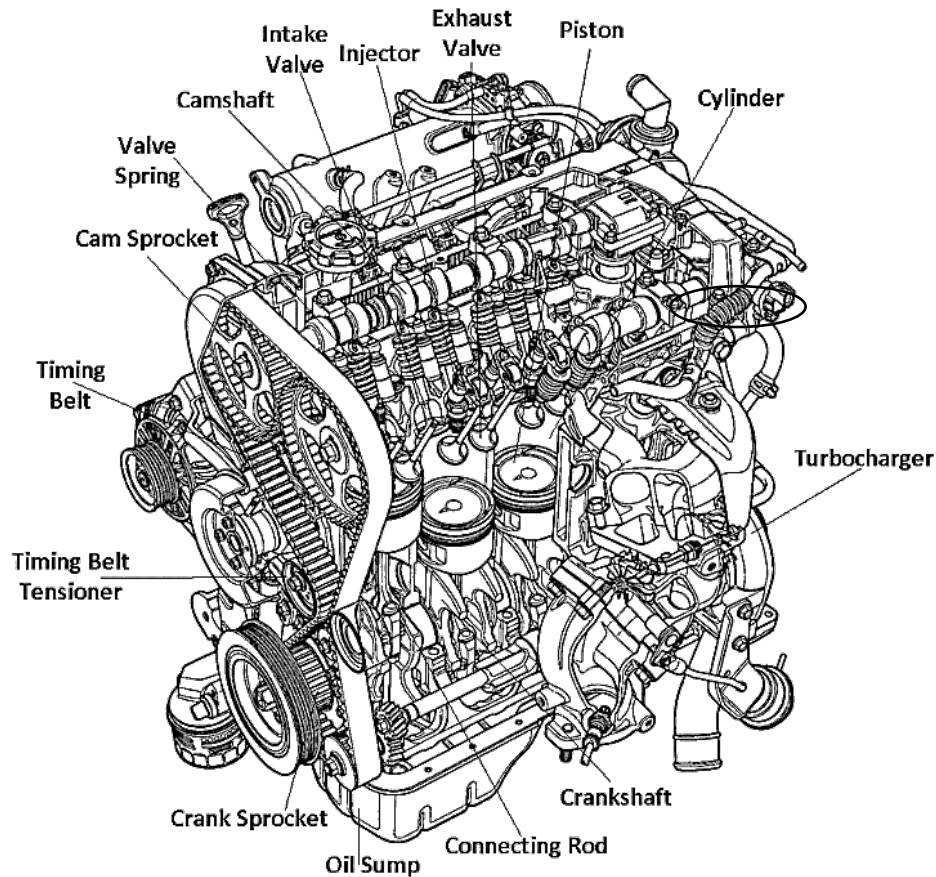


Figure 1.1 Schematic Diagram of an Internal Combustion Engine [6]

## 1.2 Construction of a Turbocharger

Figure 1.2 illustrates the main components of a turbocharger whilst Table 1.1 defines these components so that clear understanding of the individual component and its operation within the turbocharger is established.

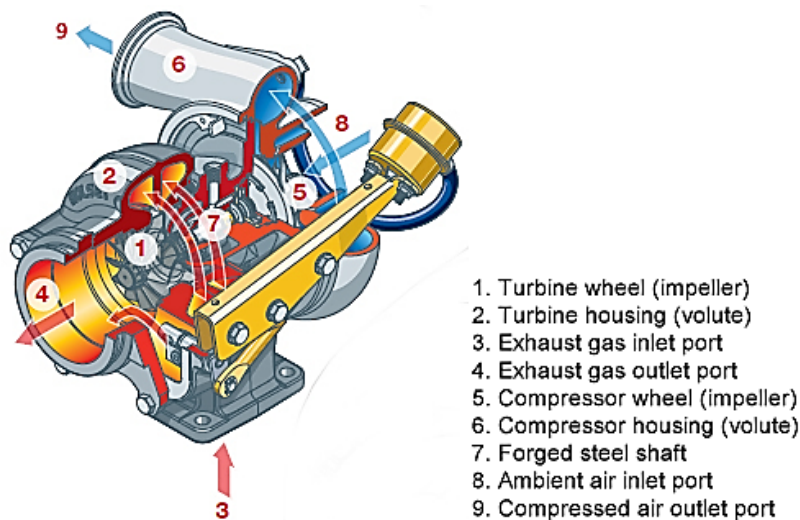


Figure 1.2 Turbocharger [7]

*Table 1.1 Main Turbocharger Components*

<b>COMPONENT</b>	<b>DEFINITION</b>
Exhaust Inlet Port	Entrance for exhaust gases to enter the turbocharger from the engine.
Turbine Volute	Exhaust travels through this housing to the turbine impeller.
Turbine Impeller	Turbine wheel that spins rapidly creating momentum.
Exhaust Outlet Port	Exit for exhaust gases from turbocharger into the exhaust system.
Shaft	Forged steel shaft connected to the turbine wheel and the compressor wheel. The momentum of the turbine impeller travels along this shaft driving the compressor impeller.
Compressor Impeller	Wheel driven by the forged steel shaft through momentum, drawing ambient air into the system
Air Inlet Port	Entrance for the ambient air to enter the turbocharger.
Diffuser	This can have vanes or be vaneless. Air passes through the diffuser converting kinetic energy into pressure energy and directs it into the compressor volute.
Compressor Volute	Air travels through this housing to the air outlet port.
Air Outlet Port	Exit for compressed air from turbocharger into the intercooler then into the engine.

### 1.3 Operation of a Turbocharger

The operation process diagram of a turbocharger within the internal combustion engine is illustrated in Figure 1.3.

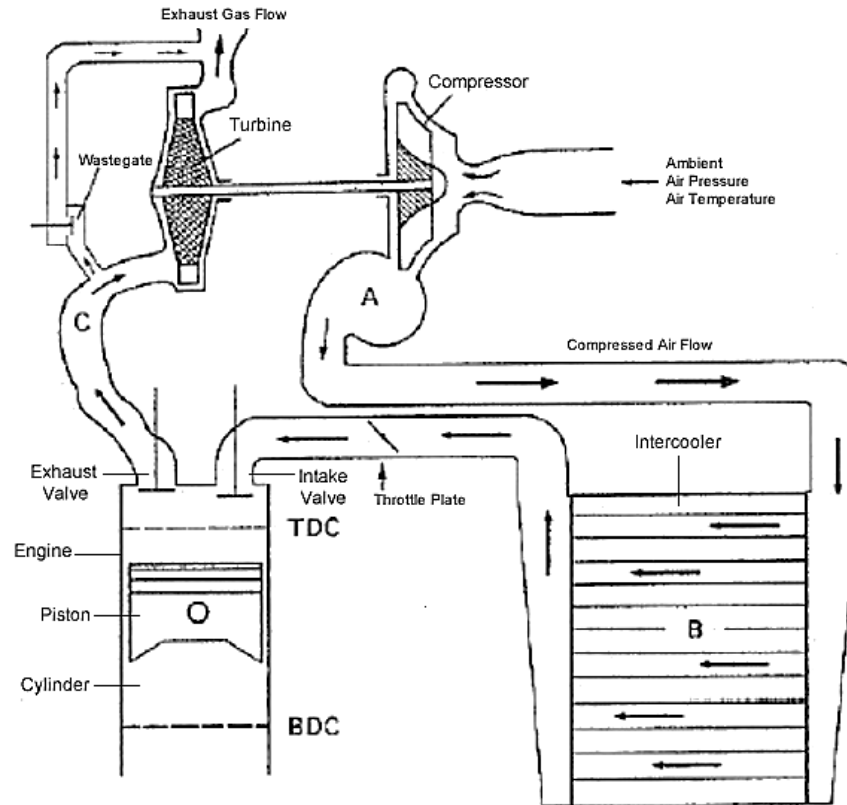


Figure 1.3 Diagram of Turbocharger Operation [8]

On the turbine side, the exhaust gas which is wasted power in engines without a turbocharger is directed into the turbine inlet at high pressures and temperatures. This exhaust gas is the working fluid on the turbine side of the turbocharger. From the turbine inlet, the fluid travels through the turbine housing, guiding the flow to the turbine wheel. The fluid hits the turbine wheel at a high velocity, making the turbine wheel rotate at a high speed converting pressure energy into mechanical energy. The turbine wheel is connected to the compressor wheel via a shaft. The high speed rotation of the turbine wheel creates significant amount of momentum, producing the power required to drive the compressor wheel. The flow exits the turbine wheel and travels into the exhaust system [4, 8, 9].

As aforementioned, the compressor side is connected to the turbine side via a forged steel shaft. This shaft links the turbine wheel to the compressor wheel and passes through the bearing housing, which is lubricated by oil. This oil acts as a coolant since it removes the heat

generated by the turbine. At both ends of the bearing housing, there are specially designed oil seals that withstand extreme pressures and temperatures produced by the turbocharger, and help ensure that oil does not leak into the compressor or turbine housing.

On the compressor side, momentum of the transferred energy from the shaft, which is generated by the turbine side to drive the compressor wheel, draws in ambient air into the compressor inlet at high velocity and low pressure. This air is the working fluid on the compressor side, which is compressed as the compressor wheel rotates at a rapid rate. The fluid travels through the passages of the compressor wheel blades, imparting kinetic energy into the fluid. The fluid enters the diffuser at a high velocity, which decreases inside the diffuser, prior to exiting into the compressor housing, also known as volute or collector. The diffuser transforms the kinetic energy in the flow to potential energy as a form of pressure, which is known as the diffusion process. This process is completed by decreasing the tangential velocity by increasing the radius [10]. In the volute, this diffusion process continues further through its spiral geometry, increasing the pressure and decreasing the velocity. The ambient air is drawn in at an ambient temperature; however, it exits at a high temperature reducing its density at the compressor outlet. In order to improve efficiency of the engine via the air intake, the fluid from the compressor passes through an intercooler, increasing the density. The intercooler uses air or water to cool the high temperature fluid prior to entering the engine. Once this compressed air enters the engine, it enables the engine to burn fuel more efficiently, enhancing the engine performance.

#### **1.4 Turbocharger Stages**

It is important to understand the fundamental concepts of a turbocharger and for this purpose each stage of the turbocharger system will be elaborated in further detail. There are three integral stages within turbochargers [4]. These are:

- Turbine Stage
- Rotor Bearing Housing Stage
- Compressor Stage

### 1.4.1 Turbocharger Turbine Stage

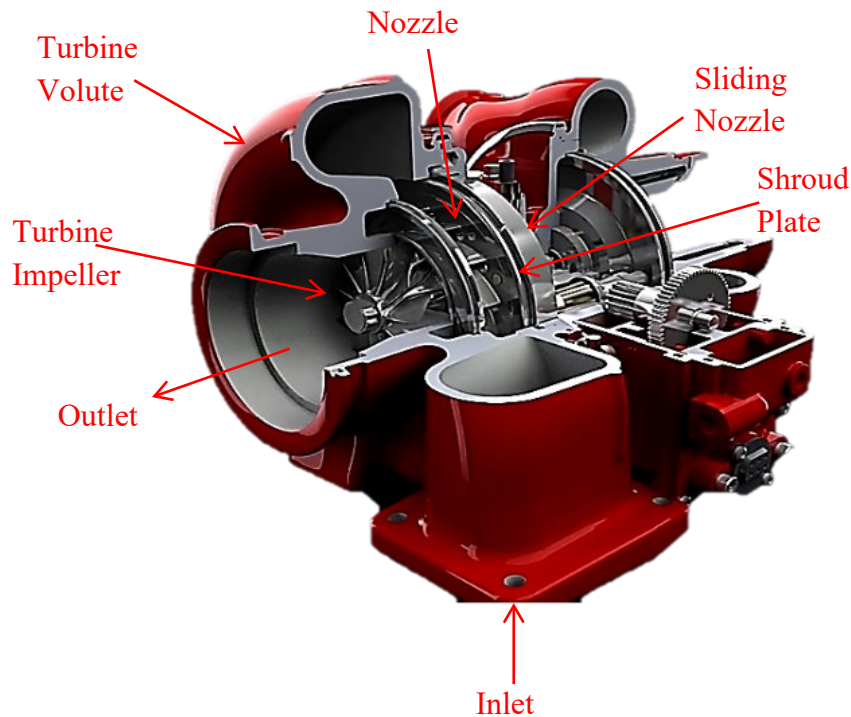


Figure 1.4 Turbocharger Turbine Stage [11]

Figure 1.4 depicts a turbocharger turbine stage identifying its components. Exhaust gases expelled from the engine travels through the exhaust manifold to enter the inlet of the turbine stage. Once entering the turbine stage, these gases are directed into the turbine housing. The turbine housing can be either a single-entry volute or twin-entry volute. A single-entry volute is as shown in Figure 1.4 and is ideal for high engine speeds. This is advantageous since it provides approximately 1% brake specific fuel consumption (BSFC) at rated speed conditions and increases the turbine efficiency by approximately 3-4%. However, its disadvantage exists in its poor transient response. A twin-entry volute has two passages to separate the front cylinders of the engine from the rear. This is considered to be better suited for low engine speeds and transient response. This is advantageous since it provides approximately 1% BSFC at peak torque conditions, captures pulsating effects and is used to enhance stage performance. However, it is not ideal for when there is a great deal of flow travelling through the wastegate [4].

When exhaust gases travel into the housing, it is directed through the sliding nozzle and nozzle vanes onto the turbine impeller. The sliding nozzle alters the inflow opening onto the turbine impeller, which increases the boost as the nozzle closes. Decreasing this opening

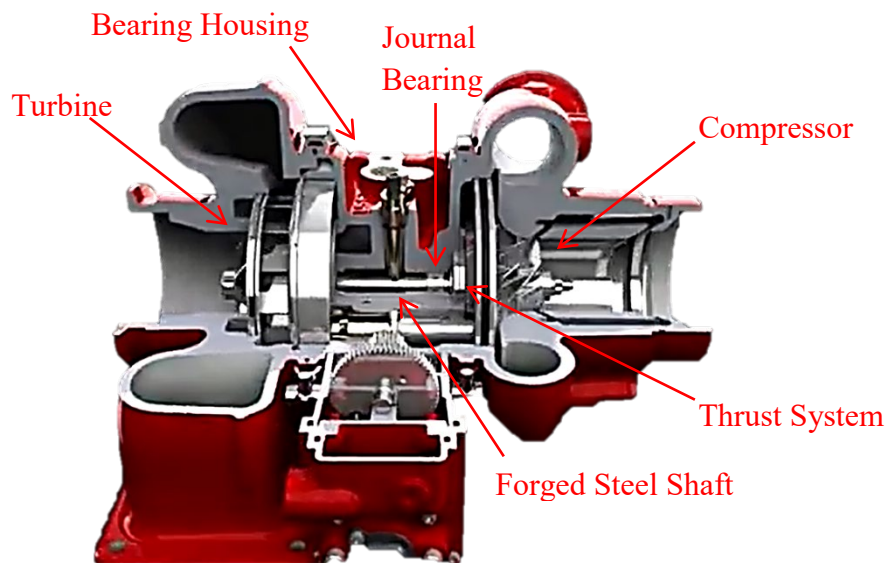


causes the exhaust manifold pressure and the turbocharger speed to increase. As the nozzle opens, there is a decrease in exhaust pressure causing the turbocharger to produce rapid boost at low engine speeds and then maintain high boost at higher engine speeds. The nozzle vanes slide axially to ensure maximum durability and reliability. These vanes are fixed in the best position producing the angle of attack for the exhaust gases to travel through the blade passages of the turbine impeller. This, in turn increases the average turbine efficiency throughout its operating range. The shroud plate seals the vanes and the turbine housing [4].

When exhaust gases flow into the turbine wheel, the gases cause the impeller to rapidly rotate, extracting energy from the exhaust gases and converting it into mechanical energy by transferring it through the forged steel shaft to drive the compressor wheel. After the energy has been extracted at the turbine impeller, exhaust gases exit the turbocharger through the outlet of the turbine stage and is directed downstream of the exhaust system [4].

#### 1.4.2 Turbocharger Rotor Bearing Stage

Figure 1.5 illustrates the bearing system of the turbocharger.



*Figure 1.5 Turbocharger Bearing System [11]*

The rotor bearing system is located in the bearing housing of the turbocharger. It connects the turbine impeller to the compressor impeller through a forged steel shaft with thrust bearing and journal bearings. The purpose of the thrust bearing is to maintain the axial moment of the rotor system as a result of gas loading on the turbine and compressor impellers. The thrust system accommodates for the forces towards the turbine and compressor and is designed to

withstand high levels of torque, primarily directed towards the compressor. This is since the compressor impeller has a greater rear face area and experiences higher-pressure ratios. The shaft is exposed to axial loads in the compressor stage near the surge condition, whereas this exposure occurs in the turbine stage near the choke condition. The purposes of journal bearings are to maintain the position of the shaft at the centre and to provide clearance to dampen vibrations at the shaft. Losses can occur in this system in terms of work done since it does approximately 2% of the turbine work at a given condition and even more at other conditions. There are frictional losses occurring in the thrust system, therefore it is important to be very careful in the design otherwise it can lead to power losses as well [4].

### 1.4.3 Turbocharger Compressor Stage

Figure 1.6 depicts the turbocharger compressor stage identifying the components and particular geometries of interest within this research.

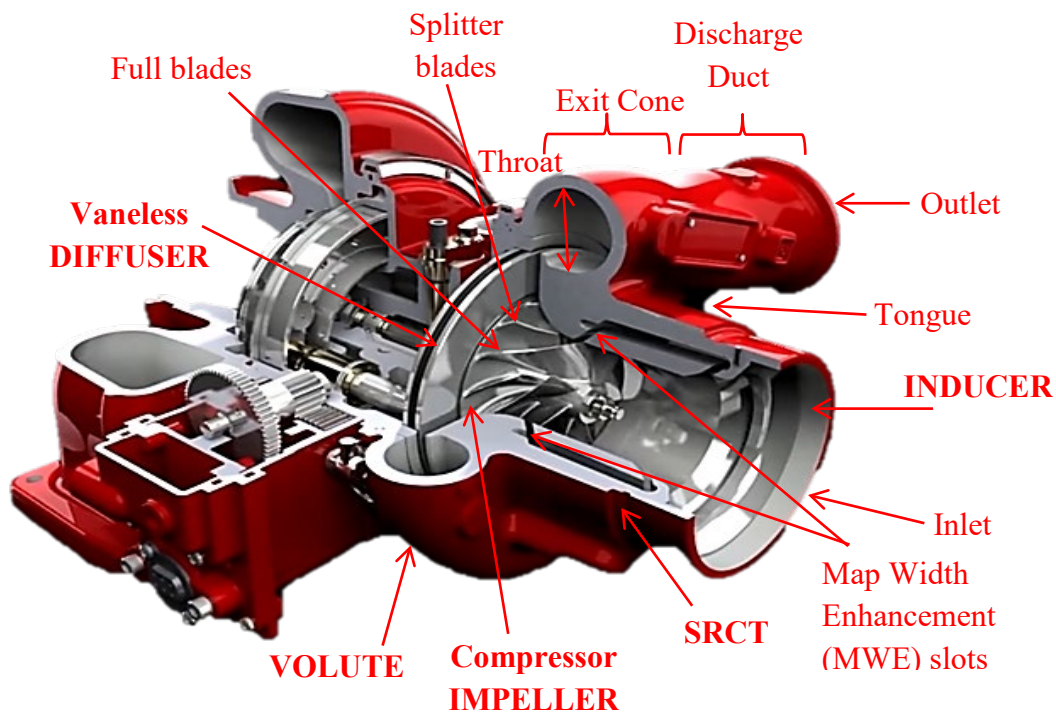


Figure 1.6 Turbocharger Compressor Stage [11]

The compressor impeller rapidly rotates using the mechanical energy converted from the energy extracted from exhaust gases in the turbine stage. The impeller rotation causes the blades to create a suction effect drawing ambient air into the compressor stage through the inlet. The impeller predominantly consists of full blades and splitter blades. The more blades there are, the better guidance there is for the air to travel through the system. When the

ambient air flows into the compressor through the inducer, it is directed to the compressor impeller. During this process, flow also travels through the Self-Recirculating Casing Treatment (SRCT), which consists of Map Width Enhancement (MWE) slots. These slots allow the impeller to operate under extreme conditions, such as surge and choke (see section 1.6) to cover a wider operating range, increasing the width of the compressor map. Once the fluid passes the impeller, it is directed into the diffuser. The diffuser is a radial annular passage that reduces the air velocity before it enters the volute with minimal losses so that pressure and temperature can rise. Diffusers can either be vaned or vaneless. When the compressor volute collects the compressed fluid from the diffuser, it is directed into the discharge duct then finally the outlet. The compressor volute can either be symmetric, also known as external, or asymmetric, also known as internal or overhung [4].

### 1.5 Fundamental Fluid Principles in a Turbocharger Compressor Stage

When analysing the turbocharger, within the compressor map total parameter conditions are used to determine its performance characteristics. Whereas when analysing the engine, within the performance stage the static measurements, particularly pressure are used for simplicity. The static conditions neglect the kinetic components of the flow parameters acting on the fluid. The gauge pressure is measured relative to the atmospheric pressure and is zero referenced against the ambient air pressure and commonly used in the real world. Absolute pressure is zero referenced against a perfect vacuum. Gauge, absolute and atmospheric pressures are all interrelated by [4]:

$$p_{atm} = p_{abs} - p_{gauge}$$

*Equation 1.1 Atmospheric Pressure*

Incompressible flow is defined as a flow without a change in density. From Bernoulli's equation [4]:

$$p_1 + \frac{1}{2}\rho v_1^2 + \rho g h_1 = p_2 + \frac{1}{2}\rho v_2^2 + \rho g h_2$$

$\nearrow$   
 Pressure  
Energy

$\uparrow$   
 Kinetic  
Energy

$\nwarrow$   
 Potential  
Energy

*Equation 1.2 Bernoulli's Principle*

Equation 1.3 and Equation 1.4 are used to calculate the total pressure and total temperature, respectively [4].

$$p_T = p_S + \left[ \frac{\rho \times v^2}{2} \right]$$

*Equation 1.3 Total Pressure*

$$T_T = T_S + \left[ \frac{v^2}{2 \times C_p} \right]$$

*Equation 1.4 Total Temperature*

Compressible flow is defined as a flow where there is a great deal of variation in the fluid density. The total pressure for compressible flow is calculated by [4]:

$$p_T = p_S \times \left[ \frac{T_t}{T_S} \right]^{\left( \frac{\gamma}{\gamma-1} \right)}$$

*Equation 1.5 Total Pressure for Compressible Flow*

The specific heat ratio ( $\gamma$ ) is 1.4 for air on the compressor stage, whereas on the turbine stage this ratio is 1.3 for exhaust gases [4].

Mach number is defined as the ratio between the speed of an object in motion through a fluid and the speed of sound, given by [4]:

$$M = \frac{v}{c} \text{ or } M = \frac{v}{\sqrt{\gamma R T}}$$

*Equation 1.6 Mach number*

The larger the Mach number means the larger difference there is between the static and total pressures due to the higher contribution of the kinetic parameter. As the Mach number increases the loss coefficient also increases [4].

Flow corrections are required to standardise the compressor map and hence the performance at various operating conditions. This is used to evaluate the performance characteristics supplied by the manufacturers of a specific turbocharger. For a specific compressor, the characteristics are defined by the mass flow rate, pressure ratio and operating speed. The pressure ratio is a non-dimensional parameter whereas the mass flow rate and operating speed

are dimensional and the value can vary with various units. In order to standardise the mass flow rate and operating speed, manufacturers use a corrected version of the compressor map that they produce to ease the process for compressor performance evaluations. The compressor performance map is generated using the actual and physical measured flow parameters during experimentation with the specified units, therefore any change in the units will alter the performance map. Through flow correction, there are clear variances in the pressure and temperature therefore it becomes much simpler and easier for the performance of the same turbocharger to be compared from tested in one country, to being tested in another. Flow correction can be carried out using the principles of ‘similitude’ and ‘dimensional analysis’. Similitude is when the state or quality is similar to something. In this case, the flow similarity requirements are considered, for which consists of [4]:

- similar geometry
- velocities at corresponding points that are in the same ratio
- velocities that have the same direction relative to some reference direction
- the same ratio of forces on the fluids in each system

The equations of mass flow rate, ideal gas and Mach number are formulated below.

$$\dot{m} = \rho A v$$

*Equation 1.7 Mass Flow Rate*

$$p = \rho R T$$

*Equation 1.8 Ideal Gas*

$$M = \frac{v}{\sqrt{\gamma R T}}$$

*Equation 1.9 Mach Number*

These formulas can be rearranged to provide a new expression for mass flow rate

$$\frac{\dot{m}}{A} = p_T \times \sqrt{\frac{\gamma}{R \times T_T}} \times \frac{M}{\left(1 + \left(\frac{\gamma-1}{2}\right) M^2\right)^{\frac{\gamma+1}{2(\gamma-1)}}}$$

Through rearranging, the following is achieved:

$$\frac{\dot{m} \times \sqrt{T_T}}{A \times p_T} = \sqrt{\frac{\gamma}{R}} \times \frac{M}{\left(1 + \left(\frac{\gamma-1}{2}\right) M^2\right)^{\frac{\gamma+1}{2(\gamma-1)}}} = \text{Constant for given } \gamma, R \text{ and } M$$

*Equation 1.10 Corrected Mass Flow Rate*

The ‘corrected flow’ usually found on compressor maps are there for others to review units of mass flow at a reference condition specific to the manufacturer that are familiar through the turbocharger, but not the physical mass flow. There are a couple of steps for the process of using the corrected flow. These are as follows [4]:

1. Define the manufacturer’s standard pressure and temperature.
2. Define the customer’s standard pressure and temperature.
3. Manufacturer measures the physical parameters then convert to ‘corrected’ flow and generate the map.
4. Customer measures the physical parameters then convert to their own ‘corrected’ flow.
5. Convert the customer’s corrected flow into the manufacturers corrected flow, and then generate that map on the original manufacturer’s corrected flow map.

A corporate standard was developed in 1995 in order to avoid confusion. The flow parameter for the turbine and compressor is calculated by [4]:

$$\text{Flow Parameter} = \left[ \frac{\dot{m}_{\text{physical}} \times \sqrt{T_{Tin}}}{p_{Tin}} \right] \quad \text{in units of} \quad \frac{\frac{\text{kg}}{\text{s}} \times \sqrt{K}}{\text{MPa}}$$

*Equation 1.11 Flow Parameter*

Therefore, from the isentropic flow equation the term ‘A’ disappears since it is the area and is a constant for the given compressor. Additionally, the corporate standard speed parameter for the compressor and turbine is given by [4]:

$$\text{Speed Parameter} = \left[ \frac{N_{\text{physical}}}{\sqrt{T_{Tin}}} \right] \quad \text{in units of} \quad \frac{\text{rps}}{\sqrt{K}}$$

*Equation 1.12 Speed Parameter*

Entropy is the order and disorder of a thermodynamic system and is a property that determines the amount of thermal energy that is unavailable to undertake work. If the fluid molecules in the system are ordered, then the entropy within the system is low, and it is high

when the molecules are disordered. The entropy is the number of microstates (being all the quantum states gathered that are occupied by the molecules at any point) of a system in equilibrium condition and is given by [12]:

$$S = k_B \ln \Omega$$

*Equation 1.13 Entropy*

The change in entropy is defined as the change in heat over temperature, given by:

$$\Delta S = \frac{\Delta Q}{T}$$

*Equation 1.14 Change in Entropy*

In a turbocharger compressor stage, as the ambient air is drawn into the inlet duct, the entropy is low since the molecules are ordered, whereby the molecules exhibit less or no collisions nor agitation. Entropy increases by adding heat into the system in an internal reversible process. Therefore, as this air hits the impeller blades, it transfers energy; creating work within the system, which in turn increases the heat and therefore the entropy begins to increase. Here, since the fluid is passing through several impeller-blade passages, there is a decrease in pressure and an increase in velocity. Since the impeller transfer energy into the fluid, heat takes place and hence the entropy increases further. When the air is at the impeller exit, the fluid is at its highest velocity and lowest pressure prior diffusion. When the air is compressed in the diffuser and reaches the diffuser exit, there is a rapid decrease in velocity, an increase in pressure and temperature. When this compressed fluid is directed into the volute, it converts the kinetic energy ( $\frac{1}{2}\rho v^2$ ) into potential (pressure) energy. When pressure increases since  $p = \rho RT$ , temperature increases, which leads to a further increase in entropy. The compressed air then exits via the discharge duct of the volute at low velocity, high pressure, high temperature and high entropy. Whereby, the molecules are random, agitated, vibrating, energised and with collisions taking place.

Enthalpy is a “state function” meaning that it is dependent on the state of the thermodynamic system as it is, rather than how the system reached that state. It relies on internal energy, pressure and volume, whereby the relationship is given by [12-14]:

$$H = U + pV$$

*Equation 1.15 Enthalpy*

The change in enthalpy is given by:

$$\Delta H = \Delta U + \Delta p \Delta V$$

*Equation 1.16 Change in Enthalpy*

Since the change in internal energy is given by:

$$\Delta U = Q - W \text{ and hence } \Delta H = Q - p\Delta V + \Delta pV$$

It can be said that when there is constant pressure in the thermodynamic system:

$$\Delta U = Q$$

The enthalpy defines energy changes in a thermodynamic system and its change takes into consideration the energy transfer at constant pressure caused by heating and expansion. When the change in enthalpy is positive, the system is essentially absorbing the energy from its surroundings as heat. This process is an endothermic reaction. When the change in enthalpy is negative, the system is essentially releasing the energy from the system as heat. This process is an exothermic reaction.

Enthalpy can be applied to the turbocharger compressor stage in a similar principle as how entropy varies through the system. Thus, since enthalpy is a state function and is dependent on the properties, it is considered that as the volume, pressure and temperature of the fluid varies, the enthalpy of the system would then also change accordingly, which in turn describe the variances of energy in the compressor.

## 1.6 Turbocharger Compressor Stage Performance Characteristics

Figure 1.7 is a graphical representation of the performance characteristics in the form of a compressor map. It can be seen that the corrected mass flow rate is plotted against pressure ratio for various speeds. The compressor map is an essential chart used to determine the performance characteristics of the particular compressor at design and off-design conditions. These performance characteristics include the isentropic efficiency, mass flow range, boost pressure capability (total-to-total pressure ratio), and turbocharger operating speeds. The compressor map is also used to validate various designs and illustrates variations in the mass flow rate of air through the compressor with respect to total-to-total pressure ratio at various operating speeds of the turbocharger. This in turn allows the isentropic efficiency of the system to be determined. There are six points on a compressor map per speed. The first point



in each speed line is near the surge condition and this is located by capturing the pressure fluctuation. The last point in each speed line is near the choke condition and beyond this point, oil leakage and thrust bearing failure tends to occur [4].

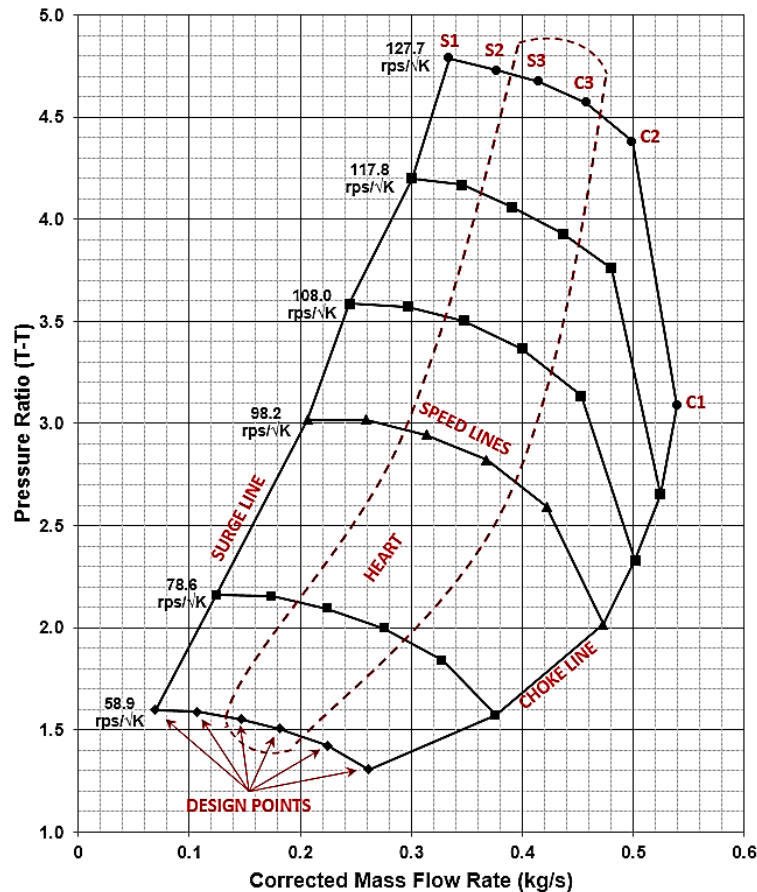


Figure 1.7 Turbocharger Compressor Map

The middle ring on the compressor map is the heart of the map and is also known as the efficiency island. The highest efficiency falls within this area and the design point with the highest efficiency is known as Best Efficiency Point (BEP). As the ring expands and extends, the efficiency decreases. The speed lines are the constant operating speed of the turbocharger. The surge condition is a complex and extreme phenomenon related to the inducer stall and wheel outlet recirculation as a result of separation. It is a condition when the compressor is unable to add sufficient energy to beat the system resistance, or backpressure. Excessive boost pressure builds up under surging conditions, causing the compressor wheel to stall. The air flow stops through the compressor, and is reversed until the pressure is stabilised and positive mass flow is achieved. At this point, the pressure builds up again and the cycle repeats. During this condition, pressure is at its maximum and the mass flow is at its minimum for the specified operating speed. The choke condition is a complex and extreme

phenomenon. It is the condition where the mass flow rate in the compressor has reached its maximum limit and a further increase in the differential pressure does not increase the mass flow rate of air through the system. During this condition the mass flow is at its highest and the pressure is at its lowest for the specified operating speed [15, 16]. Unfortunately the real surge and choke conditions are unknown and can be very challenging to determine, hence the presented surge and choke conditions are considered to be near these extreme conditions. The pressure ratio is the total-to-total compressor pressure ratio of absolute total outlet pressure over the absolute total inlet pressure. The corrected mass flow rate is the mass of air flowing through the system when the inlet pressure and temperature resembles ambient conditions.

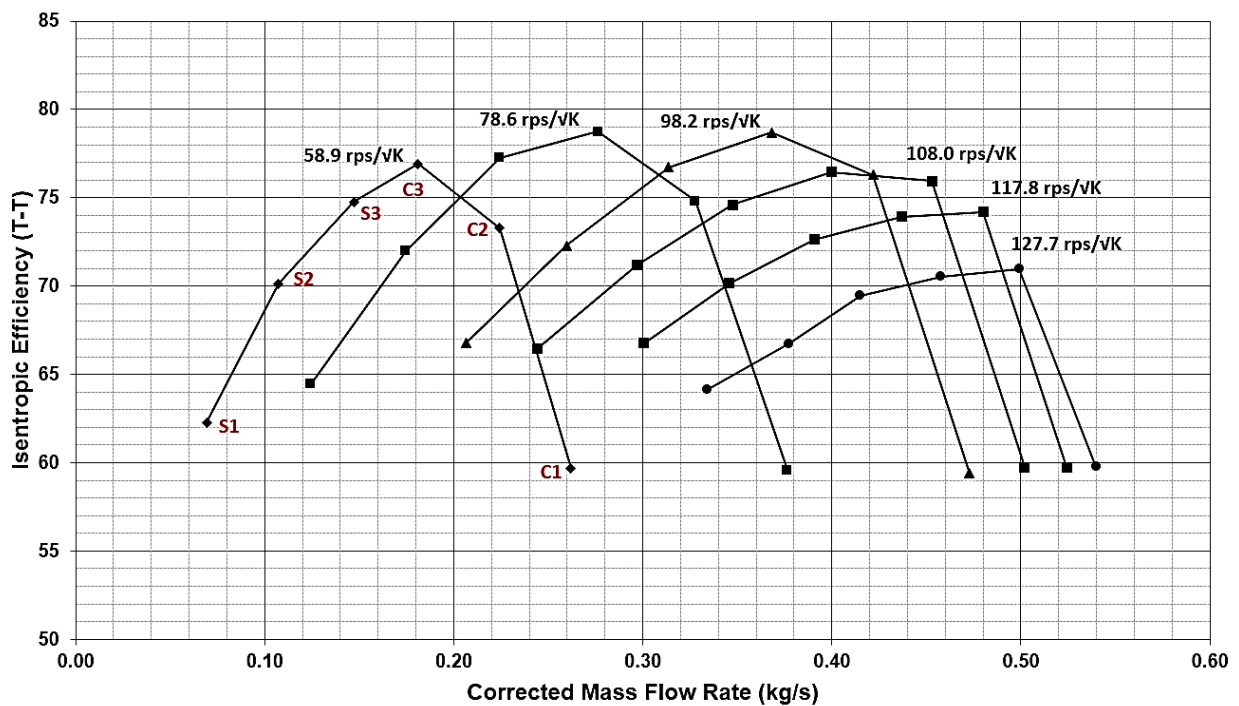


Figure 1.8 Turbocharger Efficiency Map

Isentropic process in the compressible flow is a reversible process that maintains constant entropy and has no heat transfer to the fluid or from the fluid [4, 13]. The isentropic efficiency determines the amount of input work needed to increase the pressure of the fluid to an ideal value to that of actual input work [14]. The calculation to determine the total-to-total isentropic efficiency of the compressor for the work between the inlet and outlet pressures is given by:

$$\eta_c = \left[ \frac{W_{IDEAL}}{W_{ACTUAL}} \right]$$

The isentropic efficiency of the compressor expressed as the ratio of temperature differences is given by:

$$\eta_c = \left[ \frac{T_{Tout,is} - T_{Tin}}{T_{Tout} - T_{Tin}} \right]$$

By using the relationship between temperature and pressure,  $T_{Tout,is}$  can be substituted so that the compressor efficiency can be given by:

$$\eta_c = \left[ \frac{T_{Tin} \times \left[ PR^{\left( \frac{\gamma-1}{\gamma} \right)} - 1 \right]}{T_{Tout} - T_{Tin}} \right]$$

*Equation 1.17 Total-to-Total Compressor Isentropic Efficiency*

$$PR = \frac{P_{Tout}}{P_{Tin}}$$

*Equation 1.18 Total-to-Total Pressure Ratio*

## 1.7 Centrifugal Compressor Volute Geometry

The volute is considered to be the third most important component within the compressor stage and has therefore, not received the attention that is needed [2, 3]. Within the volute, there are a number of geometrical sections that can be explored [2, 5, 17, 18]:

- The scroll, which is a logarithmic spiral passage designed to collect the volume of compressed air and convert the kinetic energy in the fluid into potential (pressure) energy by increasing the cross-sectional area with the azimuth angle.
- The tongue that is the joint of its smallest area, largest area, and exit cone. The tongue acts as a dividing plane where flow is divided and directed either into the discharge duct to exit the compressor, or re-enters forcing to recirculate around the volute.
- The throat, which is a cross-sectional area in the volute at the tip of the tongue (dividing plane) and entrance of the exit cone. Also known as the critical area or the full collection plane. It is the location at which the mass flow from the diffuser has fully been collected. Modifications to this geometry can alter the efficiency levels. The larger throat area will provide improved efficiency at low pressure ratios,

whereas the smaller throat area will provide improved efficiency at high pressure ratios.

- The exit cone that is the area in the volute between the tongue tip and the discharge duct.
- The discharge duct, which is the area in the volute before the compressed air leaves the compressor through the outlet at high pressure, temperature, density and low velocity to pass into the intercooler.

The purpose of the volute/scroll is to collect the fluid from the diffuser outlet and deliver it to the discharge pipe, and to convert kinetic energy into potential (pressure) energy. The scroll has different cross-sectional areas to minimise losses and leakages and to maintain constant velocity. Volute is generally designed to the desired best efficiency point (BEP) flow and the best volutes are designed to maintain constant velocity. The performance of the volute is affected primarily by five geometric parameters. These are [2, 18-22]:

- (1) Cross-Sectional Area: Circumferential increase in cross-sectional area collects more mass flow along the volute inlet and delivers uniform flow to maintain constant swirl and tangential velocity through the volute [5]. If this area is designed inadequately, it can result non-uniformities in the flow that can lead to many adverse effects upon the compressor itself.
- (2) Cross-Sectional Shape: this has a significant impact on the operating range stability of the centrifugal compressor and can affect the system performance. A poor design of the cross-sectional area causes distorted pressure distributions, which can affect upstream flow and aeromechanical forces that can affect the impeller [1, 18, 23].
- (3) Radial Location of the Cross-Section: this has the strongest influence on the performance of the volute since the conservation of angular momentum can be applied here. Theory of angular momentum states that the tangential velocity in a swirling flow is inversely proportional to the radius. Thus, if the volute inlet radius is smaller than the diffuser outlet radius then the tangential velocity inside the volute is higher in the volute than at the diffuser outlet. This means at the diffuser outlet where

the flow of the fluid decelerates to its lowest point, is then accelerated again at the volute inlet, which results to an unwanted static pressure drop and more losses.

(4) Location of the Volute Inlet: Asymmetric type volutes provide a more desired performance than symmetric type volutes because the double vortex in the symmetric type volutes causes significant separation [24].

(5) Tongue Geometry: This is a dividing plane and is a blend of the volute's smallest and largest cross-sectional areas. Closed tongue does not allow recirculation, whereas open tongue allows recirculation. Its length and angle can be adjusted.

It is important to understand the parameters involved in expressing the volute design. The azimuth angle ( $\theta$ ) is also known as the wrap angle, or circumferential angle. Due to the limitation of space available, the scroll is wrapped as a curved section having a cut-off between  $\theta = 300^\circ$  and  $340^\circ$ . The radius is dependent on the azimuth angle, hence is a function of  $\theta$ . From the throat, the volute consists of an exit cone which is designed such that the cross-section slightly increases to decelerate the flow and increase the pressure further prior to discharging through the outlet. This geometric region is also referred to as the discharge pipe. The radius to the volute centroid ( $R_c$ ) is the distance from the centre-point of the volute to the centre-point of the volute throat diameter. This parameter describes the geometric characteristics of all compressor and turbine housings. It is defined as [15, 21]:

$$\frac{\text{Area of Throat}}{\text{Radius of Center}} = k\theta$$

Where,  $k$  denotes the  $\frac{\text{area}}{\text{radius}}$  ratio.

The fluid is compressed in the diffuser where its purpose is to achieve static pressure recovery. Fluid is tangentially directed out of the diffuser and into the volute, thus the exhibited inflow velocity is a significant factor to the cross-sectional area and shape of the volute. The impeller outlet affects the volute more in pumps than in compressors since pumps commonly do not have diffusers, as a result the flow phenomena interactions between impeller blade and volute tongue is much more predominant in pumps.

## 1.8 Centrifugal Compressor Volute Loss Mechanisms

There are many different types of losses with respect to individual components during the stage efficiency, for example, the impeller, diffuser, volute will all suffer from frictional losses between the fluid and the wall of the component. There are losses in pressure when restrictions are in place, for example, when the airflow passes the impeller, pressure losses are incurred in the flow at the blades results.

Achieving optimal efficiency is the target for designing a turbocharger compressor stage since the prime purpose is to transfer energy from the shaft into the fluid in order to generate more power. During compressor operation, various loss mechanisms are encountered degrading the energy throughout the system resulting in a decrease in efficiency. These loss mechanisms are referred to as head loss, which are expressed as total pressure loss (pressure drop). There are four common sources of head loss by which the volute suffers in particular. These are [2, 9, 17, 21, 25, 26]:

### (1) Meridional velocity dump loss

The radial velocity dissipates to the swirl velocity component at the volute inlet, forming the meridional velocity dump loss, which cannot be recovered. It is defined as:

$$\Delta p_{mdl} = \frac{1}{2} \rho C_{r4}^2$$

*Equation 1.19 Meridional velocity dump loss*

### (2) Skin friction loss

As the fluid particles travel through the volute path, surface roughness of the component causes the fluid to encounter skin friction loss. In order to determine this loss, the average path length of the volute channel is taken into account, as well as the hydraulic diameter of the volute at the critical area, also referred to as the throat located at an azimuth angle of 360°, and the volume flow. This loss is determined upon the flux through the volute, whether it is laminar, turbulent, transition, smooth turbulent, or rough turbulent. The friction coefficient parameter ( $C_f$ ) is a function of the Reynolds number and is determined from the Moody's chart for pipes.

$$\Delta p_{sfl} = c_f \cdot \frac{L}{D_h} \frac{1}{2} \rho C_{u4}^2$$

*Equation 1.20 Skin friction loss*

Where,

$$L = \frac{\pi (r_4 + r_{th})}{2}$$

*Equation 1.21 Average path length of flow*

$$D_h = \sqrt{\frac{4A_{th}}{\pi}}$$

*Equation 1.22 Hydraulic diameter*

### (3) Exit cone loss

The exit cone starts at 360° azimuth angle whereby the cross-sectional area varies smoothly to the outlet. This has been previously calculated as a sudden expansion loss as opposed to a gradual expansion loss. Due to this, there are more losses generated in the volute however, the additional loss is employed in order to account as much as possible, for any swirl components entering the exit cone. The exit cone loss is dependent on the total opening angle of the exit cone. The exit cone loss coefficient varies with the opening angle from 0.15 for a 10° to 1.1 for a 60°. Research has recommended that for achieving a good volute design, this opening angle should not be greater than 10° and hence the exit cone loss coefficient should maintain a constant value of 0.15. The exit cone loss is defined taking the distorted flow entering the exit cone, and the transition from a swirling annular flow (log-spiral flow path) to a linear flow path, into account. Hence it is defined as:

$$\Delta p_{ecl} = c_{ecl} \frac{1}{2} \rho (C_{th} - C_5)^2$$

*Equation 1.23 Exit cone loss*

### (4) Tangential velocity dump loss

The tangential velocity effectively delivers the fluid from the volute inlet to the outlet and is proportional to the difference of the actual kinetic energy head related to the tangential velocity component at the volute inlet. It is important to account for the change in area and

average radius in the circumferential direction since these force a change in the angular momentum, causing the tangential velocity head to be partially lost.

$$\Delta p_{udl} = \frac{1}{2} \rho \cdot \frac{r_4 C_{u4}^2}{r_{th} C_4^2} \left[ 1 - \frac{1}{SP^2} \right]; \quad SP \geq 1$$

$$\Delta p_{udl} = \rho \cdot \frac{r_4 C_{u4}^2}{r_{th} C_4^2} \left[ 1 - \frac{1}{SP} \right]^2; \quad SP < 1$$

*Equation 1.24 Tangential velocity dump loss*

$$SP = \frac{r_4 C_{u4}}{r_{th} C_{th}}$$

*Equation 1.25 Sizing Parameter*

In the initial stages of the flow entering the volute inlet, the scroll tries to diffuse this incoming flow to zero velocity, which can cause total tangential velocity head loss. Therefore, the overall tangential velocity is computed as the sum of the two values obtained from Equation 1.24.

#### (5) Head Loss

The total pressure head loss of the volute from the inlet to the outlet is given by the sum of all the head losses.

$$\Delta p_{45} = \Delta p_{mdl} + \Delta p_{sfl} + \Delta p_{ecl} + \Delta p_{udl}$$

*Equation 1.26 Total head loss of volute*

When fluid travels through a volume, it requires a certain amount of energy. However, when resistive forces exist such as viscosity in a fluid or friction on the surface, the fluid needs to work harder to overcome this resistance. The pressure head loss equation applicable for this case is given by [27, 28]:

$$H_L = \frac{\Delta p_L}{\rho g}$$

*Equation 1.27 Head Loss*



Where,

$$\Delta p_L = f \left[ \frac{L_{eq.}}{D} \frac{\rho v_{avg}^2}{2} \right]$$

*Equation 1.28 Pressure Loss*

Where,

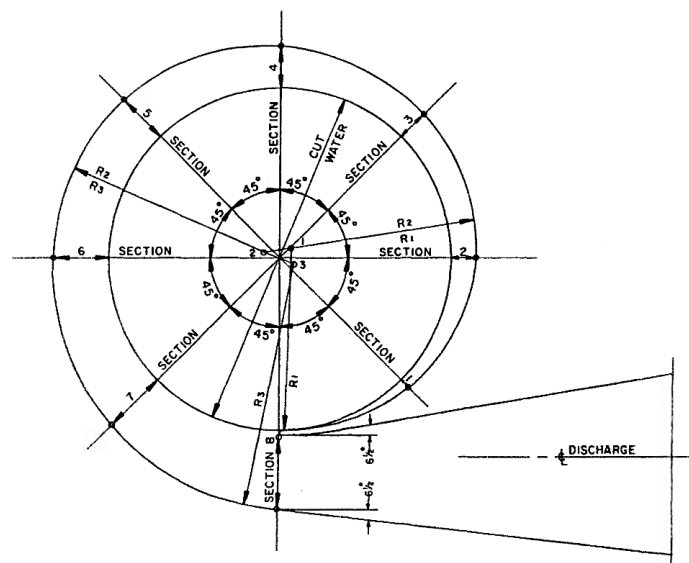
$$f = \frac{8\tau_w}{\rho v_{avg}^2}$$

*Equation 1.29 Darcy's Friction Factor*

These equations are appropriate for laminar and turbulent flow regimes as well as for circular and non-circular pipes [27, 28].

## 1.9 Volute Design Practices

A centrifugal compressor volute is very much similar to a centrifugal fan volute and a centrifugal pump volute in that the systems are designed to increase the energy of the flow by smoothly increasing the cross-sectional area. The compressor differs from a pump in that it uses gas as the working fluid which is compressible, as opposed to a pump that uses liquid as the working fluid which is incompressible. The compressor differs from a fan in that it operates at higher speeds in order to produce a higher rise in pressure. Due to the similarities in the job of the volute, there are also similarities in the way in which they are designed. A classic volute layout is shown in Figure 1.9 where profiles have been created at an azimuth angle of every 45° [20].



*Figure 1.9 Centrifugal Compressor Volute Layout [20]*

There are certain universal guidelines for volute designs that have been developed over experience to provide good results, ease manufacturing, as well as reducing costs and time. These guidelines are as follows [20]:

1. Ensure that the angles used on the sidewalls of the volute are constant instead of using different angles at each section.
2. Ensure symmetrical volute space on both sides of the impeller shrouds.
3. Ensure that all the areas of the volute are design to exhibit smooth change of areas.
4. Ensure that the total angle the discharge duct, diverges is between  $7^\circ$  and  $13^\circ$  since this behaves as a conical diffuser where the final diffusion process takes place, fully converting kinetic energy into potential energy.

It is vital for the centrifugal compressor volute to be well matched with the impeller and the diffuser at the BEP with even static pressure distribution along the periphery of the volute inlet. This can ensure even static pressure distribution along the impeller exit, which is a condition for impeller performance. If the static pressure distribution is uneven along here, it can cause load changes on the impeller with the efficiency and operating range suffering from adverse effects. During off-design conditions, the mismatch of the volute and the impeller can cause pressure losses [15]. In order to minimise losses in the volute, it is designed such that the tangential velocity varies inversely proportional with the radius. These are the ideal conditions however in real conditions, friction alters this ideal flow, and there are variances in the tangential velocity with respect to the length of its followed path [22]. Taking this into account, different cross-sectional areas of the volute can be designed with realistic efficiency by undertaking sufficient calculations and experimentation, achieving reasonable results with a reasonable degree of accuracy.

The cross-sectional area of the volute is a significant geometric parameter that has great impingement on the volute performance. These various cross-section geometries that can be used are predominantly circular or elliptical for cast volutes; and rectangular for fabricated volutes. The essential aspect of volute design is to determine the variations of the mean circumferential radius and the cross-sectional area. There are two methods:

1. Simple Area Schedule (SAS) – the area of the full-collection plane is fixed by using the desired flow velocity, allowing the volute area to then change linearly with the polar angle  $\theta$ .

2. CAM –a more precise method to establish area distribution using the principles of conservation of mass and angular momentum.

Since the CAM approach disregards some factors such as non-uniformities of flow in the volute over the cross-sectional area, and the generation of a significantly higher mean velocity than the calculated from the ideal model due to distorted profiles, viscosity and secondary flows, it is suggested to use a generalised basic design volute equation, given by [21]:

$$A = \theta \cdot SP \cdot r_c \cdot b_5 \cdot \tan \alpha_5$$

Whereby,  $\theta$  is the polar angle; SP is the sizing parameter that represents the ratio of the actual area of the volute to the value satisfying the ideal conservation of angular momentum;  $r_c$  is the radius of the mean passage cross-section parameter;  $b_5$  is the hub to shroud passage width at the volute inlet condition; and  $\alpha_5$  is the tangential flow angle at the volute inlet condition. If the volute is undersized then considerable losses are incurred, therefore a  $SP > 1$  is commonly used in practice as a safety margin. Large SP are used for volutes where vaneless diffusers are present to adapt to the requirements for off-design conditions. With regards to design conditions or where vaned diffusers are present, SP between 1.0-1.2 are used [21].

### 1.10 Motivation

Many manufacturers are interested in making the volute more compact since it is the largest component of the compressor [2, 5, 10, 29]. Volute designs have remained the same for decades due to the little pressure gain and is therefore considered as components that does not need to be improved [30]. However, without investigating the volute and studying the incurred losses and considering these losses in its design, would result in a decrease in pressure through the component and an instantaneous rise in pressure at the tongue, resulting in poor performance due to poor matching with the impeller [17]. Therefore, studying the centrifugal compressor volute design to have a realistic methodology where losses in the volute are minimal and real conditions, such as frictional effects are accounted for is important.

Researchers have investigated the performance of the volute using similar design methodologies. However, there is only limited amount of literature available that focuses on the design of the turbocharger compressor volute considering frictional effects. In addition to this, transient response studies in this regard are severely limited and to the best of the

author's knowledge there are no literatures available yet that establishes an expression for designing the turbocharger compressor volute for realistic conditions. Hence, there is a need to carry out extensive investigation to understand the flow field inside the centrifugal compressor volute and how the very design methodology approach taken for the turbocharger compressor volute can affect the aerodynamic mechanisms and flow characteristics of a turbocharger compressor stage. This has therefore, motivated the author to carry out research in this particular area.

There is a need to explore how the design methodology of a turbocharger compressor volute can affect its geometry, performance, energy losses and entire flow structure under steady and transient conditions at various operating speeds and design points. Therefore, in this study, since Computational Fluid Dynamics (CFD) has a significant role in the aerodynamic design of turbomachinery [31], this numerical technique has been employed using to develop a thorough understanding of the flow behaviour the turbocharger compressor stage experiences, under steady and transient conditions from a macroscopic level to a microscopic level. Detailed qualitative and quantitative flow field analyses have been carried out to create a solid foundation to develop a realistic design methodology for a turbocharger compressor volute application.

### **1.11 Research Aim**

Analyse the flow characteristics of the turbocharger compressor and its volute during steady and unsteady response to develop a novel design methodology for the turbocharger compressor volute.

### **1.12 Organisation of Thesis**

On the basis of the previous discussions, this section presents the structure of work carried out for this research study.

Chapter 1 captivates an overview of turbochargers, their construction and operation, alongside the fluid flow mechanisms exhibited in the centrifugal compressor stage. It also includes the design practices implemented onto the component of focus. This essentially provides a fundamental understanding of the presented research field. From this overview, the motivation expresses the driving force carried out towards pursuing this study, followed by the research aims that identify key elements to be addressed.

Chapter 2 provides extensive and detailed review of the research that has been undertaken in volutes. It includes the review of published literature regarding the analytical, experimental and numerical studies of volute geometry, design methodologies and performance evaluations under steady and transient conditions. Details of the scope of research are provided in the form of research objectives, creating a canvas for conducting this study.

Chapter 3 documents the stages involved when employing Computational Fluid Dynamics (CFD). It includes the modelling of the turbocharger compressor stage, the solver settings that have been specified for this study, and references of the locations specified for the analyses to be carried out in the upcoming chapters.

Chapter 4 captures detailed steady flow field analyses of the turbocharger compressor stage behaviour. It includes global and local qualitative and quantitative flow maps; depicting complex flow structures of the baseline model operating near the two opposing extreme compressor conditions, as well as the best efficiency point (BEP) during low and high operating speeds.

Chapter 5 sheds light onto the detailed instantaneous flow field analyses of a turbocharger compressor stage behaviour. It includes global and local qualitative and quantitative flow maps; depicting complex flow structures of the baseline model operating at the BEP during low and high operating speeds. This section focuses on the impeller blade position with respect to the volute tongue.

Chapter 6 presents the journey that discovers the novel methodology for designing the volute, taking frictional effects into account. This section presents expressions for volute design and includes the application of these expressions that characterises the volute geometry. This has facilitated in developing a realistic volute design methodology employed for the turbocharger compressor stage application. The final presented developed model is compared and evaluated against that, which currently exists.

Chapter 7 concludes the discoveries of the presented research study, clearly highlighting the goals achieved and additions to existing knowledge regarding the volute design methodology for a turbocharger compressor stage. This is in terms of the design process and flow mapping, correlating the local performance indicators with the global performance indicators under steady and unsteady conditions. Recommendations for future work have also been included in this chapter.

## CHAPTER 2

# LITERATURE REVIEW

---

On the basis of the research aim aforementioned in the previous chapter, a detailed literature review has been presented in this chapter, which highlights the knowledge gaps in the existing analytical, numerical and experimental studies. It includes the published works regarding the flow characteristics and losses incurred through the volute during steady and unsteady conditions, as well as volute design methodologies. Based on the knowledge gaps found in the literature review, scope of research has been defined and research objectives of this study have been formulated.

## 2.1 Fluid Flow Characteristics inside a Centrifugal Compressor Volute during Steady Response

Braembussche and Hände (1990) carried out an experimental and theoretical study of the swirling flow in centrifugal compressor volutes [34]. The authors conducted the experimental part of their study in their test facility using an overhung volute, which they had straightened and set up with a blower, inlet duct and guide vanes to simulate the compressor stage. The measurements had been taken with probe traverses at axial locations. The theoretical part of their study made comparisons with an analytical model. Their findings revealed that there were no variations in the radial distribution of swirl velocity, while different operating conditions at volute cross-sections showed that there were significant variations in the distribution of through-flow velocity. The authors also discovered that the flow and pressure measurements in vicinity of the walls were not representing the average values. The fall in velocity in the freestream at minimum mass flow varies into above average velocity at maximum mass flow, which also has the same influence as a positive and negative blockage and hence, effects the optimum volute dimensions. The authors presented that total pressure losses did not appear where they were produced. The radial pressure gradient thrusts low-energy fluid into the central area. They stated that the isentropic flow calculation demonstrated high through-flow velocity depicted in the freestream of the volute and the negative blockage factor are used in design methodologies. In addition to this, non-isentropic flow calculations demonstrated how total pressure losses impinge the through-flow velocity and cause blockage in the freestream of the volute. It also demonstrates the evaluation of total pressure losses as a role of flow parameters and friction coefficient. However, the authors have some doubt regarding the total pressure distribution across the cross-section of the volute. Furthermore, non-isentropic flow calculations are found to enable higher accuracy in design for the optimum volute geometry and allow the prediction of outlet flow. The authors anticipate there to be disturbances in the flow pattern between the gap at the volute and tongue region. Moreover, the volute curvature in real conditions is stated to result in smaller tangential velocity at the outer volute radius and larger velocity at the inner volute radius. The authors mention that additional research is required to assess the influence the gap between the volute and tongue has, as well as the influence the volute curvature has on losses and optimum volute dimensions.

Ayder et al. (1993) undertook an experimental and theoretical analysis of the flow in a centrifugal compressor volute [35]. In this study, the operating speed was set at 14,364rpm

with three different mass flow rates: 0.933kg/s (high); 0.575 kg/s (medium); 0.255kg/s (low) and collating pressure measurements at the outlet. The results of this study showed that there was a decrease in static pressure on the periphery of the volute, which led to an increase of radial velocity exhibited at the diffuser outlet. It also showed that the mass flow rate at the volute inlet also increases from the tongue to the outlet. The case for low mass flow indicated that there was uniform distribution of static pressure exhibited at the volute inlet. The fluid flowing in proximity of the tongue exhibits swirls at the centre of the volute cross-section. It concludes that the distribution of static pressure is dependent on the centrifugal forces caused by swirling velocity in the cross-section as opposed to the centrifugal forces caused by the velocity as a result of static and total pressure variations exhibited at the periphery of the volute. The gap in the study could be to strengthen the confidence of this investigation by calculating the energy losses through the centrifugal compressor volute using the numerical data obtained from the simulation.

Ayder et al. (1994) conducted a numerical analysis of the three-dimensional swirling flow in centrifugal compressor volutes [36]. Since it has been identified that volute flow is affected more predominantly by the losses in the core than the boundary layer, the investigation was solved by implementing the second-order dissipation and wall shear forces to the Euler solver. The volute uses hexahedral mesh cells with special attention regarding discretisation of the flow in the tongue area. The same number of cells was used for each cross-section of the volute in order to enhance the flow pattern resolution in small sections. The results state that the diffuser flow showed a variation of velocity and static pressure. At high mass flow rates, this static pressure decreases at the periphery in the direction of rotation of the impeller with a sudden increase in static pressure at the periphery of the diffuser outlet around the tongue region. In addition to this, the high pressure losses at the centre of the cross-section are stated to be due to the dissipation of the swirl kinetic energy. For high mass flow rates, there were no distinct explanation of the phenomena occurring with regards to the high mass flows and high total pressures exhibited at small cross-sections, however; a potential explanation has been stated as being as result of separation at the tongue. For low mass flow rates, the results state that there are no large gradients of total pressure led by viscous effects. Furthermore, the phenomenon of this investigation has discovered that when the fluid enters the volute in proximity of the tongue, it travels through the centre of the volute along the mean streamline until it reaches the outlet. Since the phenomena at high mass flow could not



be explained, the gap in this study is to observe flow patterns through the centrifugal compressor volute exhibited during various flow rates.

Nursen and Ayder (2003) undertook a numerical calculation of the three-dimensional swirling flow inside the centrifugal pump volutes, whereby an incompressible flow solver was developed for the pump volute [37]. This was then validated against experimental data in literature by other researchers. The authors have measured and analysed the variation of static pressure circumferentially at the volute inlet, the swirling velocity distribution at two cross-sections, as well as the through-flow velocity distribution at four cross-sections. In order to achieve this, the authors created an external pump volute having a rectangular cross-section with a 55mm constant axial width, a constant inner radius of 0.106m, and a logarithmic spiral as the outer wall. Hexahedron mesh was implemented onto the volute with 15 x 15 nodes on each of the 47 cross-sections. The authors implemented a unique fusing method at the tongue where the first cross-section was positioned at the diffuser exit, and created as a line laterally to the width of the volute, thus having tetrahedron mesh elements in this region. The study was conducted using three mass flow rates: 0.0029m<sup>3</sup>/s (low); 0.0045m<sup>3</sup>/s (medium); and 0.0062m<sup>3</sup>/s (high). The results showed that for low mass flow rates, the calculations predicted that flow tends to decelerate inside the volute, which causes the static pressure to increase throughout the volute from the tongue region. For high mass flow rates the static pressure has the vice versa effect, whilst for medium mass flow rates, the static pressure is almost maintained at a constant inside the volute. The authors concluded that the calculated and measured variations of circumferential flow inside a pump volute was well-matched. With respect to static pressure at the volute inlet, this was also in good agreement, which meant that the developed code can be used for investigations involving the interaction between the impeller and volute. However, due to the assumptions made during modelling the tongue, there were slight discrepancies observed between the numerical and experimental data. It was also mentioned that the inlet conditions of the volute, such as the distributions of total pressure, radial velocity and the through-flow velocity were not experimentally captured, and thus the total pressure and flow angles were assumed in the calculations as being circumferentially uniform at the volute inlet. No investigations have been carried out of the variation between different blade positions, such as when the blade is aligned with the tongue and when the tongue is between two blades in centrifugal compressors.

Zheng et al. (2010) numerically investigated the influence of a volute on the flow in a centrifugal compressor of a high-pressure ratio turbocharger [33]. This study was then validated using experimental methodology, more specifically, a turbocharger test bench. The conclusions that were drawn from the simulations and the experimental results were that at low mass flow rates, the volute suffers from a flow instability. The influence of the stable flow range (SFR), which is a prime issue for the automotive industry to expand at high-pressure ratios, was found to increase at the design speed, causing distorted perturbations in the compressor. In addition to this, it was found that the link between variations in the incidence angle with the impeller speed and the high sensitivity to variations in the incidence angle, are accountable for severe effects on the volute with regards to the SFR. This was discovered to exhibit an increased magnitude of losses in passages at high pressure ratios. This steady simulation with the conditions implemented found that detailed instantaneous flow field could not be accurately predicted. The investigation observes the asymmetric flow mechanisms at off-design conditions, however, this was not completely understood, and thus the gap in this study yet remains. It is stated that it is highly important to understand the flow mechanisms that cause instabilities within the system in order to make suggestions for compressor design. By understanding the asymmetric flow mechanisms, a development for the asymmetric flow control methods to stabilise the influence of the volute can be achieved by expanding the map width enhancement (MWE) slots. Further to this, another gap in this study is to conduct an unsteady simulation of a high pressure ratio compressor, since this particular investigation was conducted as being a steady simulation.

Abdelmadjid et al. carried out a numerical investigation in 2013 of the volute geometry effect on the turbulent air flow through a turbocharger compressor using CFD analysis [32]. This study focussed on the interaction between the impeller, diffuser and volute with respect to the variations of volute geometry to explore the performance characteristics using numerical solution with sliding mesh technique and steady flow. The various volute geometries analysed were circular cross-section with tangential inlet location; circular cross-section with symmetrical inlet location; and semi-circular cross-section with tangential inlet location. There are two distinct aspects that are predominant in this study, where the volute geometry was based on the overall performance and operating range. This has been distinguished by the shape of the cross-section, whereby the circular has been compared to the semi-circular; and the location of the volute inlet, whereby the tangential has been compared to the symmetrical. The results indicated a range of performance characteristics such as pressure

ratios, efficiencies, mass flow rate, velocity and vorticity that have all been explored within this study. The findings overall discovered that modification to the shape of the volute cross-section affects the operating range greater than the peak efficiency, while modification to the volute inlet location affects the peak efficiency more than the operating range. It also indicated that there is higher peak efficiency when the volute inlet location is tangential, there are wider operating ranges when the volute shape is circular, and there is non-uniform pressure present at high flow rates. Although there is a great deal of ground covered in this study, a detailed flow analysis across each profile can provide much more detailed understanding inside the compressor the volute.

## **2.2 Fluid Flow Characteristics inside a Centrifugal Compressor Volute during Instantaneous Response**

In 1995, Chu et al. researched the relationship between unsteady flow, pressure fluctuations and noise in a centrifugal pump and the effects of blade-tongue interactions using Planar Doppler Velocimetry (PDV) data [38]. The experimental results showed that there is low pressure around the blade and a vortex train is generated in proximity caused by the non-uniform outflux the jet/wake phenomenon from the impeller. The pressure distribution is constantly varying throughout and is dependent on the location of the impeller relative to the tongue. When the blade of the impeller passes by aligning with the tip of the tongue, the pressure distribution is at its lowest near the impeller, and at its highest within the wake behind the impeller blade as well as when it is far away from the tongue. Additionally, the noise peaks are produced when the pressure difference across the tongue is at its maximum due to the tongue oscillations forced by the local pressure fluctuations and when the wake is strongly influenced on the tongue tip. The study found that minor changes to the tongue gap created major changes to the entire flow structure, pressure fluctuations, and the far-field noise. Since the findings discovered that the leading phenomena are a result of blade-tongue interactions and non-uniform outflux from the impeller, it is desired to investigate the flow field inside a centrifugal compressor of the two blade positions.

Hillewaert and Van den Braembussche (1999) studies the numerical simulation of impeller tongue interaction in a centrifugal compressor [39]. The authors carried out a three-dimensional unsteady calculation of flow in the impeller and a three-dimensional time-averaged calculation in the volute. The purpose of this particular study was to predict circumferential distortion of flow in the volute; unsteady periodic blade loading and the

resulting radial force exerted on the impeller shaft. The findings depicted that unsteady flow in the impeller is related to the fluctuations circumferential total pressure and temperature distributions. It has also been documented that the interaction between the impeller and volute is the reason behind the static pressure rise is slower near the tongue. Further detailed numerical analysis can be conducted focussing on the position of the impeller blade in relation to the volute tongue in a centrifugal compressor.

An experimental and numerical study on the steady and unsteady radial forces for a centrifugal pump with impeller and tongue gap variation was carried out by González Pérez et al. in 2006 [40]. The experimental study was carried out using pressure transducers and was compared against the numerical study computed using CFD. Both studies were carried out using two impellers, one with radial gaps between the blade and the tongue of 10% and the other of 15.8% of the impeller radius with different outlet diameters for the same volute. Steady radial forces was calculated from the measured average pressure field and the model over various flow rates whilst the unsteady radial forces was analysed from the pressure pulsations relative to momentum exchange in the impeller, which accounts for the static and dynamic effects of flow. The steady and unsteady radial forces of the blade passing frequency were calculated using the radial integration of the pressure distributions on the shroud side of the volute. The gaps between the sides of the impeller and the lateral walls of the casing means that the effective cross-section of the volute is higher in reality than in the model, which is relative to the tongue region in that it accounts for positive (for low flow rates) or negative (for high flow rates) flow exchange through the radial gap that contributes to a reduction in pressure difference across the tongue gap. The pressure fluctuations of the blade-passing frequency can predict the radial forces that are similar to unsteady forces, which when aligned produces a radial force directed towards the volute tongue position. The results showed that the difference in tongue gap did not create impingement on the pressure fluctuations. The findings found that for the larger diameter although there are unsteady forces present, at the blade passing frequency there is 10% increase therefore as the impeller diameter decreases, there is a much higher increase in unsteady forces exerted than that of the larger diameter at higher flow rates. Since the effects of radial forces have been established in this study on the impeller size, with the volute tongue as a key factor in conducting specific calculations during this study, further improvements can be made by focussing on the instantaneous influence of the impeller blade position with the volute tongue.

Mentzos et al. (2014) numerically studied the evolution of the velocity profile as the impeller passes in front on the volute tongue of a centrifugal pump [41]. CFD had been employed to conduct this investigation using Gambit® for the geometry and meshing, and Fluent® for setup and calculation. The pump geometry employed in this study had a gap of 30% of the impeller outer radius between the impeller exit and the tongue, six full blades and six splitter blades on both impellers: one with an outlet vane angle of 20° and the other with 35°. Three-dimensional steady flow had been simulated using RANS equations and standard k- $\epsilon$  turbulence model with SIMPLE algorithm. The results for both impellers depicted that as the blade passed the tongue, the pressure decreased and as the blades moved away, the pressure increased. The impeller exit showed high velocities in the pressure side of the blade passages and zero velocities in the suction side facing the volute tongue. There had been no recirculation shown in the case of the impeller with the outlet vane angle on 20°, but there had been recirculation exhibited in the case of the impeller with the outlet vane angle on 35°. The recirculation region in this case had been depicted in the suction side of the blades as they moved towards the tongue region. As the blades moved away from the volute tongue, the flow appeared to reattach on the surface of the blades. This study had only been investigated at a single operating speed of 1400rpm. No work on how the velocity profile evolves across each volute profiles and how this would affect centrifugal compressors throughout different operating ranges.

### **2.3 Volute Design Methodologies Performance and Losses**

Weber and Koronowski (1986) analytically investigated the mean-line performance prediction of volutes in centrifugal compressors, which had been validated against previous test data undertaken by Elliott Company's European affiliate, Thomassen Holland [25]. The authors created twelve test cases whereby ten were internal volutes, one was an external volute and one was a plenum. The authors identified the requirement for a loss coefficient expression from the inlet to the outlet of the volute in terms of efficiency. There are four sources of head loss exhibited throughout the volute: meridional loss; skin friction loss; exit cone loss; and tangential velocity dump loss. New models for exit cone head loss and tangential velocity dump loss were derived and compared against the old loss models. The results identified that although both loss models displayed poor correlation against the test data, the new model matched closer than the old model. The new exit cone loss coefficient model significantly decreased the occurrence of negative tangential velocity dump loss values from the test data. In addition to this, the superiority of the new tangential velocity dump loss

model had been made evident for  $SP < 1$ . Furthermore, the authors discovered that the new models for  $SP \geq 1$  displayed minor improvements, though providing a solid base for future generalisation in differentiating between volutes that are created using various engineering design methods, such as Conservation of angular momentum (CAM); CAM with friction; or Simple Area Schedule (SAS), etc. Moreover, the authors concluded that the equivalent sizing parameter (SP) concept for volute performance prediction based on a concept from volute design is a valuable parameter to compare the tangential velocity dump loss against the test data. There has been no expression established for using the CAM with friction method for volute design to determine the effect on the magnitude of losses.

Qi et al. (1996) conducted an analytical and experimental study in using a two-dimensional inverse method to achieve a new approach to the design of fan volute profiles [44]. This paper confirms that in general, there is only one optimal volute profile that enables the system to achieve optimal performance. It is one where there is a direct relationship between the volute profile and the volute inlet flow. In traditional methods for designing the volute it is assumed that the flow is uniform at ideal conditions, however this investigation was undertaken in order to understand the non-uniform distribution of flow laws and parameters that are involved at the volute inlet when various volutes are matched with the impeller. This study was undertaken by using some basic assumptions and the governing equations, followed by implementing a numerical procedure whereby the volute inlet parameters are controlled in order to calculate the volute profile. The findings discovered that using non-uniform flow parameters showed a significant improvement in volute design that has high potential for being used in engineering applications. Unfortunately, due to the author's limited resources available the study required further work in order to achieve the optimal volute profile since the optimal distribution of volute inlet flow could not be determined. This work presents the methodology of how parameters can be controlled to achieve the goal of the study, along with the assumptions and considerations to be made. No expression for volute design considering friction effects has been established.

Pan et al. (1999) carried out a numerical and experimental study on the design considerations for the volutes of centrifugal fans and compressors [45]. In this study the volute design has been developed to accommodate for the asymmetric (overhung) type volutes. This design uses the expression as that derived by Eck (1973), given by:

$$r = \sqrt{\frac{\theta R_c q_v}{360\pi C_{u4} r_4} - \left(\frac{\theta q_v}{720\pi C_{u4} r_4}\right)^2}$$

For symmetric volutes,

$$R_c - r = r_4$$

For asymmetric volutes,

$$R_c - r \neq r_4$$

For the asymmetric volute, the overhang magnitude is defined by:

$$\delta = r_4 - (R_c - r)$$

It is specified as the linear function of the azimuth angle and is stated to accurately describe the overhang of the volute:

$$(R_c - r) = a + b\theta$$

Where  $r_4$ ,  $a$  and  $b$  are constants.

The purpose of this investigation was to improve the volute performance characteristics over a wide range by modifying the volute geometry. Three test cases were analysed: one asymmetric circular cross-section volute, and two asymmetric square cross-section volutes with one having a larger flow area under the tongue. The asymmetric circular cross-section model had been analysed through experimentation and two square cross-section volutes had been analysed through CFD. The results established that by increasing the flow area in proximity of the tongue region improves the volute performance. This reduces fluctuations in pressure and flow with the wrap angle as well as showing improved vaneless diffuser performance of upstream of the volute. There has been no consideration of frictional effects in this investigation.

Miyanga et al. (2001) investigated the volute tongue and passage design on the performance of centrifugal turbomachines [46]. This was carried out by analysing the size influence of the recirculation port as well as the tongue design on the volute performance through experimentation. The volute was designed using the same expression as the previous study, as that derived by Eck (1973). The overhang magnitude was also specified and computed in the same manner. The volutes constructed for this study were as follows:

FA: A turbocharger volute designed using the basic free vortex method with full tongue, no recirculating port.

FC: Same design method as FA but with a recirculating flow port.

NA: A modified passage design using a method that applied a high flow angle at small azimuth angles.

NC: Same design as NA but with a recirculating flow port.

FCT: A modification of design FC consisting of rounded tongue geometry at the inlet to the recirculating flow port.

FCT2: Same as design FCT, with rounded tongue geometry, but with a reduced recirculating port area to reduce the frictional loss of the recirculating flow.

The results established that by constructing a recirculation port does improve the performance of the volute; however it is only the case for symmetric designs where the nature of the swirl flow are set with two counter-rotating vortices rather than overhang designs as carried out in this study, where the nature of the swirl flow generates a single passage vortex. Therefore, by using a symmetric design for the volute geometry would increase blockage, and through modifying the design to also increase the passage area, would be an effective means of improving the performance. Furthermore, there was impingement occurring on the volute performance at high flow rates due to the design of the tongue's leading edge. It was discovered that a rounded tongue design decreases the amount of flow separation and magnitude of the wake in the volute exit, and flow in the recirculation passage was analysed as being additionally systematic. There has been no consideration of frictional effects in this investigation.

Additionally in 2002, Whitfield et al. investigated the effect of volute design on the performance of a turbocharger compressor through experimentation using three fabricated turbocharger compressor volutes (two bigger and one smaller than the original cast), where the radius of the volute passage was calculated as a function of the azimuth angle using a derived equation [47]. The volute was designed using the same expression as the previous study, as that derived by Eck (1973). The area profile of the volute was modified by keeping the same minimal areas at the tongue and modifying the area leading to the volute exit. The results showed that the 25% larger volute had an improvement in performance throughout the operating range, whilst the smaller volute had a smaller discharge area, which indicated poor performance at high flow rates, due to the high levels of flow separation from the leading



edge of the tongue. It was found that the size of the volute has a direct impact on the stage performance of the turbocharger compressor, more predominantly at high mass flow rates. As the volute size reduced, the stage efficiency and pressure ratio had decreased at high flow rates, and if the operating efficiency limit is fixed, then this has a significant reduction in operating range as the size of the volute decreases. Therefore, the smallest volute size showed better performance in terms of pressure ratio and efficiency. The design of the volute also had an influence on the performance upstream of the vaneless diffuser with the original cast. This exhibited maximum pressure recovery coefficient, while the fabricated volutes showed a progressive increase throughout the flow range, however, when reaching to high flow rates, this increase was very slight. There has been no consideration of frictional effects in this investigation.

Phuong et al. (2002) carried out a two part analytical study. The first part describes a new volute design system for centrifugal compressors by Bezier application, specifically, B-spline and Bezier polynomials [48]. The findings report that any desired industrial component can be defined accurately using the developed code. The authors have demonstrated the success of the code to generate 2D and 3D cross-section models of the volute with parameters defined by the user. Automated mesh generation code has also been developed producing structured grids of high quality. It is stated that volutes are to be designed in accordance to the designer needs instead of geometrical categories. The developed code can produce over 95% volute designs with ease, allowing parametric studies to be carried out. [49] The second part describes the design methodology of the developed codes for centrifugal compressor volute design. The findings were positive in that the design methodology is effective and efficient with high quality structured mesh. The tool correlates directly with CFD and can be used to carry out parametric and optimisation studies. This study however, does not account for losses present in real conditions or the flow characteristics. There is a gap to develop a novel design methodology for centrifugal compressors based on real flow conditions.

Steglich et al. (2008) experimentally and numerically studied the improved diffuser/volute combinations for centrifugal compressors [50]. The authors present simultaneous optimisation of the diffuser and volute. Two modifications have been made: one where frictional losses are reduced between the diffuser and volute by eliminating the wall in between; and the other where the secondary vortex in the volute is weakened by decelerating the radial velocity at the diffuser outlet. The findings report that the asymmetric diffuser presenter slightly higher circumferential pressure variation at the impeller outlet during off-

design conditions, which increases the dynamic loads on the impeller and bearings. Further to this, low solidity diffuser combination with the internal volute depicted pressure ratios and efficiencies near to the combination if a concentric diffuser with and larger external volute. This study manipulates the flow characteristics by modifying the geometry. It is useful to investigate how incorporating certain flow parameters, such as accounting for frictional effects, into the expression is used to design improved and realistic compressor volutes.

Qiang et al. (2010) numerically studied the influence of various volute designs on volute overall performance using CFD by analysing the affected parameters being the volute's cross-sectional area, the shape of the cross-section, radial location of the cross-section, location of the volute inlet, and the tongue geometry [19]. The three various tongue geometries conducted for this sector of the investigation are, at  $45^\circ$ ,  $40^\circ$ , and  $50^\circ$ . The volute was designed using the same expression as the previous study, as that derived by Eck (1973). The overhang magnitude was also specified and computed in the same manner. The results identified that there were variations at extreme off-design conditions such as stall. This is where the difference margin for total pressure loss coefficient and static pressure loss coefficient is approximately 4.9% and approximately 2.4%, respectively. These are smaller when the system was operating near the choke condition. This study established that the optimal performance during design and off-design conditions is of the volute design consisting of medium  $360^\circ$  cross-section radius with  $45^\circ$  tongue angle. There has been no consideration of frictional effects in this investigation.

In 2011, Yang et al. undertook a numerical study on the design of the pump volute using Computational Fluid Dynamics (CFD) to investigate the volute throat region, volute cross-section geometry, design rule of spiral development region, and radial gap between the impeller and volute tongue, which is a sensitive parameter specifically of interest [43]. When this gap is too small, the impingement it creates has an impact on the system in that although it improves efficiency, it however decreases the vibration characteristics and causes cavitation to occur near the volute tongue. By increasing this gap, although it would improve the vibration and cavitation downfalls, it will however, decrease the efficiency of the system. This study researched radial gaps of between 5mm to 20mm where the optimal distance with the highest efficiency was achieved at 15mm, being  $0.053 \times$  the impeller diameter, or the volute base circle diameter is  $1.107 \times$  the impeller outlet diameter. Furthermore, as the radial gap increases the pressure head and shaft power variation is excessively small and when the

gap is 20mm the head starts to decrease. The optimal radial gap has been determined with the highest efficiency. The gap in this study is to explore the instantaneous flow behaviour of the centrifugal compressor with respect to the volute design and the head loss incurred.

In 2012 and 2013, Mojaddam et al. carried out an experimental and numerical study investigating the effect of centrifugal compressor volute cross-section shape on performance characteristics and flow field [1, 51]. For the volute design method, the authors employed some basic principles and assumptions on the basis of neglecting friction. The conservation of angular momentum which is also known as the free vortex law is defined as:

$$r_c C_c = K$$

This states that the flow velocity at the location of the radius centroid of the cross-section maintains at a constant.

Assuming that from the diffuser exit there is equal distribution of tangential flow at any given circumference, where  $\theta = 0$  to  $2\pi$  giving:

$$\rho_c C_c A_c = \frac{\theta}{2\pi} \dot{m}$$

Furthermore, assuming the gas density is constant since the Mach number is low providing the following approximation for the desired cross-section as a function of  $\theta$ :

$$\frac{A_c}{r_c} = \dot{m} \frac{\theta}{2\pi \rho K}$$

When considering friction, the flow inside the volute causes total pressure loss which is also determined by friction head loss, given by:

$$dh = c_f \frac{C_{av}^2}{2g} \frac{dL}{D_h}$$

Where  $h$  is the head,  $c_f$  is the friction factor,  $C_{av}$  is the average flow velocity,  $D_h$  is the hydraulic diameter and  $dL = r_c d\theta$ .

The other cross-section increments are calculated using the principle of the continuity equation, given by:

$$A_1 C_1 = A_2 C_2$$

And the Bernoulli equation, given by:

$$\frac{p_1}{\rho g} + \frac{C_1^2}{2g} = \frac{p_2}{\rho g} + \frac{C_2^2}{2g} + h$$

$$h = \frac{C_1^2}{2g} \left[ 1 - \left( \frac{A_1}{A_2} \right) \right]$$

The authors modified the volute shape by altering the shape factor,  $a$  where  $H = ar$  and  $W = r/a$  with  $H$  denoting the height and  $W$  denoting the width, and  $r$  denoting the radius of the volute cross-section. Altering this shape factor has an effect on the horizontal and vertical ellipse with the constant area.

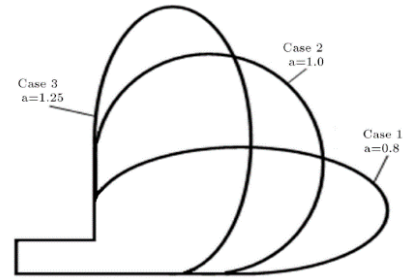


Figure 2.1 Volute Cross-Section Shapes[1]

Three asymmetric centrifugal compressor volute test cases were designed for the investigation. One test case had shape factor of 0.8 for horizontal ellipse cross-section; another test case had shape factor of 1 for circular cross-section; and the last test case had shape factor of 1.25 for vertical ellipse cross-section as shown in. The radius centroid for determining the overhang magnitude had been given by:

$$R_c = r_4 + 0.475W$$

The numerical study generated these geometries and employed unstructured tetrahedral mesh elements consisting of refinements at the tongue regions due to steep gradients. The results state that all cases almost have the same values for the compressor performance characteristics. Additionally the elliptical cross-section volute (case 3) exhibits improved performance, total pressure ratio and total-to-total isentropic efficiency in comparison with the other cross-section volutes. Moreover, it was identified that there was less static pressure non-uniformity around the impeller compared to the other cases at low mass flow rates, and case 2 identified as causing the least amount of net radial force on the impeller as a result of circumferential pressure non-uniformity. The numerical data was validated against the experimental, which identified good agreement. There has been no expression established for the volute design incorporating friction as a parameter.

Shyam and Vithuraj (2013) developed a Mathcad tool that can create 3D structures of centrifugal air compressor volutes from cross-sectional profiles that can be imported into any

CAD software for modelling [52]. The authors generated six different profiles with the assistance of suitable algorithms. These cross-sectional volute profiles are: (i) Rectangular External; (ii) Rectangular Semi-External; (iii) Elliptical External; (iv) Elliptical Semi-External; (v) Circular External; (vi) Circular Semi-External. The algorithms provide geometrical properties and 3D co-ordinates for the full-collection plane for each volute type. For the two rectangular profiles, there are also these algorithms separately for the exit cone. For the outputs, the Mathcad software converted the algorithms into programs for each volute, thus 24 programs were created for the six volutes, which was combined together as a single Mathcad file. A program known as Choice was added to enable users to select between the six volutes. The output program comprises of 12 parts. These are: (i) Full Collection Plane Geometrical Properties; (ii) Coordinates for the Full Collection Plane; (iii) Exit Cone Geometrical Properties; (iv) Length of the Exit Cone; (v) Coordinates for the Exit Cone; (vi) Area Variation of Full Collection Plane; (vii) Circumferential Area Increase of Full Collection Plane; (viii) Radial Orientation of Full Collection Plane; (ix) Variation of Full Collection plane around Diffuser; (x) 3D Contour Plot of the Volute; (xi) Variation of the Exit Cone; (xii) Radial Orientation of the Exit Cone. The results were authenticated and validated using a commercial software COMPAERO©, which showed that tool was an excellent match and successfully developed. No expression has been established for the volute design incorporating friction effects.

Doustmohammadi et al. (2013) conducted experimental and numerical investigation of losses in centrifugal compressor components [26]. The losses in each component were studied separately and the decrease in compressor efficiency for various mass flow rates and operating speeds has been captured. The volute loss has been predicted using the correlation of enthalpy and entropy. The enthalpy loss calculation is given by:

$$\Delta h_{loss} = K \frac{C_4^2}{2}$$

Where K has been recommended to be a value of 0.5, thus the entropy gain factor from the volute inlet to the volute outlet is denoted by:

$$\sigma_{45} = \left( 1 - \frac{\Delta h_{loss}}{C_p T_3} \right)^{\frac{\gamma}{\gamma-1}}$$

For this study, the authors have used a 1D model to predict the compressor characteristics since it was believed to have reasonable accuracy and reduced simulation time. Unfortunately, the results discovered that the flow structure could not accurately be captured in the volute since the flux within this component is complex and three-dimensional. The results have identified that the volute is the second prime source of entropy generation after the impeller. The numerical data was validated against the experimental results, identifying good agreement. The head loss throughout the centrifugal compressor volute could be integrated as a parameter into the expression for a realistic volute design.

Following from this, in 2014 Mojaddam et al. carried out an experimental and numerical investigation of radial flow compressor component losses [53]. Since 1D and 2D was discovered to be of limited interest due to the unreliability of results, a 3D model was employed into this study using unstructured tetrahedral mesh elements with refinements at the tongue region and inflation layers on the impeller and at the volute inlet and outlet boundaries in order to capture the flow in proximity of the walls. The results identify that the total pressure loss coefficient for the volute reduces down to its lowest value at the maximum efficiency at low mass flow rates, and then rises to its highest values at high mass flow rates. It has also been discovered that at low mass flow rates, there is a constant increase in static pressure due to the volute construction being excessively large for low mass flow rates, thus operating as a diffuser. Conversely, at high mass flow rates, the flow accelerates and results in a pressure drop due to the volute being excessively small to allow high mass through-flow, thus operating as a nozzle in a circumferential direction. The numerical data was validated against the experimental results, identifying good agreement, though the variation between the two is said to be due to leakages among the components, effect of heat transfer and roughness. Given this, there has been no consideration of frictional effects or head loss in this investigation.

In 2014, Mojaddam et al. conducted an experimental and numerical study on the optimal design of the volute for a turbocharger radial flow compressor [54]. This investigation focuses on the identifying the optimum values for the effective parameters of the volute; being the exit cone, tongue, and the cross-sectional area of the scroll. This was undertaken by modelling different volutes with the same impeller and vaneless diffuser. The authors created six asymmetric volutes where one had been designed using the Stepanoff model, three had been designed using the Pfleiderer model and two had been designed using non-constant

angular momentum. The overhang is generated through the ratio of area centroid and radius centroid, given by:

$$\frac{A_c}{R_c} = \frac{r^2(1 + 3\pi/4)}{r_4 + r(1 + 1/9\pi)}$$

The cross-section shape is comprised of three quadrants of circular arcs and the fourth quadrant being a square. The velocity field at the diffuser exit is required for the design. The tongue areas investigated had been at tongue angles of 32.9° (reference), 35°, 37°, 40° and 43°. A 1D code had been developed by the authors to predict the flow characteristics at each station of the compressor, which had been validated by the experimental data. Using this, the mean radial and tangential velocity components had been extracted at the vaneless diffuser exit at the mass flow rate design point. These models had been analysed at design and off-design conditions. The results confirm the geometries that affect the volute performance are the throat, cross-sectional area, exit cone opening and tongue location. In order to analyse the overall performance, the authors investigated the total pressure ratio, static pressure recovery, total pressure loss coefficient and radial force on the impeller for different mass flow rates at each design point and off-design condition, which had been calculated. The results depicted good performance at design and off-design conditions on the volute designed using the Pfleiderer model with its constant at 0.5, which showed an almost linear area distribution. This model depicted the highest performance and causes lowest net radial force on the impeller at desired mass flow rates. Additionally, it was found that if the pressure ratio is improved and total pressure loss is reduced, it can cause an increase in radial force on the impeller and provide poor results at off-design conditions. Furthermore, an increase in tongue angle results in approximately 7% total pressure loss and decrease in pressure recovery of approximately 2%, which shows that altering the tongue geometry at design mass flow rates leads to a decrease in volute performance. Moreover, the optimum values for the volute geometry was discovered to be at 10° for the exit cone opening, 43° round tongue angle, and at 360° for the cross-sectional area of the scroll. Although this study determined the optimum values for volute design, there has been no consideration of friction in the design to compensate for losses for a turbocharger compressor stage, which would provide realistic solutions.

Zhou and Lee numerically compared the performance between two types of three-arc overhung volute for an automobile turbocharger compressor in 2014 using ANSYS CFX

[55]. Overhung volute has been selected for this study since they are commonly used to restrict the radial space needed for gaining entrance to the rear face of the compressor, where the bearing housing is attached via a flange or a clamp. The author states the volute performance falls due to swirl velocity since radial velocity cannot be recovered at the exit of the diffuser. This results in radial velocity losses due to the shape change of the volute cross-section, which in turn, becomes the swirl velocity component. Since the swirl velocity component is responsible for radial velocity loss, friction loss and heat, the authors aim to reduce swirl losses in this study. In addition to this, the authors also aim to achieve high pressure recovery and low pressure loss. All these factors are focussed on to improve volute performance. The authors have conducted this study with two volutes. The first volute consists on radially long cross-section, while the second volute consists on axially long cross-section, both comprised of 3 arcs. The results depicted that the second volute exhibited more uniform pressure and velocity distribution through all cross-section, including the tongue region. Additionally, the second volute showed higher static pressure recovery and lower total pressure loss. Furthermore, even though both volutes did not perform well at off-design conditions, the second volute still identified higher volute performance through all flow rates compared to the first volute. The gap in this study is to identify the energy losses through the centrifugal compressor volute to gain a better understanding. Lv et al. (2015) numerically investigated the design of volute shape of centrifugal fans [42]. Three models had been studied: original fan (OF); modified fan with area constraint (MF); and modified fan without area constraint (MFW). The authors had developed a multi-objective genetic algorithm in MATLAB to determine the volute radius of a centrifugal fan to achieve improved performance under variable working conditions. The authors developed an equation based on three assumptions: the flow inside the volute is stable; fluid viscosity has been ignored because viscous force is very small with respect to the inertial force; the effluent speed of the fluid from the impeller is uniform. The equation that had been developed for the volute radius profile, applicable when designing without considering the performance under variable working condition is:

$$R_\phi = R_2 e^{\frac{Q}{2\pi B C'_{2u} R_2} \phi}$$

Where,  $Q$  is the designed flow (m<sup>3</sup>/s);  $B$  is the volute inlet width (m);  $C'_{2u}$  is the circumferential velocity at the impeller outlet (m/s);  $R_2$  is the impeller radius (m); and  $\phi$  is the



rotation angle (rad). When designing to take the variable working condition as a performance consideration, the equation for modified volute radius profile is:

$$R'_{\varphi} = R_2 e^{\frac{\phi Q}{2\pi BC'_{2u} R_2} \varphi}$$

Where,  $\varphi$  is the flow rate correction coefficient given by:

$$\phi = \left( K_1 \frac{\varphi}{2\pi} \right)^{K_2}$$

Where  $K_1$  and  $K_2$  are the optimisation parameters determined under the effects of variable conditions found through integration. The three centrifugal fans had been modelled and CFD based analysis had been used to compare the performance and verify the validity of the proposed design system. The results concluded that the volute designed with modified area constraint (MF) depicted the highest efficiency with stable static pressure under variable working conditions. The original fan (OF) depicted leakages and losses at the volute tongue; with large vortices and prominent static pressure fluctuations at the outlet. The MF volute demonstrated prevention of fluid leakage from the outlet to the volute tongue with smaller vortices and suppressed secondary flows. The authors stated that in-depth analysis of dynamic characteristics with the optimised fan volute is in demand under transient conditions. There has been no consideration of friction, which can be implemented with centrifugal compressors.

Henrich and Swarze (2015) presented a numerical investigation on a scripted CFD tool for the automated design of volutes for centrifugal compressors [56]. The authors used C++ to create a script for generating the volute design, which is represented by B-splines as a function of the azimuth angle. The purpose of this script is to have the freedom to easily adjust the volute geometry in order to produce large variations, optimisations and design parameters automatically without a manual design process. The authors also investigated the effect of volute tongue radius on the overall performance. The shape of the volute had been divided into three parts: radial diffuser; volute; axial diffuser, having 11 parameters within these three parts. Representations of the volute geometry have been made by a third order spline using eight knots each. By adding more knots to the spline can achieve the generation of more complex geometries. Three models had been created for this study to investigate the volute flow using OpenFOAM: complete model comprising of the inlet, impeller and volute; simplified model comprising of impeller and volute; and the volute-only model. The volute

tongue radius and cross-section shape had been investigated with the volute-only model. The radii studied were 1.5mm and 5.5mm, respectively. The results depicted that there had been only 2% difference between the complete model and simplified model, indicating the inlet does not play a very important role in the volute flow. The influence of shape showed that symmetric cross-sections performed the weakest, having lowest pressure recovery and highest pressure losses. The asymmetric cross-sections showed improved performance with one slanted circular cross-section, having higher pressure recovery and lower pressure losses. The authors have suggested additional work to be undertaken via optimisation study to determine the optimal volute shape. For the investigation sector of the tongue radius, it had been discovered that the small tongue radius had no influence on volute performance at small cross-sections; however at large cross-section, the larger radius indicated improved performance since the separation at the tongue region had been suppressed. The scripted CFD tool has not been presented in the article and surface roughness has not been considered in the study.

Tanganelli and Cencherie (2018) investigated loss generation mechanisms inside different centrifugal compressor volutes for turbochargers [5]. The authors have observed the sources of thermodynamic irreversibilities inside different compressor volutes. The three cases investigated are circular symmetric with “ideal” shaped tongue, which allows flow to be collected at  $\theta = 0^\circ$  where the area of the volute is very small; circular symmetric without tongue; and elliptical asymmetric. The authors carried out this investigation at three mass flow rates, namely, low, design and high. The results analysed the loss indicators, total pressure loss and entropy generation in the three volutes. It had been found that using only total pressure fields would lead to incomplete considerations, therefore using entropy generation rate to emphasise on the significance of evaluating losses, accurately allows the irreversibilities to be localised. Further to this, it had also been found that it was not possible during the investigation to determine if the low pressure areas are characterised by a local source of loss, or if it is the sum of upstream losses experienced by the fluid. Since this study focused on the total pressure loss and entropy generation, it is useful to investigate the other flow characteristics and its behaviour in volutes with different cross-sections.

## 2.4 Scope of Research

Knowledge for defining a realistic expression to design a centrifugal compressor volute for a turbocharging application is severely limited. The expression that is currently available is an approximation derived originally for a symmetric type circular cross-section volute for a fan application assuming ideal conditions. Researchers are generally implementing this approximation upon various cross-sectional geometries for the design of centrifugal compressor volutes, including the overhung type.

Majority of the research is carried out regarding volutes are on centrifugal pumps and centrifugal fan applications rather than on centrifugal compressors. It therefore, becomes difficult to monitor and analyse predicted flow structure for a turbocharging application where alternate phenomena and additional components are at work. Although all three volute are designed using the same principles, the application for the volute differs according to the system. With the introduction of modern computational tools and sophisticated software to model and simulate fluid flow in turbomachinery, there is great potential to study the complex flow structure within a turbocharger compressor stage focusing predominantly on the volute. Extensive literature review has suggested the designing a centrifugal compressor volute should focus on evaluating the flow structure and pressure losses around the volute, as well as the interaction between the impeller and volute [1, 10, 19, 57, 58]. Based on the review of published literature, key areas for the volute design methodology have been discovered.

The first area explores the flow mechanics inside the turbocharger compressor stage and its volute. This is carried out by numerically simulating the steady response at design and off-design conditions. Global analyses are carried out to understand the flow structure across the entire turbocharger compressor stage and local analyses are carried out to understand the flow structure inside its volute. In order to understand the flow features at design and off-design conditions, this sector of the study explores the flow field at low operating speed and high operating speed at low flow rate, design flow rate and high flow rate.

The second area explores the interaction between the impeller blade positions with respect to the volute tongue. This is carried out by numerically simulating the instantaneous response, analysing the centrifugal compressor stage and its volute. Global analyses are carried out to understand the flow structure across the entire turbocharger compressor stage and local analyses are carried out to understand the flow structure inside the volute. Since volutes are

designed to design conditions, this sector of the study explores the flow field at low operating speed and high operating speed at the design flow rate.

The third area investigates various volute cross-sections for the centrifugal compressor. The centrifugal compressor volute has been designed to ideal conditions and actual conditions. The volutes designed to ideal conditions neglect frictional effects in its design approximation, while the volutes designed to actual conditions incorporate frictional effects into its design approximation. The existing approximation for the volute is employed as the base for the derivation of a symmetric volute expression incorporating frictional effects as a parameter to account for 'real' conditions. In order to achieve this, an iterative method is used to match the pressure head at the volute. Following on from this, the same approach has been taken to develop a methodology for designing an asymmetric volute since this volute type are commonly known to achieve optimum performance. This final model is compared and evaluated against that which currently exists. This sector of the study focuses on the novel design methodology; hence this investigation has been carried out on the design flow.

## **2.5 Research Objectives**

1. Analyse the flow characteristics of the turbocharger compressor stage and its volute at design and off-design conditions at low and high operating speeds during steady response.
2. Analyse the flow characteristics of the turbocharger compressor stage and its volute at the design conditions of low and high operating speeds during instantaneous response, focussing on the effect of impeller blade position with respect to the volute tongue.
3. Develop a design methodology for symmetric type turbocharger compressor volutes of various cross-sections neglecting frictional effects and incorporating frictional effects, as well as asymmetric type turbocharger compressor volute incorporating frictional effects.
4. Analyse the flow characteristics of the symmetric type centrifugal compressor volute with various volute cross-sections and investigate the incurred energy loss through the volute during steady response.

5. Analyse the flow characteristics of the asymmetric type centrifugal compressor volute, investigate the incurred energy loss through the volute and compare this model with the original existing model during steady and unsteady responses.

The next chapter discusses details of the numerical methodology employed throughout the present study for achieving the above objectives.

## CHAPTER 3

# NUMERICAL MODELLING OF THE TURBOCHARGER COMPRESSOR STAGE

---

On the basis of the research objectives that have been formulated in the previous chapter, advanced Computational Fluid Dynamics (CFD) techniques have been used to computationally simulate the turbocharger compressor stage. This chapter documents various stages involved during numerical investigations. It includes the pre-processing stage, detailing the geometry and mesh of the system; the solver execution stage, detailing the solver-settings, boundary conditions that have been specified, turbulence modelling, discretization, convergence criteria; and the post-processing stage, detailing the locations of data extraction for analyses carried out in this research study.

### 3.1 Numerical Methodology

The numerical investigation of this study has been undertaken using Computational Fluid Dynamics (CFD) based tools that uses complex algorithms and iteratively solves the numerical equations governing the fluid flow in systems dictated by specified boundary conditions. Further details on CFD are described in APPENDIX 1.

This section will focus and elaborate on the working principles of using CFD; the governing equations relative to this project; pre-processing involving the geometry and meshing of the volute designs; and the solver execution stating the boundary conditions and numerical parameters setup for the models.

FLUENT v.17 is a commercial code used for Computational Fluid Dynamics (CFD) based analysis due to its simplicity, ease of use and polyhedral meshing capabilities, which provides efficient simulation time with high levels of accuracy in the results achieved. During this investigation, FLUENT v.17 has been used to solve a compressible flow based problem within a turbocharger compressor stage. This flow problem involves both, rotating and stationary domains within a turbocharger. For steady state conditions, Multi Reference Frame (MRF) approach is used to define the motion of the impeller blades since this is the rotating domain of the turbocharger. This approach however, does not resolve the transient effects i.e. flow interactions with the impeller blades. Therefore, for transient conditions, Sliding Mesh (SM) approach is used whereby flow interactions with the moving blades of the impeller can be simulated and investigated.

### 3.2 Pre-Processing

The pre-processing in CFD is partitioned into two main classifications, which are the creation of the geometry and the meshing of the flow domain. This section provides details of the geometry and the meshing of the turbocharger compressor stage using FLUENT in the ANSYS Workbench.

#### 3.2.1 Geometry

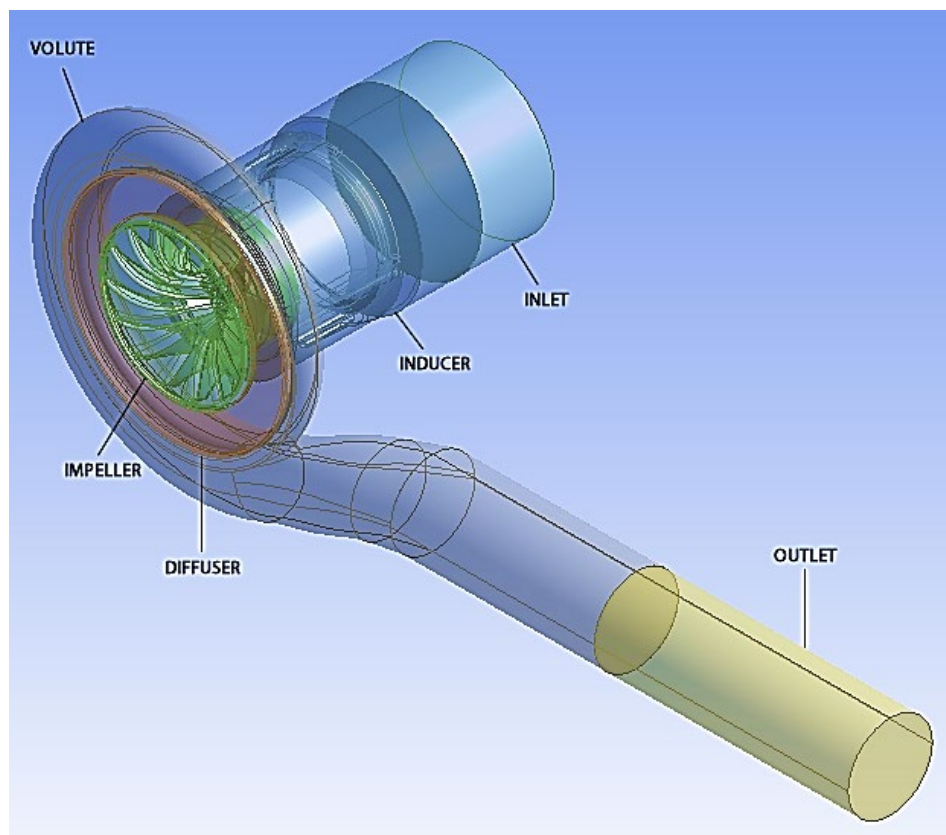
Figure 3.1 depicts the geometry of the turbocharger compressor stage which had been provided by Cummins Turbo Technologies as .igs file. In Design Modeller of the geometry stage, the model had been separated by creating two sketches. This enabled specific mesh sizing to be set for various components and faces. It also enabled the impeller to be set as “rotating” in the solver whilst other components remained as “stationary”.

Inlet and outlet extension pipes had been created at the inlet and outlet of the compressor stage. The purposes for installing these extensions are to ensure that fully developed flow at the compressor stage inlet and outlet are achieved during numerical simulation. The length of these extension pipes have been calculated on the basis of the flow type for its given application. According to theory, for turbulent flow the extension length is approximated at [27]:

$$L_{turbulent} \approx 10D$$

*Equation 3.1 Extension Length Approximation*

However for this application, such long extensions are no needed since there is negligible variances in results achieved. Therefore these extensions have been designed in correspondence with that of the company. The length of inlet extension upstream of the turbocharger compressor stage has the axial length of the impeller, whilst the length of the outlet extension downstream of the turbocharger compressor stage has the length of  $3D_{out}$  which is suffice to obtain the most accurate boundary conditions with a reasonable velocity profile and with minimal numerical flow instabilities.



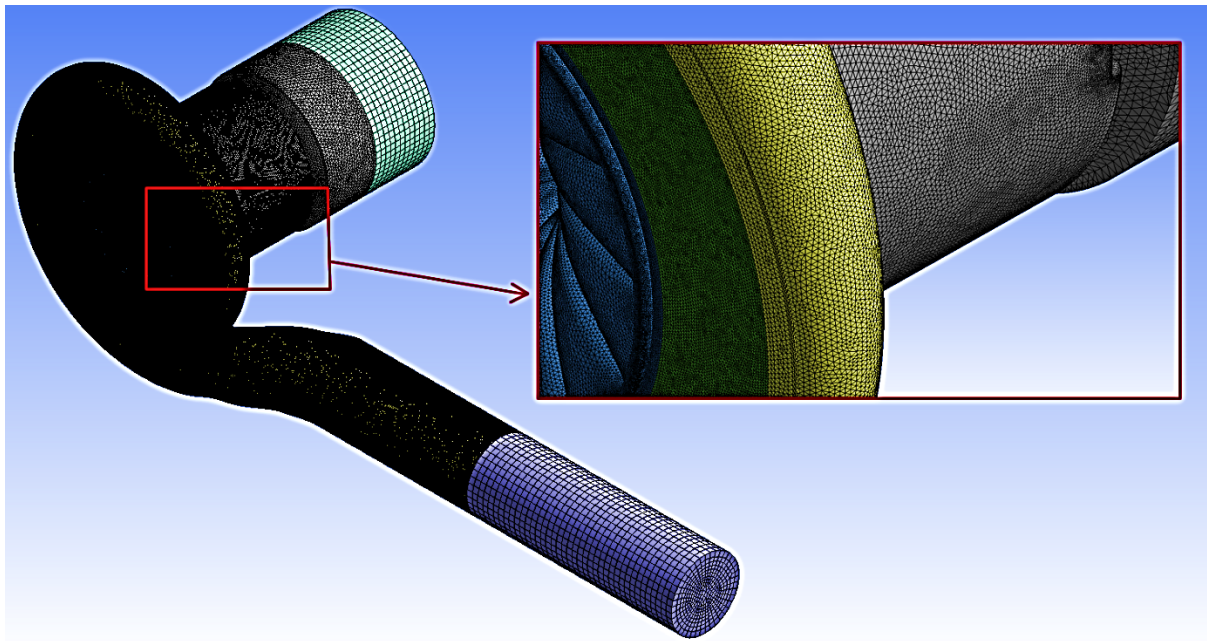
*Figure 3.1 Turbocharger Compressor Stage Geometry in ANSYS Design Modeller*



### 3.2.2 Meshing

There are six bodies within the geometry, namely being, inlet; inducer; impeller; diffuser; volute; outlet. Named selections had been set on every face of the turbocharger compressor stage assembly.

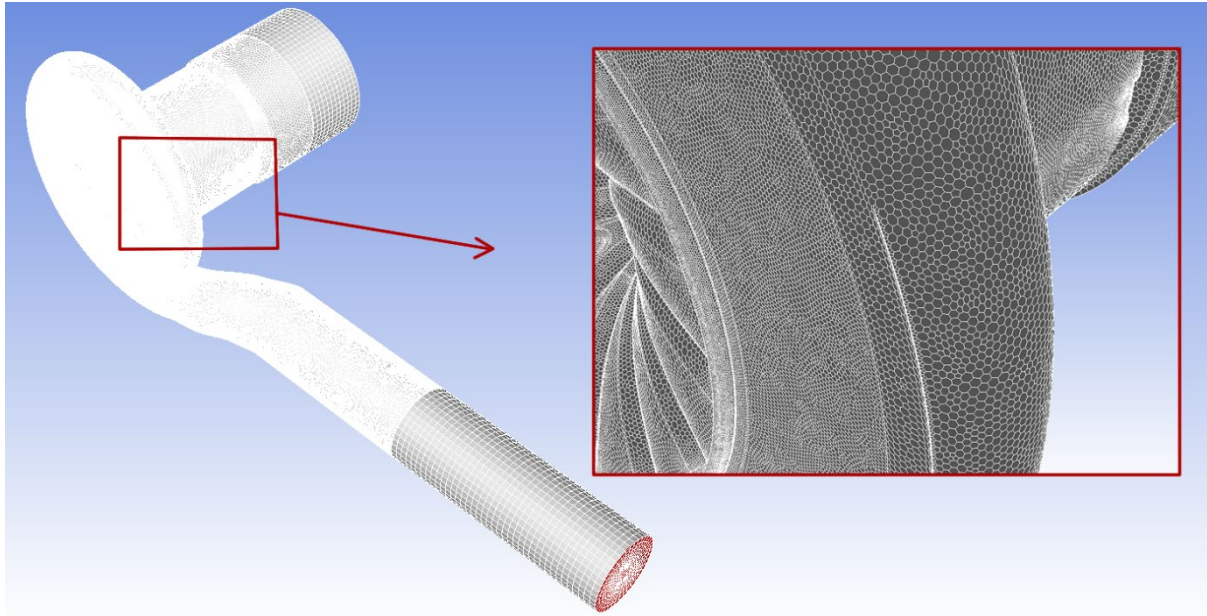
The mesh element size set for the blades, blades-leading-edge, blades-trailing-edge are 1mm; blades-tips are 0.2mm; impeller hub is 1mm; diffuser is 0.5mm; volute is 0.8mm; volute-tongue is 0.2mm; shroud is 0.2mm; shroud-blind is 0.2mm; recess is 0.5mm; SRCT is 1mm and inlet duct is 2mm. In order to achieve superior mesh quality, the global mesh was set as fine, medium smoothing, slow transition and curvature size function with a growth rate of 1.1. The minimum global mesh size was set at 0.2mm, whilst the maximum face and mesh sizes are set at 4mm. Having specified these mesh sizes resulted in 20million mesh elements. This initial tetrahedral mesh on the compressor stage and hexahedral mesh on the extensions are displayed in Figure 3.2.



*Figure 3.2 Mesh Generation in ANSYS Meshing*

After reaching this stage, the mesh had been exported into FLUENT and converted into polyhedral elements as displayed in Figure 3.3. Using polyhedral mesh elements demonstrated benefits of being able to use higher number of ANSYS Meshing elements with good accuracy and significantly less time consumption. This was possible since the number of elements in the initial mesh had been reduced by a considerable amount. For example, 20

million tetrahedral and hexahedral meshing elements converted into only 4 million polyhedral elements.



*Figure 3.3 Conversion to Polyhedral Mesh in FLUENT*

The mesh independence study had been carried out at the BEP of the experimental data, as shown in Figure 3.4. It became evident there were negligible variances after 4 million elements and had the least variation in pressure ratio and isentropic efficiency against the experimental data. For these reasons, 4 million elements had been selected to be reasonable for pursuing this research study.

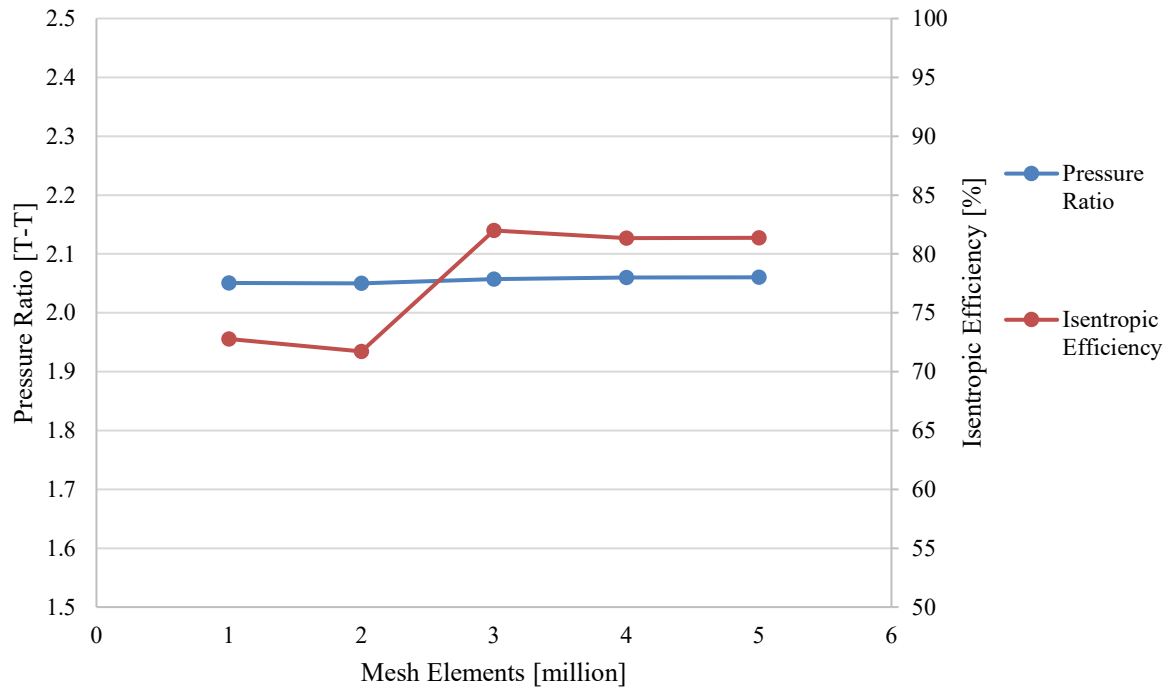


Figure 3.4 Mesh Independence Study

### 3.3 Solver Execution

The commercial code for solver execution used in the present study is FLUENT v.17. The details of the settings implemented on the numerical analysis are presented in this section.

#### 3.3.1 Solver Settings

The solver settings are set enabling reasonably accurate calculations and predictions for the flow fields. In solver control, the equation class were set for continuity, momentum and energy with Green Gauss Node Based Second Order advection scheme and convergence criteria of  $1e-06$ . For the unsteady cases, second order implicit method has specified for the transient formulation.

#### 3.3.2 Boundary Conditions

Reviewing back to Figure 1.7 it can be seen there are six points per speed line. The inlet, inducer, diffuser, volute and outlet are stationary parts while the impeller is rotating at various operating speeds.

Operating conditions have been specified as 0 atm. Pressure has been selected for the outlet boundary condition, while mass flow rate has been selected for the inlet boundary condition with total temperature of 288K. The values specified for the boundary conditions are respectively to the design point for the operating condition provided by the company. Turbulence intensity of 5% has been specified it the inlet boundary condition, and 10% at the

outlet boundary condition as specified by the software guidelines for turbomachine applications [61, 62].

For the compressor stage of the turbocharger, no-slip conditions have been applied at all walls. This means viscous effects causing the fluid to stick to the surface result in zero velocity at the wall boundary. Slip conditions are used where viscous effects at the wall are negligible and/or the mesh is much coarser than the boundary layer thickness. Smooth wall implies there are no protrusions in the wall surface whereas rough wall implies there are protrusions in the wall surface and require this to be specified relative to the sand grain equivalence. If the wall roughness is smaller than the viscous sub-layer then the flow can be considered as hydraulically smooth as its effects are negligible. However, if the wall roughness is larger than the viscous sub-layer, this protrude and destroy the viscous sub-layer and is known as a fully rough wall or hydraulically rough. Calculations can be carried out to determine whether the protrusions are of significant size, which would affect the numerical solution. Equivalence sand grain wall roughness of 8 microns had been specified for walls in the inlet, inducer, impeller, diffuser and outlet domains, and 32 microns for the volute domain. These have been calculated based on the casting data of the original volute and the machined equivalent surface roughness data of the other components. After undertaking some calculations to determine whether the wall roughness would have an effect on the numerical solutions, the results identified transitional roughness. This means protrusions on the surface are slightly larger than the viscous sub-layer, which can cause disturbances and therefore, it has an effect on the flow [63-67].

### 3.3.3 Turbulence Modelling

The turbulence model used is Shear Stress Transport (SST), which is an eddy-viscosity model consisting of two equations that comprises of the “best of both worlds” using a combination of  $k-\omega$  and  $k-\epsilon$  formulations. It is selected to enhance accuracy of flow predictions with extreme adverse pressure gradients and boundary-layer separation induced by pressure [68, 69].

The optimum features of the  $k-\omega$  model are employed through the viscous sub-layer of the boundary since there are no requirements of any damping functions. This enables reliable accuracy for considerably higher numerical stability than the  $k-\epsilon$  model. Additionally, the  $k-\omega$  model is superior to the  $k-\epsilon$  model in that it can be used in its logarithmic sector of the

boundary-layer whereby, its behaviour is exceptional in adverse pressure gradients and in compressible flows [68, 69].

The optimum features of the  $k-\varepsilon$  model are employed in the wake region of the boundary-layer since the  $k-\omega$  model is exceptionally profound to the inlet free-stream turbulence properties. Additionally, the  $k-\varepsilon$  model is superior to the  $k-\omega$  model in that it can be utilised in the free shear layers as it characterises a reasonable compromise in accuracy for wakes, jets, and mixing layers [68, 69].

### 3.3.4 Discretization

In order to discretize a model, it is essentially being broken into many mesh elements. In three-dimensional models these mesh elements can be characterised as tetrahedral, hexahedral or polyhedral. Hexahedral mesh elements are much more accurate than tetrahedral mesh elements, though it can take a great deal of computation time. It is possible that not every point in the mesh elements are being solved due to numerical diffusion. Therefore, it is necessary to reduce this by increasing the number of mesh elements, which in turn would also improve and optimise the quality of the mesh. Polyhedral mesh elements are much more accurate and less time consuming than using tetrahedral elements. The way in which discretization operates is through interpolation, whereby a single point is solved, then that solution will be interpolated to solve the next point and so forth [60, 61, 70]. SIMPLE scheme has been employed as the pressure-velocity coupling. For the spatial discretization, Green Gauss Node Based has been selected as the gradient with second order discretization to achieve higher accuracy.

### 3.3.5 Convergence Criteria

Convergence criteria are vital for reaching system stability by ensuring that any variations in flow parameters respective to the iterative process have dampened. This creates a sense of confidence in achieving reasonable and reliable results [61].

The convergence criterion for continuity, velocities in three dimensions and turbulence parameters in Ansys 17 in its default state is 0.001. This means that when the change in continuity, velocities and turbulence parameters drops down to the fourth place after the decimal, the solution is treated as a converged solution. However, in many practical applications, the default criterion does not necessarily indicate that the changes in the solution parameters have dampened and is therefore beneficial to manually monitor the convergence rather than relying on the default convergence criteria.

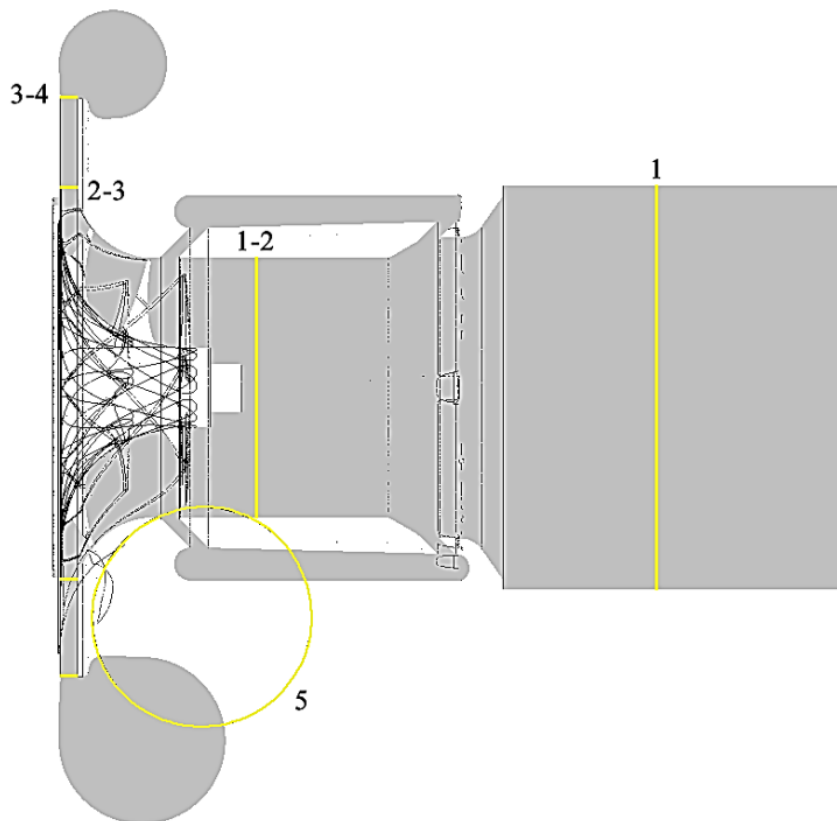
In the present study, mass flow rate on the inducer inlet and volute outlet faces of the compressor stage have been monitored throughout the iterative process. Convergence of the solution has been considered once the mass flow rates at both these faces have become stable. Here, a stable solution can either be when the mass flow rate fluctuations have dampened completely or have become recurring having same amplitude in each cycle.

### 3.4 Post- Processing

This section illustrates the locations at which the data has been extracted from through the following chapters.

#### 3.4.1 Global Data Extraction Locations through the Centrifugal Compressor Stage

For global analyses, in order to understand how variations occur within each component in the turbocharger compressor stage on a macroscopic level, data has been extracted from the inlet and outlet locations of each component at the interfaces as illustrated in Figure 3.5. Where, 1 is the inducer inlet, 1-2 are inducer outlet and impeller inlet, 2-3 are impeller outlet and diffuser inlet, 3-4 are diffuser outlet and volute inlet, and 5 is the volute outlet.



*Figure 3.5 Centrifugal Compressor Stage Global Analyses Locations*

### 3.4.2 Local Data Extraction through the Centrifugal Compressor Volute

For local analyses in order to understand the flow characteristics on a microscopic level, Figure 3.6 illustrates plane locations created to extract data and conduct analyses for this research. It is important to understand that flow inside a centrifugal compressor volute is three-dimensional, compressible and turbulent. At  $0^\circ$ , the smallest cross-section is wrapped into the largest cross-section of the scroll and hence has been consumed by the tongue. Given this, the first cross-section of the scroll has been taken as the first plane to extract data, which is situated above the tongue and differs from symmetric to asymmetric type volutes. The location for extracting data have been selected throughout the volute at every  $45^\circ$  from  $0^\circ$  to  $315^\circ$ . Following this, various locations are specified according to the design stages of the volute, namely, the cut off location, mid-exit cone, the discharge duct and the outlet. For continuity purposes downstream of the cut-off location, the azimuth angle from  $0^\circ$  to the central locations of the exit cone, discharge duct and outlet have been added to  $360^\circ$ .

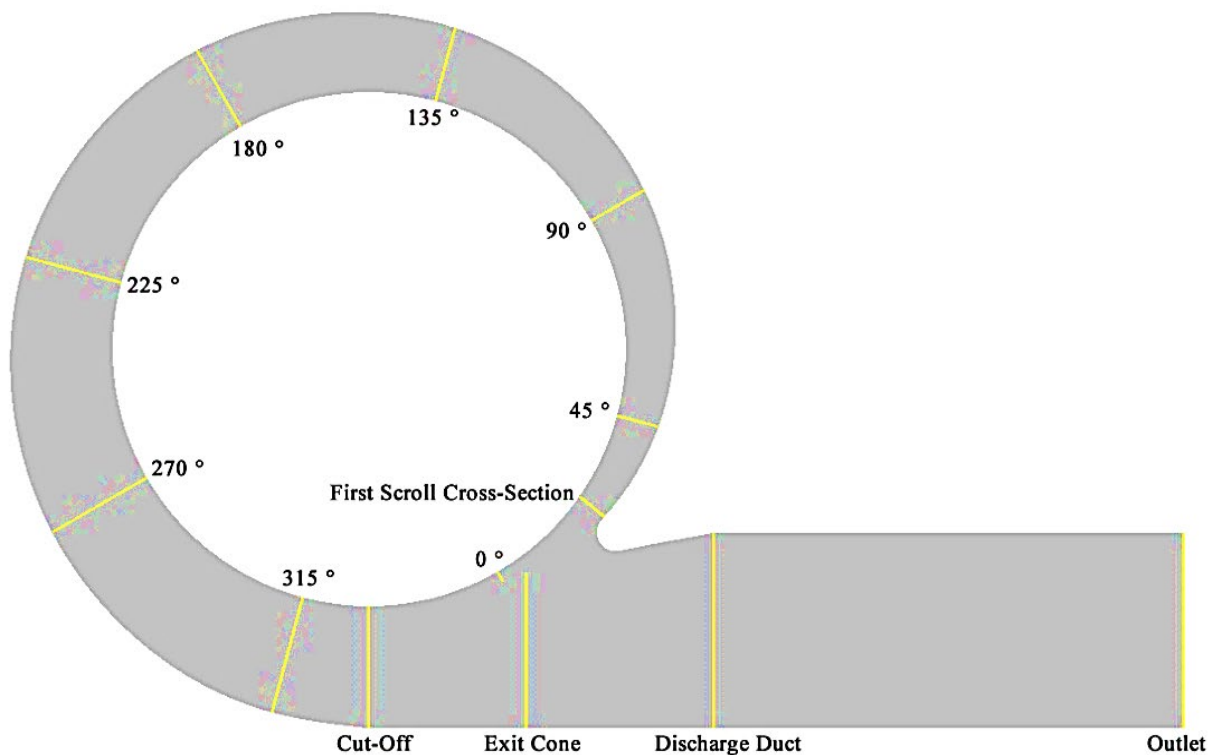


Figure 3.6 Centrifugal Compressor Volute Local Analyses Locations

Figure 3.7 illustrates the lines on the profile that have been post-processed in the radial direction and axial direction. On every profile, data have been extracted in increments of 10% along these lines in the radial direction and axial direction in order to determine how the flow varies. The line in the axial direction begins at the rear face (H1) and ends at the front face of

the volute (H2), whilst the line in the radial direction begins at the volute inlet (V1) and ends at the outer curve of the volute (V2).

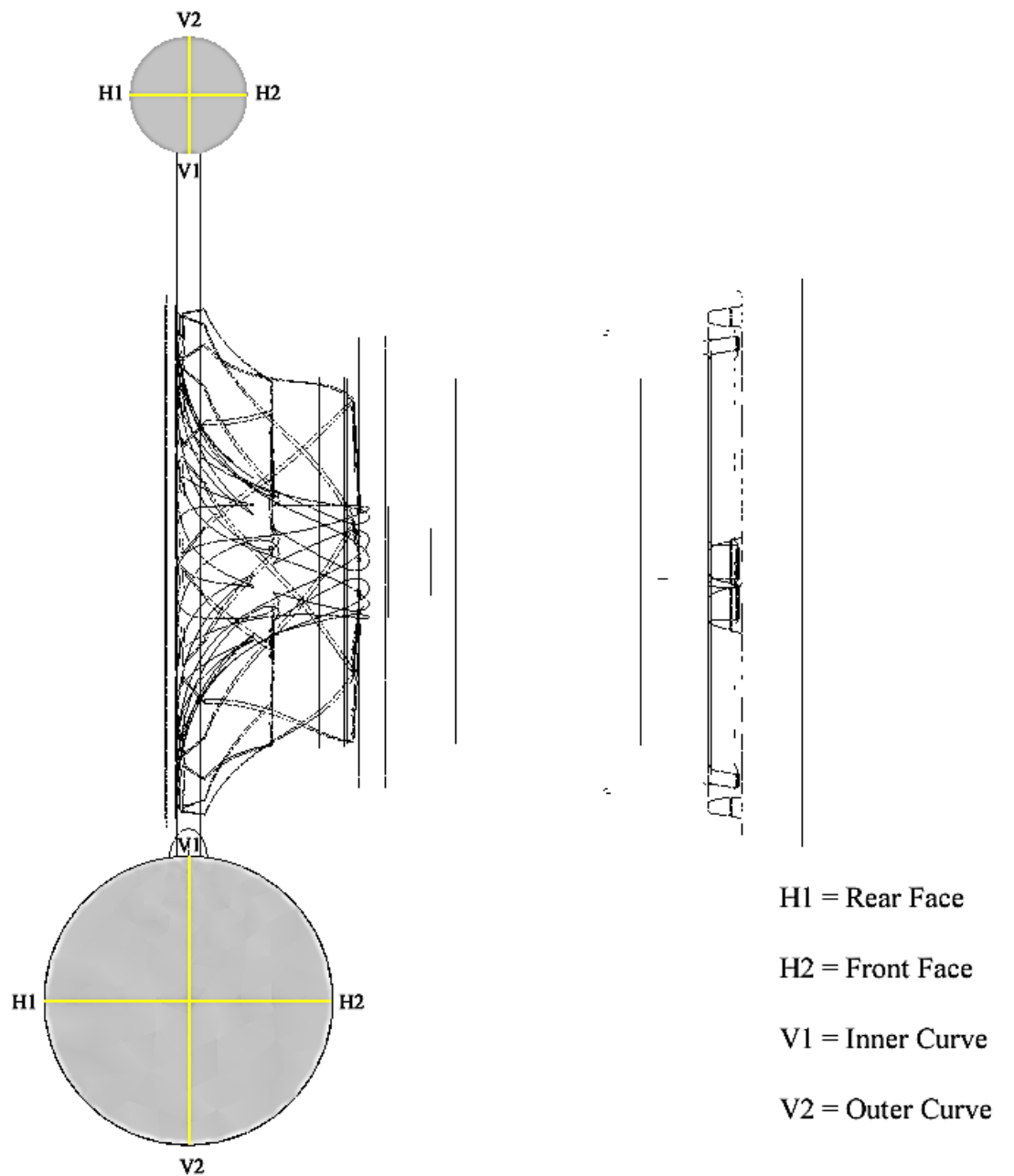


Figure 3.7 Profiles for Data Extraction along the Radial Direction and Axial Direction



### 3.5 Scope of the Numerical Investigations

Based on the above results, Chapter 4 comprises of steady simulations using the multiple reference frame approach. These simulations are conducted across low operating speed of 58.9rps/ $\sqrt{K}$  and high operating speed of 98.2rps/ $\sqrt{K}$  at low flow rate, design flow rate and high flow rate. This is because there are variations in flow conditions as the volute performs further away from its design point. When the volute is operating at a low flow rate, the fluid becomes diffusive, whereas when the volute is operating at a high flow rate, the fluid velocity increases, resulting in loss-generation mechanisms. Therefore, in turbocharging applications where covering a wide range is crucial, makes exploring these variations, relevant [5]. Chapter 5 comprises of transient simulations using the sliding mesh approach. These simulations are conducted across low operating speed of 58.9rps/ $\sqrt{K}$  and high operating speed of 98.2rps/ $\sqrt{K}$  at low flow rate, design flow rate and high flow rate and predominately focus on the design flow rate at the two speeds at two impeller blade positions with respect to the volute tongue. Chapter 6 comprises of steady simulations of six symmetric type volute models and one asymmetric type volute model since the volute shape is frequently driven by limitations and constraints in space available in the vehicle [5]. A transient simulation of the asymmetric model using the novel volute design methodology has been simulated and is compared against the original existing volute model at the BEP at a high operating speed of 98.2rps/ $\sqrt{K}$ . This has been selected as a result of the experimental data and numerical data being in good agreement at this design point in the compressor efficiency map.

## CHAPTER 4

# FLOW CHARACTERISTICS INSIDE A CENTRIFUGAL COMPRESSOR VOLUTE DURING STEADY CONDITIONS

---

This chapter numerically captures the aerodynamic flow characteristics of a turbocharger compressor stage, as well as the flow structure through the volute across numerous profiles. These investigations are carried out using Multiple Reference Frame (MRF) model within CFD based techniques for simulating steady response at the specified operating speeds and their corresponding design points. A thorough understanding is gained in this section where the strengths and weaknesses of the existing model have been identified, correlating local performance indicators with the global performance indicators to explore the flow behaviour against that which is expected in theory. Fluid flow structures have been captured along the radial direction and axial direction of each profile, which has been used to compute the asymmetric ratio to determine the flow field dominance during steady response.

#### 4.1 Baseline Turbocharger Compressor Stage Numerical Verification against Experimental

It is important to verify the numerical results against the experimental data in the initial stage of the study. Therefore, key performance parameters of the numerical simulations have been compared with the experimental of the centrifugal compressor stage, being pressure ratio and isentropic efficiency. This is to identify the accuracy margin for the numerical prediction and to ensure the numerical setup satisfies the application to pursue developments. The turbocharger compressor stage has been simulated during two operating speeds. These are that at low operating speed of 58.9rps/ $\sqrt{K}$  and high operating speed of 98.2rps/ $\sqrt{K}$  across three mass flow rates. At low mass flow rate, the compressor is performing near surge condition and this is referred as low flow during the analyses. At design flow rate, the compressor is performing at the best efficiency point (BEP) and this is referred as design flow during the analyses. At high mass flow rate, the compressor is performing near choke condition and this is referred as high flow during the analyses. Mass flow rate convergence had been monitored achieving no more than 0.06% variation between the inlet and outlet of the compressor stage.

Figure 4.1 (a) depicts the turbocharger compressor map at low operating speed of 58.9rps/ $\sqrt{K}$  and at a high operating speed of 98.2rps/ $\sqrt{K}$ , verifying the numerical solutions against the experimental data. It can be seen that the numerical results match the experimental data quite closely at 58.9rps/ $\sqrt{K}$  and is in reasonable agreement 98.2rps/ $\sqrt{K}$ . At low flow, total-to-total pressure ratio is the highest; while at high flow total-to-total pressure ratio is the lowest. At 58.9rps/ $\sqrt{K}$ , the difference in pressure ratio at low flow is 5.1% more than that at design flow. At high flow, there is a pressure ratio difference of 10.8% less than that at design flow. At 98.2rps/ $\sqrt{K}$ , the difference in pressure ratio at low flow is 9.7% more than that at design flow. At high flow, there is a pressure ratio difference of 18.2% less than that at design flow. This identifies that as the operating speed increases of the centrifugal compressor, the deviations of total-to total pressure ratio between off-design conditions with the design condition also increases.

Figure 4.1 (b) depicts the turbocharger compressor isentropic efficiency map at low operating speed of 58.9rps/ $\sqrt{K}$  and at a high operating speed of 98.2rps/ $\sqrt{K}$ . It can be seen at 58.9rps/ $\sqrt{K}$ , the difference in isentropic efficiency at low flow is 30.6% less than that at design flow. At high flow, there is an isentropic efficiency difference of 13% less than that at

design flow. At 98.2rps/ $\sqrt{K}$ , the difference in isentropic efficiency at low flow is 13.8% less than that at design flow. At high flow, there is an isentropic efficiency difference of 12.7% less than that at design flow. This identifies that as the operating speed increases of the centrifugal compressor, the deviations of isentropic efficiency between off-design conditions with the design condition decreases.

Since the volute is designed to the BEP, it is of prime interest that an extensively detailed analysis is conducted to understand the aerodynamic flow characteristics through the turbocharger compressor stage and its volute. Given these results, the focus of this design study can be satisfied by simulating at low speed of 58.9rps/ $\sqrt{K}$  and at high speed of 98.2rps/ $\sqrt{K}$  at design and off-design conditions, namely design points, S1, which is near surge at low flow rate, C3, which is BEP at design flow rate and C1, which is near choke at high flow rate. Due to the complexity of capturing the actual extreme conditions of surge and choke, the reference to S1 and C1 are taken as the choke and surge conditions on the compressor map and throughout this study.

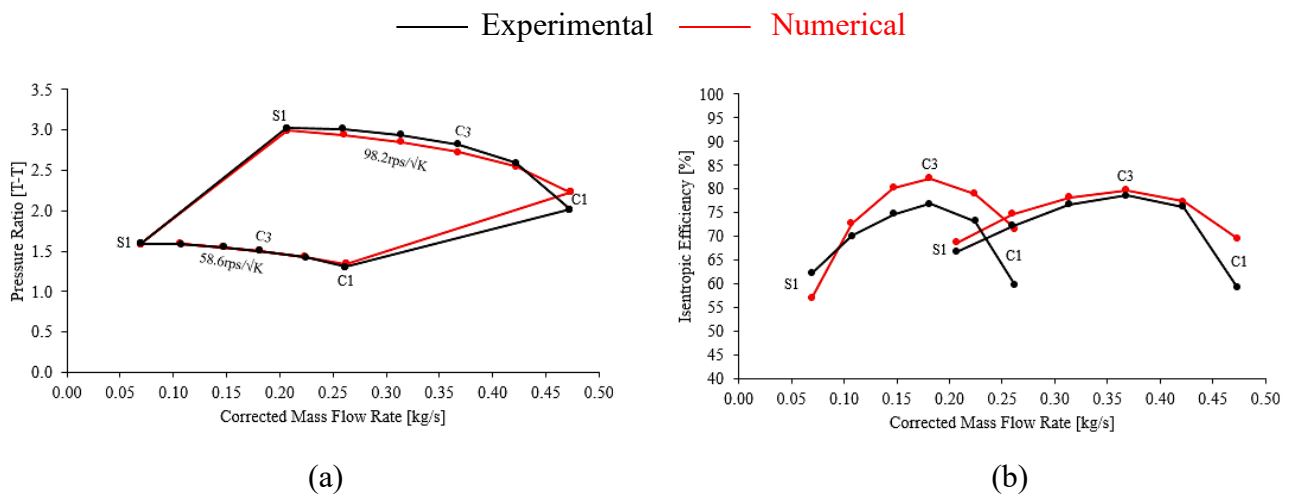


Figure 4.1 Turbocharger Compressor Stage (a) Performance Map (b) Efficiency Map

## 4.2 Turbocharger Compressor Volute Performance

The overall volute performance is analysed by quantifying the total pressure loss coefficient denoted by  $K_p$  [1, 2, 17, 46], which is calculated using Equation 4.1 and static pressure recovery coefficient, denoted by  $C_p$ , which is calculated using Equation 4.2.

$$K_p = \frac{P_{Tin} - P_{Tout}}{P_{Tin} - P_{Sin}}$$

*Equation 4.1 Total Pressure Loss Coefficient*

$$C_p = \frac{P_{Sout} - P_{Sin}}{P_{Tin} - P_{Sin}}$$

*Equation 4.2 Static Pressure Recovery Coefficient*

Figure 4.2 (a) depicts the total pressure loss coefficient through the turbocharger compressor volute at low operating speed of 58.9rps/ $\sqrt{K}$  and at a high operating speed of 98.2rps/ $\sqrt{K}$ . It can be seen at both operating speeds that from low flow to design flow, total pressure loss decreases then increase from design flow to high flow, as expected [2]. The presented results through the centrifugal compressor volute depicts at 58.9rps/ $\sqrt{K}$ , the difference of total pressure loss for the surge condition at low flow is 16.1% more than that at depicted at BEP, which is the design flow. For the choke condition at high flow, there is a total pressure loss difference of 63.1% more than that depicted at BEP. At 98.2rps/ $\sqrt{K}$ , the difference in total pressure loss for the surge condition at low flow is 20.1% more than that at BEP, which is the design flow. For the choke condition at high flow, there is a total pressure loss difference of 38.4% more than that at BEP. This identifies that for low flow, as the operating speed increases the deviation of total pressure loss between off-design conditions with the design condition decreases. At high flow, as the operating speed increases, the deviation of total pressure loss between off-design conditions with the design condition increases. Since the flow into the volute is at a relatively high velocity, ensuring low total pressure loss is essential to avoid any shortcomings of the compressor efficiency [5].

Figure 4.2 (b) depicts the static pressure recovery coefficient through the turbocharger compressor volute at low operating speed of 58.9rps/ $\sqrt{K}$  and at a high operating speed of 98.2rps/ $\sqrt{K}$ . It can be seen for both operating speeds that from low flow to high flow, static pressure recovery decreases, as expected [2]. The presented results through the centrifugal compressor volute depicts at 58.9rps/ $\sqrt{K}$ , the difference in static pressure recovery for the surge condition at low flow is 45.8% more than that at BEP, which is the design flow. For the

choke condition at high flow, there is a static pressure recovery difference of 136.4% less than that at BEP. It is also noticed that static pressure recovery coefficient falls below 0 at low operating speed, indicating that there are more pressure losses taking place at the choke condition than pressure recovery. This is a due to secondary flows causing head loss as a result of friction. At 98.2rps/ $\sqrt{K}$ , the difference in static pressure recovery for the surge condition at low flow is 12.6% more than that at BEP, which is the design flow. For the choke condition at high flow, there is a static pressure recovery difference of 85% less than that at BEP. This identifies that as the operating speed increases the deviation of static pressure recovery between off-design conditions with the design condition decreases.

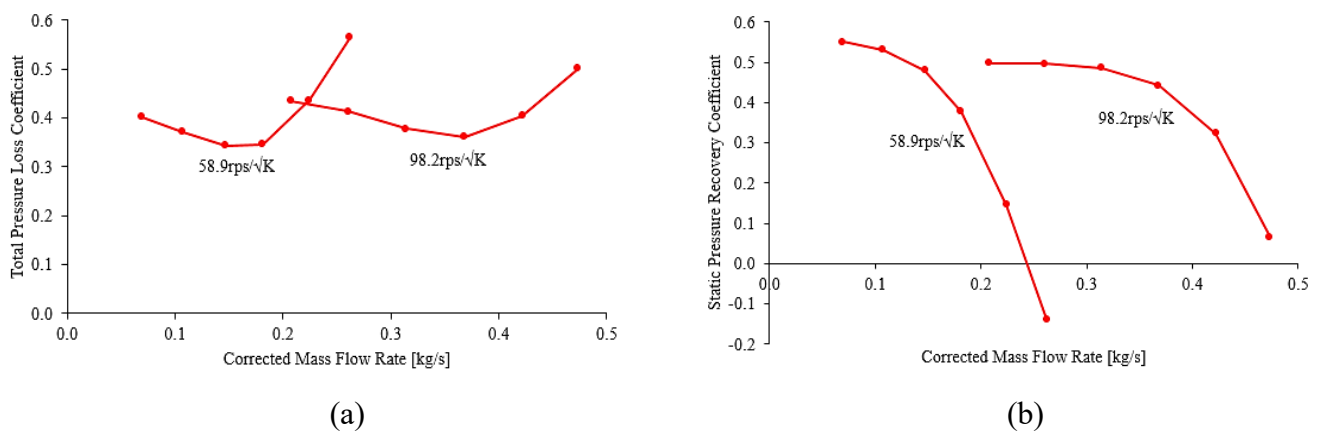


Figure 4.2 Turbocharger Compressor Volute Performance (a) Total Pressure Loss Coefficient (b) Static Pressure Recovery Coefficient

### 4.3 Global Static Pressure Distribution around the Centrifugal Compressor during Steady Conditions

This section details the global distribution of static pressure around the compressor stage of the turbocharger. The BEP has initially been analysed since at this condition, the compressor stage performs at its optimum in the specified operating speed. The two extreme conditions have been analysed after the BEP in order to distinguish the variations between the conditions.

In general, ambient air is drawn into the compressor stage via the inducer as result of force and moment generated from the rotation of the blades, caused by the mechanical energy transferred to the impeller from the shaft. When the ambient air enters the inducer, it is at a very low pressure. This low pressure decreases even further when the fluid is directed into the impeller. As the fluid flows radially outwards through the passages of the impeller, Coriolis

forces and diffusion simultaneously take place, acting as a rotating diffuser and imparting kinetic energy and pressure rise into the fluid. When the flow leaves the impeller, centrifugal forces push the fluid into the diffuser where compressibility and diffusion takes place. The idea behind diffusion is to increase the pressure in the flow by compressing the fluid. This in turn, increases the density of the air and hence affects the rate at which mass flow is delivered into the volute. The diffusion process occurs by squeezing the fluid into an annular passage and directing it along a radial length prior to entering the volute. When the compressed fluid is leaving the diffuser, the pressure is comparatively high as to when it first entered the stage. Fluid enters the volute circumferentially and radially, converting kinetic energy in the fluid into pressure energy. This is achieved through the linear increase of the cross-sectional area of the scroll [17, 21, 71]. As the fluid enters the volute at any arbitrary azimuth angle, upstream fluid also merges with the inflow in the passage. Flow at the tongue is complex. The tongue is the blend between the smallest cross-sectional area and the largest cross-sectional area of the volute. It is essentially a dividing plane where fluid is either directed into the discharge duct or recirculated back around the scroll. From the cut-off, the exit cone and discharge duct fundamentally behaves as a conical diffuser, where pressure in the flow increases further and reaches its highest in the stage. At the BEP, uniform pressure is expected to incur around the periphery of the volute inlet with reasonably uniform total pressure across the cross-sections. At the choke side of the map where mass flow rates are higher than that at the BEP, losses have been seen to increase due to greater velocity gradients and shear stresses. Since the passage of the scroll is narrow it becomes difficult to build up the pressure causing the flow to accelerate and restricting pressure rise. At the surge side of the map where mass flow rates are lower than that at the BEP, it is found that pressure rises from the inlet to the outlet having a fall in total pressure in the centre of the passage as a result of shear stresses occurring internally [17].

Figure 4.3 in the top row, depicts static pressure variation in the turbocharger compressor stage during the operating speed of  $58.9\text{ rps}/\sqrt{K}$  at (a) BEP (b) choke (c) surge. Observing (a), which is the turbocharger compressor stage operation at design flow rate, ambient air flows into the compressor stage through the inducer at a static pressure of 1atm. From here, there is 1.8% decrease in static pressure when the fluid enters the impeller. When air particles pass through the impeller passages and exits into the diffuser, static pressure rises by 33.3%. After compressibility and diffusion have taken place in the diffuser, static pressure continues to increase by 10%. Once the flow has been collected in the volute and kinetic energy in the

flow has been converted into potential energy, the final static pressure increases at the outlet by 2.9%.

Viewing the operating speed of 58.9rps/ $\sqrt{K}$  at (b), which is the turbocharger compressor stage operation at high flow rate, the inflow also enters the inducer at a static pressure of 1atm. When fluid reaches the exit of the inducer and enters the impeller, there is a fall in static pressure by 2.6%. After the ambient air has passed through the impeller, changing the fluid properties, static pressure increases by 15.4%. After further altering the fluid properties through the diffuser passage, static pressure increases by an additional 15% prior to entering the volute. When the fluid reaches the outlet, the results show a fall in static pressure by 1.5% rather than a further increase. This anomaly at the specified off-design condition where the mass flow is greater than the BEP is as expected.

Inspecting the operating speed of 58.9rps/ $\sqrt{K}$  at (c), which is the turbocharger compressor stage operation at low flow rate, incoming flow of the air also exhibits 1atm of static pressure. This static pressure increases by 0.1% when the fluid reaches the inlet of the impeller. By the time, the fluid leaves the impeller, static pressure has increased by 43.5% at the diffuser inlet. From here, post compressibility and diffusion of the fluid, a further increase of 7.3% in static pressure has incurred. After the kinetic energy has been converted into pressure energy, the compressed fluid leaves the stage with a 2.8% greater rise in static pressure.

It can be seen from the results that by the end of each station, there are variations between the design and off-design conditions. Reviewing static pressure variations under the choke condition against the BEP, there is 0.1% increase at the end of the inducer; 15.4% decrease at the end of the impeller; 10.4% decrease at the end of the diffuser; and 15.3% decrease at the end of the volute. Reviewing static pressure variations under the surge condition against the BEP, there is 1.1% increase at the end of the inducer; 8.8% increase at the end of the impeller; 6.1% increase at the end of the diffuser; and 6% increase at the end of the volute.

The results also show the variations through each station between the design and off-design conditions. Reviewing static pressure variations under the choke condition against the BEP, there is 32.5% increase through the inducer; 115.8% decrease through the impeller; 22.9% increase through the diffuser; and 317.2% increase through the volute. Reviewing static pressure variations under the surge condition against the BEP, there is 103.3% decrease



through the inducer; 32% increase through the impeller; 20.7% decrease through the diffuser; and 1.2% increase through the volute.

Figure 4.3 in the bottom row, depicts static pressure variation in the turbocharger compressor stage during the operating speed of 98.2rps/ $\sqrt{K}$  at (a) BEP (b) choke (c) surge. Observing (a), which is the turbocharger compressor stage operation at design flow rate, ambient air flows into the compressor stage through the inducer at a static pressure of 1atm. From here, there is 6.4% decrease in static pressure when the fluid enters the impeller. When air particles pass through the impeller passages and exits into the diffuser, static pressure rises by 117.8%. After compressibility and diffusion have taken place in the diffuser, static pressure continues to increase by 22.7%. Once the flow has been collected in the volute and kinetic energy in the flow has been converted into potential energy, the final static pressure increases at the outlet by 6.9%.

Viewing the operating speed of 98.2rps/ $\sqrt{K}$  at (b), which is the turbocharger compressor stage operation at high flow rate, the ambient inflow also enters the inducer at a static pressure of 1atm. When fluid enters the impeller, there is a fall in static pressure by 9.5%. After the ambient air has passed through the impeller, imparting energy into the fluid, static pressure increases by 21.5%. After altering the fluid properties even more during compressibility in the diffuser passage, static pressure increases by an additional 85.2% prior to entering the volute. When the fluid reaches the outlet, the results show a rise in static pressure by 1.5%.

Inspecting the operating speed of 98.2rps/ $\sqrt{K}$  at (c), which is the turbocharger compressor stage operation at low flow rate, ambient air inflow is exhibited at 1atm of static pressure. This static pressure falls by 2.7% when the fluid approaches the impeller inlet. By the time the fluid is energised and leaves the impeller, static pressure has risen by 141.9%. From here, after the fluid has been through the compressibility and diffusion process in the diffuser, a further static pressure increase of 18.5% has incurred. Post energy conversion, the compressed fluid leaves the volute with a 6.7% greater rise in static pressure.

It can be seen from the results that by the end of each station, there are variations between the design and off-design conditions. Reviewing static pressure variations under the choke condition against the BEP, there is 11.7% decrease at the end of the inducer; 100.1% decrease at the end of the impeller; 32.6% decrease at the end of the diffuser; and 39.7% decrease at the end of the volute. Reviewing static pressure variations under the surge condition against the BEP, there is a fall of 0.1% at the end of the inducer; 11% increase at the end of the

impeller; 7.1% increase at the end of the diffuser; and 6.9% increase at the end of the volute. The results also show the variations through each station between the design and off-design conditions. Reviewing static pressure variations under the choke condition against the BEP, there is 27.5% increase through the inducer; 511.4% decrease through the impeller; 46.6% increase through the diffuser; and 501.5% decrease through the volute. Reviewing static pressure variations under the surge condition against the BEP, there is a fall of 59.2% through the inducer; 20.4% increase through the impeller; fall of 9.7% through the diffuser; and rise of 3.2% through the volute.

Table 4.1 details the speed comparison of static pressure variation at  $98.2\text{rps}/\sqrt{K}$  compared to that at  $58.9\text{rps}/\sqrt{K}$ . It can be seen at low flow rate, highest static pressure variation at the inlet and the outlet occurs in the volute, where the turbocharger compressor stage operating at  $98.2\text{rps}/\sqrt{K}$  increases substantially compared to that at  $58.9\text{rps}/\sqrt{K}$ . The lowest static pressure variation at the inlet and outlet occurs in the inducer, where the operating condition  $98.2\text{rps}/\sqrt{K}$  increases slightly compared to that at  $58.9\text{rps}/\sqrt{K}$ . At the design flow rate, highest static pressure variation at the inlet and the outlet occurs in the volute, where the turbocharger compressor stage operating at  $98.2\text{rps}/\sqrt{K}$  increases substantially compared to that at  $58.9\text{rps}/\sqrt{K}$ . The lowest static pressure variation at the inlet and outlet occurs in the impeller and inducer, respectively, where the operating condition  $98.2\text{rps}/\sqrt{K}$  decreases slightly compared to that at  $58.9\text{rps}/\sqrt{K}$ . At the high flow rate, highest static pressure variation at the inlet and the outlet occurs in the volute, where the turbocharger compressor stage operating at  $98.2\text{rps}/\sqrt{K}$  increases by just over 50% compared to that at  $58.9\text{rps}/\sqrt{K}$ . The lowest static pressure variation at the inlet and outlet occurs in the inducer and impeller, respectively, where the operating condition  $98.2\text{rps}/\sqrt{K}$  decreases compared to that at  $58.9\text{rps}/\sqrt{K}$ .

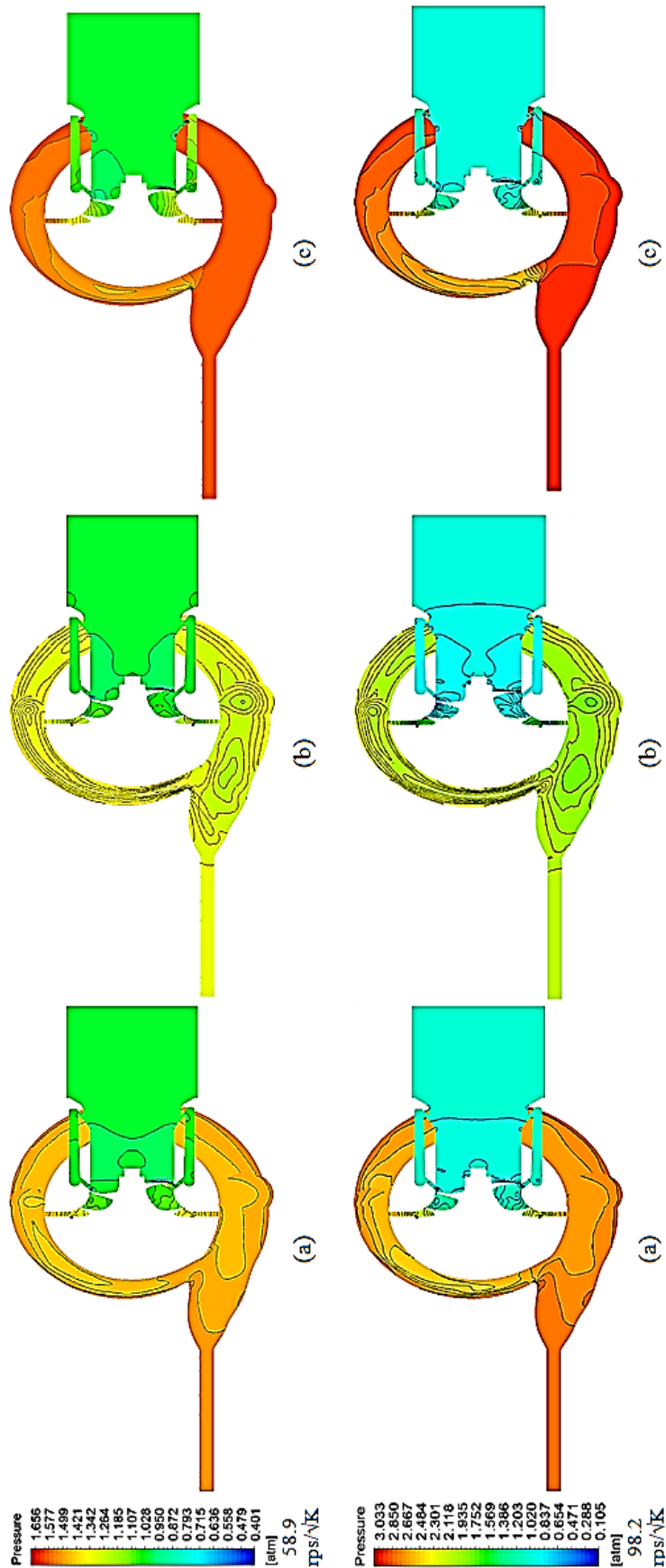


Table 4.1 Global Speed Comparison of Static Pressure Variation

Compressor Component	Static Pressure In [%]			Static Pressure Out [%]		
	Low Flow	Design Flow	High Flow	Low Flow	Design Flow	High Flow
Inducer	0.6	3.8	-4.7	-2.2	-1	-11.5
Impeller	-2.2	-1	-11.5	65	61.7	-6.8
Diffuser	65	61.7	-6.8	82.2	80.4	50.2
Volute	82.2	80.4	50.2	89.1	87.5	54.7

Figure 4.3 Static Pressure Variation in the Turbocharger Compressor Stage during the operating speed of 58.9rps/√K and 98.2rps/√K at (a) BEP (b) choke (c) surge

Figure 4.4 depicts static pressure variations through each station in the compressor stage during the operating speed of (a) 58.9rps/ $\sqrt{K}$  and (b) 98.2rps/ $\sqrt{K}$ , both under design and off-design conditions. Overall, it is clear that static pressure variation through each component is much higher at 98.2rps/ $\sqrt{K}$  than at 58.9rps/ $\sqrt{K}$ .

Figure 4.4 (a) represents the variation of static pressure through each station in the compressor stage during the operating speed of 58.9rps/ $\sqrt{K}$  under design and off-design conditions. It can be seen during the surge condition, negligible static pressure variation occurs through the inducer, whereas for BEP and choke conditions, static pressure decreases through the component. Through the impeller, all three conditions show static pressure varying significantly in the form of an increase. The highest variation in static pressure is exhibited during the surge condition, while the lowest variation in static pressure is exhibited during the choke condition. It is identified that as the mass flow rate increases, variation in static pressure decreases through the impeller. Static pressure varies considerably in the diffuser, also showing an increase. Highest static pressure variation is exhibited during the choke condition, while the lowest static pressure variation is exhibited during the surge condition. It is identified that as the mass flow rate increases, variation in static pressure also increases through the diffuser. In the volute during surge and BEP, variations in static pressure are almost the same showing an increase, whereas during the choke condition, static pressure varies in the form of a decrease.

Figure 4.4 (b) represents the variation of static pressure through each station in the compressor stage during the operating speed of 98.2rps/ $\sqrt{K}$  under design and off-design conditions. It can be seen that for all three conditions, static pressure falls through the inducer considerably and exhibits a significant increase through the impeller, diffuser and volute. It is noticed that the highest static pressure variation through the inducer occurs during the choke condition, while the lowest static pressure variation occurs during surge condition. It seems in this case, as the mass flow rate increases, static pressure variation also increases through the inducer in the form of a decrease. Static pressure rises significantly through the impeller showing substantial variance during the surge condition and at BEP as compared to that during the choke condition. Static pressure varies through the diffuser quite considerably during the choke condition compared to that during the surge condition and to that previously depicted in the impeller. Through the volute, static pressure variance during the surge condition and at BEP are very similar, however during the choke condition, the variance of static pressure is much lower.

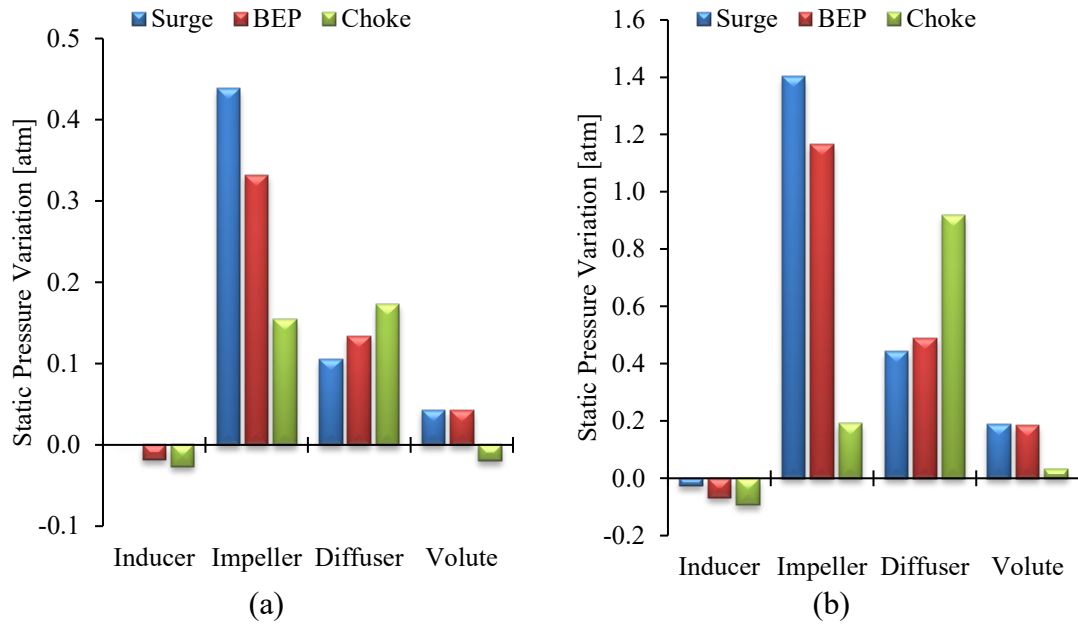


Figure 4.4 Static pressure difference through each station in the turbocharger compressor stage during (a) 58.9rps/√K (b) 98.2rps/√K

#### 4.4 Local Static Pressure around the Centrifugal Compressor Volute at Low Operating Speed during Steady Conditions

Figure 4.5 depicts static pressure distribution through the turbocharger compressor volute during the operating speed of 58.9rps/√K at (a) BEP (b) choke (c) surge. Twelve cross-sections through the volute channel have been presented from the first cross-section of the scroll situated above the tongue, through to the outlet of the compressor stage.

Observing (a), which is the volute operation at design flow rate at 58.9rps/√K, static pressure at the periphery appears to be reasonably uniform similar to that observed by Rezaei (2001) and increasing downstream of the volute [17]. Further to this, static pressure appears to be lower around the inlet, whereas towards the outer curve, static pressure increases. This trend is similar to that of Reunanen (2001) [2]. Static pressure disturbances are expected in the tongue area with adverse pressure gradients, which can affect the start of the scroll and the exit cone. In the tongue region, flow becomes distorted upon entrance into the volute due to flow from upstream of the scroll merging with the inflow and either recirculating the fluid back around the volute or directing the fluid into the discharge duct. In this case however, static pressure appears to have minimal distinctive variations. After the fluid has passed through the exit cone and directed into the discharge duct, static pressure distribution is high and uniform. From the profiles, it is noticed that static pressure is predominantly follows the curvature of the scroll. Further to this,

low static pressure distribution is exhibited in the central region and increases towards the outer walls.

At  $15^\circ$ , static pressure distribution is 1.5atm, which compared to the outlet is 1.5% less than the static pressure exhibited at the outlet. It can be seen static pressure distribution increases towards the outer curve on the rear side. At  $45^\circ$ , static pressure falls from that depicted at  $15^\circ$  by 0.5% and hence the static pressure distribution is 2% less compared to the outlet. In the central region, leaning towards the overhang depicts lower pressure than the previous profile. However, static pressure appears to increase and has a greater distribution toward the outer curve on the rear side. At  $90^\circ$ , static pressure falls further by 1.2% resulting in 3.2% less static pressure incurring than that at the outlet. It can be seen the static pressure distribution behaves in the same manner as previous, however, the low static pressure inflow is more localised to the central region of the cross-section and the area distribution for the variations are smaller. For this reason, there is a much smaller region of higher static pressures on the outer curve towards the rear side and is less than that depicted at  $45^\circ$ . At  $135^\circ$ , static pressure increases by 0.4% and exhibits 2.9% less static pressure than that depicted at the outlet. It can be seen that low static pressure is directed towards the centre of the cross-section, which propagates towards the front face and is superimposed by the flow upstream of the scroll. Although static pressure increases towards the outer curve, the highest static pressure area exhibited for the cross-section reduces from the aforementioned profile. At  $180^\circ$ , static pressure increases by 0.4%, which is 2.5% less static pressure compared to that at the outlet. This distribution depicts a region of higher static pressure along the outer curve and more centralised than that aforementioned in the previous profiles. The lowest static pressure region is smaller and more localised to the centre of the cross-section and within the overhang. At  $225^\circ$ , static pressure increases by 0.3% and hence, is 2.3% less static pressure compared to that at the outlet. The lowest static pressure is exhibited on the flow superimposed upstream of the scroll. The highest static pressure region along the outer wall has a greater distribution than that depicted previously. At  $270^\circ$ , static pressure increases by 0.1% resulting in 2.1% less static pressure compared to that at the outlet. It can be seen that static pressure behaves in the same manner as that aforementioned profile. Though, lowest static pressure area appears to have reduced and highest static pressure area appears to have increased in its more profound distribution along the outer wall and towards the central region. At  $315^\circ$ , static pressure decreases by 0.1% and exhibits 2.2% less static pressure compared to that at the outlet. It can be seen that static pressure behaves in the same manner as that previously described. At the cut-off location, static pressure falls by 0.7%, which is 2.9% less static pressure compared to that at the

outlet. The lowest static pressure region is reduced and more localised to the centre of the cross-section, while having higher static pressure from the inflow and upstream flow. Static pressure along the outer curve appears to have reduced from the previous profile. At the exit cone, static pressure rises by 2.2% and exhibits 0.8% less static pressure than that depicted at the outlet. The lowest static pressure region remains localised to the freestream area and has propagated circumferentially. It can also be seen that static pressure from upstream has also risen significantly across the profile. At the discharge duct, static pressure has risen by 0.7% with no change in its variation compared to the outlet. Lowest static pressure is higher than that previously depicted and is localised from the central rear face of the profile, which appears to increase circumferentially towards the front face of the profile. At the outlet, there are no static pressure variations from the discharge duct though, it can be seen the lowest static pressure is same as that previously depicted. However, this static pressure is localised in the freestream of the cross-section and higher almost uniform static pressure manifests concentric to this localised low static pressure region.

Viewing (b), which is the volute operation at high flow rate at  $58.9\text{rps}/\sqrt{K}$ , depicts fairly consistent static pressure in the periphery of the volute inlet. It is immediately noticed that static pressure throughout the volute operating at high flow rate depicts comparatively low static pressure throughout the volute than that depicted at BEP. Static pressure follows the curvature of the scroll, having higher static pressure at the volute inlet and at the outer wall with lower static pressure through the freestream region. Uniform static pressure is seen throughout the volute and is more profound downstream the discharge duct. Lowest static pressures of the profiles are localised in the freestream of the cross-section. Furthermore, static pressure gradients across the profiles through the volute appear to be reasonably uniform and concentric. At  $15^\circ$ , static pressure distribution is 1.4atm, which compared to the outlet is 3.8% more than the static pressure exhibited at the outlet. Since this is the first cross-section situated above the tongue, there are adverse pressure gradients depicted here. The low static pressure zone is depicted at the interface in the curvature of the overhang. This is due to the tongue region, where flow is superimposed and is forced to be directed either back around the scroll or towards the outlet. Significantly high pressure areas are depicted towards the overhang and the outer wall. At  $45^\circ$ , static pressure rises from that depicted at  $15^\circ$  by 1.7% and hence, static pressure distribution has increased significantly by 5.5% compared to the outlet. Low static pressure appears to be localised to the close to the centre with slightly higher inflow static pressure. This distribution has minimal variance. At  $90^\circ$ , static pressure falls by 1.6% resulting in 3.9% rise in static

pressure incurring than that at the outlet. It can be seen the static pressure distribution emits similar static pressure gradients as the previous profile. At 135° static pressure decreases by 1.5% and exhibits 2.3% more static pressure than that depicted at the outlet. It can be seen that static pressure has propagated low pressure localised in the freestream and higher static pressure concentric to this. At 180°, static pressure decreases by 1.2%, which is 1% more static pressure compared to that at the outlet. It can be seen that there is minimal variation in the distribution of static pressure as the aforementioned profile. At 225°, static pressure decreases by a further 1.2% and hence, is 0.2% less static pressure compared to that at the outlet. Low static pressure localised in the freestream has propagated to inner side of the volute with a slight fall at the outer walls. At 270°, static pressure decreases by 1.4% resulting in 1.6% less static pressure compared to that at the outlet. It can be seen that low static pressure manifests across the profile with slightly higher static pressure along the circumference of the outer wall of the volute. At 315°, static pressure decreases by 2% and exhibits 3.6% less static pressure compared to that at the outlet. It can be seen that static pressure behaves in the same manner as that previously described however with lower pressure and a more focal zone in the freestream. At the cut-off location, static pressure falls by 3.3%, which is 6.8% less static pressure compared to that at the outlet. Low static pressure zone is exhibited and localised in the freestream. Slightly higher static pressure is concentric to this focal low static pressure zone, which appears to have manifested from the previous profile. At the exit cone, static pressure significantly rises by 4.5% and exhibits 2.6% less static pressure than that depicted at the outlet. The freestream area depicts a slight rise in static pressure and higher static pressure is reintroduced. At the discharge duct, static pressure has risen by 2.3% with 0.4% less static pressure compared to the outlet. Static pressure appears to be maintained with a greater distribution of higher static pressure towards the walls. At the outlet, static pressure rises by 0.4% and depicts higher static pressure behaving in a concentric manner.

Inspecting (c), which is the volute operation at low flow rate at 58.9rps/ $\sqrt{K}$ , show high and uniform static pressure upstream of 135° and even higher uniform static pressure downstream of 135°. It is immediately noticed that static pressure throughout the volute operating at low flow rate depicts comparatively high static pressure throughout the volute than that depicted at BEP. It is also noticed that static pressure appears rises throughout the volute. At 15°, static pressure distribution is 1.5atm, which is 5.2% less than the static pressure exhibited at the outlet. It can be seen that there is a distinctive low static pressure region in the central top of the cross-section. Since this is the first cross-section of the scroll, which is located above the tongue, the



disturbances caused by the tongue appears to directly influence this first cross-section. Static pressure increases concentric to the low static pressure region. At  $45^\circ$ , static pressure increases from that depicted at  $15^\circ$  by 0.8% and hence the static pressure distribution is 4.4% less compared to the outlet. It can be seen there is static pressure increase from the inflow to the outer wall across the cross-section. The lowest static pressure is exhibited from the upstream superimposed flow in the central region towards the front face of the volute. The highest static pressure is exhibited along the outer curve. At  $90^\circ$ , static pressure increases further by 0.2% resulting in 4.2% less static pressure incurring than that at the outlet. Highest static pressure distribution along the outer curve becomes much more profound. Lowest static pressure exists in this cross-section as a result of the superimposed flow. At  $135^\circ$ , static pressure increases by 1.5% and exhibits 2.8% less static pressure than that depicted at the outlet. From the bottom on the cross-section in the overhang to the freestream, shows the lowest static pressure in the cross-section. Static pressure increases towards the outer curve however, there are minimal variations of this distribution. At  $180^\circ$ , static pressure increases by 1.2%, which is 1.6% less static pressure compared to that at the outlet. Static pressure continues to rise showing higher static pressure across the top half of the cross-section. At  $225^\circ$ , static pressure increases by 0.6% and hence, is 1% less static pressure compared to that at the outlet. Static pressure becomes almost uniform across this cross-section showing a further rise. However, the distribution of the lower static pressure appears to be greater than the distribution of the higher static pressure. At  $270^\circ$ , static pressure increases by 0.4% resulting in 0.7% less static pressure compared to that at the outlet. Almost constant static pressure is depicted across this cross-section. The higher static pressure has a greater distribution than that of the lower static pressure. At  $315^\circ$ , static pressure increases by 0.1% and exhibits 0.5% less static pressure compared to that at the outlet. It is evident that uniform static pressure is achieved through this cross-section, behaving at a constant. This is also the case at the cut-off location. Additionally, there is 0.6% less static pressure compared to the outlet. At the exit cone, static pressure increases by 0.5% and exhibits 0.1% less static pressure compared to that at the outlet. Lower static pressure appears to have predominantly greater distribution than the higher static pressure that has been depicted. The rise in static pressure along the top of the cross-section is a result of disturbance encountered at the tongue. At the discharge duct, static pressure increases by 0.1% and exhibits no variation compared to that at the outlet. Higher static pressure is exhibited towards the front face of the volute, while lower static pressure is exhibited towards the rear face of the volute. At the outlet, the high static pressure from the aforementioned cross-section appears to manifest across the outlet, showing almost constant static pressure.

## CHAPTER FOUR: FLOW CHARACTERISTICS INSIDE A CENTRIFUGAL COMPRESSOR VOLUTE DURING STEADY CONDITIONS

Overall at low operating speed of the centrifugal compressor, it can be seen that static pressure increases from choke to surge in the volute, as expected. The choke condition depicts the decrease in static pressure from the first profile to the cut-off prior to increasing downstream to the outlet. At BEP, static pressure decreases from the first profile prior to increasing downstream of the cut-off location, whilst near surge condition static pressure linearly increases.

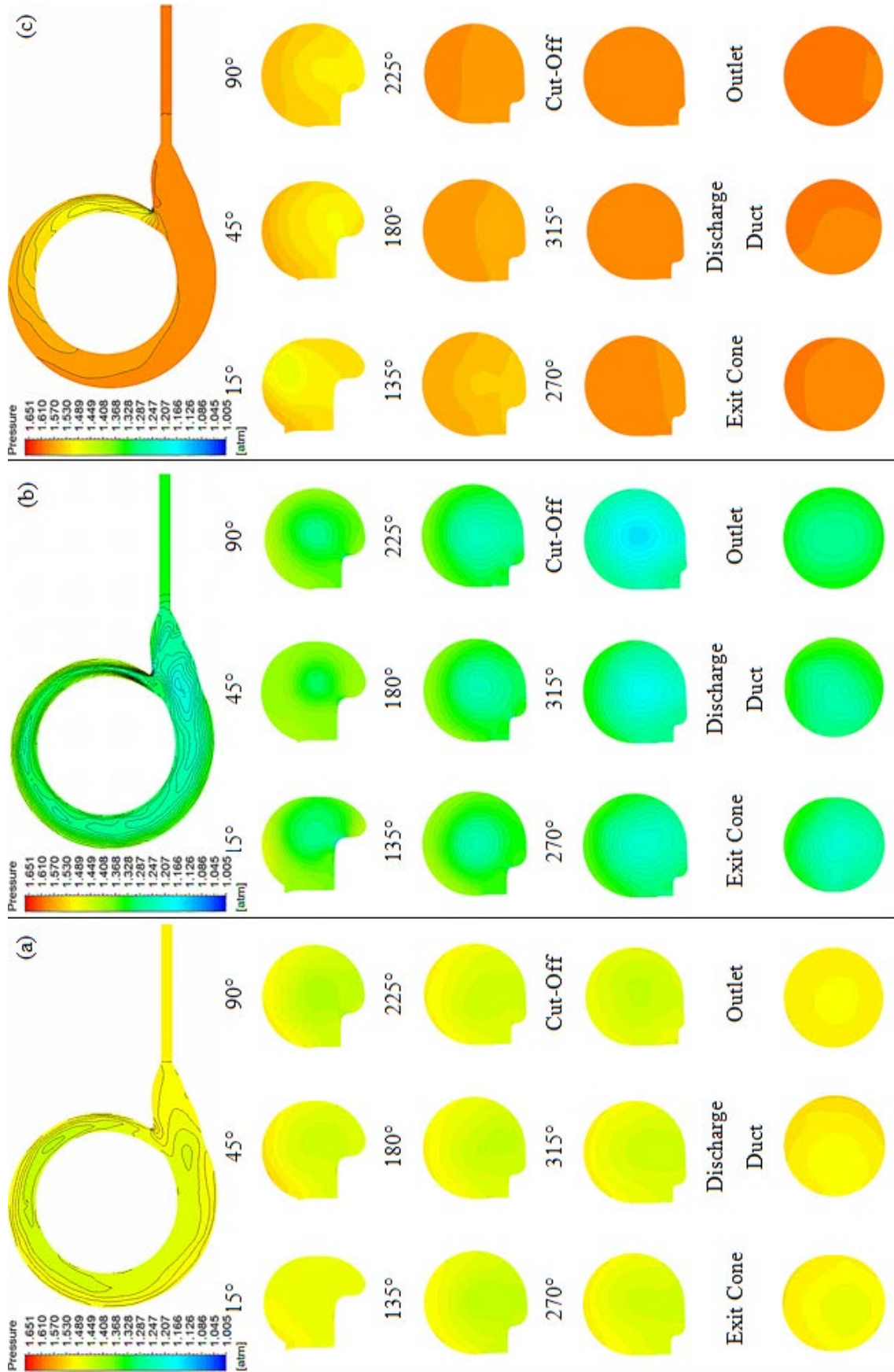


Figure 4.5 Static Pressure around the Compressor Volute during the operating speed of 58.9rps/√K at (a) BEP (b) choke (c) surge

Figure 4.6 depicts the variation of static pressure across each cross-section around the centrifugal compressor volute during the operating speed of 58.9rps/ $\sqrt{K}$  at low flow rate, being near the surge condition; design flow rate, being the best efficiency point; and high flow rate, being near the choke condition. It is clear that the low flow shows higher static pressure than the design flow, while high flow shows lower static pressure than the design flow throughout the centrifugal compressor volute. At 15°, low flow depicts an increase in static pressure of 1.9% compared to the design flow, while high flow depicts a static pressure decrease of 9.4% compared to the design flow. At 45°, surge condition depicts a static pressure increase of 3.3% compared to the BEP, while choke condition depicts a decrease in static pressure of 7% compared to the BEP. At 90°, low flow depicts a static pressure increase of 4.8% compared to the design flow, while high flow depicts a decrease in static pressure of 7.4% compared to the design flow. At 135°, surge condition depicts an increase in static pressure of 6% compared to the BEP, while choke condition depicts a static pressure decrease of 9.5% compared to the BEP. At 180°, low flow depicts an increase in static pressure of 6.9% compared to the design flow, while high flow depicts a static pressure decrease of 11.3% compared to the design flow. At 225°, surge condition depicts a static pressure increase of 7.3% compared to the BEP, while choke condition depicts a decrease in static pressure of 12.9% compared to the BEP. At 270°, low flow depicts a static pressure increase of 7.5% compared to the design flow, while high flow depicts a decrease in static pressure of 14.7% compared to the design flow. At 315°, surge condition depicts an increase in static pressure of 7.7% compared to the BEP, while choke condition depicts a static pressure decrease of 16.9% compared to the BEP. At 345°, which is the cut-off location, low flow depicts an increase in static pressure of 8.5% compared to the design flow, while high flow depicts a static pressure decrease of 20.1% compared to the design flow. At 390°, which is the exit cone location, surge condition depicts a static pressure increase of 6.6% compared to the BEP, while choke condition depicts a decrease in static pressure of 17.5% compared to the BEP. At 393°, which is the discharge duct location, low flow depicts a static pressure increase of 5.9% compared to the design flow, while high flow depicts a decrease in static pressure of 15.7% compared to the design flow. At 400°, which is the outlet location, surge condition depicts an increase in static pressure of 5.9% compared to the BEP, while choke condition depicts a static pressure decrease of 15.3% compared to the BEP. Overall, this quantifies the static pressure variation across each cross-section around the centrifugal compressor volute as a function of flow rates and how the off-design conditions vary against the design condition at low operating speed.

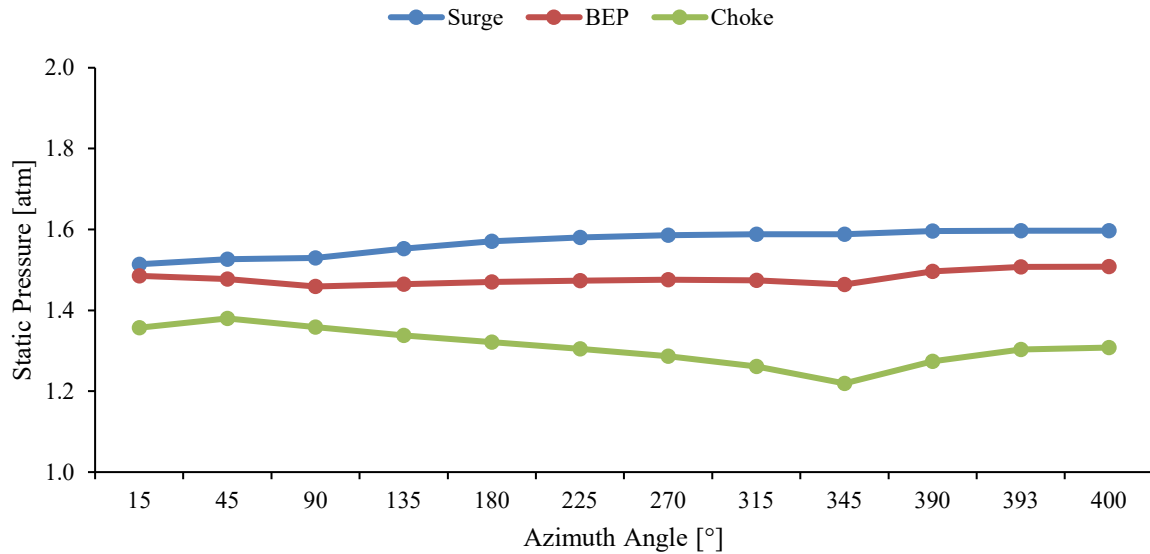


Figure 4.6 Static Pressure across each cross-section around the Compressor Volute during the operating speed of 58.9rps/ $\sqrt{K}$

Figure 4.7 is a graphical representation depicting the asymmetric ratio of static pressure along the radial direction of the profiles, which is from V1 to V2 illustrated in Figure 3.7 around the cross-sections of the centrifugal compressor volute at the operating speed of 58.9rps/ $\sqrt{K}$ . When the asymmetric ratio is at 1, the flow variable is symmetric and signifies desirable flow characteristics. Asymmetric ratio that is not 1 signifies the presence of secondary flows, which means more energy is required due to losses taking place as a result of friction. Secondary flows are a direct cause for head loss therefore, the more symmetric the ratio means the better the volute performs. When the asymmetric ratio is less than 1, the flow variable is asymmetric towards the outer curve. When the asymmetric ratio is more than 1, the flow variable is asymmetric towards the inner curve. It can be seen that static pressure along the radial direction of the profiles through the volute predominantly depicts asymmetry towards the outer curve. It is identified for low flow rate near the surge condition, static pressure displays asymmetry in the flow along the radial direction at 15° towards the inner curve, while downstream of this to 315°, static pressure depicts asymmetry towards the outer curve. From the cut-off location at 345° to the outlet location at 400°, symmetric static pressure in the flow along the radial direction is presented. It is identified for design flow rate at the BEP, static pressure in the flow at 15° is almost symmetric however dominance leans slightly towards the outer curve, which remains downstream of this to 345°. At 390°, static pressure in the flow along the radial direction depicts slight asymmetry towards the inner curve. At 393° and 400°, static pressure in the flow is symmetric along the radial direction. It is identified for high flow rate near the choke condition, there is significant static pressure asymmetry in the flow along the radial direction from 15° to

345° towards the outer curve. At 390°, significant asymmetry of static pressure is displayed towards the inner curve along the radial direction. At 393° and 400°, static pressure in the flow is symmetric. Overall at low operating speed, it is observed that flow rate has an influence on the imbalance of static pressure along the radial direction of the cross-section profiles inside the centrifugal compressor volute. High flow conditions are seen to have the most significant imbalance in static pressure in comparison with low flow and design flow conditions. More detailed graphical representations are depicted in APPENDIX 2.

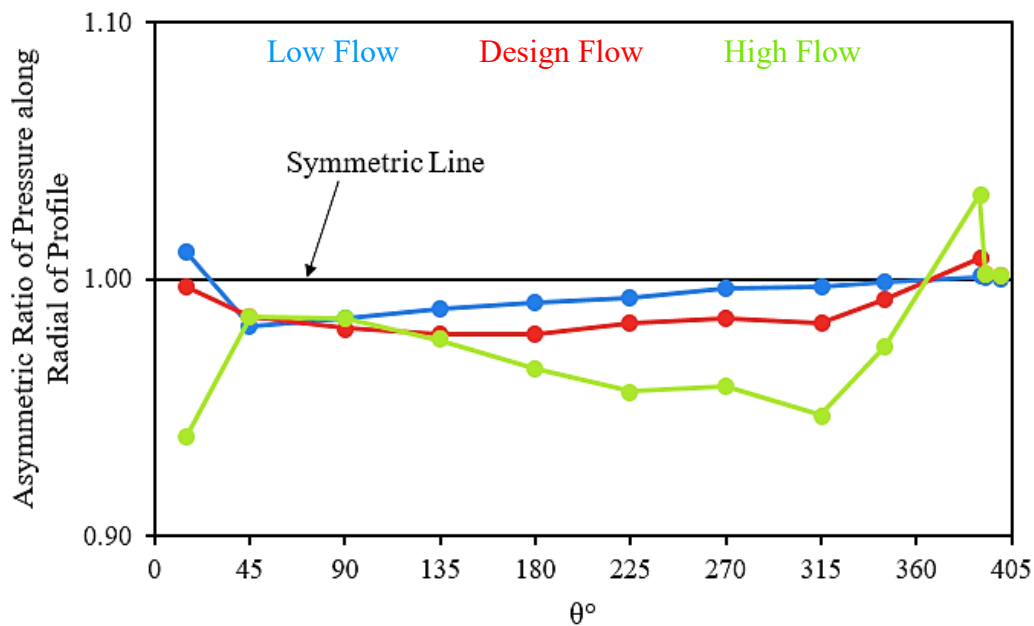


Figure 4.7 Asymmetric Ratio of Static Pressure along the Radial Direction on the Profiles around the Centrifugal Compressor Volute at Operating Speed of 58.9rps/√K during Low Flow Rate, Design Flow Rate and High Flow Rate

Figure 4.8 is a graphical representation depicting the asymmetric ratio of static pressure along the axial direction of the profiles, which is from H1 to H2 illustrated in Figure 3.7 around the cross-sections of the centrifugal compressor volute at the operating speed of 58.9rps/√K. When the asymmetric ratio is at 1, the flow variable is symmetric and signifies desirable flow characteristics. Asymmetric ratio that is not 1 signifies the presence of secondary flows, which means more energy is required due to losses taking place as a result of friction. Secondary flows are a direct cause for head loss therefore, the more symmetric the ratio means the better the volute performs. When the asymmetric ratio is less than 1, the flow variable is asymmetric towards the front face. When the asymmetric ratio is more than 1, the flow variable is asymmetric towards the rear face. It can be seen that low flow and design flow conditions share similar symmetry and asymmetry along the axial direction of the profiles through the volute. Both conditions have static pressure that is almost symmetric through the volute along the axial

direction of the profiles. The behaviour of static pressure along the axial direction at high flow rate present greater asymmetries than low flow and design flow conditions. For low flow rate near the surge condition, it can be seen that static pressure in the flow is asymmetric towards the rear face along the axial direction from  $15^\circ$  to  $90^\circ$ . Downstream of  $135^\circ$ , static pressure in the flow along the axial is seen to be symmetric. For design flow rate at BEP, it is identified that static pressure in the flow along the axial direction is symmetric at  $15^\circ$  then is slightly asymmetric towards the rear face at  $45^\circ$ . At  $90^\circ$ , static pressure in the flow along the axial direction is symmetric. At  $135^\circ$ , static pressure depicts slight asymmetry towards the rear face. At  $180^\circ$  and  $225^\circ$ , static pressure in the flow along the axial direction exhibits asymmetries towards the front face. From  $270^\circ$  to  $345^\circ$ , static pressure in the flow along the axial direction once again displays slight asymmetry towards the rear face, prior to displaying asymmetry towards the front face at  $390^\circ$  and  $393^\circ$ . At  $400^\circ$ , static pressure in the flow achieves symmetry along the axial direction. For high flow rate near the choke condition, there are significant asymmetries of static pressure displayed in the flow along the axial direction towards the rear face from  $15^\circ$  to  $90^\circ$ . At  $135^\circ$  static pressure in the flow is symmetric prior to displaying asymmetries of static pressure along the axial direction towards the rear face of the profile at  $180^\circ$ . Static pressure in the flow along the axial direction is almost symmetric at  $225^\circ$  and  $270^\circ$  however, dominance leans towards the front face. At  $315^\circ$ , static pressure along the axial direction achieves symmetry prior to displaying asymmetry in static pressure towards the rear face at  $345^\circ$ . At  $390^\circ$  and  $393^\circ$ , static pressure exhibits asymmetry towards the front face followed by symmetric static pressure at  $400^\circ$  along the axial direction of the profile. Overall at low operating speed, it is observed that flow rate has an influence on the imbalance of static pressure along the axial direction of the cross-section profiles inside the centrifugal compressor volute. High flow rate depicts the most imbalance in static pressure in comparison with low flow and design flow conditions. More detailed graphical representations are depicted in APPENDIX 2.

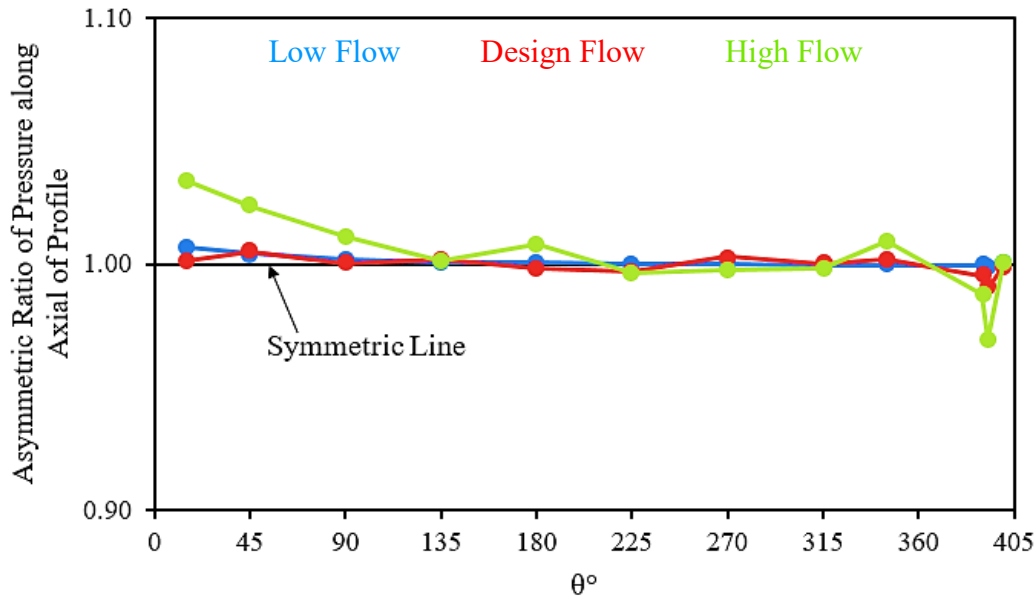


Figure 4.8 Asymmetric Ratio of Static Pressure along the Axial Direction on the Profiles around the Centrifugal Compressor Volute at Operating Speed of 58.9rps/√K during Low Flow Rate, Design Flow Rate and High Flow Rate

#### 4.5 Local Static Pressure around the Centrifugal Compressor Volute at High Operating Speed during Steady Conditions

Figure 4.9 depicts static pressure distribution through the turbocharger compressor volute during the operating speed of 98.2rps/√K at (a) BEP (b) choke (c) surge. Twelve cross-sections through the volute channel have been presented from the first cross-section of the scroll situated above the tongue, through to the outlet of the compressor stage.

Observing (a), which is the volute operation at design flow rate at 98.2rps/√K, static pressure behaviour is similar as aforementioned at BEP and to that also described by Reunanen (2001) [2] and Rezaei (2001) [17]. Static pressure at the periphery appears to be reasonably uniform and increasing downstream of the volute. Further to this, static pressure appears to be lower around the inlet, whereas towards the outer curve, static pressure increases. Static pressure disturbances depicted at the tongue due to flow from upstream of the scroll merging with the inflow and either recirculating the fluid back around the volute or directing the fluid into the discharge duct. After the fluid has passed through the exit cone and directed into the discharge duct, static pressure distribution is high and uniform. From the profiles, it is noticed that static pressure upstream of 180° is slightly lower than that during the operating speed of 58.9rps/√K, while static pressure downstream of 180° is slightly higher than that during the operating speed of 58.9rps/√K. Further to this, low static pressure distribution is exhibited in vicinity of the central region and increases



towards the outer walls. At  $15^\circ$ , static pressure distribution is 2.7atm, which is 6.1% less than the static pressure exhibited at the outlet. Static pressure disturbances can be seen here as a result of the distortions generated at the tongue. Inflow static pressure appears to be lower, as well as that at the outer curve. Further to this, higher static pressure is exhibited at the rear face of the volute. At  $45^\circ$ , static pressure falls from that depicted at  $15^\circ$  by 0.9% and hence the static pressure distribution is 7% less compared to the outlet. Inflow static pressure appears to behave at a comparatively lower static pressure in the central region than the increased static pressure at the outer curve. At  $90^\circ$ , static pressure falls further by 1.7% resulting in 8.6% less static pressure incurring than that at the outlet. It can be seen the static pressure show the same trend as the aforementioned profile however, losses are depicted across the profile. At  $135^\circ$ , static pressure increases by 2.2% and exhibits 6.6% less static pressure than that depicted at the outlet. It can be seen that low static pressure is localised in the centre of the cross-section, which is superimposed by the flow upstream of the scroll. It is also noticed that static pressure has recovered from the aforementioned profile. At  $180^\circ$ , static pressure increases by 1.6%, which is 5.2% less static pressure compared to that at the outlet. This distribution appears to rise further in static pressure over the cross-section. Static pressure increases from the inner curve to the outer curve and these variations appear to be more profound, depicting highest static pressure along the outer curve and comparatively low static pressure localised within the overhang towards the front face of the cross-section. At  $225^\circ$ , static pressure increases by 0.8% and hence, is 4.4% less static pressure compared to that at the outlet. The lowest static pressure in the cross-section is exhibited on the flow superimposed upstream of the scroll at the inner curve. The highest static pressure is exhibited along the outer wall, which seems to have slightly risen further. At  $270^\circ$ , static pressure increases by 0.6% resulting in 3.9% less static pressure compared to that at the outlet. Static pressure slightly rises across the profile, depicting lower static pressure at the inner curve, while depicting higher static pressure along the outer curve. At  $315^\circ$ , static pressure increases by 0.2% and exhibits 3.7% less static pressure compared to that at the outlet. It can be seen that static pressure behaves in the same manner as that previously described. At the cut-off location, static pressure falls by 0.9%, which is 4.5% less static pressure compared to that at the outlet. From the previous profile, it appears the flow has incurred in pressure losses. The lowest static pressure region is more localised to the centre of the cross-section rather than at the inner curve as previously depicted. Higher static pressure incurs concentric to this with the highest cross-section static pressure located partially on the outer curve at the rear face. At the exit cone, static pressure rises by 3.7% and exhibits 1% less static pressure than that depicted at the outlet. From

the previous profile, it appears static pressure has been recovered. Lower cross-section static pressure manifests across the profile with higher pressure incurring above this. At the discharge duct, static pressure has risen by 0.9% with 0.1% less static pressure compared to that at the outlet. A small area of low static pressure is localised at the centre of the profile towards the rear face. This is surrounded by higher static pressure, which appears to propagate circumferentially from the rear face towards the front face of the profile. At the outlet, static pressure rises by 0.1% from the discharge duct. Static pressure appears to be almost uniform however; it rises slightly concentric to the profound lower static pressure area depicted in the centre of the cross-section.

Viewing (b), which is the volute operation at high flow rate at  $98.2\text{rps}/\sqrt{K}$ , depicts reasonably consistent static pressure in the periphery of the volute inlet. The static pressure trend appears to be same as that previously discussed for the operating speed  $58.9\text{rps}/\sqrt{K}$ , however with much lower static pressure. It is immediately noticed that static pressure throughout the volute operating at high flow rate depicts comparatively low static pressure throughout the volute than that depicted at BEP. Static pressure appears to predominantly follow the curvature of the scroll, having higher static pressure at the volute inlet and at the outer wall with lower static pressure through the freestream region of the cross-section. Furthermore, static pressure gradients across the profiles through the volute appear to be consistent and increase in a concentric manner to the low static pressure region. At  $15^\circ$ , static pressure distribution is  $2.1\text{atm}$ , which compared to the outlet is 1.8% more than the static pressure exhibited at the outlet. Low static pressure is depicted at the interface in the curvature of the overhang and in the centre of the cross-section towards the front face of the volute. Static pressure is higher along the outer wall. At  $45^\circ$ , static pressure rises from that depicted at  $15^\circ$  by 2.6% and hence, static pressure distribution has increased significantly by 4.4% compared to the outlet. Static pressure behaves in the same manner as that described for the previous profile. The low pressure region in the centre has however, reduced in its distribution across the profile and moved a little lower in the overhang. At  $90^\circ$ , static pressure falls by 2.8% resulting in 1.5% rise in static pressure incurring than that at the outlet. It is noticed the low pressure region in the centre has increased in its distribution across the profile and moved more central to the profile. Further to this, the higher static pressure surrounding this low static pressure area appears to follow the curvature of the profile. At  $135^\circ$  static pressure decreases by 1.8% and exhibits 0.3% less static pressure than that depicted at the outlet. It can be seen that static pressure in the centre has decreased further signifying pressure losses in the freestream. Higher static pressure surrounding the low pressure area has also decreased towards the inner curve and the rear face of the profile. At  $180^\circ$ , static pressure decreases by 1.2%, which

is 1.6% less static pressure compared to that at the outlet. Low static pressure is depicted at the centre with the behaviour from the previous cross-section propagating across the profile. At 225°, static pressure decreases by a further 1.2% and hence, is 2.8% less static pressure compared to that at the outlet. Low static pressure localised in the freestream has propagated even further across the profile towards the inner curve. It can be seen upstream of this location, there have been minimal static pressure variation. At 270°, static pressure decreases by 1.6% resulting in 4.3% less static pressure compared to that at the outlet. It can be observed that low static pressure continues to manifest across the profile and higher static pressure along the outer curve has decreased, which suggests pressure losses have incurred. At 315°, static pressure decreases by 2.4% and exhibits 6.6% less static pressure compared to that at the outlet. The fluid experiences further pressure losses since static pressure has decreased and low static pressure region in the freestream has also reduced its distribution. At the cut-off location, static pressure falls significantly by 5.5%, which is 11.7% less static pressure compared to that at the outlet. Lowest static pressure zone is exhibited in this cross-section and has propagated across the profile. It appears significant pressure losses have incurred at this location. This fall is the result of the disturbances occurring at the tongue due to inflow and the direction of flow downstream of this location at the tongue. At the exit cone, static pressure significantly rises by 8.7% and exhibits 4.1% less static pressure than that depicted at the outlet. From the previously described profile, static pressure has been recovered significantly. Since this profile is located after the tongue, flow in this location is being directed to the outlet, which means there are currently no disturbances here to maintain lowest pressure incurred at the cut-off location. At the discharge duct, static pressure has risen by 3.9% with 0.3% less static pressure compared to the outlet. Low static pressure appears to have moved from the centre of the profile, slightly to the rear face with static pressure rising towards the front face of the volute. At the outlet, static pressure rises by 0.3% and depicts higher concentric static pressure.

Inspecting (c), which is the volute operation at low flow rate at 98.2rps/ $\sqrt{K}$ , presents secondary flows as a result of static pressure non-uniformities upstream of 135° and minimal variations in static pressure downstream of 135°. It is immediately noticed that static pressure throughout the volute operating at low flow rate depicts comparatively high static pressure throughout the volute than that depicted at BEP. It can be seen upstream 135°, static pressure appears to be lower than that depicted at 58.9rps/ $\sqrt{K}$ , while downstream 135°, static pressure appears to be higher. At 15°, static pressure distribution is 2.6atm, which is 14.4% less than the static pressure exhibited at the outlet. Comparatively low static pressure is depicted at the outer curve with slightly higher

variations distributed across the profile. At  $45^\circ$ , static pressure increases from that depicted at  $15^\circ$  by 4.7% with 10.4% less compared to the outlet. Static pressure is observed to be low in the overhang and rises towards the outer curve. At  $90^\circ$ , static pressure increases further by 2% resulting in 8.6% less static pressure incurring than that at the outlet. Static pressure variations are distributed in the same manner aforementioned. At  $135^\circ$ , static pressure increases by 3.2% with 5.7% less static pressure than that depicted at the outlet. From the bottom of the cross-section in the overhang to the freestream, lowest static pressure in the cross-section is exhibited. Static pressure increases towards the outer curve however; there are minimal variations of this distribution. At  $180^\circ$ , static pressure increases by 2.1%, which is 3.8% less static pressure compared to that at the outlet. Static pressure continues to raise showing lower static pressure at the inner curve, which rises towards the outer curve of the cross-section. At  $225^\circ$ , static pressure increases by 1.1% and hence, is 2.7% less static pressure compared to that at the outlet. Static pressure behaves in the same manner as aforementioned. At  $270^\circ$ , static pressure increases by 0.5% resulting in 2.2% less static pressure compared to that at the outlet. Once more, static pressure behaves in the same manner aforementioned at  $180^\circ$  however; the higher pressure is much less prominent in this cross-section. At  $315^\circ$ , static pressure increases by 0.5% and exhibits 1.8% less static pressure compared to that at the outlet. It is observed, lower static pressure region is depicted in the overhang towards the front face of the volute and at the inflow. Similar to that previously described, higher static pressures exhibited in this cross-section are less pronounced as previously encountered. At the cut-off location, there are no variations in static pressure from the previous profile however; there is 1.8% less static pressure compared to the outlet. This cross-section appears to have almost uniform static pressure however; higher static pressure is exhibited at the walls. At the exit cone, static pressure increases by 1.5% and exhibits 0.3% less static pressure compared to that at the outlet. Superimposed flow emerging from the bottom of the cross-section towards the rear face of the volute depicts lower static pressure than that propagated in the cross-section. At the discharge duct, static pressure increases by 0.3% with 0.1% less static pressure compared to that at the outlet. High static pressure from the previous cross-section has manifested across this profile achieving uniformity. At the outlet, static pressure increases by 0.1% and depicts the same constant and uniform high static pressure as that in the previous profile.

## CHAPTER FOUR: FLOW CHARACTERISTICS INSIDE A CENTRIFUGAL COMPRESSOR VOLUTE DURING STEADY CONDITIONS

Overall at high operating speed of the centrifugal compressor, static pressure increases from choke to surge, as expected in the volute. The choke condition depicts the decrease in static pressure from the first profile to cut-off prior to increasing downstream to the outlet. At BEP, static pressure decreases from the first profile to 90° before increasing downstream of the outlet. The surge condition depicts a linear increase in static pressure.

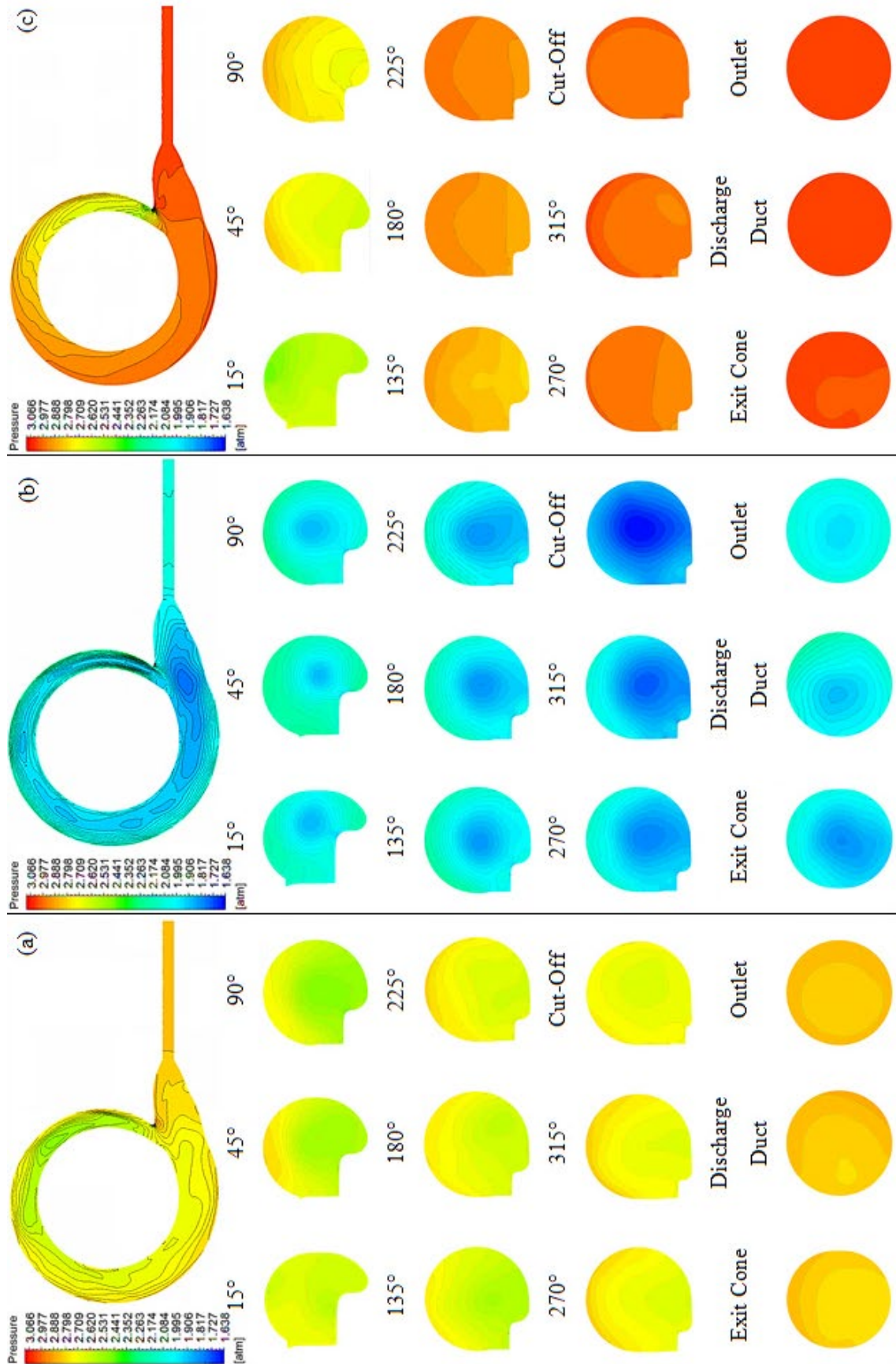


Figure 4.9 Static Pressure around the Compressor Volute during the operating speed of 98.2rps/√K at (a) BEP (b) choke (c) surge

Figure 4.10 depicts the variation of static pressure across each cross-section around the centrifugal compressor volute during the operating speed of 98.2rps/ $\sqrt{K}$  at low flow rate, being near the surge condition; design flow rate, being the best efficiency point; and high flow rate, being near the choke condition. This section is carried out in order to understand how the low and how the high flow rates near extreme phenomena differ in static pressure from the design flow rate. With the exception of 15°, it is clear that the low flow shows higher static pressure than the design flow, while high flow shows lower static pressure than the design flow throughout the centrifugal compressor volute. At 15°, low flow depicts a decrease in static pressure of 2.6% compared to the design flow, while high flow depicts a static pressure decrease of 28.8% compared to the design flow. At 45°, surge condition depicts a static pressure increase of 3% compared to the BEP, while choke condition depicts a decrease in static pressure of 24.3% compared to the BEP. At 90°, low flow depicts a static pressure increase of 6.8% compared to the design flow, while high flow depicts a decrease in static pressure of 25.7% compared to the design flow. At 135°, surge condition depicts an increase in static pressure of 7.9% compared to the BEP, while choke condition depicts a static pressure decrease of 30.9% compared to the BEP. At 180°, low flow depicts an increase in static pressure of 8.5% compared to the design flow, while high flow depicts a static pressure decrease of 34.5% compared to the design flow. At 225°, surge condition depicts a static pressure increase of 8.8% compared to the BEP, while choke condition depicts a decrease in static pressure of 37.3% compared to the BEP. At 270°, low flow depicts a static pressure increase of 8.7% compared to the design flow, while high flow depicts a decrease in static pressure of 40.3% compared to the design flow. At 315°, surge condition depicts an increase in static pressure of 9% compared to the BEP, while choke condition depicts a static pressure decrease of 44% compared to the BEP. At 345°, which is the cut-off location, low flow depicts an increase in static pressure of 9.9% compared to the design flow, while high flow depicts a static pressure decrease of 51.1% compared to the design flow. At 390°, which is the exit cone location, surge condition depicts a static pressure increase of 7.6% compared to the BEP, while choke condition depicts a decrease in static pressure of 44.1% compared to the BEP. At 393°, which is the discharge duct location, low flow depicts a static pressure increase of 6.9% compared to the design flow, while high flow depicts a decrease in static pressure of 39.9% compared to the design flow. At 400°, which is the outlet location, surge condition depicts an increase in static pressure of 6.9% compared to the BEP, while choke condition depicts a static pressure decrease of 39.7% compared to the BEP. Overall, this quantifies the static pressure variation across each cross-section around the centrifugal

compressor volute as a function of flow rates and how the off-design conditions vary against the design condition at high operating speed.

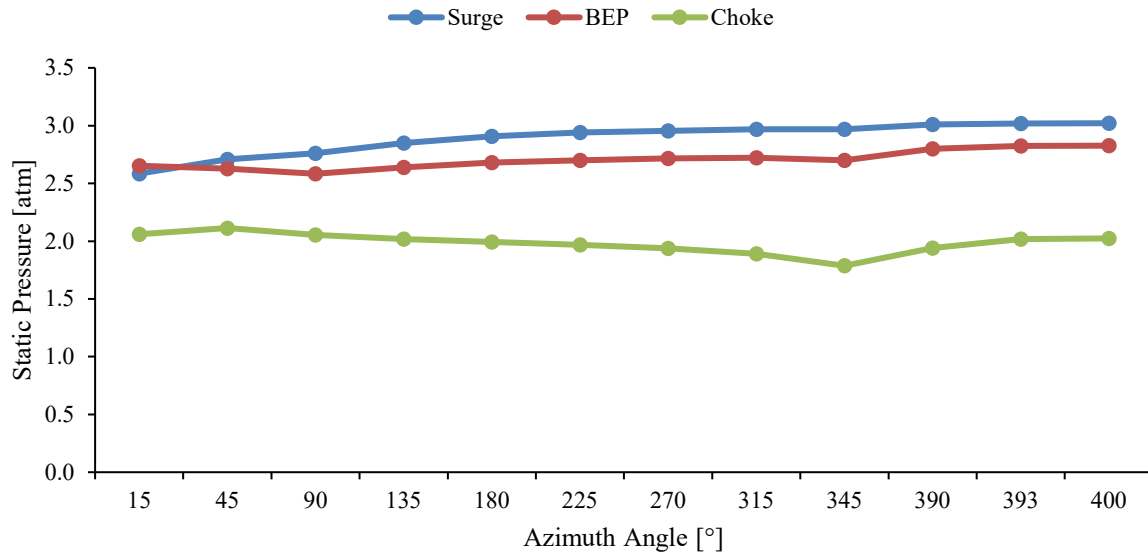


Figure 4.10 Static Pressure across each cross-section around the Compressor Volute during the operating speed of 98.2rps/√K

Figure 4.11 is a graphical representation depicting the asymmetric ratio of static pressure along the radial direction of the profiles, which is from V1 to V2 illustrated in Figure 3.7 around the cross-sections of the centrifugal compressor volute at the operating speed of 98.2rps/√K. It is observed that static pressure along the radial direction of the profiles at low flow and design flow, show almost parallel asymmetries. At low flow being near the surge condition, considerable asymmetry is seen towards the inner curve at 15°, whereas downstream to 345° depicts asymmetry of static pressure towards the outer curve along the radial direction of the profiles. At 390°, there is static pressure asymmetry towards the inner curve prior to being symmetric downstream to the outlet. At design flow being the BEP, static pressure in the flow from 15° to 345° depict significant asymmetry towards the outer curve along the radial direction of the profiles. At 390°, static pressure is depicted towards the inner curve prior to being symmetric downstream to the outlet. At high flow being near the choke condition, there are substantial asymmetries of static pressure towards the outer curve along the radial direction from 15° to 345°. At 390° and 393°, static pressure displays asymmetries towards the inner curve prior to being symmetric at the outlet. Overall at high operating speed, it is observed that flow rate has a significant influence on the imbalance of static pressure along the radial direction of the cross-section profiles inside the centrifugal compressor volute. It is noticed that high flow conditions have significant imbalance in static pressure in comparison with low flow and design flow conditions. More detailed graphical representations are depicted in APPENDIX 2.



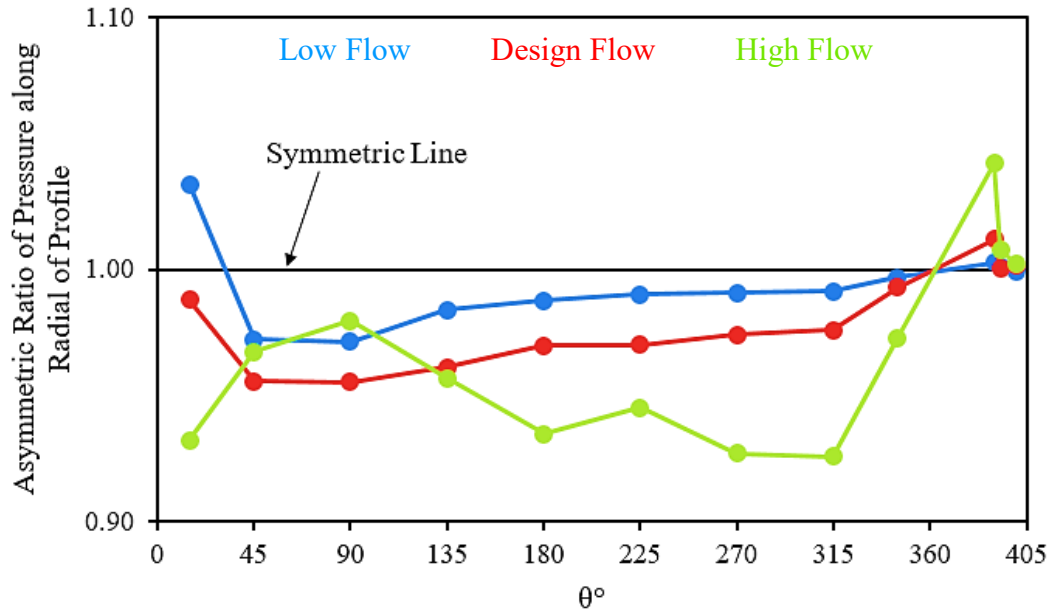


Figure 4.11 Asymmetric Ratio of Static Pressure along the Radial Direction on the Profiles around the Centrifugal Compressor Volute at Operating Speed of 98.2rps/√K during Low Flow Rate, Design Flow Rate and High Flow Rate

Figure 4.12 is a graphical representation depicting the asymmetric ratio of static pressure along the axial direction of the profiles, which is from H1 to H2 illustrated in Figure 3.7 around the cross-sections of the centrifugal compressor volute at the operating speed of 98.2rps/√K. It is observed that the low flow condition predominantly depicts symmetry in static pressure along the axial direction through the volute, while the high flow condition predominantly depicts asymmetry in static pressure along the axial direction through the volute. At low flow being near the surge condition, static pressure in the flow depicts asymmetry towards the rear face at 15° and 45°. At 90°, symmetric static pressure along the axial direction is achieved prior to presenting slight asymmetries towards the front face at 135° and 180°. Thereafter, downstream to 345° static pressure in the flow is symmetric. Slight asymmetry is exhibited towards the front face at 390° and 393°. Static pressure in the flow at 400° is once again symmetric along the axial direction. At design flow being the BEP, static pressure in the flow depicts asymmetry towards the rear face from 15° to 225°. Static pressure in the flow along the axial direction displays symmetry at 270° prior to displaying asymmetry in the flow towards the front face at 315°. Following on from here at 345°, static pressure along the axial direction once again exhibits asymmetry towards the rear face. Downstream from 390°, static pressure in the flow is asymmetric towards the front face. At high flow being near the choke condition, the flow depicts significant asymmetry of static pressure along the axial direction on the profiles at 15° and 45°. From 90° to 180°, static pressure in the flow displays comparatively less asymmetry towards the rear face to that aforementioned. At 225°, static pressure in the flow is asymmetric towards the

front face. From  $270^\circ$  to  $345^\circ$ , static pressure in the flow depicts asymmetry towards the rear face, prior to displaying asymmetry towards the front face downstream of  $390^\circ$ . In addition to this, comparatively greater asymmetries of static pressure are noticed at  $345^\circ$  and  $393^\circ$  along the axial direction. Overall at high operating speed, flow rate is seen to have a significant influence on the imbalance of static pressure along the axial direction of the cross-section profiles inside the centrifugal compressor volute. High flow conditions depict prominent imbalance is static pressure along the axial direction through the tongue section due its blended geometry and narrow passage. More detailed graphical representations are depicted in APPENDIX 2.

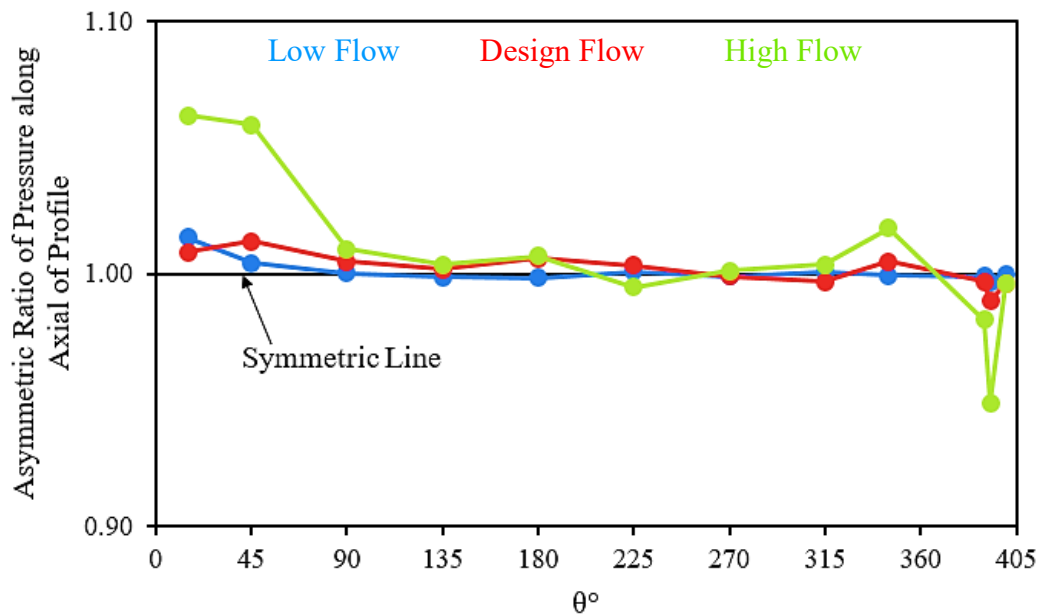


Figure 4.12 Asymmetric Ratio of Static Pressure along the Axial Direction on the Profiles around the Centrifugal Compressor Volute at Operating Speed of  $98.2\text{rps}/\sqrt{K}$  during Low Flow Rate, Design Flow Rate and High Flow Rate

#### 4.6 Local Speed Comparison of Static Pressure around the Centrifugal Compressor Volute during Steady Conditions

Table 4.2 depicts the steady response of the local speed comparison, where the high operating speed of  $98.2\text{rps}/\sqrt{K}$  is compared against the low operating speed of  $58.9\text{rps}/\sqrt{K}$  for static pressure across each of the selected cross-section through the turbocharger compressor volute. It can be seen that static pressure at  $98.2\text{rps}/\sqrt{K}$  increases at design and off-design conditions compared to that at  $58.9\text{rps}/\sqrt{K}$ . The lowest static pressure increase through the volute occurs at high flow conditions, while highest static pressure increase through the volute occurs at low flow conditions. For low flow and design flow, highest static pressure variation is found at the outlet, being  $400^\circ$ , while lowest static pressure variation is found at  $15^\circ$  and  $90^\circ$ , respectively. At high

flow, the highest static pressure variation is found at the discharge duct, being 393°, while lowest static pressure variation is found at the cut-off, being 345°.

*Table 4.2 Local Speed Comparison of Static Pressure Variation during Steady Response*

$\theta^\circ$	Static Pressure [%]		
	Low Flow	Design Flow	High Flow
15	70.7	78.6	51.8
45	77.4	77.9	53.2
90	80.4	77.0	51.2
135	83.5	80.2	50.7
180	85.1	82.3	50.8
225	86.0	83.3	50.8
270	86.3	84.1	50.5
315	86.8	84.7	49.9
345	86.9	84.4	46.5
390	88.7	87.0	52.4
393	89.1	87.3	54.9
400	89.2	87.4	54.8

#### 4.7 Global Velocity Magnitude Distribution around the Centrifugal Compressor during Steady Conditions

As the impeller rapidly rotates due to the mechanical energy transferred from the shaft, momentum generated by the impeller wheel causes the ambient air to be exposed to suction force, drawing fluid into inducer. Flow enters the compressor stage at a high velocity magnitude and as it approaches the impeller, it follows the path of the blades. As the flow passes through the impeller, Coriolis forces and work input in the form of diffusion occurs at the same time, imparting kinetic energy resulting in a velocity magnitude increase and static pressure rise into the fluid. Centrifugal forces act on the fluid, pushing particles outwards, radially into the diffuser. Velocity magnitude is comparatively higher at the trailing edge of the impeller blades than the leading edge. As the flow is squeezed into the annular diffuser passage, diffusion causes velocity magnitude to decrease converting kinetic energy into potential energy [17]. The radial flow velocity is converted into secondary vortex flow when entering the volute passage [21]. Velocity magnitude decreases around the volute due to the increase in area as well as the curvature of scroll [17]. At the BEP, constant circumferential velocity is exhibited at the periphery of the volute inlet with reasonable uniform flow velocity across the cross-sections,

having a slight increase in the freestream. At the choke side of the map where mass flow rates are higher than that at the BEP, radial velocity at the periphery of the volute inlet is found to be greater than the tangential velocity, forming a greater swirl velocity that increases with the cross-section around the volute. This is a result of the volute passage being smaller for the large amount of mass flow attempting to pass through. At the surge side of the map where mass flow rates are lower than that at the BEP, flow initially accelerates in the tongue region and then decelerates downstream to the outlet. This is a result of the volute passage being bigger for the small amount of mass flow attempting to pass through. Tangential velocity is greater with very low radial velocity, which causes tangential velocity to decrease towards the outlet hence; the volute behaves as a nozzle or a diffuser [72]. The exhibited radial velocity at the periphery of the volute inlet causes constant swirl velocity to occur.

Figure 4.13 in the top row, depicts flow velocity magnitude variation in the turbocharger compressor stage during the operating speed of  $58.9\text{rps}/\sqrt{K}$  at (a) BEP (b) choke (c) surge. Observing (a), which is the turbocharger compressor stage operation at design flow rate, ambient air flows into the compressor stage through the inducer at a  $20\text{m/s}$ . From here, flow accelerates by  $180.5\%$  as entering the impeller. Flow velocity magnitude accelerates by  $27.5\%$  when air particles pass through the impeller passages and exits into the diffuser. After compressibility and diffusion have taken place in the diffuser, flow decelerates by  $38.3\%$ . Once the flow has been collected in the volute and kinetic energy in the flow has been converted into potential energy, the flow decelerates even further at the outlet by  $45.7\%$ .

Viewing the operating speed of  $58.9\text{rps}/\sqrt{K}$  at (b), which is the turbocharger compressor stage operation at high flow rate, the ambient air enters the inducer at  $29\text{m/s}$ . When the fluid reaches the exit of the inducer and enters the impeller, the flow accelerates by  $141.4\%$ . After the ambient air has passed through the impeller, changing the fluid properties, further acceleration incurs by  $61.5\%$ . After altering the fluid properties even more through the diffuser passage, velocity magnitudes fall by  $38.2\%$  prior to entering the volute. When the fluid reaches the outlet, the results show the flow decelerates by  $20.3\%$ .

Inspecting the operating speed of  $58.9\text{rps}/\sqrt{K}$  at (c), which is the turbocharger compressor stage operation at low flow rate, ambient air enters the inducer at  $8\text{m/s}$ . Fluid flow accelerates by  $484.4\%$  as it reaches the inlet of the impeller. By the time, the fluid is energised and has accelerated by  $7.9\%$  at the diffuser inlet. From here, after compressibility and diffusion have

taken place, flow decelerates by 47.5%. After the energy conversion has taken place, the compressed fluid decelerates further by 76.9% to the outlet.

It can be seen from the results that by the end of each station, there are variations between the design and off-design conditions. Generally, it appears that velocity magnitude increases in the inducer and impeller then decreases downstream thereafter. Reviewing variations in velocity magnitude under the choke condition against the BEP, flow accelerates by 18.9% at the end of the inducer; accelerates by 25.1% at the end of the impeller; decelerates by 13.7% at the end of the diffuser; and decelerates even further by 41% at the end of the volute. Reviewing variations in velocity magnitude under the surge condition against the BEP, flow decelerates by 19.8% at the end of the inducer; decelerates by 23.5% at the end of the impeller; decelerates by 19.8% at the end of the diffuser; and decelerates even further by 65.9% at the end of the volute.

The results also show the variations through each station between the design and off-design conditions. Reviewing variations in velocity magnitude under the choke condition against the BEP, the flow accelerates by 10.9% through the inducer; accelerates by 57.5% through the impeller; accelerates by 13.6% through the diffuser; and decelerates by 94% through the volute. Reviewing variations in velocity magnitude under the surge condition against the BEP, the flow accelerates by 3.4% through the inducer; decelerates by 74.1% through the impeller; accelerates by 17.3% through the diffuser; and accelerates by 34.8% through the volute.

Figure 4.13 in the bottom row, depicts flow velocity magnitude variation in the turbocharger compressor stage during the operating speed of  $98.2\text{ rps}/\sqrt{K}$  at (a) BEP (b) choke (c) surge. Observing (a), which is the turbocharger compressor stage operation at design flow rate, ambient air flows into the compressor stage through the inducer at a  $40\text{ m/s}$ . From here, flow accelerates entering the impeller by 171.3%. When air particles pass through the impeller passages and exits into the diffuser, flow velocity magnitude accelerates further by 18.2%. After passing through the diffuser having altered the fluid properties, flow decelerates by 41.6%. Once the flow has been collected in the volute flow decelerates even further at the outlet by 53.1%.

Viewing the operating speed of  $98.2\text{ rps}/\sqrt{K}$  at (b), which is the turbocharger compressor stage operation at high flow rate, the ambient air enters the inducer at  $55\text{ m/s}$ . When the fluid enters the impeller, flow accelerates by 146.1%. After the ambient air has passed through the impeller, energising fluid properties, further acceleration incurs by 72%. After the fluid properties changing even more through the diffuser passage due to compressibility and diffusion, velocity

magnitudes falls by 50.6% prior to entering the volute. When the fluid reaches the outlet, the results show the flow decelerates by 29.7%.

Inspecting the operating speed of 98.2rps/ $\sqrt{K}$  at (c), which is the turbocharger compressor stage operation at low flow rate, ambient air enters the inducer at 23m/s. Fluid flow accelerates by 261.6% as it leaves the inducer and enters the impeller. By the time, the flow properties have altered due to the energy imparted on the fluid; it has accelerated only by 0.4% at the diffuser inlet during this condition. From here, flow decelerates by 42.9% into the volute. Post energy through the volute, the compressed fluid decelerates by 72.8% to the outlet.

It can be seen from the results that by the end of each station, there are variations between the design and off-design conditions. Reviewing variations in velocity magnitude under the choke condition against the BEP, flow accelerates by 20.4% at the end of the inducer; accelerates by 35.3% at the end of the impeller; accelerates by 16.3% at the end of the diffuser; and accelerates even further by 44.2% at the end of the volute. Reviewing variations in velocity magnitude under the surge condition against the BEP, flow decelerates by 21.9% at the end of the inducer; decelerates by 21.1% at the end of the impeller; decelerates by 1.8% at the end of the diffuser; and decelerates by 43.3% at the end of the volute.

The results also show the variations through each station between the design and off-design conditions. Reviewing variations in velocity magnitude under the choke condition against the BEP, the flow accelerates by 15.3% through the inducer; accelerates by 76.1% through the impeller; accelerates by 41.7% through the diffuser; and decelerates by 49.6% through the volute. Reviewing variations in velocity magnitude under the surge condition against the BEP, the flow decelerates by 10.5% through the inducer; decelerates by 97.8% through the impeller; accelerates by 3.2% through the diffuser; and accelerates by 34.3% through the volute.

Table 4.3 details the speed comparison of velocity magnitude variation at 98.2rps/ $\sqrt{K}$  compared to that at 58.9rps/ $\sqrt{K}$ . It can be seen at low flow rate, highest velocity magnitude variation at the inlet and the outlet occurs in the inducer and volute, respectively, where the turbocharger compressor stage operating at 98.2rps/ $\sqrt{K}$  increases by over 100% compared to that at 58.9rps/ $\sqrt{K}$ . The lowest velocity magnitude variation at the inlet and outlet occurs in the diffuser and impeller, respectively, where the operating condition 98.2rps/ $\sqrt{K}$  increases compared to that at 58.9rps/ $\sqrt{K}$ . At the design flow rate, highest velocity magnitude variation at the inlet and the outlet occurs in the inducer, while lowest velocity magnitude variation at the inlet and outlet occurs in the volute, where the operating condition 98.2rps/ $\sqrt{K}$  increases for both compared to

that at 58.9rps/ $\sqrt{K}$ . At the high flow rate, highest velocity magnitude variation at the inlet and the outlet occurs in the diffuser and outlet, respectively, while lowest velocity magnitude variation at the inlet and outlet occurs in the volute, where the operating condition 98.2rps/ $\sqrt{K}$  increases compared to that at 58.9rps/ $\sqrt{K}$ .

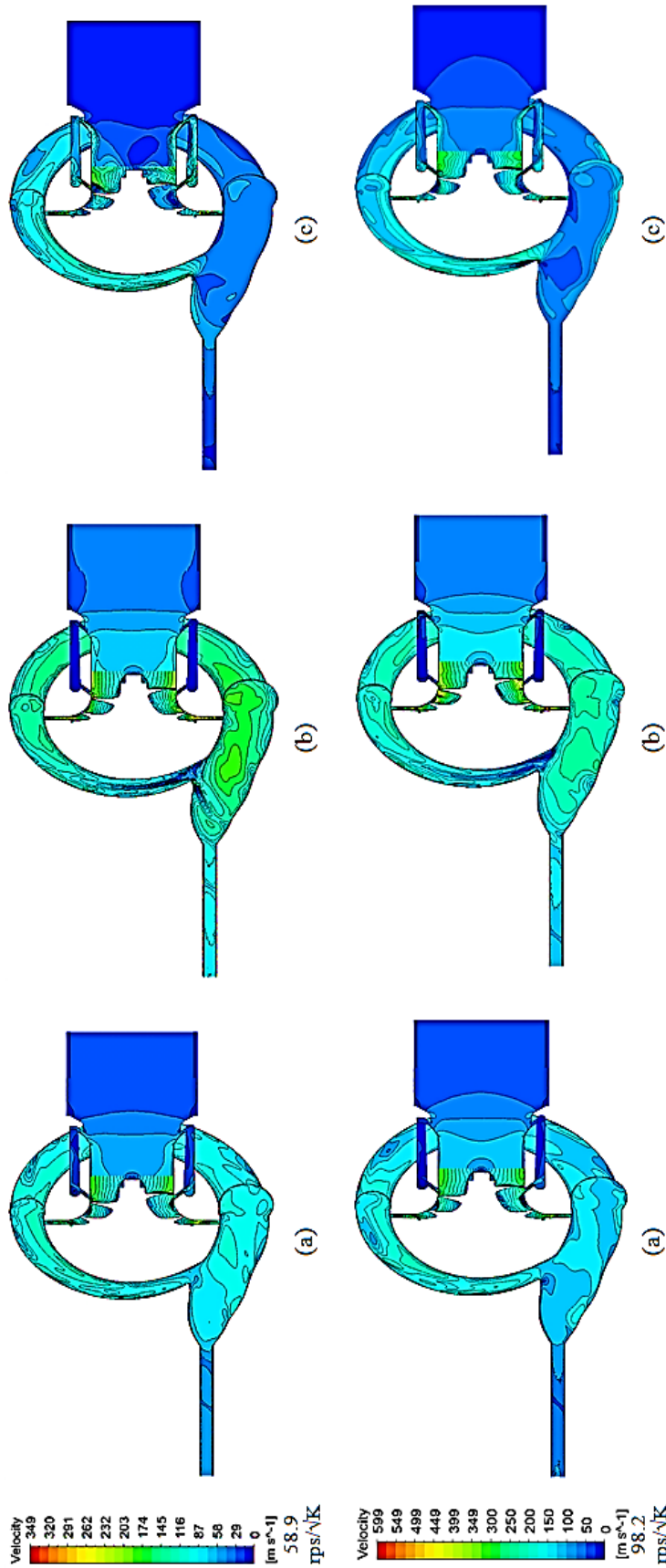


Table 4.3 Global Speed Comparison of Velocity Magnitude Variation

Compressor Component	Velocity Magnitude In [%]			Velocity Magnitude Out [%]		
	Low Flow	Design Flow	High Flow	Low Flow	Design Flow	High Flow
Inducer	197.3	95.4	88.8	84	89	92.5
Impeller	76.7	72	73.3	64.5	59.5	84.5
Diffuser	69.9	59.9	95	85	51.1	55.8
Volute	84.6	51	55.9	116.6	30.3	37.5

Figure 4.13 Velocity Magnitude Variation in the Turbocharger Compressor Stage during the operating speed of 58.9 rps/°K and 98.2 rps/°K at (a) BEP (b) choke (c) surge



Figure 4.14 depicts velocity magnitude variations through each station in the compressor stage during the operating speed of (a) 58.9rps/ $\sqrt{K}$  and (b) 98.2rps/ $\sqrt{K}$ , both under design and off-design conditions. Overall, it is clear that velocity magnitude variation through each component is much higher at 98.2rps/ $\sqrt{K}$  than at 58.9rps/ $\sqrt{K}$ .

Figure 4.14 (a) represents the variation of velocity magnitude through each station in the compressor stage during the operating speed of 58.9rps/ $\sqrt{K}$  under design and off-design conditions. Velocity magnitude in the inducer show similar variances between the three conditions. Highest flow velocity magnitude variance occurs during the choke condition while lowest variance occurs at BEP. Through the impeller, velocity magnitude varies substantially during the choke condition and comparatively very little during the surge condition. Through the diffuser, velocity magnitude variances during the surge and choke conditions are very similar, whereas flow velocity magnitude at BEP decelerated the least. Through the volute, flow velocity during the choke condition decelerated the least whereas, during the surge condition flow velocity decelerated the most. It appears as the mass flow rate increases, variance in velocity magnitude decreases through the volute. In all three operating conditions, flow velocity magnitude varies in the form of acceleration through the inducer and impeller and substantially varies in the form of deceleration through the diffuser and volute.

Figure 4.14 (b) represents the variation of velocity magnitude through each station in the compressor stage during the operating speed of 98.2rps/ $\sqrt{K}$  under design and off-design conditions. As mass flow rate increases, variance in flow velocity magnitude through the inducer also increases in the form of acceleration. Through the impeller, velocity magnitude variation during surge condition is negligible whereas this variation during the choke condition is significantly high. Flow velocity magnitude through the diffuser varies in the form of deceleration. This variance is considerably high for the three conditions, where BEP and surge conditions are very similar and choke condition varies significantly. Velocity magnitude through the volute varies considerably in the form of deceleration. It can be seen as the mass flow rate increases, the flow velocity magnitude through the volute decreases. In all three operating conditions, flow velocity magnitude varies in the form of acceleration through the inducer and impeller while through the diffuser and volute, flow velocity magnitude varies in the form of deceleration.

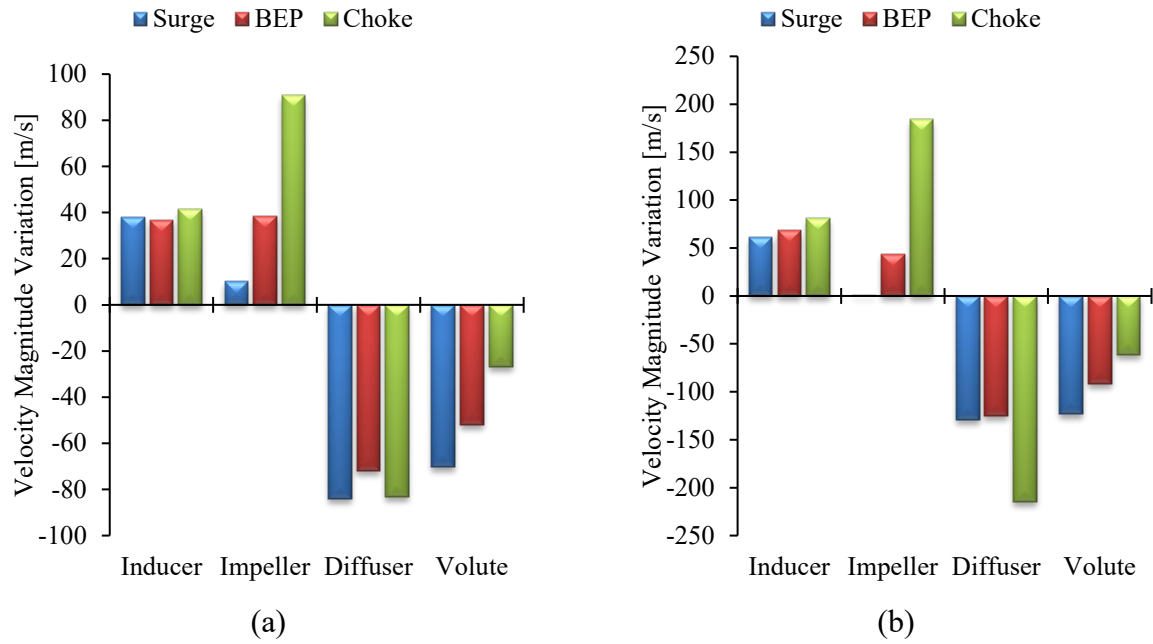


Figure 4.14 Velocity Magnitude difference at the inlet and outlet of each component in the turbocharger compressor stage during (a) 58.9rps/√K (b) 98.2rps/√K

#### 4.8 Local Velocity Magnitude Distribution around the Centrifugal Compressor Volute at Low Operating Speed during Steady Conditions

Figure 4.15 depicts velocity magnitude distribution through the turbocharger compressor volute during the operating speed of 58.9rps/√K at (a) BEP (b) choke (c) surge. Twelve cross-sections through the volute channel have been presented from the first cross-section of the scroll situated above the tongue, through to the outlet of the compressor stage.

It can be seen that there is zero velocity at the walls due to no-slip boundary conditions. Skin friction at the walls incur in flow close to the wall to retard the flow causing it to eventually stop at the wall. When flow enters the volute from the diffuser, radial velocity component is converted into a secondary vortex flow, namely, swirl velocity. When this phenomenon takes place, turbulence mixing or the motion of large scale eddies incurring cause turbulence and viscosity in the flow regime, causing the swirl flow velocity component to dissipate. This results in meridional velocity dump losses and its recovery is highly unlikely. Due to this dissipation, tangential velocity superimposes on the flow in the volute periphery. Since the presented volute is external, flow is expected to increase its static pressure and have minimal losses as flow velocity decelerates through the freestream of the volute. This, in addition to the curvature of the volute, causes variations in velocity magnitude. Furthermore, disturbances at the tongue has a

ricochet effect upstream the tongue, specifically the beginning sector of the scroll; downstream the tongue, specifically the exit cone; and at the cut-off location [15, 17, 21, 73].

Observing (a), which is the volute operation at design flow rate at  $58.9\text{rps}/\sqrt{K}$ , it is noticed, there is a great deal of non-uniformities occurring, which signifies the magnitude of secondary flows incurring in the flow regime. Low flow velocity magnitude pockets are depicted near the walls along the periphery of the outer curve and the volute inlet. At  $15^\circ$ , velocity magnitude is  $78\text{m/s}$ , which compared to the outlet, has an accelerated flow of  $25.4\%$  compared to that exhibited at the outlet. It can be seen flow velocity magnitude enters the volute and decelerates significantly in the overhang. At  $45^\circ$ , velocity magnitude accelerates from that depicted at  $15^\circ$  by  $36.6\%$  hence, having accelerated flow of  $71.2\%$  compared to that exhibited at the outlet. High velocity magnitude is noticed when the flow enters the volute at this cross-section, which decelerates in the overhang. At  $90^\circ$ , velocity magnitude accelerates by  $10.3\%$ , which in turn resulted in having  $88.9\%$  accelerated flow than that at the outlet. There is a significant increase in flow velocity magnitude across this cross-section, with higher velocities depicted at the inlet and in the overhang. At  $135^\circ$ , velocity magnitude decelerates by  $8.8\%$  from the previous and exhibits  $72.4\%$  accelerated flow velocity magnitude than that depicted at the outlet. It can be seen inflow velocity magnitude is significantly greater, while the distribution of flow velocity magnitude over the cross-section has reduced, predominantly showing lower regions of velocity magnitude in vicinity of the outer curve. At  $180^\circ$ , flow velocity magnitude decelerates by  $6.9\%$ , which is  $60.4\%$  accelerated flow compared to that at the outlet. It is noticed that incoming flow has decreased as well as flow distributed across the profile. The flow from the rear face of the volute depicts low velocity magnitude, which propagates towards the front face of the volute. At  $225^\circ$ , velocity magnitude decelerates by  $4\%$  and hence, the flow is  $53.9\%$  accelerated compared to that at the outlet. Velocity magnitude across this cross-section shows the previous high velocity regions to reduce and decelerate further, showing a very low velocity region at the outer curve. At  $270^\circ$ , flow velocity magnitude decelerates by  $2\%$  resulting in  $50.8\%$  accelerated flow compared to that at the outlet. Low inflow velocity magnitude is distributed across the profile with slightly higher flow velocity magnitude remaining in the overhang. At  $315^\circ$ , flow accelerates by  $1.1\%$  and exhibits  $52.5\%$  accelerated flow velocity magnitude compared to that at the outlet. In this profile, inflow velocity magnitude increases further to that exhibited in the previously mentioned profile. Velocity magnitude remains low on the rear face of the volute and the region of slightly higher velocity exhibited in the overhang appears to have propagated. At the cut-off location, flow velocity magnitude accelerates further by  $7.7\%$ , which depicts an

acceleration of 64.3% compared to that at the outlet. It is noticed that there is significantly higher flow velocity magnitude exists at the inlet, with much lower flow velocity magnitude along the outer curve and inner curve. This is a result of being in vicinity of the tongue. The region of slightly high velocity magnitude in the overhang aforementioned also remains to exist in this cross-section. At the exit cone, flow velocity magnitude decelerates by 27.2%, exhibiting 19.7% accelerated flow velocity magnitude than that depicted at the outlet. Low velocity magnitude is depicted on the front face of the volute with distribution propagating from top of the profile. It is noticed flow velocity magnitude has reduced considerably in comparison with the cut-off location. At the discharge duct, flow velocity magnitude has decelerated by 13.4% with 3.6% acceleration compared to the outlet. Distribution of low velocity magnitude zones are identified across this profile, predominantly somewhat in the freestream as well as from the top of the profile. This appears to be from the upstream flow depicted in the exit cone. At the outlet, flow velocity magnitude decelerates even further by 3.5%, showing low regions in the freestream.

Viewing (b), which is the volute operation at high flow rate at  $58.9\text{rps}/\sqrt{K}$ , it can be seen that there are high non-uniformities in the fluid, indicating the presence of secondary flows. These are from the radial velocity component forming into swirl velocity. Distinct pockets of low flow velocity magnitude peaks are depicted near the walls along the periphery of the outer curve and the volute inlet. Rezaei (2001) [17] describes at higher flow rates, throughflow velocity increases from the tongue to the outlet as a result of flow incoming to the volute with a negative incidence. This indicates the volute passage is large for the small amount of mass flow passing through and is as expected at this off-design condition near choke. However, what is seen in this case are low flow velocity zones displayed upstream the tongue, downstream the tongue and in the tongue region, which propagates into the exit cone. This flow deceleration indicates the volute passage is small for the large amount of mass flow passing through and is unexpected at this off-design condition near choke. Downstream of  $45^\circ$  however, it can be seen that flow velocity magnitude begins to continuously accelerate until the flow reaches the cut-off location, where flow velocity magnitude decelerates, which is somewhat similar to that described by Rezaei (2001) [17]. Furthermore, the increase in flow velocity through the volute passage is also due to secondary flows, such as swirl velocity component, which increases with the cross-sectional area. At  $15^\circ$ , velocity magnitude is  $86\text{m/s}$ , which compared to the outlet has decelerated flow of 17.9% compared to that exhibited at the outlet. Here, flow enters the volute at a high velocity magnitude which decelerates rapidly, prominent in the central region of the profile. Distinctive high velocity magnitude is also displayed in vicinity of the wall in the front face and in the overhang at the

interface. At  $45^\circ$ , velocity magnitude decelerates from that depicted at  $15^\circ$  by 6.7% hence, having decelerated flow of 23.5% compared to that exhibited at the outlet. This is the result of that aforementioned regarding disturbance in the flow caused by the tongue. Low velocity magnitude zone is depicted in the freestream of the cross-section, which increases concentric to this low velocity magnitude zone. Additionally, there is a region of low velocity magnitude on the rear face of the profile, which appears to increase along the outer curve towards the front face. Higher velocity magnitude regions are located at the inlet on the rear face of the profile and in the overhang at the interface. At  $90^\circ$ , velocity magnitude accelerates by 53.3%, which in turn resulted in having 17.4% accelerated flow than that at the outlet. Low velocity magnitude is depicted in the freestream as well as on the rear face, at the inlet towards the overhang and in the vicinity of the overhang wall. Higher flow velocity magnitude is exhibited surrounding the low velocity region in the freestream with even higher areas of velocity magnitude close to the outer curve wall and at the inlet. At  $135^\circ$ , velocity magnitude accelerates by 8.1% from the previous and exhibits 26.8% accelerated flow velocity magnitude than that depicted at the outlet. Low flow velocity magnitude region is localised in proximity of the outer curve and at the inlet close to the overhang. Higher velocity magnitude is seen across the lower sector of the profile. At  $180^\circ$ , flow velocity magnitude accelerates by 2.6%, which is 30.1% accelerated flow compared to that at the outlet. High velocity magnitude is exhibited at the inflow along the rear face and appears to accelerate from the outer curve towards the overhang. Low velocity magnitude is exhibited near the inlet towards the overhang as well as along the outer curve. At  $225^\circ$ , velocity magnitude accelerates by 1.6% and hence, the flow is 32.1% accelerated compared to that at the outlet. Throughflow velocity magnitude in this profile is similar to that previously discussed, however with higher velocity magnitude across the lower sector of the profile and low velocity propagating from the outer curve towards the rear face. At  $270^\circ$ , flow velocity magnitude accelerates by 2.9% resulting in 36% accelerated flow compared to that at the outlet. Low velocity magnitude is depicted along the outer curve and at the inlet close to the overhang. From the outer curve to the lower sector of the profile in the overhang, throughflow velocity magnitude increases. At  $315^\circ$ , flow accelerates by 4.8% and exhibits 42.5% accelerated flow velocity magnitude compared to that at the outlet. Behaviour of flow velocity magnitude is the same as that previously described, however the distribution is propagated, especially with high velocity magnitude region localised in the lower sector of the profile, towards the overhang. At the cut-off location, flow velocity magnitude accelerates further by 10.3%, which depicts an acceleration of 57.2% compared to that at the outlet. Prominent low throughflow velocity magnitude can be seen along the outer curve towards the rear face and near the inlet towards the overhang. Higher

velocity magnitude exhibits along the front face and increases from the walls inwards towards the central region. In this case, highest throughflow velocity is depicted in the lower sector of the profile towards the front face. Significant variations in throughflow velocity magnitudes are exhibited, again, indicating that secondary flows are present. At the exit cone, flow velocity magnitude decelerates by 20.5%, exhibiting 24.9% accelerated flow velocity magnitude than that depicted at the outlet. Low velocity magnitude regions are depicted along the rear face, top curve and front face of the profile, while towards the central region, the flow appears to accelerate. The highest velocity region is depicted in the central lower sector of the profile towards the front face. At the discharge duct, flow velocity magnitude has decelerated by 12.7% with 9% acceleration compared to the outlet. High velocity magnitude decelerates from the rear face and to the front face, showing prominent region of the highest velocity magnitude in the central lower sector of the profile towards the rear face. At the outlet, flow velocity magnitude decelerates even further by 8.2%, showing higher regions in the freestream with slightly lower surrounding this.

Inspecting (c), which is the volute operation at low flow rate at 58.9rps/ $\sqrt{K}$ , it can be seen that there is a region on high velocity magnitude along the outer curve downstream the upper sector of the tongue. Rezaei (2001) [17] describes at lower flow rates, throughflow velocity decreases from the tongue to the outlet as a result of flow incoming to the volute with a positive incidence. This indicates the volute passage is small for the large amount of mass flow passing through and is as expected at this off-design condition near surge. In this case, throughflow velocity magnitude decelerates from the tongue to the outlet, indicating that at this off-design condition near surge, flow velocity magnitude behaves as expected. At 15°, velocity magnitude is 124m/s, which compared to the outlet, has accelerated flow of 487.9% compared to that exhibited at the outlet. It is observed that inflow velocity magnitude is high on the rear face and decreases slightly following the curvature of the outer wall prior to decreasing further across the profile towards the overhang. There is also a region of low velocity on the front face of the profile. Non-uniformities at this location are expected due to being the first cross-section downstream the upper sector of the tongue. At 45°, velocity magnitude decelerates from that depicted at 15° by 1.9% hence, having accelerated flow of 476.8% compared to that exhibited at the outlet. Similar to the previous discussion at 15°, high flow velocity magnitude is seen at the entrance towards the rear face, however at this cross-section, distribution of high velocity magnitude is much smaller than that previously observed. The velocity magnitude from the rear face decelerating slightly along the curvature of the outer wall in the previous cross-section appears to have

propagated even further following the curvature along the front face wall towards the overhang in this cross-section. Low velocity magnitude area is localised next to the inlet near the overhang. At  $90^\circ$ , velocity magnitude decelerates by 15%, which in turn resulted in having 390.6% accelerated flow than that at the outlet. Inflow exhibit low velocity magnitude the rear face of the profile as well as higher velocity magnitude towards the overhang. From the rear face of the volute, velocity magnitude appears to slightly increase across the profiles towards the overhang following the curvature of the wall. The high velocity magnitude area following the curvature along the front face wall towards the overhang from the previous cross-section appears to have moved further into the overhang leaning towards the front face in this cross-section and has slightly higher velocity magnitude in the centre of this moving high velocity region. At  $135^\circ$ , velocity magnitude decelerates by 21.4% from the previous and exhibits 285.8% accelerated flow velocity magnitude than that depicted at the outlet. The region of high velocity magnitude in the previous section has decreased in this cross-section and remains in the overhang but now appears to be leaning towards the rear face. Low velocity zone is depicted at the top of the profile slightly at the rear face and accelerates towards the front face. Low velocity is also distinctly depicted in the centre of this cross-section. At  $180^\circ$ , flow velocity magnitude decelerates by 19.2%, which is 211.8% accelerated flow compared to that at the outlet. In the previous cross-section, low velocity magnitude region at the top of the profile slightly at the rear face appears to have moved slightly towards the front face in this cross-section. At  $225^\circ$ , velocity magnitude decelerates by 20.1% and hence, the flow is 149.2% accelerated compared to that at the outlet. Low velocity magnitude has manifested across this profile depicting lowest region at the inflow towards the overhang, with slightly higher flow velocity magnitude at the inflow along the rear face and along the front face curvature near the wall. At  $270^\circ$ , flow velocity magnitude decelerates by 21.6% resulting in 95.5% accelerated flow compared to that at the outlet. Lowest velocity magnitude regions are observed at the outer curve of the profile, which appears to slightly increase to the highest velocity magnitude region within the profile. The slightly high velocity magnitude region depicted along the front face curvature near the wall in the previous profile appears to have decelerated further and reduced its distribution in length, but slightly increased its distribution in width. At  $315^\circ$ , flow decelerates by 8.7% and exhibits 78.5% accelerated flow velocity magnitude compared to that at the outlet. Low velocity magnitude is exhibited here with minimal variations across the cross-section. At the cut-off location, flow velocity magnitude accelerates further by 5.7%, which depicts an acceleration of 88.7% compared to that at the outlet. Inflow velocity magnitude has significantly increased at this cross-section. This appears to be caused by the disturbances at as well as in vicinity of the tongue

region. Aside from this, velocity magnitude is low across the profile. At the exit cone, flow velocity magnitude decelerates by 35.2%, exhibiting 22.3% accelerated flow velocity magnitude than that depicted at the outlet. Low velocity magnitude zone is seen near the wall along the curvature of the front face, while the highest region of velocity magnitude is seen near the wall of the rear face. At the discharge duct, flow velocity magnitude has decelerated by 15.2% with 3.6% acceleration compared to the outlet. The variations of velocity magnitude are similar to that previous discussed, however in this cross-section, the velocity magnitude variation regions appear to have a slightly greater distribution area. At the outlet, flow velocity magnitude decelerates even further by 3.5%, showing low velocity magnitude across the cross-section with minimal variations.

Overall at low operating speed of the centrifugal compressor, it can be seen that velocity magnitude increases from surge to choke in the volute, as expected. The surge condition depicts a linear decrease in velocity magnitude. At BEP, velocity magnitude initially increases to 90° before decreasing downstream to the outlet. The choke condition depicts an increase in velocity magnitude to the cut-off location, prior to decreasing downstream to the outlet.



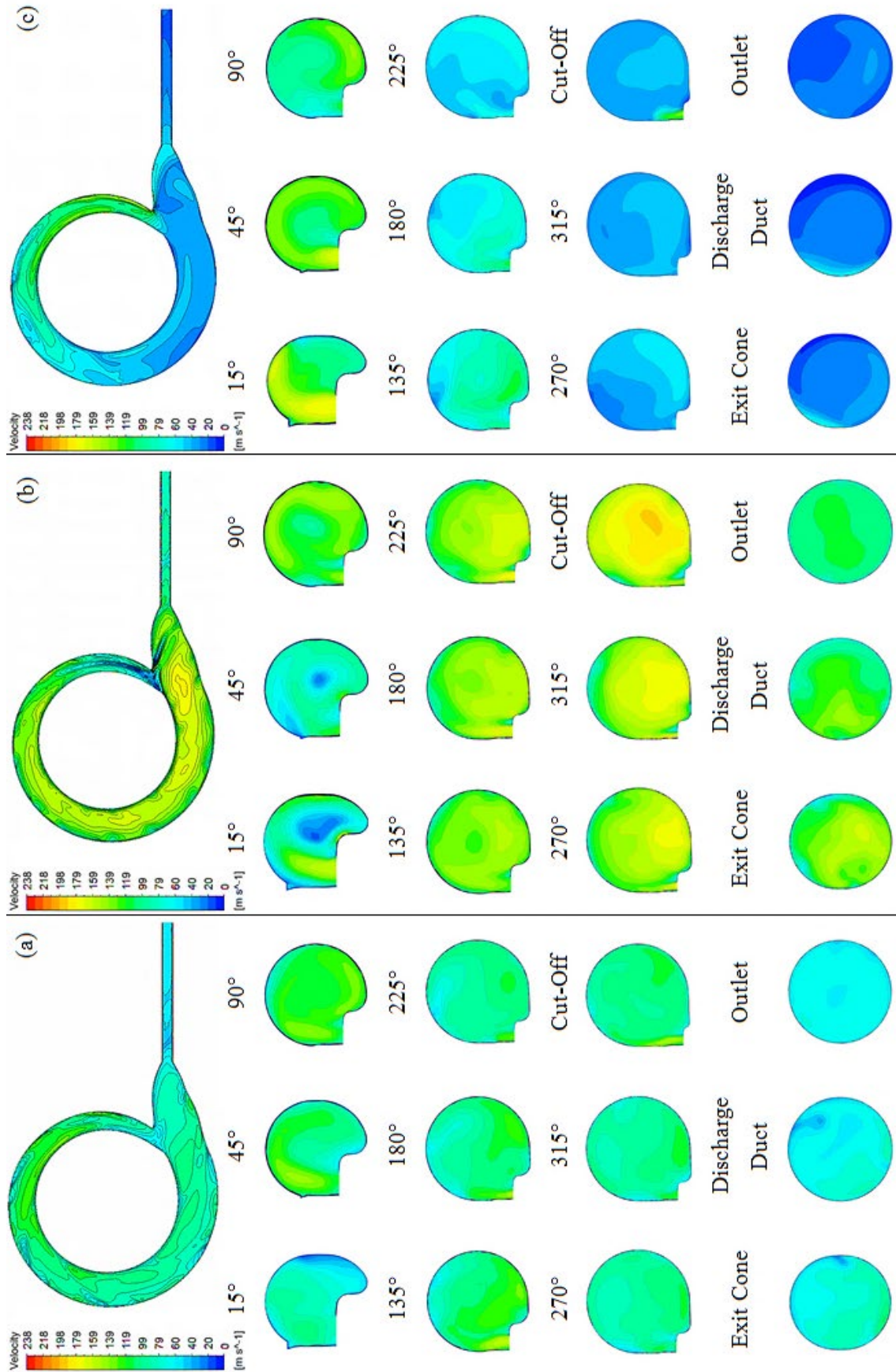


Figure 4.15 Velocity Magnitude around the Compressor Volute during the operating speed of 58.9rps/√K at (a) BEP (b) choke (c) surge

Figure 4.16 depicts the variation of velocity magnitude across each cross-section around the centrifugal compressor volute during the operating speed of 58.9rps/ $\sqrt{K}$  at low flow rate, being near the surge condition; design flow rate, being the best efficiency point; and high flow rate, being near the choke condition. This section is carried out in order to understand how the low and how the high flow rates near extreme phenomena differ in velocity magnitude from the design flow rate. It is clear that downstream 90°, the low flow shows lower velocity magnitude than the design flow, while high flow shows higher velocity magnitude than the design flow throughout the centrifugal compressor volute. At 15°, low flow depicts an increase in velocity magnitude of 60% compared to the design flow, while high flow depicts a velocity magnitude increase of 9.9% compared to the design flow. At 45°, surge condition depicts a velocity magnitude increase of 15% compared to the BEP, while choke condition depicts a decrease in velocity magnitude of 31.9% compared to the BEP. At 90°, low flow depicts a velocity magnitude decrease of 11.4% compared to the design flow, while high flow depicts an increase in velocity magnitude of 5.1% compared to the design flow. At 135°, surge condition depicts a decrease in velocity magnitude of 23.6% compared to the BEP, while choke condition depicts a velocity magnitude increase of 19.9% compared to the BEP. At 180°, low flow depicts a decrease in velocity magnitude of 33.7% compared to the design flow, while high flow depicts a velocity magnitude increase of 27.3% compared to the design flow. At 225°, surge condition depicts a velocity magnitude decrease of 44.7% compared to the BEP, while choke condition depicts an increase in velocity magnitude of 31.3% compared to the BEP. At 270°, low flow depicts a velocity magnitude decrease of 55.8% compared to the design flow, while high flow depicts an increase in velocity magnitude of 34.6% compared to the design flow. At 315°, surge condition depicts a decrease in velocity magnitude of 60.1% compared to the BEP, while choke condition depicts a velocity magnitude increase of 36.9% compared to the BEP. At 345°, which is the cut-off location, low flow depicts a decrease in velocity magnitude of 60.8% compared to the design flow, while high flow depicts a velocity magnitude increase of 38.4% compared to the design flow. At 390°, which is the exit cone location, surge condition depicts a velocity magnitude decrease of 65.1% compared to the BEP, while choke condition depicts an increase in velocity magnitude of 43.5% compared to the BEP. At 393°, which is the discharge duct location, low flow depicts a velocity magnitude decrease of 65.9% compared to the design flow, while high flow depicts an increase in velocity magnitude of 44% compared to the design flow. At 400°, which is the outlet location, surge condition depicts a decrease in velocity magnitude of 65.9% compared to the BEP, while choke condition depicts a velocity magnitude increase of 41% compared to the BEP. Overall, this quantifies the velocity magnitude variation across each

cross-section around the centrifugal compressor volute as a function of flow rates and how the off-design conditions vary against the design condition at low operating speed.

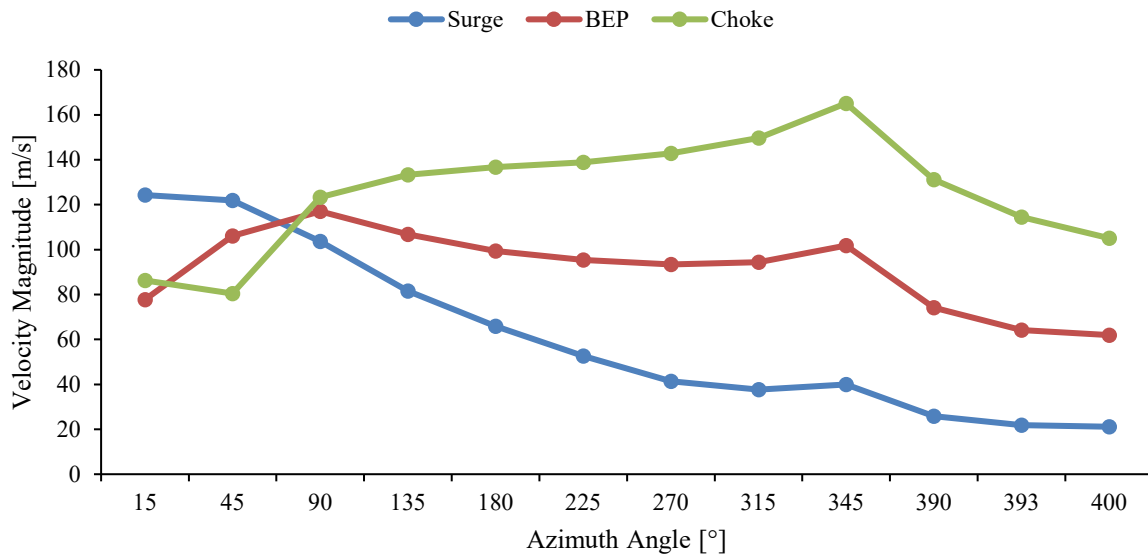


Figure 4.16 Velocity Magnitude across each cross-section around the Compressor Volute during the operating speed of 58.9 rps/√K

Figure 4.17 is a graphical representation depicting the asymmetric ratio of velocity magnitude along the radial direction of the profiles around the centrifugal compressor volute at the operating speed of 58.9 rps/√K. When the asymmetric ratio is at 1, the velocity magnitude in the flow is symmetric. When the asymmetric ratio is less than 1, velocity magnitude in the flow is asymmetric towards the outer curve. When the asymmetric ratio is more than 1, velocity magnitude in the flow is asymmetric towards the inner curve. It can be seen that velocity magnitude along the radial direction of the profiles through the volute is significantly asymmetric at design and off-design conditions. At 15° and from 90° to 270°, flow velocity magnitudes along the radial direction exhibit asymmetry towards the inner curve. At 45°, velocity magnitude along the radial direction depicts asymmetry towards the outer curve for low flow and design flow, while high flow remains asymmetric towards the inner curve. At 315°, low flow depicts asymmetry towards the outer curve, while design flow and high flow remain asymmetric towards the inner curve. At 345°, all flow conditions depict dominant velocity magnitude along the radial direction towards the inner curve. At 390° and 393°, design flow and high flow displays asymmetric velocity magnitude along the radial direction towards the outer curve, whereas low flow exhibits asymmetry towards the inner curve. At 400°, low flow and high flow conditions present asymmetry of velocity magnitude along the radial direction towards the outer curve, while the design flow condition present asymmetry towards the inner curve. Overall at low operating speed, flow rate is seen to have a significant influence on the imbalance of velocity

magnitude along the radial direction on the cross-section profiles inside the centrifugal compressor volute due to the effects of friction. More detailed graphical representations are depicted in APPENDIX 2.

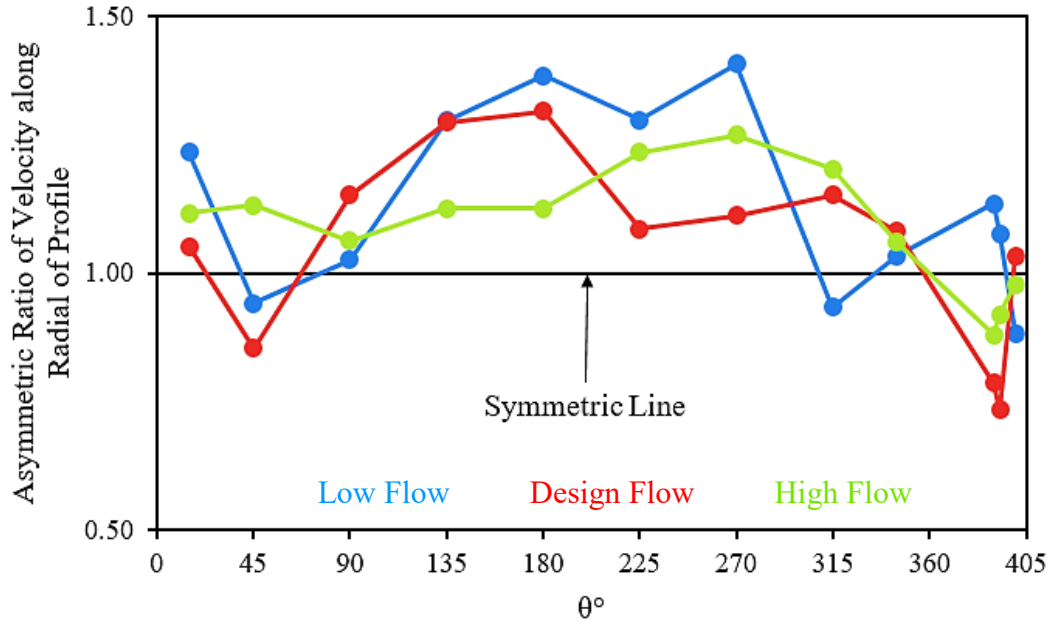


Figure 4.17 Asymmetric Ratio of Velocity Magnitude along the Radial Direction on the Profiles around the Centrifugal Compressor Volute at Operating Speed of 58.9rps/√K during Low Flow Rate, Design Flow Rate and High Flow Rate

Figure 4.18 is a graphical representation depicting the asymmetric ratio of velocity magnitude along the axial direction of the profiles around the centrifugal compressor volute at the operating speed of 58.9rps/√K. It can be seen that velocity magnitude along the axial direction on the profiles through the volute is significantly asymmetric at design and off-design conditions. At 15° of the low flow condition, symmetric velocity magnitude along the axial direction is identified. At 45°, asymmetric flow velocity magnitude is observed towards the rear face. At 90° and 135°, flow velocity magnitude exhibits significant asymmetry towards the front face. At 180°, flow velocity magnitude exhibits asymmetry towards the rear face, followed by symmetry at 225°. At 270° flow velocity magnitude again, exhibits asymmetry towards the rear face, prior to displaying asymmetry towards the front face at 315° and 345°. Thereafter at 390° and 393°, flow velocity magnitude depicts asymmetry towards the rear face once more, before displaying asymmetry that is localised towards the front face at 400°. At 15° and 45° of the design flow and high flow conditions, velocity magnitude depicts asymmetry towards the rear face. For the design flow condition, asymmetry of velocity magnitude along the axial direction remains towards the rear face at 90° and 135°, whereas for the high flow condition, asymmetry is observed towards the front face and rear face, respectively. At 180° and 225°, asymmetry is seen

towards the front face for the design flow condition, while the high flow condition remains asymmetric towards the rear face. At 270° and 315°, flow velocity magnitude along the axial direction depicts asymmetry towards the front face and the rear face, respectively, for both design flow and high flow conditions. At 345°, asymmetry of velocity magnitude is identified towards the front face for the design flow condition, whereas the high flow condition shows that asymmetry remains towards the rear face. At 390° and 393°, both flow conditions depict asymmetry of velocity magnitude towards the rear face along the axial direction on the profiles. At 400°, the design flow condition depicts asymmetry towards the front face, whereas the high flow condition depicts symmetric velocity magnitude along the axial direction. Overall at low operating speed, it is observed that flow rate has a significant influence on the imbalance of velocity magnitude along the axial direction of the cross-section profiles inside the centrifugal compressor volute due to friction. It is noticed that as the flow rate increases, the asymmetry of velocity magnitude along the axial direction decreases. More detailed graphical representations are depicted in APPENDIX 2.

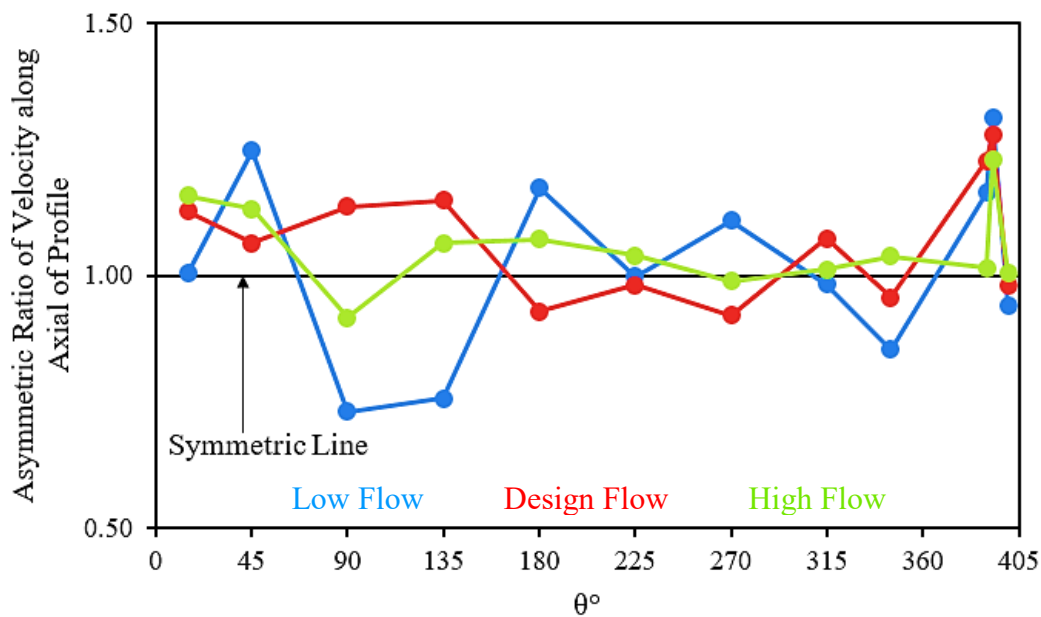


Figure 4.18 Asymmetric Ratio of Velocity Magnitude along the Axial Direction on the Profiles around the Centrifugal Compressor Volute at Operating Speed of 58.9rpm/°K during Low Flow Rate, Design Flow Rate and High Flow Rate

#### 4.9 Local Velocity Magnitude around the Centrifugal Compressor Volute at High Operating Speed during Steady Conditions

Figure 4.19 depicts velocity magnitude distribution through the turbocharger compressor volute during the operating speed of 98.2rps/ $\sqrt{K}$  at (a) BEP (b) choke (c) surge. Twelve cross-sections through the volute channel have been presented from the first cross-section of the scroll situated above the tongue, through to the outlet of the compressor stage.

Observing (a), which is the volute operation at design flow rate at 98.2rps/ $\sqrt{K}$ , it can be seen that throughflow velocity magnitude is highly non-uniform until reaching the discharge duct, where comparatively low flow velocity was achieved. Similar to 58.9 rps/ $\sqrt{K}$ , pockets of low velocity magnitude is seen along periphery of the outer curve and along the periphery of the volute inlet. At 15°, velocity magnitude is 145m/s, which compared to the outlet, has an accelerated flow of 79.9%. Inflow velocity magnitude is significantly high compared to the flow near the rear face and the front face of the volute. As the inflow is directed further into the cross-section velocity magnitude decelerates. At 45°, velocity magnitude accelerates from that depicted at 15° by 21.2% hence, having accelerated flow of 118% compared to that exhibited at the outlet. Flow velocity magnitude behaviour is similar here, as to that previously discussed. Distribution of velocity magnitude is high at the entrance, which propagates towards the front face with even higher velocity magnitude depicted in the central region of this high velocity zone. Low velocity magnitude is identified near the wall of the overhang and the outer curve from the rear face. At 90°, velocity magnitude accelerates by 4.2%, which in turn resulted in having 127.2% accelerated flow than that at the outlet. From the previously described profile, high velocity magnitude has manifested across this profile, depicting high velocity in the overhang and low velocity along the periphery of the outer curve, near the wall. At 135°, velocity magnitude decelerates by 14.3% from the previous and exhibits 94.7% accelerated flow velocity magnitude than that depicted at the outlet. Here, inflow velocity magnitude is high and as the flow travels further into the profile, velocity magnitude decreases. Along the overhang, a region of slightly lower velocity is exhibited from the upstream flow. At 180°, flow velocity magnitude decelerates by 12.2%, which is 70.9% accelerated flow compared to that at the outlet. Very small area of high velocity is identified at the inlet and rear face. Flow velocity magnitude in this profile is predominantly comparatively lower than the previous. Distinct low velocity magnitude area is depicted in the central region towards the outer curve. At 225°, velocity magnitude decelerates by 3.4% and hence, the flow is 65.1% accelerated compared to that at the outlet. Low flow velocity magnitude distribution manifests across this profile with higher velocity magnitude near



the wall, along the outer curve and near the inlet, along the overhang. A very small low velocity zone is identified on the rear face of this cross-section and again, high inflow velocity magnitude is exhibited. There are minimal variations between  $270^\circ$ ,  $315^\circ$  and the cut-off location. At  $270^\circ$ , flow velocity magnitude decelerates by 3.8% resulting in 58.9% accelerated flow compared to that at the outlet. Low flow velocity magnitude is distributed across this profile with higher regions of velocity magnitude near the wall along the outer curve more towards the rear face and near the wall along the overhang more towards the front face. Small distribution of high inflow velocity magnitude is depicted. At  $315^\circ$ , flow decelerates by 0.3% and exhibits 58.5% accelerated flow velocity magnitude compared to that at the outlet. Variation and distribution of velocity magnitude in this profile is similar to previous, however there is an even smaller distribution of high inflow velocity magnitude and there is higher velocity magnitude identified near the wall along the outer curve more towards the rear face. At the cut-off location, flow velocity magnitude accelerates by 6.4%, which depicts an acceleration of 68.6% compared to that at the outlet. Again, variation and distribution of velocity magnitude across this profile is similar to that previously discussed. There is a greater area of high inflow velocity magnitude depicted with lower velocity magnitude near the wall along the rear face, front face and in vicinity of the overhang. At the exit cone, flow velocity magnitude decelerates by 30%, exhibiting 18% accelerated flow velocity magnitude than that depicted at the outlet. Low velocity magnitude manifests across this profile with low zones along the front face near the wall. A region of higher velocity magnitude on the lower sector of the cross-section on the rear face has also been identified. At the discharge duct, flow velocity magnitude has decelerated by 12.9% with 2.8% acceleration compared to the outlet. Variation and distribution of velocity magnitude across this profile is similar to previous. The low velocity magnitude zone appears to have propagated and the higher velocity area appears to have shrunk. At the outlet, flow velocity magnitude decelerates even further by 2.7%, showing low velocity magnitude across the profile.

Viewing (b), which is the volute operation at high flow rate at 98.2rps/ $\sqrt{K}$ , shows similar behaviour to that at 58.9 rps/ $\sqrt{K}$ . Low velocity magnitude zones are depicted in vicinity of the tongue region with pockets of low velocity magnitude along the curvature near the outer wall and the volute inlet. Low flow velocity magnitude between the tongue region and  $45^\circ$  is a result of the volute passage being too large for the little amount of mass flow passing through [17]. Higher areas of velocity magnitude are depicted near the volute inlet and cut-off location. At  $15^\circ$ , velocity magnitude is 90m/s, which compared to the outlet has decelerated flow of 37.8%. Flow entering the volute at this cross-section near the rear face exhibits very low velocity magnitude,

while flow entering the volute closer to the front face shows higher velocity magnitude. It appears inflow follows the curvature of the outer wall against the rear face. There are also low velocity magnitude zone depicted in the overhang and in the freestream. At  $45^\circ$ , velocity magnitude accelerates from that depicted at  $15^\circ$  by 49.3% hence, having decelerated flow of 7.1% compared to that exhibited at the outlet. Here, incoming flow velocity magnitude is high with low velocity near the wall along the outer curve and in the freestream. Velocity magnitude appears to increase concentric to the low zone in the centre of the profile. Small area of high velocity is exhibited near the wall between the inlet and the overhang. At  $90^\circ$ , velocity magnitude accelerates by 41.1%, which in turn resulted in having 31.1% accelerated flow than that at the outlet. Incoming flow velocity magnitude is high as well as that near the wall along the outer curve. Distribution of lower velocity magnitude region is depicted central of the profile with concentric slightly higher velocity towards the outer wall. At  $135^\circ$ , velocity magnitude accelerates by 5.9% from the previous and exhibits 38.8% accelerated flow velocity magnitude than that depicted at the outlet. Again, high inflow velocity magnitude is exhibited with higher velocity magnitude zone. Low velocity magnitude is depicted in the central region of the profile. At  $180^\circ$ , flow velocity magnitude decelerates by 0.7%, which is 37.9% accelerated flow compared to that at the outlet. Flow enters this cross-section at a very high velocity with significantly lower velocity near the wall between the volute inlet and the overhang. High velocity magnitude is distributed in the overhang with lower velocity magnitude in the central region of the cross-section. At  $225^\circ$ , velocity magnitude decelerates by 0.2% and hence, the flow is 37.6% accelerated compared to that at the outlet. There is the small pocket of high velocity magnitude exhibited at the inflow close to the rear face and also a pocket of low velocity magnitude exhibited at the inflow close to the front face. A small region of high inflow velocity magnitude is exhibited close to the rear face, while a small region of low inflow velocity magnitude is exhibited close to the front face. In this profile, high velocity magnitude region is exhibited in the overhang with lower velocity magnitude distribution towards the outer curve. At  $270^\circ$ , flow velocity magnitude accelerates by 1.8% resulting in 40% accelerated flow compared to that at the outlet. Low inflow velocity magnitude near the front face and high inflow velocity magnitude near the rear face appears to have shrunk in this profile. Low velocity pocket is seen to be emerging from the outer curve into the profile. There is also distribution of high velocity magnitude, which appears to be localised in the overhang. At  $315^\circ$ , flow accelerates by 3.4% and exhibits 44.8% accelerated flow velocity magnitude compared to that at the outlet. The distribution of low inflow velocity magnitude near the front face appears to remain unchanged, while the distribution of high inflow velocity magnitude near the rear face appears to have



extended. From the previously discussed profile, the pocket of low velocity magnitude localised along the outer curve appears to have elongated towards the rear face of the profile and the distribution of high velocity magnitude depicted in the overhang, appears to have manifested. At the cut-off location, flow velocity magnitude accelerates by 11.7%, which depicts an acceleration of 61.7% compared to that at the outlet. A Pocket of high velocity magnitude is observed near the outer curve near the read face with slightly lower velocity previously depicted in the overhang, appears to have propagated substantially across this profile. At the exit cone, flow velocity magnitude decelerates by 22.7%, exhibiting 25% accelerated flow velocity magnitude than that depicted at the outlet. Velocity magnitude appears to have decreased significantly, showing low regions near the wall of the outer curve in the upper half of the profile. Slightly higher velocity magnitude is seen in the profile in the lower half, towards the rear face. At the discharge duct, flow velocity magnitude has decelerated further by 15.1% with 6.2% acceleration compared to the outlet. Low flow velocity magnitude zone is depicted central near the wall of the front face towards and along the outer curve near the wall towards the rear face. Higher velocity magnitude is seen in the central region of the profile, localised more towards the upper half and near the rear face. At the outlet, flow velocity magnitude decelerates even further by 5.8%, showing low velocity magnitude near the wall and slightly higher velocity magnitude distributed across the profile.

Inspecting (c), which is the volute operation at low flow rate at  $98.2\text{rps}/\sqrt{K}$ , it can be seen that there are many disturbances in terms of non-uniformities near the tongue region to  $90^\circ$ , which signifies that secondary flows are introduced. Downstream  $135^\circ$ , it can be seen that uniformity in velocity magnitude is beginning to be achieved. At  $15^\circ$ , velocity magnitude is  $194\text{m/s}$ , which compared to the outlet has accelerated flow of 324.2%. High velocity magnitude is distributed across this cross-section with even higher inflow velocity magnitude. Low velocity magnitude zone near the outer curve is exhibited caused by the upstream disturbance occurring at the tongue and the frictional effects take place between the fluid flow and the wall. At  $45^\circ$ , velocity magnitude decelerates from that depicted at  $15^\circ$  by 11.7% hence, having accelerated flow of 274.6% compared to that exhibited at the outlet. Here, high inflow velocity magnitude is exhibited against the rear face, which propagates following the curvature of the outer wall of the cross-section and also distributes with a slight deceleration into the overhang. Low velocity magnitude appears to be emerging in the freestream with surrounding accelerated flow. At  $90^\circ$ , velocity magnitude decelerates by 8.7%, which in turn resulted in having 242.2% accelerated flow than that at the outlet. It is observed the high velocity magnitude depicted in the previous

profile appears to have moved against the front face and the overhang. It is also noticed there is a small area of high inflow velocity magnitude. Low inflow velocity magnitude appears to have propagated towards low velocity depicted in the freestream in the previous cross-section. At 135°, velocity magnitude decelerates by 25.2% from the previous and exhibits 155.8% accelerated flow velocity magnitude than that depicted at the outlet. It can be seen the low velocity magnitude from the previous profile has manifested across this profile and the high velocity area near the wall of the overhang has also decelerated significantly. Additionally, high inflow velocity magnitude discussed in the previous profile has slightly increased in its distribution. At 180°, flow velocity magnitude decelerates by 18.4%, which is 108.7% accelerated flow compared to that at the outlet. Aside from the high in flow velocity magnitude propagating in toward the centre of the cross-section, velocity magnitude across this profile is low and almost uniform. At 225°, velocity magnitude decelerates by 12.3% and hence, the flow is 83% accelerated compared to that at the outlet. The region of high inflow velocity has decreased substantially due to the low velocity across the profile previously discussed, propagating further and closer to uniformity. At 270°, flow velocity magnitude decelerates by 7.5% resulting in 69.2% accelerated flow compared to that at the outlet. Significantly high inflow velocity magnitude is exhibited in comparison to this previous profile, which has also increased in its distribution. Aside from this, the cross-section remains to present low velocity magnitude. At 315°, flow accelerates by 9.5% and exhibits 85.3% accelerated flow velocity magnitude compared to that at the outlet. High inflow velocity magnitude propagates against the rear face near the wall with a slight increase along the curvature of the outer wall. Low velocity magnitude continues to be the distributed predominantly across the profile. Further to this, a zone of low velocity magnitude is seen at the base of the overhang near the volute inlet. At the cut-off location, flow velocity magnitude accelerates by 2.1%, which depicts an acceleration of 89.2% compared to that at the outlet. The low velocity magnitude across the profile appears to have manifested even more, reduced the high inflow velocity magnitude region. At the exit cone, flow velocity magnitude decelerates by 37.7%, exhibiting 17.8% accelerated flow velocity magnitude than that depicted at the outlet. Low velocity magnitude is exhibited across this cross-section with even lower velocity magnitude in its freestream. At the discharge duct, flow velocity magnitude has decelerated further by 16.3% with 1.4% decelerated flow compared to the outlet. Flow velocity magnitudes remains to be low across this profile with an even further decrease in flow velocity magnitude in the freestream. At the outlet, flow velocity magnitude accelerates slightly by 1.4%, showing low velocity magnitude distributed across the profile.

Overall at high operating speed of the centrifugal compressor, it can be seen that velocity magnitude increases from surge to choke in the volute, as expected. The surge condition exhibits a linear decrease in velocity magnitude. At BEP, velocity magnitude increases from the first profile to  $90^\circ$ , before decreasing downstream to the outlet. The choke condition shows an increase in velocity magnitude to the cut-off location, prior to decreasing downstream to the outlet.

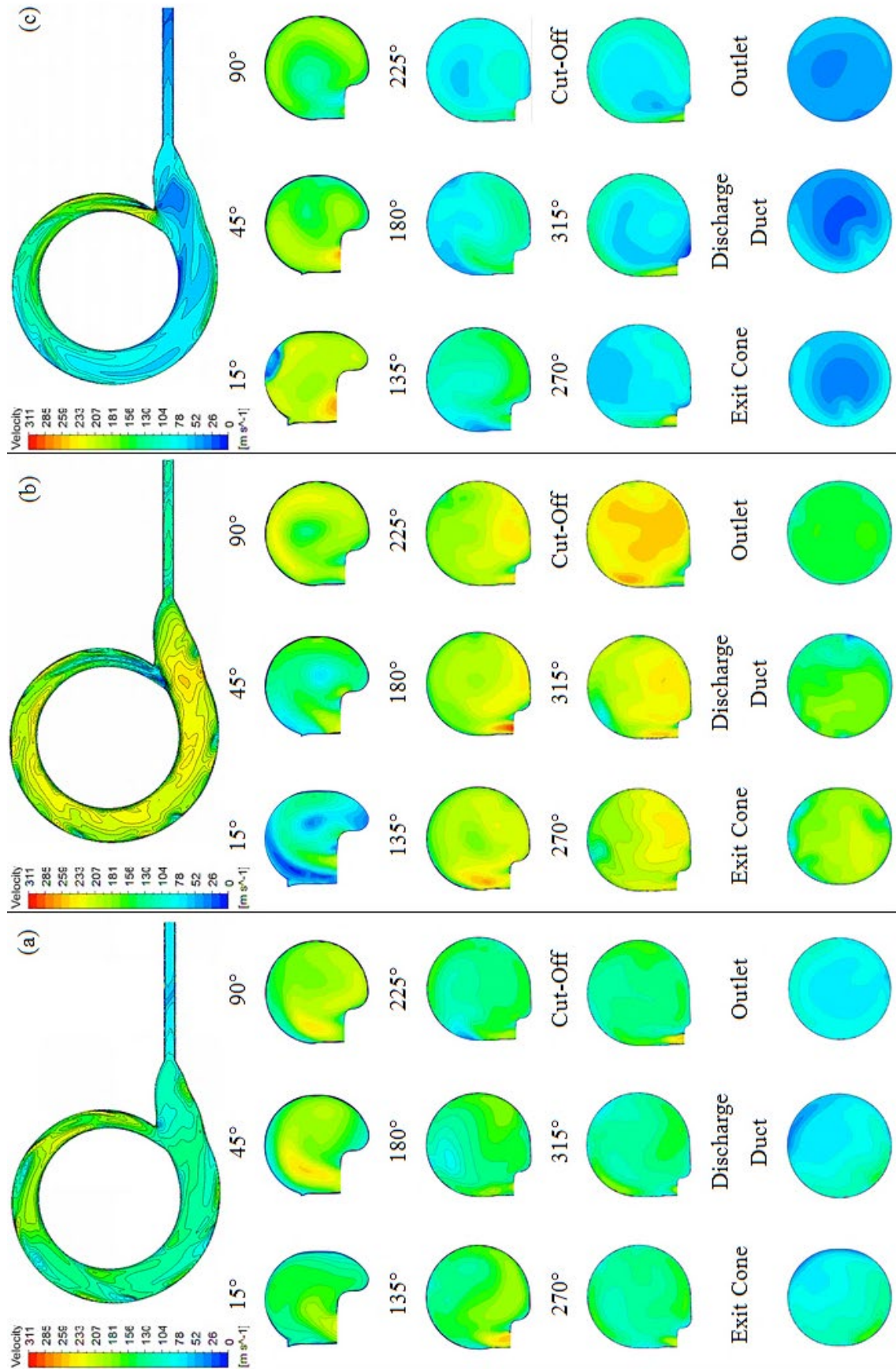


Figure 4.19 Velocity Magnitude around the Compressor Volute during the operating speed of 98.2rps/√K at (a) BEP (b) choke (c) surge

Figure 4.20 depicts the variation of velocity magnitude across each cross-section around the centrifugal compressor volute during the operating speed of 58.9rps/ $\sqrt{K}$  at low flow rate, being near the surge condition; design flow rate, being the best efficiency point; and high flow rate, being near the choke condition. This section is carried out in order to understand how the low and how the high flow rates near extreme phenomena differ in velocity magnitude from the design flow rate. It is clear that downstream 90°, the low flow shows lower velocity magnitude than the design flow, while high flow shows higher velocity magnitude than the design flow throughout the centrifugal compressor volute. At 15°, low flow depicts an increase in velocity magnitude of 33.8% compared to the design flow, while high flow depicts a velocity magnitude decrease of 61.5% compared to the design flow. At 45°, surge condition depicts a velocity magnitude decrease of 2.5% compared to the BEP, while choke condition depicts a decrease in velocity magnitude of 31% compared to the BEP. At 90°, low flow depicts a velocity magnitude decrease of 14.5% compared to the design flow, while high flow depicts an increase in velocity magnitude of 3.2% compared to the design flow. At 135°, surge condition depicts a decrease in velocity magnitude of 25.4% compared to the BEP, while choke condition depicts a velocity magnitude increase of 21.7% compared to the BEP. At 180°, low flow depicts a decrease in velocity magnitude of 30.7% compared to the design flow, while high flow depicts a velocity magnitude increase of 30.8% compared to the design flow. At 225°, surge condition depicts a velocity magnitude decrease of 37.1% compared to the BEP, while choke condition depicts an increase in velocity magnitude of 33% compared to the BEP. At 270°, low flow depicts a velocity magnitude decrease of 39.6% compared to the design flow, while high flow depicts an increase in velocity magnitude of 36.6% compared to the design flow. At 315°, surge condition depicts a decrease in velocity magnitude of 33.7% compared to the BEP, while choke condition depicts a velocity magnitude increase of 38.9% compared to the BEP. At 345°, which is the cut-off location, low flow depicts a decrease in velocity magnitude of 36.3% compared to the design flow, while high flow depicts a velocity magnitude increase of 41.8% compared to the design flow. At 390°, which is the exit cone location, surge condition depicts a velocity magnitude decrease of 43.3% compared to the BEP, while choke condition depicts an increase in velocity magnitude of 47.3% compared to the BEP. At 393°, which is the discharge duct location, low flow depicts a velocity magnitude decrease of 45.6% compared to the design flow, while high flow depicts an increase in velocity magnitude of 45.9% compared to the design flow. At 400°, which is the outlet location, surge condition depicts a decrease in velocity magnitude of 43.3% compared to the BEP, while choke condition depicts a velocity magnitude increase of 44.2% compared to the BEP. Overall, this quantifies the velocity magnitude variation across each cross-

section around the centrifugal compressor volute as a function of flow rates and how the off-design conditions vary against the design condition at high operating speed.

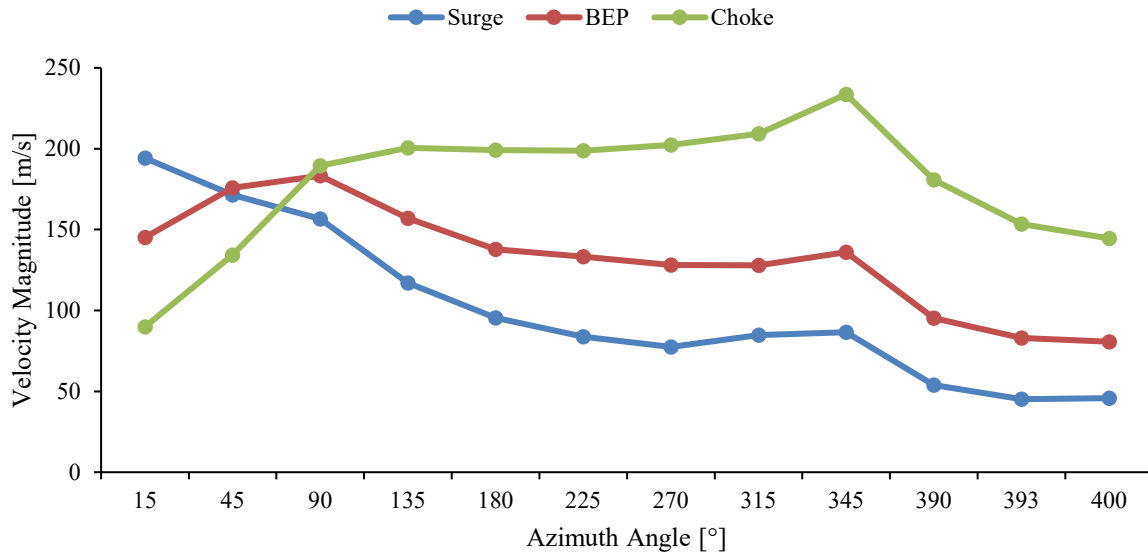


Figure 4.20 Velocity Magnitude across each cross-section around the Compressor Volute during the operating speed of 98.2rps/√K

Figure 4.21 is a graphical representation depicting the asymmetric ratio of velocity magnitude along the radial direction of the profiles around the centrifugal compressor volute at the operating speed of 98.2rps/√K. It can be seen there are significant asymmetry occurring in flow velocity magnitude toward the inner curve. For low flow and design flow conditions, velocity magnitude along the radial direction depicts asymmetry towards the inner curve at 15° followed by asymmetry towards the outer curve at 45°. From 90°, flow velocity magnitude displays asymmetry towards the inner curve to 270°. At 315°, velocity magnitudes for the low flow condition is asymmetric towards the outer curve, while remaining towards the inner curve for the design flow condition. At 345°, velocity magnitude at low flow condition exhibits asymmetry towards the inner curve and continues to remain at design flow. At 390° and 393°, low flow condition remains asymmetric towards the inner curve, whereas velocity magnitude at design flow depicts asymmetry towards the outer curve. At 400°, low flow and design flow conditions identify asymmetry of velocity magnitudes towards the outer curve and towards the inner curve, respectively. For the high flow condition, flow velocity magnitude along the radial direction depicts asymmetry towards the inner curve from 15° to 345°. Thereafter, velocity magnitude depicts asymmetry towards the outer curve downstream of 390°. Overall at high operating speed, it is observed that flow rate has a significant influence on the imbalance of velocity magnitude along the radial direction of the cross-section profiles inside the centrifugal compressor volute

due to the effects of friction. More detailed graphical representations are depicted in APPENDIX 2.

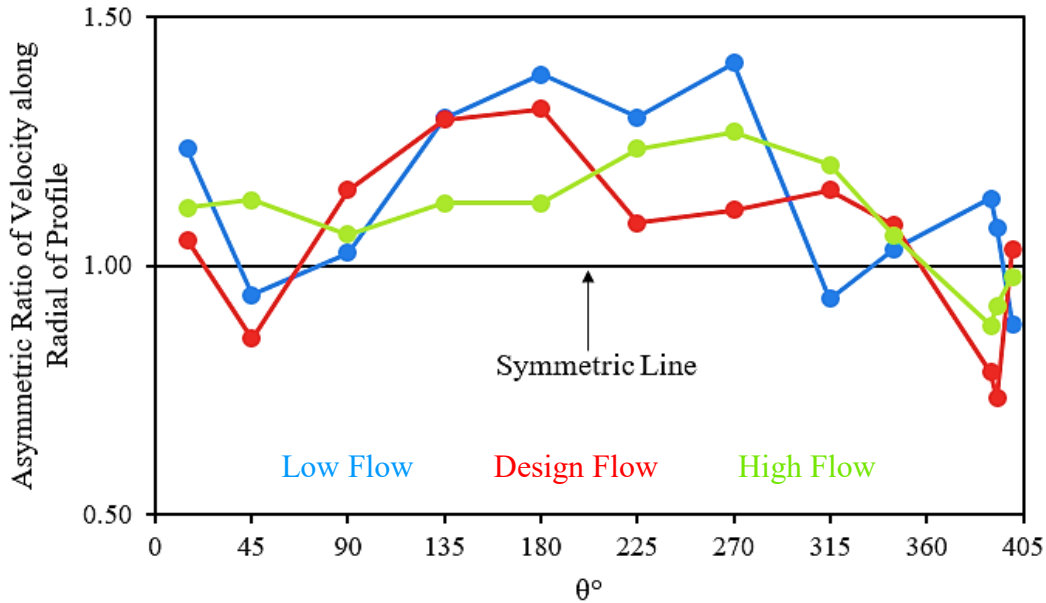


Figure 4.21 Asymmetric Ratio of Velocity Magnitude along the Radial Direction on the Profiles around the Centrifugal Compressor Volute at Operating Speed of 98.2rps/ $\sqrt{K}$  during Low Flow Rate, Design Flow Rate and High Flow Rate

Figure 4.22 is a graphical representation depicting the asymmetric ratio of velocity magnitude along the axial direction of the profiles around the centrifugal compressor volute at the operating speed of 98.2rps/ $\sqrt{K}$ . It can be seen that velocity magnitude along the axial direction on the profiles through the volute is significantly asymmetric at design and off-design conditions. For the low flow condition at 15°, flow velocity magnitude along the axial direction is symmetric. At 45°, flow velocity magnitude is asymmetric towards the rear face prior to displaying asymmetry towards the front face at 90° and 135°. At 180°, flow velocity magnitude depicts asymmetry towards the rear face, then identifies symmetry at 225°. At 270°, flow velocity magnitude displays asymmetry towards the rear face, followed by asymmetry towards the front face at 315° and 345°. Flow velocity magnitude at 390° exhibits asymmetry towards the rear face, which remains at 393°. At 400°, flow velocity magnitude along the axial direction displays asymmetry towards the front face. For the design flow condition from 15° to 135°, flow velocity magnitude along the axial direction is seen to be asymmetric towards the rear face, prior being asymmetric towards the front face from 180° to 270°. At 315°, flow velocity magnitude observes asymmetry towards the rear face and then towards the front face at 345°. At 390°, flow velocity magnitude exhibits asymmetry towards the rear face, which remains at 393°. At 400°, flow velocity magnitude along the axial direction is asymmetric towards the front face. For the high flow



condition at 15° and 45°, flow velocity magnitude along the axial direction is seen to be asymmetric towards the rear face, prior to displaying asymmetry towards the front face at 90°. From 135° to 225°, flow velocity magnitude displays asymmetry towards the rear face, followed by slight asymmetry towards the front face at 270°. Downstream from 315°, asymmetry is exhibited towards the rear face, prior to achieving symmetric flow velocity magnitude along the axial direction at 400°. Overall at high operating speed, it is observed that flow rate has a significant influence on the imbalance of velocity magnitude along the axial direction of the cross-section profiles inside the centrifugal compressor volute due to frictional effects. It is noticed that as the flow rate increases, the asymmetry of velocity magnitude along the axial direction decreases. More detailed graphical representations are depicted in APPENDIX 2.

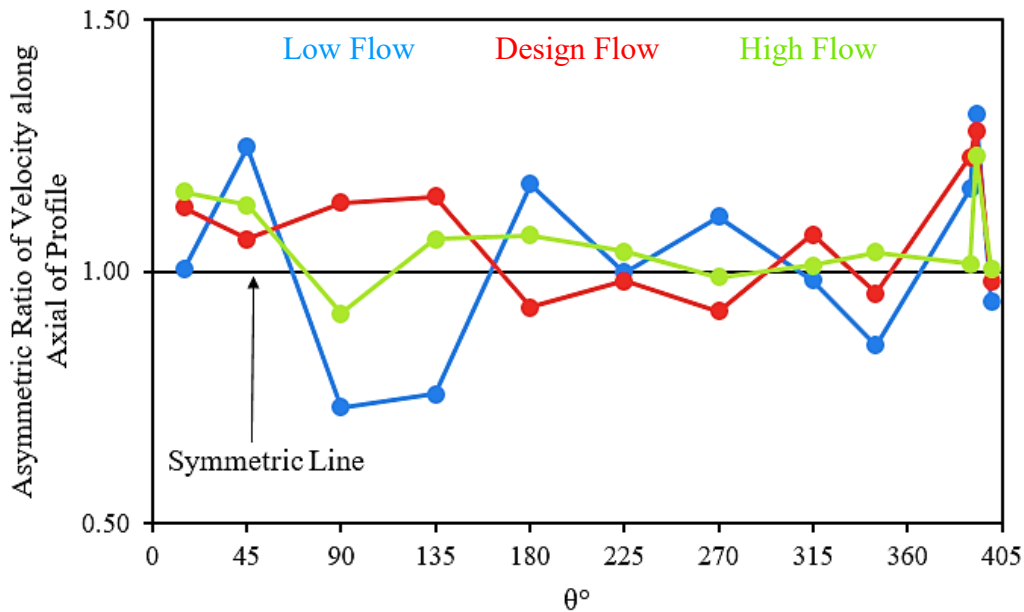


Figure 4.22 Asymmetric Ratio of Velocity Magnitude along the Axial Direction on the Profiles around the Centrifugal Compressor Volute at Operating Speed of 98.2rps/√K during Low Flow Rate, Design Flow Rate and High Flow Rate

#### 4.10 Local Speed Comparison of Velocity Magnitude around the Centrifugal Compressor Volute during Steady Conditions

Table 4.4 depicts the steady response of the local speed comparison, where the high operating speed of 98.2rps/√K is compared against the low operating speed of 58.9rps/√K for velocity magnitude across each of the selected cross-section through the turbocharger compressor volute. It can be seen that velocity magnitude at 98.2rps/√K increases at design and off-design conditions compared to that at 58.9rps/√K. Aside from that depicted at 15°, lowest velocity magnitude increase through the volute occurs at design flow conditions, while highest velocity



magnitude increase through the volute occurs at low flow conditions. For low flow, highest velocity magnitude variation is found at 315°, while lowest velocity magnitude variation is found at 45°. At design flow, highest velocity magnitude variation is found at 15°, while lowest velocity magnitude variation is found at the exit cone, being at 390°. At high flow, the highest velocity magnitude variation is found at 45°, while lowest velocity magnitude variation is found at 15°.

*Table 4.4 Local Speed Comparison of Velocity Magnitude Variation during Steady Response*

$\theta^\circ$	Velocity Magnitude [%]		
	Low Flow	Design Flow	High Flow
15	56.3	86.9	4.3
45	40.7	65.8	66.9
90	51.1	56.6	53.6
135	43.6	47.1	50.5
180	45.0	38.8	45.8
225	59.0	39.7	43.2
270	87.4	37.2	41.7
315	124.8	35.4	39.7
345	117.1	33.7	41.5
390	108.8	28.5	37.7
393	106.2	29.3	34.0
400	116.6	30.3	37.5

#### 4.11 Global Static Temperature Distribution around the Centrifugal Compressor during Steady Conditions

According to the gas law, behaviour of temperature is directly proportional to behaviour of pressure, hence as the ambient air enters the compressor stage through the inducer, temperature is relatively low. This low temperature decreases even further when the fluid enters the impeller. As the energy imparts into the fluid and flows radially outwards simultaneous with some occurrence of diffusion, temperature rises towards the trailing edge as the centrifugal forces in the impeller push the fluid particles into the diffuser. As the flow is squeezed into the diffuser, temperature continues to increase due to compressibility and diffusion. As the fluid is collected in the volute and directed towards the outlet, temperature increases even further since the volute behaves as a conical diffuser.

Figure 4.23 in the top row, depicts static temperature variation in the turbocharger compressor stage during the operating speed of 58.9rps/ $\sqrt{K}$  at (a) BEP (b) choke (c) surge. Observing (a),

which is the turbocharger compressor stage operation at design flow rate, ambient air flows into the compressor stage through the inducer at a static temperature of 288K. From here, there is 0.1% decrease in static temperature when the fluid enters the impeller. When air particles pass through the impeller passages and exits into the diffuser, static temperature rises by 8.9%. After compressibility and diffusion have taken place in the diffuser, static temperature continues to increase by 3.4%. Once the flow has been collected in the volute and kinetic energy in the flow has been converted into potential energy, the final static temperature increases at the outlet by 1.7%.

Viewing the operating speed of  $58.9\text{ rps}/\sqrt{K}$  at (b), which is the turbocharger compressor stage operation at high flow rate, the ambient inflow also enters the inducer at a static temperature of 288K. When fluid reaches the exit of the inducer and enters the impeller, there is a fall in static temperature by 0.7%. After the ambient air has passed through the impeller, changing the fluid properties, static temperature increases by 4.9%. After further altering the fluid properties through the diffuser passage, static temperature increases by an additional 4.7% prior to entering the volute. When the fluid reaches the outlet, the results show an increase in static temperature by 1.3%.

Inspecting the operating speed of  $58.9\text{ rps}/\sqrt{K}$  at (c), which is the turbocharger compressor stage operation at low flow rate, incoming flow of the ambient air also exhibits 288K of static temperature. This static temperature increases by 5.6% when the fluid reaches the inlet of the impeller. By the time, the fluid is energised, static temperature has increased by 13.2% at the diffuser inlet. From here, post compressibility and diffusion, a further increase by 2.8% in static temperature has incurred. After the kinetic energy has converted into potential energy in the volute, the compressed fluid leaves the stage with a 1.2% greater rise in static temperature.

It can be seen from the results that by the end of each station, there are variations between the design and off-design conditions. Reviewing static temperature variations under the choke condition against the BEP, there is 0.7% decrease at the end of the inducer; 4.6% decrease at the end of the impeller; 3.3% decrease at the end of the diffuser; and 3.7% decrease at the end of the volute. Reviewing static temperature variations under the surge condition against the BEP, there is 5.7% increase at the end of the inducer; 10% increase at the end of the impeller; 9.5% increase at the end of the diffuser; and 8.8% increase at the end of the volute.

The results also show the variations through each station between the design and off-design conditions. Reviewing static temperature variations under the choke condition against the BEP,

there is 87.2% increase through the inducer; 83.8% decrease through the impeller; 24.4% increase through the diffuser; and 38.1% decrease through the volute. Reviewing static temperature variations under the surge condition against the BEP, there is 6168.9% decrease through the inducer; 55.8% increase through the impeller; 7.5% decrease through the diffuser; and 26.2% decrease through the volute.

Figure 4.23 in the bottom row, depicts static temperature variation in the turbocharger compressor stage during the operating speed of 98.2rps/ $\sqrt{K}$  at (a) BEP (b) choke (c) surge. Observing (a), which is the turbocharger compressor stage operation at design flow rate, ambient air flows is drawn into the compressor stage via the inducer at a static temperature of 288K. From here, static temperature decreases by 1.4% when the fluid enters the impeller. As air particles pass through the impeller passages and exits into the diffuser, static temperature increases by 27.4%. Post the apparition of compressibility and diffusion in the diffuser, static temperature continues to rise by 7.5%. When flow has been collected in the volute and kinetic energy in the flow has been converted into potential energy, there is a final increase by 4.1% static temperature at the outlet.

Viewing the operating speed of 98.2rps/ $\sqrt{K}$  at (b), which is the turbocharger compressor stage operation at high flow rate, ambient inflow enters the inducer at a static temperature of 288K. When fluid reaches the exit of the inducer and enters the impeller, static temperature decreases by 2.7%. After the fluid has passed through the impeller, by changing its properties as a result of energy conversion, static temperature increases by 8.3%. After further altering the fluid properties through the diffuser passage as a result of compressibility and diffusion, static temperature increases by an additional 22% prior to entering the volute. When the fluid reaches the outlet, the results show an increase in static temperature by 3.5%.

Inspecting the operating speed of 98.2rps/ $\sqrt{K}$  at (c), which is the turbocharger compressor stage operation at low flow rate, incoming flow of the ambient air also exhibits 288K of static temperature. Static temperature increases by 5.9% when the fluid exits the inducer and reaches the inlet of the impeller. After energising the fluid, static temperature has increased by 29.3% at the diffuser inlet. From here, post compressibility and diffusion, a further increase by 6.8% in static temperature has incurred. After the kinetic energy has converted into potential energy in the volute, the compressed fluid leaves the stage with a 4.6% greater rise in static temperature.

It can be seen from the results that by the end of each station, there are variations between the design and off-design conditions. Reviewing static temperature variations under the choke

condition against the BEP, there is 1.5% decrease at the end of the inducer; 19.4% decrease at the end of the impeller; 4.8% decrease at the end of the diffuser; and 5.3% decrease at the end of the volute. Reviewing static temperature variations under the surge condition against the BEP, there is 7.6% increase at the end of the inducer; 9.2% increase at the end of the impeller; 8.5% increase at the end of the diffuser; and 9% increase at the end of the volute.

The results also show the variations through each station between the design and off-design conditions. Reviewing static temperature variations under the choke condition against the BEP, there is 46.3% increase through the inducer; 235.5% decrease through the impeller; 59.5% increase through the diffuser; and 22.8% decrease through the volute. Reviewing static temperature variations under the surge condition against the BEP, there is 505.9% decrease through the inducer; 15.1% increase through the impeller; 1% decrease through the diffuser; and 20.6% increase through the volute.

Table 4.5 details the speed comparison of static temperature variation at 98.2rps/ $\sqrt{K}$  compared to that at 58.9rps/ $\sqrt{K}$ . It can be seen at low flow rate, highest static temperature variation at the inlet and the outlet occurs in the volute, where the turbocharger compressor stage operating at 98.2rps/ $\sqrt{K}$  increases compared to that at 58.9rps/ $\sqrt{K}$ . There are no static lowest static temperature variations at the inlet of the impeller and the lowest static temperature variation at the outlet occurs in the inducer, where the operating condition 98.2rps/ $\sqrt{K}$  increases slightly compared to that at 58.9rps/ $\sqrt{K}$ . At the design flow rate, highest static temperature variation at the inlet and the outlet occurs in the volute, where the turbocharger compressor stage operating at 98.2rps/ $\sqrt{K}$  increases substantially compared to that at 58.9rps/ $\sqrt{K}$ . The lowest static temperature variation at the inlet and outlet occurs in the inducer, where the operating condition 98.2rps/ $\sqrt{K}$  decreases slightly compared to that at 58.9rps/ $\sqrt{K}$ . At the high flow rate, highest static temperature variation at the inlet and the outlet occurs in the volute, where the turbocharger compressor stage operating at 98.2rps/ $\sqrt{K}$  increases compared to that at 58.9rps/ $\sqrt{K}$ . The lowest static temperature variation at the inlet occurs in the inducer depicting a decrease at high speed compared to low speed. At the outlet, lowest static temperature variation occurs in the impeller, where the operating condition 98.2rps/ $\sqrt{K}$  increases compared to that at 58.9rps/ $\sqrt{K}$ .

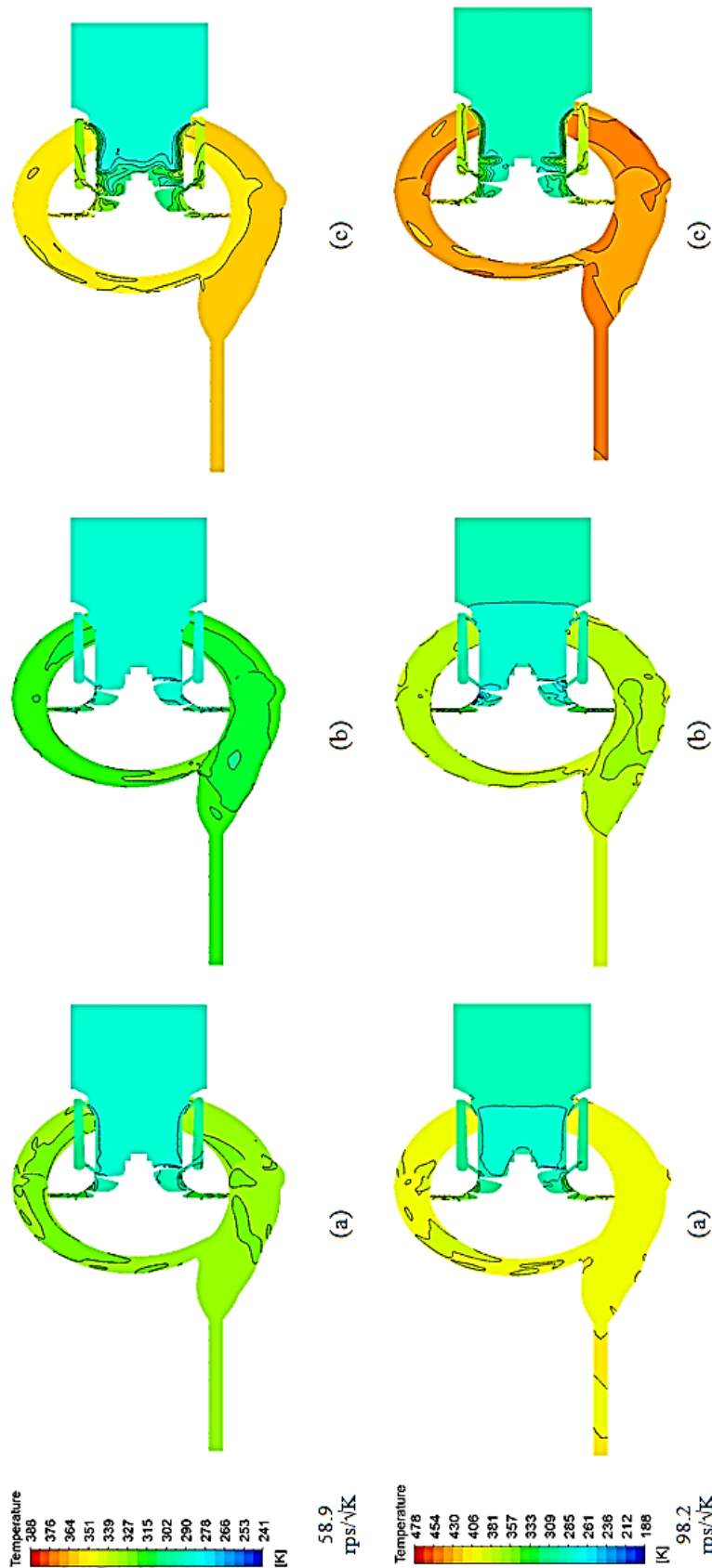


Figure 4.23 Static Temperature Variation in the Turbocharger Compressor Stage during the operating speed of 58.9 rps/√K at (a) BEP (b) choke (c) surge

Table 4.5 Global Speed Comparison of Static Temperature Variation

Compressor Component	Static Temperature In [%]			Static Temperature Out [%]		
	Low Flow	Design Flow	High Flow	Low Flow	Design Flow	High Flow
Inducer	-0.1	-0.2	-0.4	0.2	-1.6	-2.4
Impeller	0	-1.6	-2.4	14.2	15.1	0.8
Diffuser	14.3	15.2	1.3	18.7	19.8	18.1
Volute	18.8	19.9	18.2	22.9	22.7	20.8

Figure 4.24 depicts static temperature variations through each station in the compressor stage during the operating speed of (a) 58.9rps/ $\sqrt{K}$  and (b) 98.2rps/ $\sqrt{K}$ , both under design and off-design conditions. Overall, it is clear that static temperature variation through each component is much higher at 98.2rps/ $\sqrt{K}$  than at 58.9rps/ $\sqrt{K}$ .

Figure 4.24 (a) represents the variation of static temperature through each station in the compressor stage during the operating speed of 58.9rps/ $\sqrt{K}$  under design and off-design conditions. Through the inducer during the surge condition, static temperature varies considerably compared to during the BEP and choke condition. There is a very slight static temperature fall at BEP and little greater fall in the inducer during the choke condition. From the impeller, static temperature rises for all three conditions. Through the impeller, all three conditions vary significantly. It is noticed that as mass flow rate increases, static temperature variation through the impeller decreases. Vice versa trend is depicted through the diffuser. Though, there is little difference during the BEP and surge conditions. Through the volute, there is little difference the static temperature variation between the surge and choke conditions, however at BEP, static temperature varies the most.

Figure 4.24 (b) represents the variation of static temperature through each station in the compressor stage during the operating speed of 98.2rps/ $\sqrt{K}$  under design and off-design conditions. It can be seen that static temperature variance at the end of the inducer rises, while that at BEP and choke conditions, depicts a fall in static temperature. There are substantial variances in all three conditions through the impeller. Static temperature increases the most during the surge condition, followed by BEP, whereas variations during the choke condition are comparatively lower. Through the diffuser, static temperature varies significantly from the impeller. Static temperature during surge condition and at BEP are very similar however variance have greatly reduced, whereas, variations during the choke condition has significantly increased through the diffuser from the impeller. Static temperature variances through the volute has reduced further and this appears to decrease as the mass flow rate decreases.

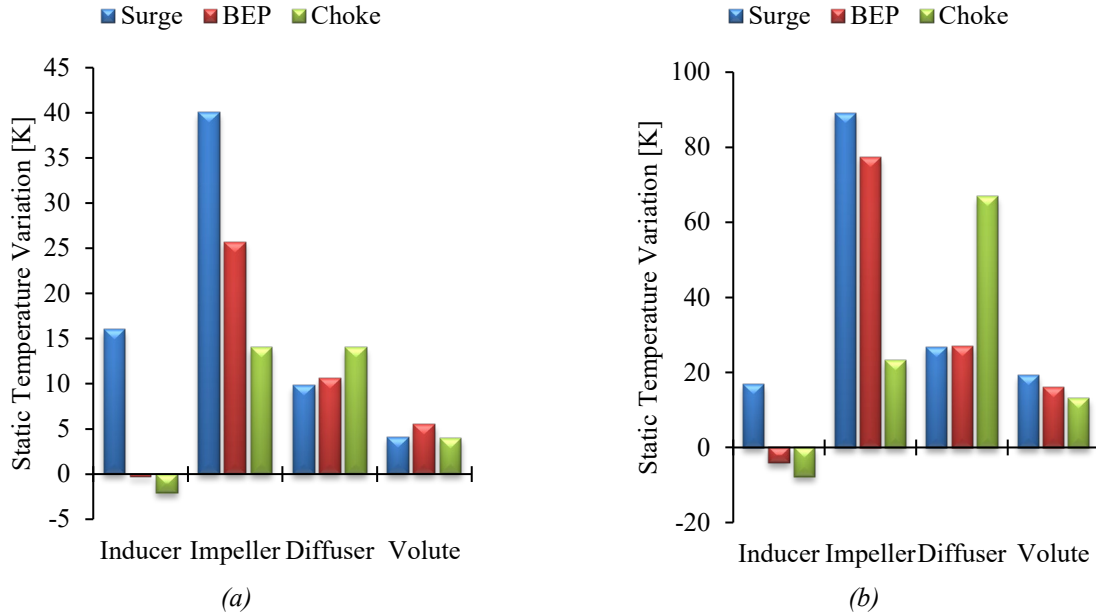


Figure 4.24 Static Temperature difference at the inlet and outlet of each component in the turbocharger compressor stage during (a) 58.9 rps/√K (b) 98.2 rps/√K

#### 4.12 Local Static Temperature Distribution around the Centrifugal Compressor Volute at Low Operating Speed during Steady Conditions

Figure 4.25 depicts static temperature distribution through the turbocharger compressor volute during the operating speed of 58.9 rps/√K at (a) BEP (b) choke (c) surge. Twelve cross-sections through the volute channel have been presented from the first cross-section of the scroll situated above the tongue, through to the outlet of the compressor stage.

It can be seen that static temperature uniformity is achieved through the centrifugal compressor volute for the design flow and high flow rate, while low flow rate is almost uniform in static temperature. It is clear that static temperature is the highest through the volute during the surge condition and static temperature is the lowest through the volute during the choke condition. Static temperature is expected to be higher at the walls due to the frictional effects taking place between the fluid and the wall. Observing (a), which is the volute operation at design flow rate at 58.9 rps/√K, it can be seen minimal and very slight static temperature variance occurs throughout the volute. At 15°, static temperature distribution is 328K, which is 0.4% less than the static temperature exhibited at the outlet. There is a very slight decrease in static temperature at the volute inlet and at the wall against the rear face towards the outer curve. At 45°, static temperature decreases from that depicted at 15° by 0.5% and hence the static temperature distribution is 0.9% less compared to the outlet. Slight decrease in static temperature is exhibited from the volute inlet along the rear face as well as from the outer curve near the front face

towards the overhang. At  $90^\circ$ , static temperature decreases further by 0.4% resulting in 1.3% less static temperature incurring than that at the outlet. Lower static temperature is seen to manifest across this cross-section from the rear face towards the front face. At  $135^\circ$ , static temperature increases by 0.2% and exhibits 1.1% less static temperature than that depicted at the outlet. The propagated region of slightly less static temperature has reduced in its distribution across the cross-section. This slight decrease is depicted from the volute inlet along the rear face and towards the central of the cross-section near the outer curve. Additionally, another area of slight decrease in static temperature is distributed from the central of the cross-section to the wall of the overhang. At  $180^\circ$ , static temperature increases further by 0.2%. This is 1% less static temperature compared to that at the outlet. Static temperature distribution is similar to the previously discussed cross-section however; the slight decrease in static temperature has reduced in its distribution across this cross-section. At  $225^\circ$ , static temperature increases by 0.1% and hence, is 0.8% less static temperature compared to that at the outlet. There are small areas from the volute inlet along the rear face, front face near the overhang and near the overhang in the central region, which display slightly decreased static temperature. At  $270^\circ$ , static temperature increases further by 0.1% resulting in 0.8% less static temperature compared to that at the outlet. Slight decrease in static temperature is displayed along the rear face and near the overhang in the central region of the cross-section. At  $315^\circ$ , there is no change in static temperature from the previously described cross-section, hence 0.8% less static temperature remains to exist compared to that at the outlet. Static temperature distribution appears to be the same, if not similar to has previously described. At the cut-off location, static temperature decreases by 0.2%, having 1% less static temperature compared to the outlet. Distribution of decreased static temperature regions have propagated from the volute inlet along the rear face and from the central region towards the front face of the profile. At the exit cone, static temperature increases by 0.7% and exhibits 0.3% less static temperature compared to that at the outlet. Static temperature appears constant here displaying uniformity. At the discharge duct, static temperature increases by 0.2% and exhibits 0.1% less static temperature compared to that at the outlet. Similar to the previous profile, static temperature appears constant here displaying uniformity. At the outlet, static temperature increases by 0.1% and depicts uniform static temperature.

Viewing (b), which is the volute operation at high flow rate at  $58.9\text{rps}/\sqrt{K}$ , shows lower static temperature to that at BEP with minimal and very slight static temperature variance occurring throughout the volute. At  $15^\circ$ , static temperature distribution is 319K, which is 0.3% more than the static temperature exhibited at the outlet. Slightly higher static temperature is exhibited in the



central region of the profile into the overhang with lower static temperature emerging from the volute inlet and between the volute inlet and overhang. At  $45^\circ$ , static temperature increases from that depicted at  $15^\circ$  by 0.2% and hence the static temperature distribution is 0.5% more compared to the outlet. The slightly higher static temperature from the previously discussed profile appears to have reduced in its distribution, while the slightly lower static temperature from the previously discussed profile appears to have propagated. At  $90^\circ$ , static temperature decreases by 0.6% resulting in 0.1% less static temperature incurring than that at the outlet. Slightly lower static temperature from the previously discussed profile appears to have manifested even more across this profile. At  $135^\circ$ , static temperature decreases by 0.4% and exhibits 0.5% less static temperature than that depicted at the outlet. Slightly lower static temperature appears to emerge from the lower sector inside the manifested low static temperature depicted in the previous profile. At  $180^\circ$ , static temperature decreases by 0.3%, which is 0.8% less static temperature compared to that at the outlet. From the previous profile, the low static temperature appears to have propagated across the lower of the profile. At  $225^\circ$ , static temperature decreases by 0.2% and hence, is 1% less static temperature compared to that at the outlet. Slight decrease in static temperature is emerging in the lower sector of the profile inside the previously mentioned low static temperature region. Further to this, increase in static temperature is also seen towards the outer curve. At  $270^\circ$ , static temperature decreases by 0.3% resulting in 1.3% less static temperature compared to that at the outlet. Slight decrease in static temperature emerging in the lower sector from the previous profile has propagated in this cross-section, also showing slight increase in static temperature towards the outer curve. At  $315^\circ$ , static temperature decreases by 0.5% and hence, is 1.8% less static temperature compared to that at the outlet. Slight decrease in static temperature exhibited in the lower sector from the previous profile has manifested even more across this profile, again, depicting an increase in static temperature towards the outer curve. At the cut-off location, static temperature decreases by 0.9%, having 2.6% less static temperature compared to the outlet. Slight decrease in static temperature is exhibited in the lower sector from the previous profile appears to have decreased further. At the exit cone, static temperature increases by 1.6% and exhibits 1.1% less static temperature compared to that at the outlet. Slightly lower static temperature emerges from the central region and propagates across the profile. At the discharge duct, static temperature increases by 0.7% and exhibits 0.4% less static temperature compared to that at the outlet. Slightly lower static temperature is depicted from the rear face and manifests across the profile towards the front face. At the outlet, static temperature increases by 0.4% and depicts uniform

static temperature with a small distribution of slightly lower static temperature in the central region of the profile near the front face.

Inspecting (c), which is the volute operation at low flow rate at  $58.9\text{ rps}/\sqrt{K}$ , shows higher static temperature to that at BEP with uniform static temperature downstream the discharge duct. At  $15^\circ$ , static temperature distribution is  $350\text{K}$ , which is 2.3% less than the static temperature exhibited at the outlet. Lower static temperature is seen to emerge from the volute inlet, which increases as it propagates into the cross-section. At  $45^\circ$ , static temperature increases from that depicted at  $15^\circ$  by 0.1% and hence the static temperature distribution is 2.2% less compared to the outlet. Lower static temperature is exhibited from the volute inlet along the rear face towards the outer curve of the profile. Higher static temperature appears to emerge between the volute inlet and the overhang, which is distributed into the cross-section. At  $90^\circ$ , static temperature increases by 0.2% resulting in 2.1% less static temperature incurring than that at the outlet. The lower static temperature region appears to have reduced in its distribution, while the region of higher static temperature has manifested in the central region of the profile. At  $135^\circ$ , static temperature increases by 0.7% and exhibits 1.4% less static temperature than that depicted at the outlet. Small regions of slightly higher static temperature appear to emerge from the volute inlet towards the rear face and near the outer curve central in the profile. At  $180^\circ$ , static temperature increases by 0.5%, which is 0.9% less static temperature compared to that at the outlet. The small region of slightly higher static temperature previously exhibited to emerge from the volute inlet appears to have manifested across the profile with a small region of high static temperature emerges inside this at the volute inlet. At  $225^\circ$ , static temperature increases by 0.4% and hence, is 0.5% less static temperature compared to that at the outlet. High static temperature at the volute inlet appears to have increased in its distribution along the rear face of the profile. At  $270^\circ$ , static temperature increases by 0.2% resulting in 0.4% less static temperature compared to that at the outlet. Static temperature appears to be almost consistent; however, high static temperature is exhibited along the outer curve towards the rear face, which increases in its distribution towards the centre of the profile. At  $315^\circ$ , static temperature increases by 0.1% and hence, is 0.3% less static temperature compared to that at the outlet. Again, higher static temperature emerges from the inflow. In addition to this, higher static temperature from the previously discussed cross-section appears to have moved to the outer curve towards front face and has increased its distribution towards the central of the profile. At the cut-off location, there is no change in static temperature hence 0.3% less static temperature remains to exist compared to the outlet. Higher static temperature region at the inflow appears to have propagated along the

rear face, while the higher static temperature region previously discussed appears to have moved to the front face and has elongated its distribution. At the exit cone, static temperature increases by 0.2% and exhibits 0.1% less static temperature compared to that at the outlet. It can be seen lower static temperature is localised at the upper sector of the profile near the rear face and along the periphery at the outer wall, which has reduced in its distribution from the previous profile. A small area of higher static temperature along the mid-section of the periphery is depicted at the rear face. At the discharge duct, there is no change in static temperature hence 0.1% less static temperature remains to exist compared to the outlet. Almost uniform static temperature is depicted here with a small distribution of slightly lower static temperature in the upper sector of the profile near the rear face, which has reduced from the previous profile. There is also a trim of higher static temperature along the mid-section of the periphery is depicted at the rear face and is reduced from the previously discussed profile. At the outlet, static temperature increases by 0.1% and depicts uniform static temperature across this profile.

Overall at low operating speed of the centrifugal compressor, it can be seen that static temperature increases from choke to surge in the volute, as expected. The choke condition exhibits static temperature decrease downstream towards the cut-off location, before to increasing towards the outlet. At BEP, there is a decrease in static temperature to 90° prior to increasing downstream towards the outlet. The surge condition depicts a linear increase in static temperature from the first profile downstream towards the outlet.

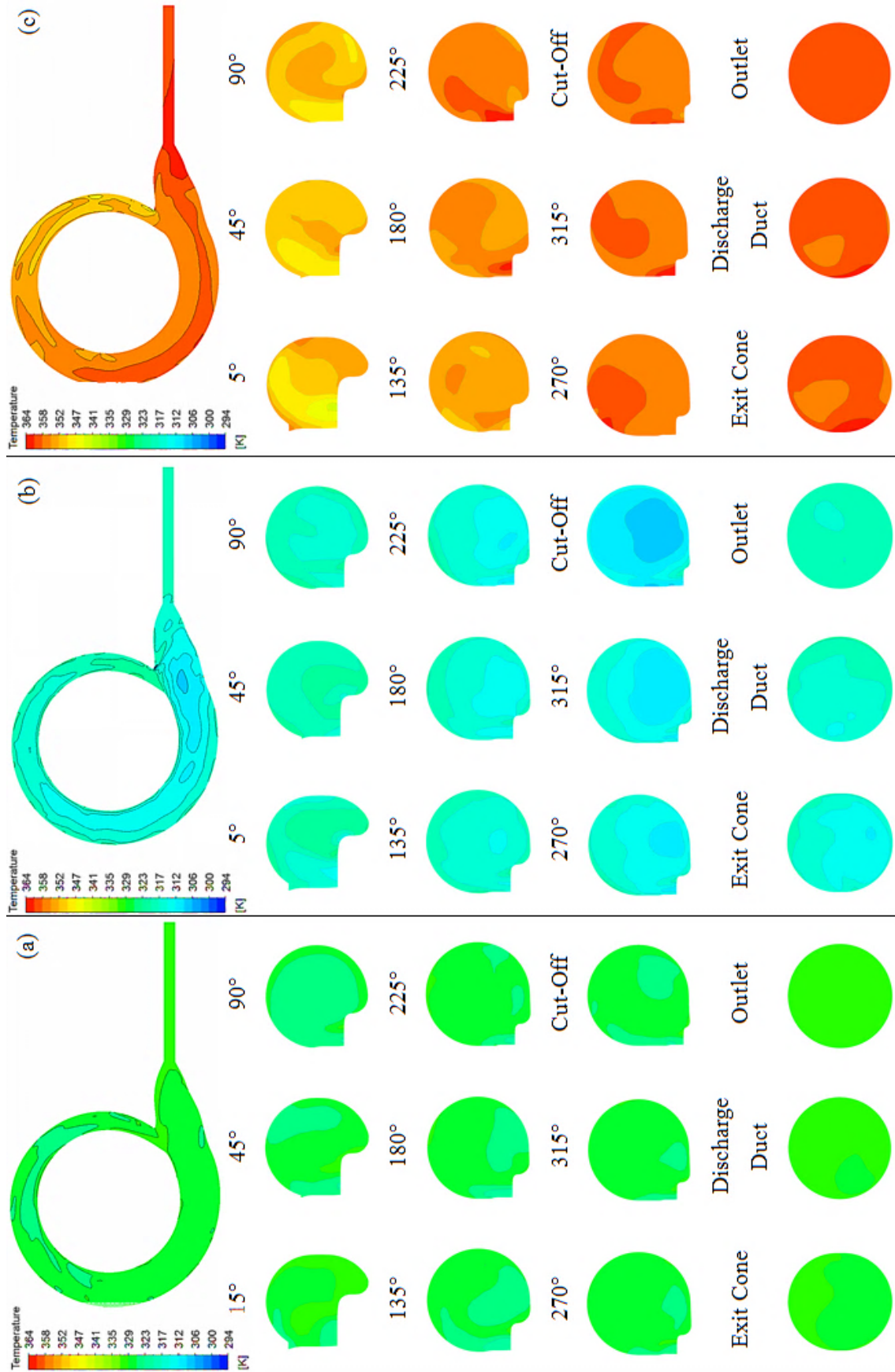


Figure 4.25 Static Temperature around the Compressor Volute during the operating speed of 58.9rps/√K at (a) BEP (b) choke (c) surge

Figure 4.26 depicts the variation of static temperature across each cross-section around the centrifugal compressor volute during the operating speed of 58.9rps/ $\sqrt{K}$  at low flow rate, being near the surge condition; design flow rate, being the best efficiency point; and high flow rate, being near the choke condition. This section is carried out in order to understand how the low and how the high flow rates near extreme phenomena differ in static temperature from the design flow rate. It is clear that the low flow shows higher static temperature than the design flow, while high flow shows lower static temperature than the design flow throughout the centrifugal compressor volute. At 15°, low flow depicts an increase in static temperature of 6.7% compared to the design flow, while high flow depicts a static temperature decrease of 2.9% compared to the design flow. At 45°, surge condition depicts a static temperature increase of 7.4% compared to the BEP, while choke condition depicts a decrease in static temperature of 2.2% compared to the BEP. At 90°, low flow depicts a static temperature increase of 8% compared to the design flow, while high flow depicts a decrease in static temperature of 2.4% compared to the design flow. At 135°, surge condition depicts an increase in static temperature of 8.6% compared to the BEP, while choke condition depicts a static temperature decrease of 3% compared to the BEP. At 180°, low flow depicts an increase in static temperature of 8.9% compared to the design flow, while high flow depicts a static temperature decrease of 3.5% compared to the design flow. At 225°, surge condition depicts a static temperature increase of 9.1% compared to the BEP, while choke condition depicts a decrease in static temperature of 3.9% compared to the BEP. At 270°, low flow depicts a static temperature increase of 9.3% compared to the design flow, while high flow depicts a decrease in static temperature of 4.2% compared to the design flow. At 315°, surge condition depicts an increase in static temperature of 9.4% compared to the BEP, while choke condition depicts a static temperature decrease of 4.7% compared to the BEP. At 345°, which is the cut-off location, low flow depicts an increase in static temperature of 9.6% compared to the design flow, while high flow depicts a static temperature decrease of 5.4% compared to the design flow. At 390°, which is the exit cone location, surge condition depicts a static temperature increase of 9.1% compared to the BEP, while choke condition depicts a decrease in static temperature of 4.5% compared to the BEP. At 393°, which is the discharge duct location, low flow depicts a static temperature increase of 8.8% compared to the design flow, while high flow depicts a decrease in static temperature of 4% compared to the design flow. At 400°, which is the outlet location, surge condition depicts an increase in static temperature of 8.8% compared to the BEP, while choke condition depicts a static temperature decrease of 3.7% compared to the BEP. Overall, this quantifies the static temperature variation

across each cross-section around the centrifugal compressor volute as a function of flow rates and how the off-design conditions vary against the design condition at low operating speed.

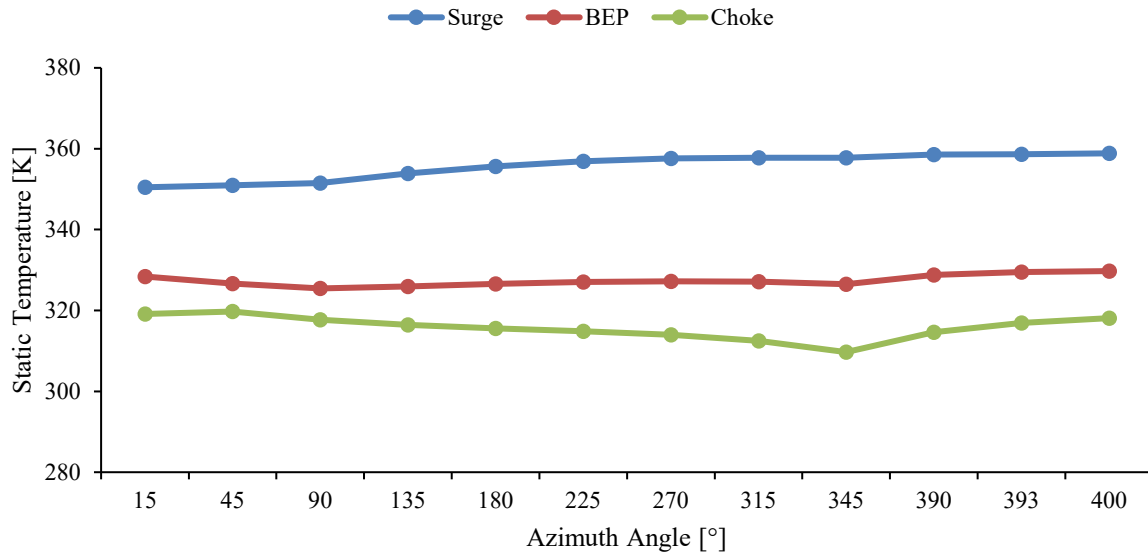


Figure 4.26 Static Temperature across each cross-section around the Compressor Volute during the operating speed of 58.9rps/ $\sqrt{K}$

Figure 4.27 is a graphical representation depicting the asymmetric ratio of static temperature along the radial direction of the profiles around the centrifugal compressor volute at the operating speed of 58.9rps/ $\sqrt{K}$ . When the asymmetric ratio is at 1, the static temperature in the flow is symmetric. When the asymmetric ratio is less than 1, static temperature in the flow is asymmetric towards the outer curve. When the asymmetric ratio is more than 1, static temperature in the flow is asymmetric towards the inner curve. It can be seen that static temperature at all flow conditions through the centrifugal compressor volute predominantly depicts slight asymmetry. At low flow, which is near the surge condition, asymmetry of static temperature is depicted along the radial direction towards the inner curve at 15°. At 45°, static temperature in the flow achieves symmetry along the radial direction. Downstream from 90° to 345°, static temperature is slightly asymmetric towards the outer curve. At 390° and 393°, symmetric static temperature is achieved in the flow along the radial direction, prior to presenting almost symmetric static temperature at 400°. At design flow, which is the BEP, there are slight asymmetries in static temperature in the flow along the radial direction from 15° to 90° towards the inner curve. From 135° to 345°, static temperature in the flow depicts asymmetry towards the outer curve. Slight asymmetries of static temperature towards the inner curve are displayed at 390°, followed by achieving symmetric static temperature downstream from 393°. At high flow, which is near the choke condition, slight asymmetry of static temperature along the radial direction is exhibited towards the outer curve at 15°. At 45°, static temperature in the flow

achieves symmetry, prior to exhibiting asymmetry towards the outer curve at  $90^\circ$ , which remains downstream to  $345^\circ$ . Static temperature in the flow depicts asymmetry along the radial direction towards the inner curve at  $390^\circ$ , followed by achieving symmetry at  $393^\circ$  and  $400^\circ$ . Overall at low operating speed, it is seen that flow rate has a little influence on the imbalance of static temperature along the radial direction of the cross-section profiles inside the centrifugal compressor volute. More detailed graphical representations are depicted in APPENDIX 2.

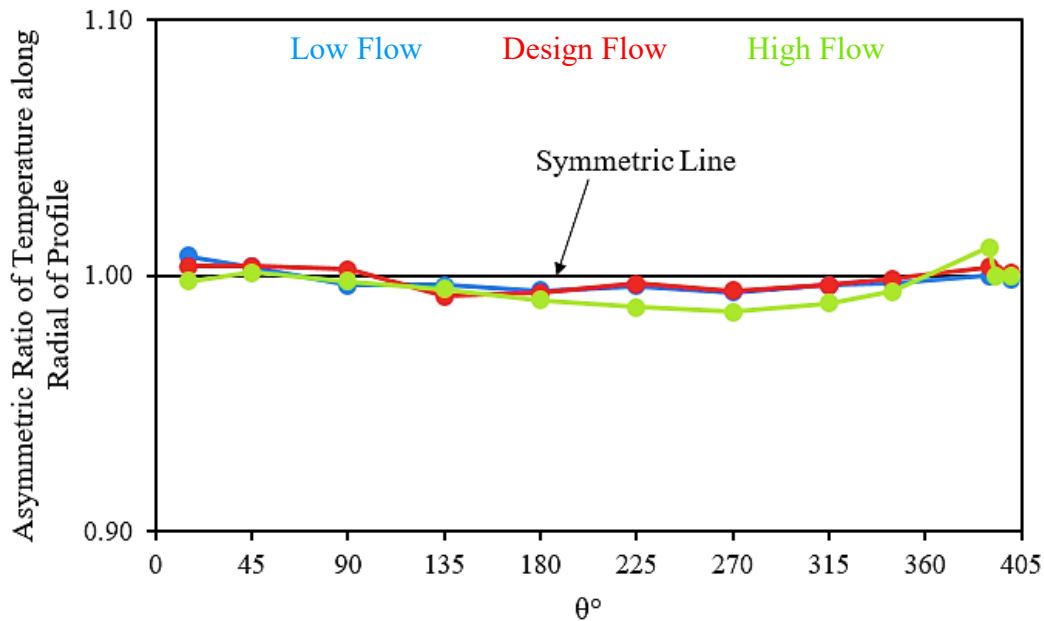


Figure 4.27 Asymmetric Ratio of Static Temperature along the Radial Direction on the Profiles around the Centrifugal Compressor Volute at Operating Speed of  $58.9\text{rps}/\sqrt{K}$  during Low Flow Rate, Design Flow Rate and High Flow Rate

Figure 4.28 is a graphical representation depicting the asymmetric ratio of static temperature along the axial direction of the profiles around the centrifugal compressor volute at the operating speed of  $58.9\text{rps}/\sqrt{K}$ . It can be seen that for all flow conditions, static temperature along the axial direction behave in a similar manner through the centrifugal compressor volute. For low flow near the surge condition, static temperature in the flow is asymmetric towards the front face from  $15^\circ$  to  $90^\circ$ . Thereafter, static temperature in the flow is slightly asymmetric towards the rear face at  $135^\circ$ , prior to depicting symmetric static temperature in the flow at  $180^\circ$ . Slight asymmetry towards the rear face is exhibited at  $225^\circ$ , which remains at  $270^\circ$ . From here, symmetric static temperature along the axial direction is achieved at  $315^\circ$  and at  $345^\circ$ . Slight asymmetry is presented towards the rear face at  $390^\circ$ , prior to achieving almost symmetric static temperature in the flow at  $393^\circ$  and  $400^\circ$  along the axial direction. For design flow at the BEP, symmetric static temperature is exhibited in the flow at  $15^\circ$ . At  $45^\circ$ , slight asymmetry is depicted towards the rear face, prior to depicting slight asymmetry towards the front face at  $90^\circ$  and  $135^\circ$ . At  $180^\circ$ , static

temperature is almost symmetric, prior to presenting symmetric static temperature along the axial direction from 225° to 345°. Downstream from 390°, static temperature is once again almost symmetric with dominance leaning slightly towards the front face. For high flow near the choke condition, static temperature in the flow along the axial direction identifies asymmetry towards the front face at 15°. At 45° and 90°, static temperature in the flow is almost symmetric with slight asymmetries towards the front face and rear face, respectively. Symmetric static temperature in the flow along the axial direction is observed at 135°, followed by an almost symmetric static temperature at 180°. Downstream from 225° to 345°, symmetric static temperature in the flow along the axial direction is achieved. At 390°, slight asymmetry of static temperature is identified towards the front face, which remains at 393°. At 400°, static temperature in the flow once again, achieves symmetry along the axial direction. Overall at low operating speed, it is observed that flow rate has a little influence on the imbalance of static temperature along the axial direction of the cross-section profiles inside the centrifugal compressor volute. More detailed graphical representations are depicted in APPENDIX 2.

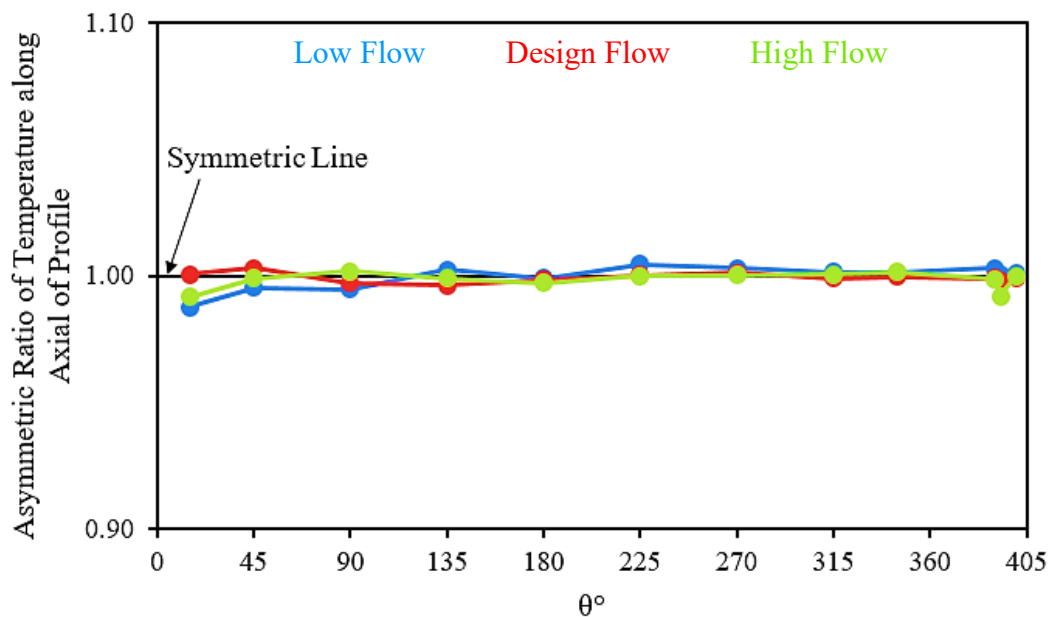


Figure 4.28 Asymmetric Ratio of Static Temperature along the Axial Direction on the Profiles around the Centrifugal Compressor Volute at Operating Speed of 58.9rps/√K during Low Flow Rate, Design Flow Rate and High Flow Rate



#### 4.13 Local Static Temperature around the Centrifugal Compressor Volute at High Operating Speed during Steady Conditions

Figure 4.29 depicts static temperature distribution through the turbocharger compressor volute during the operating speed of 98.2rps/ $\sqrt{K}$  at (a) BEP (b) choke (c) surge. Twelve cross-sections through the volute channel have been presented from the first cross-section of the scroll situated above the tongue, through to the outlet of the compressor stage.

It can be seen that static temperature is somewhat uniform through the centrifugal compressor volute for the design flow and high flow rate, while low flow rate depicts non-uniform static temperature. It is clear that static temperature is the highest through the volute during the surge condition and static temperature is the lowest through the volute during the choke condition. Static temperature is expected to be higher at the walls due to the frictional effects taking place between the fluid and the wall. Observing (a), which is the volute operation at design flow rate at 98.2rps/ $\sqrt{K}$ , it can be seen there are minimal static temperature variances. At 15°, static temperature distribution is 396K, which is 2.2% less than the static temperature exhibited at the outlet. Low static temperature can be seen to be emerging from the volute inlet against the rear face towards the centre of the cross-section. From here, static temperature appears to increase towards the front face. At 45°, static temperature decreases from that depicted at 15° by 0.8% and hence the static temperature distribution is 2.9% less compared to the outlet. Similar trend from the previous profile is exhibited here however, low static temperature region appears to have moved from the volute inlet to the rear face. There is also slightly higher static temperature seen between the volute inlet and across the overhang. At 90°, static temperature decreases further by 0.3% resulting in 3.3% less static temperature incurring than that at the outlet. The slightly higher region of static temperature has reduced in its distribution to being localised only at the volute inlet close to the overhang. At 135°, static temperature increases by 0.8% and exhibits 2.5% less static temperature than that depicted at the outlet. Low static temperature is displayed at the inflow along the rear face, as well as in the overhang. At 180°, static temperature increases by 0.7%, which is 1.8% less static temperature compared to that at the outlet. The low static temperature region at the inflow seems to have reduced in its distribution here. There is a small region of low static temperature depicted near the overhang close to the front face of the profile and slight higher static temperature along the outer curve near the front face. At 225°, static temperature increases by 0.2% and hence, is 1.6% less static temperature compared to that at the outlet. Slightly high static temperature along the outer curve appears to have moved from near the front face to near the rear face. Low static temperature appears to have elongated along

the wall of the rear face. At  $270^\circ$ , static temperature increases further by 0.2% resulting in 1.4% less static temperature compared to that at the outlet. Low static temperature is exhibited at the volute inlet along the rear face wall with slightly higher static temperature in the central region across the lower sector of the profile in the overhang. At  $315^\circ$ , there is negligible change in static temperature from the previously described cross-section, showing 1.3% less static temperature remains to exist compared to that at the outlet. Lower static temperature remains at the volute inlet with the slightly higher static temperature depicted in the previous profile is seen to manifest across the rear face and along the outer curve. At the cut-off location, static temperature decreases by 0.2%. This is the same as that depicted at  $58.9\text{rps}/\sqrt{K}$ , having 1.5% less static temperature compared to the outlet. Slightly higher static temperature discussed previous has propagating across this cross-section with lower static temperature remaining at the inflow. At the exit cone, static temperature increases by 1.1% and exhibits 0.4% less static temperature compared to that at the outlet. Static temperature is almost uniform with slightly lower static temperature beginning to reduce in its distribution across this profile. At the discharge duct, static temperature increases by 0.3% and exhibits 0.2% less static temperature compared to that at the outlet. Similar to the previous cross-section, static temperature is almost uniform with slightly lower static temperature reducing even more in its distribution across this profile. At the outlet, static temperature increases by 0.2% and depicts almost uniform static temperature with slightly lower static temperature localised in the central region of the profile.

Viewing (b), which is the volute operation at high flow rate at  $98.2\text{rps}/\sqrt{K}$ , it can be seen there are minimal static temperature variances. At  $15^\circ$ , static temperature distribution is 379K, which is 1.3% less than the static temperature exhibited at the outlet. Low static temperature is exhibited at the inflow, which is elongating into the upper sector of the profile towards the curvature of the outer wall. There is also a small region of low static temperature localised between the volute inlet and the overhang. Additionally, low static temperature is also depicted along the front face of the profile with higher static temperature elongated from the centre of the cross-section into the overhang and along the wall of the rear face and outer curve. At  $45^\circ$ , static temperature increases from that depicted at  $15^\circ$  by 0.3% and hence the static temperature distribution is 1% less compared to the outlet. Lower static temperature is seen at the inflow elongating into the central upper sector of the profile and a small region between the volute inlet and overhang. At  $90^\circ$ , static temperature decreases by 1% resulting in 2% less static temperature incurring than that at the outlet. From the previously discussed profile, the low static temperature exhibited at the inflow has reduced in its distribution, while the low static temperature region

between the volute inlet and the overhang has manifested across most of the profile leaving higher static temperature near the rear face and along the periphery of the wall. At 135°, static temperature decreases by 0.4% and exhibits 2.4% less static temperature than that depicted at the outlet. Low static temperature has manifested across the rear face of the profile with even lower static temperatures emerging from the rear face. Slightly higher static temperature remains in the upper sector of the profile towards the front face along the outer curve and at the volute inlet. At 180°, static temperature decreases by 0.1% and exhibits 2.5% less static temperature than that depicted at the outlet. Regarding the static temperature distribution, low static temperature is localised at the inflow. Higher static temperature in the upper sector has manifested from the front face across towards the rear face in the upper sector. Lower static temperature region is emerging from the low region at the central lower sector of the profile. At 225°, there is no change in static temperature from the previously described cross-section, hence 2.5% less static temperature remains to exist compared to that at the outlet. Low static temperature at the inflow remains in this cross-section with a slight reduction in its distribution. From the previously discussed profile, the small region of lower static temperature that emerged in the low region at the central lower sector of the profile appears to have propagated. At 270°, static temperature decreases by 0.1% resulting in 2.6% less static temperature compared to that at the outlet. Low static temperature at the inflow as significantly reduced its distribution and low static regions are depicted in the overhang. At 315°, static temperature decreases by 0.4% with 3% less static temperature compared to that at the outlet. Low static temperature regions localised in the overhang in the previous profile, has propagated in this cross-section. At the cut-off location, static temperature decreases by 1.3% with 4.3% less static temperature compared to that at the outlet. Predominantly low static temperature has manifested across this profile with distinctive higher static temperature localised at the front face as a minor distribution. In addition to this, another distinctive higher static temperature region is seen to be propagating from the volute inlet towards the overhang, to the wall along rear face. At the exit cone, static temperature increases by 2.8% and exhibits 1.7% less static temperature compared to that at the outlet. The higher static temperature discussed in the previous cross-section has manifested across this profile, depicting a slightly lower static temperature in the central region of the cross-section. At the discharge duct, static temperature increases by 1.2% and exhibits 0.5% less static temperature compared to that at the outlet. Almost uniform static temperature is exhibited, however slightly higher static temperatures are exhibited along the front face of the profile. At the outlet, static temperature increases by 0.5% and has uniform static temperature across the profile.

Inspecting (c), which is the volute operation at low flow rate at 98.2rps/ $\sqrt{K}$ , it can be seen there are significant static temperature variances signifying the presence of non-uniformity. At 15°, static temperature distribution is 425K, which is 3.7% less than the static temperature exhibited at the outlet. Lower static temperature is exhibited at the inflow along the wall of the rear face and towards the outer curve. This static temperature increases across profile to the wall of the front face. At 45°, static temperature increases from that depicted at 15° by 1.3% and hence the static temperature distribution is 2.4% less compared to the outlet. High static temperature is localised at the inflow near the overhang, while lower static temperature regions at the inflow along the rear face wall propagates following the outer wall curvature towards the front face. At 90°, static temperature increases by 0.7% resulting in 1.7% less static temperature incurring than that at the outlet. Lower static temperature is distributed across the inflow and increases in the cross-section. Higher static temperature is displayed along the periphery of the front face. At 135°, static temperature increases by 0.5% and exhibits 1.3% less static temperature than that depicted at the outlet. Lower inflow static temperature remains with lower regions also exhibited in the central region of the profile. Higher static temperature is exhibited along the overhang wall. At 180°, static temperature increases by 0.3%, which is 0.9% less static temperature compared to that at the outlet. Lower inflow static temperature elongates along the rear face wall and depicts a glimpse of higher static temperature emerging from between the volute inlet and the overhang. At 225°, static temperature increases further by 0.3% and hence, is 0.6% less static temperature compared to that at the outlet. Lower static temperature exhibited previously at the inflow along the rear face has elongated towards the outer curve and is displayed as a mere glimpse. Furthermore, a small region of higher static temperature is depicted at the inflow. At 270°, static temperature increases by 0.4% resulting in 0.2% less static temperature compared to that at the outlet. The lower static temperature region previously discussed has reduced to be distributed across a very small area at the volute inlet. Higher static temperature is depicted along the rear face wall, which appears to manifest almost half way across the profile. At 315°, static temperature decreases by 0.1% and hence, is 0.3% less static temperature compared to that at the outlet. Lower static temperature at the inflow appears to have elongated along the rear face wall with higher static temperature exhibited along the periphery of the front face wall. At the cut-off location, static temperature decreases by 0.2%. This is the same as that depicted at BEP, having 0.5% less static temperature compared to the outlet. Lower inflow static temperature is more prominent at the rear face wall and higher static temperature is displayed at the periphery along the overhang wall. At the exit cone, static temperature increases by 0.3% and exhibits 0.1% less static temperature compared to that at the outlet. Lower static temperature is exhibited in the

lower sector rear face wall, while higher static temperature is exhibited in the upper sector rear face wall. At the discharge duct, static temperature increases by 0.1% and exhibits 0.1% less static temperature compared to that at the outlet. Static temperature behaviour here is the same as that exhibited in the previously discussed cross-section. At the outlet, static temperature increases by 0.1% and depicts almost uniform static temperature with slightly higher static temperature variation occurring from the lower sector towards the upper sector of the profile.

Overall at high operating speed of the centrifugal compressor, it can be seen that static temperature increases from choke to surge in the volute, as expected. The choke condition depicts a decrease in static temperature downstream to the cut-off location, prior to increasing towards the outlet. At BEP, static temperature exhibits a decrease to 90° prior to increasing downstream towards the outlet. The surge condition depicts a linear increase in static temperature from the first profile downstream towards the outlet.

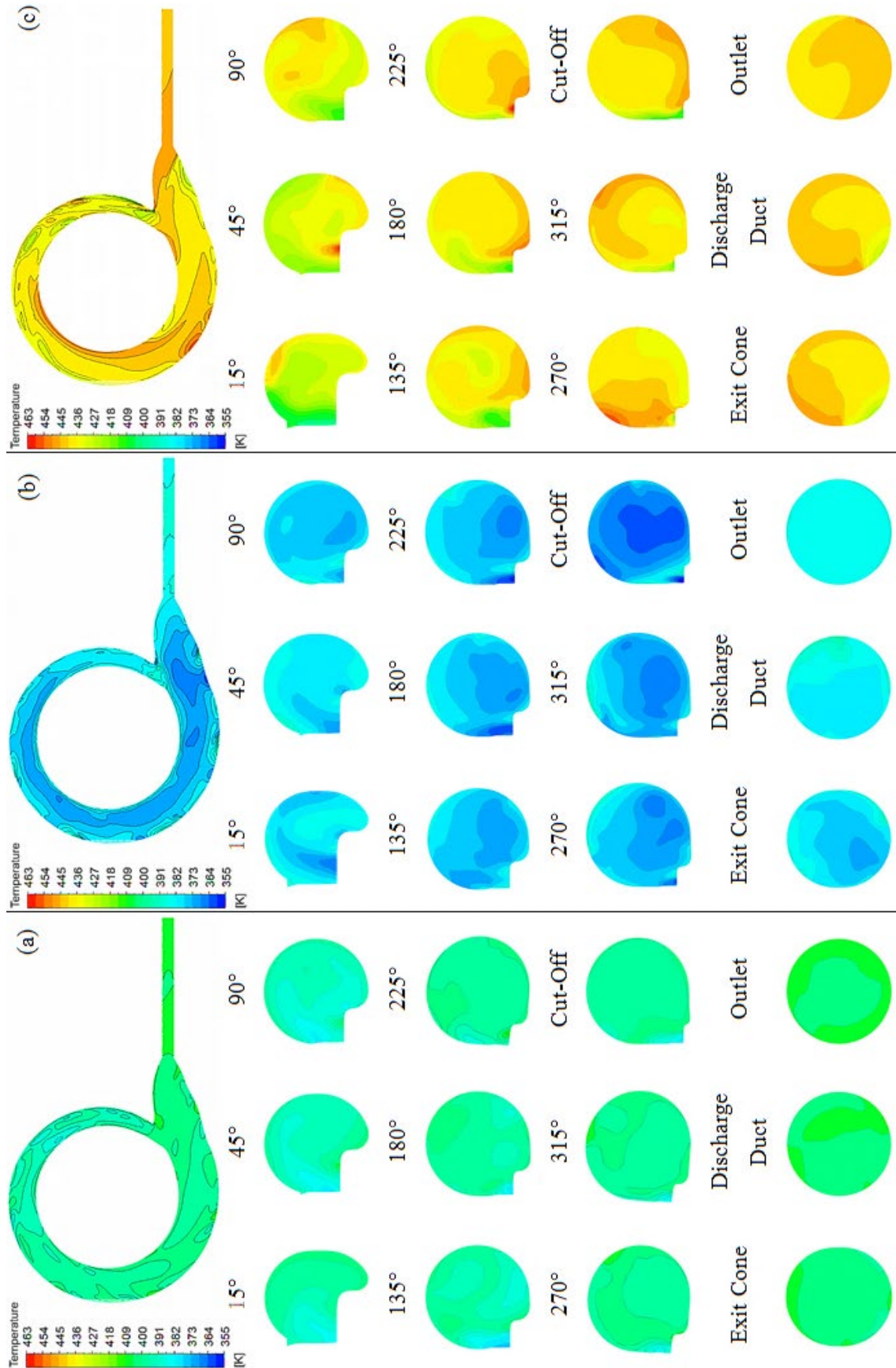


Figure 4.29 Static Temperature around the Compressor Volute during the operating speed of 98.2 rps/√K at (a) BEP (b) choke (c) surge

Figure 4.30 depicts the variation of static temperature across each cross-section around the centrifugal compressor volute during the operating speed of 98.2rps/ $\sqrt{K}$  at low flow rate, being near the surge condition; design flow rate, being the best efficiency point; and high flow rate, being near the choke condition. This section is carried out in order to understand how the low and how the high flow rates near extreme phenomena differ in static temperature from the design flow rate. It is clear that the low flow shows higher static temperature than the design flow, while high flow shows lower static temperature than the design flow throughout the centrifugal compressor volute. At 15°, low flow depicts an increase in static temperature of 7.3% compared to the design flow, while high flow depicts a static temperature decrease of 4.4% compared to the design flow. At 45°, surge condition depicts a static temperature increase of 9.6% compared to the BEP, while choke condition depicts a decrease in static temperature of 3.3% compared to the BEP. At 90°, low flow depicts a static temperature increase of 10.7% compared to the design flow, while high flow depicts a decrease in static temperature of 4% compared to the design flow. At 135°, surge condition depicts an increase in static temperature of 10.3% compared to the BEP, while choke condition depicts a static temperature decrease of 5.3% compared to the BEP. At 180°, low flow depicts an increase in static temperature of 9.9% compared to the design flow, while high flow depicts a static temperature decrease of 6.1% compared to the design flow. At 225°, surge condition depicts a static temperature increase of 10% compared to the BEP, while choke condition depicts a decrease in static temperature of 6.3% compared to the BEP. At 270°, low flow depicts a static temperature increase of 10.3% compared to the design flow, while high flow depicts a decrease in static temperature of 6.7% compared to the design flow. At 315°, surge condition depicts an increase in static temperature of 10.1% compared to the BEP, while choke condition depicts a static temperature decrease of 7.2% compared to the BEP. At 345°, which is the cut-off location, low flow depicts an increase in static temperature of 10.2% compared to the design flow, while high flow depicts a static temperature decrease of 8.4% compared to the design flow. At 390°, which is the exit cone location, surge condition depicts a static temperature increase of 9.3% compared to the BEP, while choke condition depicts a decrease in static temperature of 6.6% compared to the BEP. At 393°, which is the discharge duct location, low flow depicts a static temperature increase of 9.1% compared to the design flow, while high flow depicts a decrease in static temperature of 5.6% compared to the design flow. At 400°, which is the outlet location, surge condition depicts an increase in static temperature of 9% compared to the BEP, while choke condition depicts a static temperature decrease of 5.3% compared to the BEP. Overall, this quantifies the static temperature variation

across each cross-section around the centrifugal compressor volute as a function of flow rates and how the off-design conditions vary against the design condition at high operating speed.

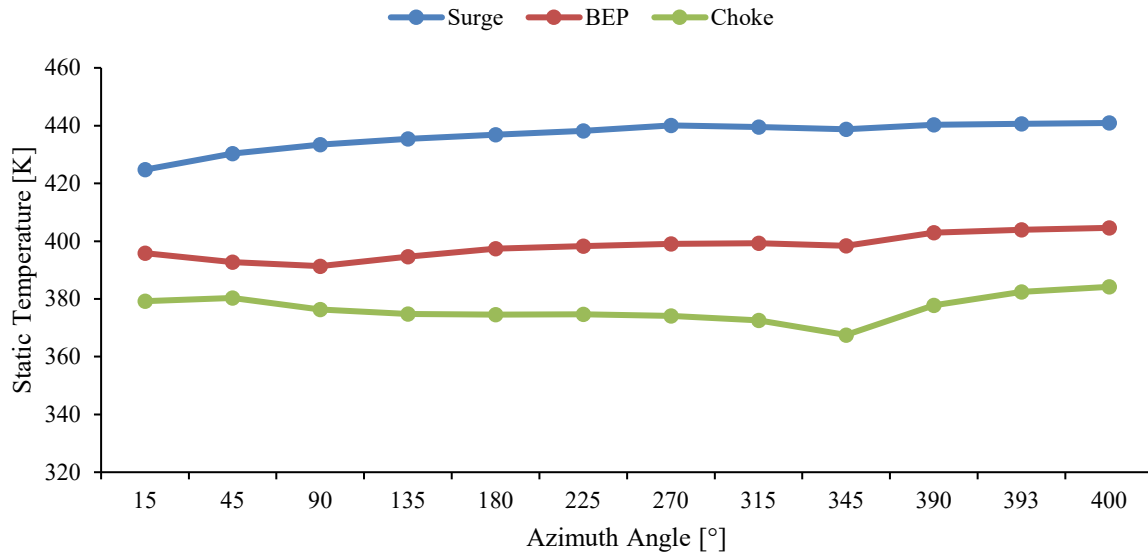


Figure 4.30 Static Temperature across each cross-section around the Compressor Volute during the operating speed of 98.2rps/ $\sqrt{K}$

Figure 4.31 is a graphical representation depicting the asymmetric ratio of static temperature along the radial direction of the profiles around the centrifugal compressor volute at the operating speed of 98.2rps/ $\sqrt{K}$ . It can be seen static temperature along the radial direction at low flow, which is near the surge condition, depicts asymmetric fluctuations through the volute between the inner curve and outer curve. The trend for asymmetry at high flow, which is near the choke condition, and design flow, which is the BEP, are very similar through the volute. For low flow near the surge condition, there is slight asymmetry in static temperature towards the outer curve at 15°. At 45°, static temperature in the flow depicts asymmetry towards the inner curve prior to displaying asymmetry towards the outer curve at 90°. From 135° to 225°, static temperature in the flow depicts asymmetry towards the inner curve. At 270°, static temperature identifies asymmetry towards the outer curve, which remains at 315°. Static temperature in the flow along the radial direction exhibits asymmetry towards the inner curve from 345° to 393°. At 400°, static temperature along the radial direction observes slight asymmetry towards the outer curve. At design and high flow conditions, static temperature along the radial direction is symmetric at 15°. For design flow condition at 45°, static temperature is asymmetric towards the inner curve. Thereafter from 90° to 345°, static temperature in the flow along the radial direction identifies asymmetry towards the outer curve. Downstream of 390°, static temperature in the flow exhibits slight asymmetry towards the inner curve. The high flow condition displays asymmetric static temperature in the flow along the radial direction from 45° to 345° towards the



outer curve. At  $390^\circ$  and  $393^\circ$ , static temperature is asymmetric towards the inner curve, prior to achieving symmetry along the radial direction at  $400^\circ$ . Overall at high operating speed, it has been exhibited that flow rate has a significant influence on the imbalance of static temperature along the radial direction of the cross-section profiles inside the centrifugal compressor volute. More detailed graphical representations are depicted in APPENDIX 2.

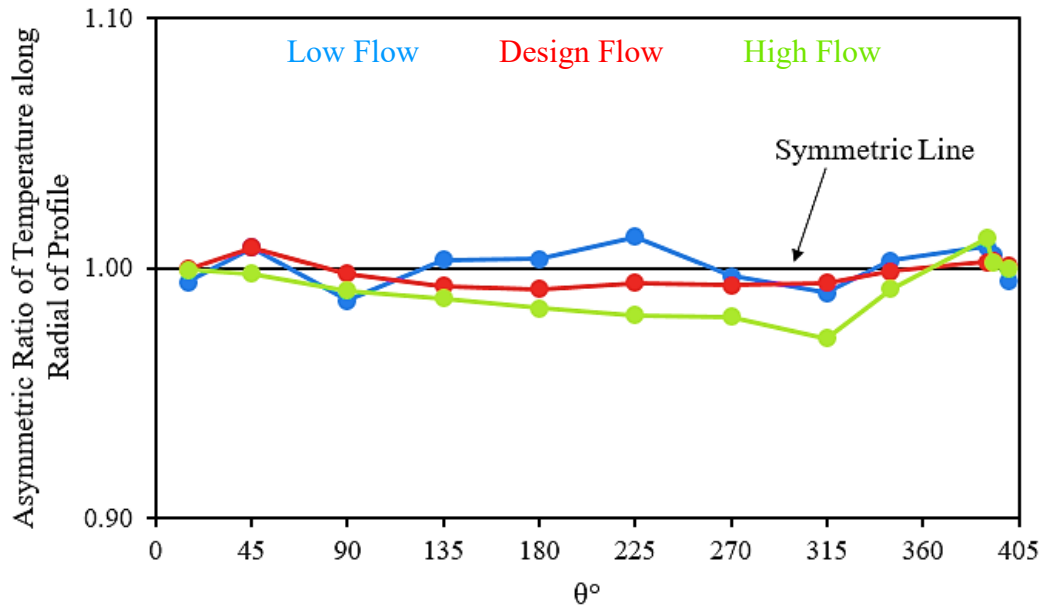


Figure 4.31 Asymmetric Ratio of Static Temperature along the Radial Direction on the Profiles around the Centrifugal Compressor Volute at Operating Speed of  $98.2\text{ rps}/\sqrt{K}$  during Low Flow Rate, Design Flow Rate and High Flow Rate

Figure 4.32 is a graphical representation depicting the asymmetric ratio of static temperature along the axial direction of the profiles around the centrifugal compressor volute at the operating speed of  $98.2\text{ rps}/\sqrt{K}$ . At low flow, being near the surge condition, it can be seen that static temperature in the flow along the axial direction is asymmetric towards the front face from  $15^\circ$  to  $180^\circ$ . At  $225^\circ$  and  $270^\circ$ , static temperature identifies asymmetry towards the rear face, prior to presenting asymmetry towards the front face at  $315^\circ$ , which remain at  $345^\circ$ . Thereafter, static temperature in the flow along the axial direction displays asymmetry towards the rear face at  $390^\circ$  and  $393^\circ$ , followed by slight asymmetry towards the front face at  $400^\circ$ . For design flow, being the BEP, it is observed that from  $15^\circ$  to  $225^\circ$ , static temperature along the axial direction shows asymmetry towards the front face. At  $270^\circ$ , there is slight asymmetry of static temperature towards the rear face, followed by a display of asymmetry towards the front face at  $315^\circ$ . Static temperature depicts asymmetry towards the rear face at  $345^\circ$ , prior to achieving symmetric static temperature at  $390^\circ$  along the axial direction. At  $393^\circ$ , there is a slight asymmetry in static temperature towards the front face prior to once again, achieving symmetric static temperature

along the axial direction at  $400^\circ$ . For high flow, being near the choke condition, it is observed that static temperature at  $15^\circ$  and  $45^\circ$  is asymmetric towards the front face, followed by displaying asymmetry towards the rear face at  $90^\circ$ . Slight asymmetries in static temperature is observed towards the front face from  $135^\circ$  to  $270^\circ$ . Symmetric static temperature in the flow along the axial direction is achieved at  $315^\circ$ . At  $345^\circ$ , static temperature in the flow present slight asymmetry towards the rear face. Thereafter, static temperature is seen to display asymmetry at  $390^\circ$  towards the front face, which remains at  $393^\circ$ . At  $400^\circ$ , symmetric static temperature in the flow along the axial is achieved. Overall at high operating speed, it is noticed that flow rate has a significant influence on the imbalance of static temperature along the axial direction of the cross-section profiles inside the centrifugal compressor volute. More detailed graphical representations are depicted in APPENDIX 2.

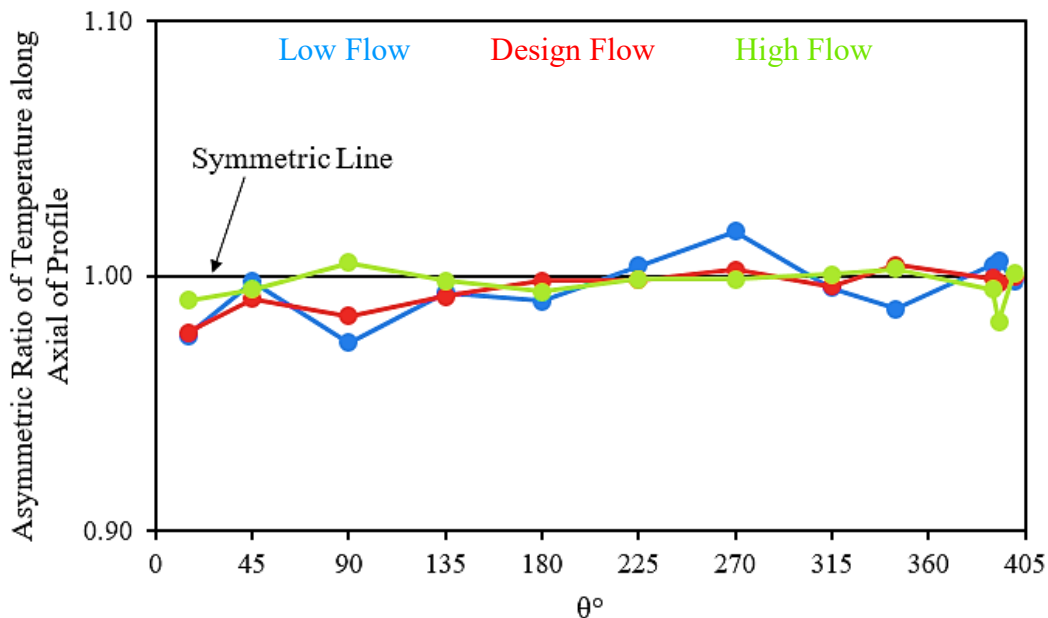


Figure 4.32 Asymmetric Ratio of Static Temperature along the Axial Direction on the Profiles around the Centrifugal Compressor Volute at Operating Speed of  $98.2\text{rps}/\sqrt{K}$  during Low Flow Rate, Design Flow Rate and High Flow Rate

#### 4.14 Local Speed Comparison of Static Temperature around the Centrifugal Compressor Volute during Steady Conditions

Table 4.6 depicts the steady response of the local speed comparison, where the high operating speed of  $98.2\text{rps}/\sqrt{K}$  is compared against the low operating speed of  $58.9\text{rps}/\sqrt{K}$  for static temperature across each of the selected cross-section through the turbocharger compressor volute. It can be seen that static temperature at  $98.2\text{rps}/\sqrt{K}$  increases at design and off-design conditions compared to that at  $58.9\text{rps}/\sqrt{K}$ . The lowest static temperature increase through the

volute occurs at high flow conditions, while highest static temperature increase through the volute occurs at low flow conditions. For all flow conditions, highest static temperature increase occurs at the outlet, being at 400°, while lowest static temperature increase occurs at 15° for low flow condition; 45° at design flow condition and 135° at high flow condition.

*Table 4.6 Local Speed Comparison of Static Temperature Variation during Steady Response*

$\theta^\circ$	Static Temperature [%]		
	Low Flow	Design Flow	High Flow
15	21.2	20.5	18.8
45	22.6	20.2	18.9
90	23.3	20.2	18.5
135	23.0	21.1	18.4
180	22.8	21.7	18.7
225	22.8	21.8	19.0
270	23.1	22.0	19.2
315	22.9	22.0	19.2
345	22.6	22.0	18.7
390	22.8	22.5	20.1
393	22.9	22.6	20.7
400	22.9	22.7	20.8

#### 4.15 Summary

This chapter has numerically investigated the steady response of the turbocharger compressor stage and its volute using CFD techniques. This section has employed Multi-Reference Frame techniques using CFD to investigate and thoroughly understand some of the aerodynamic flow characteristics inside the turbocharger compressor stage and its volute. This extensively detailed investigation enables one to better understand the flow mechanics and to use these findings gathered from this section to provide improvements during experimentation and during the design process. For example, during experimentation, the presented flow structures are difficult to capture, therefore a control section can be installed at the presented locations. During the design process, determining the strengths and weaknesses of flow behaviour inside the volute can be used to set a foundation to design an improved turbocharger compressor volute to real operating conditions. From the extensively detailed analysis carried out on the aerodynamic flow characteristics of the turbocharger compressor stage and through its volute, the findings of the presented results are summarised:

- Static pressure recovery coefficient falls below 0 at low operating speed [2], indicating that there are more pressure losses taking place at the choke condition than pressure recovery. This is due to secondary flows causing head loss as a result of friction.
- Globally, in comparison with low operating conditions, high operating speeds predominantly increases in static pressure through the inducer inlet, impeller outlet, diffuser and volute; increases throughout for velocity magnitude; and predominantly increases in static temperature through the impeller outlet, diffuser and volute.
- Locally, in comparison with low operating conditions, high operating speeds increases across the cross-sections for static pressure, velocity magnitude and static temperature through the turbocharger compressor volute.
- Since secondary flows are a direct cause for head loss as a result of friction, more specifically, an imbalance between static pressure and kinetic energy [74]. For this reason, asymmetries along the radial direction and axial direction of the cross-section profiles around the centrifugal compressor volute are more prominent for pressure and velocity.
- The extent of secondary flows inside the centrifugal compressor volute is a function of flow rate.

The conducted analyses provides sufficient knowledge the local performance indicators offers the global performance indicators for the volute and the turbocharger compressor stage. However, it is still unknown how these flow structures vary during unsteady operation. For this reason, the next section explores and captures these presented performance indicators during two different instances by employing the Sliding Mesh technique using CFD.

## CHAPTER 5

# INSTANTANEOUS FLOW CHARACTERISTICS INSIDE A CENTRIFUGAL COMPRESSOR VOLUTE

---

This chapter numerically captures the aerodynamic flow characteristics of a turbocharger compressor stage, as well as the flow structure through the volute across numerous profiles. These investigations are carried out using Sliding Mesh (SM) model within CFD based techniques for simulating unsteady response at two instances during the specified operating speeds and their corresponding design points. The two instances are with regards to the impeller blade position with respect to the volute tongue. A thorough understanding is gained in this section where the strengths and weaknesses of the existing model have been identified, correlating local performance indicators with the global performance indicators to explore the flow behaviour during unsteady response against that during steady response. This includes capturing fluid flow structures along the radial direction and axial direction of each profile, which has been used to compute the asymmetric ratio to determine the flow field imbalance.

### 5.1 Turbocharger Compressor Stage Unsteady Performance Comparison

Although the Multiple Reference Frame model is simple to employ and provides reasonable approximations, it has its limitations. In order to capture the aerodynamic interaction of the impeller blade with the volute tongue, unsteady simulations are necessary using the transient Sliding Mesh model [75].

Numerical investigations during steady response have been thoroughly analysed in the previous chapter. It is now of interest to understand the unsteady response of the turbocharger compressor stage and its volute during two different instances. The two different instances are referred as Blade Position 1, where the impeller blade is aligned with the volute tongue shown in Figure 5.1 (a), which has been taken at  $180^\circ$  impeller rotation; and Blade Position 2, where the impeller blade has passed the volute tongue and another blade is approaching the tongue shown in Figure 5.1 (b), which has been taken at  $225^\circ$  impeller rotation.

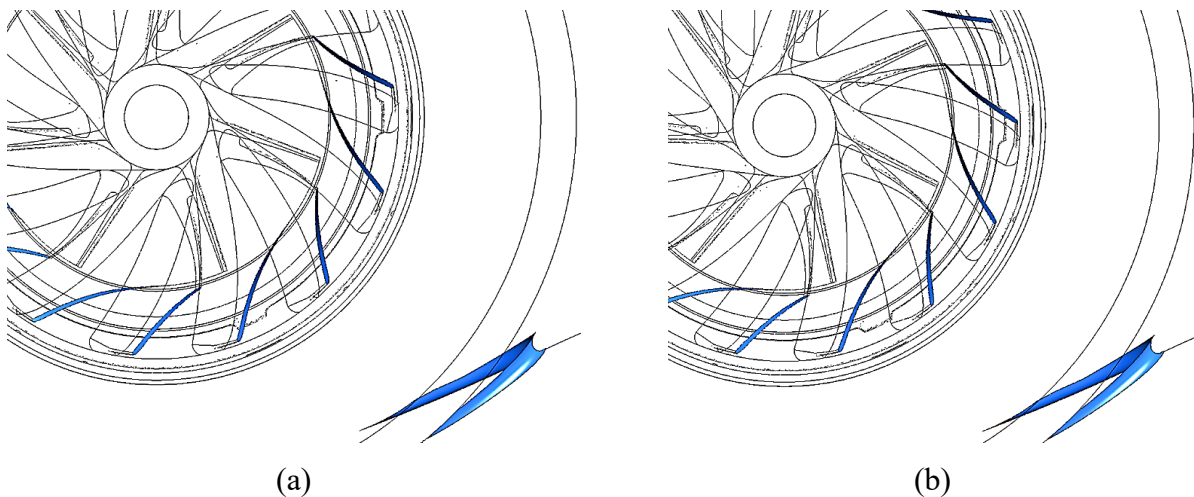


Figure 5.1 Two instances of impeller blade with respect to volute tongue (a) impeller blade aligned with volute tongue (b) volute tongue between two impeller blades

Figure 5.2 depicts the performance comparison of the experimental data and steady response with the revolution averaged unsteady response of the turbocharger compressor. Figure 5.2 (a) depicts the turbocharger compressor map and Figure 5.2 (b) depicts the turbocharger compressor isentropic efficiency map. It can be seen in Figure 5.2 (a) at  $58.9\text{rps}/\sqrt{K}$ , the revolution averaged unsteady response is in good agreement with the steady response and experimental data. At  $98.2\text{rps}/\sqrt{K}$ , total-to-total pressure ratio for the unsteady case is higher than experimental and the steady case. Figure 5.2 (b) appears to overestimate the isentropic efficiency of the turbocharger compressor for the unsteady case compared to the experimental data and the steady case. This is more significant compared to the experimental data than the steady case and could be due to errors in the temperature values during computation.

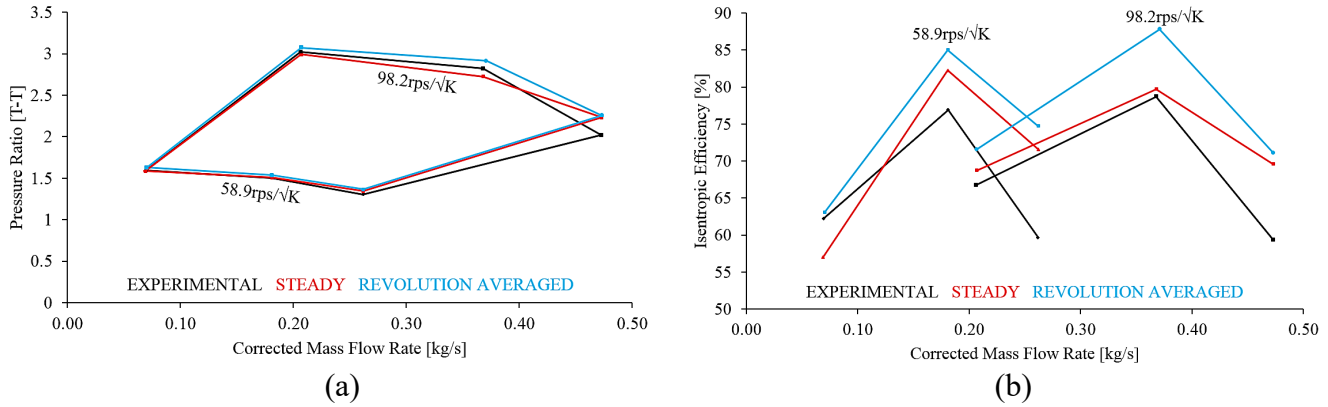


Figure 5.2 Steady and Revolution Averaged Turbocharger Compressor Performance Comparison of (a) Compressor Map (b) Isentropic Efficiency Map

Table 5.1 details the results of the total-to-total pressure ratio and isentropic efficiency of the turbocharger compressor stage, experimentally and numerically during steady and unsteady conditions. For the pressure ratio at low speed, it can be seen that the steady case and experimental data are in good agreement. The unsteady cases are higher at high flow rate with good agreement at design flow rate and low flow rate. For the pressure ratio at high speed, it can be seen that the steady case is higher than the experimental data at high flow rate and unsteady cases are even higher than the steady case. At design flow rate, pressure ratio for the steady case is lower than the experimental, while the unsteady cases are higher. At low flow rate, pressure ratio for the steady case is in good agreement with the experimental data, while unsteady cases are higher. For the isentropic efficiency unsteady cases are higher throughout the flow rates at both speeds compared to the steady case and experimental. At low speed, the steady case is higher than the experimental at high flow and design flow and lower at low flow rate, while at high speed, isentropic efficiency is higher than the experimental through all flow rates.

Table 5.1 Turbocharger Compressor Performance Comparison

Operating Speed	Design Point	Pressure Ratio [T-T]					Isentropic Efficiency [%]				
		Experimental	Steady	Blade Position 1	Blade Position 2	Revolution Averaged Unsteady	Experimental	Steady	Blade Position 1	Blade Position 2	Revolution Averaged Unsteady
58.9rps/√K	High Flow	1.3	1.3	1.4	1.4	1.4	59.7	71.6	74.7	74.7	74.7
	Design Flow	1.5	1.5	1.5	1.5	1.5	76.9	82.3	85.0	85.0	85.0
	Low Flow	1.6	1.6	1.6	1.6	1.6	62.3	57.0	63.0	63.2	63.1
98.2rps/√K	High Flow	2.0	2.2	2.3	2.3	2.3	59.4	69.6	71.1	71.1	71.1
	Design Flow	2.8	2.7	2.9	2.9	2.9	78.7	79.7	88.0	87.9	87.8
	Low Flow	3.0	3.0	3.1	3.1	3.1	66.8	68.8	71.7	71.7	71.6

Figure 5.3 depicts the overall turbocharger compressor volute performance comparison of the steady response with the revolution averaged unsteady response. Figure 5.3 (a) depicts the static pressure recovery through the compressor volute and Figure 5.3 (b) depicts total pressure loss through the compressor volute. It can be seen in Figure 5.3 (a) at low speed, the steady case

identifies higher static pressure recovery than the unsteady case at low flow rate; however, they are both in good agreement at high flow rate. At high flow rate, static pressure recovery coefficient falls below 0, indicating more pressure losses incurring at the choke condition than pressure recovery due to secondary flows causing head loss as a result of friction. For high speed, the unsteady case has negligible variance in static pressure recovery in comparison with the steady case through all flow rates and is therefore in good agreement. It can be seen in Figure 5.3 (b) at low speed, total pressure loss at low flow rate is higher for the unsteady case and lower at design flow, followed by having little variance at high flow rate. At high speed, there is little variance in total pressure loss at low flow and design flow rate. At high flow rate, the unsteady case depicts less total pressure loss through the compressor volute than that for the steady case.

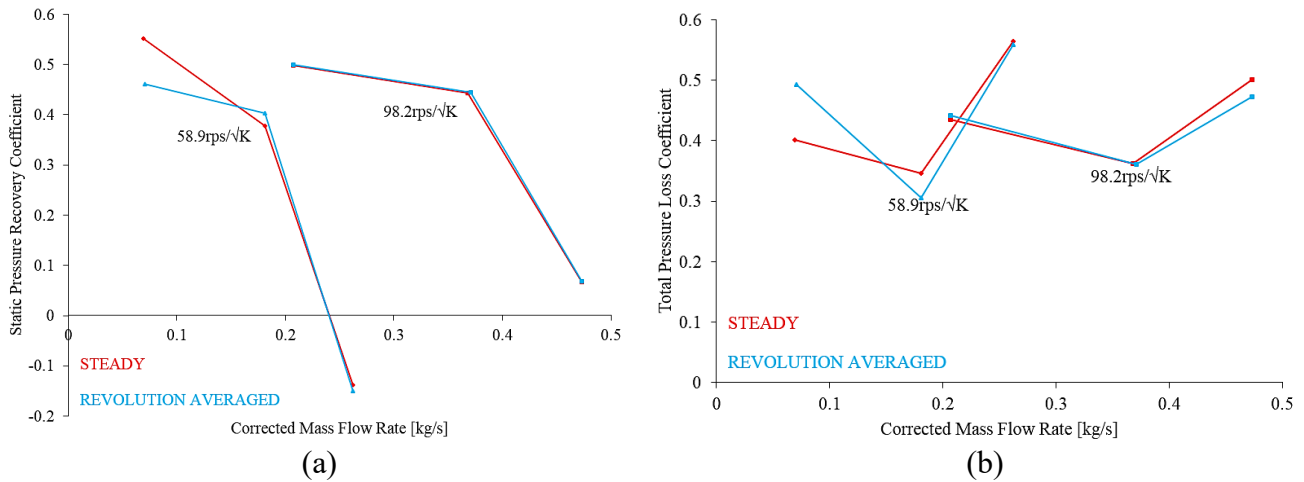


Figure 5.3 Steady and Revolution Averaged Turbocharger Compressor Volute Performance Comparison of (a) Static Pressure Recovery Coefficient (b) Total Pressure Loss Coefficient

Table 5.2 details the results of the overall turbocharger compressor volute performance via the static pressure recovery and total pressure loss incurring during steady and unsteady conditions. At low speed it can be seen that at high flow rate and low flow rate, static pressure recovery is lower during unsteady conditions than that during steady conditions, while at design flow rate, there appears to be no change. At high speed, there are no changes in static pressure recovery between the steady and unsteady cases at high flow rate and low flow rate, however at design flow rate, there appears to be higher static pressure recovery at blade position 1 when the impeller blade is aligned with the volute tongue. At both speeds, it can be seen that there are no variations in total pressure loss between the steady and unsteady cases at high flow rate and design flow rate. At low flow rate for low speed, blade position 1 and the revolution averaged unsteady results depict higher total pressure loss through the volute. At low flow rate for high speed, blade position 1 depicts higher total pressure loss through the volute.



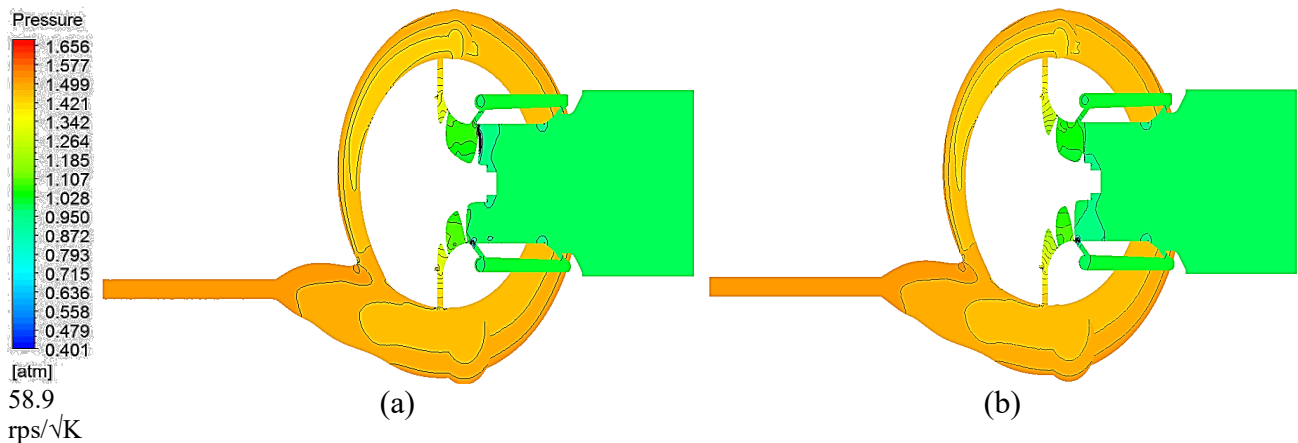
Table 5.2 Turbocharger Compressor Volute Performance Comparison

Operating Speed	Design Point	Static Pressure Recovery Coefficient				Total Pressure Loss Coefficient			
		Steady	Blade Position 1	Blade Position 2	Revolution Averaged Unsteady	Steady	Blade Position 1	Blade Position 2	Revolution Averaged Unsteady
58.9rps/ $\sqrt{K}$	High Flow	-0.1	-0.2	-0.2	-0.2	0.6	0.6	0.6	0.6
	Design Flow	0.4	0.4	0.4	0.4	0.3	0.3	0.3	0.3
	Low Flow	0.6	0.4	0.5	0.5	0.4	0.5	0.4	0.5
98.2rps/ $\sqrt{K}$	High Flow	0.1	0.1	0.1	0.1	0.5	0.5	0.5	0.5
	Design Flow	0.4	0.5	0.4	0.4	0.4	0.4	0.4	0.4
	Low Flow	0.5	0.5	0.5	0.5	0.4	0.5	0.4	0.4

Given the turbocharger compressor volute being designed to the BEP, this chapter focuses solely on the turbocharger compressor BEP at a low operating speed of 58.9rps/ $\sqrt{K}$  and at a high operating speed of 98.2rps/ $\sqrt{K}$ .

## 5.2 Global Static Pressure Distribution at Two Instances during Unsteady Conditions

Figure 5.4 depicts the static pressure variation in the turbocharger compressor stage during the operating speed of 58.9rps/ $\sqrt{K}$  and 98.2rps/ $\sqrt{k}$ . Figure 5.4 (a) depicts blade position 1, also referred as BP1, which is when the impeller blade is aligned with the volute tongue and Figure 5.4 (b) depicts blade position 2, also referred as BP2, which is when the impeller blade is passed the tongue and another blade is approaching the tongue. At both speeds, minimal variances in static pressure are seen between the two instances. At low speed, higher static pressure is displayed upstream of the diffuser than at high speed. At high speed, higher static pressure is displayed around the volute than at low speed.



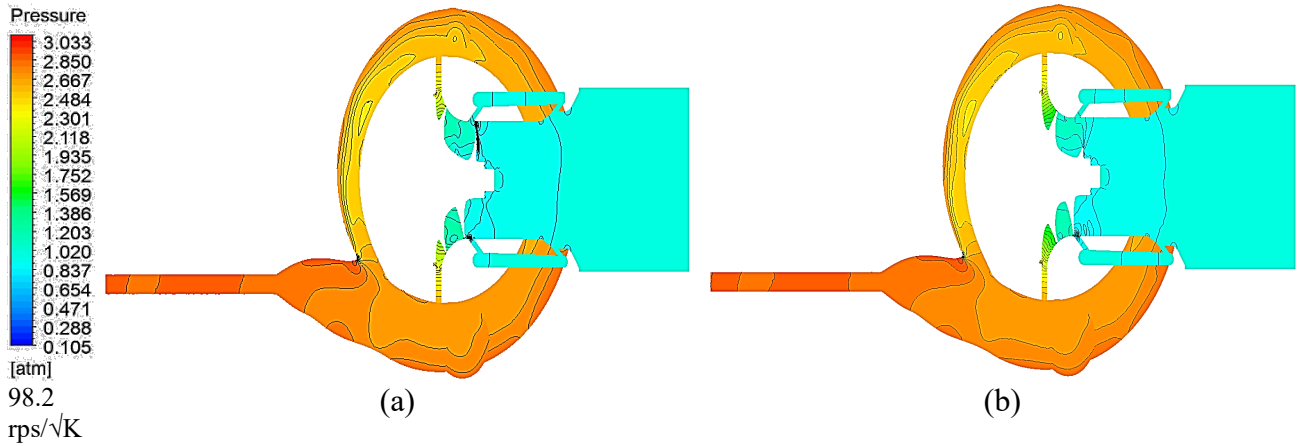


Figure 5.4 Static Pressure Variation in the Turbocharger Compressor Stage during the operating speed of 58.9 rps/√K and 98.2 rps/√K at (a) Blade Position 1 (b) Blade Position 2

Figure 5.5 depicts the comparison of static pressure variations through each station in the compressor stage between the steady conditions and unsteady conditions at low operating speed of (a) 58.9 rps/√K and at high operating speed of (b) 98.2 rps/√K. There is a greater static pressure variation through each component at high speed than at low speed. It can be seen that for both speeds, static pressure decreases through the inducer for all cases and increases downstream of this. There appears to be no variance in static pressure through the inducer between the unsteady cases and steady case. Through the impeller, unsteady cases display higher static pressure than that displayed for the steady case. This increase appears to be more prominent at low speed than at high speed. At low speed, there appears to be no variance in static pressure through the compressor between the two unsteady instances, BP1 and BP2 from the inducer to the diffuser. At the volute there is negligible variance in static pressure where, BP2 is very slightly higher. Further to this, static pressure variance through the diffuser and volute increases very slightly for unsteady cases in comparison with the steady case. At high speed, there appears to be no variance in static pressure upstream the volute between the two unsteady instances, BP1 and BP2, however, there appears to be slightly higher static pressure variance for BP1 than BP2 through the volute. Further to this, static pressure variance through the diffuser and volute increases for unsteady cases in comparison with the steady case. Details of these through-flow variances for the unsteady response at two instances against the steady response are presented in Table 5.3.

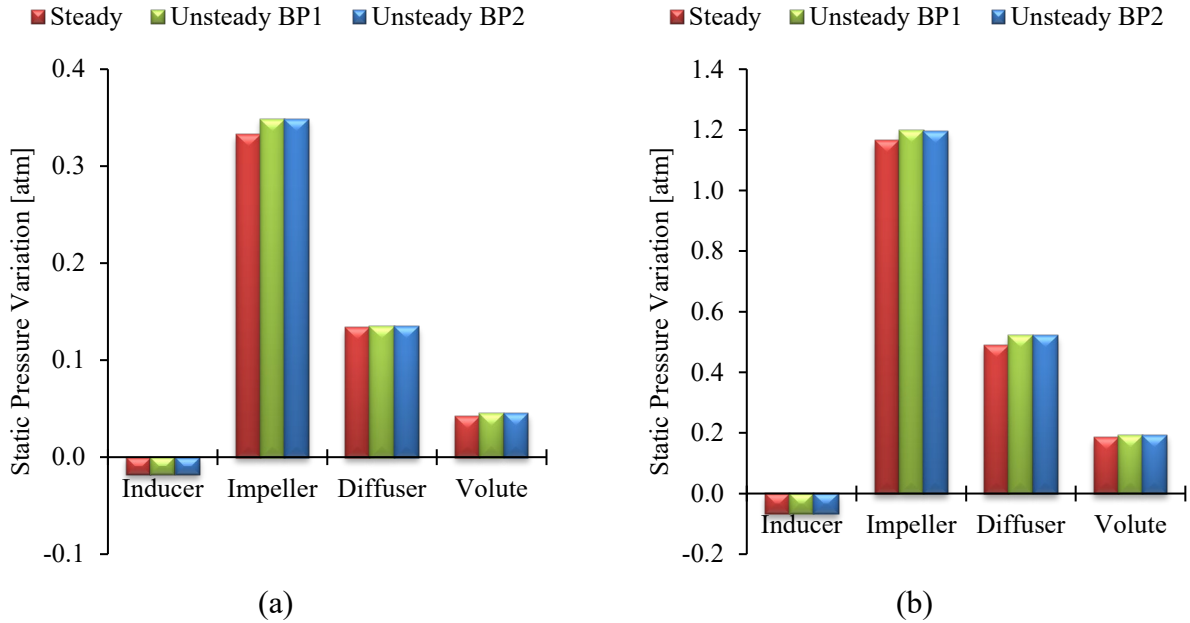


Figure 5.5 Comparison of steady and unsteady response of static pressure difference through each station in the turbocharger compressor stage during (a) 58.9rps/√K (b) 98.2rps/√K

Table 5.3 details the static pressure variance comparison of the unsteady response at two instances, being blade position 1 and blade position 2, with the steady response at low operating speed of 58.9rps/√K and at high operating speed of 98.2rps/√K. The inlet static pressure variation shows that both unsteady instances for both speeds vary the same amount against the steady response through the compressor. The highest inlet static pressure variance for unsteady response against the steady response is at the impeller inlet when the compressor is operating at high speed, whereas the lowest is at the volute inlet for both speeds. The outlet static pressure variation shows that both unsteady instances for both speeds vary the same amount against the steady response with the exception of the volute. For high speed, BP1 at the volute outlet depicts slightly higher static pressure against the steady response than BP2. The highest outlet static pressure variance for unsteady response against the steady response is at the inducer outlet when the compressor is operating at high speed, whereas the lowest static pressure depicts no variance when the compressor is operating at low speed and is localised at the volute outlet.

Table 5.3 Comparison of unsteady and steady response of static pressure variation at the inlet, outlet and through-flow across each station at low speed of 58.9rps/√K and high speed of 98.2rps/√K

Compressor Component	Inlet Variation [%]				Outlet Variation [%]				Through-flow Variation [%]			
	Blade Position 1		Blade Position 2		Blade Position 1		Blade Position 2		Blade Position 1		Blade Position 2	
	Low Speed	High Speed	Low Speed	High Speed	Low Speed	High Speed	Low Speed	High Speed	Low Speed	High Speed	Low Speed	High Speed
Inducer	-1.9	-6.3	-1.9	-6.3	-2.0	-6.7	-2.0	-6.7	1.0	0.5	0.4	0.4
Impeller	-2.0	-6.7	-2.0	-6.7	-0.3	-1.6	-0.3	-1.6	4.9	2.8	4.8	2.7
Diffuser	-0.3	-1.6	-0.3	-1.6	-0.1	-0.1	-0.1	-0.1	1.1	6.4	1.1	6.5
Volute	-0.1	-0.1	-0.1	-0.1	0.0	0.3	0.0	0.2	5.3	5.5	5.8	4.9

### 5.3 Local Static Pressure Distribution at Low Speed during Unsteady Conditions

Figure 5.6 depicts the static pressure around the compressor volute during the operating speed of 58.9rps/ $\sqrt{K}$  at (a) blade position 1, where the impeller blade is aligned with the volute tongue and (b) blade position 2, where the impeller blade has passed the volute tongue and another impeller blade is approaching the volute tongue. It can be seen that both instances show the same static pressure trends across the volute and its cross-sections. Lower static pressure is exhibited at the periphery of the volute inlet, which increases towards the outer curve as well as downstream to the outlet. At 15°, lower static pressure is distributed from the inlet, more towards the front face, and manifests across towards the outer curve. Higher static pressure emerges from the inlet along the rear face and propagates towards the outer curve. From 45° to the cut off location at 345°, static pressure distribution appears to be the same with higher static pressure along the circumference of the cross-section towards the outer curve. Lower static pressure propagates across the profile to the overhang. From the exit cone to the outlet, static pressure increases across the cross-section. Lower static pressure emerges from between the inlet and the overhang at 45°. At 135°, this low static pressure region is localised in the centre of the cross-sections. At 180° and 225°, this low static pressure region elongates towards the overhang, then localises back to the centre of the cross-section at 270°. This follows through to the outlet with higher static pressure surrounding the lower static pressure. Overall at low operating speed, it can be seen there are negligible variances in static pressure between the two instances.

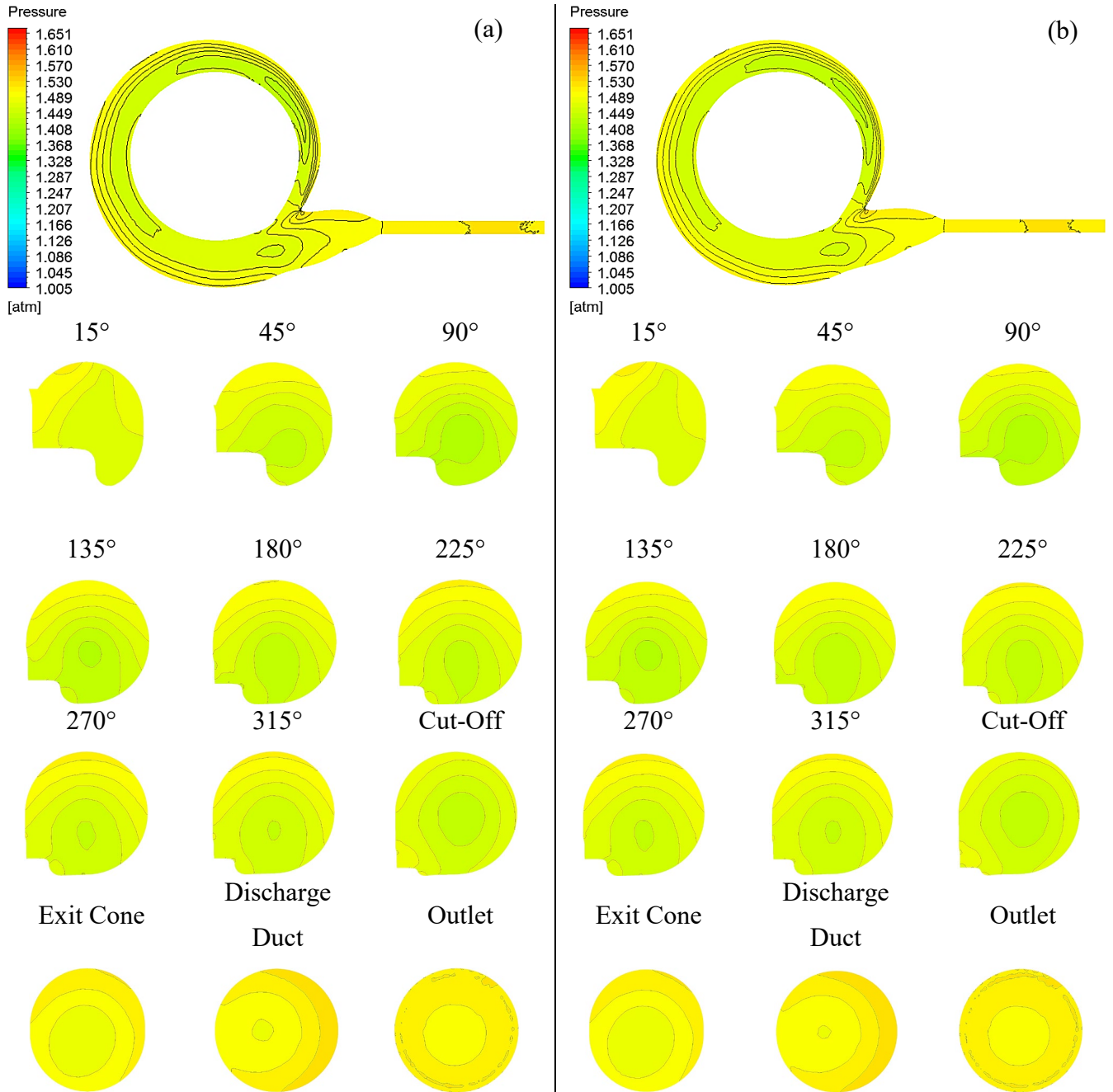


Figure 5.6 Static Pressure around the Compressor Volute during the operating speed of  $58.9\text{rps}/\sqrt{\text{K}}$  at  
(a) Blade Position 1 (b) Blade Position 2

Figure 5.7 graphically represents steady response and unsteady response at two instances of static pressure variation across each profile at low operating speed of  $58.9\text{rps}/\sqrt{\text{K}}$ . For all cases, static pressure decreases from  $15^\circ$  to  $90^\circ$ , then increases from  $135^\circ$  to  $270^\circ$ . From here, static pressure decreases once more to the cut-off location at  $345^\circ$ , prior to increasing downstream to the outlet. It is identified steady response indicates higher static pressure than that depicted with the unsteady response for both instances throughout the volute. Additionally, unsteady BP1 clearly depicts higher static pressure than unsteady BP2 from  $135^\circ$  to  $270^\circ$ . Aside from this,

there are negligible static pressure fluctuations between the two unsteady instances. Table 5.4 details the percentage difference in static pressure variation at 58.9rps/ $\sqrt{K}$  from one cross-section location to the next, specified by the azimuth angle. Table 5.4 also details the percentage difference in static pressure variation at 58.9rps/ $\sqrt{K}$  occurring at each cross-section around the volute against that depicted at the outlet. This provides an understanding of how much variation is taking place around the volute and at BP1 and BP2 compared to that at steady response. The maximum static pressure variation that occurs from one azimuth angle to the next between the unsteady responses and the steady response is at 45° to 90°, where the steady case depicts more variation. It is also found that there are no static pressure variations against the steady response from 90° to 270° for both unsteady responses. The maximum static pressure variation that occurs against the steady response between the cross-section around the volute and the outlet is at 45° for both unsteady responses, depicting a greater variation than the steady response. Further to this, there is no variation compared to the steady response in static pressure at 390° for both unsteady cases. Overall, this quantifies and compares the static pressure variation between the steady and the two instantaneous responses at low operating speed. Both instances present lower static pressure through the volute than the steady case.

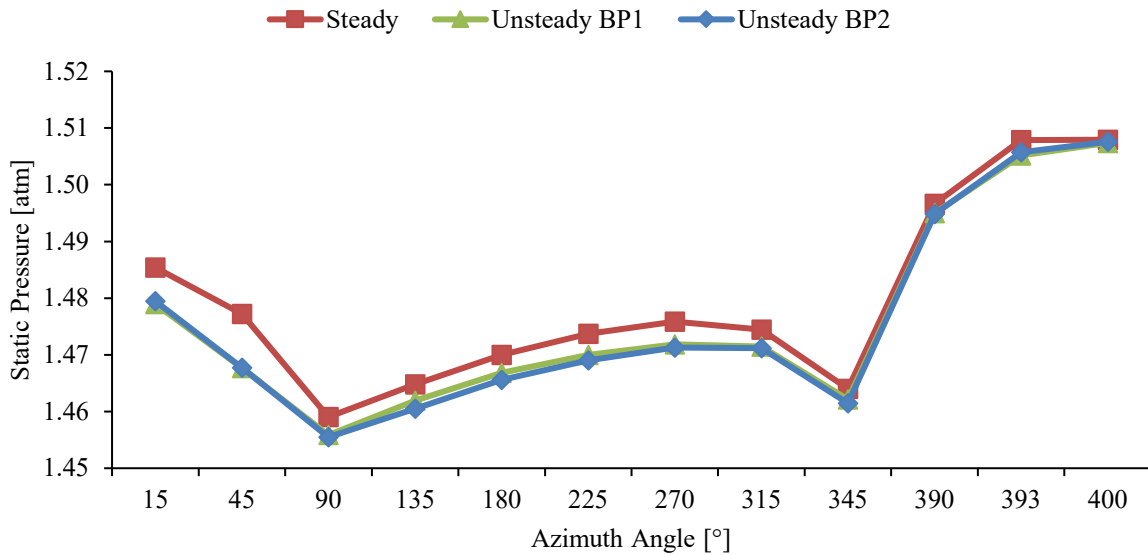


Figure 5.7 Comparison of steady and unsteady response for static pressure across each cross-section around the compressor volute during the operating speed of 58.9rps/ $\sqrt{K}$

*Table 5.4 Comparison of steady and unsteady response of plane to plane and outlet to plane static pressure variation at 58.9 rps/√K*

θ° to θ° Static Pressure Variation [%]				Outlet @ 400° to θ° Static Pressure Variation [%]			
θ°	Steady	Unsteady BP1	Unsteady BP2	θ°	Steady	Unsteady BP1	Unsteady BP2
15 - 45	-0.5	-0.8	-0.8	15	-1.5	-1.9	-1.9
45 - 90	-1.2	-0.8	-0.8	45	-2.0	-2.6	-2.6
90 - 135	0.4	0.4	0.3	90	-3.2	-3.4	-3.5
135 - 180	0.4	0.3	0.3	135	-2.9	-3.0	-3.1
180 - 225	0.3	0.2	0.2	180	-2.5	-2.7	-2.8
225 - 270	0.1	0.1	0.2	225	-2.3	-2.5	-2.6
270 - 315	-0.1	0.0	0.0	270	-2.1	-2.4	-2.4
315 - 345	-0.7	-0.6	-0.7	315	-2.2	-2.4	-2.4
345 - 390	2.2	2.3	2.3	345	-2.9	-3.0	-3.1
390 - 393	0.7	0.7	0.7	390	-0.8	-0.8	-0.8
393 - 400	0.0	0.1	0.1	393	0.0	-0.1	-0.1

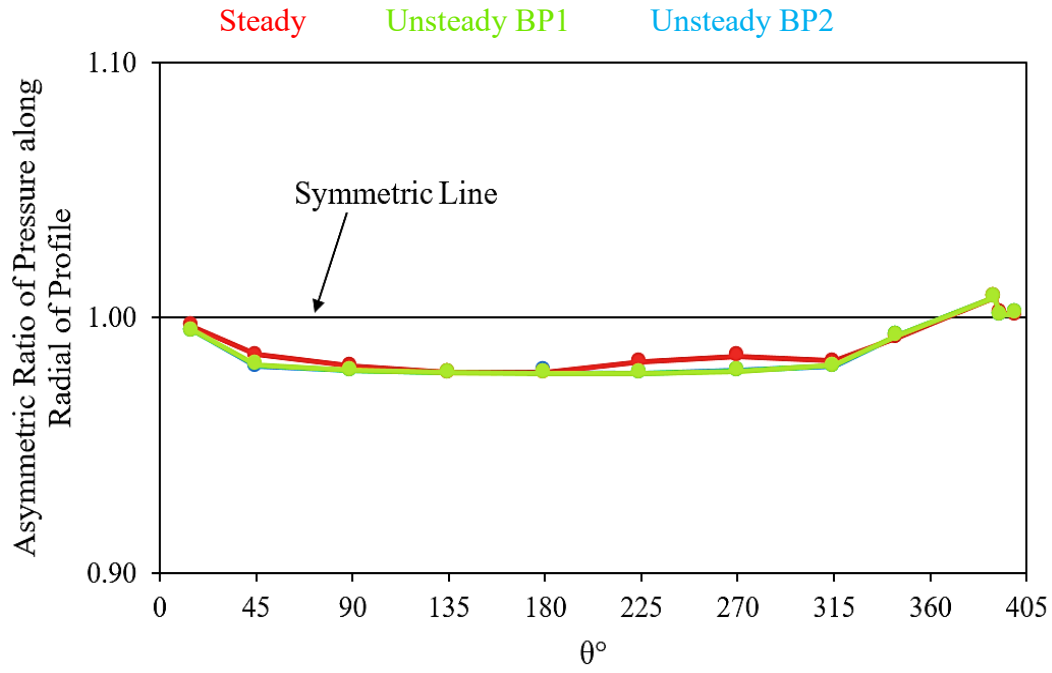
#### 5.4 Local Asymmetric Ratios of Static Pressure Distribution Profiles along the Radial Direction and Axial Direction at Low Speed during Steady and Unsteady Conditions

This section presents the asymmetric ratios of the static pressure profiles along the radial direction and axial direction of each cross-section around the turbocharger compressor volute. The asymmetric ratio has been calculated in order to determine symmetric variations or asymmetric variations of static pressure along the radial direction and axial direction of the cross-sections. These profiles depict the unsteady responses at two instances, being blade position 1 (BP1), where the impeller blade is aligned with the volute tongue and blade position 2 (BP2), where the impeller blade has passed the volute tongue and another impeller blade is approaching the volute tongue. These unsteady responses are compared with that depicted with the steady response.

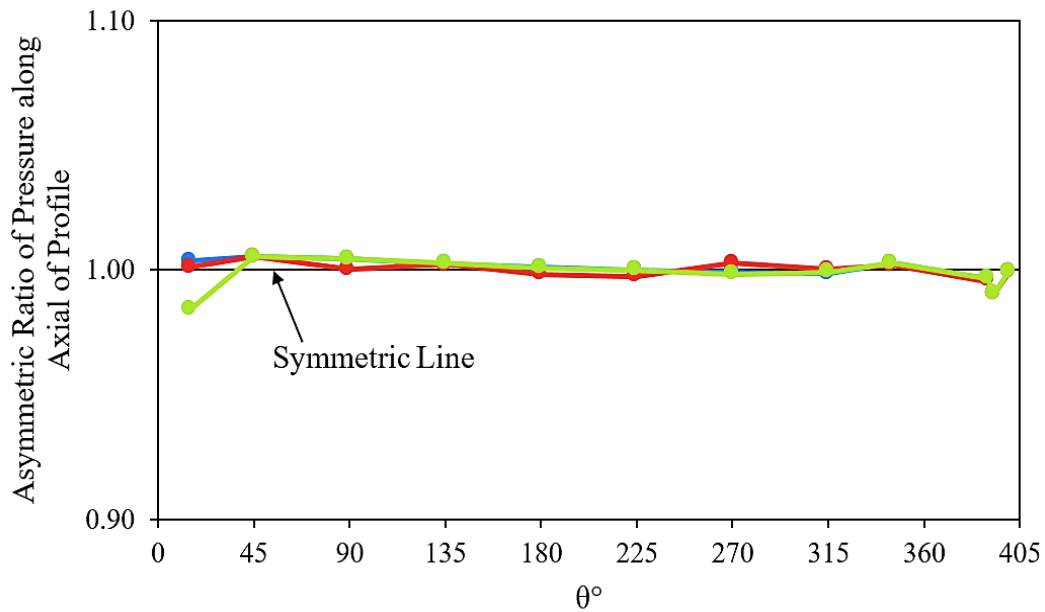
Figure 5.8 is a graphical representation depicting the asymmetric ratio of static pressure along the radial direction of the cross-section profiles in (a) and axial direction of the cross-section profiles in (b) around the centrifugal compressor volute at low operating speed of 58.9rps/√K. In both radial direction and axial direction cases, when the asymmetric ratio is 1, the flow variable is symmetric and signifies desirable flow characteristics. Asymmetric ratio that is not 1 signifies the presence of secondary flows, which means more energy is required due to losses taking place

as a result of friction. Secondary flows are a direct cause for head loss therefore, the more symmetric the ratio means the better the volute performs. When the asymmetric ratio is more than 1, flow variable in the case of the radial direction is localised towards the inner curve, and in the case of the axial direction, the flow variable is localised towards the rear face. When the asymmetric ratio is less than 1, flow variable in the case of the radial direction is localised towards the outer curve, and in the case of the axial direction, the flow variable is localised towards the front face. Viewing Figure 5.8 (a), it can be seen there is no variance between the two unsteady instances and aside from the slight variance depicted at  $45^\circ$ ,  $225^\circ$  and  $270^\circ$ , the unsteady cases are in good agreement with the steady case. It can be seen, upstream of  $390^\circ$ , static pressure along the radial direction of the profiles are asymmetric towards the outer curve. At  $390^\circ$ , static pressure is asymmetric towards the inner curve and downstream of this, static pressure along the radial direction is symmetric. Viewing Figure 5.8 (b), it can be seen aside from  $15^\circ$ , there is no variance between the two unsteady instances. Additionally, aside from the variance depicted at  $15^\circ$  and the slight variance depicted at  $90^\circ$  and  $270^\circ$ , the unsteady cases are in good agreement with the steady case. At  $15^\circ$  unsteady response at BP2 is almost the same as the static pressure variation along the axial direction depicted for the steady case, where both show slight asymmetry towards the rear face. The unsteady response at BP1 shows static pressure asymmetry towards the front face followed by slight asymmetry towards the rear face from  $45^\circ$ , being in proximity of that depicted for the steady case. From  $180^\circ$  to  $315^\circ$ , unsteady cases depict symmetric static pressure along the axial direction of the profiles with very slight variances against the steady case. At  $390^\circ$  and  $393^\circ$ , all cases show static pressure asymmetry towards the front face then show symmetry at  $400^\circ$ . Overall at low operating speed, it is observed that there is no influence on the imbalance of static pressure along the radial direction of the cross-section profiles inside the centrifugal compressor volute between the two instances. However, with respect to the axial direction, it is noticed that the only influence on the imbalance of static pressure is presented at  $15^\circ$ , which is the first profile of the scroll in proximity of the tongue. Furthermore, there is only a slight influence on the imbalance of static pressure between the steady response and the two unsteady responses along both, radial direction and axial direction. More detailed graphical representations are depicted in APPENDIX 3.





(a)



(b)

Figure 5.8 Asymmetric Ratio of Steady and Unsteady Static Pressure around the Centrifugal Compressor Volute at the operating speed of 58.9rps/ $\sqrt{K}$  along the (a) Radial of the profiles and (b) Axial of the profiles

## 5.5 Local Static Pressure Distribution at High Speed during Unsteady Conditions

Figure 5.9 depicts the static pressure around the compressor volute during the operating speed of 98.2rps/ $\sqrt{k}$  at (a) blade position 1, where the impeller blade is aligned with the volute tongue and (b) blade position 2, where the impeller blade has passed the volute tongue and another impeller blade is approaching the volute tongue. It can be seen that both instances show similar static pressure trends across the volute and its cross-sections. Lower static pressure is exhibited from 15° to 90°, which increases downstream of the volute to the outlet with a small region of higher static pressure localised at the outer curve of the profiles. Lowest static pressure across the profiles is seen predominantly in the lower sector of the central region. From 135° to 315°, higher static pressure manifests across the profile towards the central region. At 345°, which is the cut-off location, static pressure appears to have decreased in comparison to that depicted upstream. As the azimuth angle increases, it can be seen via the profiles that static pressure also increases, as a result of the area increase. These low static pressure regions are localised more in the overhang, while higher static pressure increases along the outer curve of the profiles downstream of 90°. From the exit cone at 390° to the outlet at 400°, static pressure increases across the cross-sections, depicting almost uniform static pressure at the outlet. Overall at high operating speed, it can be seen there are negligible variances in static pressure between the two instances.

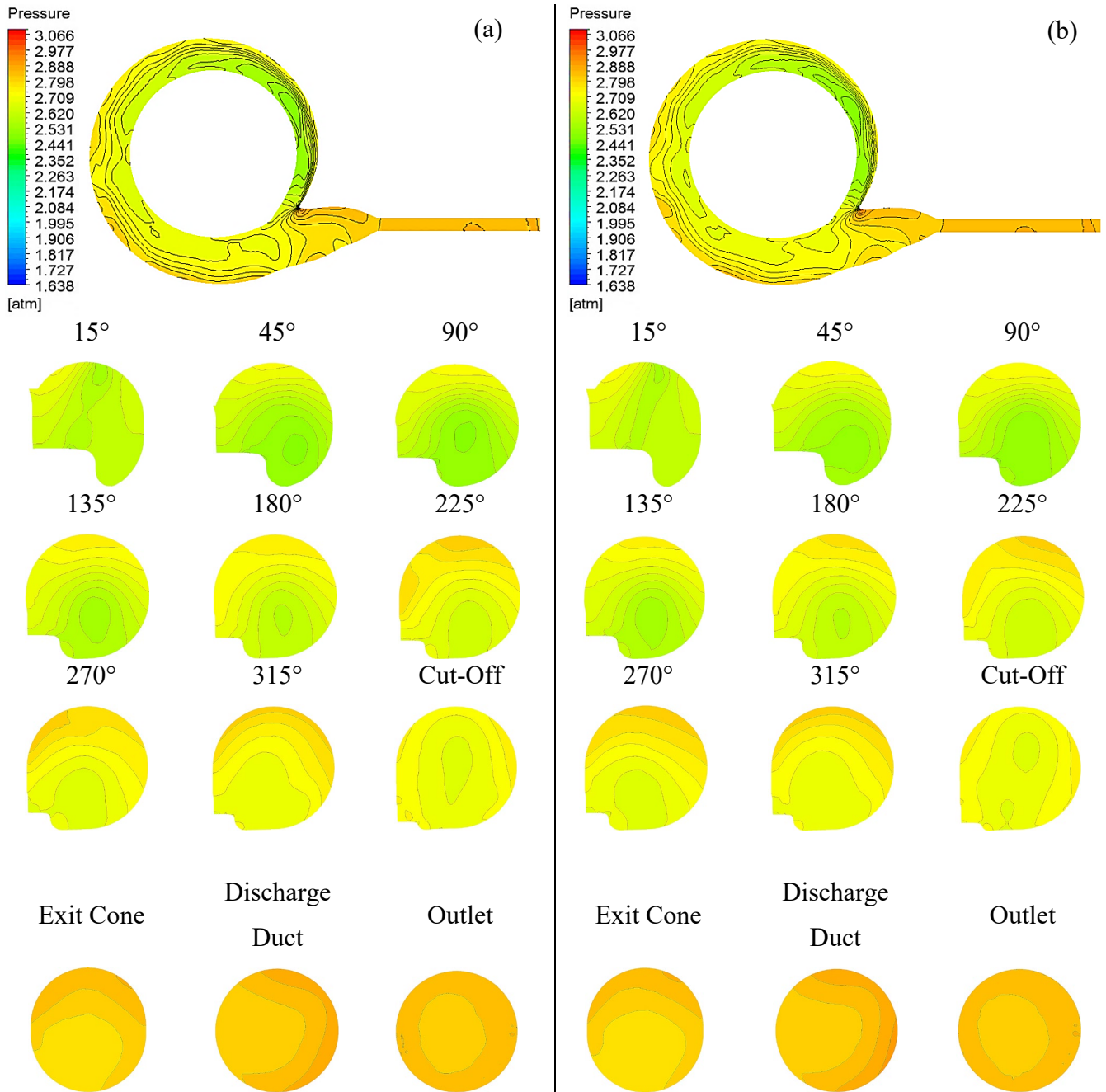


Figure 5.9 Static Pressure around the Compressor Volute during the operating speed of 98.2rps/√K at (a) Blade Position 1 (b) Blade Position 2

Figure 5.10 graphically represents steady response and unsteady response at two instances of static pressure variation across each profile at high operating speed of 98.2rps/√K. For all cases, static pressure initially decreases from 15° to 90°, which then increases downstream to 315°. There is a slight decrease at the cut-off located at 345° prior to increasing once more downstream to the outlet. It is identified there are variations between the two unsteady instances. The most prominent static pressure variation between all three cases is identified at 45°. The steady response is seen to have predominantly higher static pressure than that depicted with the

unsteady response for both instances at 15° and 45°. Unsteady BP2 has higher static pressure exhibited from 15° to 90° than unsteady BP1. At 90° and from 225° to the outlet at 400°, steady response is lower than both unsteady responses. At 135°, unsteady BP1 matches with the steady response to static pressure while unsteady BP2 is slightly lower. At 180° and from 315° to the outlet, there appears to be negligible variations between the two unsteady instances. At 225°, unsteady BP1 is predominantly higher than unsteady BP2, while being lower at 270°. Table 5.5 details the percentage difference in static pressure variation at 98.2rps/√K from one cross-section location to the next, specified by the azimuth angle. Table 5.5 also details the percentage difference in static pressure variation at 98.2rps/√K occurring at each cross-section around the volute against that depicted at the outlet. The maximum static pressure variation that occurs from one azimuth angle to the next is between unsteady BP1 and the steady response at 45° to 90°, where unsteady BP1 has a higher variation. There are no static pressure variations occurring against the steady response at 315° to 345° and 345° to 390° for unsteady BP2. The maximum static pressure variation that occurs between the cross-section around the volute and the outlet is at 45° for unsteady BP1 against the steady response, where unsteady BP1 shows a higher variation. Further to this, there are no static pressure variations occurring at 315° and 390° between the two unsteady cases and the steady case. Overall, this quantifies and compares the static pressure variation between the steady and the two instantaneous responses at high operating speed.

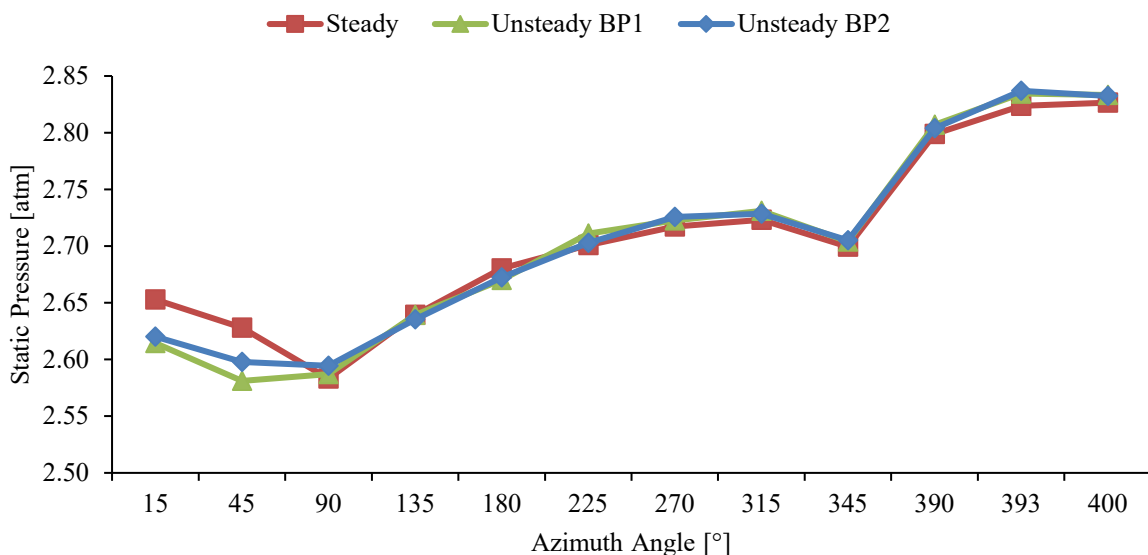


Figure 5.10 Comparison of steady and unsteady response for static pressure across each cross-section around the compressor volute during the operating speed of 98.2rps/√K

*Table 5.5 Comparison of steady and unsteady response of plane to plane and outlet to plane static pressure variation at 98.2rps/√K*

$\theta^\circ$ to $\theta^\circ$ Static Pressure Variation [%]				Outlet @ $400^\circ$ to $\theta^\circ$ Static Pressure Variation [%]			
$\theta^\circ$	Steady	Unsteady BP1	Unsteady BP2	$\theta^\circ$	Steady	Unsteady BP1	Unsteady BP2
15 - 45	-0.9	-1.3	-0.8	15	-6.1	-7.7	-7.5
45 - 90	-1.7	0.2	-0.1	45	-7.0	-8.9	-8.3
90 - 135	2.2	2.0	1.6	90	-8.6	-8.7	-8.4
135 - 180	1.6	1.2	1.4	135	-6.6	-6.9	-7.0
180 - 225	0.8	1.5	1.1	180	-5.2	-5.8	-5.6
225 - 270	0.6	0.4	0.9	225	-4.4	-4.3	-4.6
270 - 315	0.2	0.3	0.1	270	-3.9	-3.9	-3.8
315 - 345	-0.9	-1.0	-0.9	315	-3.7	-3.6	-3.7
345 - 390	3.7	3.8	3.7	345	-4.5	-4.6	-4.5
390 - 393	0.9	1.0	1.2	390	-1.0	-0.9	-1.0
393 - 400	0.1	0.0	-0.2	393	-0.1	0.0	0.2

## 5.6 Local Asymmetric Ratios of Static Pressure Distribution Profiles along the Radial Direction and Axial Direction at High Speed during Steady and Unsteady Conditions

Figure 5.11 is a graphical representation depicting the asymmetric ratio of static pressure along the radial direction of the cross-section profiles in (a) and axial direction of the cross-section profiles in (b) around the centrifugal compressor volute at low operating speed of 98.2rps/√K. It can be seen in Figure 5.11 (a), both unsteady cases depicts negligible static pressure variances along the radial against each other. At  $15^\circ$ , the two unsteady instances depict slight asymmetry towards the inner curve, while the steady case depicts slight asymmetry towards the outer curve. From  $45^\circ$  to  $345^\circ$ , all three case exhibit asymmetry towards the outer curve. From  $135^\circ$  to  $270^\circ$ , there are slight variances between the steady case and the two unsteady cases. All cases are seen to have asymmetry towards the inner curve at  $390^\circ$ , followed by depicting symmetric static pressure along the radial downstream of this. It can be seen in Figure 5.11 (b) both unsteady cases depict negligible static pressure variances along the axial against each other upstream of  $135^\circ$ . From  $15^\circ$  to  $90^\circ$  all cases exhibit asymmetric static pressure along the axial towards the rear face with slight variations at  $15^\circ$  and  $45^\circ$  and obvious variations at  $90^\circ$  between the unsteady cases and the steady case. At  $225^\circ$ , the steady case depicts symmetric static pressure along the axial, while the unsteady cases continue to show asymmetry towards the rear face. At  $180^\circ$  and  $225^\circ$ , asymmetry towards the rear face is identified for all cases, where unsteady BP2 matches

reasonably with the steady case. At  $270^\circ$  and  $315^\circ$ , all cases depict asymmetry towards the front face. The steady case exhibits slight asymmetry towards the rear face at  $345^\circ$ , while the unsteady cases exhibit slight asymmetry towards the front face. Downstream of  $390^\circ$ , all cases show asymmetry towards the front face in static pressure along the axial. Unsteady cases show the same as that as the steady case at  $400^\circ$ . Overall at high operating speed, it is observed that there is negligible influence on the imbalance of static pressure along the radial direction of the cross-section profiles inside the centrifugal compressor volute between the two instances. However, with respect to the axial direction, it is noticed that the most prominent influence on the imbalance of static pressure is presented between  $180^\circ$  and  $270^\circ$ . Furthermore, there is a minor influence on the imbalance of static pressure between the steady response and the two unsteady responses along the radial direction. With respect to the axial direction, these influence of imbalances are more prominent through the volute. More detailed graphical representations are depicted in APPENDIX 3.

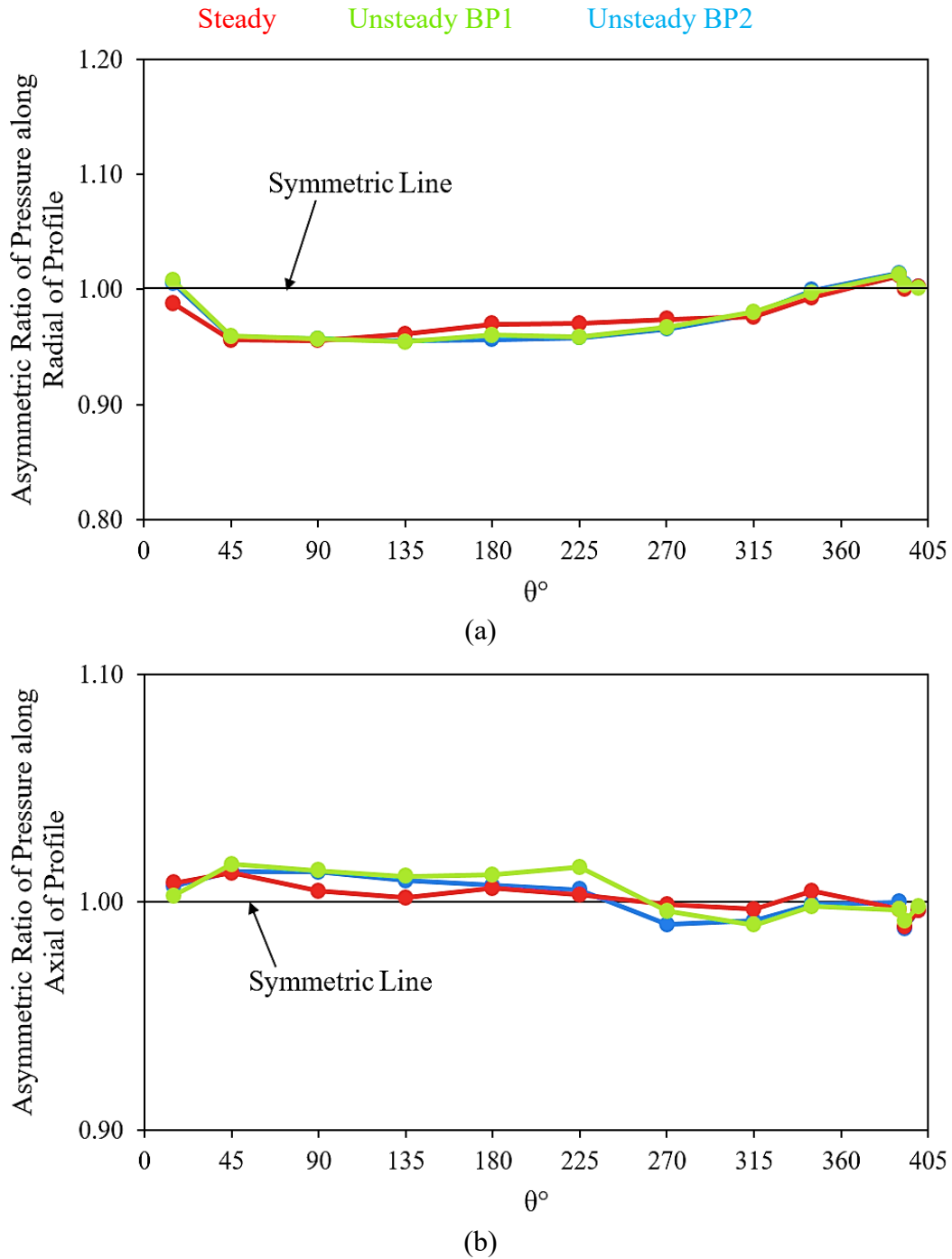


Figure 5.11 Asymmetric Ratio of Steady and Unsteady Static Pressure around the Centrifugal Compressor Volute at the operating speed of 98.2rps/ $\sqrt{K}$  along the (a) Radial of the profiles and (b) Axial of the profiles

### 5.7 Static Pressure Speed Comparison during Unsteady Conditions

Table 5.6 depicts the unsteady response of the local speed comparison, where the high operating speed of 98.2rps/ $\sqrt{K}$  is compared against the low operating speed of 58.9rps/ $\sqrt{K}$  for static pressure across each of the selected cross-section through the turbocharger compressor volute. The unsteady responses are at two instances, being at blade position 1 where the impeller blade is aligned with the volute tongue and at blade position 2, where the impeller blade has passed the volute tongue and another impeller blade is approaching the volute tongue. It is identified there are minimal variances throughout the turbocharger compressor volute between the two instances. Static pressure at 98.2rps/ $\sqrt{K}$  increases at both unsteady instances until the outlet compared to that at 58.9rps/ $\sqrt{K}$ . At the 400°, which is the outlet, although static pressure increases at 98.2rps/ $\sqrt{K}$  over that depicted at 58.9rps/ $\sqrt{K}$ , it slightly decreases from the 393°, which is the discharge duct. Between the two unsteady responses, BP2 shows higher increase in static pressure from 15° to 90°. Downstream from here, there are slight fluctuations between the two unsteady cases for the higher increase in static pressure.

*Table 5.6 Local Speed Comparison of Static Pressure Variation during Unsteady Response*

$\theta^\circ$	Static Pressure [%]	
	Unsteady BP1	Unsteady BP2
15	76.8	77.1
45	75.9	77.0
90	77.7	78.3
135	80.5	80.4
180	82.0	82.3
225	84.4	84.0
270	85.0	85.3
315	85.6	85.5
345	84.9	85.1
390	87.8	87.6
393	88.3	88.4
400	88.0	87.9



## 5.8 Global Velocity Magnitude Distribution at Two Instances during Unsteady Conditions

Figure 5.12 depicts the velocity magnitude variation in the turbocharger compressor stage during the operating speed of 58.9rps/ $\sqrt{K}$  and 98.2rps/ $\sqrt{k}$ . Figure 5.12 (a) depicts blade position 1, also referred as BP1, which is when the impeller blade is aligned with the volute tongue and Figure 5.12 (b) depicts blade position 2, also referred as BP2, which is when the impeller blade is passed the tongue and another blade is approaching the tongue. At both speeds, minimal variances in velocity magnitude are seen between the two instances. At low speed, higher velocity magnitude is displayed upstream of the diffuser than at high speed. At high speed, lower velocity magnitude is displayed around the volute than at low speed.

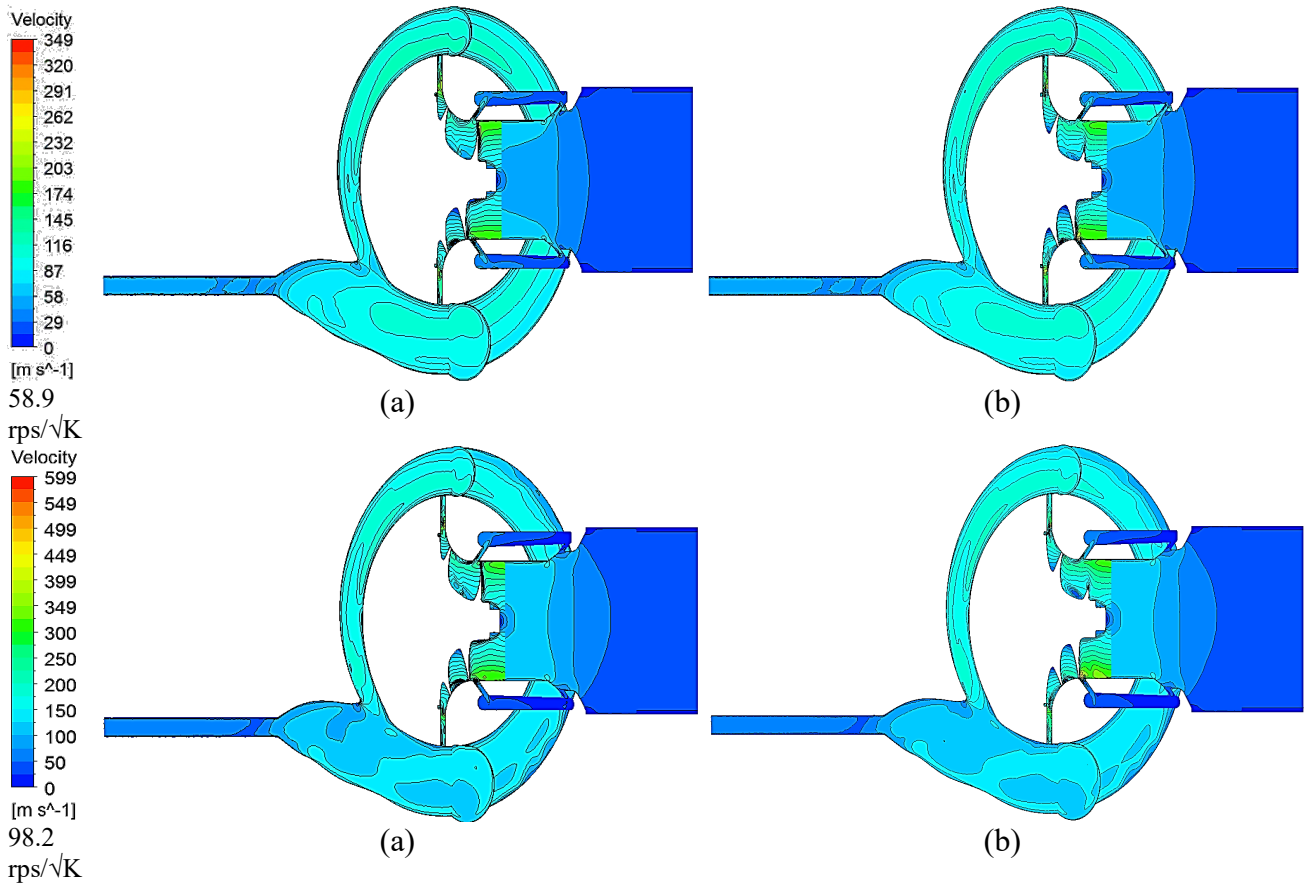


Figure 5.12 Velocity Magnitude Variation in the Turbocharger Compressor Stage during the operating speed of 58.9rps/ $\sqrt{K}$  and 98.2rps/ $\sqrt{K}$  at (a) Blade Position 1 (b) Blade Position 2

Figure 5.13 depicts the comparison of velocity magnitude variations through each station in the compressor stage between the steady conditions and unsteady conditions at low operating speed of (a) 58.9rps/ $\sqrt{K}$  and at high operating speed of (b) 98.2rps/ $\sqrt{K}$ . There is a greater velocity magnitude variation through each component at high speed than at low speed. It can be seen that for both speeds, velocity magnitude accelerates through the inducer and impeller and decelerates

through the diffuser and volute, as expected. There are negligible velocity magnitude variances between unsteady BP1 and unsteady BP2. Slightly higher velocity magnitude is exhibited through the inducer for the unsteady cases at both speeds. At low speed, the unsteady cases depicts the same velocity magnitude through the impeller as that of the steady case, while exhibiting prominent lower velocity magnitude than the steady case at high speed. At both speeds, velocity magnitude decelerates more for the steady case than that depicted for the unsteady cases through the diffuser. Velocity magnitude is decelerates more through the volute for the unsteady cases at both speeds. Details of these through-flow variances for the unsteady response at two instances against the steady response are presented in Table 5.7.

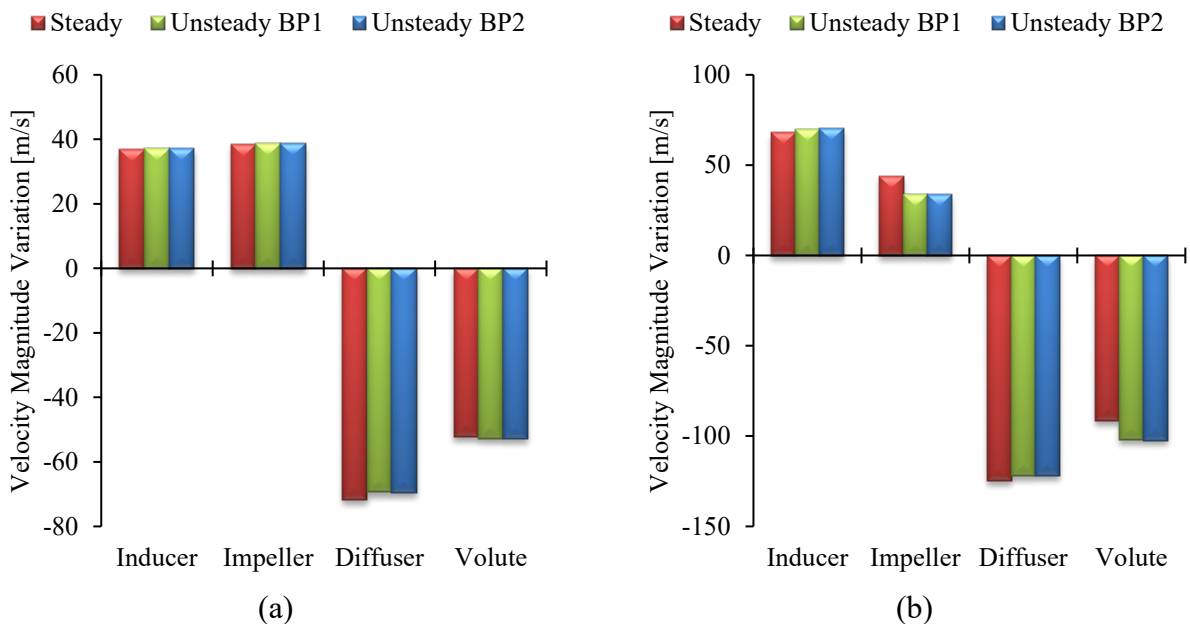


Figure 5.13 Comparison of steady and unsteady response of velocity magnitude difference through each station in the turbocharger compressor stage during (a) 58.9rps/√K (b) 98.2rps/√K

Table 5.7 details the velocity magnitude variance comparison of the unsteady response at two instances, being blade position 1 and blade position 2, with the steady response at low operating speed of 58.9rps/√K and at high operating speed of 98.2rps/√K. The inlet velocity magnitude variation shows that both unsteady instances for low speed vary the same amount against the steady response through the compressor. At high speed, the inlet velocity magnitude increases slightly against the steady response at the inducer and diffuser at blade position 1 in comparison with blade position 2. At the impeller, both unsteady instances vary by the same amount against the steady response and at the volute, blade position 2 increases slightly more than that at blade position 1, against the steady response. The highest inlet velocity magnitude variance for unsteady response against the steady response is at the volute inlet when the compressor is operating at high speed, whereas the lowest is at the diffuser inlet for low speed. The outlet

velocity magnitude variation shows that both unsteady instances for low speed vary the same amount against the steady response at the impeller and volute, while at the inducer and diffuser, blade position 1 shows a slight velocity magnitude increase against the steady case in comparison with blade position 2. At high speed, the outlet velocity magnitude shows that both unsteady instances vary the same amount against the steady response at the impeller, while velocity magnitude at the inducer, diffuser and volute are slightly higher for blade position 2 against the steady case in comparison with blade position 1. The highest outlet velocity magnitude variance for unsteady response against the steady response is at the diffuser outlet when the compressor is operating at high speed, whereas the lowest is at the impeller outlet for low speed.

*Table 5.7 Comparison of steady and unsteady response of velocity magnitude at the inlet, outlet and through-flow across each station at low speed of 58.9rps/√K and high speed of 98.2rps/√K*

Compressor Component	Inlet Variation [%]				Outlet Variation [%]				Through-flow Variation [%]			
	Blade Position 1		Blade Position 2		Blade Position 1		Blade Position 2		Blade Position 1		Blade Position 2	
	Low Speed	High Speed	Low Speed	High Speed	Low Speed	High Speed	Low Speed	High Speed	Low Speed	High Speed	Low Speed	High Speed
Inducer	1.9	6.2	1.9	6.1	1.5	4.0	1.4	4.1	1.2	2.8	1.2	2.9
Impeller	0.5	1.1	0.5	1.1	0.4	-2.7	0.4	-2.7	0.2	-23.8	0.3	-23.5
Diffuser	-0.2	3.2	-0.2	3.1	1.7	7.0	1.6	7.1	-3.2	-2.2	-3.2	-2.4
Volute	1.6	7.0	1.6	7.1	1.8	1.5	1.8	1.6	1.5	11.8	1.3	11.9

## 5.9 Local Velocity Magnitude Distribution at Low Speed during Unsteady Conditions

Figure 5.14 depicts the velocity magnitude around the compressor volute during the operating speed of 58.9rps/√K at (a) blade position 1, where the impeller blade is aligned with the volute tongue and (b) blade position 2, where the impeller blade has passed the volute tongue and another impeller blade is approaching the volute tongue. It can be seen that both instances show the same velocity magnitude trends across the volute and its cross-sections. Inflow velocity magnitude through the volute cross-sections is comparatively high from 15° to the cut-off location at 345°. At 15°, low velocity magnitude zone is depicted at the front face of the cross-section. From 45° to 90° velocity magnitude increases, predominantly at the inflow and in the overhang. Downstream of this velocity magnitude decelerates through the cross-sections to the outlet. From the exit cone to the outlet, significantly low velocity magnitude propagates across the profiles, depicting low zones of velocity magnitude along the inner curve of the exit cone and along the front face of the discharge duct, followed by uniform velocity magnitude at the outlet.

Overall at low operating speed, it can be seen there are negligible variances in velocity magnitude between the two instances.

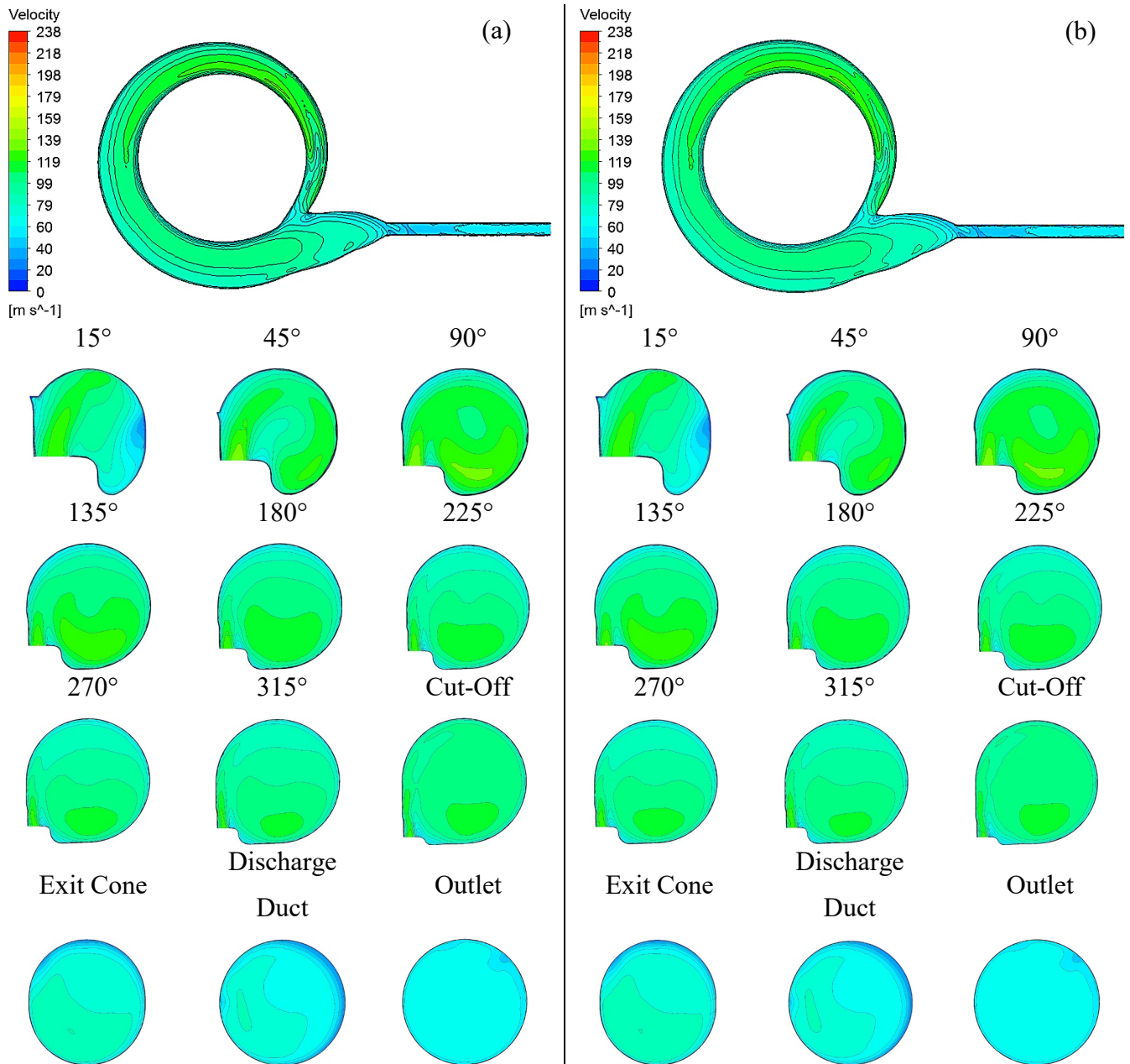


Figure 5.14 Velocity Magnitude around the Compressor Volute during the operating speed of 58.9rps/√K at (a) Blade Position 1 (b) Blade Position 2

Figure 5.15 graphically represents steady response and unsteady response at two instances of velocity magnitude variation across each profile at low operating speed of 58.9rps/√K. For all cases, velocity magnitude increases from 15° to 90° prior to decreasing downstream to 270°. From here, velocity magnitude increases once more to the cut-off location at 345° followed by a considerable decrease downstream to the outlet. There appears to be no if not negligible velocity

magnitude variations between the two unsteady instances. At 15°, the steady case has prominently lower velocity magnitude than the unsteady cases. From 45° to 135°, the steady case has higher velocity magnitude than the unsteady cases. At 180°, all cases appear to have the same velocity magnitude occurring across the profile. Downstream of this, the steady case exhibits slight deceleration in comparison to the unsteady cases. Table 5.8 details the percentage difference in velocity magnitude variation at 58.9rps/ $\sqrt{K}$  from one cross-section location to the next, specified by the azimuth angle. Table 5.8 also details the percentage difference in velocity magnitude variation at 58.9rps/ $\sqrt{K}$  occurring at each cross-section around the volute against that depicted at the outlet. The maximum velocity magnitude variation that occurs from one azimuth angle to the next between unsteady BP2 and the steady response is at 15° to 45°, where the steady response has a greater variation. The minimum velocity magnitude variation occurs at 225° to 270°, where velocity magnitude varies by the same amount for both unsteady cases. The maximum velocity magnitude variation that occurs between the cross-section around the volute and the outlet against the steady response is at 15° with unsteady BP2, which has a greater variation. There is no variation at 390° between unsteady BP2 and the steady response. Overall, this quantifies and compares the velocity magnitude variation between the steady and the two instantaneous responses at low operating speed.

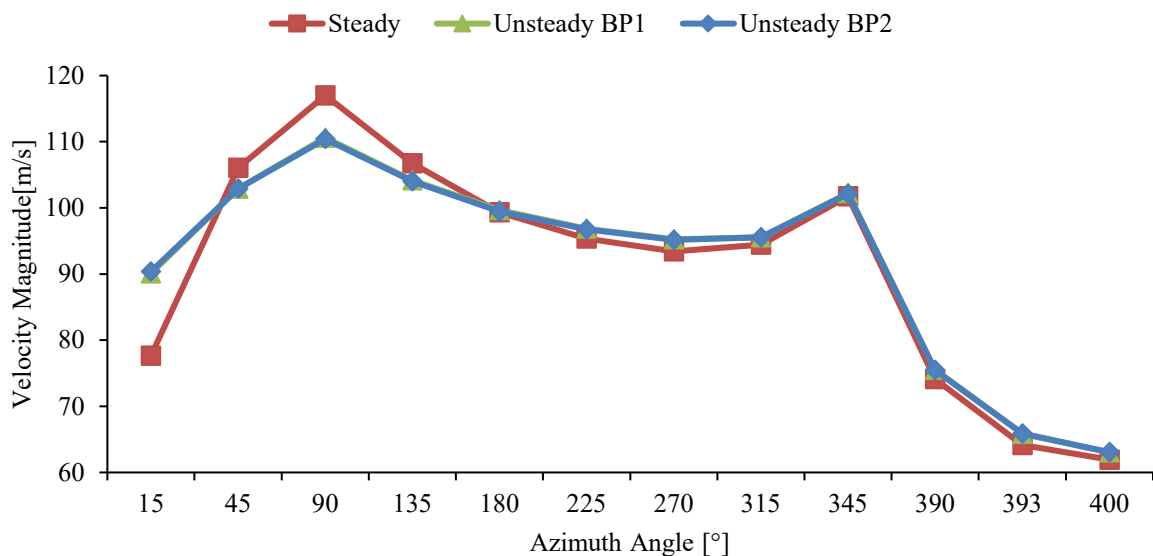


Figure 5.15 Comparison of steady and unsteady response for velocity magnitude across each cross-section around the compressor volute during the operating speed of 58.9rps/ $\sqrt{K}$

Table 5.8 Comparison of steady and unsteady response of plane to plane and outlet to plane velocity magnitude variation at 58.9 rps/ $\sqrt{K}$

$\theta^\circ$ to $\theta^\circ$ Velocity Magnitude Variation [%]				Outlet @ $400^\circ$ to $\theta^\circ$ Velocity Magnitude Variation [%]			
$\theta^\circ$	Steady	Unsteady BP1	Unsteady BP2	$\theta^\circ$	Steady	Unsteady BP1	Unsteady BP2
15 - 45	36.6	14.3	13.9	15	25.4	42.9	43.3
45 - 90	10.3	7.5	7.3	45	71.2	63.3	63.2
90 - 135	-8.8	-5.8	-5.8	90	88.9	75.5	75.1
135 - 180	-6.9	-4.3	-4.4	135	72.4	65.3	64.9
180 - 225	-4.0	-2.8	-2.7	180	60.4	58.1	57.7
225 - 270	-2.0	-1.6	-1.6	225	53.9	53.6	53.4
270 - 315	1.1	0.3	0.4	270	50.8	51.1	50.9
315 - 345	7.7	7.0	6.9	315	52.5	51.6	51.5
345 - 390	-27.2	-26.1	-26.1	345	64.3	62.2	61.9
390 - 393	-13.4	-12.8	-12.7	390	19.7	19.8	19.7
393 - 400	-3.5	-4.2	-4.3	393	3.6	4.4	4.5

### 5.10 Local Asymmetric Ratios of Velocity Magnitude Distribution Profiles along the Radial Direction and Axial Direction at Low Speed during Steady and Unsteady Conditions

Figure 5.16 is a graphical representation depicting the asymmetric ratio of velocity magnitude along the radial direction of the cross-section profiles in (a) and axial direction of the cross-section profiles in (b) around the centrifugal compressor volute at low operating speed of 58.9rps/ $\sqrt{K}$ . In the case of Figure 5.16 (a) at  $15^\circ$ , both unsteady cases show asymmetry towards the outer curve, while the steady case shows asymmetry towards the inner curve. At  $45^\circ$ , all cases are asymmetric towards the outer curve and from  $90^\circ$  to  $345^\circ$ , all cases are asymmetric towards the inner curve. At  $90^\circ$ , there are no variations between two unsteady cases and depict negligible variance to  $225^\circ$ . Downstream of this, there are no velocity magnitude variations between the two unsteady cases along the radial. At  $135^\circ$  and  $180^\circ$ , the steady case is significantly more asymmetric than the two unsteady cases, while depicting significantly less asymmetry at  $225^\circ$  and  $270^\circ$ . From  $315^\circ$ , velocity magnitude asymmetry variation along the radial between the steady case and the unsteady cases reduce. At  $390^\circ$  and  $393^\circ$ , all cases are asymmetric towards the outer curve prior to depicting symmetry and asymmetric towards the inner curve at the outlet for the two unsteady cases and the steady case, respectively. In the case of Figure 5.16 (b), both unsteady cases depict negligible velocity magnitude variation along the

axial throughout the volute. At  $15^\circ$ , all cases are asymmetric towards the rear face, where substantial variance is exhibited between the unsteady cases and the steady case. Here, the unsteady cases exhibit considerably higher asymmetry than the steady case. At  $45^\circ$  and  $90^\circ$ , the unsteady cases show symmetric velocity magnitude along the axial of the profiles, while the steady case is asymmetric towards the rear face from  $45^\circ$  to  $135^\circ$ . At  $135^\circ$ , unsteady cases are slightly asymmetric towards the front face. From  $180^\circ$  to  $270^\circ$ , the steady case depicts velocity magnitude asymmetry towards the front face. The unsteady cases exhibit slight asymmetry towards the rear face from  $180^\circ$  to  $315^\circ$ , followed by depicting velocity magnitude symmetry at  $345^\circ$ . At  $315^\circ$  and  $345^\circ$ , the steady case exhibits asymmetric towards the rear face and towards the front face, respectively. At  $390^\circ$  and  $393^\circ$ , all cases depict asymmetry once more towards rear face, where there are significant velocity magnitude variations along the axial between the steady case and the two unsteady cases. At the outlet, there appears to be no variations at the between cases and shows slight asymmetry towards the front face. Overall at low operating speed, it is observed that the only influence on the imbalance of velocity magnitude along the radial direction is exhibited at  $45^\circ$  between the two instances. Aside from this, there is no influence on imbalance of velocity magnitude between the two instances along the radial direction and axial direction through the centrifugal compressor volute. Furthermore, there is a significant influence on the imbalance of velocity magnitude through the centrifugal compressor volute between the steady response and the two unsteady responses along both, radial direction and axial direction. More detailed graphical representations are depicted in APPENDIX 3.



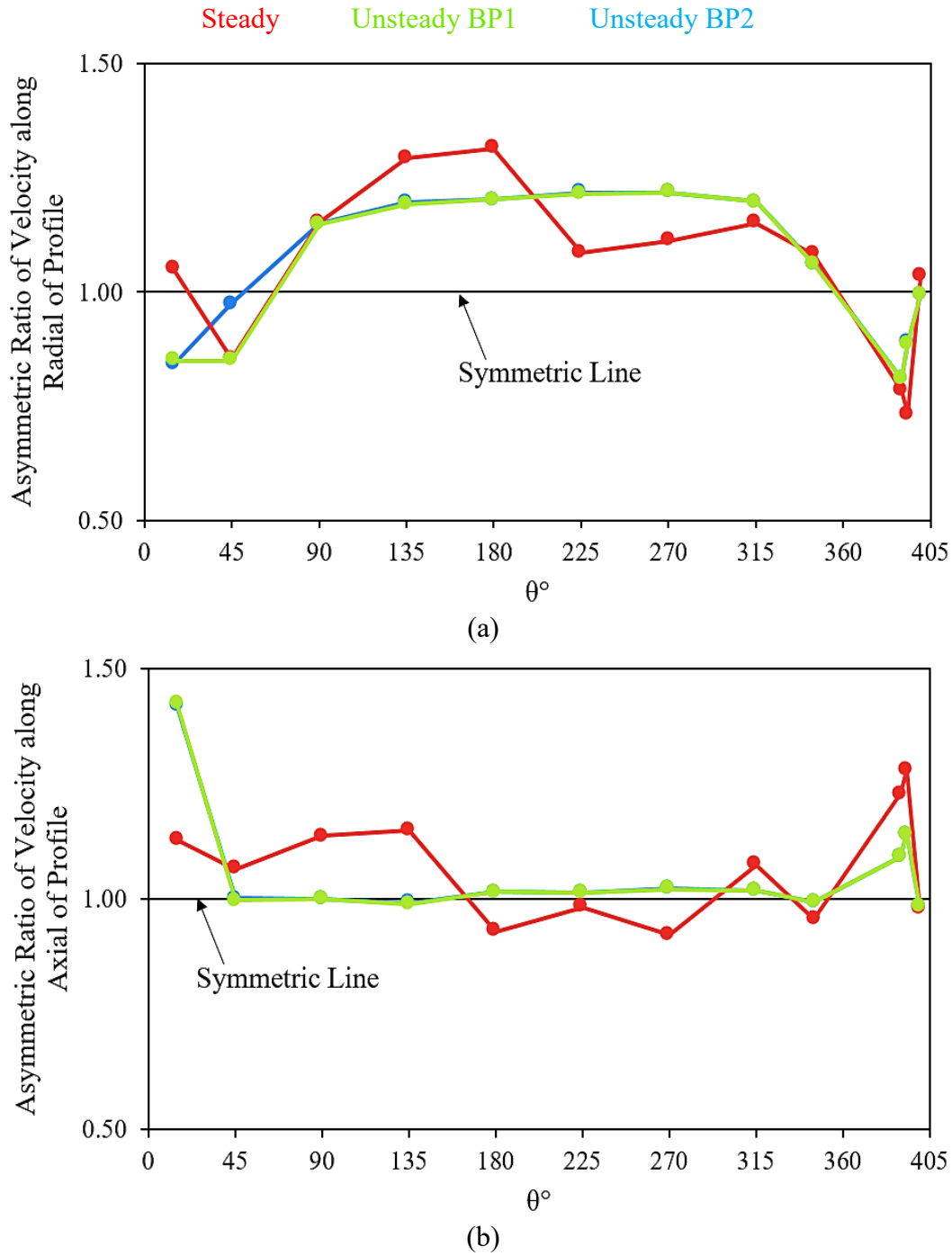


Figure 5.16 Asymmetric Ratio of Steady and Unsteady Velocity Magnitude around the Centrifugal Compressor Volute at the operating speed of 58.9rps/ $\sqrt{K}$  along the (a) Radial of the profiles and (b) Axial of the profiles



### 5.11 Local Velocity Magnitude Distribution at High Speed during Unsteady Conditions

Figure 5.17 depicts the velocity magnitude around the compressor volute during the operating speed of 98.2rps/ $\sqrt{k}$  at (a) blade position 1, where the impeller blade is aligned with the volute tongue and (b) blade position 2, where the impeller blade has passed the volute tongue and another impeller blade is approaching the volute tongue. It can be seen that both instances show the almost the same velocity magnitude trends across the volute and its cross-sections. Velocity magnitude appears to be high from 15° to 90°, prior to decelerating downstream, as well as exhibiting low flow velocity magnitude towards the outer curve. From 15° to the cut-off location at 345°, inflow velocity magnitude appears to be comparatively higher than that depicted in across the cross-sections. At 15°, there is accelerated flow velocity also exhibited at in the central region near of the outer curve of the profile. From 90°, lower flow velocity magnitude emerges along the rear face and the outer curve of the profile, which propagates downstream to 270°. At 315°, higher flow velocity magnitude exhibited across lower sector and central region of the profiles manifest to the lower flow velocity magnitude regions depicted upstream. At 345°, flow velocity magnitude is seen to be accelerated further, predominantly from the inflow following the curvature of the outer wall. From the exit cone to the outlet, significantly low velocity magnitude propagates across the profiles, depicting low zones of velocity magnitude along the inner curve of the exit cone and along the front face of the discharge duct, followed by uniform velocity magnitude at the outlet. Overall at high operating speed, it can be seen there are negligible variances in velocity magnitude between the two instances.

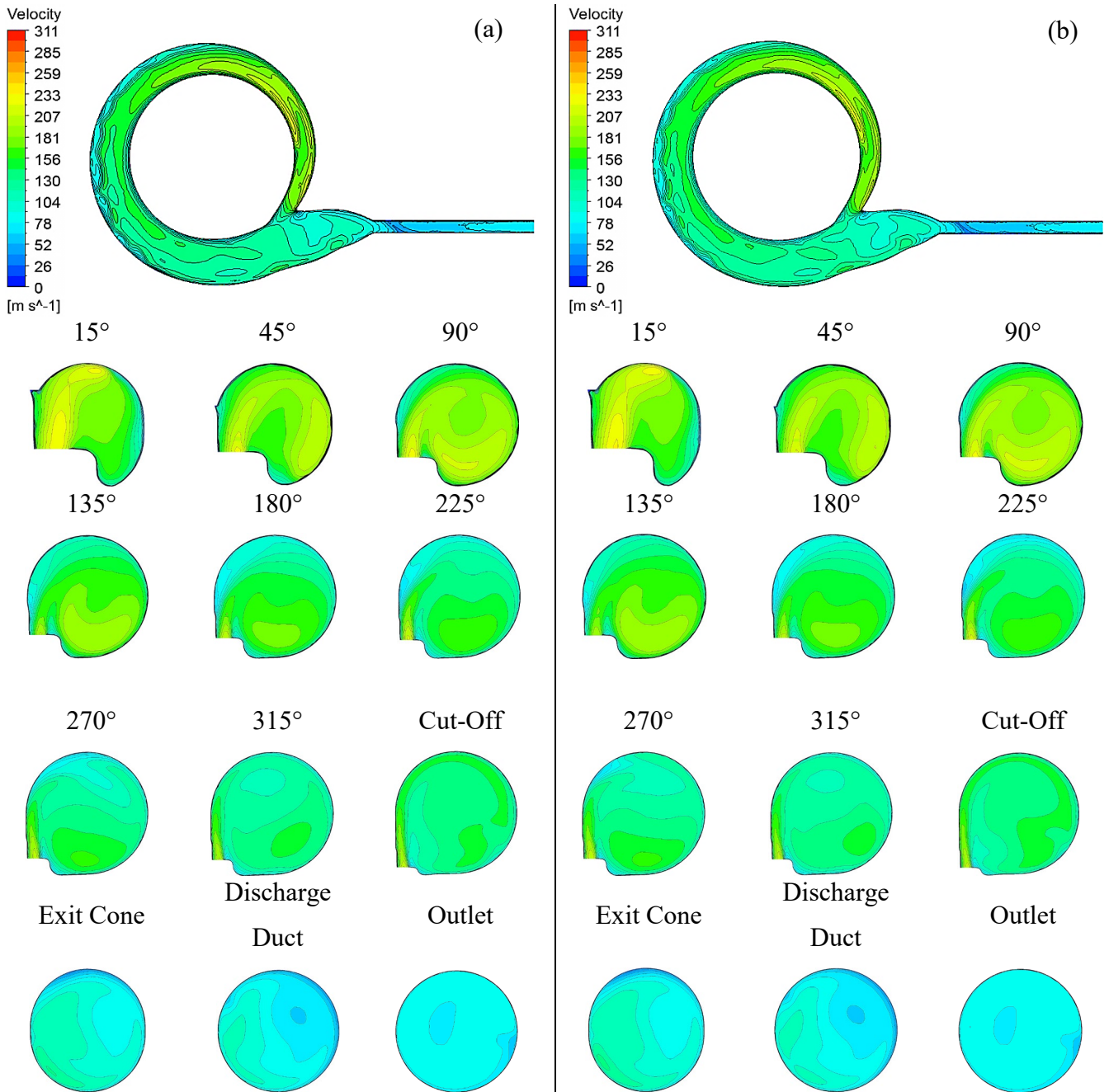


Figure 5.17 Velocity Magnitude around the Compressor Volute during the operating speed of 98.2rps/√K at (a) Blade Position 1 (b) Blade Position 2

Figure 5.18 graphically represents steady response and unsteady response at two instances of velocity magnitude variation across each profile at high operating speed of 98.2rps/√K. For all cases, velocity magnitude increases from 15° to 90° prior to decreasing downstream to 315°. From here, velocity magnitude increases once more at the cut-off location at 345° followed by a considerable decrease downstream to the outlet. There appears to be negligible velocity magnitude variations between the unsteady cases, where BP2 is slightly higher than BP1. The most prominent velocity magnitude variation between the steady response and unsteady

responses occur at  $15^\circ$ , where steady response has much lower velocity magnitude. At  $90^\circ$ , steady response exhibits higher velocity magnitude in comparison with unsteady responses. At  $45^\circ$  and  $135^\circ$ , velocity magnitude is slightly less and slightly more for the steady case than unsteady cases, respectively. From  $180^\circ$  to  $390^\circ$ , slightly accelerated velocity magnitude is depicted for the steady case than the unsteady cases. At  $393^\circ$ , the steady case presents slightly accelerated velocity magnitude prior to decelerating slightly at the outlet in comparison to the unsteady responses. Table 5.9 details the percentage difference in velocity magnitude variation at  $98.2\text{rps}/\sqrt{K}$  from one cross-section location to the next, specified by the azimuth angle, as well as the velocity magnitude variation occurring at each cross-section around the volute against that depicted at the outlet. The maximum velocity magnitude variation occurring from one azimuth angle to the next between unsteady BP1 and steady response is at  $15^\circ$  to  $45^\circ$ , where the steady response depicts a higher variation. The minimum velocity magnitude variation occurs between unsteady BP2 and the steady response at  $315^\circ$  to  $345^\circ$ , where the steady response depicts more variation. The maximum velocity magnitude variation occurring between the cross-section around the volute and the outlet against the steady response is at  $15^\circ$  with unsteady BP2, while the minimum occurs at  $180^\circ$  with unsteady BP1, where both unsteady response depict more variations. Overall, this quantifies and compares the velocity magnitude variation between the steady and the two instantaneous responses at high operating speed.

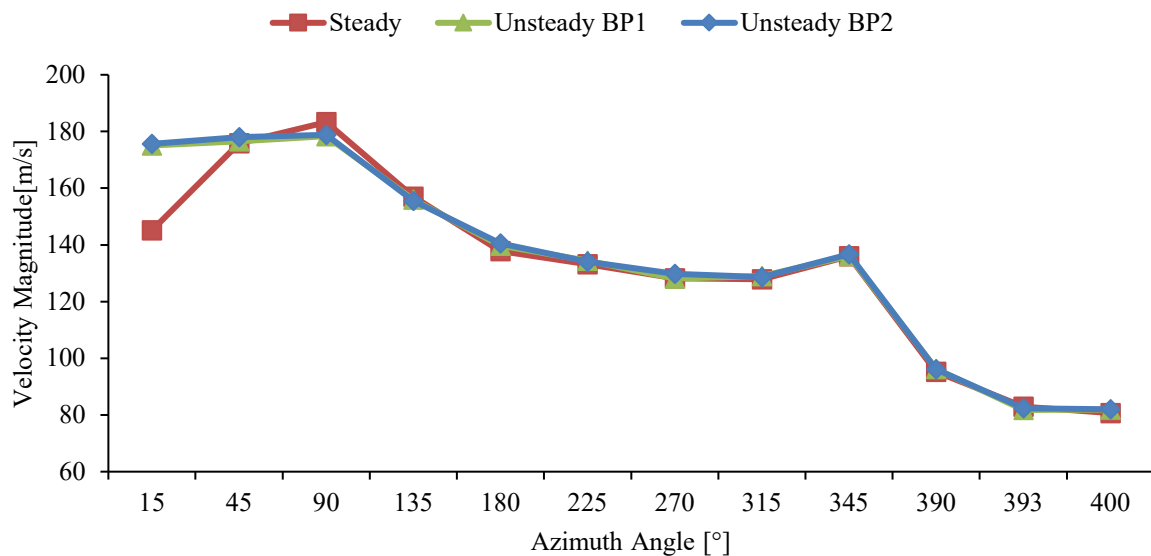


Figure 5.18 Comparison of steady and unsteady response for velocity magnitude across each cross-section around the compressor volute during the operating speed of  $98.2\text{rps}/\sqrt{K}$

*Table 5.9 Comparison of steady and unsteady response of plane to plane and outlet to plane velocity magnitude variation at 98.2 rps/√K*

$\theta^\circ$ to $\theta^\circ$ Velocity Magnitude Variation [%]				Outlet @ $400^\circ$ to $\theta^\circ$ Velocity Magnitude Variation [%]			
$\theta^\circ$	Steady	Unsteady BP1	Unsteady BP2	$\theta^\circ$	Steady	Unsteady BP1	Unsteady BP2
15 - 45	21.2	0.9	1.3	15	79.9	113.8	114.2
45 - 90	4.2	1.0	0.5	45	118.0	115.6	117.0
90 - 135	-14.3	-12.5	-13.0	90	127.2	117.8	118.1
135 - 180	-12.2	-10.5	-9.7	135	94.7	90.5	89.7
180 - 225	-3.4	-3.8	-4.6	180	70.9	70.6	71.4
225 - 270	-3.8	-4.7	-3.2	225	65.1	64.1	63.5
270 - 315	-0.3	0.6	-0.9	270	58.9	56.5	58.3
315 - 345	6.4	5.6	6.2	315	58.5	57.5	56.9
345 - 390	-30.0	-29.3	-29.7	345	68.6	66.3	66.6
390 - 393	-12.9	-15.0	-14.4	390	18.0	17.5	17.2
393 - 400	-2.7	0.1	-0.4	393	2.8	-0.1	0.4

### 5.12 Local Asymmetric Ratios of Velocity Magnitude Distribution Profiles along the Radial Direction and Axial Direction at High Speed during Steady and Unsteady Conditions

Figure 5.19 is a graphical representation depicting the asymmetric ratio of velocity magnitude along the radial direction of the cross-section profiles in (a) and axial direction of the cross-section profiles in (b) around the centrifugal compressor volute at high operating speed of 98.2rps/√K. Observing Figure 5.19 (a), both unsteady cases show asymmetry towards the outer curve, while the steady case shows asymmetry towards the inner curve at 15°. At 45°, all cases are asymmetric towards the outer curve with slight variances between each other. From 90° to 345°, all cases are asymmetric towards the inner curve. At 90°, 135° and 225°, there are no variations between two unsteady cases, while at 180° negligible variance is depicted. From 90° to 180°, the steady case depicts greater asymmetry than the two unsteady cases, while at 225° and 270°, the unsteady cases depict greater asymmetry than the steady case. At 270°, unsteady BP1 exhibits much higher asymmetry and matches with the steady case at 315°. Here, unsteady BP2 depicts negligible variance with the steady case and unsteady BP1. At 345°, all cases exhibit asymmetry towards the inner curve, showing no velocity magnitude variations between the two unsteady cases at 345°, however the steady case depicts higher asymmetry. At 390° and 393°, all cases are asymmetric towards the outer curve, where the steady case depicts higher asymmetry than the unsteady cases and there is negligible variance between the two unsteady cases at 393°.

At  $400^\circ$ , the two unsteady cases exhibit symmetry in velocity magnitude along the radial, while the steady case exhibits asymmetry towards the inner curve. Observing Figure 5.19 (b), all cases are asymmetric towards the rear face at  $15^\circ$ , where the steady case exhibits the least asymmetry and unsteady BP1 depicts the most. From  $45^\circ$  to  $225^\circ$ , there is negligible velocity magnitude variance along the axial between the two unsteady cases and depicts asymmetry towards the front face. From  $45^\circ$  to  $135^\circ$ , steady case exhibits asymmetry towards the rear face prior to exhibiting asymmetry towards the front face from  $180^\circ$  to  $270^\circ$ . At  $180^\circ$ , the steady case has more asymmetry than the two unsteady cases and at  $225^\circ$ , there is negligible velocity magnitude variation along the axial between the steady and the two unsteady cases. At  $270^\circ$ , both unsteady cases depict asymmetry towards the rear face, where unsteady BP1 is slightly higher. At  $315^\circ$ , steady case is asymmetric towards the rear face while unsteady BP1 and unsteady BP2 are slight asymmetric towards the front face and rear face, respectively. At  $345^\circ$ , all cases are asymmetric towards the front face, where the two unsteady cases depict no velocity magnitude variation along the axial of the profile. Additionally, the steady case identifies slightly more asymmetry than the unsteady cases. At  $390^\circ$  and  $393^\circ$ , all cases depict asymmetry once towards rear face, where there is a slight variation and a prominent variation, respectively, along the axial between the steady case and the two unsteady cases. At the outlet, there appears to be negligible variations between the cases and shows slight asymmetry towards the front face. Overall at high operating speed, it is observed that there is a prominent influence on the imbalance of velocity magnitude along the radial direction at  $270^\circ$  between the two instances. Aside from this, there is predominantly only a slight influence on the imbalance of velocity magnitude between the two instances along the radial direction and axial direction through the centrifugal compressor volute. Furthermore, there is a significant influence on the imbalance of velocity magnitude through the centrifugal compressor volute between the steady response and the two unsteady responses along both, radial direction and axial direction. More detailed graphical representations are depicted in APPENDIX 3.

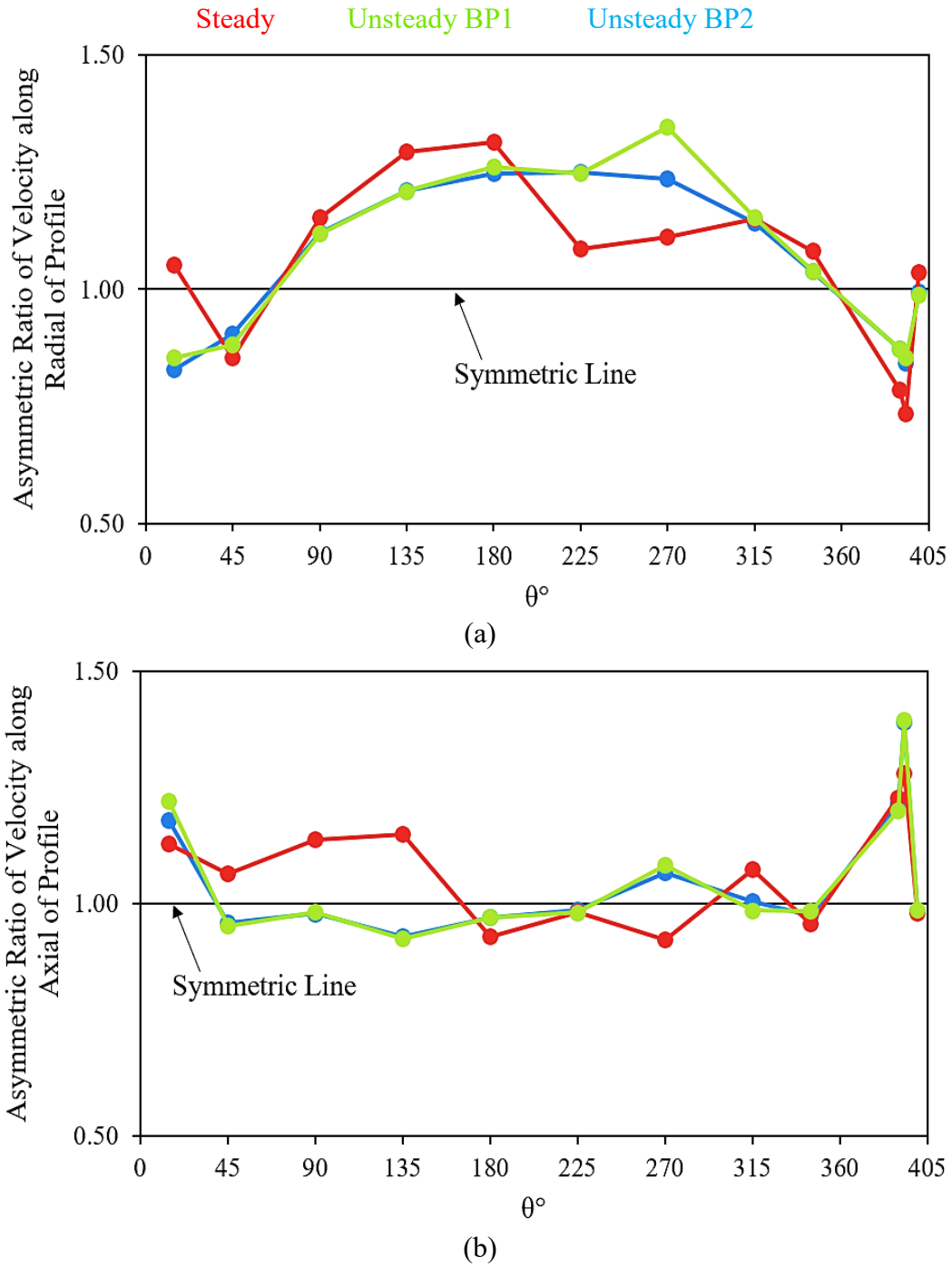


Figure 5.19 Asymmetric Ratio of Steady and Unsteady Velocity Magnitude around the Centrifugal Compressor Volute at the operating speed of 98.2rps/ $\sqrt{K}$  along the (a) Radial of the profiles and (b) Axial of the profiles

### 5.13 Velocity Magnitude Speed Comparison during Unsteady Conditions

Table 5.10 depicts the unsteady response of the local speed comparison, where the high operating speed of 98.2rps/ $\sqrt{K}$  is compared against the low operating speed of 58.9rps/ $\sqrt{K}$  for velocity magnitude across each of the selected cross-section through the turbocharger compressor volute. The unsteady responses are at two instances, being at blade position 1 where the impeller blade is aligned with the volute tongue and at blade position 2, where the impeller blade has passed the volute tongue and another impeller blade is approaching the volute tongue. It is identified there are minimal variances throughout the turbocharger compressor volute between the two instances. Velocity magnitude at 98.2rps/ $\sqrt{K}$  increases at both unsteady instances compared to that at 58.9rps/ $\sqrt{K}$  and decreases in its variance compared to that at 58.9rps/ $\sqrt{K}$  through the volute. The maximum difference between the two unsteady cases when comparing 98.2rps/ $\sqrt{K}$  with 58.9rps/ $\sqrt{K}$  is located at 45°, where BP2 shows higher increase in velocity magnitude.

*Table 5.10 Local Speed Comparison of Velocity Magnitude Variation during Unsteady Response*

$\theta^\circ$	Velocity Magnitude [%]	
	Unsteady BP1	Unsteady BP2
15	94.4	94.3
45	71.6	72.9
90	61.2	62.0
135	49.7	49.6
180	40.2	41.3
225	38.8	38.6
270	34.5	36.4
315	35.0	34.7
345	33.2	33.8
390	27.5	27.4
393	24.2	25.0
400	29.9	30.0

### 5.14 Global Static Temperature Distribution at Two Instances during Unsteady Conditions

Figure 5.20 depicts the static temperature variation in the turbocharger compressor stage during the operating speed of  $58.9\text{rps}/\sqrt{\text{K}}$  and  $98.2\text{rps}/\sqrt{\text{K}}$ . Figure 5.20 (a) depicts blade position 1, also referred as BP1, which is when the impeller blade is aligned with the volute tongue and Figure 5.20 (b) depicts blade position 2, also referred as BP2, which is when the impeller blade is passed the tongue and another blade is approaching the tongue. At both speeds, minimal variances in static temperature are seen between the two instances. Higher static temperature is displayed at high speed, while lower static temperature is displayed at low speed. Uniform static temperature is identified through the turbocharger compressor in both cases.

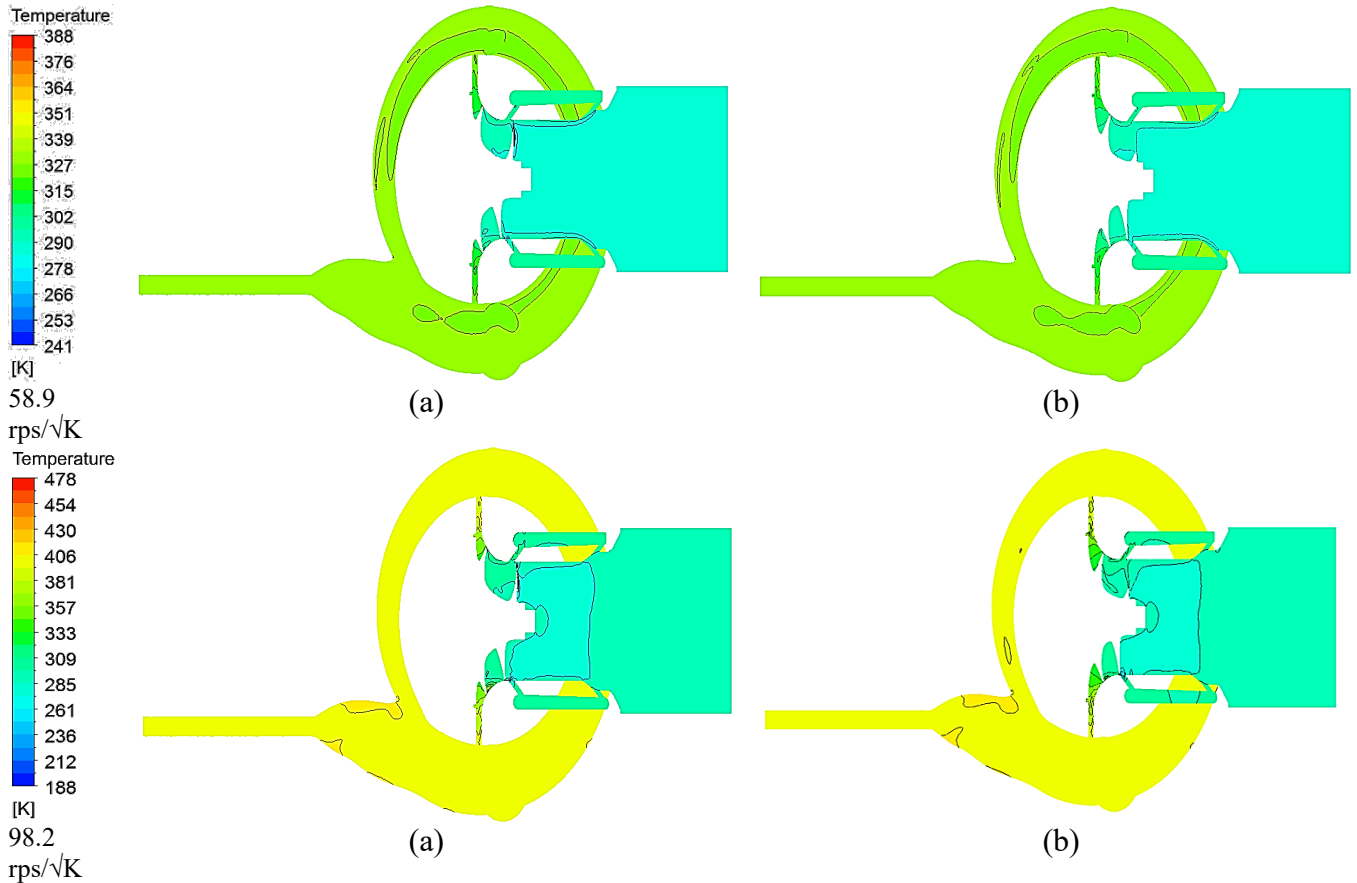


Figure 5.20 Static Temperature Variation in the Turbocharger Compressor Stage during the operating speed of  $58.9\text{rps}/\sqrt{\text{K}}$  and  $98.2\text{rps}/\sqrt{\text{K}}$  at (a) Blade Position 1 (b) Blade Position 2

Figure 5.21 depicts the comparison of static temperature variations through each station in the compressor stage between the steady conditions and unsteady conditions at low operating speed of (a)  $58.9\text{rps}/\sqrt{\text{K}}$  and at high operating speed of (b)  $98.2\text{rps}/\sqrt{\text{K}}$ . There is a greater static temperature variation through each component at high speed than at low speed. It can be seen that for both speeds, static temperature decreases in the inducer for all cases and increases



downstream of this. There appears to be no variance in static temperature between the two unsteady cases at low speed from the inducer to the diffuser, while high speed depicts no variance through the inducer and volute. At low speed, unsteady BP2 depicts slightly more of a decrease in static temperature through the impeller and slightly higher static temperature through the volute than unsteady BP1. Through the inducer and impeller static temperature is observed to be lower at the steady case than the two unsteady cases and higher through the diffuser and volute. At high speed, unsteady BP1 depicts slightly higher static temperature through the impeller and slightly lower static temperature through the diffuser than unsteady BP2. There is no static temperature variance between the steady case and the two unsteady cases through the inducer. Static temperature is observed to be lower at the steady case than the two unsteady cases through the impeller and diffuser. Further to this, higher static temperature is exhibited from the steady case through the volute. Details of these through-flow variances for the unsteady response at two instances against the steady response are presented in Table 5.11.

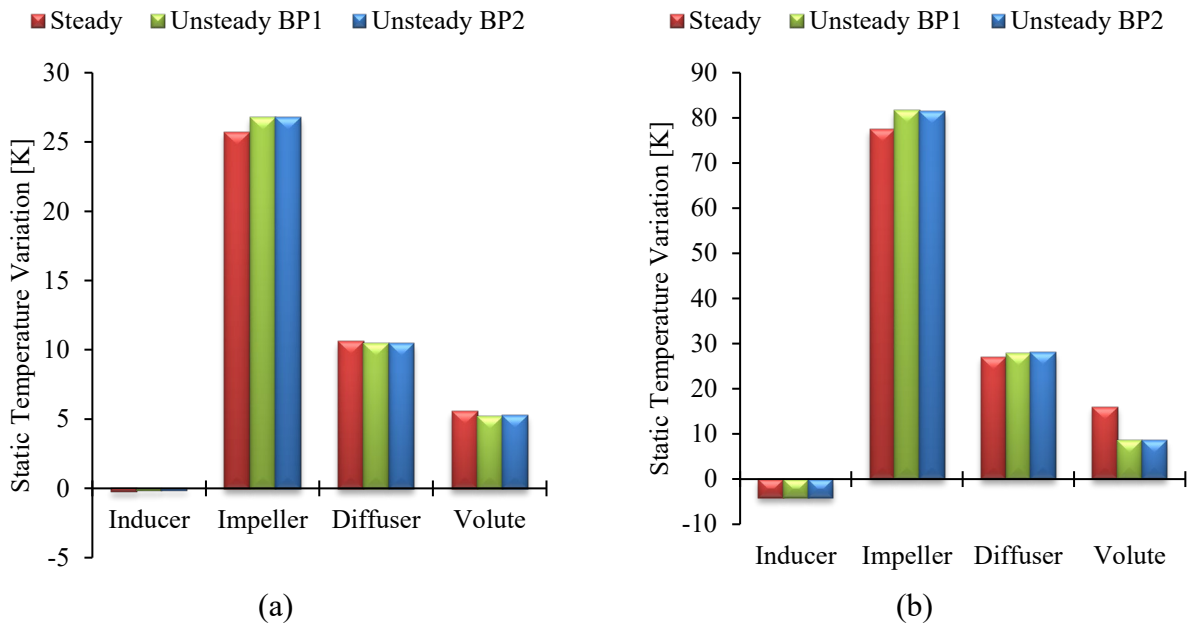


Figure 5.21 Comparison of steady and unsteady response of static temperature difference through each station in the turbocharger compressor stage during (a) 58.9rps/√K (b) 98.2rps/√K

Table 5.11 details the static temperature variance comparison of the unsteady response at two instances, being blade position 1 and blade position 2, with the steady response at low operating speed of 58.9rps/√K and at high operating speed of 98.2rps/√K. There are no static temperature variations depicted at the inducer inlet and impeller inlet at low speed, while at high speed there is negligible variances. At low speed, static temperature at the inlet location of each component varies by the same amount at both unsteady instances. This is also the case at high speed aside from that at the diffuser, where blade position 2 depicts slightly lower static temperature

variation than that depicted at blade position 1. At low speed, static temperature at the outlet location of each component varies by the same amount at both unsteady instances. This is also the case at high speed aside from that at the impeller, where blade position 2 depicts slightly lower static temperature variation than that depicted at blade position 1.

*Table 5.11 Comparison of steady and unsteady response of static temperature at the inlet, outlet and through-flow across each station at low speed of 58.9rps/ $\sqrt{K}$  and high speed of 98.2rps/ $\sqrt{K}$*

Compressor Component	Inlet Variation [%]				Outlet Variation [%]				Through-flow Variation [%]			
	Blade Position 1		Blade Position 2		Blade Position 1		Blade Position 2		Blade Position 1		Blade Position 2	
	Low Speed	High Speed	Low Speed	High Speed	Low Speed	High Speed	Low Speed	High Speed	Low Speed	High Speed	Low Speed	High Speed
Inducer	0.0	0.1	0.0	0.1	0.0	0.1	0.0	0.1	-42.8	1.7	-48.5	1.3
Impeller	0.0	0.1	0.0	0.1	0.4	1.3	0.4	1.2	4.1	5.3	4.0	5.1
Diffuser	0.4	1.3	0.4	1.2	0.3	1.4	0.3	1.4	-1.4	2.7	-1.5	3.6
Volute	0.3	1.4	0.3	1.4	0.2	-0.5	0.2	-0.5	-5.7	-46.6	-5.0	-46.3

### 5.15 Local Static Temperature Distribution at Low Speed during Unsteady Conditions

Figure 5.22 depicts the static temperature around the compressor volute during the operating speed of 58.9rps/ $\sqrt{K}$  at (a) blade position 1, where the impeller blade is aligned with the volute tongue and (b) blade position 2, where the impeller blade has passed the volute tongue and another impeller blade is approaching the volute tongue. It can be seen that both instances show the same uniform static temperature trends across the volute and its cross-sections. At 15°, there are small regions of slightly lower static temperature depicted at the inlet and near the outer curve more towards the rear face. From 45° to 135°, the lower static temperature region at the inlet increases in its distribution prior to reducing its distribution at the inlet downstream of 135°. At 45°, the lower static temperature is also depicting in the overhang at the front face, which propagates into the overhang at 90°. Downstream of 90°, this lower static temperature region localised in the overhang reduces its distribution until the flow reaches the cut-off location at 345°, where flow depicts predominant uniformity in its static temperature distribution across the profile. Very small regions of lower static temperature remains at the inlet and at the rear face near the inlet. Downstream of the cut-off location, static temperature distribution is uniform. Overall at low operating speed, it can be seen there are no variances in static temperature between the two instances.

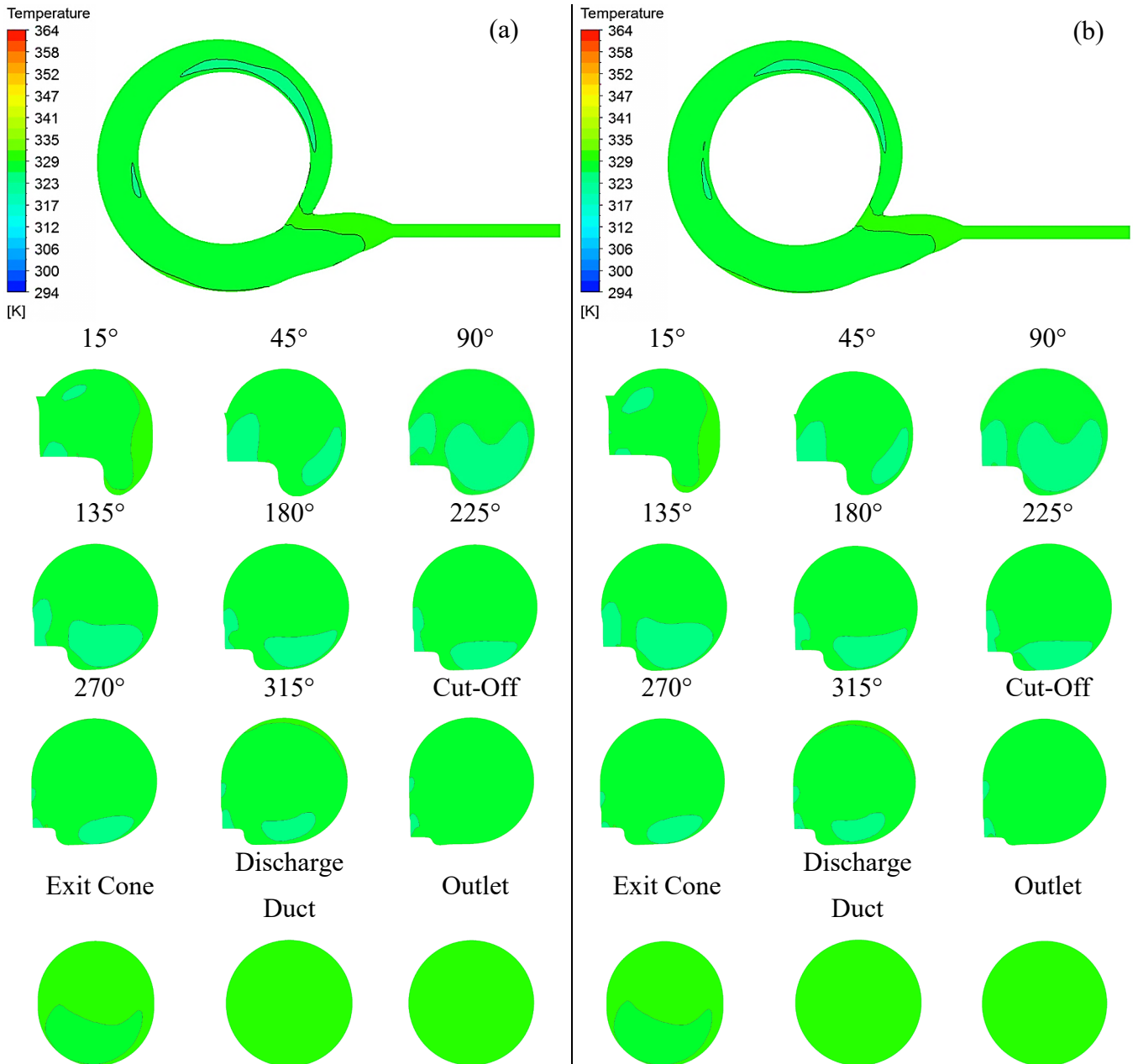


Figure 5.22 Static Temperature around the Compressor Volute during the operating speed of  $58.9\text{ rps}/\sqrt{\text{K}}$  at (a) Blade Position 1 (b) Blade Position 2

Figure 5.23 graphically represents steady response and unsteady response at two instances of static temperature variation across each profile at low operating speed of  $58.9\text{ rps}/\sqrt{\text{K}}$ . For all cases, static temperature decreases from  $15^\circ$  to  $90^\circ$ , then increases from  $135^\circ$  to  $315^\circ$ . From here, static temperature decreases once more to the cut-off location at  $345^\circ$ , prior to increasing downstream to the outlet. It is identified at  $15^\circ$ , the steady case depicts prominently higher static temperature than that depicts for the two unsteady cases, while at  $45^\circ$  this variation is very slight. Downstream of  $45^\circ$ , the steady response indicates lower static temperature than that depicted with the unsteady response for both instances. There are minor variations between unsteady BP1

and unsteady BP2. Table 5.11 details the percentage difference in static temperature variation at  $58.9\text{rps}/\sqrt{K}$  from one cross-section location to the next, specified by the azimuth angle. Table 5.11 also details the percentage difference in static temperature variation at  $58.9\text{rps}/\sqrt{K}$  occurring at each cross-section around the volute against that depicted at the outlet. The maximum static temperature variation that occurs from one azimuth angle to the next between the unsteady responses and the steady response is at  $15^\circ$  to  $90^\circ$ , where the steady response has more variation. There are no static temperature variation occurring between the unsteady and steady responses downstream of  $180^\circ$ . The maximum static temperature variation that occurs between the cross-section around the volute and the outlet is at  $15^\circ$  with the unsteady cases exhibiting more of a variation than the steady case. There are no static temperature variations occurring at  $90^\circ$  and  $393^\circ$  where all cases vary by the same amount across the profile. Overall, this quantifies and compares the static temperature variation between the steady and the two instantaneous responses at low operating speed.

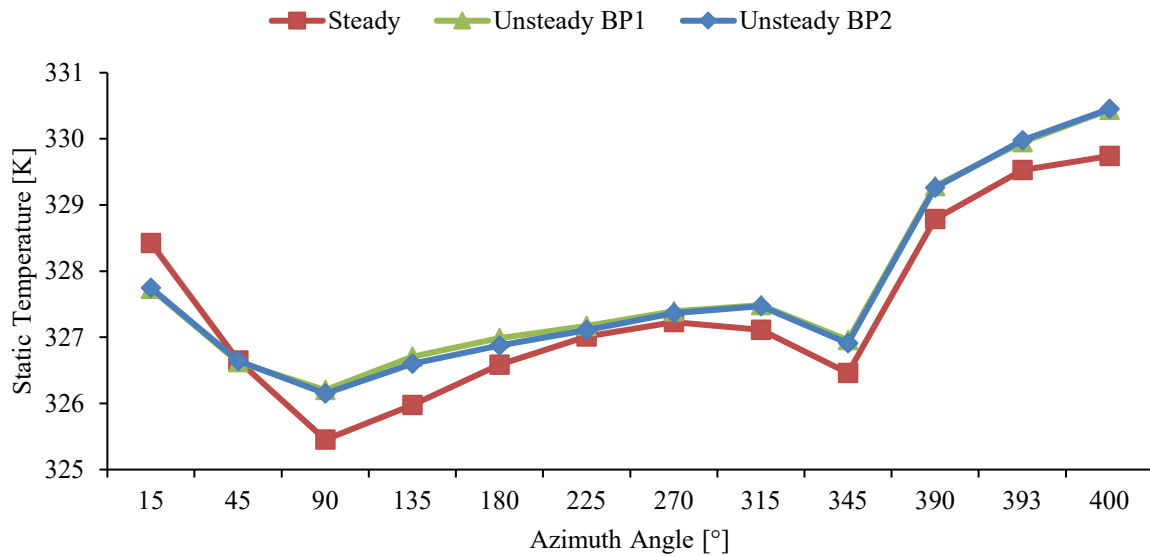


Figure 5.23 Comparison of steady and unsteady response for static temperature across each cross-section around the compressor volute during the operating speed of  $58.9\text{rps}/\sqrt{K}$

Table 5.12 Comparison of steady and unsteady response of plane to plane and outlet to plane static temperature variation at 58.9 rps/ $\sqrt{K}$

$\theta^\circ$ to $\theta^\circ$ Static Temperature Variation [%]				Outlet @ $400^\circ$ to $\theta^\circ$ Static Temperature Variation [%]			
$\theta^\circ$	Steady	Unsteady BP1	Unsteady BP2	$\theta^\circ$	Steady	Unsteady BP1	Unsteady BP2
15 - 45	-0.5	-0.3	-0.3	15	-0.4	-0.8	-0.8
45 - 90	-0.4	-0.1	-0.2	45	-0.9	-1.2	-1.2
90 - 135	0.2	0.2	0.1	90	-1.3	-1.3	-1.3
135 - 180	0.2	0.1	0.1	135	-1.1	-1.1	-1.2
180 - 225	0.1	0.1	0.1	180	-1.0	-1.0	-1.1
225 - 270	0.1	0.1	0.1	225	-0.8	-1.0	-1.0
270 - 315	0.0	0.0	0.0	270	-0.8	-0.9	-0.9
315 - 345	-0.2	-0.2	-0.2	315	-0.8	-0.9	-0.9
345 - 390	0.7	0.7	0.7	345	-1.0	-1.1	-1.1
390 - 393	0.2	0.2	0.2	390	-0.3	-0.3	-0.4
393 - 400	0.1	0.1	0.1	393	-0.1	-0.1	-0.1

### 5.16 Local Asymmetric Ratios of Static Temperature Distribution Profiles along the Radial Direction and Axial Direction at Low Speed during Steady and Unsteady Conditions

Figure 5.24 is a graphical representation depicting the asymmetric ratio of static temperature along the radial direction of the cross-section profiles in (a) and axial direction of the cross-section profiles in (b) around the centrifugal compressor volute at low operating speed of 58.9rps/ $\sqrt{K}$ . In the case of Figure 5.24 (a) the two unsteady responses depict the same asymmetric ratio for static temperature along the radial through the volute. At  $15^\circ$  and  $45^\circ$  all cases depict slight asymmetry towards the inner curve, where the steady case is higher. At  $90^\circ$ , the steady response exhibit slight asymmetry towards the inner curve, while the unsteady responses exhibit slight asymmetry towards the outer curve. From  $135^\circ$  to  $345^\circ$ , all cases identify slight asymmetry towards the outer curve where the steady case depicts high asymmetry at  $135^\circ$  and  $180^\circ$ , then slightly less asymmetry at  $225^\circ$  and  $315^\circ$ . At  $270^\circ$  and  $345^\circ$ , all cases identify the same amount of asymmetry. At 390 and  $393^\circ$  all case depicts the same minor asymmetry towards the inner curve. At  $400^\circ$ , unsteady cases depict symmetric static temperature along the radial, while the steady case continues to depict minor asymmetry towards the inner curve. In the case of Figure 5.24 (b) the two unsteady responses depict the same asymmetric ratio for static temperature along the axial through the volute. The two unsteady responses depict the same asymmetric ratio for static temperature along the axial downstream of  $135^\circ$ . Upstream of this are

very minor variances. From  $15^\circ$  to  $135^\circ$ , the unsteady cases depict slight asymmetry towards the front face, while the steady case identifies symmetric static temperature at  $15^\circ$ , followed by slight asymmetry towards the rear face at  $45^\circ$  and then slightly more asymmetry than the unsteady cases towards the front face from  $90^\circ$  to  $180^\circ$ . From  $180^\circ$  to  $270^\circ$ , the unsteady cases depict symmetric static temperature along the axial, whereas the steady case depicts slight asymmetry towards the rear face. All cases exhibit very minor asymmetry towards the front face at  $315^\circ$  followed by symmetric static temperature along the axial at  $345^\circ$ . At  $390^\circ$ , unsteady cases continue to exhibit symmetry, while the steady case shows very minor asymmetry towards the front face. At  $393^\circ$  unsteady cases join the steady case by also showing very minor asymmetry towards the front face prior to deviating away from the steady case at  $400^\circ$ . Here, unsteady cases are symmetric along the axial, while the steady case continues to exhibit very minor asymmetry towards the front face. Overall at low operating speed, it is observed that there is no influence on the imbalance of static temperature along the radial direction or the axial direction of the cross-section profiles inside the centrifugal compressor volute between the two instances. Furthermore, there is only a slight, if not negligible, influence on the imbalance of static temperature between the steady response and the two unsteady responses along both, radial direction and axial direction. More detailed graphical representations are depicted in APPENDIX 3.

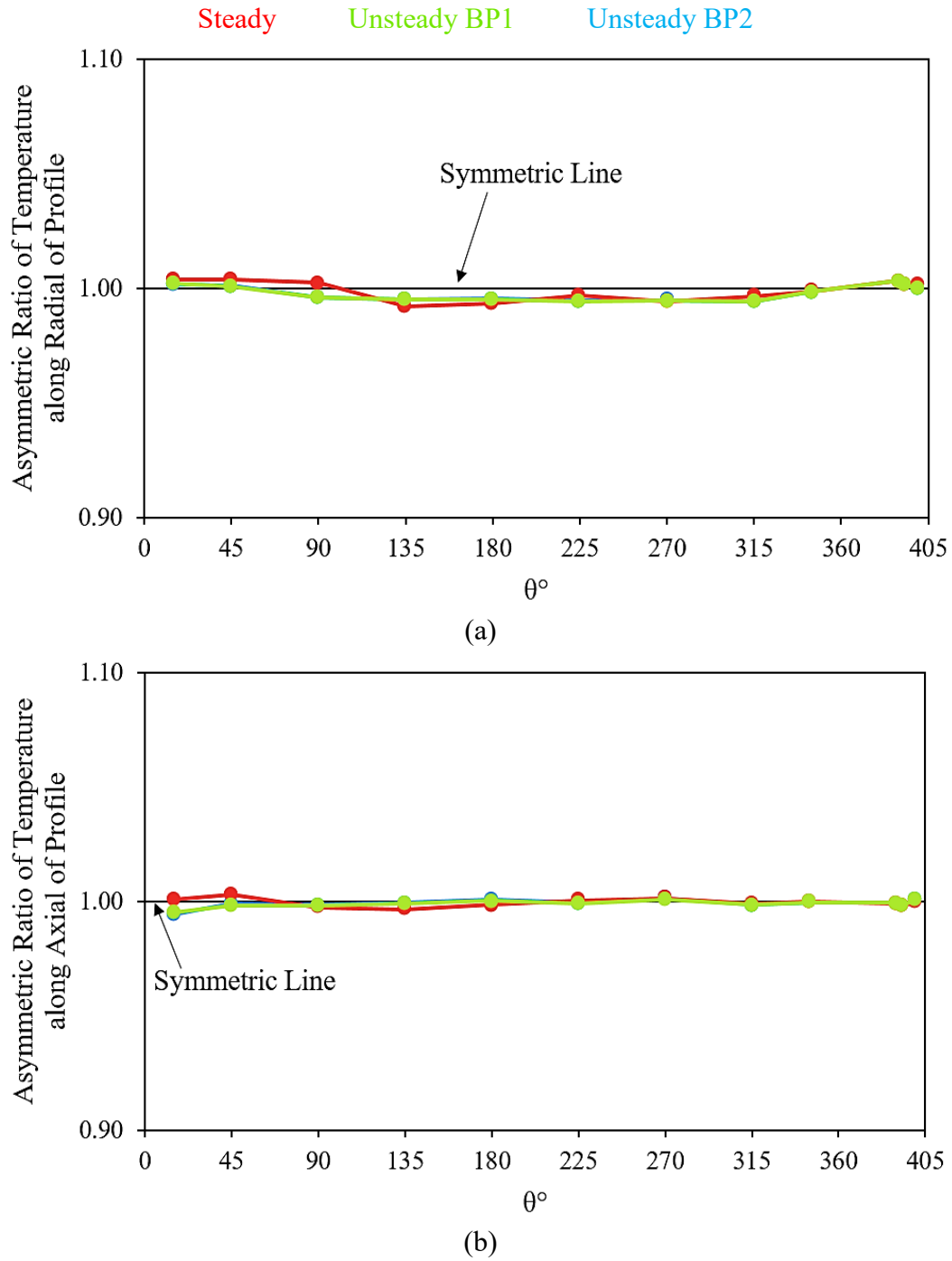


Figure 5.24 Asymmetric Ratio of Steady and Unsteady Static Temperature around the Centrifugal Compressor Volute at the operating speed of 58.9rps/ $\sqrt{K}$  along the (a) Radial of the profiles and (b) Axial of the profiles

### 5.17 Local Static Temperature Distribution at High Speed during Unsteady Conditions

Figure 5.25 depicts the static temperature around the compressor volute during the operating speed of 98.2rps/ $\sqrt{k}$  at (a) blade position 1, where the impeller blade is aligned with the volute tongue and (b) blade position 2, where the impeller blade has passed the volute tongue and another impeller blade is approaching the volute tongue. It can be seen that both instances show the almost uniform static temperature trends across the volute and its cross-sections. Very slight static temperature variations are identified at and upstream of 315°. Downstream of this depicts areas of slightly high static temperatures, predominately from the exit cone. At 15°, slightly lower static temperature is exhibited at the inlet, along the rear face and in the central upper sector of the profile. These regions reduce in its distribution from 45° and depict another slightly lower static temperature region across the profiles, predominately in the overhang, which propagates to 135°. Downstream of 135° until reaching 315° of the volute, the slightly lower static temperature region localised in the overhang reduces in its distribution. From 225° to 315°, there is a region of higher static temperature in the central region more towards the upper sector of the profile. At 270°, this region is greater at (b) than at (a), also depicting slightly high static temperature along the outer curve, which is absent in the case of (a). At the cut-off for both instances, slightly lower static temperature is identified once more in the overhang of the profile. The exit cone and discharge duct depicts higher static temperature across the profiles with regions of lower static temperatures in the lower sector and at the rear face of the cross-sections, respectively. At the outlet, uniform static temperature is identified for both instances. Overall at high operating speed, it can be seen there are negligible variances in static temperature between the two instances.



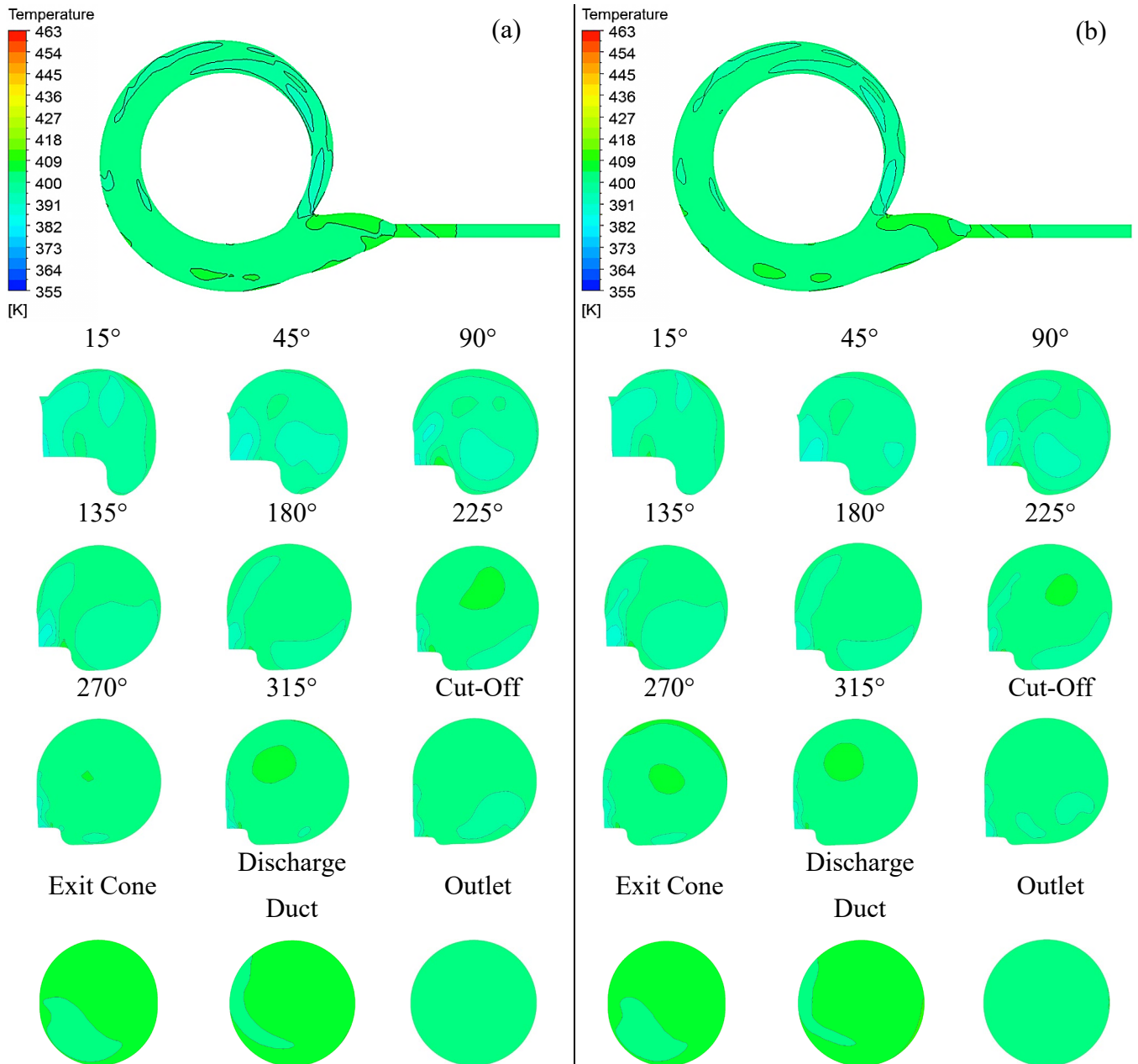


Figure 5.25 Static Temperature around the Compressor Volute during the operating speed of  $98.2\text{rps}/\sqrt{\text{K}}$  at (a) Blade Position 1 (b) Blade Position 2

Figure 5.26 graphically represents steady response and unsteady response at two instances of static temperature variation across each profile at high operating speed of  $98.2\text{rps}/\sqrt{\text{K}}$ . For all cases, static temperature decreases from  $15^\circ$  to  $90^\circ$ , then increases from  $135^\circ$  to  $315^\circ$ . From here, static temperature again decreases at  $345^\circ$ , prior to increasing downstream to the outlet for the steady response. For both unsteady responses however, static temperature increases then decreases at the outlet. It is identified steady response indicates lower static temperature than that depicted with the unsteady response for both instances throughout the volute. BP2 is predominately higher than BP1 aside from both instances depict the same static temperature at  $315^\circ$  and  $390^\circ$  and BP1 being higher than BP2 at  $225^\circ$  and  $135^\circ$ . Table 5.13 details the

percentage difference in static temperature variation at 98.2rps/ $\sqrt{K}$  from one cross-section location to the next, specified by the azimuth angle. Table 5.13 also details the percentage difference in static temperature variation at 98.2rps/ $\sqrt{K}$  occurring at each cross-section around the volute against that depicted at the outlet. The maximum static temperature variation that occurs from one azimuth angle to the next between the unsteady responses and the steady response is at 393° to 400°, where steady case depicts higher variation than the two unsteady. There are no static temperature variations occurring between both unsteady responses and the steady response at 390° to 393°. The maximum and minimum static temperature variation that occurs between the cross-section around the volute and the outlet is at 90° and 15°, respectively with the steady cases exhibiting more of a variation than the unsteady cases. Overall, this quantifies and compares the static temperature variation between the steady and the two instantaneous responses at high operating speed.

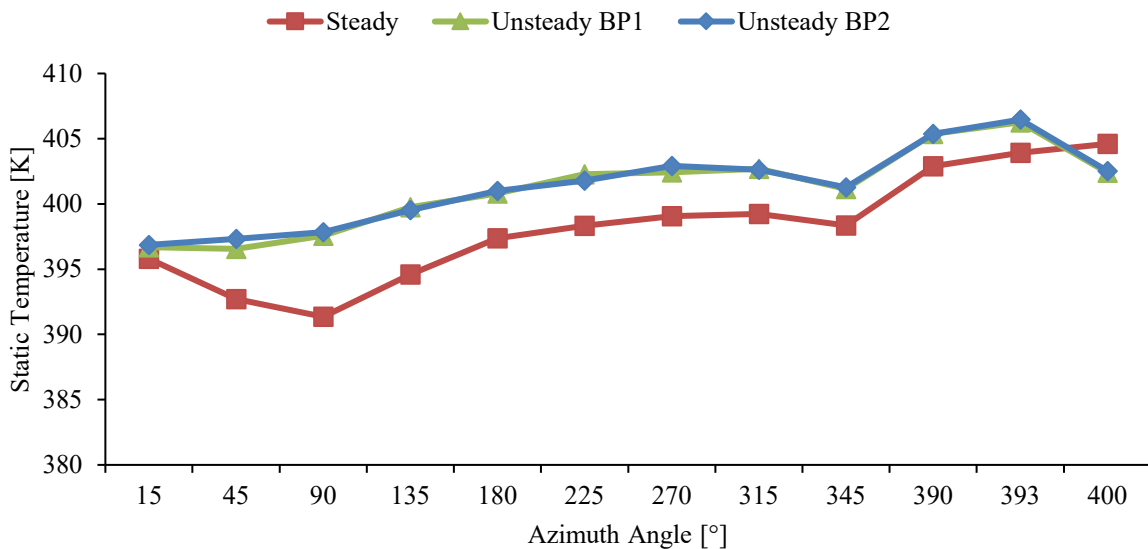


Figure 5.26 Comparison of steady and unsteady response for static temperature across each cross-section around the compressor volute during the operating speed of 98.2rps/ $\sqrt{K}$

*Table 5.13 Comparison of steady and unsteady response of plane to plane and outlet to plane static temperature variation at 98.2rps/ $\sqrt{K}$*

$\theta^\circ$ to $\theta^\circ$ Static Temperature Variation [%]				Outlet @ $400^\circ$ to $\theta^\circ$ Static Temperature Variation [%]			
$\theta^\circ$	Steady	Unsteady BP1	Unsteady BP2	$\theta^\circ$	Steady	Unsteady BP1	Unsteady BP2
15 - 45	-0.8	0.0	0.1	15	-2.2	-1.4	-1.4
45 - 90	-0.3	0.3	0.1	45	-2.9	-1.5	-1.3
90 - 135	0.8	0.5	0.4	90	-3.3	-1.2	-1.2
135 - 180	0.7	0.3	0.4	135	-2.5	-0.7	-0.7
180 - 225	0.2	0.4	0.2	180	-1.8	-0.4	-0.4
225 - 270	0.2	0.0	0.3	225	-1.6	0.0	-0.2
270 - 315	0.0	0.1	-0.1	270	-1.4	0.0	0.1
315 - 345	-0.2	-0.4	-0.3	315	-1.3	0.1	0.0
345 - 390	1.1	1.1	1.0	345	-1.5	-0.3	-0.3
390 - 393	0.3	0.2	0.3	390	-0.4	0.7	0.7
393 - 400	0.2	-0.9	-1.0	393	-0.2	1.0	1.0

### 5.18 Local Asymmetric Ratios of Static Temperature Distribution Profiles along the Radial Direction and Axial Direction at High Speed during Steady and Unsteady Conditions

Figure 5.27 is a graphical representation depicting the asymmetric ratio of static temperature along the radial direction of the cross-section profiles in (a) and axial direction of the cross-section profiles in (b) around the centrifugal compressor volute at high operating speed of 98.2rps/ $\sqrt{K}$ . In the case of Figure 5.27 (a), both unsteady cases depict symmetric static temperature at  $15^\circ$ , while the steady case appears to be asymmetric towards the outer curve. From  $45^\circ$  to  $345^\circ$  both unsteady cases exhibit asymmetry towards the outer curve and consist of the same asymmetry at  $135^\circ$ ,  $225^\circ$  and  $315^\circ$ . At  $45^\circ$  the steady case identifies asymmetry towards the inner curve until  $345^\circ$ , asymmetry towards the outer curve is depicted. Slight variations are seen between the steady case and unsteady cases. Downstream of  $345^\circ$ , all cases show slight static temperature asymmetry along the radial towards the inner curve. In the case of Figure 5.27 (b), there are no static temperature variances along the axial between the two unsteady cases at  $90^\circ$  and downstream of  $345^\circ$ . Aside from this and the slight variance localised at  $270^\circ$ , there is negligible variance between the two unsteady cases. From  $15^\circ$  to  $90^\circ$ , all cases exhibit asymmetry towards the front face with the steady case depicting more asymmetry. At  $135^\circ$ , unsteady cases are symmetric while the steady case continues to depict asymmetry towards the front face. All cases are slightly asymmetric towards the front face at  $180^\circ$ , followed by

symmetric static temperature along the axial at 225°. At 270°, unsteady BP1 depicts symmetry while unsteady BP2 and the steady case depict slight asymmetry towards the front face and rear face, respectively. At 315°, unsteady BP1 depicts symmetry while unsteady BP2 and the steady case depict vice versa to previous. At 345°, both unsteady cases exhibit symmetric static temperature along the axial, while the steady condition exhibits asymmetry towards the rear face. At 390° and 393°, unsteady cases depict asymmetry towards the front face and the steady case depicts asymmetry towards the rear face prior to all cases presenting symmetric static temperature at 400°. Overall at high operating speed, it is observed that there is no influence on the imbalance of static temperature along the radial direction of the cross-section profiles inside the centrifugal compressor volute between the two instances. With respect to the axial direction however, the only influence on the imbalance of static temperature between the two instances is exhibited at 270°. Aside from this, there is also no influence on the imbalance of static temperature between the two instances along the axial direction. Furthermore, between the steady response and the two unsteady responses, there is a prominent influence on the imbalance of static temperature presented at 45° along the radial direction and upstream of 180° along the axial direction. Aside from this, there is only a slight influence on the imbalance of static temperature between the steady response and the two unsteady responses along both, radial direction and axial direction. More detailed graphical representations are depicted in APPENDIX 3.

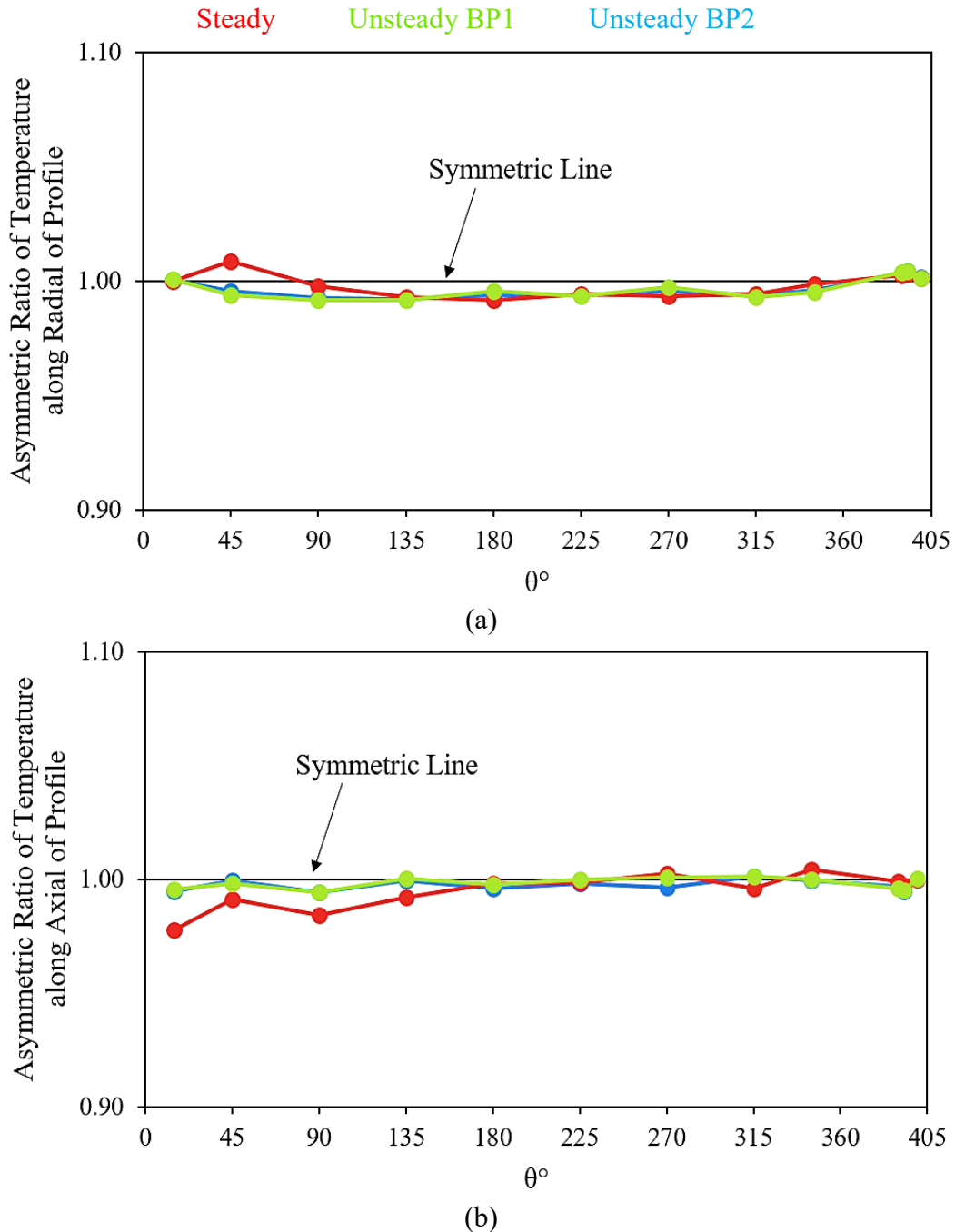


Figure 5.27 Asymmetric Ratio of Steady and Unsteady Static Temperature around the Centrifugal Compressor Volute at the operating speed of 98.2rps/ $\sqrt{K}$  along the (a) Radial of the profiles and (b) Axial of the profiles

### 5.19 Static Temperature Speed Comparison during Unsteady Conditions

Table 5.14 depicts the unsteady response of the local speed comparison, where the high operating speed of 98.2rps/ $\sqrt{K}$  is compared against the low operating speed of 58.9rps/ $\sqrt{K}$  for static temperature across each of the selected cross-section through the turbocharger compressor volute. The unsteady responses are at two instances, being at blade position 1 where the impeller blade is aligned with the volute tongue and at blade position 2, where the impeller blade has

passed the volute tongue and another impeller blade is approaching the volute tongue. It is identified there are minimal variances throughout the turbocharger compressor volute between the two instances. For both unsteady cases, static temperature increases at 98.2rps/ $\sqrt{K}$  in comparison with that at 58.9rps/ $\sqrt{K}$ . For unsteady BP1, static temperature at 98.2rps/ $\sqrt{K}$  increases its variation through the volute until 225°. Downstream from here, there are fluctuations from that depicted in the previous profile. This is also the case for unsteady BP2, except static temperature at 98.2rps/ $\sqrt{K}$  increases its variation through the volute until 270° prior to depicting fluctuations downstream from that in the previous profile. Aside from that at 393°, there are no static temperature variations between the two cases against that at 58.9rps/ $\sqrt{K}$  downstream of 315°.

*Table 5.14 Local Speed Comparison of Static Temperature Variation during Unsteady Response*

$\theta^\circ$	Static Temperature [%]	
	Unsteady BP1	Unsteady BP2
15	21.0	21.1
45	21.4	21.6
90	21.9	22.0
135	22.4	22.3
180	22.6	22.7
225	23.0	22.8
270	22.9	23.1
315	23.0	23.0
345	22.7	22.7
390	23.1	23.1
393	23.1	23.2
400	21.8	21.8

## 5.20 Summary

This chapter has numerically investigated the instantaneous responses of the turbocharger compressor stage and its volute using CFD techniques. This section has employed Sliding Mesh techniques using CFD to investigate and thoroughly understand some of the aerodynamic flow characteristics inside the turbocharger compressor stage and its volute when the blade is aligned with the tongue and when the tongue is in between two blades. This extensively detailed investigation enables one to better understand the flow mechanics and to use these findings gathered from this section to provide improvements during experimentation and during the

design process. For example, during experimentation, the presented flow structures are difficult to capture, therefore a control section can be installed at the presented locations. During the design process, determining the strengths and weaknesses of flow behaviour inside the volute can be used to set a foundation to design an improved turbocharger compressor volute to real operating conditions. From detailed analyses carried out on the aerodynamic flow characteristics of the turbocharger compressor stage and through its volute, the findings of the presented results are summarised:

- The isentropic efficiency is overestimated in comparison with the experiment data and the steady case, which could be a result of incurred numerical errors.
- Both globally and locally, there are negligible variations between the two instances. This is because the centrifugal compressor employed in the presented study has a vaneless diffuser between the impeller and the volute. Further to this, both operating speeds are relatively high in this case compared to that of fans and pumps thus, capturing these effects is challenging. Studies for Meakhail and Park (2005) also obtained poor quantitative unsteady results when studying the interaction between impeller, vaned diffuser and volute in a centrifugal fan and required improved to capture true transient interaction [76].
- The asymmetric ratio for static pressure along the radial direction is predominantly asymmetric towards the outer curve at both operating speeds. Static pressure along the axial direction is almost symmetric at low operating speed and is asymmetric towards the rear face downstream to  $225^\circ$ , prior to depicting asymmetry towards the front face downstream to the outlet at high operating speed.
- At low operating speed, there is no influence on the imbalance of static pressure along the radial direction between the two instances; the only influence on the imbalance of static pressure along the axial direction is presented at the first profile downstream of the tongue; and only a slight influence on the imbalance of static pressure is identified between the steady response and the two unsteady responses along both directions.
- At high operating speed, there is negligible influence on the imbalance of static pressure along the radial direction between the two instances; most prominent influence on the imbalance of static pressure along the axial direction is presented between  $180^\circ$  and  $270^\circ$ ; minor influence on the imbalance of static pressure is seen between the steady response and the two unsteady responses along the radial direction; and these influence of imbalances are more prominent along the axial direction.

- The asymmetric ratio for velocity magnitude along the radial direction is predominantly asymmetric towards the inner curve for both operating speeds. Velocity magnitude along the axial direction is asymmetric towards the rear face for all cases at low operating speed; is asymmetric towards the rear face for the steady case at high operating speed; and is asymmetric towards the front face for both instantaneous cases at high operating speed.
- At low operating speed, the only influence on the imbalance of velocity magnitude along the radial direction is at  $45^\circ$  between the two instances; there is no influence on the imbalance of velocity magnitude along the axial direction between the two instances; and there is a significant influence on the imbalance of velocity magnitude between the steady response and the two unsteady responses along both directions.
- At high operating speed, there is a prominent influence on the imbalance of velocity magnitude along the radial direction at  $270^\circ$  between the two instances; there is predominantly only a slight influence on the imbalance of velocity magnitude between the two instances along both directions; and there is a significant influence on the imbalance of velocity magnitude between the steady response and the two unsteady responses along both directions.
- The asymmetric ratio for static temperature along the radial direction is predominantly asymmetric towards the outer curve for both operating speeds. Static temperature along the axial direction is predominantly symmetric at low operating speed and asymmetric towards the front face for all cases at high operating speed.
- At low operating speed, there is no an influence on the imbalance of static temperature along the radial direction or the axial direction between the two instances; there is only a slight, if not negligible, influence on the imbalance of static temperature between the steady response and the two unsteady responses along both directions.
- At high operating speed, there is no influence on the imbalance of static temperature along the radial direction between the two instances; the only influence on the imbalance of static temperature along the axial direction between the two instances is at  $270^\circ$ ; there is a prominent influence on the imbalance of static temperature between the steady response and the two unsteady responses at  $45^\circ$  along the radial direction and upstream of  $180^\circ$  along the axial direction.
- The extent of secondary flows inside the centrifugal compressor volute is not a predominant function of impeller blade position with respect to the volute tongue.



The conducted analyses provides sufficient knowledge the local performance indicators offers the global performance indicators for the volute and the turbocharger compressor stage. Given the information collated, the next section presents the design methodology for the turbocharger compressor volute for both, symmetric and asymmetric volute types. Steady and instantaneous investigations have been carried out and the existing volute has been compared against the newly designed centrifugal compressor volute.

## CHAPTER 6

# DESIGN METHODOLOGY FOR A TURBOCHARGER COMPRESSOR VOLUTE

---

This chapter sheds light onto the journey that discovers the approach taken for designing a volute. This section explores the design methodology for various symmetric and asymmetric volute cross-sections, which includes that designed to ideal conditions neglecting frictional effects and that designed to actual conditions where frictional effects are incorporated into the compressor volute design methodology. This methodology has been used to finally design an asymmetric type compressor volute, which is evaluated against the baseline geometry during steady conditions discussed for the design flow in Chapter 4; and instantaneous conditions similar to Chapter 5 however, in this chapter, the two instances are the maximum and minimum flow variations with respect to the revolution averaged.

## 6.1 Centrifugal Compressor Volute Design Methodology

Design practices of a turbomachine volute has been extensively and thoroughly investigated in detail in Chapter 1 and Chapter 2. This is in order to understand the basic principles and aerodynamic flow characteristics involved to facilitate in the development of deriving a realistic expression, which has not yet been established. This section presents the design methodology for the centrifugal compressor volutes designed to ideal conditions, where frictional effects have been neglected and designed to actual conditions, where frictional effects incorporated into the expression employed to develop the centrifugal compressor volute. These have been applied into practice with the same compressor stage to numerically understand the difference in flow structure and behaviour.

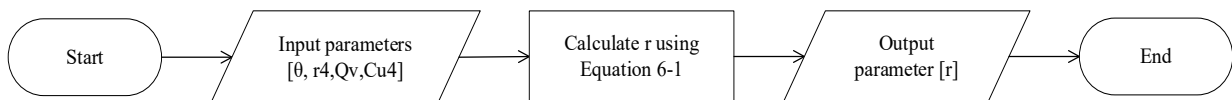
### 6.1.1 Symmetric Volute Design Approximation Neglecting Friction

Initiating from the foundation, most common existing volute design methodology is defined by Eck (1973) [24]. Eck derived an approximation for symmetric circular cross-section volute design that neglects friction. This expression identifies the radius of the spiral passage profile as a function of the azimuth angle, meaning that as the spiral passage wraps further round, its profile radius increases proportionally. This approximation is given by:

$$r = \sqrt{\frac{\theta r_c q_v}{360\pi C_{u4} r_4} - \left(\frac{\theta q_v}{720\pi C_{u4} r_4}\right)^2}$$

*Equation 6.1 Eck's Frictionless Symmetric Circular Volute Design Approximation*

The assumptions of this equation are discussed by Mojaddam et al. (2012) (2013) [1, 51] in Section 2.3. The application of this approximation follows the process depicted in Figure 6.1. It is necessary for the user to specify some parameters in the equation prior to achieving the output parameter. In this case, numerical investigation of the baseline model had been used to extract the input parameters of the volume flow rate through the volute, denoted by  $q_v$  and the tangential velocity at the volute inlet, denoted by  $C_{u4}$ . The radius of the volute inlet denoted by  $r_4$  is fixed by the radius of the diffuser outlet.



*Figure 6.1 Process chart for the application of Eck's volute design approximation*

Figure 6.1 depicts the flow chart which visually represents the start to finish process of applying Equation 6.1 into practice. This identifies the input parameters in the expression

required for the calculation process using Equation 6.1, which in turn provides an output parameter required for the next stage of the calculation process until the result is achieved. This is repeated to determine the radius from  $\theta = 0^\circ$  to  $360^\circ$ .

Following this process in applying Eck's volute design approximation for symmetric circular cross-section volutes, the meanline as shown in Figure 6.2 is generated. This geometry is imported into a modelling software, namely SolidWorks, where the meanline is used as the centre point for generating the profiles for the scroll, appropriately at numerous azimuth angles around the volute.

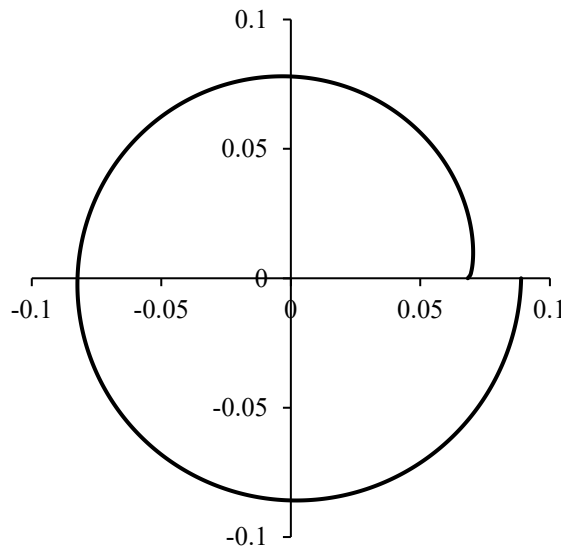


Figure 6.2 Volute Design Methodology using Eck's Volute Design Approximation

Ayder (1993) reported that the symmetric elliptical volute cross-section shape is more efficient [1, 2]. Therefore, following on from Eck based on Equation 6.1, Baker (2018) [77] derived an approximation for a volute with elliptical cross-section profiles, which is defined by Equation 6.2. In order to make the area as close as possible to the symmetric circular profile for a valid evaluation, the a:b ratio for the ellipse had been specified as 3:2 and 2:3 as depicted in Figure 6.3.

$$\frac{2b}{r_4 k} = \varphi \pm 2\sqrt{\frac{\varphi}{k}}$$

Equation 6.2 Baker's Elliptical Volute Design Approximation

Where,  $\varphi$  is that defined in Equation 6.1.

$$k = b/a$$

Equation 6.3 Elliptical Ratio

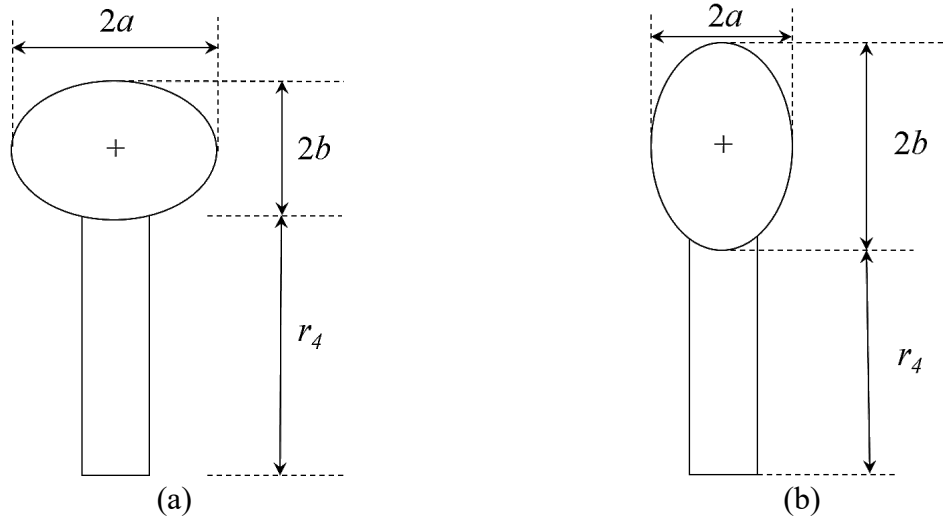


Figure 6.3 Symmetric Elliptical Volute Cross-Section where (a) is Elliptical 3:2 and (b) is Elliptical 2:3

The process of applying this design methodology is presented in Figure 6.4.

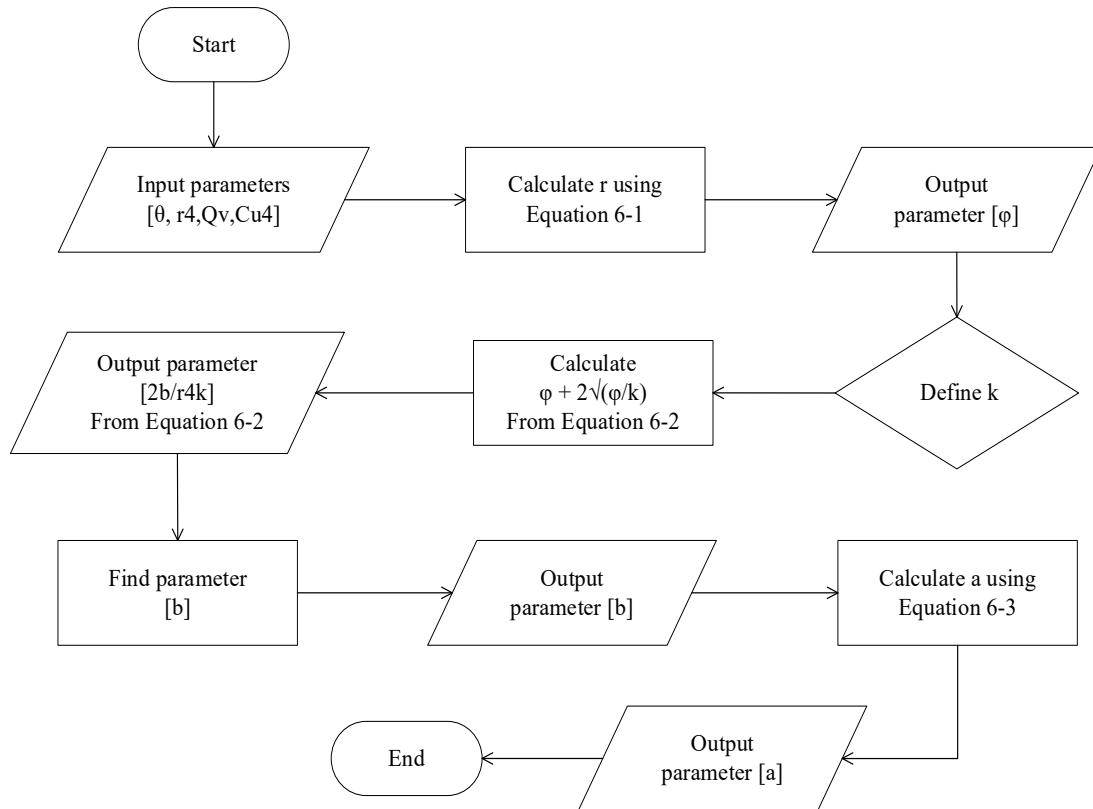


Figure 6.4 Process chart for the application of Baker's volute design approximation

These approximations are derived for ideal conditions where frictional effects are not considered and the results obtained neglect frictional losses. Even though studies have been carried out on volute design considering frictional effects, such as that of Mojaddam et al. [1] and Rezaei [17], no realistic expressions have been established in literature to the authors knowledge in the centrifugal compressor volute design methodology. Equation 6.1 had been derived for fans, however this approximation has been widely employed for pumps and

compressors. Centrifugal systems that have larger volutes such as fans and pumps have negligible frictional effect and can afford to ignore this parameter. Conversely, compressors especially those operating at high pressure conditions, have a much narrower volute passage where frictional effects are highly important and hence cannot be ignored in any calculations [24].

Applications of these expressions are illustrated in APPENDIX 5 and volute models created using these expressions are illustrated APPENDIX 6.

### 6.1.2 Symmetric Volute Design Approximation Incorporating Friction

Skin friction are the highest cause of losses within the centrifugal compressor [78]. These losses in the volute manifest as total pressure loss (pressure drop) or as entropy gain in the direction of flow, meaning that this fall in energy will take place at the volute origin, i.e.  $\theta = 0^\circ$ . The volute is designed to ensure that static pressure remains constant over the periphery of the impeller. The periodic pressure fluctuations that transpire in the impeller causes unsteady flow, hence it is assumed that impeller losses will increase. There are two effects that friction has in the volute:

- (1) Frictional head loss in the volute (fall in energy)
- (2) Flow reduction through the impeller as an effect of unsteady static pressure at the impeller periphery.

These can be overcome by slightly increasing the cross-sectional area of the volute. The volute design considering friction is based on the principles of [1, 17, 24, 51]:

- (1) Continuity:

$$C_{(1)}A_{(1)} = C_{(2)}A_{(2)}$$

*Equation 6.4 Volute Design Principle of Continuity*

- (2) Energy Equation:

$$\frac{P_{(1)}}{\rho g} + \frac{C_{(1)}^2}{2g} = \frac{P_{(2)}}{\rho g} + \frac{C_{(2)}^2}{2g} + h$$

*Equation 6.5 Volute Design Principle of Energy Equation*

In order to compensate for the pressure loss due to frictional effects, it is assumed that there pressure will be the same [1, 24].

(3) Friction Head Loss:

The effect of friction resulting pressure loss is approximated using Equation 6.6.

$$dh = \frac{c_f C^2 dL}{2gD_h}$$

*Equation 6.6 Volute Design Principle of Friction Head Loss*

Using the principles in Equation 6.4, Equation 6.5 and Equation 6.6 under the assumptions stated, gives Equation 6.7:

$$\Delta h = \frac{C_{(1)}^2}{2g} \left[ 1 - \left( \frac{A_{(1)}}{A_{(2)}} \right)^2 \right]$$

*Equation 6.7 Volute Design Principle of Head Loss*

From this, the approximation for symmetric circular cross-section volute design incorporating friction as a parameter has been derived giving Equation 6.8:

$$r' = \frac{rC_{av}}{\sqrt{C_{av}^2 - 2gh}}$$

*Equation 6.8 Symmetric Circular Cross-Section Volute Design Expression Incorporating Friction*

Where h is computed from Equation 1.27, where  $L_{eq}$  and D from Equation 1.28 is computed from in APPENDIX 7 and APPENDIX 8, respectively; r is computed from Equation 6.1; and  $C_{av}$  is obtained from the numerical simulation of the symmetric circular cross-sectioned volute designed using Equation 6.1.

When considering friction into the calculation for volute design, new quantities of fluid are introduced into the volute cross-sectional area, as well as through-flow velocity distribution following other laws. Within the volute, the flow slows down and follows a spiral path meaning the curvature of the volute inlet produces disturbances. Where streamlines are curved and flow is decelerates in a duct, secondary flow transpires. The streamlines are steeper at the centre of the volute cross-section than at the boundaries and the path of each fluid particle during secondary flow elongates, having a greater average velocity than without secondary flow. Consequently, the influence of friction on the volute is much larger than calculations solely based on the mean velocities. There is greater centrifugal force through the centre of the volute profiles than at the sides due to the fluid particles in the freestream, having greater flow

velocity than that decelerated at the walls of the duct as a result of friction. These fluid particles are vigorously pushed outwards whilst at the exit cone, a double vortex transpires superimposing on the main flow causing a significant separation of the central layer of flow, predominantly that entering the exit cone sector of the volute [24]. The process of applying this design methodology is presented in Figure 6.5.

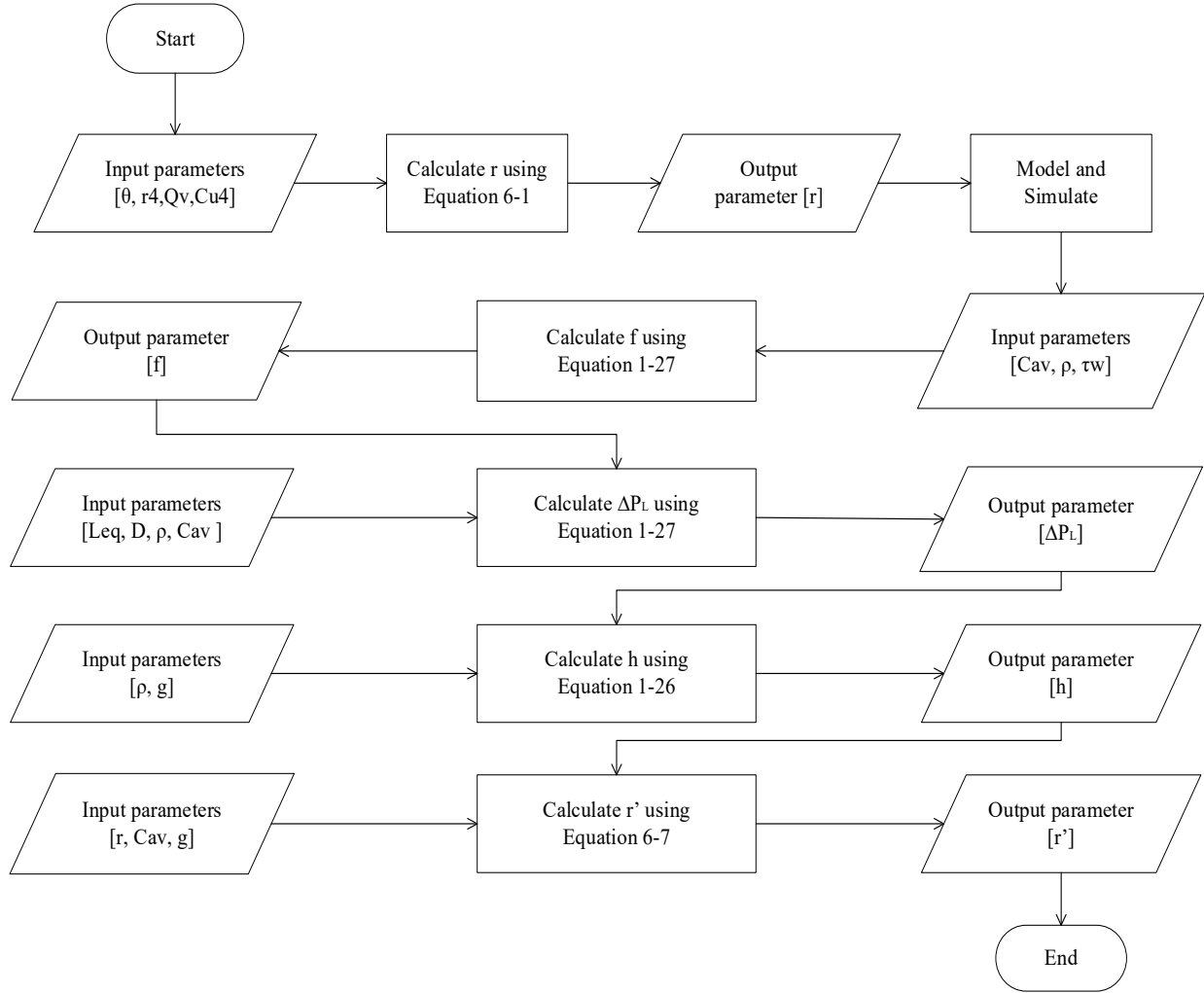


Figure 6.5 Process Flow Chart for the Application of Symmetric Circular Cross-Section Volute Design  
Incorporating Friction

For the elliptical cross-sections, the friction incorporated expression is given by:

$$a' = \frac{aC_{av}}{\sqrt{C_{av}^2 - 2gh}} \quad b' = \frac{bC_{av}}{\sqrt{C_{av}^2 - 2gh}}$$

Equation 6.9 Symmetric Elliptical Cross-Section Volute Design Expression Incorporating Friction



The process of applying this design methodology is presented in Figure 6.6.

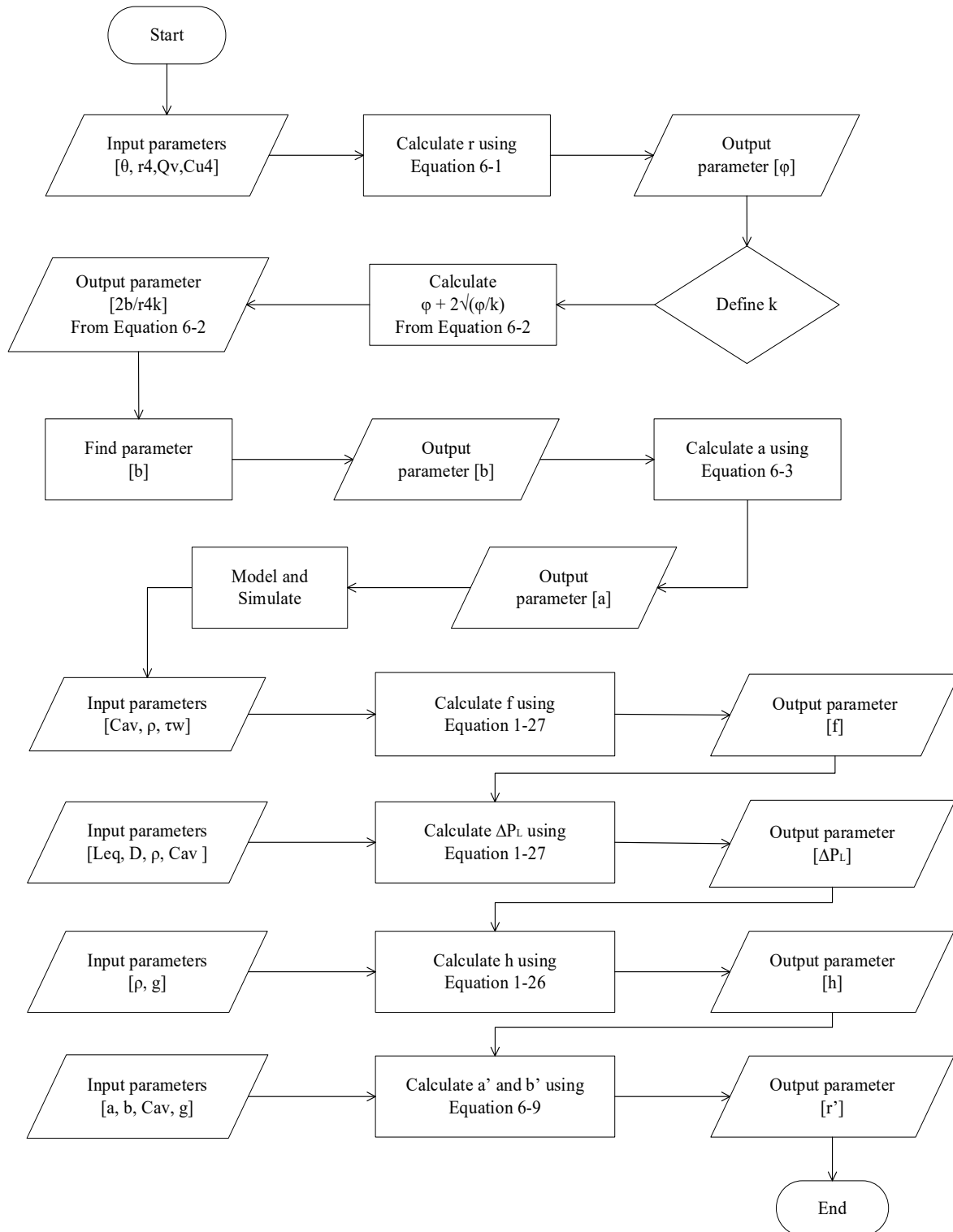


Figure 6.6 Process Flow Chart for the Application of Symmetric Elliptical Cross-Section Volute Design Incorporating Friction

Applications of these expressions are illustrated in APPENDIX 5 and volute models created using these expressions are illustrated in APPENDIX 6.

### 6.1.3 Asymmetric Volute Design Approximation

In order to grasp the foundations of volute design, symmetric type volutes with various cross-sections are explored. From here, the next step is to develop a design methodology for the asymmetric type volute since the existing volute is also asymmetric. The asymmetric type volute has been proven to perform more efficiently than the symmetric type volute due to having lower loss coefficient. The double vortex in the symmetric type volute results in significant separation, predominantly with the inflow to the discharge duct, hence Oosterlen (1935) proposed the asymmetric volute. The experimental findings verified the single vortex inside the asymmetric volute had significantly lower losses and some undesired separation had been avoided [24, 79]. For this reason, the asymmetric type volute is more commonly used and the design of this is defined by:

$$r^* = r'e^{k\theta}$$

*Equation 6.10 Baker's Asymmetric Volute Design Approximation*

Where k is the constant and is defined by:

$$k = \frac{1}{(2\pi)} \ln \left[ \left( \frac{b_4}{r'} \right) + 1 \right]$$

*Equation 6.11 Baker's Asymmetric Volute Design Approximation Constant Parameter*

Similar to the elliptical cross-sections, this generates cross-section profiles. The process of applying this design methodology is presented in Figure 6.7.

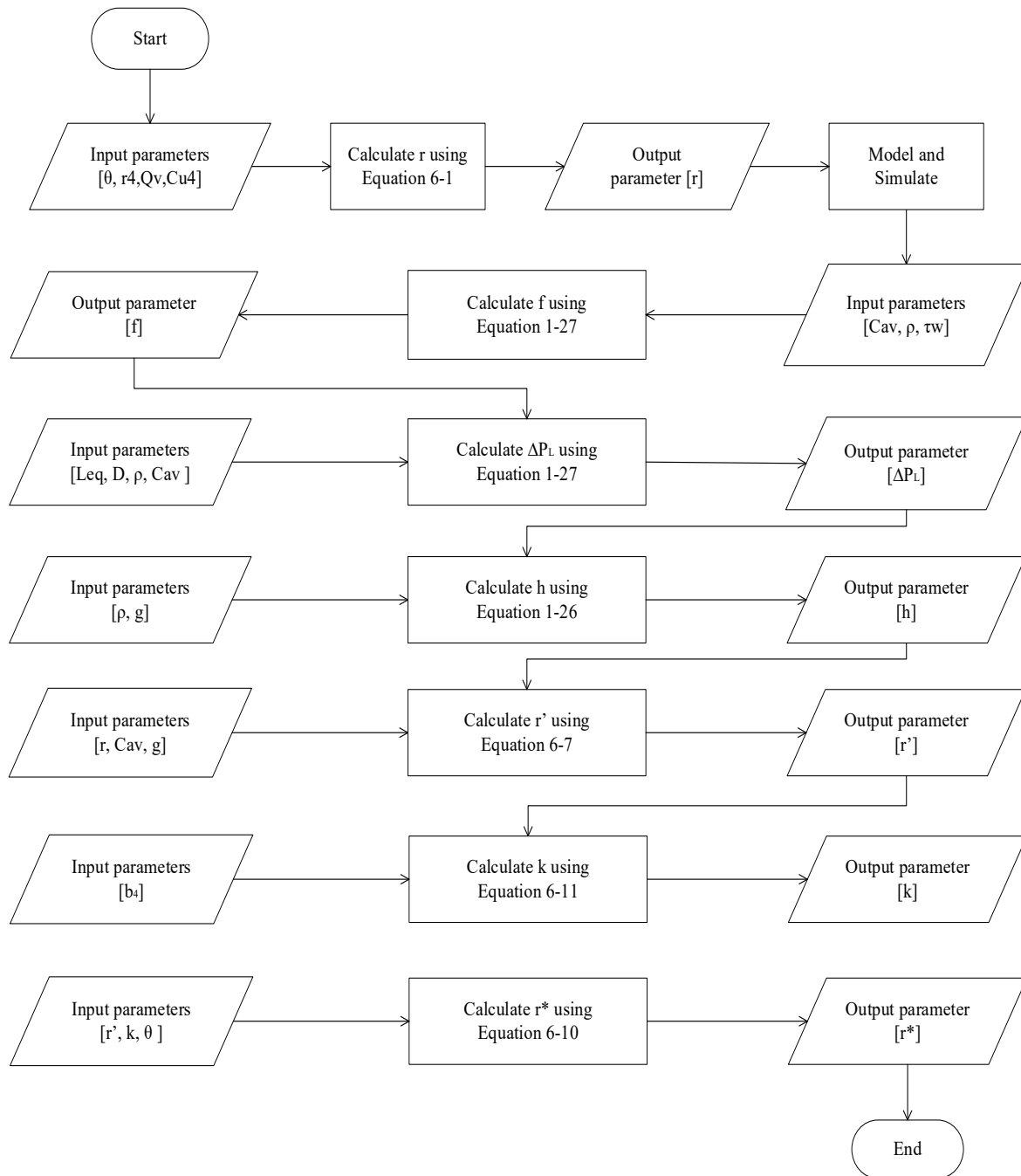


Figure 6.7 Process Flow Chart for the Application of Asymmetric Circular Cross-Section Volute Design Incorporating Friction

The application of this expression is illustrated APPENDIX 5 and the volute model created using this expression is illustrated in APPENDIX 6.

## 6.2 Centrifugal Compressor Volute Investigation Details

This section places the aforementioned calculations and research collated into practice for volute design. The following investigates the effect of volute designed neglecting friction and incorporating friction. Six different symmetric type volutes have been designed in order to investigate the frictional effects within centrifugal compressors. Additionally, one asymmetric volute incorporating frictional effects in its design has been developed in order to compare and evaluate this with that which currently exists, analysed in the previous two chapters. Details of these models are given in Table 6.1.

*Table 6.1 Details of the Investigated Centrifugal Compressor Volute Models*

TYPE	CROSS-SECTION	EXPRESSION	FRICTIONAL EFFECTS
Symmetric	Circular	Equation 6.1	No
Symmetric	Elliptical 3:2	Equation 6.2	No
Symmetric	Elliptical 2:3	Equation 6.2	No
Symmetric	Circular	Equation 6.8	Yes
Symmetric	Elliptical 3:2	Equation 6.9	Yes
Symmetric	Elliptical 2:3	Equation 6.9	Yes
Asymmetric	Circular	Equation 6.10	Yes

The ideal models are referred to those which have been designed to neglect frictional effects, while the actual models are referred to those which have been designed to incorporate frictional effects, providing a realistic expression for designing the centrifugal compressor volute.

The volute has been cut off at  $330^\circ$  in compliance with Lüdtke (2004) due to the lack of space for the volute to wrap around. From this cut-off, the geometric modelling of the exit cone to the outlet has followed the same procedure for all models, in terms of the angles and distances specified in order to maintain consistency between both models, for the new profiles to be generated. These new profiles within the exit cone increases significantly in area compared to the scroll. Due to the nature of the cross-section shape, the first profile after the tongue and the geometry downstream of the cut-off are located at different azimuth angles for each model. Extended inlet and outlet pipes had been extruded from the inlet duct and discharge duct, respectively, in accordance with that aforementioned in section 3.2.1 Geometry.

### 6.3 Global Performance Evaluation of the Symmetric Type Volute for Centrifugal Compressor

This section presents the performance of the turbocharger compressor stage and its symmetric type volute across low operating speed of 58.9 rps/ $\sqrt{K}$  and high operating speed of 98.2 rps/ $\sqrt{K}$  at high, design and low flow rates. The emphasis in the following sections are to characterise the flow features where losses are present and must be accounted for by incorporating this into the design process. Since the volute is designed to the best efficiency design point at high operating speed, it has been selected to carry out flow field investigations through the components of the turbocharger compressor stage have also been presented.

#### 6.3.1 Turbocharger Compressor and Volute Performance with Symmetric Type Volumes

Table 6.2 details the total-to-total pressure ratio (PR) and the isentropic efficiency ( $\eta$ ) of the turbocharger compressor stage, which provides information on the system performance. Table 6.2 also details the total pressure loss coefficient ( $K_p$ ) and static pressure recovery coefficient ( $C_p$ ) of the volute, which provides information on the component performance. Although the volute had been design to the design flow at 98.2 rps/ $\sqrt{K}$ , this sector of the investigation has been carried out across low operating speed of 58.9 rps/ $\sqrt{K}$  and high operating speed of 98.2 rps/ $\sqrt{K}$  at high, design and low flow rates. This is to gain a clear understanding of how these various cross-sections behave over a wide range of mass flow rates. The results comprise of the compressor volute designed to ideal conditions; where the effects of friction are not considered in the expressions employed to design the compressor volute, and of the compressor volute designed to actual conditions; where the effects of friction are incorporated in the expressions employed to design the compressor volute. Results in Table 6.2 identify the ellipse 2:3 cross-section shapes have the highest centrifugal compressor isentropic efficiency, which occurs at design flow of 58.9 rps/ $\sqrt{K}$  operating speed for the volute designed to both, ideal and actual conditions. The volute designed to actual conditions depicts higher isentropic efficiency results. The lowest centrifugal compressor performance occurs at low flow of 58.9 rps/ $\sqrt{K}$  operating speed for the volute designed to actual conditions with all cross-sections. For the volute designed to ideal conditions, the lowest centrifugal compressor performance occurs only with the ellipse 3:2 cross-section shape and remains to be slightly higher than that designed to actual conditions. The highest total pressure loss occurs at high flow of 58.9 rps/ $\sqrt{K}$  operating speed for the volute designed to both, ideal and actual conditions with ellipse 3:2 cross-section shape. The volute designed to ideal conditions depicts higher total pressure loss. The lowest total pressure loss occurs at low flow of 58.9 rps/ $\sqrt{K}$  for the circular cross-section shape regarding

the volute designed to ideal conditions and for the ellipse 2:3 cross-section shape regarding the volute designed to actual conditions. The highest static pressure recovery occurs at low flow of 58.9 rps/ $\sqrt{K}$  operating speed for volutes designed to both, ideal and actual conditions with the circular and ellipse 2:3 cross-section shapes. Additionally, the ellipse 2:3 cross-section shape also depicts highest static pressure recovery at 98.2 rps/ $\sqrt{K}$  operating speed. The lowest static pressure recovery occurs at high flow of 58.9 rps/ $\sqrt{K}$  operating speed for volutes designed to both, ideal and actual conditions with the ellipse 3:2 cross-section shapes. With respect to the static pressure recovery through the compressor volute against the total pressure loss, it is noticed at low flow of 58.9 rps/ $\sqrt{K}$  operating speed, the volute designed to ideal conditions show improved recovery against that which is lost for the circular cross-section shape, while the volute designed to actual conditions show improved recovery against that which is lost for the ellipse 2:3 cross-section shape.

Table 6.2 Compressor and Volute Performance of various Symmetric Cross-Sections Designed to Ideal and Actual Conditions

Cross-Section Shape	Speed [rps/ $\sqrt{K}$ ]	Flow Rate	VOLUTE DESIGN TO IDEAL CONDITIONS				VOLUTE DESIGN TO ACTUAL CONDITIONS			
			Compressor Performance		Volute Performance		Compressor Performance		Volute Performance	
			PR [T-T]	$\eta$ [%]	Kp	Cp	PR [T-T]	$\eta$ [%]	Kp	Cp
Circular	58.9	High	1.3	64	0.8	-0.2	1.3	65	0.8	-0.2
		Design	1.5	79	0.5	0.3	1.5	79	0.5	0.3
		Low	1.6	59	0.3	0.6	1.6	56	0.4	0.6
	98.2	High	2.1	64	0.8	-0.1	2.1	66	0.8	-0.1
		Design	2.7	79	0.5	0.4	2.7	78	0.5	0.4
		Low	2.9	66	0.4	0.5	2.8	65	0.4	0.5
Ellipse 2:3	58.9	High	1.3	64	0.8	-0.2	1.3	66	0.7	-0.2
		Design	1.5	81	0.4	0.4	1.5	82	0.4	0.4
		Low	1.6	58	0.4	0.6	1.6	56	0.3	0.6
	98.2	High	2.0	62	0.6	0.1	2.2	67	0.6	0.0
		Design	2.7	80	0.4	0.4	2.7	80	0.4	0.5
		Low	2.9	70	0.4	0.6	2.9	66	0.4	0.6
Ellipse 3:2	58.9	High	1.3	61	1.0	-0.4	1.3	62	0.9	-0.4
		Design	1.5	80	0.5	0.3	1.5	80	0.5	0.3
		Low	1.6	57	0.4	0.5	1.6	56	0.5	0.5
	98.2	High	2.1	65	0.8	-0.2	2.2	66	0.8	-0.1
		Design	2.7	78	0.5	0.4	2.7	78	0.5	0.3
		Low	2.9	67	0.4	0.5	2.9	65	0.4	0.5

Onwards from here, the focus is solely on that simulated at the design point at which all the models have been designed to, namely, at the operating speed of 98.2 rps/ $\sqrt{K}$  at design flow.

### 6.3.2 Global Static Pressure through Symmetric Type Volute

Figure 6.8 depicts the static pressure at (a) the inlet and (b) the outlet of each of the components in the turbocharger compressor stage. It can be seen that static pressure decreases slightly at the outlet of the inducer from the inlet, while downstream components increase in static pressure at the outlet from the inlet. The most significant increase in outlet static pressure from the inlet static pressure is at the impeller. In Figure 6.8 (a), minimal static pressure variations at the inlet is depicted between the ideal and actual cases at the inducer and impeller, however at the diffuser and volute, these variations are more prominent. In Figure 6.8 (b), minimal static pressure variations at the outlet is depicted between the ideal and actual cases at the inducer and volute, however at the impeller and diffuser, these variations are more prominent.

Table 6.3 details static pressure difference in the volutes designed to actual conditions against volutes designed to ideal conditions. At the inlet, it can be observed the highest variations occur in the diffuser for ellipse 3:2 cross-section shape, where the volute designed to actual conditions identifies 0.5% increase in static pressure compared to that depicted for the volute designed to ideal conditions. For the ellipse 2:3 cross-section shape, there is 0.2% static pressure decrease in the inducer and impeller for the volute designed to actual conditions compared to that depicted for the volute designed to ideal conditions. At the outlet, it can be observed the highest variations occur in the impeller for the ellipse 3:2 cross-section shape where the volute designed to actual conditions identifies 0.5% increase in static pressure compared to that depicted for the volute designed to ideal conditions. For the ellipse 2:3 cross-section shape, there is 0.2% decrease in static pressure at the inducer for the volute designed to actual conditions compared to that depicted for the volute designed to ideal conditions. The highest static pressure variation through the component between the inlet and outlet occurs in the volute for ellipse 3:2 cross-section shape. This depicts 4.5% static pressure decrease for the volute designed to actual conditions compared to that depicted for the volute designed to ideal conditions. Furthermore, there is a static pressure increase of 1.9% for the ellipse 2:3 cross-section shape in volute designed to actual conditions compared to that depicted for the volute designed to ideal conditions.

■ Ideal Circular ■ Ideal Ellipse 2:3 ■ Ideal Ellipse 3:2 ■ Actual Circular ■ Actual Ellipse 2:3 ■ Actual Ellipse 3:2

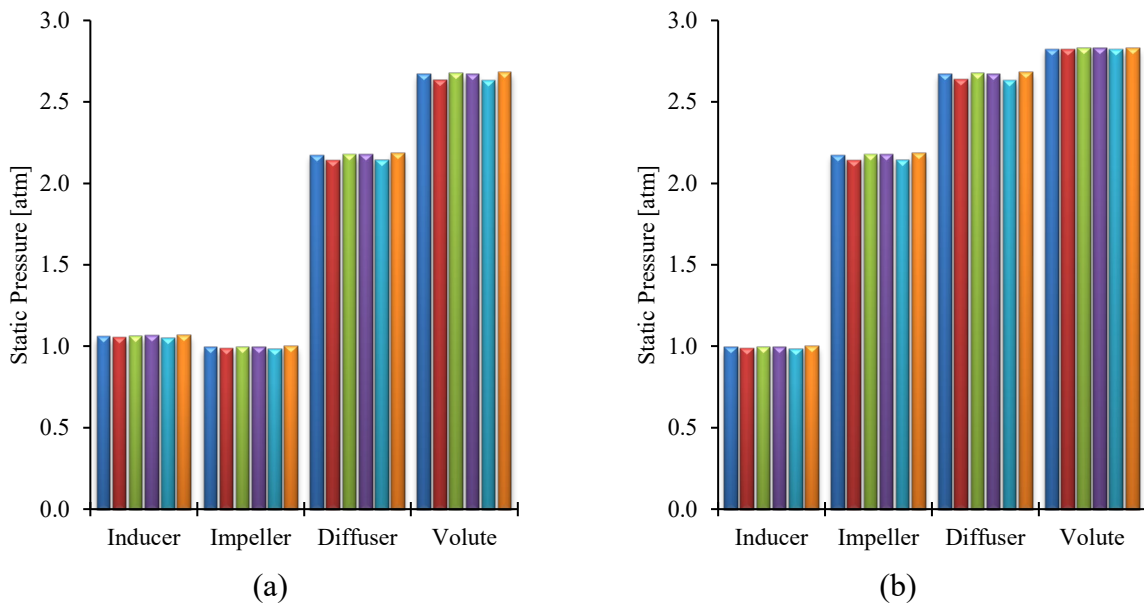


Figure 6.8 Static pressure at (a) inlet and (b) outlet of each station in the turbocharger compressor stage

Table 6.3 Static Pressure Variation of volute designed to actual conditions against volute designed to ideal conditions

Component	Inlet Static Pressure Variation [%]			Outlet Static Pressure Variation [%]			Static Pressure Variation [%]		
	Circular	Ellipse 2:3	Ellipse 3:2	Circular	Ellipse 2:3	Ellipse 3:2	Circular	Ellipse 2:3	Ellipse 3:2
Inducer	0.4	-0.2	0.3	0.4	-0.2	0.3	0.1	-0.4	0.0
Impeller	0.4	-0.2	0.3	0.2	0.0	0.5	0.0	0.2	0.6
Diffuser	0.2	0.0	0.5	0.0	-0.1	0.3	-0.9	-0.8	-0.7
Volute	0.0	-0.1	0.3	0.0	0.0	0.0	1.2	1.9	-4.5

### 6.3.3 Global Velocity Magnitude through Symmetric Type Volute

Figure 6.9 depicts the velocity magnitude at (a) the inlet and (b) the outlet of each of the components in the turbocharger compressor stage. It can be seen that velocity magnitude increases at the outlet of the inducer and impeller from the inlet, while downstream components decrease in velocity magnitude at the outlet from the inlet. In Figure 6.9 (a), minimal velocity magnitude variations at the inlet of the impeller is depicted between the ideal and actual cases, however these variations are more prominent at the inducer. In Figure 6.9 (b), minimal velocity magnitude variations at the outlet is depicted between the ideal and actual cases at the inducer, however these variations are more prominent in the volute.

Table 6.4 details velocity magnitude difference in the volutes designed to actual conditions against volutes designed to ideal conditions. At the inlet, it can be observed the highest variations occur in the volute for the ellipse 3:2 cross-section shape where the volute designed



to actual condition identifies 0.5% velocity magnitude increase compared to that depicted for the volute designed to ideal conditions. For the circular cross-section shape, there is 0.4% velocity magnitude decrease in the inducer for the volute designed to actual condition compared to that depicted for the volute designed to ideal conditions. At the outlet, it can be observed the highest variations occur in the volute for the ellipse 2:3 cross-section shape where the volute designed to actual conditions identifies 7.4% velocity magnitude increase compared to that depicted for the volute designed to ideal conditions. For the circular cross-section shape, there is 1% decrease in velocity magnitude for the volute designed to actual conditions compared to that depicted for the volute designed to ideal conditions. The highest velocity magnitude variation through the component between the inlet and outlet occurs in the volute for ellipse 2:3 cross-section shape. This depicts a decrease of 5.3% for the volute designed to actual conditions compared to that depicted for the volute designed to ideal conditions. Furthermore, there is 0.8% increase in velocity magnitude through the volute of the circular and ellipse 3:2 cross-section shapes for the volute designed to actual conditions compared to that depicted for the volute designed to ideal conditions.

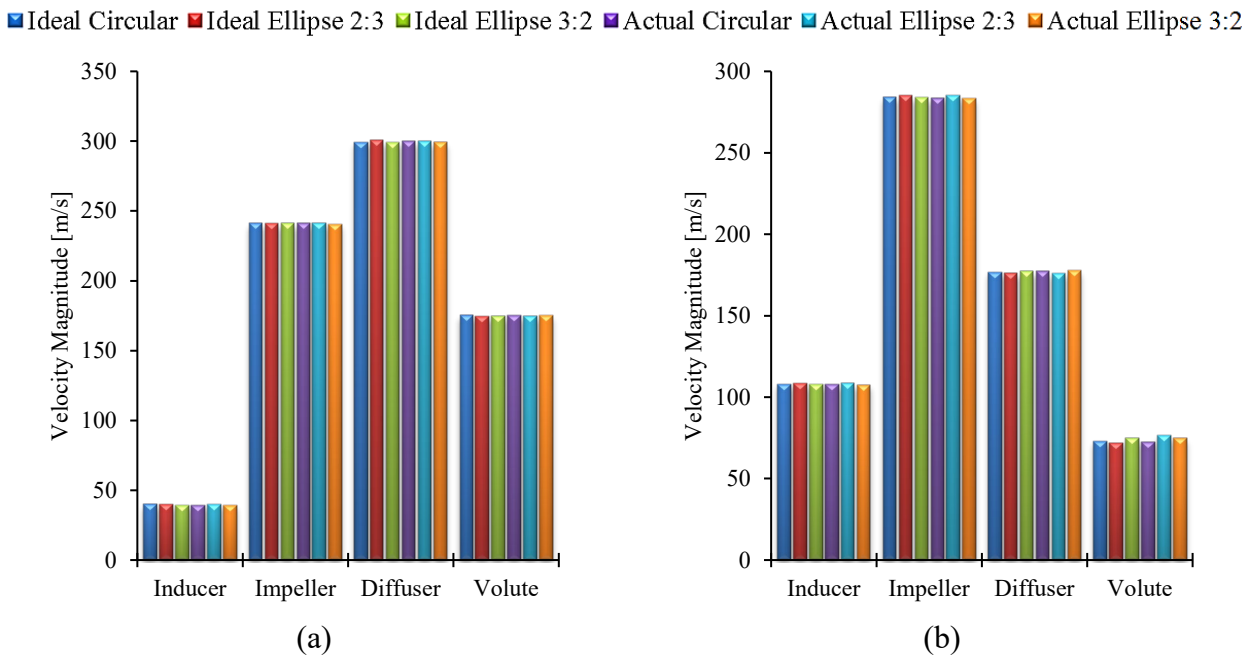


Figure 6.9 Velocity Magnitude at (a) inlet and (b) outlet of each station in the turbocharger compressor stage

Table 6.4 Velocity Magnitude Variation of volute designed to actual conditions against volute designed to ideal conditions

Component	Inlet Velocity Magnitude Variation [%]			Outlet Velocity Magnitude Variation [%]			Velocity Magnitude Variation [%]		
	Circular	Ellipse 2:3	Ellipse 3:2	Circular	Ellipse 2:3	Ellipse 3:2	Circular	Ellipse 2:3	Ellipse 3:2
Inducer	-0.4	0.2	-0.3	-0.3	0.0	-0.2	-0.2	-0.1	-0.1
Impeller	0.0	0.0	0.0	-0.1	0.1	-0.1	-0.4	0.8	-0.7
Diffuser	0.0	-0.1	-0.1	0.1	-0.1	0.4	-0.1	-0.1	-0.8
Volute	0.1	-0.1	0.5	-1.0	7.4	0.1	0.8	-5.3	0.8

#### 6.3.4 Global Static Temperature through Symmetric Type Volumes

Figure 6.10 depicts the static temperature at (a) the inlet and (b) the outlet of each of the components in the turbocharger compressor stage. It can be seen that static temperature slightly decreases at the outlet of the inducer from the inlet, while downstream components increase in static temperature at the outlet from the inlet. The most significant increase in outlet static temperature from the inlet static temperature is at the impeller. In Figure 6.10 (a) and Figure 6.10 (b), there are no or negligible static temperature variations depicted between the ideal and actual cases.

Table 6.5 details static temperature difference in the volutes designed to actual conditions against volutes designed to ideal conditions. At the inlet, it can be observed the highest variations occur in the volute for ellipse 2:3 cross-section shape, where the volute designed to actual conditions identifies 0.2% increase in static temperature compared to that depicted for the volute designed to ideal conditions. At the outlet, it can be observed the highest variations occur in the diffuser for the ellipse 2:3 cross-section shape where the volute designed to actual conditions identifies 0.2% increase in static temperature compared to that depicted for the volute designed to ideal conditions. The highest static temperature variation through the component between the inlet and outlet occurs in the volute for ellipse 2:3 cross-section shape. This depicts 4.9% static temperature decrease for the volute designed to actual conditions compared to that depicted for the volute designed to ideal conditions. Furthermore, there is a static temperature increase of 0.9% for the ellipse 3:2 cross-section shape in volute designed to actual conditions compared to that depicted for the volute designed to ideal conditions.

■ Ideal Circular ■ Ideal Ellipse 2:3 ■ Ideal Ellipse 3:2 ■ Actual Circular ■ Actual Ellipse 2:3 ■ Actual Ellipse 3:2

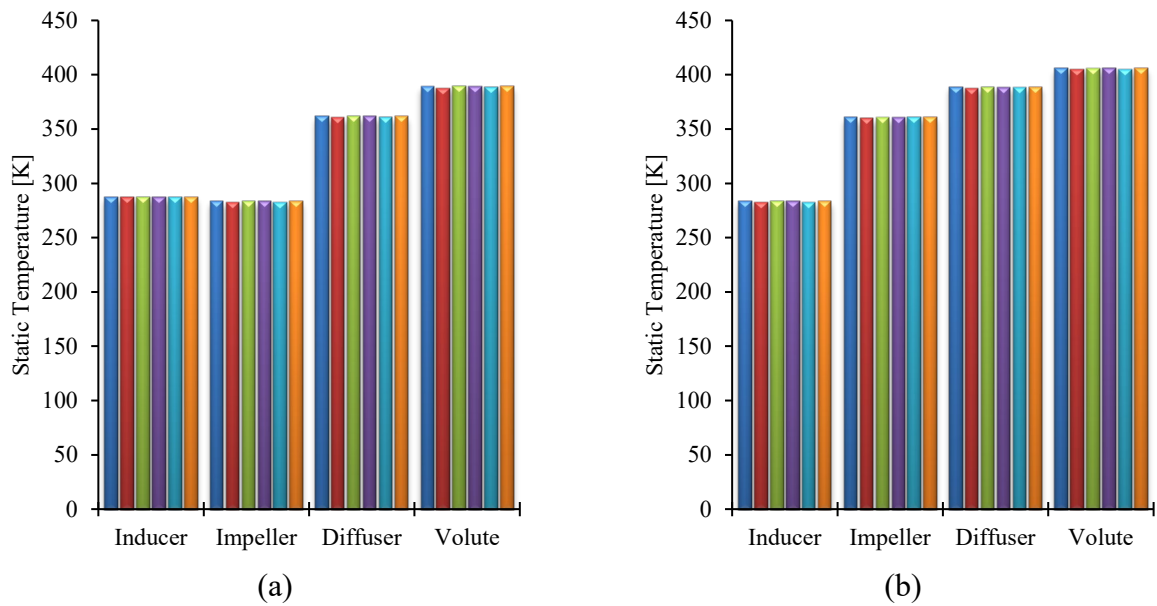


Figure 6.10 Static Temperature at (a) inlet and (b) outlet of each station in the turbocharger compressor stage

Table 6.5 Static Temperature Variation of volute designed to actual conditions against volute designed to ideal conditions

Component	Inlet Static Temperature Variation [%]			Outlet Static Temperature Variation [%]			Static Temperature Variation [%]		
	Circular	Ellipse 2:3	Ellipse 3:2	Circular	Ellipse 2:3	Ellipse 3:2	Circular	Ellipse 2:3	Ellipse 3:2
Inducer	0.0	0.0	0.0	0.0	0.0	0.0	0.0	1.1	-0.7
Impeller	0.0	0.0	0.0	0.0	0.1	0.1	-0.2	0.7	0.2
Diffuser	0.0	0.1	0.1	0.0	0.2	0.0	-0.1	1.0	-0.8
Volute	0.0	0.2	0.0	0.0	0.0	0.1	0.3	-4.9	0.9

## 6.4 Local Performance Evaluation of the Symmetric Type Volute for Centrifugal Compressor

This section explores the performance and flow behaviour inside centrifugal compressor symmetric type volutes and how various symmetric cross-sections behave against the other. Variations between volutes designed to neglect frictional effects and to that which incorporates frictional effects into its equation have been quantified.

### 6.4.1 Local Static Pressure through Symmetric Type Volutes

Figure 6.11 depicts the behaviour of static pressure through symmetric type volutes, namely, those designed to ideal conditions and those designed to actual conditions with circular, ellipse 2:3 and ellipse 3:2 cross-section shapes. In the case of volutes designed to ideal conditions with circular and ellipse 3:2 cross-section shapes, static pressure increases considerably from the

first profile to  $45^\circ$ . From here, it maintains fairly uniform to  $90^\circ$  prior to increasing at  $135^\circ$  and maintaining fairly uniform to  $330^\circ$ , where static pressure increases significantly to the outlet of the volutes. In the case of volutes designed to actual conditions with circular and ellipse 3:2 cross-section shapes, static pressure increases considerably from the first profile to  $90^\circ$ . From here, it maintains fairly uniform prior to decreasing at  $315^\circ$  to  $330^\circ$ , where static pressure significantly increases to the outlet of the volutes. For the ellipse 2:3 cross-section shape volute designed to ideal conditions, static pressure decreases from the first profile to  $90^\circ$  before increasing to  $135^\circ$ . From here to  $330^\circ$ , static pressure maintains fairly uniform prior to decreasing at  $315^\circ$  to  $330^\circ$ , where static pressure significantly increases to the outlet of the volute. For the ellipse 2:3 cross-section shape volute designed to actual conditions, static pressure increases to  $90^\circ$  from which attains reasonable uniformity to  $315^\circ$ . From here to  $330^\circ$ , static pressure decreases before increasing considerably to the outlet of the volute.

Table 6.6 details static pressure variation through symmetric type volutes from one plane to the next around the volute and the static pressure variation at each plane against that depicted at the outlet. These volutes are namely, those designed to ideal conditions and those designed to actual conditions with circular, ellipse 2:3 and ellipse 3:2 cross-section shapes. Analysing the plane to plane variation, it is identified for all volute cross-section shapes designed to ideal and actual conditions, the highest static pressure variation occurs from the cut-off location to the outlet. In the cases for the volute designed to ideal conditions, there are no static pressure variations exhibited from  $315^\circ$  to  $330^\circ$  for the cases of circular and ellipse 3:2 cross-section shapes, while ellipse 2:3 cross-section shape depicts no variation at  $135^\circ$  to  $180^\circ$ . In the cases for the volute designed to actual conditions, minimal static pressure variations are exhibited from  $270^\circ$  to  $315^\circ$  for the cases of circular and ellipse 3:2 cross-section shapes, while ellipse 2:3 cross-section shape depicts minimal variations at  $135^\circ$  to  $180^\circ$ . Analysing the static pressure variation of that depicted at the plane against that depicted at the outlet, it is identified the highest variation in the cases for the volutes designed to ideal conditions occur in the first profile with circular and ellipse 3:2 cross-section shapes, while for ellipse 2:3 cross-section shape the highest static pressure variation occurs at  $90^\circ$ . In the cases for the volute designed to actual conditions, highest static pressure variations occur in the first profile for all cross-section shapes. Further to this, lowest static pressure variations occur at  $315^\circ$  for all cases.

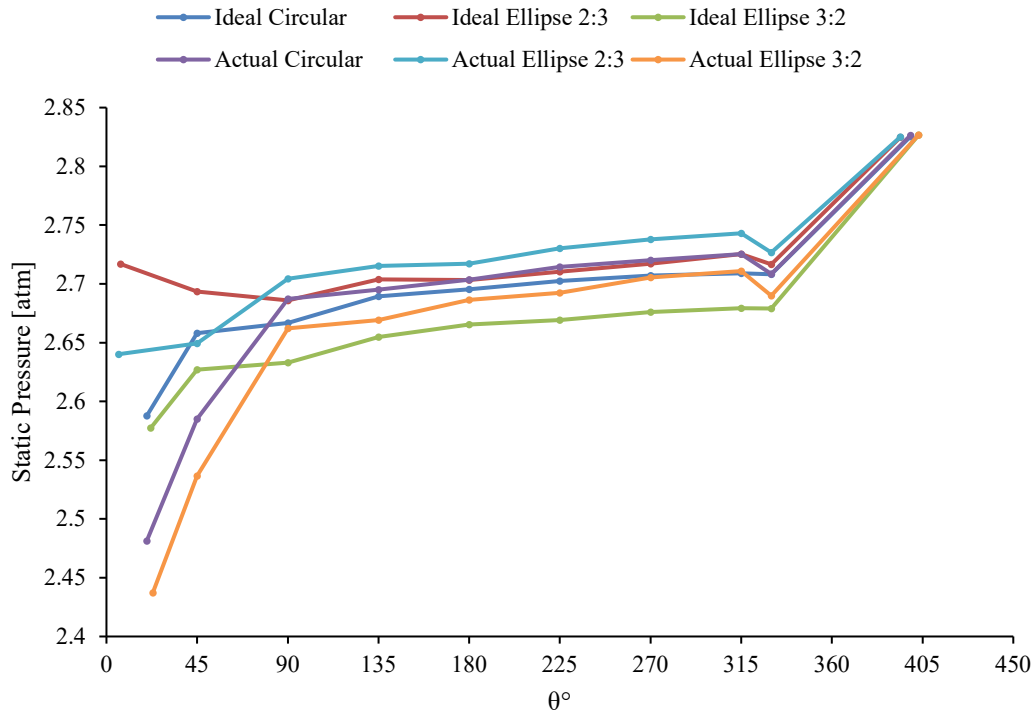


Figure 6.11 Static Pressure through the Symmetric Type Volute

Table 6.6 Static Pressure Variation through Symmetric Type Volutes

Static Pressure Through the Symmetric Volute Design to Ideal Conditions											
θ°			Plane to Plane Variation [%]			θ°			Outlet to Plane Variation [%]		
Circular	Ellipse 2:3	Ellipse 3:2	Circular	Ellipse 2:3	Ellipse 3:2	Circular	Ellipse 2:3	Ellipse 3:2	Circular	Ellipse 2:3	Ellipse 3:2
20 - 45	7 - 45	22 - 45	2.7	-0.9	1.9	20	7	22	-8.4	-3.8	-8.8
45 - 90	45 - 90	45 - 90	0.3	-0.3	0.2	45	45	45	-5.9	-4.7	-7.1
90 - 135	90 - 135	90 - 135	0.9	0.7	0.8	90	90	90	-5.6	-4.9	-6.8
135 - 180	135 - 180	135 - 180	0.2	0.0	0.4	135	135	135	-4.8	-4.3	-6.1
180 - 225	180 - 225	180 - 225	0.3	0.3	0.1	180	180	180	-4.6	-4.3	-5.7
225 - 270	225 - 270	225 - 270	0.2	0.3	0.3	225	225	225	-4.4	-4.1	-5.6
270 - 315	270 - 315	270 - 315	0.1	0.3	0.1	270	270	270	-4.2	-3.8	-5.3
315 - 330	315 - 330	315 - 330	0.0	-0.3	0.0	315	315	315	-4.1	-3.5	-5.2
330 - 399	330 - 394	330 - 403	4.3	4.0	5.5	330	330	330	-4.1	-3.8	-5.2
Static Pressure Through the Symmetric Volute Design to Actual Conditions											
θ°			Plane to Plane Variation [%]			θ°			Outlet to Plane Variation [%]		
Circular	Ellipse 2:3	Ellipse 3:2	Circular	Ellipse 2:3	Ellipse 3:2	Circular	Ellipse 2:3	Ellipse 3:2	Circular	Ellipse 2:3	Ellipse 3:2
20 - 45	6 - 45	23 - 45	4.2	0.4	4.1	20	6	23	-12.2	-6.5	-13.8
45 - 90	45 - 90	45 - 90	4.0	2.1	4.9	45	45	45	-8.5	-6.2	-10.3
90 - 135	90 - 135	90 - 135	0.3	0.4	0.3	90	90	90	-4.9	-4.3	-5.8
135 - 180	135 - 180	135 - 180	0.3	0.1	0.6	135	135	135	-4.7	-3.9	-5.6
180 - 225	180 - 225	180 - 225	0.4	0.5	0.2	180	180	180	-4.4	-3.8	-5.0
225 - 270	225 - 270	225 - 270	0.2	0.3	0.5	225	225	225	-4.0	-3.4	-4.7
270 - 315	270 - 315	270 - 315	0.2	0.2	0.2	270	270	270	-3.8	-3.1	-4.3
315 - 330	315 - 330	315 - 330	-0.6	-0.6	-0.8	315	315	315	-3.6	-2.9	-4.1
330 - 399	330 - 394	330 - 403	4.4	3.6	5.1	330	330	330	-4.2	-3.5	-4.8

#### 6.4.2 Local Velocity Magnitude through Symmetric Type Volute

Figure 6.12 depicts the behaviour of velocity magnitude through symmetric type volutes, namely, those designed to ideal conditions and those designed to actual conditions with circular, ellipse 2:3 and ellipse 3:2 cross-section shapes. Aside from the ellipse 3:2 cross-section shape volute designed to ideal conditions, all cases depict deceleration from the first profile to  $90^\circ$ . From here, deceleration continues to  $315^\circ$  with minor fluctuations. There is slight acceleration to  $330^\circ$  for those cases designed to actual conditions, while those designed to ideal conditions attain uniform velocity magnitude. From  $330^\circ$ , velocity magnitude for all cases decelerates significantly to the outlet of the volute.

Table 6.7 details flow velocity magnitude variation through symmetric type volutes from one plane to the next around the volute and the flow velocity magnitude variation at each plane against that depicted at the outlet. These volutes are namely, those designed to ideal conditions and those designed to actual conditions with circular, ellipse 2:3 and ellipse 3:2 cross-section shapes. Analysing the plane to plane variation, it is identified for all volute cross-section shapes designed to ideal and actual conditions, the highest flow velocity magnitude variation occurs from the cut-off location to the outlet. In the cases for the volute designed to ideal conditions, lowest flow velocity magnitude variations exhibited from  $315^\circ$  to  $330^\circ$  for all volute cross-section shapes. In the cases for the volute designed to actual conditions lowest flow velocity magnitude variations are exhibited from  $90^\circ$  to  $135^\circ$  for the cases of circular cross-section shape; from  $270^\circ$  to  $315^\circ$  for ellipse 2:3 cross-section shape; and from  $180^\circ$  to  $225^\circ$  for ellipse 3:2 cross-section shape. Analysing the flow velocity magnitude variation of that depicted at the plane against that depicted at the outlet, it is identified the highest variation in the cases for the volutes designed to ideal conditions occur in the first profile with circular and ellipse 2:3 cross-section shapes, while for ellipse 3:2 cross-section shape the highest flow velocity magnitude variation occurs at  $45^\circ$ . In the cases for the volute designed to actual conditions, highest flow velocity magnitude variations occur in the first profile for all cross-section shapes. Further to this, lowest flow velocity magnitude variations occur at  $330^\circ$  and  $315^\circ$  for all cases where the volute has been designed to ideal conditions and volutes designed to actual conditions, respectively.

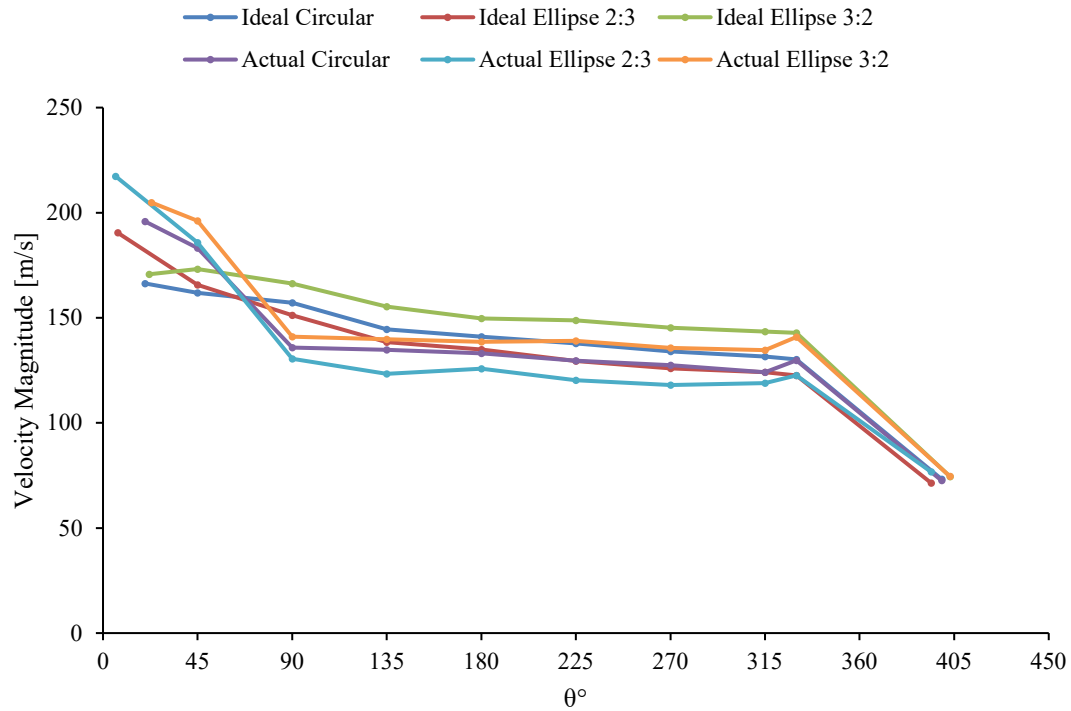


Figure 6.12 Velocity Magnitude through the Symmetric Type Volute

Table 6.7 Velocity Magnitude Variation through Symmetric Type Volute

Velocity Magnitude Through the Symmetric Volute Design to Ideal Conditions											
θ°			Plane to Plane Variation [%]			θ°			Outlet to Plane Variation [%]		
Circular	Ellipse 2:3	Ellipse 3:2	Circular	Ellipse 2:3	Ellipse 3:2	Circular	Ellipse 2:3	Ellipse 3:2	Circular	Ellipse 2:3	Ellipse 3:2
20 - 45	7 - 45	22 - 45	-2.6	-13.0	1.5	20	7	22	127.1	166.6	129.1
45 - 90	45 - 90	45 - 90	-3.0	-8.7	-4.0	45	45	45	121.1	132.0	132.5
90 - 135	90 - 135	90 - 135	-8.1	-8.5	-6.6	90	90	90	114.5	111.7	123.3
135 - 180	135 - 180	135 - 180	-2.4	-2.6	-3.6	135	135	135	97.2	93.7	108.5
180 - 225	180 - 225	180 - 225	-2.3	-4.1	-0.5	180	180	180	92.5	88.7	100.9
225 - 270	225 - 270	225 - 270	-2.7	-2.6	-2.4	225	225	225	88.1	81.1	99.8
270 - 315	270 - 315	270 - 315	-1.9	-1.5	-1.3	270	270	270	83.0	76.3	95.1
315 - 330	315 - 330	315 - 330	-1.1	-1.1	-0.4	315	315	315	79.5	73.6	92.6
330 - 399	330 - 394	330 - 403	-43.7	-41.7	-47.8	330	330	330	77.6	71.6	91.7
Velocity Magnitude Through the Symmetric Volute Design to Actual Conditions											
θ°			Plane to Plane Variation [%]			θ°			Outlet to Plane Variation [%]		
Circular	Ellipse 2:3	Ellipse 3:2	Circular	Ellipse 2:3	Ellipse 3:2	Circular	Ellipse 2:3	Ellipse 3:2	Circular	Ellipse 2:3	Ellipse 3:2
20 - 45	6 - 45	23 - 45	-6.4	-14.5	-4.3	20	6	23	169.9	183.3	174.8
45 - 90	45 - 90	45 - 90	-25.9	-29.8	-28.1	45	45	45	152.6	142.2	163.1
90 - 135	90 - 135	90 - 135	-0.8	-5.5	-0.9	90	90	90	87.1	70.0	89.2
135 - 180	135 - 180	135 - 180	-1.2	2.0	-0.9	135	135	135	85.7	60.7	87.5
180 - 225	180 - 225	180 - 225	-2.6	-4.3	0.4	180	180	180	83.5	63.9	85.8
225 - 270	225 - 270	225 - 270	-1.7	-1.9	-2.4	225	225	225	78.7	56.8	86.6
270 - 315	270 - 315	270 - 315	-2.7	0.7	-0.8	270	270	270	75.6	53.8	82.0
315 - 330	315 - 330	315 - 330	4.6	3.2	4.7	315	315	315	70.9	54.9	80.5
330 - 399	330 - 394	330 - 403	-44.1	-37.4	-47.1	330	330	330	78.8	59.8	89.0

### 6.4.3 Local Static Temperature through Symmetric Type Volutes

Figure 6.13 depicts the behaviour of static temperature through symmetric type volutes, namely, those designed to ideal conditions and those designed to actual conditions with circular, ellipse 2:3 and ellipse 3:2 cross-section shapes. Aside from the ellipse 3:2 cross-section shape volute designed to ideal conditions, all cases depict an increase in static temperature from the first profile to 90°. In the case of the ellipse 3:2 cross-section shape volute designed to ideal conditions, static temperature slightly decreases from the first profile to 45° prior to increasing to 90°. Aside for the circular and ellipse 3:3 cross-section shape volutes designed to actual conditions, all cases attain reasonable uniformity in static temperature to 315°. For the circular and ellipse 3:3 cross-section shape volutes designed to actual conditions, static temperature decreases slightly to 135° prior attaining reasonable uniformity to 315°. For those volutes designed to ideal conditions, uniform static temperature is attained to 330° followed by a substantial increase in static temperature. For those volutes designed to actual conditions, there is a slight static temperature decrease to 330° prior to the substantial static temperature increase to the outlet of the volute.

Table 6.8 details static temperature variation through symmetric type volutes from one plane to the next around the volute and the static temperature variation at each plane against that depicted at the outlet. These volutes are namely, those designed to ideal conditions and those designed to actual conditions with circular, ellipse 2:3 and ellipse 3:2 cross-section shapes. Analysing the plane to plane variation, it is identified all volute cross-section shapes designed to ideal conditions have highest static temperature variation from 330° to the outlet, while all volute cross-section shapes designed to ideal conditions have highest static temperature variation from 45° to 90°. There are no static temperature variations depicted for all cases from 315° to 330° for the volutes designed to ideal conditions. In addition to this, there are no variations in static temperature from 135° to 180° for ellipse 2:3 cross-section shape for volute designed to both actual and ideal conditions. Furthermore, ellipse 2:3 cross-section shape volute designed to actual conditions depict no variation from 270° to 315° and for the ellipse 3:2 cross-section shape volute designed to ideal conditions, depict no static temperature variation from the first profile to 45°. Analysing the static temperature variation of that depicted at the plane against that depicted at the outlet, it is identified the highest variation occurs in the first profile for all cases. It is also identified the lowest variation occurs in 315° for all cases for the volute designed to both ideal and actual conditions. In addition to this,



lowest variation also occurs for all cross section shapes at 330° for those designed to ideal conditions.

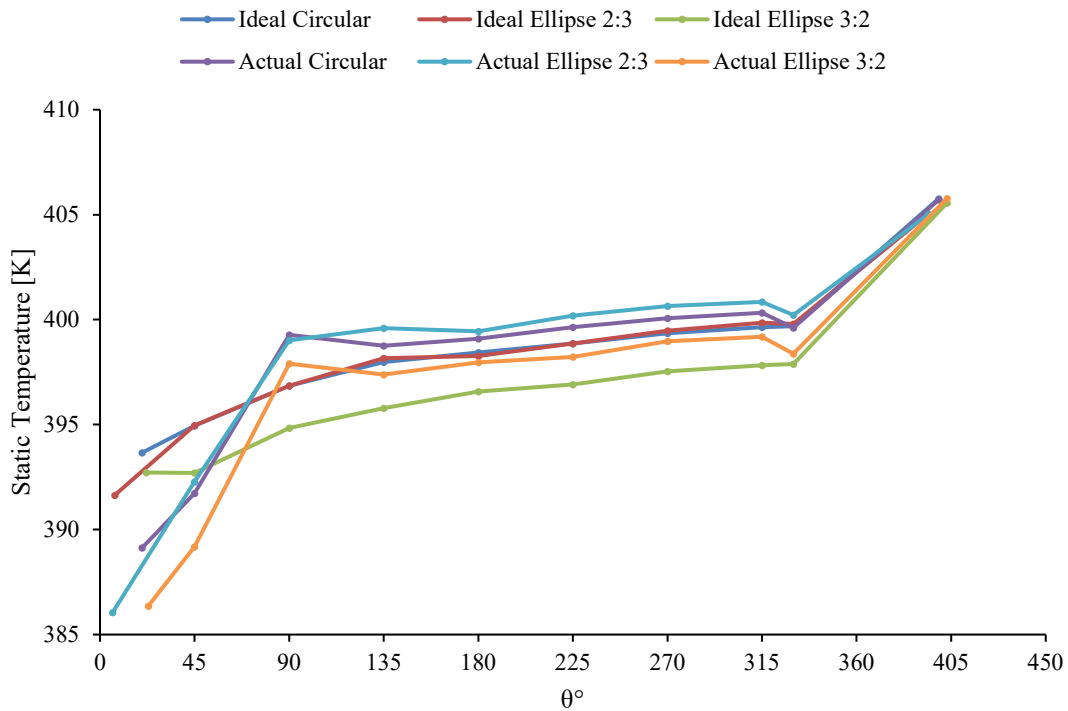


Figure 6.13 Static Temperature through the Symmetric Type Volute

Table 6.8 Static Temperature Variation through Symmetric Type Volutes

Static Temperature Through the Symmetric Volute Design to Ideal Conditions											
θ°			Plane to Plane Variation [%]			θ°			Outlet to Plane Variation [%]		
Circular	Ellipse 2:3	Ellipse 3:2	Circular	Ellipse 2:3	Ellipse 3:2	Circular	Ellipse 2:3	Ellipse 3:2	Circular	Ellipse 2:3	Ellipse 3:2
20 - 45	7 - 45	22 - 45	0.3	0.8	0.0	20	7	22	-3.0	-3.3	-3.2
45 - 90	45 - 90	45 - 90	0.5	0.5	0.5	45	45	45	-2.7	-2.5	-3.2
90 - 135	90 - 135	90 - 135	0.3	0.3	0.2	90	90	90	-2.2	-2.0	-2.6
135 - 180	135 - 180	135 - 180	0.1	0.0	0.2	135	135	135	-1.9	-1.7	-2.4
180 - 225	180 - 225	180 - 225	0.1	0.2	0.1	180	180	180	-1.8	-1.7	-2.2
225 - 270	225 - 270	225 - 270	0.1	0.2	0.2	225	225	225	-1.7	-1.5	-2.1
270 - 315	270 - 315	270 - 315	0.1	0.1	0.1	270	270	270	-1.6	-1.4	-2.0
315 - 330	315 - 330	315 - 330	0.0	0.0	0.0	315	315	315	-1.5	-1.3	-1.9
330 - 399	330 - 394	330 - 403	1.5	1.3	1.9	330	330	330	-1.5	-1.3	-1.9
Static Temperature Through the Symmetric Volute Design to Actual Conditions											
θ°			Plane to Plane Variation [%]			θ°			Outlet to Plane Variation [%]		
Circular	Ellipse 2:3	Ellipse 3:2	Circular	Ellipse 2:3	Ellipse 3:2	Circular	Ellipse 2:3	Ellipse 3:2	Circular	Ellipse 2:3	Ellipse 3:2
20 - 45	6 - 45	23 - 45	0.7	1.6	0.7	20	6	23	-4.1	-4.7	-4.8
45 - 90	45 - 90	45 - 90	1.9	1.7	2.2	45	45	45	-3.4	-3.1	-4.1
90 - 135	90 - 135	90 - 135	-0.1	0.1	-0.1	90	90	90	-1.6	-1.5	-1.9
135 - 180	135 - 180	135 - 180	0.1	0.0	0.1	135	135	135	-1.7	-1.3	-2.1
180 - 225	180 - 225	180 - 225	0.1	0.2	0.1	180	180	180	-1.6	-1.4	-1.9
225 - 270	225 - 270	225 - 270	0.1	0.1	0.2	225	225	225	-1.5	-1.2	-1.9
270 - 315	270 - 315	270 - 315	0.1	0.0	0.1	270	270	270	-1.4	-1.1	-1.7
315 - 330	315 - 330	315 - 330	-0.2	-0.2	-0.2	315	315	315	-1.3	-1.0	-1.6
330 - 399	330 - 394	330 - 403	1.5	1.2	1.9	330	330	330	-1.5	-1.2	-1.8

#### 6.4.4 Head Loss Variation through Symmetric Type Volutes

In order to quantify the frictional effects among these various symmetric type volutes, pressure head loss incurred inside the volute, is the amount of energy that needs to be risen in order to overcome frictional losses have been investigated [27]. Since the source of this head loss is viscosity and has direct relation to wall shear stress [27], the effect of wall shear stress on the volute casings have also been investigated. The correlation between head loss and wall shear stress, which are associated to the vortices in the volute cross section have different performance characteristics in symmetric volutes and asymmetric volutes [80]. This focuses on the scroll of the volute in order to evaluate the expressions employed during the design methodology of the centrifugal compressor volute.

Figure 6.14 depicts the wall shear stress incurred on sections of the scroll of the volute casing. It can be seen that wall shear stresses initially increases in the scroll then decreases. In the first section of the scroll, wall shear stresses are higher in volutes designed to actual conditions for the ellipse 2:3 and ellipse 3:2 cross-section shapes, whereas the volute designed to ideal conditions show higher wall shear stress for the circular cross-section shape. In the second section of the scroll, wall shear stresses for all cross-section shapes in volutes designed to actual conditions are higher than those designed to ideal conditions. In the third section of the scroll, wall shear stresses are higher for the circular and ellipse 2:3 cross-section shape volutes designed to actual conditions than those designed to ideal conditions, while for ellipse 3:2 wall shear stress is higher for the volute designed to ideal conditions than that designed to actual conditions. Downstream sections to the last section, all cross-section shapes for volutes designed to ideal conditions depict higher wall shear stresses than for those designed to actual conditions. In the last section, wall shear stresses are higher for circular and ellipse 3:2 cross-section shape volutes designed to ideal conditions, whereas for ellipse 2:3 cross-section shape volute designed to actual conditions has higher wall shear stress. See APPENDIX 9 for further details.

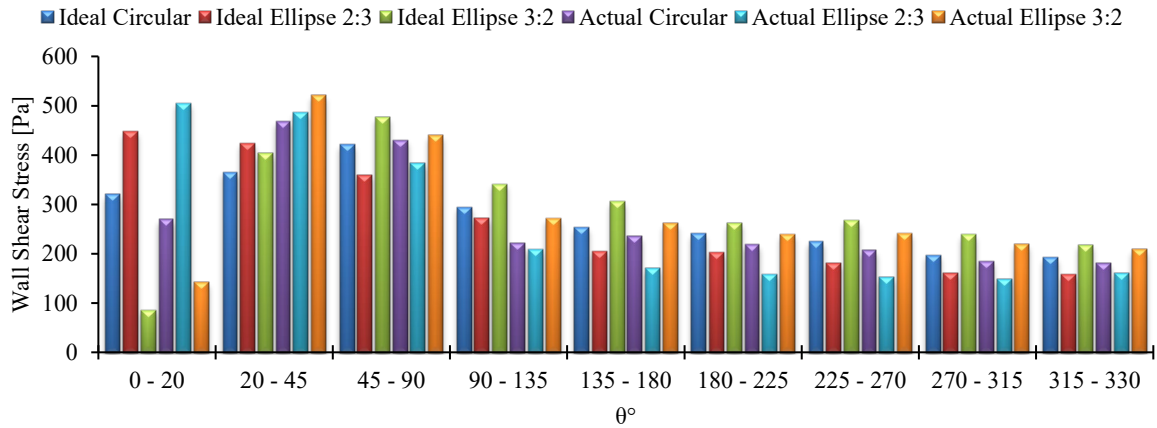


Figure 6.14 Comparison of wall shear stress on the symmetric type centrifugal compressor volute casing

Figure 6.15 depicts the head losses incurring through sections of the scroll of the volute casing. The similar trends can be identified here as that in Figure 6.14, which signifies the interrelationship between wall shear stress and head loss. In the first section of the scroll, head losses are higher in volutes designed to actual conditions for the ellipse 2:3 and ellipse 3:2 cross-section shapes, whereas the volute designed to ideal conditions show higher head loss for the circular cross-section shape. In the second section of the scroll, head losses for all cross-section shapes in volutes designed to actual conditions are higher than those designed to ideal conditions. Downstream sections to the last section, all cross-section shapes for volutes designed to ideal conditions depict higher head losses than for those designed to actual conditions. In the last section, head losses are higher for circular and ellipse 3:2 cross-section shape volutes designed to ideal conditions, whereas for ellipse 2:3 cross-section shape volute designed to both ideal and actual conditions have the same head loss. See APPENDIX 10 for further details.

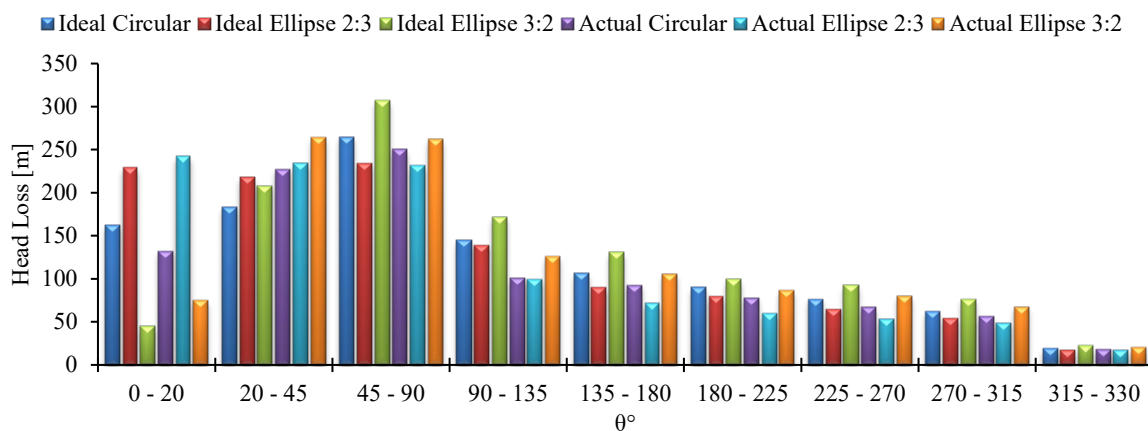


Figure 6.15 Comparison of head loss through the symmetric type centrifugal compressor volute

## 6.5 Global Performance Evaluation of the Asymmetric Type Volute for Centrifugal Compressor

Now that symmetric type volute cross-sections have been explored, an asymmetric type volute has been investigated in the forthcoming sections. Since the existing volute, (referred as CTT in the forthcoming sections), is also an asymmetric type volute, the new asymmetric volute (referred as Asymmetric in the forthcoming sections) designed to actual conditions incorporating friction as a parameter using the novel design methodology, has been developed. The Asymmetric volute has been compared and evaluated against the CTT volute to determine the locations of the flow field variations; to characterise the losses; highlight the strengths and weaknesses of the two cases; and to verify the design methodology.

### 6.5.1 Turbocharger Compressor Performance with Asymmetric Type Volutes

Figure 6.16 depicts the turbocharger compressor performance comparison of the experimental data and its corresponding numerical data, referred as CTT, with the numerical data of the turbocharger compressor stage fixed with the newly designed asymmetric volute. Figure 6.16 (a) depicts the turbocharger compressor map and Figure 6.16 (b) depicts the turbocharger compressor isentropic efficiency map. In Figure 6.16 (a), the asymmetric volute is in reasonable agreement with CTT and the experimental data at low operating speed of 58.9rps/ $\sqrt{K}$ . At high operating speed of 98.2rps/ $\sqrt{K}$ , total-to-total pressure ratio for asymmetric is lower than both the experimental data and CTT at low flow rate and design flow rate, whereas at high flow rate, total-to-total pressure ratio is slightly higher than that of the experimental data and lower than that of CTT. In Figure 6.16 (b), there are significant isentropic efficiency variations between asymmetric and experimental as well as with asymmetric and CTT. Minimal isentropic efficiency variances are depicted between asymmetric and CTT at low flow rate where asymmetric is slightly higher; and between asymmetric and experimental at design flow rate where asymmetric is slightly lower, for the low operating speed of 58.9rps/ $\sqrt{K}$ . At high operating speed of 98.2rps/ $\sqrt{K}$ , asymmetric is distinctly lower than both experimental and CTT at low flow rate and design flow rate. At high flow rate asymmetric has higher isentropic efficiency than experimental and lower than CTT.

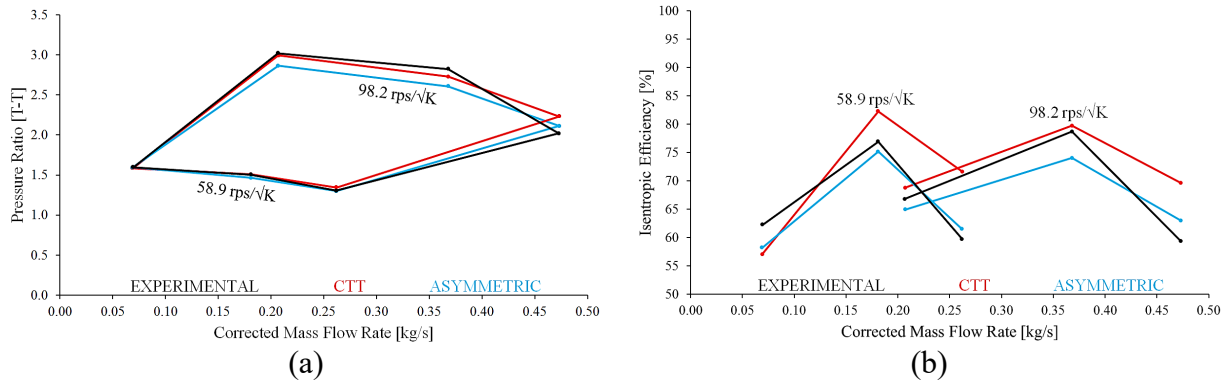


Figure 6.16 Asymmetric Volute and CTT Volute Turbocharger Compressor Performance Comparison of (a) Compressor Map (b) Isentropic Efficiency Map

### 6.5.2 Turbocharger Compressor Volute Performance with Asymmetric Type Volutes

Figure 6.17 depicts the overall turbocharger compressor volute performance comparison of asymmetric with the CTT. Figure 6.17 (a) depicts the static pressure recovery through the compressor volute and Figure 6.17 (b) depicts total pressure loss through the compressor volute. In both figures, there are substantial variations depicted between the two cases. In Figure 6.17 (a) static pressure recovery coefficient for asymmetric is less than that depicted for CTT, identifying less variation at high flow rate for both operating speeds. It is also noticed that at both operating speeds, the Asymmetric volute depict a static pressure recovery coefficient below zero. This suggests there are more pressure losses incurring at the choke condition than pressure recovery due to secondary flows causing head loss as a result of friction. In Figure 6.17 (b) total pressure loss coefficient for asymmetric is significantly higher than that depicted for CTT for both operating speeds.

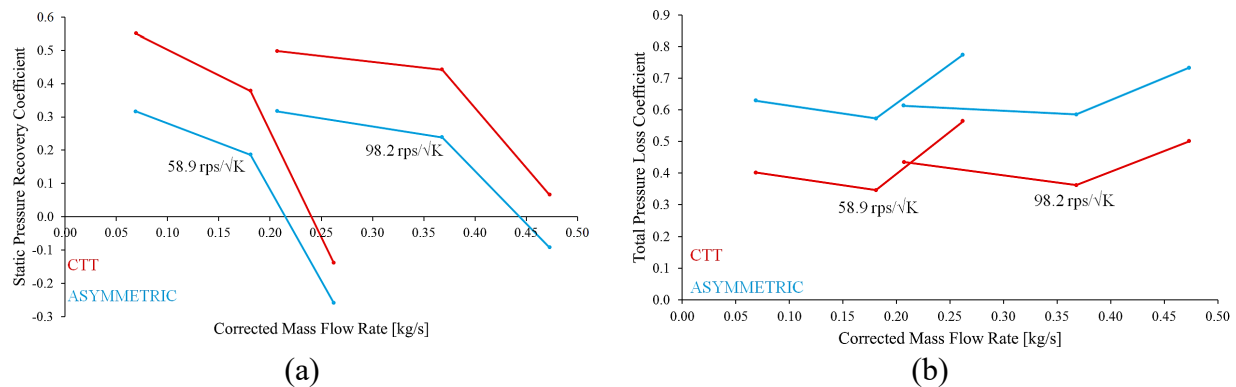
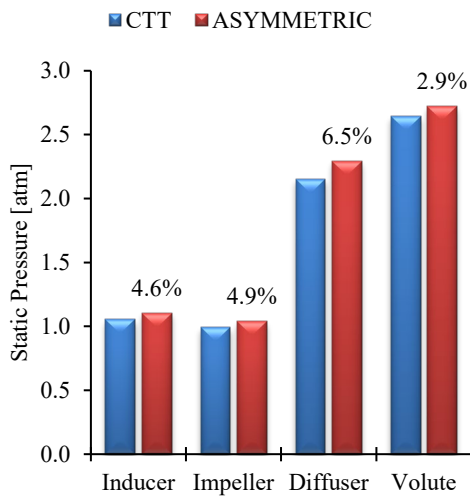
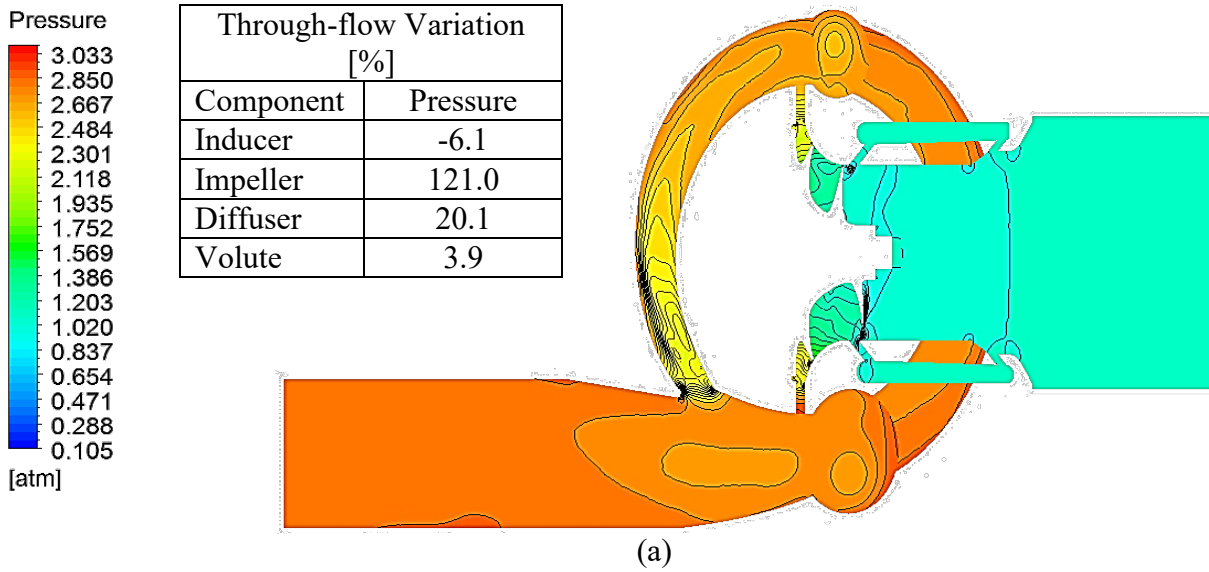


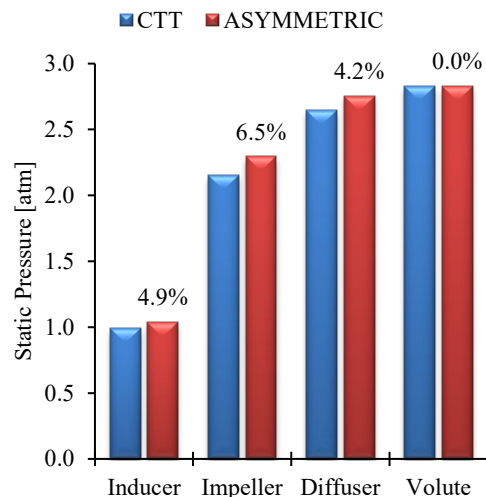
Figure 6.17 Asymmetric Volute and CTT Volute Turbocharger Compressor Volute Performance Comparison of (a) Static Pressure Recovery Coefficient (b) Total Pressure Loss Coefficient

### 6.5.3 Global Static Pressure through Asymmetric Type Volutes

Figure 6.18 depicts static pressure variation in the turbocharger compressor stage with the asymmetric volute at design flow rate operating at a speed of  $98.2\text{rps}\sqrt{K}$ , where Figure 6.18 (a) depicts the static pressure contour; Figure 6.18 (b) depicts the inlet static pressure comparison with CTT; and Figure 6.18 (c) depicts the outlet static pressure comparison with CTT. Figure 6.18 (a) depicts similar trends as that of CTT aforementioned in Chapter 4. Upstream of the volute, static pressure behaviour appears the same however in the volute, there appears to be some non-uniformities occurring in the tail of the volute in the initial stages of inflow. Downstream of this, static pressure is uniform. Highest static pressure variation inside the component occurs in the impeller where static pressure increases by 121% at the outlet compared to that at the inlet. Lowest static pressure variation inside the component occurs in the volute where static pressure increases by 3.9% at the outlet compared to that at the inlet. Figure 6.18 (b) identifies that the inflow static pressure is higher for asymmetric than for CTT for all components. This is also the case in Figure 6.18 (c) for the outflow static pressure, however, there are no variations at the volute outlet between asymmetric and CTT. Compared with the CTT case, static pressure through the component for the asymmetric case decreases by 0.1% through the inducer; increases by 7.8% through the impeller; and decreases by 5.6% and 42.3% through the diffuser and volute, respectively. Overall, it is observed that static pressure increases through all components with the asymmetric volute in comparison with the CTT volute.



(b)



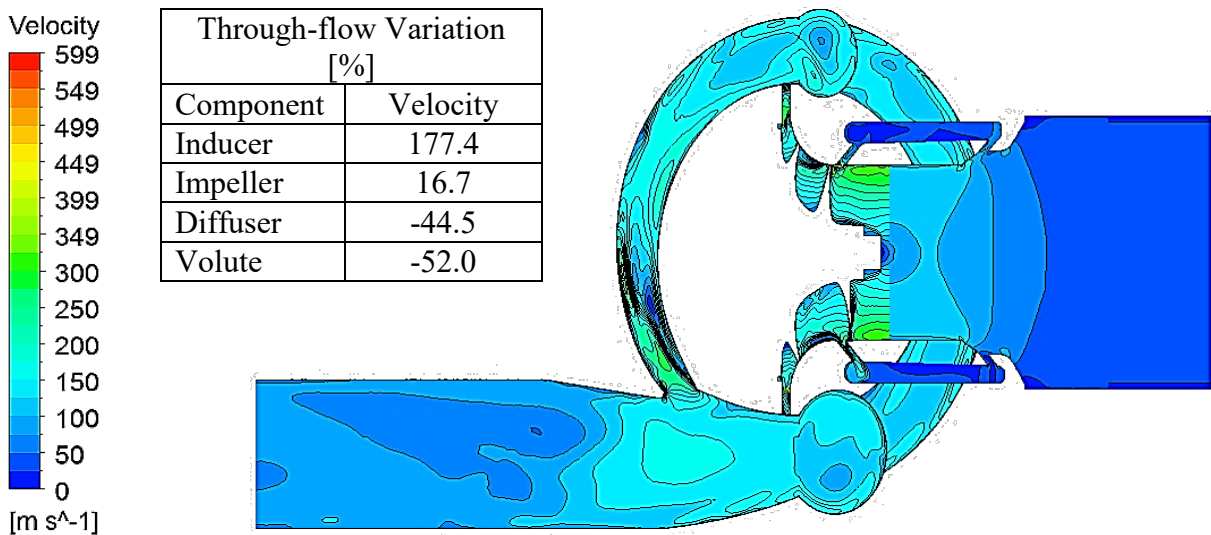
(c)

Figure 6.18 Static Pressure Variation in the Turbocharger Compressor Stage with the Asymmetric Volute where (a) static pressure contour (b) inlet static pressure comparison with CTT (c) outlet static pressure comparison with CTT

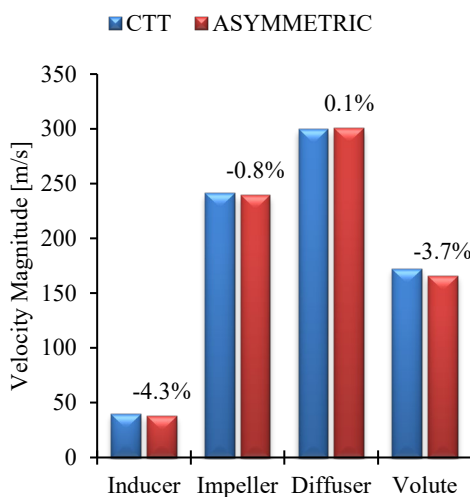
#### 6.5.4 Global Velocity Magnitude through Asymmetric Type Volutes

Figure 6.19 depicts velocity magnitude variation in the turbocharger compressor stage with the asymmetric volute at design flow rate operating at a speed of  $98.2\text{rps}\sqrt{\text{K}}$ , where Figure 6.19 (a) depicts the velocity magnitude contour; Figure 6.19 (b) depicts the inlet velocity magnitude comparison with CTT; and Figure 6.19 (c) depicts the outlet velocity magnitude comparison with CTT. Figure 6.19 (a) depicts similar trends as that of CTT aforementioned in Chapter 4. Upstream of the volute, velocity magnitude behaviour appears the same however in the volute, there appears to be some non-uniformities occurring in the tail of the volute in the initial stages of inflow. Highest velocity magnitude variation inside the component occurs in the inducer where velocity magnitude increases by 177.4% at the outlet compared to that at the inlet. Lowest velocity magnitude variation inside the component occurs in the impeller where

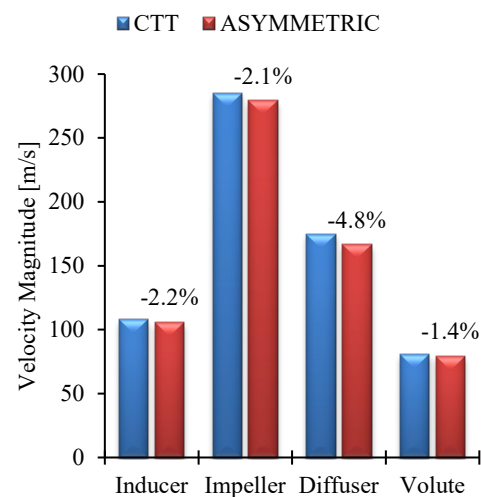
velocity magnitude increases by 16.7% at the outlet compared to that at the inlet. Figure 6.19 (b) identifies that the inflow velocity magnitude is lower at the inducer, impeller and volute for asymmetric than for CTT, while being higher at the diffuser. Figure 6.19 (c) identifies that the outflow velocity magnitude is lower for asymmetric than for CTT for all components. Compared with the CTT case, velocity magnitude through the component for the asymmetric case decreases by 1% through the inducer; decreases by 9.1% through the impeller; increases by 7.1% through the diffuser; and decreases by 5.7% through the volute. Overall, the asymmetric volute depicts that velocity magnitude only increases through the diffuser inlet in comparison with the CTT volute. Aside from this, the velocity magnitude decreases through all components for the asymmetric volute in comparison with the CTT volute.



(a)



(b)



(c)

Figure 6.19 Velocity Magnitude Variation in the Turbocharger Compressor Stage with the Asymmetric Volute where (a) velocity magnitude contour (b) inlet velocity magnitude comparison with CTT (c) outlet velocity magnitude comparison with CTT



### 6.5.5 Global Static Temperature through Asymmetric Type Volutes

Figure 6.20 depicts static temperature variation in the turbocharger compressor stage with the asymmetric volute at design flow rate operating at a speed of  $98.2\text{rps}\sqrt{K}$ , where Figure 6.20 (a) depicts the static temperature contour; Figure 6.20 (b) depicts the inlet static temperature comparison with CTT; and Figure 6-20 (c) depicts the outlet static temperature comparison with CTT. Figure 6.20 (a) depicts similar trends as that of CTT aforementioned in Chapter 4. Upstream of the volute, static temperature behaviour appears the same however in the volute, there is a slight fall in static temperature in the initial stages of inflow near the volute tongue. Downstream of this, static temperature is uniform to the outlet of the volute. Highest static temperature variation inside the component occurs in the impeller where static temperature increases by 27.5% at the outlet compared to that at the inlet. Lowest static temperature variation inside the component occurs in the inducer where static temperature decreases by 0.9% at the outlet compared to that at the inlet. Figure 6.20 (b) identifies that there is no static temperature variation between asymmetric and CTT at the inducer, though inflow static temperature is slightly higher for asymmetric than for CTT for components downstream of this. Figure 6.20 (c) identifies that the outflow static temperature is slightly higher for asymmetric than for CTT for all components. Compared with the CTT case, static temperature through the component for the asymmetric case decreases by 34.2% through the inducer; increases by 0.9% through the impeller; decreases by 1% through the diffuser; and increases by 8.4% through the volute. Overall, it is observed that there is a negligible increase in static temperature for the asymmetric volute in comparison with the CTT volute.

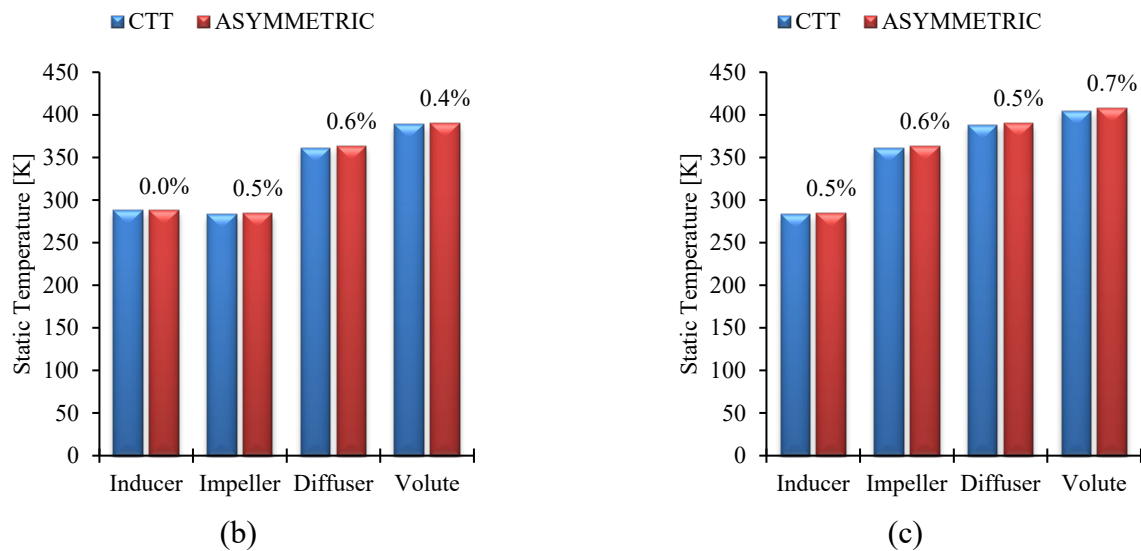
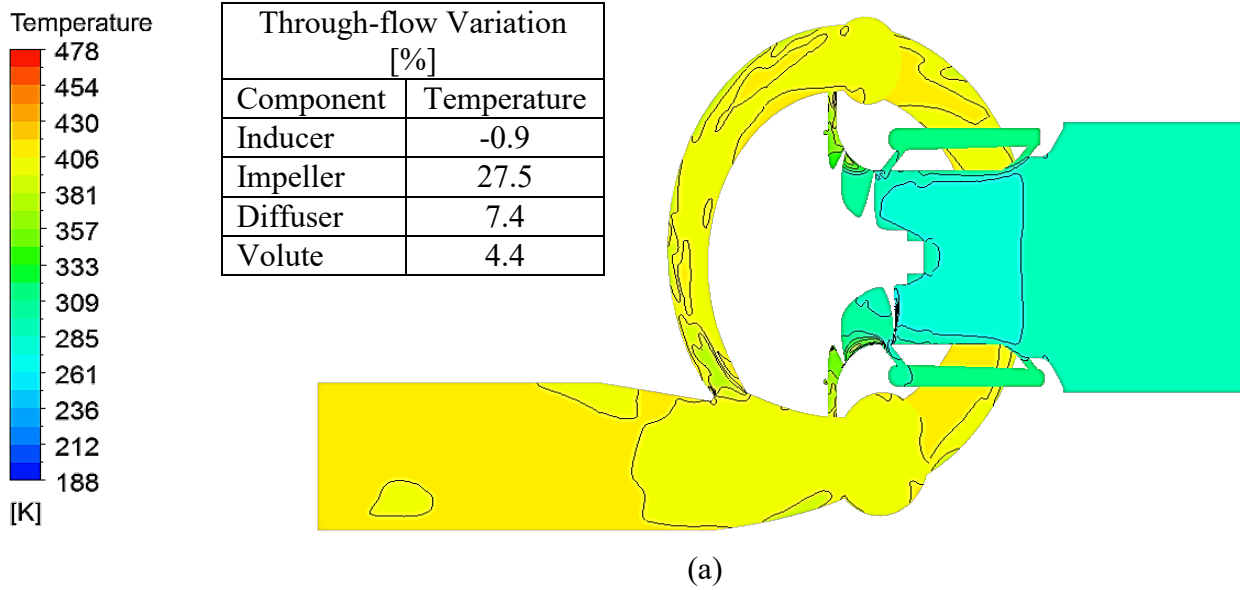


Figure 6.20 Static Temperature Variation in the Turbocharger Compressor Stage with the Asymmetric Volute where (a) static temperature contour (b) inlet static temperature comparison with CTT (c) outlet static temperature comparison with CTT

## 6.6 Local Performance Evaluation of the Asymmetric Type Volute for Centrifugal Compressor

This section explores the local flow fields through the turbocharger compressor volute and compares with that of CTT. Instantaneous analysis has also been presented for both cases and the minimum and maximum points taken at the first profile in the volute with respect to static pressure. The static pressure field has been selected specifically since this flow property has a direct relationship with the purpose and performance of the volute. Since Chapter 5 found negligible variances between the two selected instances, this chapter not only focuses on the flow behaviour at the selected minimum and maximum points, but also focuses on the

percentage difference against the revolution averaged results for the two instances with both, asymmetric and CTT cases.

### 6.6.1 Local Static Pressure through Asymmetric Type Volute

Figure 6.21 depicts static pressure distribution through the turbocharger compressor volute during the operating speed of 98.2rps/ $\sqrt{K}$  at design flow rate. Twelve cross-sections through the volute channel have been presented from the first cross-section of the scroll situated above the tongue, through to the outlet of the compressor stage. From the base of the tail at the first cross-section profile located at 20°, low static pressure is identified with a circumferential increase as the flow travels downstream from this location. From 90° to the cut-off location, lower static pressure is seen in the free-stream. Further to this, it is noticed that static pressure decreases through the exit cone due to the effects of the volute tongue; and increases to its highest static pressure through the discharge duct towards the outlet, as expected.

Figure 6.22 quantifies the static pressure distribution across each plane around the turbocharger compressor volute and compares the newly designed asymmetric volute with the CTT volute. The percentage difference of the asymmetric volute has been calculated against that of the CTT volute. It is identified the highest static pressure variation between the two volute models occur in the first profile, where the asymmetric volute depicts 16.1% less static pressure than that of CTT, while depicting no variation between the two models at the outlet.

Table 6.9 details the percentage difference in static pressure variation from one cross-section location to the next, specified by the azimuth angle. It also details the percentage difference in static pressure variation occurring at each cross-section around the volute against that depicted at the outlet. The data includes that from the asymmetric volute and that of the CTT volute, enabling observations to be made in the distinct variations between the two. With regards to the static pressure variation from one cross-section location to the next, the highest static pressure variation occurs between 90° and 135° for the CTT case with 2.2%, whereas for the newly designed asymmetric case, the highest static pressure variation occurs in the initial section of the tail between the first profile and 45° with 10.5%. For both cases, the lowest static pressure variation of 0.1% occurs between the discharge duct and the outlet. Regarding the static pressure variation occurring at each cross-section around the volute against that depicted at the outlet, the highest static pressure variance occurs at 90° and in the first profile for the CTT volute and asymmetric volute, respectively. CTT volute identifies 8.6% less static pressure than that at the outlet, while asymmetric volute identifies 21.2% less static pressure than that at the

outlet. The lowest variation for both case occur at the discharge duct with 0.1% less static pressure and higher static pressure than that at the outlet for CTT volute and symmetric volute respectively. Overall, when comparing the Asymmetric volute with the CTT volute, an increase in static pressure means that more kinetic energy is converted into potential energy, hence signifies an improvement in performance. It is identified that static pressure is initially lower until the flow reaches 45°, then higher downstream to the cut-off location, which then decreases at the exit cone, followed by exhibiting the same static pressure at the outlet.

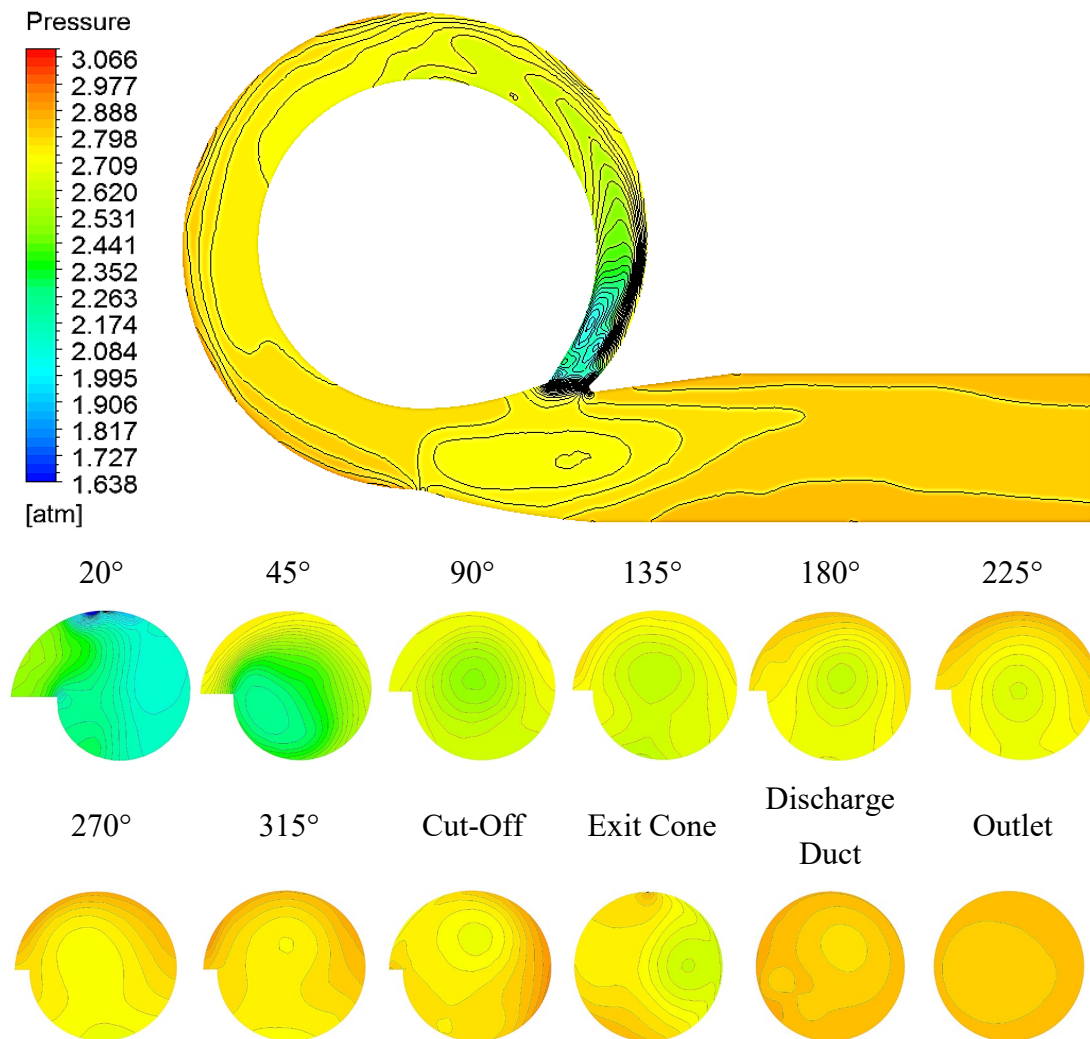


Figure 6.21 Static pressure around the asymmetric type compressor volute

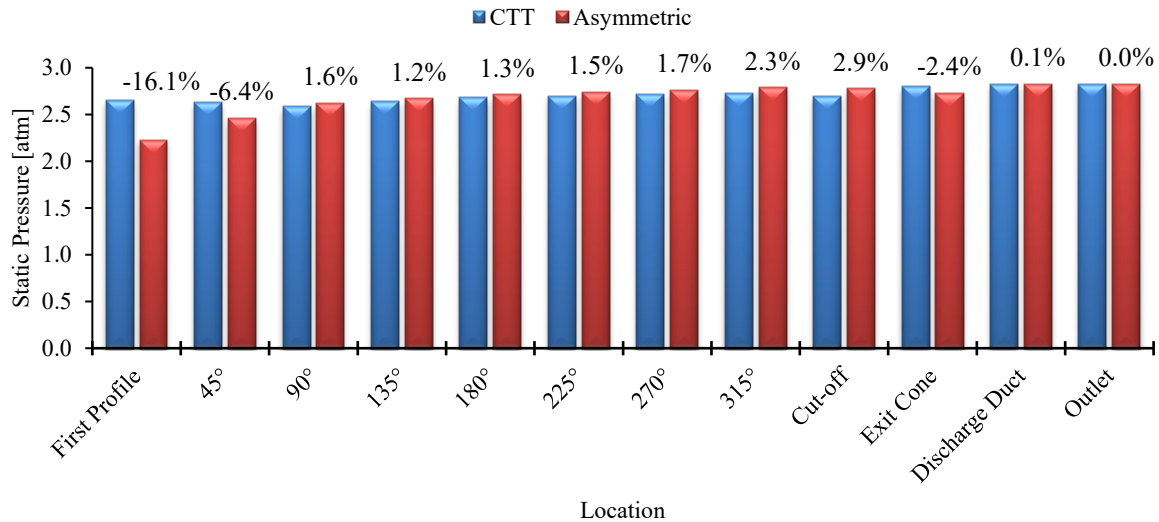


Figure 6.22 Static pressure across each cross-section around the asymmetric volute and CTT volute

Table 6.9 Asymmetric volute comparison with CTT volute of static pressure variation from plane to plane and outlet to plane

$\theta^\circ$ to $\theta^\circ$			Outlet to $\theta^\circ$		
Static Pressure Variation [%]			Static Pressure Variation [%]		
$\theta^\circ - \theta^\circ$	CTT	Asymmetric	$\theta^\circ$	CTT	Asymmetric
<b>FP - 45</b>	-0.9	10.5	<b>First Profile</b>	-6.1	-21.2
<b>45 - 90</b>	-1.7	6.7	<b>45</b>	-7.0	-12.9
<b>90 - 135</b>	2.2	1.7	<b>90</b>	-8.6	-7.1
<b>135 - 180</b>	1.6	1.7	<b>135</b>	-6.6	-5.5
<b>180 - 225</b>	0.8	1.0	<b>180</b>	-5.2	-4.0
<b>225 - 270</b>	0.6	0.8	<b>225</b>	-4.4	-3.0
<b>270 - 315</b>	0.2	0.8	<b>270</b>	-3.9	-2.2
<b>315 - CO</b>	-0.9	-0.3	<b>315</b>	-3.7	-1.5
<b>CO - EC</b>	3.7	-1.6	<b>Cut- off</b>	-4.5	-1.8
<b>EC - DD</b>	0.9	3.5	<b>Exit Cone</b>	-1.0	-3.3
<b>DD - OUT</b>	0.1	-0.1	<b>Discharge Duct</b>	-0.1	0.1

Figure 6.23 is a graphical representation depicting the asymmetric ratio of static pressure along the radial direction of the cross-section profiles in (a), and axial direction of the cross-section profiles in (b) around the centrifugal compressor volute, at design flow rate and high operating speed of 98.2rps/ $\sqrt{K}$ . The data included comprises of the minimum and maximum responses for the CTT volute and the Asymmetric volute. In both radial direction and axial direction cases, when the asymmetric ratio is 1, the flow variable is symmetric and signifies desirable flow characteristics. Asymmetric ratio that is not 1 signifies the presence of secondary flows as

a result of an imbalance in the flow between static pressure and kinetic energy [74]. This in turn, requires more energy due to losses taking place as a result of friction. Secondary flows are a direct cause for head loss [74] therefore, the more symmetric the ratio means the better the volute performs. When the asymmetric ratio is more than 1, flow variable in the case of the radial direction is localised towards the inner curve, and in the case of the axial direction, the flow variable is localised towards the rear face. When the asymmetric ratio is less than 1, flow variable in the case of the radial direction is localised towards the outer curve, and in the case of the axial direction, the flow variable is localised towards the front face. More detailed graphical representations are depicted in APPENDIX 4.

In the case of Figure 6.23 (a), static pressure along the radial direction is predominantly asymmetric towards the outer curve. In the first profile, the steady cases for the Asymmetric and CTT as well as CTT Min, depict asymmetry towards the inner curve, while the max cases for the Asymmetric and CTT as well as Asymmetric Min depict asymmetry towards the outer curve. At 45°, all cases are asymmetric towards the outer curve with all asymmetric cases identifying more asymmetry than all CTT cases. At 90°, only Asymmetric Max depicts slight asymmetry towards the inner curve, while at 315° only Asymmetric Min depicts asymmetry towards the inner curve. From 90° to 315°, all Asymmetric cases are less asymmetric in static pressure along the radial direction than all CTT cases. At the cut-off location, all Asymmetric cases identify asymmetry towards the inner curve while CTT Steady is symmetric and CTT Min and CTT Max remain asymmetric towards the outer curve. At the exit cone and discharge duct, the static pressure asymmetric behaviour along the radial direction is vice versa for the two volute cases. At the outlet, all cases identify static pressure asymmetry along the radial direction towards the inner curve.

In the case of Figure 6.23 (b), static pressure along the axial direction depicts asymmetry towards the rear face for all cases in the first profile with the Asymmetric cases displaying considerably more asymmetry than that of the CTT cases. At 45°, Asymmetric Steady depicts asymmetry towards the front face, whilst the remainder continue to display asymmetry towards the rear face. At 90°, all Asymmetric cases depict asymmetry towards the front face, while all CTT cases display asymmetry towards the rear face. At 135°, Asymmetric Steady identifies symmetry in static pressure along the axial direction and the remainder depicts asymmetry towards the rear face. At 180°, all cases display asymmetry towards the rear face and at 225°, only Asymmetric Min displays asymmetry towards the front face. At 270°, CTT Min and CTT Max are seen to have symmetric static pressure along the axial direction while the remainder

are seen to be asymmetric towards the rear face. At 315°, all cases show asymmetric static pressure along the axial direction towards the front face. At the cut-off location, all Asymmetric cases and CTT Steady remain asymmetric towards the front face while CTT Min and CTT Max display asymmetry towards the rear face. At the exit cone, all Asymmetric cases are significantly asymmetric towards the rear face. CTT Steady presents symmetric static pressure along the axial direction with CTT Min and CTT Max showing asymmetry towards the front face. At the discharge duct, all Asymmetric cases are slightly asymmetric towards the rear face and all CTT cases are asymmetric towards the front face. At the outlet, all cases display asymmetry in static pressure along the axial direction towards the front face.

Overall, the influence on the imbalance of static pressure along the radial direction through the centrifugal compressor volute for all cases of the CTT model are significantly greater than all cases of the Asymmetric model through the scroll. In the tongue region however, all Asymmetric volutes have a greater influence on the imbalance of static pressure. Further to this, the influence on the imbalance of static pressure along the axial direction through the centrifugal compressor volute for all cases are very similar. Although, the Asymmetric volute depict a higher influence on the imbalance of static pressure in comparison with the CTT volute in vicinity of the tongue region.

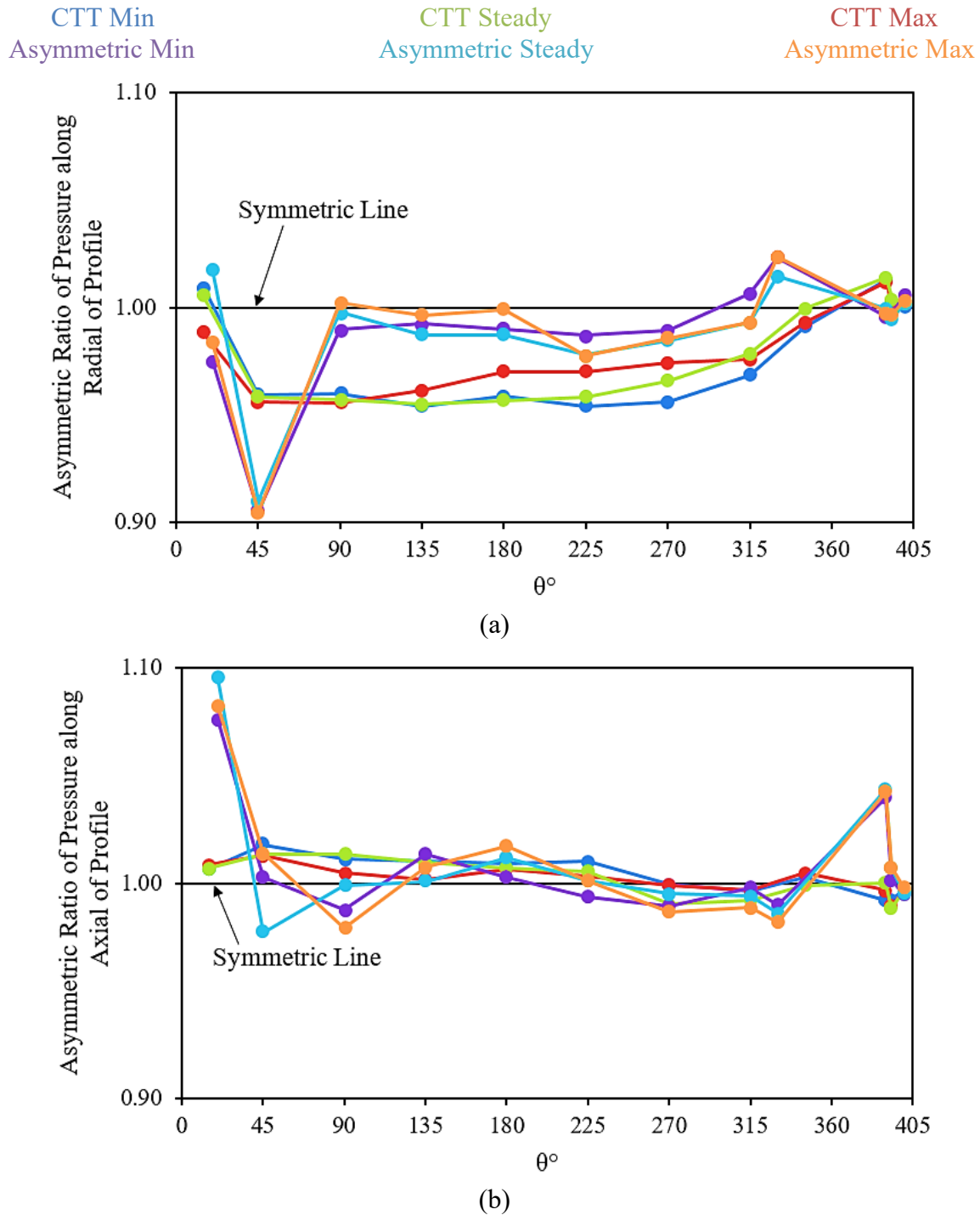


Figure 6.23 Asymmetric ratio of static pressure around the CTT and asymmetric centrifugal compressor volutes along the (a) radial direction of the profiles and (b) axial direction of the profiles

Figure 6.24 depicts the percentage difference against the revolution average of static pressure through asymmetric volute at (a) the maximum point and (b) the minimum point. Prominent variances are displayed in the freestream and along wall of both cases with distinct vice versa percentage differences between Figure 6.24 (a) and Figure 6.24 (b). At 20°, Figure 6.24 (a) high static pressure difference occurs through the volute inflow with low differences at the wall



of the outer curve, while Figure 6.24 (b) depicts low static pressure difference through the volute inflow and high static pressure difference at the wall of the outer curve. From  $45^\circ$  to  $225^\circ$ , high static pressure differences against that of the revolution averaged occurs along the outer curve in Figure 6.24 (a), whereas in Figure 6.24 (b), low static pressure differences are displayed here. At  $45^\circ$ , lowest static pressure difference against the revolution averaged occurs in the overhang of the profile, while Figure 6.24 (b) shows high static pressure differences here. From  $90^\circ$  to  $225^\circ$ , this high region for Figure 6.24 (a) and low region for Figure 6.24 (b) are localised more in the central of the profiles. In Figure 6.24 (a), although low static pressure difference is localised in the central region at  $270^\circ$  and  $315^\circ$ , the lowest static pressure difference is exhibited at the wall in the overhang, while the highest static pressure differences are exhibited along the outer curve. In the case of Figure 6.24 (b), highest static pressure differences are localised at the wall in the overhang, with  $315^\circ$  also displayed high static pressure difference in the freestream of the profile. Low static pressure difference is depicted along the outer curve close to the front face of the profile. At the cut-off location, high static pressure differences compared to that of the revolution averaged is seen at the wall along the front face in Figure 6.24 (a), with low region in the centre more towards the outer curve. For Figure 6.24 (b), low static pressure differences compared to that of the revolution averaged is viewed at the wall near the front face with high regions viewed in the centre more towards the outer curve. At the exit cone, high static pressure difference is observed in vicinity of the front face in Figure 6.24 (a) with low region in the central area of the outer curve. Figure 6.24 (b) observes low and high static pressure difference here, respectively. At the discharge duct for Figure 6.24 (a), there are two regions of low static pressure difference where one large region is localised near the front face and one small region is localised near the rear face, with high region seen along the wall of the rear face. For Figure 6.24 (b), low regions are depicted along the walls of the front and rear faces and two high regions are seen in the centre near the outer curve and near the rear face. At the outlet, Figure 6.24 (a) show high and low regions near the outer curve and near the central of the rear face, respectively, while Figure 6.24 (b) depicts the vice versa at these locations of the profile.

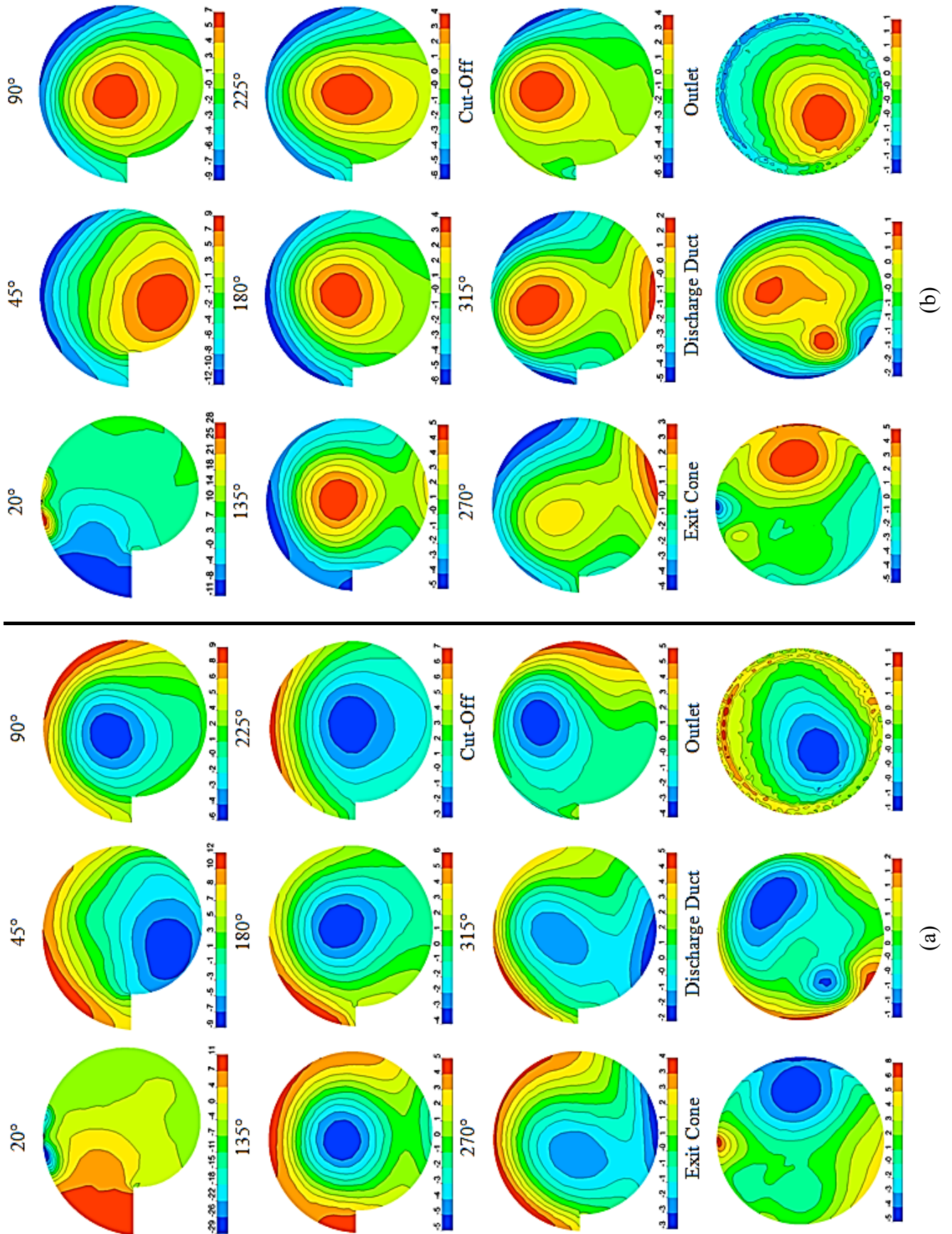


Figure 6.24 Percentage difference of static pressure through asymmetric volute at (a) maximum (b) minimum

Figure 6.25 depicts the percentage difference against the revolution average of static pressure through the CTT volute at (a) the maximum point and (b) the minimum point. Similarities are seen here as that of Figure 6.24 where the minimum case predominantly shows the vice versa high and low static pressure differences to that of the maximum case. At 15°, Figure 6.25 (a) high static pressure difference is seen at the outer curve near the rear face, while low regions are depicted at the centre of the outer curve and a small region in the centre of the inflow. Figure 6.25 (b) displays the vice versa high and low static pressure difference at these locations. Figure 6.25 (a) shows that high static pressure difference remains along the wall of the outer curve from 45° to 315°. Thereafter at the cut-off location, high regions are depicted along the wall of front and rear faces. Following this, the exit cone depicts a high static pressure difference region at the wall between the outer curve and front face, while the discharge duct and outlet identifies high regions along the wall of the front face. Further to this, low static pressure difference regions are predominantly depicted in the free-stream of all profiles. From 45° and 315°, there are very small regions of low static pressure differences emerging from the inflow and between the inflow and overhang. This is in addition to the low regions across the central of the profiles, with that at 90° and 315° depicting slightly lower static pressure differences. At the cut-off location, there are two regions of low static pressure differences with one region emerging from the inner curve and the other region in the central region towards the outer curve. The exit cone presents a low static pressure difference region emerging near the rear face, while the discharge duct shows low regions along the rear face and in the central area more towards the rear face. The outlet displays this low static pressure difference in the free-stream. Figure 6.25 (b) shows that low static pressure difference remains along the wall of the outer curve from 45° to the cut-off. Low regions at the exit cone and outlet are depicted along the wall of the outer curve slightly towards the rear face, while that at the discharge duct depicts this slightly towards the front face. At 45° and 90°, high static pressure differences are seen to emerge from the inflow and between the inflow and overhang, which becomes more prominent in the central area of these cross-sections. At 135°, cut-off location, exit cone and outlet, high static pressure differences are seen in the central region of the profiles, while from 180° to 315°, these high regions emerge from the inner curve to the central region. At the discharge duct, high static pressure difference is displayed in the central region towards and along the rear face.

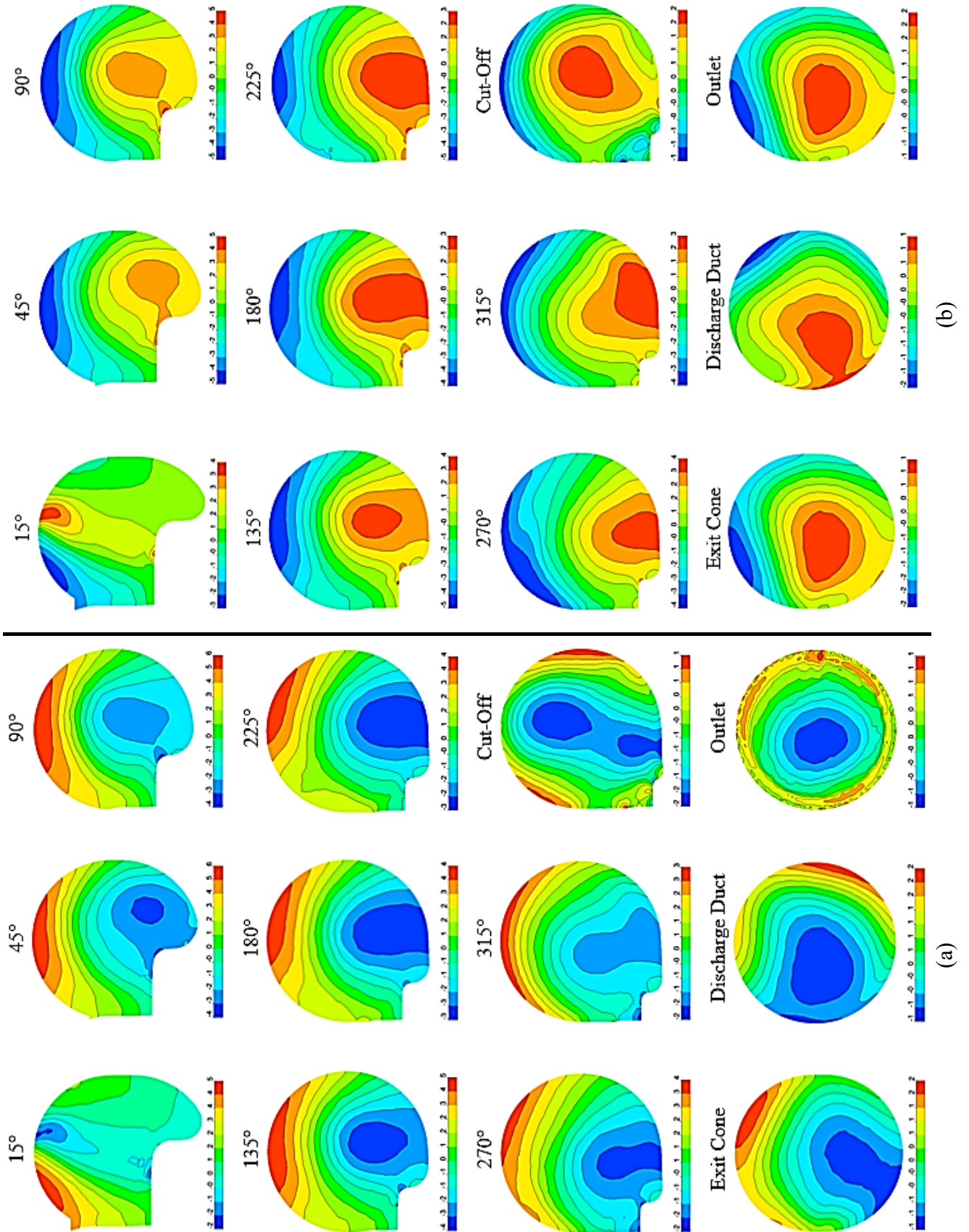


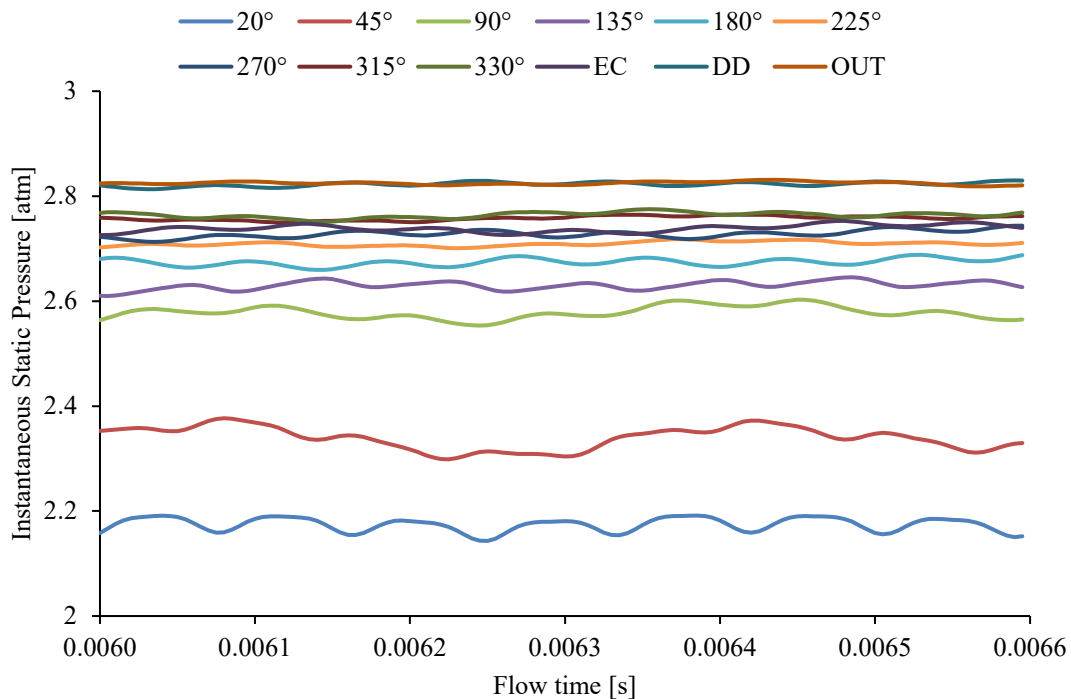
Figure 6.25 Percentage difference of static pressure through CTT volute at (a) maximum (b) minimum



Figure 6.26 depicts the instantaneous static pressure variation across a single revolution for (a) asymmetric volute and (b) CTT volute from the first profile to the outlet. The minimum, maximum, mean and standard deviation have also been presented for static pressure across each selected profile through the centrifugal compressor volute during one revolution.

In Figure 6.26 (a), it can be seen that static pressure clearly increases as the flow travels around the volute, whereas in the case of Figure 6.26 (b), there are many overlaps between the profiles. Figure 6.26 (a) table shows that minimum static pressure is at 20°, while the maximum static pressure is at the discharge duct and outlet. Furthermore, the maximum standard deviation of static pressure is at 45°.

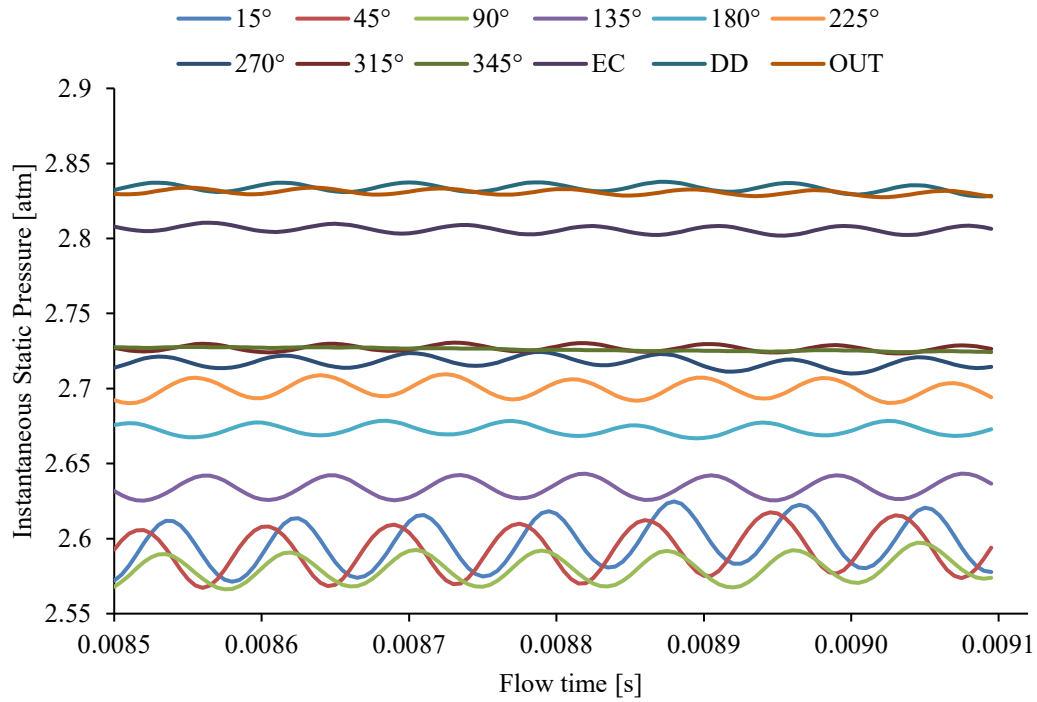
In Figure 6.26 (b), static pressure at 15° reaches higher than that at 90° at its maximum and at 90° static pressure reaches lower than that 15° at its minimum. From 135° to 270°, a clear increase in downstream static pressure is displayed. Static pressure at 315° is seen to be higher and lower at its maximum and minimum, respectively, compared to that at 345°. Further to this, static pressure at the exit cone is higher and is seen to increase as the fluid travels downstream to the outlet of the volute. Figure 6.26 (b) table shows that minimum static pressure is from 15° to 90°, while the maximum static pressure is also at the discharge duct and outlet. Moreover, the maximum standard deviation of static pressure is at 45°.



## CHAPTER SIX: DESIGN METHODOLOGY FOR A TURBOCHARGER COMPRESSOR VOLUTE

	20°	45°	90°	135°	180°	225°	270°	315°	330°	EC	DD	OUT
Min	2.14	2.30	2.55	2.61	2.66	2.70	2.71	2.75	2.75	2.73	2.81	2.82
Max	2.19	2.38	2.60	2.65	2.69	2.72	2.74	2.76	2.78	2.75	2.83	2.83
Mean	2.17	2.34	2.58	2.63	2.67	2.71	2.73	2.76	2.76	2.74	2.82	2.82
$\sigma$	0.01	0.02	0.01	0.01	0.01	0.00	0.01	0.00	0.01	0.01	0.00	0.00

(a)



	15°	45°	90°	135°	180°	225°	270°	315°	345°	EC	DD	OUT
Min	2.57	2.57	2.57	2.63	2.67	2.69	2.71	2.72	2.72	2.80	2.83	2.83
Max	2.62	2.62	2.60	2.64	2.68	2.71	2.72	2.73	2.73	2.81	2.84	2.83
Mean	2.60	2.59	2.58	2.63	2.67	2.70	2.72	2.73	2.73	2.81	2.83	2.83
$\sigma$	0.02	0.01	0.01	0.01	0.00	0.01	0.00	0.00	0.00	0.00	0.00	0.00

(b)

Figure 6.26 Instantaneous static pressure variation through (a) Asymmetric volute and (b) CTT volute

### 6.6.2 Local Velocity Magnitude through Asymmetric Type Volutes

Figure 6.27 depicts the distribution of velocity magnitude through the turbocharger compressor volute during the operating speed of 98.2rps/ $\sqrt{K}$  at design flow rate. Twelve cross-sections through the volute channel have been presented from the first cross-section of the scroll situated above the tongue, through to the outlet of the compressor stage. Velocity magnitude is zero at the walls due to no-slip boundary conditions. From the base of the tail at the first cross-section profile located at 20°, high velocity magnitude is identified with pockets of higher flow velocity magnitude along the outer curvature of the scroll. A great deal of velocity magnitude non-uniformities are displayed at 20° and at 45° is due to the influences of the volute tongue. At 20°, low velocity magnitude regions are exhibited along the curvature of the front face, while high regions are exhibited near the outer curve. At 45°, high inflow is exhibited with low regions in the overhang near the inlet. From 90° to the cut-off location, lower velocity magnitude is seen in the free-stream with higher velocity magnitudes at the inflow. Decelerated flow is displayed downstream from the cut-off location.

Figure 6.28 quantifies the velocity magnitude distribution across each plane around the turbocharger compressor volute and compares the newly designed asymmetric volute with the CTT volute. The percentage difference of the asymmetric volute has been calculated against that of the CTT volute. It is identified the highest velocity magnitude variation between the two volute models occur in the first profile where the asymmetric volute depicts 22.2% accelerated flow than that for CTT. The lowest velocity magnitude variation occurs in the discharge duct, where the asymmetric volute identifies 0.1% higher velocity magnitude than that of CTT. Table 6.10 details the percentage difference in velocity magnitude variation from one cross-section location to the next, specified by the azimuth angle for both CTT and asymmetric volutes. It also details the percentage difference in velocity magnitude variation occurring at each cross-section around the volute against that depicted at the outlet for both CTT and asymmetric volutes. Regarding the velocity magnitude variation from one cross-section location to the next, the highest velocity magnitude variation occurs between the cut-off and the exit cone for the CTT case where the flow decelerates by 30%, while the lowest variation occurs between 270° and 315° where the flow decelerates by 0.3%. For the newly designed asymmetric case, the highest velocity magnitude variation occurs between the exit cone and discharge duct where the flow decelerates by 25.6%, while the lowest variation occurs between 180° and 225° where the flow decelerates by 2.7%. Regarding the velocity magnitude variation occurring at each cross-section around the volute against that depicted at the outlet, highest

velocity magnitude variances occur at 90° and 45° for the CTT volute and asymmetric volute, respectively. CTT volute identifies 127.2% higher velocity magnitude than that at the outlet, while asymmetric volute identifies 132.6% higher velocity magnitude than that at the outlet. The lowest occurs in the discharge duct with 2.8% higher velocity magnitude than that at the outlet for the CTT volute and 2.8% higher velocity magnitude than that at the outlet for Asymmetric volute. Overall, when comparing the Asymmetric volute with the CTT volute, a decrease in velocity magnitude means that more kinetic energy is converted into potential energy, hence signifies an improvement in performance. It is identified that velocity magnitude is initially higher until the flow reaches 45°, then lower downstream to the cut-off location, which then increases at the exit cone, followed by exhibiting lower velocity magnitude at the outlet.

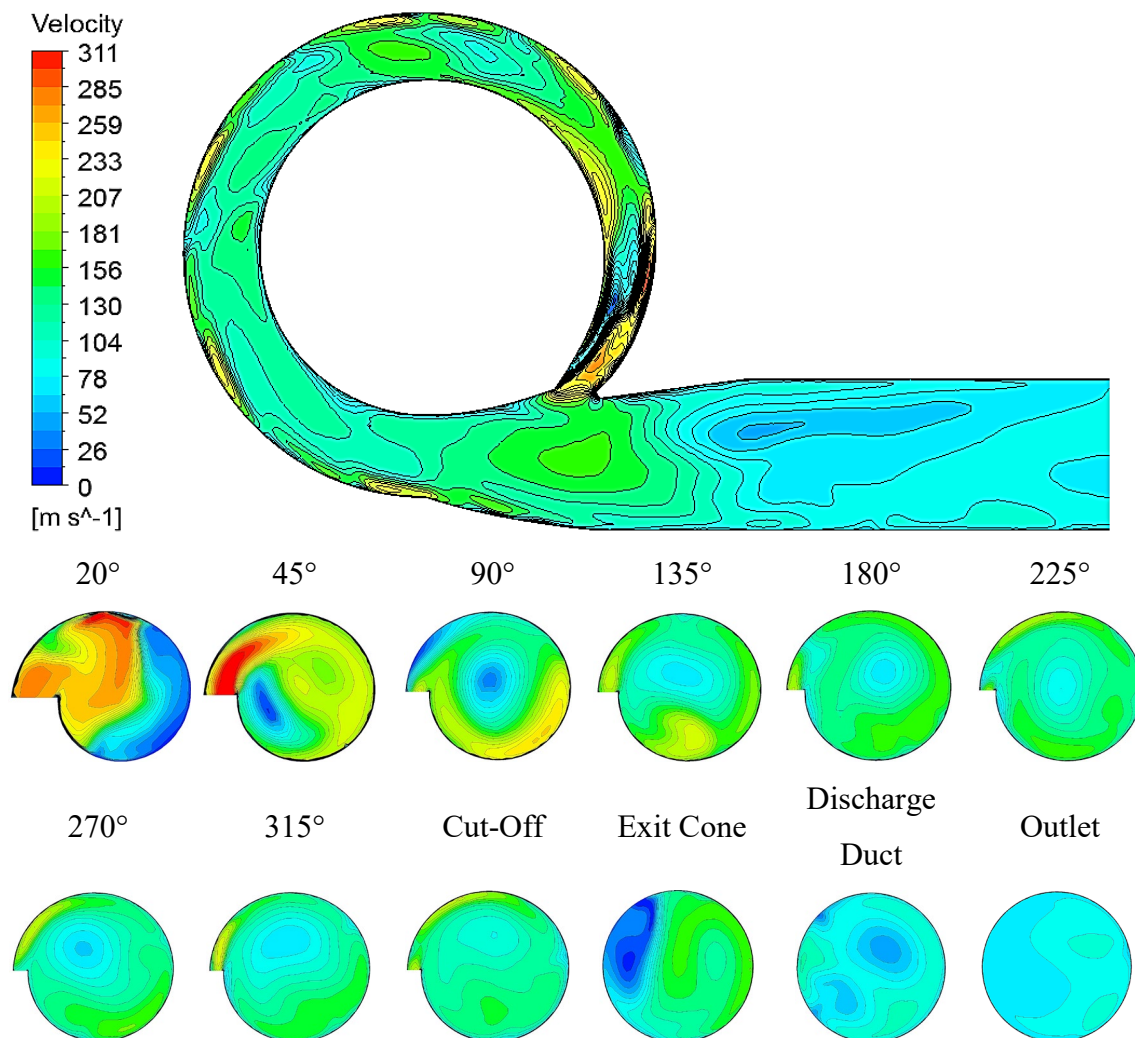


Figure 6.27 Velocity magnitude around the asymmetric type compressor volute



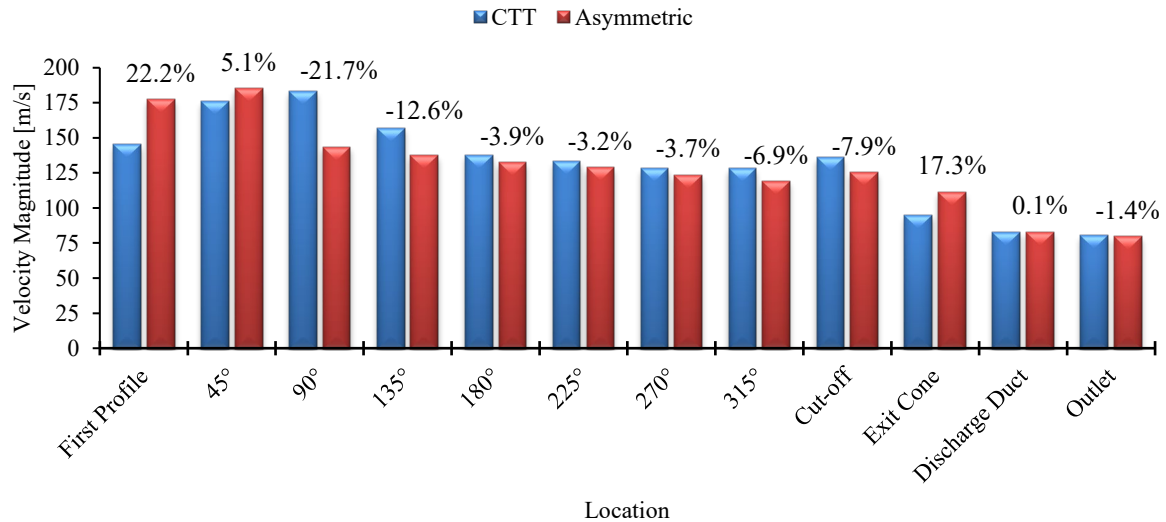


Figure 6.28 Velocity magnitude across each cross-section around the asymmetric volute and CTT volute

Table 6.10 Asymmetric volute comparison with CTT volute of velocity magnitude variation from plane to plane and outlet to plane

$\theta^\circ$ to $\theta^\circ$ Velocity Magnitude Variation [%]			Outlet to $\theta^\circ$ Velocity Magnitude Variation [%]		
$\theta^\circ - \theta^\circ$	CTT	Asymmetric	$\theta^\circ$	CTT	Asymmetric
<b>FP - 45</b>	21.2	4.2	<b>First Profile</b>	79.9	123.2
<b>45 - 90</b>	4.2	-22.4	<b>45</b>	118.0	132.6
<b>90 - 135</b>	-14.3	-4.4	<b>90</b>	127.2	80.6
<b>135 - 180</b>	-12.2	-3.5	<b>135</b>	94.7	72.7
<b>180 - 225</b>	-3.4	-2.7	<b>180</b>	70.9	66.7
<b>225 - 270</b>	-3.8	-4.2	<b>225</b>	65.1	62.2
<b>270 - 315</b>	-0.3	-3.6	<b>270</b>	58.9	55.3
<b>315 - CO</b>	6.4	5.2	<b>315</b>	58.5	49.8
<b>CO - EC</b>	-30.0	-10.9	<b>Cut- off</b>	68.6	57.5
<b>EC - DD</b>	-12.9	-25.6	<b>Exit Cone</b>	18.0	40.4
<b>DD - OUT</b>	-2.7	-4.3	<b>Discharge Duct</b>	2.8	4.5

Figure 6.29 is a graphical representation depicting the asymmetric ratio of velocity magnitude along the radial direction of the cross-section profiles in (a) and axial direction of the cross-section profiles in (b) around the centrifugal compressor volute at design flow rate and high operating speed of 98.2rps/ $\sqrt{K}$ . The data included comprises of the minimum and maximum responses for the CTT volute and the Asymmetric volute. More detailed graphical representations are depicted in APPENDIX 4.

In the case of Figure 6.29 (a), velocity magnitudes along the radial direction for the first profile are asymmetric towards the outer curve for all cases aside from CTT Max, where this depicts asymmetric towards the inner curve. At 45°, all cases depict velocity magnitude asymmetry along the radial direction towards the outer curve with the CTT cases depicting less asymmetry than Asymmetric cases. From 90° to the cut-off location, all cases are asymmetric towards the inner curve. The min and max cases are for both volutes show very close asymmetry. At 90°, 135° and from 270° to the cut-off, CTT cases show less asymmetry than Asymmetric cases, while at 180°, the Asymmetric cases show less asymmetry than CTT cases. At the exit cone, Asymmetric cases exhibit velocity magnitude asymmetry towards the inner curve along the radial direction, whereas CTT cases exhibit asymmetry towards the outer curve. At the discharge duct, all cases are asymmetric towards the outer curve. At the outlet, CTT Steady depicts symmetry in velocity magnitude along the radial direction, whilst remainder of the cases depict asymmetry towards the inner curve.

In the case of Figure 6.29 (b), velocity magnitude along the axial direction depicts asymmetry along the axial direction towards the rear face with the CTT cases identifying less asymmetry than Asymmetric cases. At 45° to 135°, CTT Max exhibits velocity magnitude asymmetry along the axial direction towards the rear face. At 45° and 90°, all Asymmetric cases and CTT Steady exhibit velocity magnitude asymmetry along the axial direction towards the front face. CTT Min show slight asymmetry towards the rear face at 45° and symmetry along the axial direction at 90°. At 135°, Asymmetric Max displays symmetric velocity magnitude along the axial direction while Asymmetric Steady displays slight asymmetry towards the rear face and remainder cases remain asymmetric towards the front face. At 180°, all CTT cases present asymmetry towards the front face, whereas all Asymmetric cases present asymmetry towards the rear face. At 225°, all CTT cases identify symmetric velocity magnitude along the axial direction while Asymmetric Steady shows very slight asymmetry towards the front face and Asymmetry Min and Asymmetry Max show asymmetry towards the rear face. At 270°, only the two Steady cases depict asymmetry towards the rear face, while the Min and Max cases for both volutes depicts asymmetry towards the front face. All CTT cases display slight velocity magnitude asymmetry along the axial direction towards the rear face at 315° and the exit cone, whereas all Asymmetric cases display slight asymmetry towards the front face. This is vice versa at the cut-off location. The discharge duct depicts velocity magnitude asymmetry along the axial direction towards the rear face for all cases, while the outlet depicts symmetry in

velocity magnitude along the axial direction for CTT cases and asymmetry towards the front face for Asymmetric cases.

Overall, the influence on the imbalance of velocity magnitude along the radial direction through the centrifugal compressor volute for all cases of the Asymmetric model are greater than all cases of the CTT model. Further to this, the influence on the imbalance of velocity magnitude along the axial direction through the centrifugal compressor volute for all cases are very similar. However, the Asymmetric volute depict a higher influence on the imbalance of velocity magnitude in comparison with the CTT volute in vicinity of the tongue region.

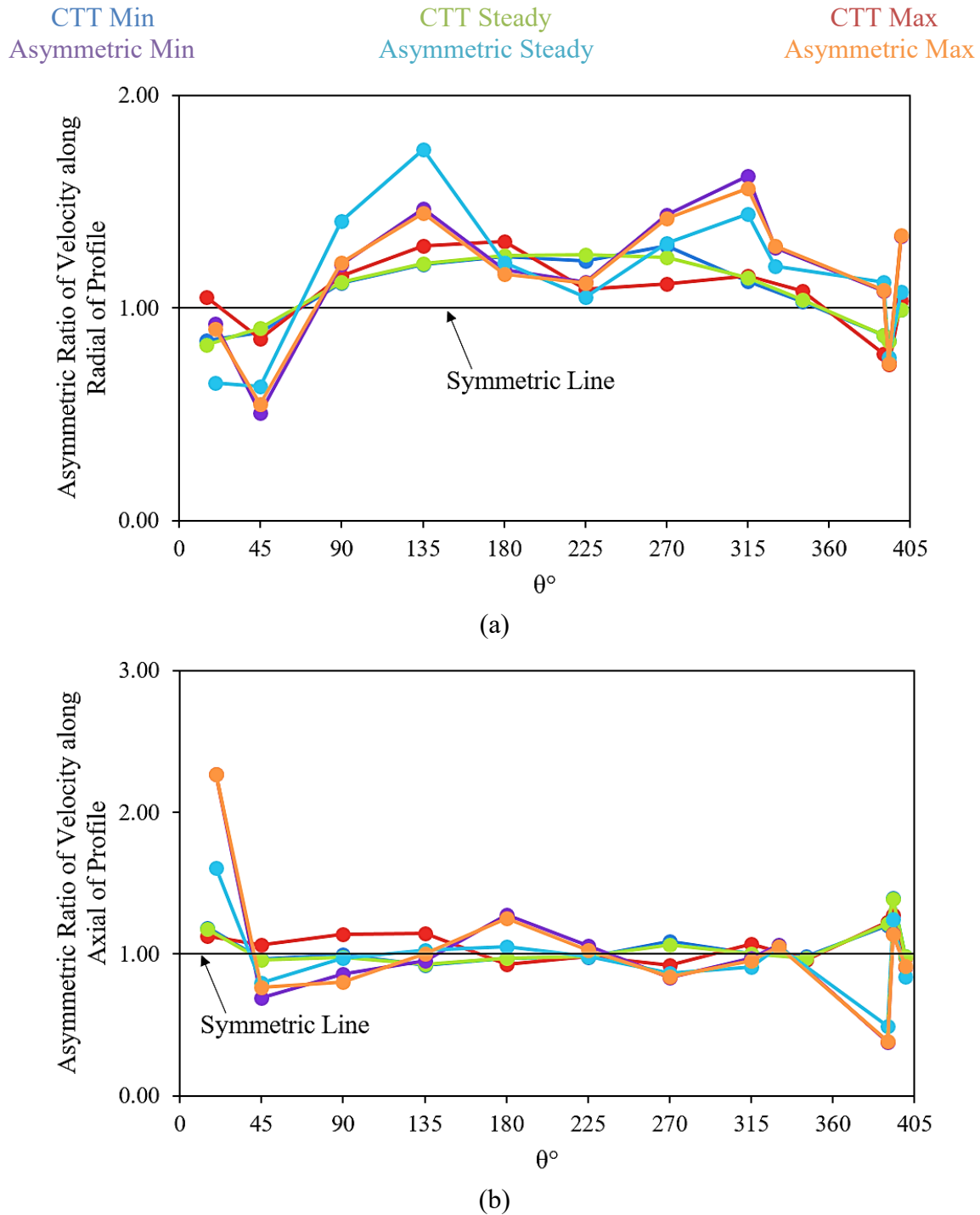


Figure 6.29 Asymmetric ratio of velocity magnitude around the CTT and asymmetric centrifugal compressor volutes along the (a) radial direction of the profiles and (b) axial direction of the profiles

Figure 6.30 depicts the percentage difference against the revolution average of velocity magnitude through asymmetric volute at (a) the maximum point and (b) the minimum point. Prominent variances are displayed with vice versa percentage differences between Figure 6.30 (a) and Figure 6.30 (b). At  $20^\circ$ , high velocity magnitude differences are displayed as a small area near the outer curve in Figure 6.30 (a) with low velocity magnitude difference in the

central region towards the front face. Figure 6.30 (b) depicts low and high velocity magnitude differences at these locations, respectively. At 45°, Figure 6.30 (a) depicts high velocity magnitude difference at the inflow and low velocity magnitude difference in the overhang near the inlet, while Figure 6.30 (b) depicts low and high velocity magnitude differences at these locations, respectively. From 90° to 270°, °, Figure 6.30 (a) depicts low velocity magnitude differences in the free-stream of the cross-sections, while Figure 6.30 (b) depicts low velocity magnitude differences here. At 90°, Figure 6.30 (a) displays high velocity magnitude differences along the front face of the profile, while at 135° and 270° high regions are depicted in the overhang of the profiles. Figure 6.30 (b) depicts low velocity magnitude differences at these locations. From 180° to the cut-off location, Figure 6.30 (a) and Figure 6.30 (b) present high and low velocity magnitude differences at the inflow, respectively. At the exit cone, Figure 6.30 (a) exhibits high velocity magnitude difference along the front face and small regions of low velocity magnitude differences in vicinity of the rear face. Figure 6.30 (b) depicts low and high velocity magnitude differences at these locations, respectively. At the discharge duct, regions of high velocity magnitude differences are localised along front and rear faces of the profile with low velocity magnitude difference localised on the upper centre of the profile for Figure 6.30 (a). Figure 6.30 (b) depicts the respective low and high velocity magnitude differences in the same locations of the profile. At the outlet, high velocity magnitude difference is localised on the upper centre of the profile with low velocity magnitude difference localised on the lower centre of the profile for Figure 6.30 (a). This is vice versa with respect to Figure 6.30 (b).

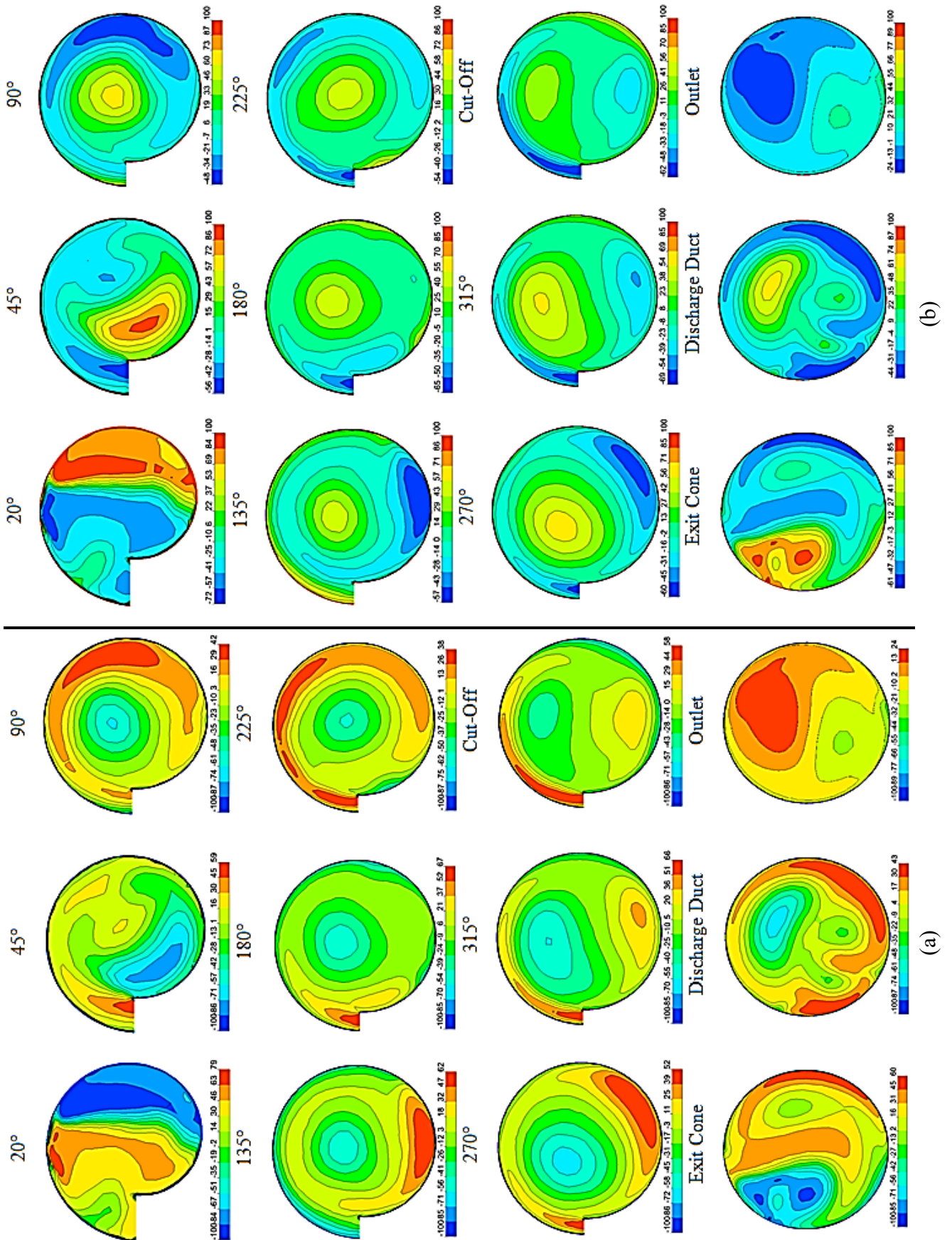


Figure 6.30 Percentage difference of velocity magnitude through asymmetric volute at (a) maximum (b) minimum

Figure 6.31 depicts the percentage difference against the revolution average of velocity magnitude through CTT volute at (a) the maximum point and (b) the minimum point. Prominent variances are displayed with distinct vice versa percentage differences between Figure 6.31 (a) and Figure 6.31 (b). From  $15^\circ$  to the cut-off location, high and low velocity magnitude differences exist at the inflow for Figure 6.31 (a) and Figure 6.31 (b), respectively. For Figure 6.31 (a), there are additional areas of high velocity magnitude differences from  $15^\circ$  to  $135^\circ$ . High regions are observed in the centre near the outer curve of  $15^\circ$ ; along the front face of  $45^\circ$ ; in the overhang at  $90^\circ$  and  $135^\circ$ . In the case of Figure 6.31 (b), lower regions are depicted at these locations. From  $15^\circ$  to  $135^\circ$ , very small regions of low and high velocity magnitude differences exist at the rear faces for Figure 6.31 (a) and Figure 6.31 (b), respectively. From  $180^\circ$  to  $270^\circ$ , these low and high regions with respect to for Figure 6.31 (a) and Figure 6.31 (b) are localised along the curvature from the rear face to the outer curve. At  $315^\circ$  and the cut-off location, these velocity magnitude differences are very small and can be viewed at between the inflow and overhang. At the exit cone, Figure 6.31 (a) depicts high velocity magnitude differences along the bottom sector of the rear face and low velocity magnitude differences along the curvature of the upper sector. Figure 6.31 (b) identifies the low and high velocity magnitude differences at these locations, respectively. At the discharge duct, high velocity magnitude differences are seen at the rear face of the profile with low velocity magnitude differences along the curvature of the front face. Again, Figure 6.31 (b) identifies the low and high velocity magnitude differences at these locations, respectively. At the outlet, high velocity magnitude difference is exhibited across the profile with a very small region of low difference at the central location of the front face. Once more, Figure 6.31 (b) presents low and high velocity magnitude differences at the same locations.



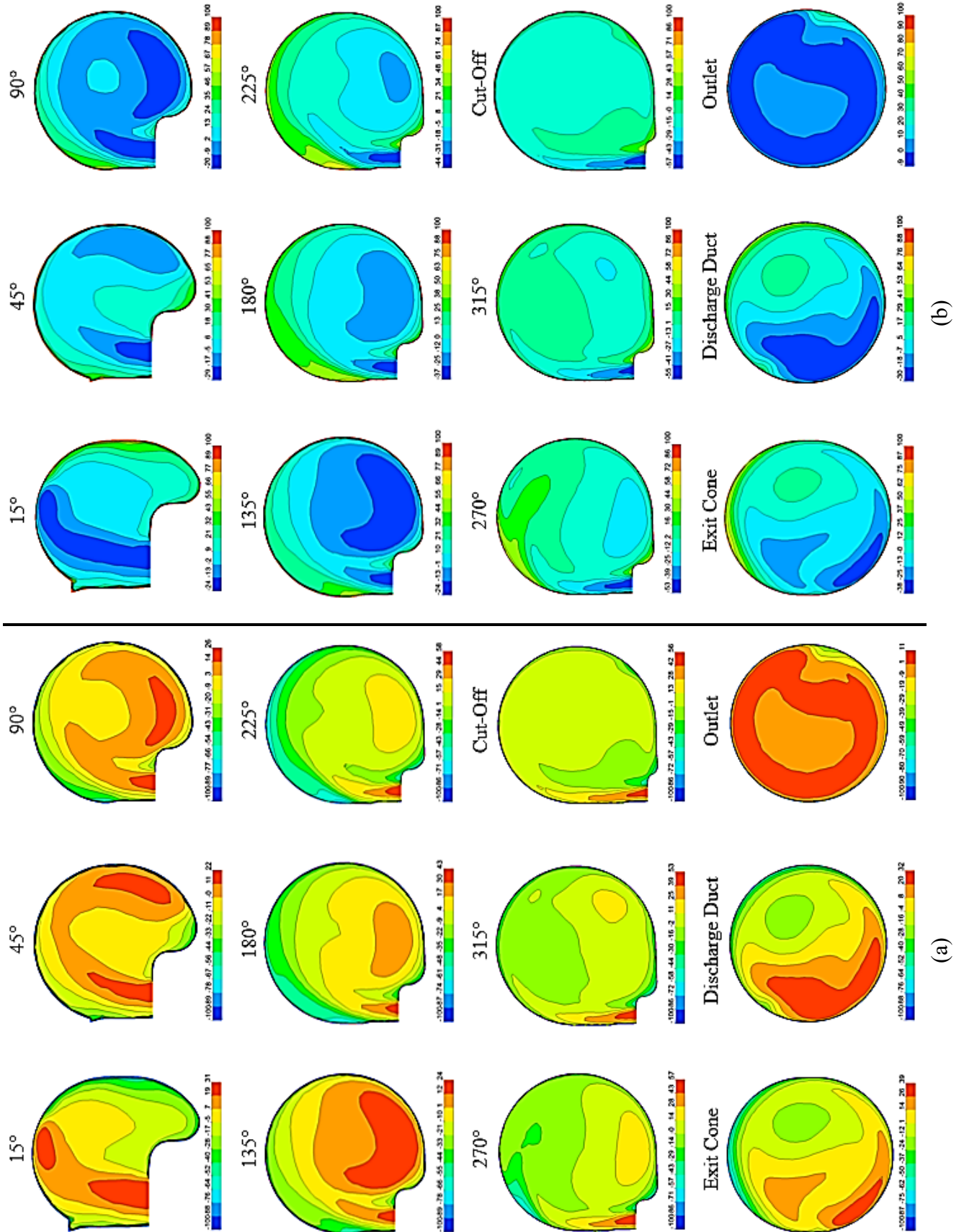


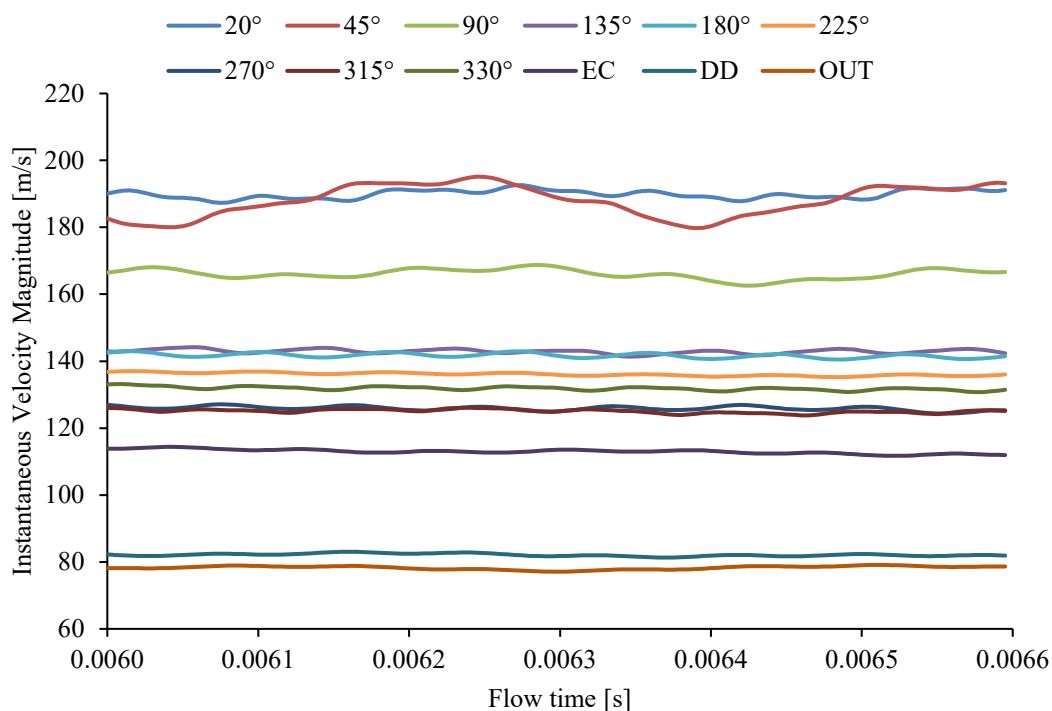
Figure 6.31 Percentage difference of velocity magnitude through CTT volute at (a) maximum (b) minimum



Figure 6.32 depicts the instantaneous velocity magnitude variation across a single revolution for (a) asymmetric volute and (b) CTT volute from the first profile to the outlet. The minimum, maximum, mean and standard deviation have also been presented for velocity magnitude across each selected profile through the centrifugal compressor volute during one revolution.

In Figure 6.32 (a), it can be seen that velocity magnitude predominantly decreases as the flow travels around the volute, though there are some fluctuations between 20° and 45°, which are expected due to the influence of the volute tongue. Figure 6.32 (a) table shows that minimum velocity magnitude is at the outlet, while the maximum velocity magnitude is at 45°. Furthermore, the maximum standard deviation of velocity magnitude is at 45°.

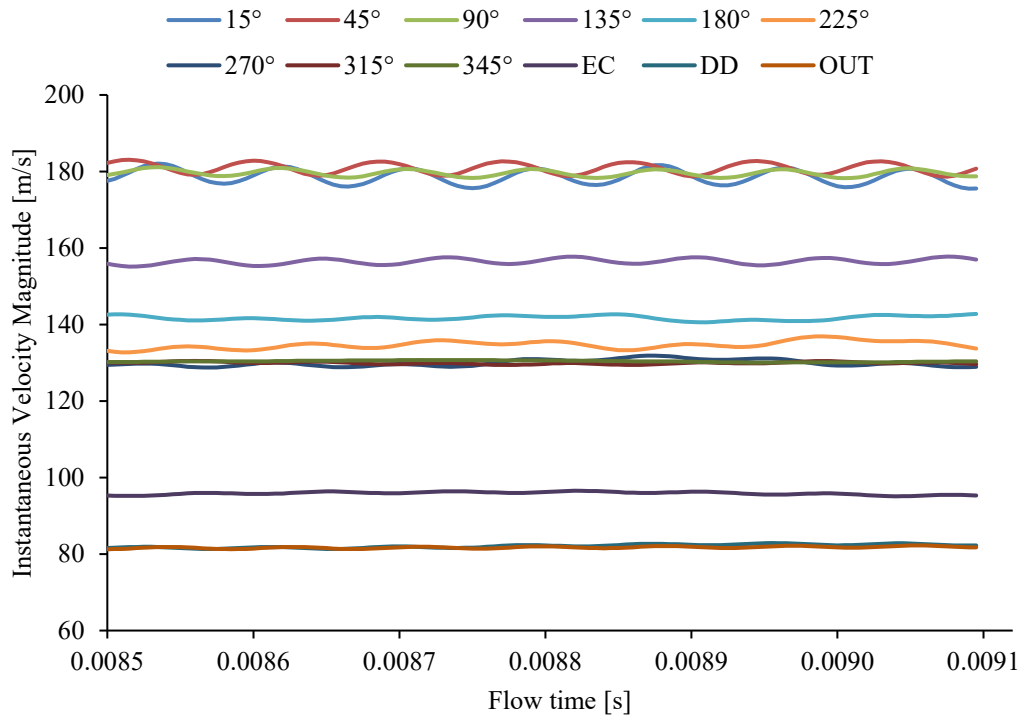
In the case of Figure 6.32 (b), there are some overlaps between 15°, 45° and 90°. Velocity magnitude at 15° is lower than that at 90° at its minimum and velocity magnitude at 45° reaches higher than that 90° at its maximum. From 135° to 225°, a clear decrease in velocity magnitude is displayed. Velocity magnitude from 270° to the cut-off appears to be overlapping, while from the exit cone it is seen to decrease as the fluid travels downstream to the outlet of the volute, with overlapping and minimal variation between that at the discharge duct and that at the outlet. Figure 6.32 (b) table shows that minimum velocity magnitude is at the outlet, while the maximum velocity magnitude is at 45°. Moreover, the maximum standard deviation of velocity magnitude is at 45°.



## CHAPTER SIX: DESIGN METHODOLOGY FOR A TURBOCHARGER COMPRESSOR VOLUTE

	20°	45°	90°	135°	180°	225°	270°	315°	330°	EC	DD	OUT
Min	187.30	179.76	162.56	141.35	140.48	135.23	124.36	123.80	130.74	111.73	81.31	77.08
Max	192.61	195.15	168.78	144.16	143.02	137.01	127.12	126.08	133.14	114.39	83.03	79.10
Mean	189.88	187.88	166.07	142.93	141.71	136.10	125.89	125.06	131.85	113.00	82.12	78.28
$\sigma$	1.28	4.70	1.48	0.64	0.68	0.48	0.65	0.56	0.54	0.66	0.41	0.53

(a)



	15°	45°	90°	135°	180°	225°	270°	315°	345°	EC	DD	OUT
Min	175.51	178.64	178.25	155.16	140.58	132.72	128.76	129.42	130.04	95.08	81.33	81.27
Max	182.06	183.06	181.14	157.76	142.76	136.90	131.85	130.48	130.70	96.53	82.87	82.25
Mean	178.62	180.88	179.57	156.50	141.70	134.69	129.94	129.94	130.37	95.88	82.09	81.74
$\sigma$	1.85	1.38	0.85	0.73	0.59	0.99	0.86	0.27	0.20	0.39	0.45	0.25

(b)

Figure 6.32 Instantaneous velocity magnitude variation through (a) Asymmetric volute and (b) CTT volute

### 6.6.3 Local Static Temperature through Asymmetric Type Volutes

Figure 6.33 depicts static temperature distribution through the turbocharger compressor volute during the operating speed of 98.2rps/ $\sqrt{K}$  at design flow rate. Twelve cross-sections through the volute channel have been presented from the first cross-section of the scroll situated above the tongue, through to the outlet of the compressor stage. Static temperature is seen to increase very slightly downstream to the outlet and is predominantly fairly consistent across the profiles. Pockets of low static temperature can be seen along the outer curve of the scroll. At 20°, low static temperature is identified at the outer curve of the profile. From 45° to the cut-off location, lower static temperatures are seen at the inflow. At the outlet, uniform static temperature is presented.

Figure 6.34 quantifies the static temperature distribution across each plane around the turbocharger compressor volute and compares the newly designed asymmetric volute with the CTT volute. The percentage difference of the asymmetric volute has been calculated against that of the CTT volute. Highest static temperature variation between the two volute models is identified at 90°, where the asymmetric volute depicts 2.4% higher static temperature than that of CTT. No variations between the two models are depicted at the exit cone. Table 6.11 details the percentage difference in static temperature variation from one cross-section location to the next, specified by the azimuth angle of the Asymmetric volute and the CTT volute. It also details the percentage difference in static temperature variation occurring at each cross-section around the volute against that depicted at the outlet of the Asymmetric volute and the CTT volute. Respective of the static temperature variation from one cross-section location to the next, the highest static temperature variation occurs between the first profile and 45° as well as between 90° and 135° for the CTT case with 0.8% fall in static temperature and rise in static temperature, respectively. There are no variations in static temperature between 270° and 315°. For the newly designed asymmetric case, the highest static temperature variation occurs between 45° and 90° with 1.3% rise in static temperature. There are no variations in static temperature between 180° and 225°. Respective the static temperature variation occurring at each cross-section around the volute against that depicted at the outlet, the highest static temperature variance occurs at 90° and in the first profile for the CTT volute and asymmetric volute, respectively. CTT volute identifies 3.3% less static temperature than that at the outlet, while asymmetric volute identifies 3.9% less static temperature than that at the outlet. The lowest occurs in the discharge duct with 0.2% less static temperature than that at the outlet for both cases. Overall, when comparing the Asymmetric volute with the CTT volute, a decrease in

static temperature signifies an improvement in performance. It is identified that static temperature is initially lower in the first profile, then higher downstream to the cut-off location, which remains the same at the exit cone, followed by exhibiting higher velocity magnitude at the outlet.

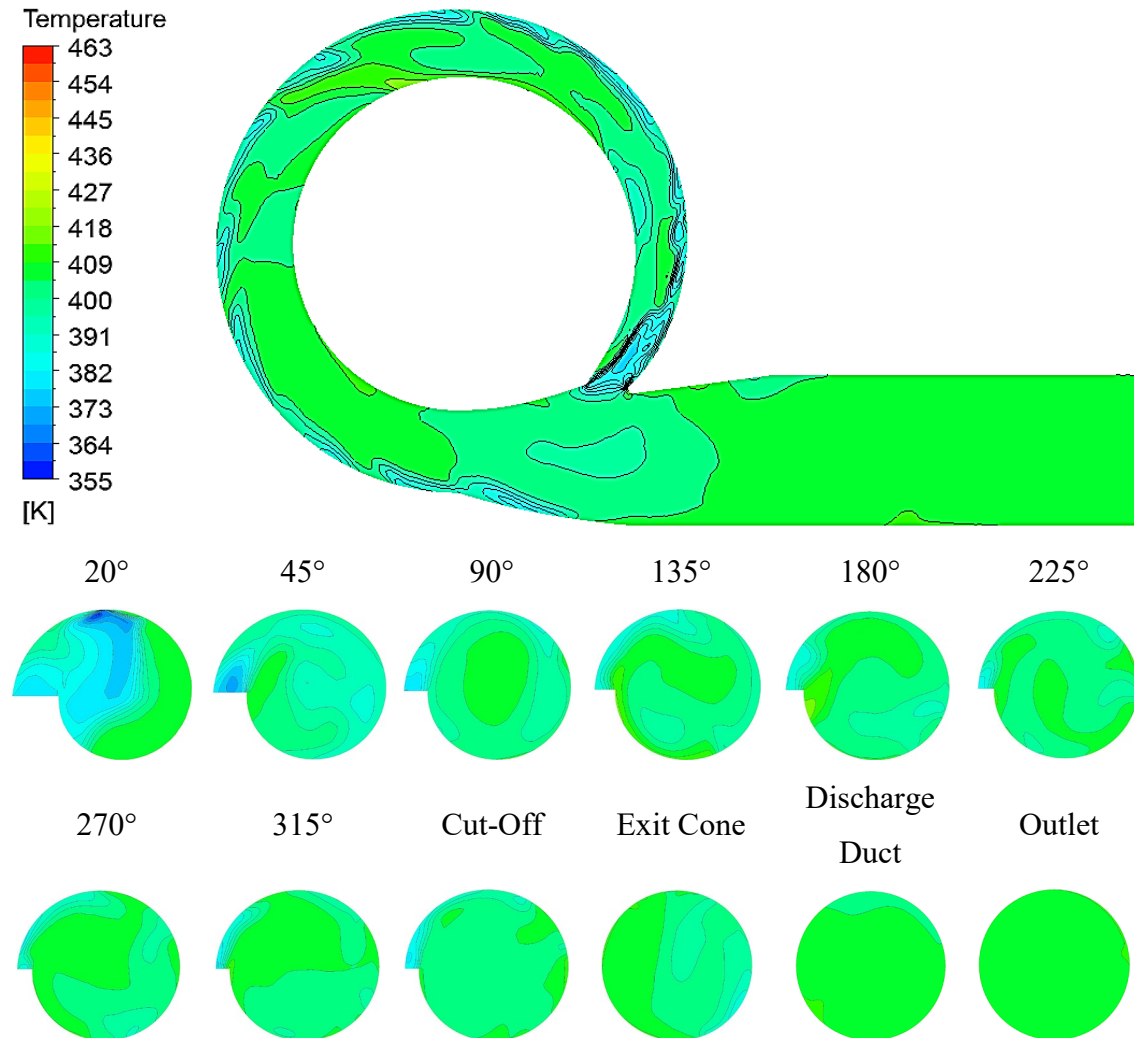


Figure 6.33 Static temperature around the asymmetric type compressor volute

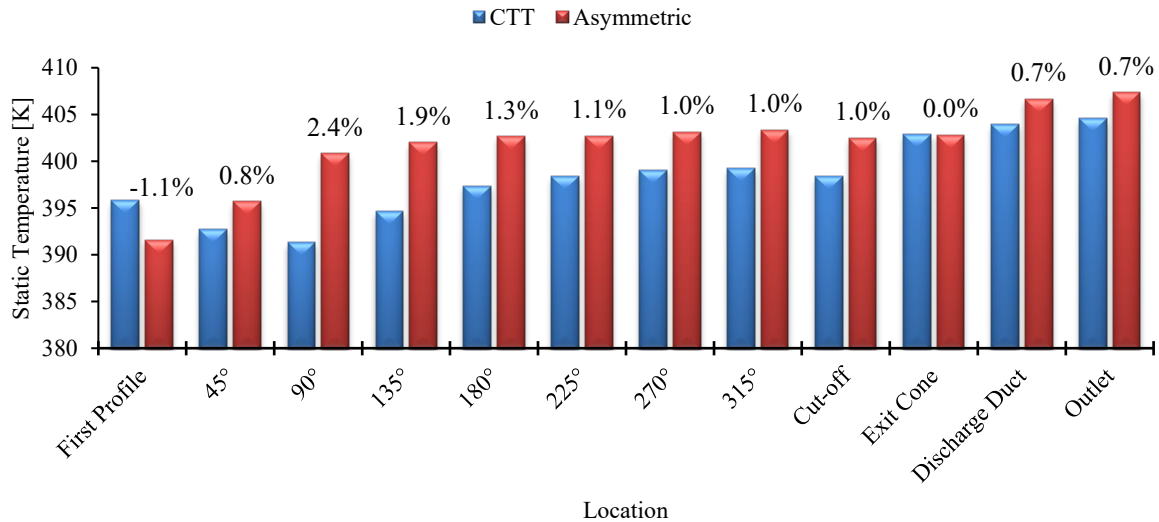


Figure 6.34 Static temperature across each cross-section around the asymmetric volute and CTT volute

Table 6.11 Asymmetric volute comparison with CTT volute of static temperature variation from plane to plane and outlet to plane

$\theta^\circ$ to $\theta^\circ$			Outlet to $\theta^\circ$		
Static Temperature Variation [%]			Static Temperature Variation [%]		
$\theta^\circ - \theta^\circ$	CTT	Asymmetric	$\theta^\circ$	CTT	Asymmetric
<b>FP - 45</b>	-0.8	1.0	<b>First Profile</b>	-2.2	-3.9
<b>45 - 90</b>	-0.3	1.3	<b>45</b>	-2.9	-2.9
<b>90 - 135</b>	0.8	0.3	<b>90</b>	-3.3	-1.6
<b>135 - 180</b>	0.7	0.2	<b>135</b>	-2.5	-1.3
<b>180 - 225</b>	0.2	0.0	<b>180</b>	-1.8	-1.2
<b>225 - 270</b>	0.2	0.1	<b>225</b>	-1.6	-1.1
<b>270 - 315</b>	0.0	0.1	<b>270</b>	-1.4	-1.0
<b>315 - CO</b>	-0.2	-0.2	<b>315</b>	-1.3	-1.0
<b>CO - EC</b>	1.1	0.1	<b>Cut- off</b>	-1.5	-1.2
<b>EC - DD</b>	0.3	1.0	<b>Exit Cone</b>	-0.4	-1.1
<b>DD - OUT</b>	0.2	0.2	<b>Discharge Duct</b>	-0.2	-0.2

Figure 6.35 is a graphical representation depicting the asymmetric ratio of static temperature along the radial direction of the cross-section profiles in (a) and axial direction of the cross-section profiles in (b) around the centrifugal compressor volute at design flow rate and high operating speed of 98.2rps/ $\sqrt{K}$ . The data included comprises of the minimum and maximum responses for the CTT volute and the Asymmetric volute. More detailed graphical representations are depicted in APPENDIX 4.

In the case of Figure 6.35 (a) static temperature along the radial direction is predominantly asymmetric towards the outer curve. For the first profile, almost symmetric static temperature is depicted for CTT Max however this is very slightly asymmetric towards the outer curve along the radial direction and symmetric static temperature is depicted for CTT Steady. The remainder of the cases show asymmetry towards the inner curve. At 45°, all Asymmetric cases and CTT Max display asymmetry towards the inner curve. At 90°, Asymmetric Max presents symmetric static temperature along the radial direction of the profile with Asymmetric Steady and Asymmetric Min displaying asymmetry towards the inner curve. At 135°, Asymmetric Steady remains asymmetric towards the inner curve for static temperature along the axial direction. At 180° Asymmetric Max depicts static temperature asymmetry towards the inner curve along the axial direction. At 225°, Asymmetric Min and Asymmetric Steady show slight asymmetry towards the inner curve. At 270° and 315°, all cases identify asymmetric static temperature towards the outer curve. At the cut-off location, Asymmetric Min and Asymmetric Max exhibit asymmetric in static temperature along the radial direction towards the inner curve, while remainder of the cases exhibit static temperature towards the outer curve. At the exit cone and discharge duct, all CTT cases depict asymmetric static temperature along the radial direction towards the inner curve, while all Asymmetric cases depict asymmetric static temperature along the radial direction towards the outer curve. At the outlet all cases are almost symmetric.

In the case of Figure 6.35 (b) static temperature along the axial direction is predominantly asymmetric towards the front face. At 45°, Asymmetric Max depicts static temperature asymmetry towards the rear face, while Asymmetric Steady displays symmetry along the axial direction. At 180°, Asymmetric Steady and Asymmetric Max present asymmetry towards the rear face. At 225°, Asymmetric Steady remains to display asymmetry towards the rear face. At 270°, the two Min cases display symmetric static temperature along the axial direction while CTT Max depicts asymmetry towards the rear face. At 315°, only Asymmetric Steady and CTT Max exhibit asymmetric static temperature along the axial direction towards the front face, while remainder of the cases exhibit asymmetry towards the rear face. At the cut-off, all Asymmetric cases and CTT Steady identify asymmetry towards the front face with CTT Max identifying asymmetry towards the rear face and CTT Min identifying symmetric static temperature along the axial direction. At the exit cone, all Asymmetric cases present asymmetry towards the rear face, while all CTT cases present asymmetry towards the front face. At the discharge duct, all CTT cases and Asymmetric Min depict asymmetry in static

temperature towards the front face, whereas Asymmetric Steady and Asymmetric Max depict asymmetry towards the rear face. At the outlet Asymmetric Min and Asymmetric Max present asymmetry towards the rear face, while CTT Steady and CTT Max present asymmetry towards the front face. CTT Min and Asymmetric Steady exhibit symmetric static temperature along the axial direction.

Overall, the influence on the imbalance of static temperature along both the radial direction and the axial direction through the centrifugal compressor volute for all cases are very similar.

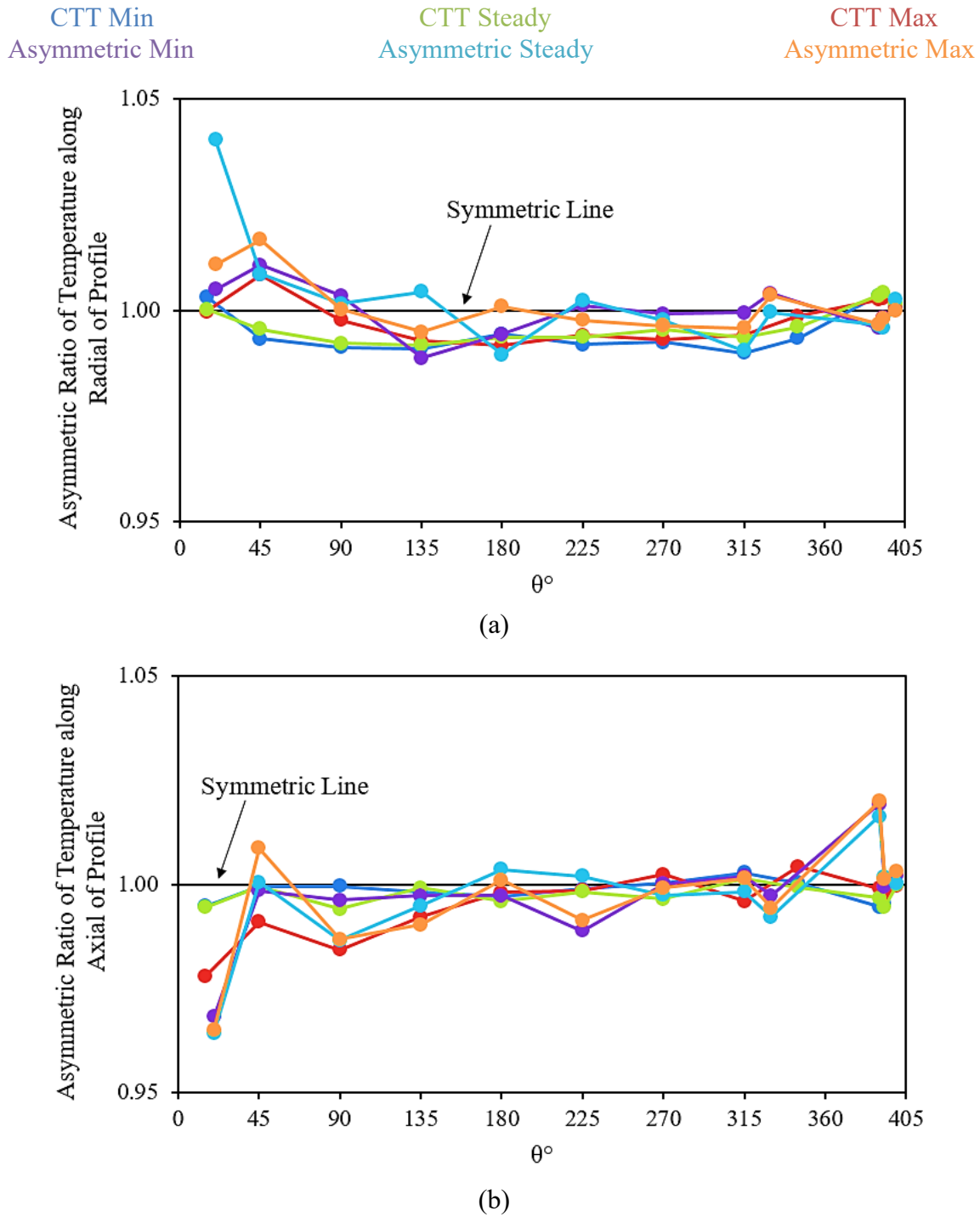


Figure 6.35 Asymmetric ratio of static temperature around the CTT and asymmetric centrifugal compressor volutes along the (a) radial direction of the profiles and (b) axial direction of the profiles

Figure 6.36 depicts the percentage difference against the revolution average of static temperature through asymmetric volute at (a) the maximum point and (b) the minimum point. At 20°, Figure 6.36 (a) displays high static temperature difference across the front face of the profile with small areas of low static temperature differences localised at the outer curve. Figure 6.36 (b) depicts low and high static temperature differences at these locations,



respectively. From 45° to the cut-off location, high and low static temperature differences are depicted at the inflow of Figure 6.36 (a) and Figure 6.36 (b), respectively. At 45°, high static temperature difference is depicted next to the inlet in the overhang in Figure 6.36 (a), while Figure 6.36 (b) displays low static temperature differences in the overhang towards the front face and in the central region towards the rear face. At 90° for Figure 6.36 (a), high static temperature differences are seen prominently in the central region of the profile, as well as slightly along the curvature of the front face near the outer curve and along the overhang curvature next to the inlet. Figure 6.36 (b) depicts low differences along the curvature of the front face and along the overhang curvature next to the inlet. At 135° and 180°, Figure 6.36 (a) depicts high regions of static temperature differences along the curvature of the overhang, while Figure 6.36 (b) depicts low regions of static temperature differences here. There is a large region of high static temperature difference exhibited at 225° in Figure 6.36 (a) across the central region of the profile, whereas in Figure 6.36 (b), a smaller area of low static temperature difference is exhibited in vicinity of the front face in the central region of the profile. At 270°, high static temperature difference is observed in the central region towards the rear face of the profile in Figure 6.36 (a). Figure 6.36 (b) depicts a large region of low static temperature difference emerging from the overhang next to the inlet across to the central region of the profile. At 315° and the cut-off, high and low static temperature differences are localised along the overhang curvature next to the inlet in Figure 6.36 (a) and Figure 6.36 (b), respectively. At the exit cone in Figure 6.36 (a), high and low static temperature differences are localised at the rear face and along the front face, respectively. Figure 6.36 (b) depicts low and high static temperature differences in the same locations, respectively. At the discharge duct, low static temperature difference is localised at the rear face, while high static temperature difference is localised in the central region of the profile in Figure 6.36 (a). Figure 6.36 (b) displays low and high static temperature differences at these locations, respectively. In Figure 6.36 (a) at the outlet, high static temperature difference is identified at the lower sector of the profile with high differences at the front face. Figure 6.36 (b) depicts this for low and higher difference, respectively, also identifying high differences in the upper sector of the profile near the front face.

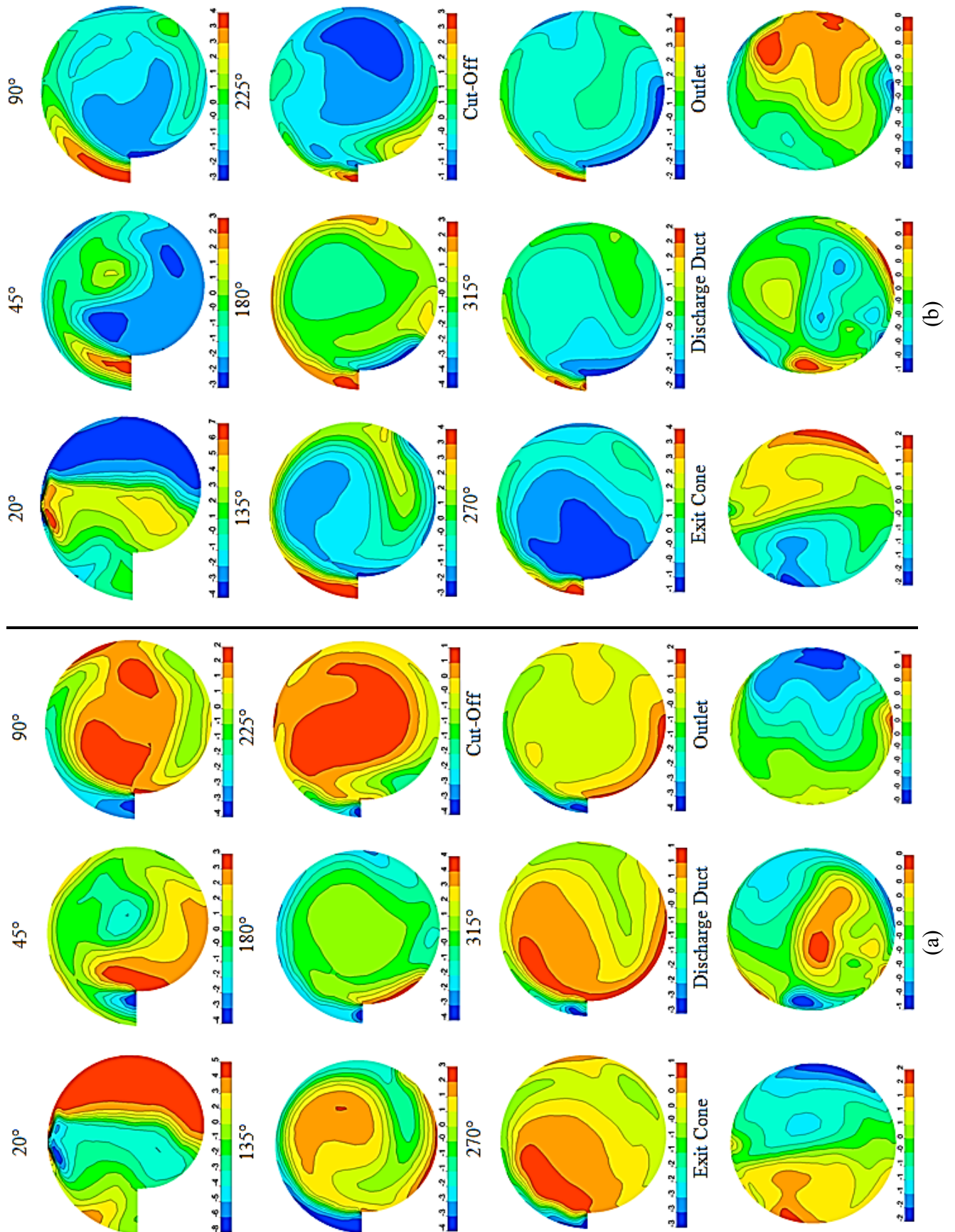


Figure 6.36 Percentage Difference of Static Temperature through Asymmetric Volute at (a) Maximum (b) Minimum

Figure 6.37 depicts the percentage difference against the revolution average of static temperature through CTT volute at (a) the maximum point and (b) the minimum point. From 15° to the cut-off location, low and high static temperature differences are localised at the inflow next to the rear face for Figure 6.37 (a) and Figure 6.37 (b), respectively. At 15°, Figure 6.37 (a) depicts high static temperature difference at the inflow next to the overhang as well as along the outer curve. In Figure 6.37 (b), low static temperature difference is exhibited along the outer curvature. At 45° in Figure 6.37 (a) high static temperature differences are seen along the outer curve, along the overhang and in the central region of the profile towards the rear face. In Figure 6.37 (b), low static temperature difference is localised at the inflow next to the overhang. High and low static temperature differences are displayed at the inflow next to the overhang from 90° to 225° for Figure 6.37 (a) and Figure 6.37 (b), respectively. Additional regions of high static temperature differences in Figure 6.37 (a) are depicted in the central of the profile at 180° and at the cut-off location. Additional regions of low static temperature differences in Figure 6.37 (b) are depicted slightly along the overhang curvature next to the inlet at 90° and from 180° to 315°. Further to this, low regions are displayed across the central of the profile at 180°, 225° and 315°, as well as along the outer curvature at 270° and 315°. At the exit cone, Figure 6.37 (a) depicts a very small area of high static temperature difference at the rear face of the profile with prominent low static temperature difference in the lower sector towards the rear face. Figure 6.37 (b) depicts high and low static temperature differences in the same locations as the low and high regions depicted in Figure 6.37 (a), respectively. Low static temperature difference in Figure 6.37 (b) is also displayed along the curvature of the front face. At the discharge duct, low and high static temperature differences are exhibited at the rear face and the front face of the profile in Figure 6.37 (a), respectively. Figure 6.37 (b) exhibits the high and more prominent low static temperature differences in the same locations, respectively. At the outlet, high static temperature difference is displayed along the front face of the profile, while low static temperature differences are displayed near the front face. Figure 6.37 (b) exhibits the high and low static temperature differences in the same locations, respectively.

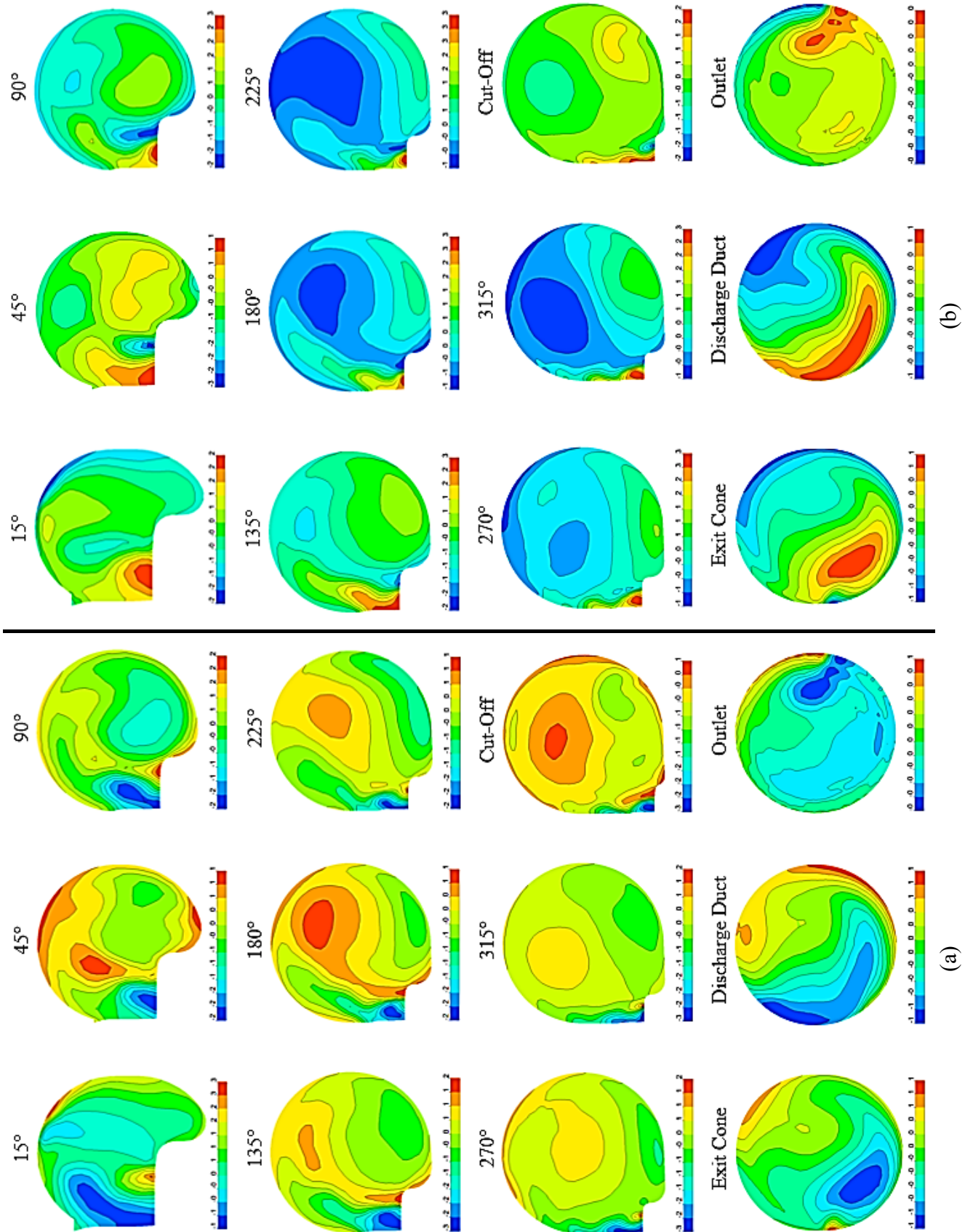
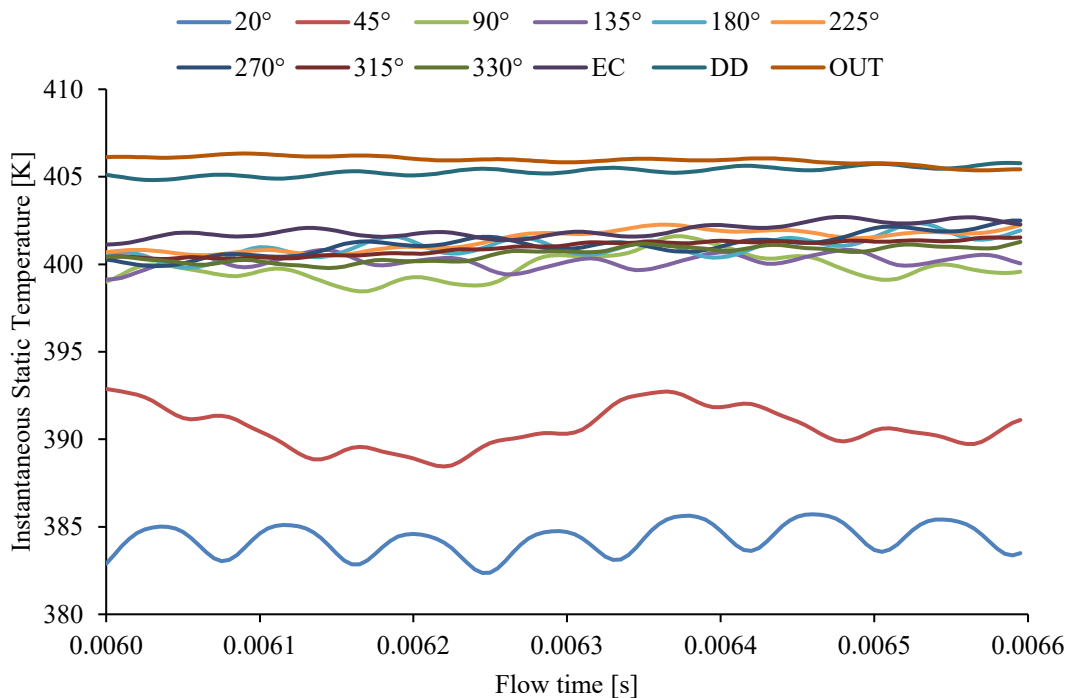


Figure 6.37 Percentage Difference of Static Temperature through CTT Volute at (a) Maximum (b) Minimum

Figure 6.38 depicts the instantaneous static temperature variation across a single revolution for (a) asymmetric volute and (b) CTT volute from the first profile to the outlet. The minimum, maximum, mean and standard deviation have also been presented for static temperature across each selected profile through the centrifugal compressor volute. In both cases, static temperature initially increases inside the volute.

In Figure 6.38 (a), there are some static temperature overlaps displayed between 90° and 330°. Aside from this, static temperature is seen to increase at 45° from 20° as well as downstream of 330°. Figure 6.38 (a) table shows that minimum static temperature is at 20°, while the maximum static temperature is at the outlet. Moreover, the maximum standard deviation of static temperature is at 45°.

In Figure 6.38 (b), static temperature increase from 15° to 270° is much clearer however there are some overlaps in static temperature downstream of 270°. It is noticed that static temperature at the outlet decreases less than that at the exit cone, leaving static temperature to be highest at the discharge duct. Figure 6.38 (b) table shows that minimum static temperature is at 15°, while the maximum static temperature is at the discharge duct. Moreover, the maximum standard deviation of static temperature is at 15°.

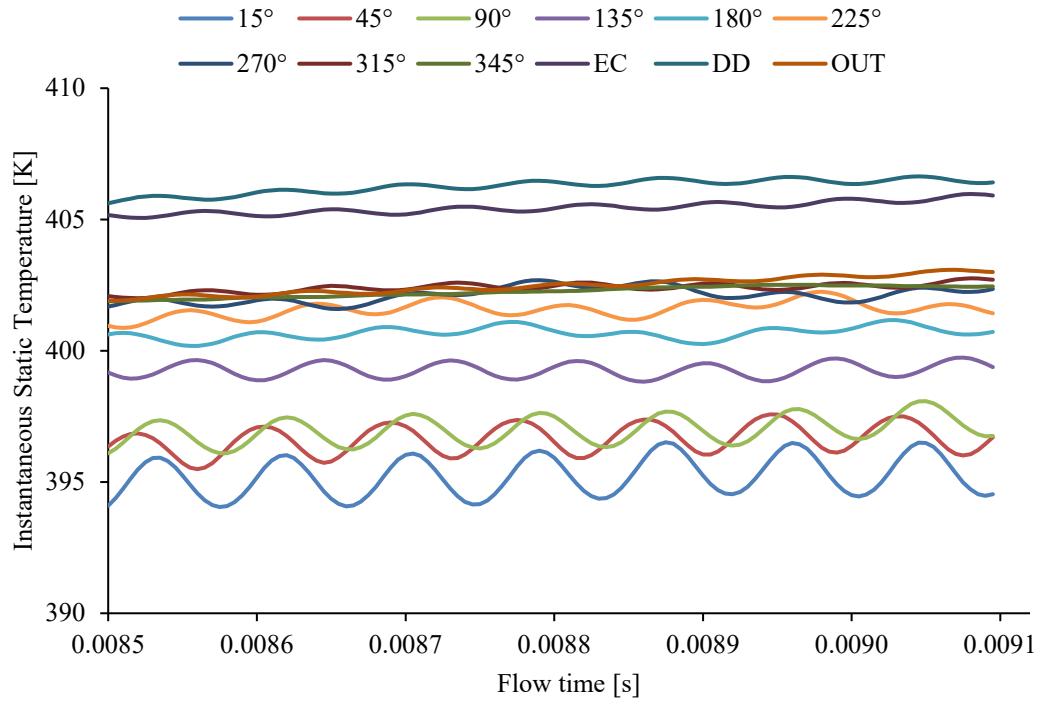




# CHAPTER SIX: DESIGN METHODOLOGY FOR A TURBOCHARGER COMPRESSOR VOLUTE

	20°	45°	90°	135°	180°	225°	270°	315°	330°	EC	DD	OUT
Min	382.36	388.45	398.45	399.13	399.81	400.49	399.89	400.30	399.78	401.13	404.81	405.37
Max	385.71	392.88	401.60	400.82	402.34	402.26	402.50	401.53	401.28	402.70	405.79	406.33
Mean	384.30	390.64	399.81	400.17	401.01	401.39	401.13	400.94	400.59	401.94	405.32	405.95
$\sigma$	0.85	1.20	0.76	0.37	0.56	0.57	0.62	0.41	0.42	0.40	0.25	0.24

(a)



	15°	45°	90°	135°	180°	225°	270°	315°	345°	EC	DD	OUT
Min	394.05	395.49	396.10	398.82	400.19	400.87	401.59	402.00	401.88	405.06	405.62	401.90
Max	396.51	397.58	398.08	399.74	401.17	402.25	402.69	402.76	402.51	405.97	406.64	403.08
Mean	395.23	396.63	396.99	399.27	400.67	401.58	402.13	402.40	402.25	405.45	406.27	402.48
$\sigma$	0.73	0.54	0.51	0.27	0.23	0.30	0.29	0.17	0.20	0.23	0.26	0.33

(b)

Figure 6.38 Instantaneous static temperature variation through (a) Asymmetric volute and (b) CTT volute

#### 6.6.4 Head Loss Variation through the Asymmetric Type Volutes

Figure 6.39 depicts the total head loss across low operating speed of 58.9rps/ $\sqrt{K}$  and high operating speed of 98.2rps/ $\sqrt{K}$  at low flow rate, design flow rate and high flow rate for the CTT volute and Asymmetric volute. It can be seen that as the mass flow rate increases, total head loss also increases across both operating speeds for the Asymmetric volute and only at high operating speed of 98.2rps/ $\sqrt{K}$  for the CTT volute. At low operating speed of 58.9rps/ $\sqrt{K}$ , total head loss is seen to slightly decrease.

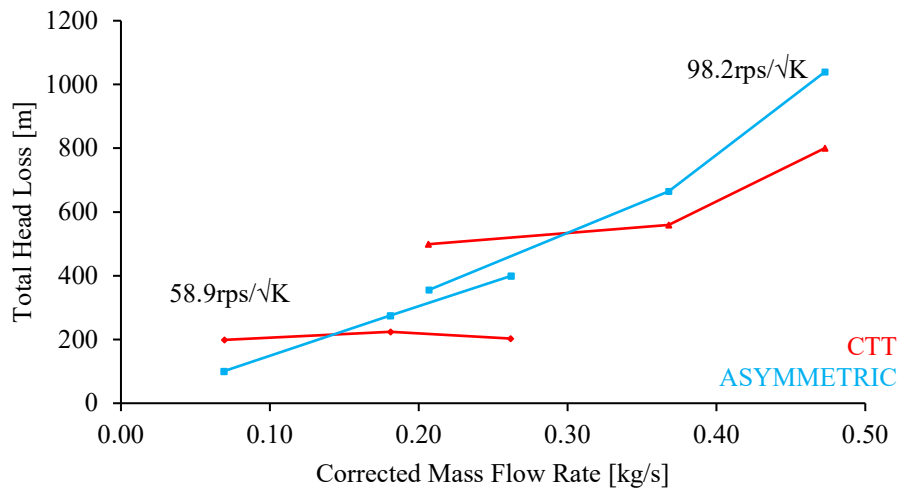
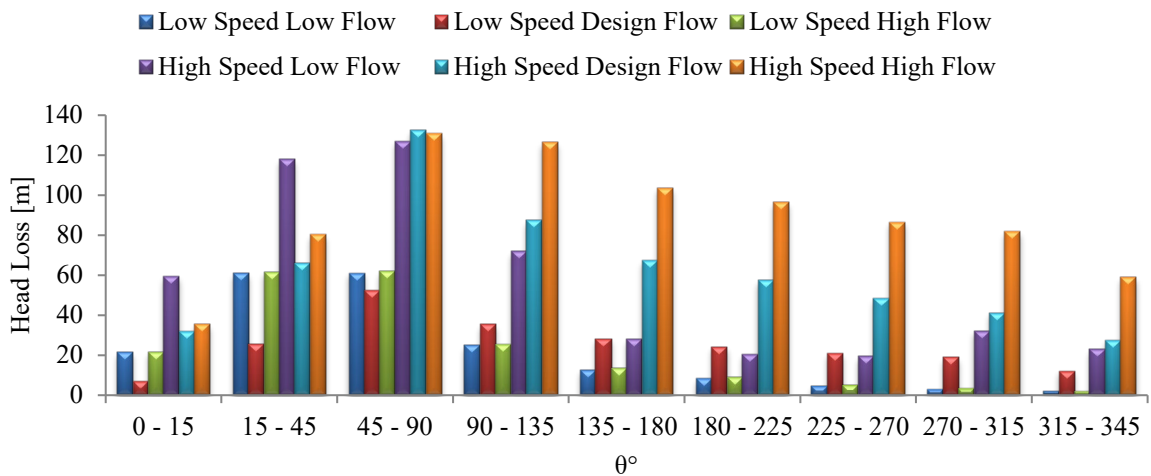


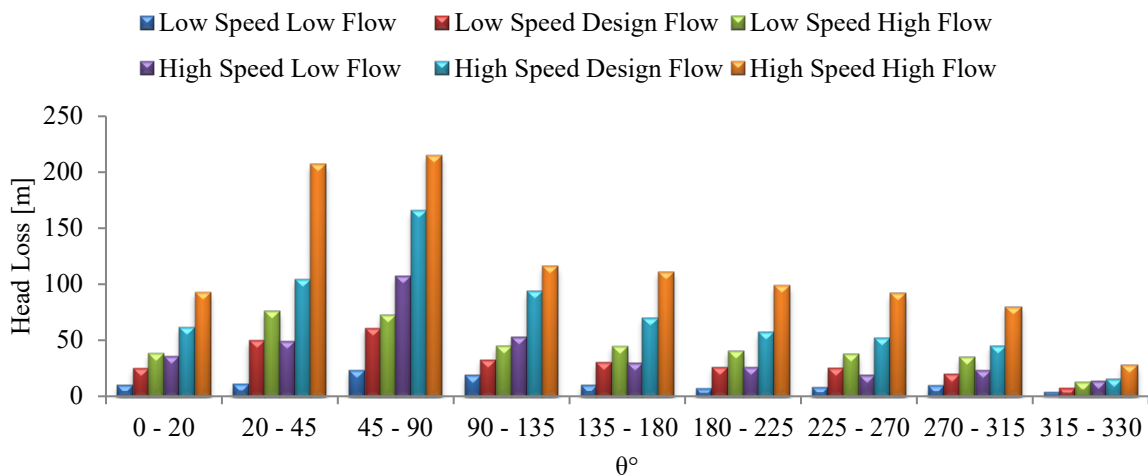
Figure 6.39 Total Head Loss through the Volute at different flow rates

Figure 6.40 depicts the head loss across low operating speed of 58.9rps/ $\sqrt{K}$  and high operating speed of 98.2rps/ $\sqrt{K}$  at low flow rate, design flow rate and high flow rate for (a) the CTT volute and (b) the Asymmetric volute. In Figure 6.40 (a), it is noticed at low operating speed of 58.9rps/ $\sqrt{K}$ , head loss for design flow is lower than low flow and high flow from 0° to 90°. Thereafter downstream of 90° to the outlet, head loss is higher through the volute during design flow conditions than that at low flow and high flow conditions. From 0° to 135° high flow conditions show only very slightly higher head loss than low flow conditions. Head loss between high flow conditions and low flow conditions are the same from 135° to 180° and downstream from 225° to the outlet. Maximum head loss at low flow conditions occur between 15° and 90°, whereas the minimum head loss occurs between 315° and 345°. For design flow conditions, maximum and minimum head loss occurs between 45° and 90° and between 0° and 15°, respectively. For high flow rate, the maximum head loss occurs between 15° and 90°, while minimum head loss occurs between 315° and 345°. At high operating speed of 98.2rps/ $\sqrt{K}$ , head loss for low flow from 0° to 90° is high than that during design flow and high flow conditions. Thereafter, downstream from 90° to the outlet, head loss through the volute increases as the flow rate increases. Maximum head loss at low flow conditions occur between

45° and 90°, whereas the minimum head loss occurs between 225° and 270°. For design flow conditions, maximum and minimum head loss occurs between 45° and 90° and between 315° and 345°, respectively. For high flow rate, the maximum head loss occurs between 45° and 90°, while minimum head loss occurs between 0° and 15°. In Figure 6.40 (b), it is noticed head loss increases as flow rate increases at both operating speeds of 58.9rps/√K and 98.2rps/√K. For both operating speeds, maximum head loss at low flow conditions occur between 45° and 90°, whereas the minimum head loss occurs between 315° and 330°. In addition to this, for design flow conditions, maximum and minimum head loss occurs between 45° and 90° and between 315° and 330°, respectively. For high flow rate at low operating speed of 58.9rps/√K, the maximum head loss occurs between 20° and 45°, while at high operating speed of 98.2rps/√K maximum head loss occurs between 45° and 90°. Furthermore, minimum head loss occurs between 315° and 330° for both operating conditions at high operating speed.



(a)



(b)

Figure 6.40 Head loss variation through (a) CTT volute and (b) Asymmetric volute



Figure 6.41 depicts the wall shear stress incurred on sections of the scroll of the volute casing. It can be seen that wall shear stresses initially increases in the scroll from  $0^\circ$  to  $90^\circ$ , prior to decreasing downstream. It can be seen that the Asymmetric volute has higher wall shear stresses acting on the casing of the scroll than that of the CTT volute. Highest wall shear stress variation between the Asymmetric volute and the CTT volute is depicted in the second section, which is between the first profile and  $45^\circ$ . Furthermore, the lowest wall shear stress variation between the Asymmetric volute and the CTT volute is depicted in the sixth section, which is between  $180^\circ$  and  $225^\circ$ . See APPENDIX 9 for details.

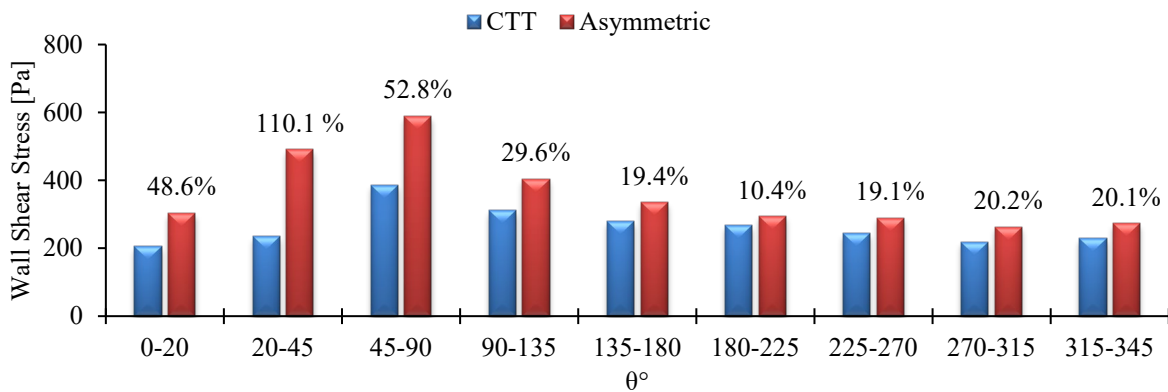


Figure 6.41 Comparison of wall shear stress on the asymmetric type centrifugal compressor volute casing

Figure 6.42 depicts head loss incurring through sections of the scroll of the volute casing. The similar trends can be identified here as that in Figure 6.41. The Asymmetric volute is seen to present higher head losses through the scroll than that of the CTT volute. In both cases, head loss increases in the scroll from  $0^\circ$  to  $90^\circ$ , prior to decreasing downstream. These trends that are same as those depicted in Figure 6.41 signifies the interrelationship between wall shear stress and head loss. Highest head losses incurred through the scroll are of that between  $0^\circ$  to the first profile, while the lowest head losses incurred through the scroll are of that between  $180^\circ$  to  $225^\circ$ . See APPENDIX 10 Head Loss through Volute Scroll Section for details.

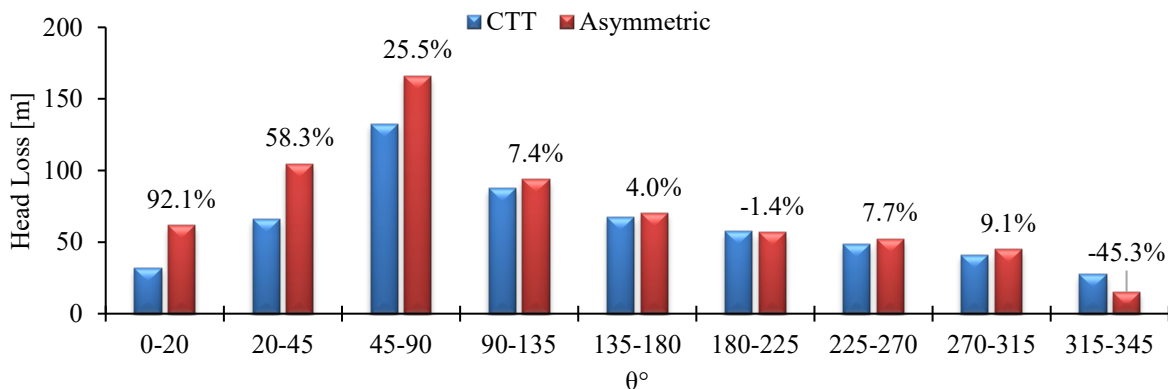
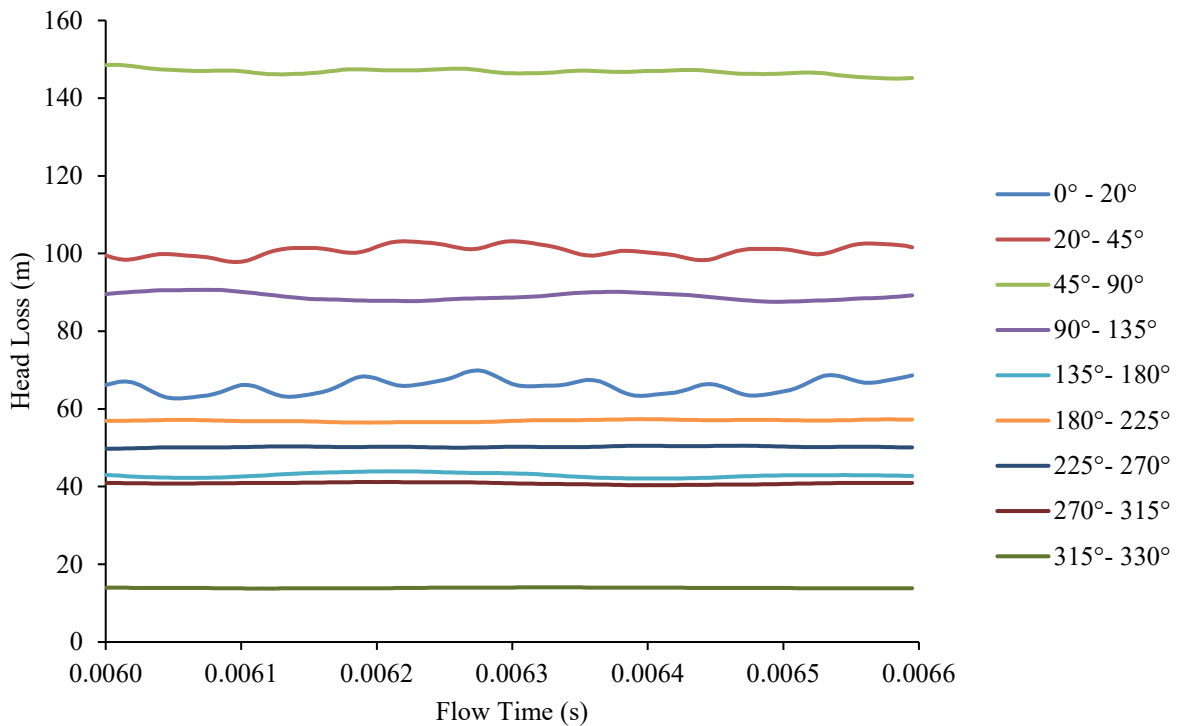


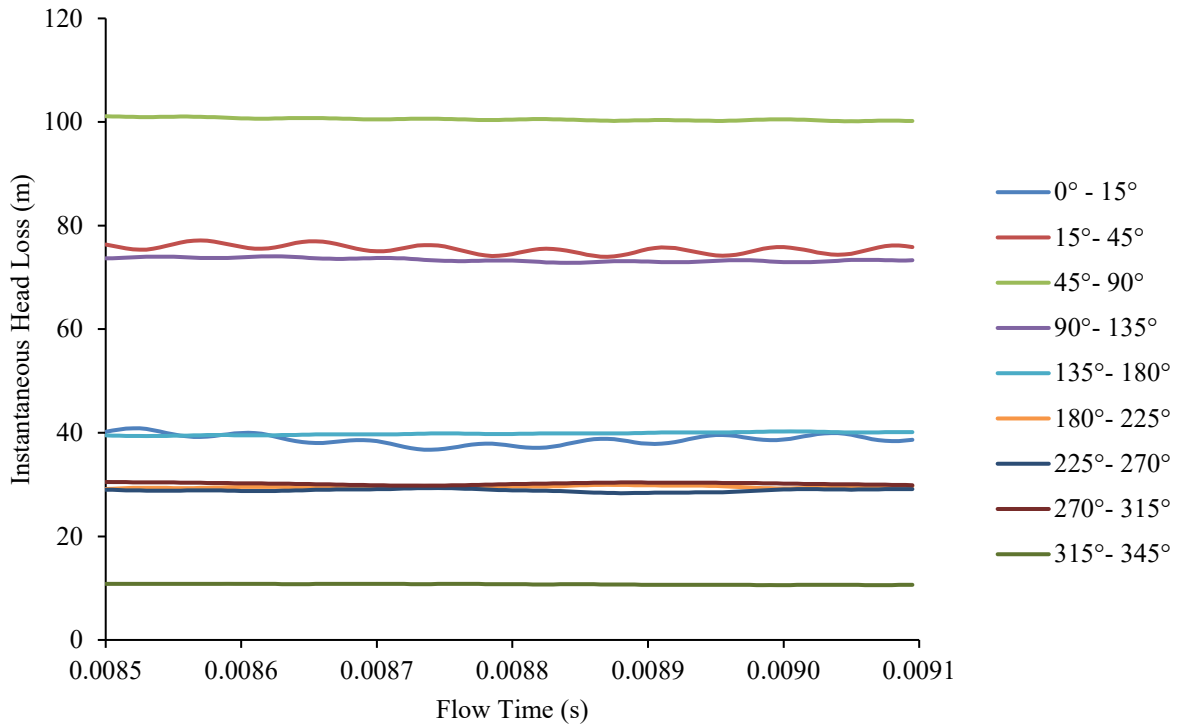
Figure 6.42 Comparison of head loss on the asymmetric type centrifugal compressor volute casing

Figure 6.43 the instantaneous head loss variation through (a) asymmetric volute and (b) CTT volute from the first profile to the cut-off location over one revolution. The minimum, maximum, mean and standard deviation have also been presented for head loss through each section of the centrifugal compressor volute scroll during one revolution. In the case of Figure 6.43 (a), head loss through the scroll of the volute is clear, whereas in the case of Figure 6.43 (b), there are distinct overlaps in head losses from 180° to 315° due to minimal variations between these sections of the scroll. Figure 6.43 (a) and Figure 6.43 (b) tables show that for both cases, minimum head loss occurs in the last section of the scroll between 315° and 330°, while the maximum head loss occurs in the third section of the scroll between 45° and 90°. Furthermore, the maximum standard deviation of head loss occurs in the first section of the scroll between 0° and 20°.



	0° - 20°	20° - 45°	45° - 90°	90° - 135°	135° - 180°	180° - 225°	225° - 270°	270° - 315°	315° - 330°
Min	62.72	97.81	145.05	87.57	42.10	56.49	49.75	40.37	13.78
Max	69.93	103.19	148.57	90.66	43.94	57.38	50.54	41.17	14.08
Mean	65.87	100.71	146.79	88.96	42.92	56.98	50.23	40.83	13.92
$\sigma$	1.80	1.42	0.71	0.96	0.57	0.25	0.17	0.24	0.08

(a)



(b)

Figure 6.43 Instantaneous head loss variation through (a) Asymmetric volute and (b) CTT volute

## 6.7 Summary

This section has employed Multi-Reference Frame and Sliding Mesh techniques using CFD to investigate and thoroughly understand some of the aerodynamic flow characteristics inside the turbocharger compressor stage and its volute. This extensively detailed investigation enables one to better understand the flow mechanics and to use these findings gathered from this section to provide improvements during experimentation and during the design process. For example, during experimentation, the presented flow structures are difficult to capture, therefore a control section can be installed at the presented locations. During the design process, determining the strengths and weaknesses of flow behaviour inside the volute can be used to set a foundation to design an improved turbocharger compressor volute to real operating conditions. From detailed analyses carried out on the aerodynamic flow

characteristics of the turbocharger compressor stage and through its volute, the findings of the presented results are summarised:

- Novel volute design methodology for a turbocharger compressor has been developed.
- All symmetric cross-section volutes designed to actual conditions have higher isentropic efficiency than that designed to ideal conditions at high flow rate.
- Ellipse 2:3 designed to actual conditions depicted the highest isentropic efficiency at design flow rate, which is displayed to be the optimal configuration for this application.
- Ellipse 2:3 designed to actual conditions depicted the highest static pressure, lowest velocity magnitude and highest static temperature through the turbocharger compressor volute from all the symmetric cross-sections that have been investigated.
- Downstream from  $45^\circ$ , all symmetric cross-sections designed to actual conditions identified less head loss compared to that designed to ideal conditions.
- From  $90^\circ$  to  $315^\circ$  all symmetric cross-sections designed to actual conditions identified less wall shear stress compared to that designed to ideal conditions.
- Asymmetric volute depicted good agreement with the experimental data and the numerical of the existing volute at low operating speed.
- Asymmetric volute depicted lower isentropic efficiency, low static pressure recovery and higher total pressure loss than the numerical of the existing volute through all flow rates and at both operating speeds.
- Asymmetric volute displayed higher static pressure and lower velocity magnitude from  $90^\circ$  to the cut-off location; and higher static temperature downstream of  $45^\circ$  than the existing volute.
- There are more secondary flows incurring along the radial direction through the centrifugal compressor volute for the CTT model than the Asymmetric model, suggesting considerably less pressure head loss incurred. This demonstrates that frictional effects have been taken into consideration in the volute design.
- There are more secondary flows incurring along the radial direction through the centrifugal compressor volute for the Asymmetric model are more prominent than for the CTT model, suggesting there are more head loss incurred that are associated with velocity for the Asymmetric model.
- Secondary flows along the axial direction through the centrifugal compressor volute for all cases are very similar for pressure and velocity. However, the Asymmetric volute depict higher secondary flows in comparison with the CTT model in the tongue area.

This could be a result of modelling the tongue from set guidelines and not having a characterised expression integrated into the volute design equation for the tongue, therefore neglecting frictional effects in this region.

- At low flow rate for both speeds, asymmetric volute depicts less total head loss than the existing volute.
- Asymmetric volute has higher wall shear stress and higher head loss than the existing volute.
- The instantaneous minimum and maximum results for asymmetric type volutes, predominantly displayed opposing low and high areas, which is similar for both cases.
- Minimum static pressure occurs at  $20^\circ$  for the asymmetric volute, while minimum static pressure occurs from  $15^\circ$  to  $90^\circ$  for the existing volute. The maximum static pressure occurs at the discharge duct and outlet with the maximum standard deviation of static pressure at  $45^\circ$  for both volutes.
- Minimum velocity magnitude is at the outlet, while the maximum velocity magnitude is at  $45^\circ$  and the maximum standard deviation of velocity magnitude is at  $45^\circ$  for both volutes.
- Minimum static temperature is at  $20^\circ$ , while the maximum static temperature is at the outlet and the maximum standard deviation of static temperature is at  $45^\circ$  for the asymmetric volute.
- Minimum static temperature is at  $15^\circ$ , while the maximum static temperature is at the discharge duct and the maximum standard deviation of static temperature is at  $15^\circ$  for the existing volute.
- Minimum head loss occurs between  $315^\circ$  and  $330^\circ$ , while the maximum head loss occurs between  $45^\circ$  and  $90^\circ$ . Maximum standard deviation of head loss occurs in the first section of the scroll between  $0^\circ$  and  $20^\circ$  for both volutes.

The conducted analyses provides sufficient knowledge the local performance indicators offers the global performance indicators for the volute and the turbocharger compressor stage. The next section provides concludes the discoveries of the presented research study, clearly highlighting the goals achieved, contributions and additions to existing knowledge regarding the volute design methodology for a turbocharger compressor stage.

## CHAPTER 7

# CONCLUSIONS

---

With regards to the aerodynamic and performance characteristics of the volute designed neglecting friction and the volute designed incorporating friction for centrifugal compressors; this chapter details the conclusions drawn from the results obtained in previous chapters. The achievements and contributions to the existing knowledge are summarised and wherever possible referenced back to the initial aims of this study. Finally, the tasks carried out in this study are evaluated and requirements for future work in the area of volute design for centrifugal compressors are defined.

## 7.1 Research Problem Synopsis

Many researchers have investigated centrifugal compressors though the volute had not been of prime focus until the 1990's [2]. The expression employed in previous studies neglects friction hence, those volute models in literature having symmetric circular cross-section appear superior [1, 19, 46, 51]. Centrifugal systems that have larger volutes such as fans and pumps have negligible frictional effects, thus are of limited use regarding turbochargers. Conversely, compressors especially those operating at high pressure conditions, have a much narrower volute whereby friction is highly important and hence cannot be ignored [24]. Literature research has established no expression for volute design incorporating friction. Hence, this particular study numerically explores the effect of volute design under ideal conditions where friction is neglected, as well as under actual conditions where friction is included as a parameter, establishing a new volute design expression tailored for centrifugal compressors. From extensive review of published literatures, a number of limitations have been discovered concerning the aforementioned points. In order to accurately predict the flow structure and performance behaviour in the centrifugal compressor volute, a set of aims and objectives have been formulated which define the scope of this research study. This chapter summarises the primary aims, achievements and contributions of the research project. For reference, the detailed objectives within each of these aims are given in Chapter 2.

## 7.2 Research Aim and Achievements

The research aims of this thesis are defined from an extensive literature review in this area.

**Research Aim: Analyse the flow characteristics of the turbocharger compressor and its volute during steady and unsteady response to develop a novel design methodology for the turbocharger compressor volute.**

**Achievement # 1:** This research study provides a detailed CFD based investigation on the global and local flow field, through the turbocharger compressor stage and its volute, respectively. The initial part of the investigation has been carried out using the Multiple Reference Frame technique for steady simulations. Two operating speeds have been presented, being 58.9rps/ $\sqrt{K}$  and 98.2rps/ $\sqrt{K}$  across three flow rates, namely being low, design and high. This is carried out in order to understand the flow behaviour over a wide range and to explore what the performance indicators offer each component within the turbocharger compressor stage, as well as inside its volute across various cross-sections. The experimental data of the turbocharger compressor stage has been used to verify the numerical data and setup for the

research study via the performance map and efficiency map. The overall performance of the turbocharger compressor volute has been analysed via the total pressure loss and static pressure recovery. Based on detailed numerical investigation on the flow characteristics, pressure, velocity and temperature fields have been qualitatively and quantitatively analysed macroscopically and microscopically. Qualitative analyses makes use of pressure, velocity and temperature contours during steady response. Quantitative analyses makes use of pressure, velocity and temperature profiles along the radial direction and the axial direction across various cross-sections around the volute during steady response. These are presented using asymmetric ratios as a method of representing flow dominance and secondary flows at different locations through the volute. The results provide a clear canvas of aerodynamic flow characteristics within a turbocharger compressor stage and its volute during steady response.

**Achievement # 2:** This research study provides a detailed CFD based investigation on the global and local flow field, through the turbocharger compressor stage and its volute, respectively. The second part of the investigation has been carried out using the Sliding Mesh technique for unsteady simulations. The unsteady responses are taken at two instances, which are referred as Blade Position 1, where the impeller blade is aligned with the volute tongue, which has been taken at  $180^\circ$  impeller rotation; and Blade Position 2, where the impeller blade has passed the volute tongue and another blade is approaching the tongue, which has been taken at  $225^\circ$  impeller rotation. Taking the revolution averaged, the unsteady response of the turbocharger compressor stage has been analysed via the performance map and efficiency map; and the overall performance of the turbocharger compressor volute has been analysed via the total pressure loss and static pressure recovery. Based on the detailed numerical investigation on the flow characteristics, pressure, velocity and temperature fields have been qualitatively and quantitatively analysed macroscopically and microscopically at design flow at low operating speed of 58.9rps/ $\sqrt{K}$  and high operating speed of 98.2rps/ $\sqrt{K}$ . Qualitative analyses makes use of pressure, velocity and temperature contours, while quantitative analyses makes use of pressure, velocity and temperature profiles along the radial direction and the axial direction across various cross-sections around the volute during two instances. These are presented using asymmetric ratios as a method of representing flow dominance and secondary flows at different locations through the volute. This has been carried out to understand the behaviour that performance indicators offer each component within the turbocharger compressor stage, as well as inside its volute across various cross-sections. The results



presented provide a clear canvas of aerodynamic flow characteristics within a turbocharger compressor stage and its volute during instantaneous response.

**Achievement # 3:** This research study provides a detailed CFD based investigation on the global and local flow field, through the turbocharger compressor stage and its volute, respectively. The final part of the investigation has been carried out using the Multiple Reference Frame and Sliding Mesh techniques for steady and unsteady simulations, respectively. It presents the design methodology for the turbocharger compressor volute for both, symmetric and asymmetric type volutes. These can be universally utilised to express the centrifugal compressor volute design of a symmetric type volute having a circular, elliptical 2:3 and elliptical 3:2 cross-section and an asymmetric type volute having a circular cross-section. Symmetric type volutes have been designed firstly using the basis of an expression that currently exists, which neglects frictional effects and is for ideal conditions. Three volute cross-sections have been investigated, namely, circular; ellipse 2:3; and ellipse 3:2. Following on from this, same cross-section shapes have been designed using another expression that has been derived from the basis of that existing. This existing expression is readily available in text and literature and is appropriate for fans and pumps, thus is inappropriate for centrifugal compressors since friction is an essential factor which must be considered in compressible flow applications due to its narrow passage at high pressure conditions. The newly developed expression for centrifugal compressor volute design incorporates frictional effects as a parameter and is unique since it demonstrates a design engineered for actual conditions. This is currently unavailable in text and literature. From here, the asymmetric volute incorporating friction as a parameter has been designed, since the existing volute provided by the company is asymmetric. Based on the detailed numerical investigation on the flow characteristics, pressure, velocity and temperature fields have been qualitatively and quantitatively analysed macroscopically and microscopically. Qualitative analyses makes use of pressure, velocity and temperature contours during steady response, while quantitative analyses makes use of pressure, velocity and temperature profiles along the radial direction and the axial direction across various cross-sections around the volute. These are presented using asymmetric ratios as a method of representing flow dominance and secondary flows at different locations through the volute. Further to this, wall shear stress and head loss have also been presented to understand the influences of friction on the volute design. The focus of this sector is at design flow during high operating speed of 98.2rps/ $\sqrt{K}$ . This design point has been selected since it is at which the numerical and experimental data were in highest agreement during the verification

process. For the symmetric sector, steady flow field behaviour across various cross-sections and how that designed to neglect frictional effects to that designed to incorporate frictional effects influences the flow field, have been studied. For the asymmetric sector, steady and instantaneous flow field behaviour have been captured and explored between the newly and realistically designed volute tailored to centrifugal compressors, to that which is in existence and in use. The minimum and maximum of instantaneous results have been captured and the percentage differences from the revolution average have been presented. The results provide a clear canvas of aerodynamic flow characteristics within a turbocharger compressor stage and its volute designed neglecting frictional effects and the incorporating frictional effects. The purpose of this is to characterise the flow features where losses are present and to reiterate the importance of accounting for the frictional effects in the centrifugal compressor volute design methodology. The development of such universal tool designed specifically for centrifugal compressors where the flow structure is far more complex, which also shows realistic results, is the main achievement of the presented research study.

### 7.3 Thesis Conclusions

A detailed study has been undertaken to support the existing literature with regards to the design of a centrifugal compressor volute. This has facilitated in novel additions to improve the current understanding of the flow characteristics, geometry related effects and design methodology for a centrifugal compressor volute. The conclusions of this research study are summarised as follows:

**Research Objective # 1: Analyse the flow characteristics of the turbocharger compressor stage and its volute at design and off-design conditions at low and high operating speeds during steady response.**

**Conclusion # 1:** From the investigations carried out in this study, it can be concluded that static pressure recovery coefficient falls below 0 at low operating speed [2]. This indicates there are more pressure losses taking place at the choke condition than pressure recovery due to secondary flows causing head loss as a result of friction. Highest static pressures are exhibited at the surge condition, while lowest static pressures are exhibited at the choke condition around the turbocharger compressor stage and its volute as expected [2]. Low flow conditions depict little static pressure variations to that at design flow compared to high flow conditions for both operating speeds. Highest velocity magnitude distributions are displayed at the choke condition, while lowest velocity magnitude distributions are displayed at the surge condition

for both operating speeds. There is a more significant difference in velocity magnitude across each plane compared to that at the outlet at the surge condition for both operating speeds. Low flow at low operating speed depicts the most velocity magnitude variation compared to that at design flow. These are expected because during surge, the system is trying to add more energy into the flow to overcome system resistance whereas, during the choke condition, mass flow has reached its maximum, hence velocity would be at its highest and pressure would be at its lowest since pressure is inversely proportional to velocity. Highest static temperatures are exhibited at the surge condition, while lowest static temperatures are exhibited at the choke condition around the turbocharger compressor stage and its volute. High flow conditions depict little static temperature variations to that at design flow compared to low flow conditions for both operating speeds. These are expected since there is a directly proportional relationship between pressure and temperature. With respect to the asymmetric ratio, symmetric ratio signifies desirable flow characteristics and asymmetric ratio signifies the presence of secondary flows, which means more energy is required due to losses taking place as a result of friction. Therefore, the more symmetric the ratio means the better the volute performs. It can be concluded that static pressure variation along the radial direction depicts significant asymmetry through the profile around the volute than static pressure variation along the axial direction at both operating speeds. For both operating speeds, flow velocity magnitude is significantly asymmetric through the centrifugal compressor volute, axially and radially. Static temperature in the flow during low operating speeds is much more symmetric than static temperature in the flow during high operating speeds. With respect to the effect of flow behaviour inside the volute on the operating speed, it can be concluded that there are more static pressure and velocity magnitude variations occurring from one plane to the next around the volute at high operating speed than at low operating speed, while static temperature depicts negligible variations occurring in the flow from one plane to the next, through the centrifugal compressor volute across both operating speeds. It can also be concluded that there are more significant differences in static pressure and static temperature across each plane compared to that at the outlet at high operating speed than at low operating speed. Moreover, it can be concluded that globally in comparison with low operating conditions, high operating speeds predominantly increases in static pressure through the inducer inlet, impeller outlet, diffuser and volute; increases throughout for velocity magnitude; and predominantly increases in static temperature through the impeller outlet, diffuser and volute. Locally in comparison with low operating conditions, high operating speeds increases across the cross-sections for static pressure, velocity magnitude and static temperature through the turbocharger compressor volute. Further

to this, asymmetries along the radial direction and axial direction of the cross-section profiles around the centrifugal compressor volute are more prominent for pressure and velocity as a result of secondary flows. Moreover, the extent of secondary flows inside the centrifugal compressor volute is a function of flow rate.

**Research Objective # 2: Analyse the flow characteristics of the turbocharger compressor stage and its volute at design conditions of low and high operating speeds during instantaneous response, focussing on the effect of impeller blade position with respect to the volute tongue.**

**Conclusion # 2:** From the investigations carried out in this study, it can be concluded that both globally and locally, there are negligible variations between the two instances. This is because the centrifugal compressor employed in the presented study has a vaneless diffuser between the impeller and the volute. Further to this, both operating speeds are relatively high in this case compared to that of fans and pumps thus, capturing these effects is challenging. It can also be concluded that isentropic efficiency is overestimated in comparison with the experiment data and the steady case. It had also been found that static pressures and static temperatures are higher at higher speeds, while velocity magnitude is lower. It can also be concluded that the asymmetric ratio for static pressure along the radial direction is predominantly asymmetric towards the outer curve at both operating speeds, while static pressure along the axial direction is almost symmetric at low operating speed. At high operating speed, static pressure along the axial direction is asymmetric towards the rear face downstream to  $225^\circ$ , prior to depicting asymmetry is towards the front face downstream to the outlet. Additionally, the asymmetric ratio for velocity magnitude along the radial direction is predominantly asymmetric towards the inner curve for both operating speeds, while velocity magnitude along the axial direction is asymmetric towards the rear face for all cases at low operating speed. At high operating speed, velocity magnitude along the axial direction is asymmetric towards the rear face for the steady case and asymmetric towards the front face for both instantaneous cases. Furthermore, the asymmetric ratio for static temperature along the radial direction is predominantly asymmetric towards the outer curve for both operating speeds, while static temperature along the axial direction is predominantly symmetric at low operating speed and asymmetric towards the front face for all cases at high operating speed. It can also be concluded that static pressure for both unsteady cases and the steady case are in agreement, while velocity magnitudes for both unsteady cases are in agreement downstream of  $45^\circ$  with prominent variations against the steady case. Moreover, static temperature for both instantaneous cases and the steady case

depict variations, which are more prominent on the flow along the axial direction than the radial direction. It is also concluded that the extent of secondary flows inside the centrifugal compressor volute is not a predominant function of impeller blade position with respect to the volute tongue.

**Research Objective # 3: Develop a design methodology for symmetric type turbocharger compressor volutes of various cross-sections neglecting frictional effects and incorporating frictional effects and asymmetric type turbocharger compressor volute incorporating frictional effects.**

**Conclusion # 3:** Using existing knowledge from text and literature, a thorough understanding provided the tools and capabilities to derive a unique expression engineered specifically, for centrifugal compressor volutes that is designed for actual operating conditions, where frictional effects have been incorporated into its very expression. Design methodology for symmetric type volutes neglecting friction and incorporating friction have been developed for various cross-sections, namely, circular, elliptical 2:3 and elliptical 3:2. Further to this, the design methodology for the asymmetric type volute has also been developed since the existing volute is also asymmetric. This design methodology can make a valid comparison to that which currently exists.

**Research Objective # 4: Analyse the flow characteristics of the symmetric type centrifugal compressor volute with various volute cross-sections and investigate the incurred energy loss through the volute during steady response.**

**Conclusion # 4:** From the investigations regarding carried out in this study, it can be concluded that all symmetric cross-section volutes designed to actual conditions have higher isentropic efficiency than that designed to ideal conditions at high flow rate. Ellipse 2:3 designed to actual conditions depicted the highest isentropic efficiency at design flow rate, as well as depicting the highest static pressure, lowest velocity magnitude and highest static temperature through the turbocharger compressor volute from all the symmetric cross-sections that have been investigated. It can also be concluded that downstream from  $45^\circ$ , all symmetric cross-sections designed to actual conditions identified less head loss compared to that designed to ideal conditions. Further to this, from  $90^\circ$  to  $315^\circ$  all symmetric cross-sections designed to actual conditions identified less wall shear stress compared to that designed to ideal conditions.

**Research Objective # 5:** Analyse the flow characteristics of the asymmetric type centrifugal compressor volute, investigate the incurred energy loss through the volute and compare this model with the original existing model during steady and unsteady responses.

**Conclusion # 5:** From the investigations carried out in this study, it can be concluded that the asymmetric volute depicted good agreement with the experimental data and the numerical of the existing volute at low operating speed. Asymmetric volute depicted lower isentropic efficiency, low static pressure recovery and higher total pressure loss than the numerical of the existing volute through all flow rates and at both operating speeds. Asymmetric volute displayed higher static pressure and lower velocity magnitude from  $90^\circ$  to the cut-off location; and higher static temperature downstream of  $45^\circ$  than the existing volute. At low flow rate for both speeds, asymmetric volute depicts less total head loss than the existing volute. It can also be concluded that the asymmetric volute has higher wall shear stress and higher head loss than the existing volute. Additionally, it can be concluded that the instantaneous minimum and maximum results for asymmetric type volutes, predominantly displayed opposing low and high areas, which is similar for both volutes. The minimum static pressure occurs at  $20^\circ$  for the asymmetric volute, while minimum static pressure occurs from  $15^\circ$  to  $90^\circ$  for the existing volute. The maximum static pressure occurs at the discharge duct and outlet with the maximum standard deviation of static pressure at  $45^\circ$  for both volutes. Furthermore, minimum velocity magnitude is at the outlet, while the maximum velocity magnitude is at  $45^\circ$  and the maximum standard deviation of velocity magnitude is at  $45^\circ$  for both volutes. Moreover, minimum static temperature is at  $20^\circ$ , while the maximum static temperature is at the outlet and the maximum standard deviation of static temperature is at  $45^\circ$  for the asymmetric volute. Minimum static temperature is at  $15^\circ$ , while the maximum static temperature is at the discharge duct and the maximum standard deviation of static temperature is at  $15^\circ$  for the existing volute. Also, minimum head loss occurs between  $315^\circ$  and  $330^\circ$ , while the maximum head loss occurs between  $45^\circ$  and  $90^\circ$ . Maximum standard deviation of head loss occurs in the first section of the scroll between  $0^\circ$  and  $20^\circ$  for both volutes.

## 7.4 Thesis Contribution

The novel contributions of this research study are summarised:

**Contribution # 1:** Existing literature has limitations on the detailed flow analysis through the turbocharger compressor volute. Hence, the first major contribution of this research study is the detailed flow characterisation during steady conditions through the turbocharger compressor and its volute, respectively. These include the fluid flow distributions across each of the specified locations around the volute, which have been compared against that depicted at the outlet; flow distributions through the volute at the off-design conditions compared against that at design conditions; and flow distributions at high operating speeds compared with that at low operating speeds. The fluid flow structures have been captured along the radial direction and axial direction of each profile, which has been used to compute the asymmetric ratio to determine the flow dominance and represent secondary flows during steady response. The available literature does not provide this information.

**Contribution # 2:** The second major contribution of this research study is detailed flow characterisation during unsteady conditions through the turbocharger compressor and its volute, respectively. The unsteady responses are taken at two instances, where the impeller blade is aligned with the volute tongue, and where the volute tongue is between two blades. Flow behaviour across each cross-section has been compared against that depicted at the outlet; unsteady conditions have been compared against steady conditions; and high operating speeds have been compared with low operating speeds. Furthermore, flow structures have been captured along the radial direction and axial direction of each profile, which has been used to compute the asymmetric ratio of flow dominance and represent secondary flows during unsteady response. The available literature does not provide this information.

**Contribution # 3:** The third major contribution of this research study is the development of a novel design methodology for a centrifugal compressor volute. Novel analytical expressions have been derived by the author and other novel expressions have been derived by Baker (2018), all of which have not yet been applied into practice nor had it been numerically investigated. Therefore, the author applied these expressions into practice and carried out the numerical investigations with novel analyses. The friction incorporated expression for the volute design had been derived by the author and numerically analysed. The flow structure of all these had been captured demonstrating the influence frictional effects have in the volute design. Complex flow structures of pressure, velocity and temperature have been investigated

where the radial direction and axial direction profiles had been captured enabling the asymmetric ratio of flow dominance to be determined and secondary flows to be quantified. In addition to this, the percentage difference contours of pressure, velocity and temperature have been presented from the maximum and minimum points captured during the instantaneous response. Furthermore, new flow field indicators for head loss, wall shear stress and asymmetric ratio have been developed and wall shear stress and energy loss have been quantified through the volute during steady and instantaneous responses. This information is currently unavailable in existing literature.

### **Supervisor Contributions**

Professor Rakesh Mishra supervised the author throughout the PhD journey. With the collaboration of Dr Paul Eynon and Dr Michael Dolton at Cummins Turbo Technologies, the need for this research project had been presented in the field of turbocharger compressor volute. The experimental data used in this research study had been provided by Cummins Turbo Technologies and the numerical facilities of Computational Fluid Dynamics had been made available at the University of Huddersfield. Dr Paul Baker contributed towards this research study through the derivation of the expressions for the symmetric elliptical 3:2, symmetric elliptical 2:3 and asymmetric circular cross-section volutes neglecting frictional effects. The expressions of the friction incorporated volutes had been derived by the author. Professor Rakesh Mishra contributed throughout this research with his ideas, insights, guidance and technical knowledge. Dr. Taimoor Asim at the University of Huddersfield and John Horsley at Cummins Turbo Technologies have contributed towards this research through the numerical expertise and suggestions. Should Professor Rakesh Mishra, Dr Paul Baker, Dr. Taimoor Asim at the University of Huddersfield as well as Dr. Paul Eynon, Dr. Michael Dolton and John Horsley at Cummins Turbo Technologies wish to use the author's data to conduct and/or publish further research, they are free to do so with the author being the author or the co-author to any publications where any work and concepts from this thesis have been used.

### **7.5 Recommendation for Future Work**

The flow characteristics during steady and instantaneous conditions as well as establishing a design methodology for centrifugal compressor volutes have been presented in this study, such that gaps identified in literature could be bridged. In light of the concluded remarks provided in the previous sections, a great potential for further research in this particular area of design has been unveiled. The main areas identified for further work are described, which are associated



with understanding the flow characteristics further, and undertaking further developments in design and optimisation of centrifugal compressor volutes.

**Recommendation # 1:** The presented flow characteristics are of pressure, velocity and temperature during steady response. Therefore, future recommendations are to explore other flow properties such as entropy and enthalpy generation, along with three-dimensional flow characteristics, such as swirling strength, tangential velocity and vorticity as well as turbulent properties such as Q criterion, inside the volute. Thorough analysis of these flow characteristics along with that presented in this study, will provide an improved understanding of flow structure and behaviour. With extensive focus on the boundary layer inside the volute, this will be a valued addition for future improvements to the friction incorporated expressions, where additional flow related terms can be integrated.

**Recommendation # 2:** The presented flow characteristics are of pressure, velocity and temperature during unsteady response. Therefore, future recommendations are to explore the instantaneous response of aforementioned flow characteristics inside the volute. The instantaneous response recommended here, is the transient behaviour in terms of acceleration and deceleration as well as across different flow rates. This will provide a more realistic and valuable set of data collation, which can be used to make improvements to the friction incorporated expression, where additional flow related terms can be integrated.

**Recommendation # 3:** The presented expressions are of the scroll and therefore future recommendations are to characterise the exit cone, discharge duct and tongue of the volute. These integrated together will provide an expression for the complete volute. Design optimisation is recommended for further developments. Additionally, only the circular cross-section of the asymmetric type volute had been studied. The symmetric type volute with the elliptical 2:3 cross-section designed to actual conditions presented positive results during this study. Further to this, since the asymmetry of the volute has a significant influence on the turbocharger compressor performance [81], it is encouraging to capture its performance as an asymmetric cross-sectioned volute for turbocharging applications.

**Recommendation # 4:** The presented research has been carried out numerically and therefore future recommendations are to explore the flow characteristics through various cross-sections using experimentation, such as Particle Image Velocimetry (PIV) with a volute manufactured using a transparent material.



# REFERENCES

---

1. Mojaddam, M., A.H. Benisi, and M.R. Movahhedi. *Investigation on effect of centrifugal compressor volute cross-section shape on performance and flow field*. in *ASME Turbo Expo 2012: Turbine Technical Conference and Exposition*. 2012. American Society of Mechanical Engineers.
2. Reunanen, A., *Experimental and numerical analysis of different volutes in a centrifugal compressor*, in *Acta Universitatis Lappeenrantaensis*. 2001.
3. Shu, M., et al., *Performance Analysis of a Centrifugal Compressor Based on Circumferential Flow Distortion Induced by Volute*. *Journal of Engineering for Gas Turbines and Power*, 2018. **140**(12): p. 122603.
4. Zala, K., *The Application of Turbo-machinery to Reciprocating Engines*. 2014, Cummins Turbo Technologies: Huddersfield, West Yorkshire, UK.
5. Tanganelli, A., et al., *An investigation on the loss generation mechanisms inside different centrifugal compressor volutes for turbochargers*. *Journal of Engineering for Gas Turbines and Power*, 2018. **141**(2): p. 021004.
6. Engines, J.S. *Mitsubishi 4G6-Series Engines*. 1996 [cited 2011; Available from: <http://www.jdmspecengines.com/mitsubishi-engines/4g6-series.html>.
7. Technologies, C.T. *How a Turbocharger Works* 2014; Available from: [http://www.cumminsturbotechnologies.com/ctt/navigationAction.do?url=SiteContent+en+HTML+ProductsAndTechnologies+How\\_a\\_Turbocharger\\_Works](http://www.cumminsturbotechnologies.com/ctt/navigationAction.do?url=SiteContent+en+HTML+ProductsAndTechnologies+How_a_Turbocharger_Works)
8. Davis, E., *Supercharging, Turbocharging and Nitrous Oxide Performance*. 2002: MotorBooks International.
9. Logan Jr, E., *Handbook of turbomachinery*. 2003: CRC Press.
10. Eynon, P. and A. Whitfield, *Pressure recovery in a turbocharger compressor volute*. *Proceedings of the Institution of Mechanical Engineers, Part A: Journal of Power and Energy*, 2000. **214**(6): p. 599-610.
11. Technologies, C.T., *Cummins Turbo Technologies HE400VG – Animation* 2013, YouTube.
12. Serway, R. and J. Faughn, *College Physics*. 5th ed. 1999: Orlando, Florida: Harcourt Brace College Publishers.
13. Gerhart, P.M. and R.J. Gross, *Fundamentals of fluid mechanics*. 2nd ed. 1992: Addison-Wesley.
14. Cengel, Y. and M. Boles, *Thermodynamics: an engineering approach*. 5th ed. 2006: Tata McGraw-Hill Publishing Company Limited, New Delhi.

15. Lüdtke, K.H., *Process centrifugal compressors: basics, function, operation, design, application*. 2004: Springer Science & Business Media.
16. Dick, E., *Fundamentals of turbomachines*. Vol. 109. 2015: Springer.
17. Rezaei, H., *Investigation of the flow structure and loss mechanism in a centrifugal compressor volute*. 2001.
18. Dumitrescu, O., G. Fetea, and B. Gherman. *Influence of the volute design on performances of a centrifugal compressor*. in *ENERGY and ENVIRONMENT (CIEM), 2017 International Conference on*. 2017. IEEE.
19. Qiang, X., J. Teng, and Z. Du, *Influence of various volute designs on volute overall performance*. *Journal of Thermal Science*, 2010. **19**(6): p. 505-513.
20. Lobanoff, V.S. and R.R. Ross, *Centrifugal Pumps: Design and Application: Design and Application*. 1992: Elsevier.
21. Aungier, R.H., *Centrifugal compressors: a strategy for aerodynamic design and analysis*. 2000: American Society of Mechanical Engineers.
22. von Kovats, A., *Design and performance of centrifugal and axial flow pumps and compressors*. 1964: Pergamon Press.
23. Stepanoff, A.J., *Centrifugal and axial flow pumps: theory, design, and application*. 1957: Wiley New York.
24. Eck, B., *Fans; design and operation of centrifugal, axial-flow, and cross-flow fans*. 1973: Pergamon.
25. Weber, C. and M. Koronowski. *Meanline performance prediction of volutes in Centrifugal compressors*. in *ASME 1986 International Gas Turbine Conference and Exhibit*. 1986. American Society of Mechanical Engineers.
26. Doustmohammadi, A.A., A. HajilouyBenisi, and M. Mojaddam. *Experimental and numerical investigation of losses in centrifugal compressor components*. in *ASME Turbo Expo 2013: Turbine Technical Conference and Exposition*. 2013. American Society of Mechanical Engineers.
27. Cengel, Y. and J. Cimbala, *Fluid Mechanics, Fundamentals and Applications*. 2006, New York: McGraw-Hill.
28. Munson, B., D. Young, and T. Okiishi, *Fundamentals of Fluid Mechanics*. 2006, Hoboken, NJ: Wiley & Sons.
29. Flaxington, D. and E. Swain, *Turbocharger aerodynamic design*. *Proceedings of the Institution of Mechanical Engineers, Part C: Journal of Mechanical Engineering Science*, 1999. **213**(1): p. 43-57.
30. Gong, X. and R. Chen, *Total pressure loss mechanism of centrifugal compressors*. *Mechanical engineering research*, 2014. **4**(2): p. 45.

31. Denton, J. and W. Dawes, *Computational fluid dynamics for turbomachinery design*. Proceedings of the Institution of Mechanical Engineers, Part C: Journal of Mechanical Engineering Science, 1998. **213**(2): p. 107-124.
32. Abdelmadjid, C., S.-A. Mohamed, and B. Boussad, *CFD Analysis of the Volute Geometry Effect on the Turbulent Air Flow through the Turbocharger Compressor*. Energy Procedia, 2013. **36**: p. 746-755.
33. Zheng, X., et al., *Influence of the volute on the flow in a centrifugal compressor of a high-pressure ratio turbocharger*. Proceedings of the Institution of Mechanical Engineers, Part A: Journal of Power and Energy, 2010. **224**(8): p. 1157-1169.
34. Van den Braembussche, R. and B. Hande. *Experimental and theoretical study of the swirling flow in centrifugal compressor volutes*. in *ASME 1989 International Gas Turbine and Aeroengine Congress and Exposition*. 1989. American Society of Mechanical Engineers.
35. Ayder, E., R. Van den Braembussche, and J. Brasz, *Experimental and theoretical analysis of the flow in a centrifugal compressor volute*. Journal of Turbomachinery Transactions of the ASME, 1993. **115**: p. 582-589.
36. Ayder, E. and R. Van den Braembussche, *Numerical analysis of the three-dimensional swirling flow in centrifugal compressor volutes*. Journal of turbomachinery, 1994. **116**(3): p. 462-468.
37. Nursen, E.C. and E. Ayder, *Numerical calculation of the three-dimensional swirling flow inside the centrifugal pump volutes*. International Journal of Rotating Machinery, 2003. **9**(4): p. 247-253.
38. Chu, S., R. Dong, and J. Katz, *Relationship between unsteady flow, pressure fluctuations, and noise in a centrifugal pump—part B: effects of blade-tongue interactions*. Journal of fluids engineering, 1995. **117**(1): p. 30-35.
39. Hillewaert, K. and R.A. Van den Braembussche. *Numerical simulation of impeller–volute interaction in centrifugal compressors*. in *ASME 1998 International Gas Turbine and Aeroengine Congress and Exhibition*. 1998. American Society of Mechanical Engineers.
40. González Pérez, J., et al., *Steady and Unsteady Radial Forces for a Centrifugal Pump With Impeller to Tongue Gap Variation*. Journal of Fluids Engineering, 2006. **128**: p. 455.
41. Mentzos, M., et al., *The evolution of the velocity profile as impeller passes in front of the volute tongue*. 2014.
42. Lv, Y., et al., *Design of volute shape of centrifugal fans*. Proceedings of the Institution of Mechanical Engineers, Part A: Journal of Power and Energy, 2015: p. 0957650915624034.
43. Yang, S., F. Kong, and B. Chen, *Research on pump volute design method using CFD*. International Journal of Rotating Machinery, 2011. **2011**.
44. Qi, D., M. Pomfret, and K. Lam, *A new approach to the design of fan volute profiles*. Proceedings of the Institution of Mechanical Engineers, Part C: Journal of Mechanical Engineering Science, 1996. **210**(3): p. 287-294.

45. Pan, D., A. Whitfield, and M. Wilson, *Design considerations for the volutes of centrifugal fans and compressors*. Proceedings of the Institution of Mechanical Engineers, Part C: Journal of Mechanical Engineering Science, 1999. **213**(4): p. 401-410.
46. Miyanaga, K., et al. *A study of volute tongue and passage design on the performance of centrifugal turbomachines*. in *Proc. of the 14th Australasian Fluid Mechanics Conference*. 2001.
47. Whitfield, A. and M.A. Johnson, *The Effect of Volute Design On The Performance Of A Turbocharger Compressor*. 2002.
48. Phuong, G., S. Abanteriba, and P. Haley. *Compressor Volute Design System: Part I—Volute Design by Bezier Application*. in *ASME 2002 Joint US-European Fluids Engineering Division Conference*. 2002. American Society of Mechanical Engineers.
49. Phuong, G., S. Abanteriba, and P. Haley. *Compressor Volute Design System: Part II—New Volute Design System Approach*. in *ASME 2002 Joint US-European Fluids Engineering Division Conference*. 2002. American Society of Mechanical Engineers.
50. Steglich, T., et al., *Improved diffuser/volute combinations for centrifugal compressors*. Journal of Turbomachinery, 2008. **130**(1): p. 011014.
51. Mojaddam, M., A. Hajilouy-Benisi, and M. Movahhedy, *Experimental and numerical investigation of radial flow compressor volute shape effects in characteristics and circumferential pressure non-uniformity*. Scientia Iranica. Transaction B, Mechanical Engineering, 2013. **20**(6): p. 1753.
52. Shyam, P. and T. Vithuraj, *Mathcad Tool for Design of Volute of Centrifugal Air Compressor*. International Journal of Scientific and Engineering Research, 2013(4): p. 6.
53. Mojaddam, M., et al., *Experimental and numerical investigations of radial flow compressor component losses*. Journal of Mechanical Science and Technology, 2014. **28**(6): p. 2189-2196.
54. Mojaddam, M., A. Hajilouy-Benisi, and M.R. Movahhedy. *Optimal design of the volute for a turbocharger radial flow compressor*. in *ASME Turbo Expo 2014: Turbine Technical Conference and Exposition*. 2014. American Society of Mechanical Engineers.
55. Zhou, T. and G.S. Lee, *Comparison of Performance between Two Types of the Three-Arcs Overhung Volute for an Automobile Turbocharger Compressor*. 2014.
56. Heinrich, M. and R. Schwarze. *Scripted CFD-Tool for the Automated Design of Volutes for Centrifugal Compressors*. in *ASME Turbo Expo 2015: Turbine Technical Conference and Exposition*. 2015. American Society of Mechanical Engineers.
57. Van den Braembussche, R. and B. Hande, *Experimental and theoretical study of the swirling flow in centrifugal compressor volutes*. Journal of turbomachinery, 1990. **112**(1): p. 38-43.
58. Xu, C. and M. Müller, *Development and design of a centrifugal compressor volute*. International Journal of rotating machinery, 2005. **2005**(3): p. 190-196.

59. Versteeg, H.K. and W. Malalasekera, *An introduction to computational fluid dynamics: the finite volume method*. 2007: Pearson Education.
60. Anderson, J.D. and J. Wendt, *Computational fluid dynamics*. Vol. 206. 1995: Springer.
61. ANSYS, I., *ANSYS FLUENT User's Manual Release 15.0*, I. ANSYS, Editor. 2011: U.S.A.
62. Samale, A. and J.E. Pacheco. *Volute CFD modeling evaluation for centrifugal compressors*. in *ASME Turbo Expo 2014: Turbine Technical Conference and Exposition*. 2014. American Society of Mechanical Engineers.
63. Adams, T., C. Grant, and H. Watson, *A simple algorithm to relate measured surface roughness to equivalent sand-grain roughness*. Journal ISSN, 2012. **2929**: p. 2724.
64. Blocken, B., T. Stathopoulos, and J. Carmeliet, *CFD simulation of the atmospheric boundary layer: wall function problems*. Atmospheric environment, 2007. **41**(2): p. 238-252.
65. Javed, A. and E. Kamphues. *Evaluation of the Influence of Volute Roughness on Turbocharger Compressor Performance From a Manufacturing Perspective*. in *ASME Turbo Expo 2014: Turbine Technical Conference and Exposition*. 2014. American Society of Mechanical Engineers.
66. Einstein, H.A. and E.-S.A. El-Samni, *Hydrodynamic forces on a rough wall*. Reviews of modern physics, 1949. **21**(3): p. 520.
67. Tennekes, H. and J.L. Lumley, *A first course in turbulence*. 1972: MIT press.
68. Blazek, J., *Computational Fluid Dynamics: Principles and Applications: (Book with accompanying CD)*. 2005: Elsevier.
69. Menter, F.R., *Two-equation eddy-viscosity turbulence models for engineering applications*. AIAA journal, 1994. **32**(8): p. 1598-1605.
70. ANSYS, I., *ANSYS FLUENT Theory Guide, Release 17.0*, I. ANSYS, Editor. 2016: U.S.A.
71. Japikse, D., *Centrifugal compressor design and performance*. 1996: Wilder, VT: Concepts ETI, Inc.
72. Ceyrowsky, T., A. Hildebrandt, and R. Schwarze. *Numerical Investigation of the Circumferential Pressure Distortion Induced by a Centrifugal Compressor's External Volute*. in *ASME Turbo Expo 2018: Turbomachinery Technical Conference and Exposition*. 2018. American Society of Mechanical Engineers.
73. Cumpsty, N., *Compressor Aerodynamics*, Harlow, Essex, England: Longman Scientific and Technical; New York: J. 1989: Wiley.
74. Brun, K. and R.J.I.J.o.R.M. Kurz, *Analysis of secondary flows in centrifugal impellers*. 2005. **2005**(1): p. 45-52.
75. Liu, Z. and D.L. Hill, *Issues surrounding multiple frames of reference models for turbo compressor applications*. 2000.
76. Meakhail, T. and S.O. Park, *A study of impeller-diffuser-volute interaction in a centrifugal fan*. Journal of Turbomachinery, 2005. **127**(1): p. 84-90.

77. Baker, P., *Extension of an Analytical Method for Novel Volute Design*. Journal of Engineering and Applied Sciences, Accepted/In press 2018.
78. Masri, J.A. and A. Sayma, *Prediction of the Characteristic Map of a Centrifugal Compressors Using Computational Fluid Dynamic*. Mapta Journal of Mechanical and Industrial Engineering (MJMIE), 2018. **2**(02): p. 13-21.
79. Sun, Z., et al., *Influence of volute design on flow field distortion and flow stability of turbocharger centrifugal compressors*. Proceedings of the Institution of Mechanical Engineers, Part D: Journal of Automobile Engineering, 2018: p. 0954407017746281.
80. Chen, H., D. Tong, and X. Wang. *Vortices and performance of internal and external volutes*. in *ASME turbo expo 2015: turbine technical conference and exposition*. 2015. American Society of Mechanical Engineers.
81. Zheng, X., Y. Lin, and Z. Sun, *Effects of volute's asymmetry on the performance of a turbocharger centrifugal compressor*. Proceedings of the Institution of Mechanical Engineers, Part G: Journal of Aerospace Engineering, 2018. **232**(7): p. 1235-1246.



# APPENDICES

---

## APPENDIX 1 Computational Fluid Dynamics

Computational Fluid Dynamics (CFD) is the numerical analysis of systems involving fluid mechanics, thermodynamics and associated phenomena using computer-based simulation. This numerical technique is a very powerful prediction tool that can be employed into investigations over a vast range of industrial and non-industrial application areas. Since the 1960s, CFD techniques have been integrated into the design, Research & Development (R&D) and manufacture of systems. More recently, this numerical methodology has been implemented to design, analyse and predict flow phenomena in order to conduct investigations on systems and their processes across a wide range of applications. Such applications range from mechanical, aerospace and motorsport engineering to simulate high performance components, systems and vehicles, to oceanography simulating ocean currents, to medicine simulating blood flows through the living and even the cause of deceased in forensics applications [59].

Elaborating this further in order to understand the expansion of how broad CFD branches out; such applications include, turbomachinery in terms of analysing the flow map inside volutes, diffusers and rotating passages, such as the impeller; power plant applications to analyse and predict the combustion process in internal combustion engines, combustion chambers of gas turbines and furnaces; aerodynamics of aircraft and vehicles to analyse and predict the effect of forces and moments; hydrodynamics of ships; electrical and electronic engineering to analyse the cooling of equipment, such as microcircuits; external and internal environment of buildings to analyse and predict wind loading as well as heating and ventilation; meteorology to predict the weather; hydrology and oceanography to analyse the flows in rivers, oceans, estuaries; environmental engineering to analyse and predict the distribution of pollutants and effluents; marine engineering to analyse the loads on offshore structures; chemical process engineering to analyse polymer moulding, mixing and separation; biomedical engineering to analyse blood flows through arteries and veins; forensics to analyse and predict causes of fires, the deceased in the scattered blood patterns at crime scenes to solve cases; and so forth [59].

The variable cost of an experiment, in terms of hiring a facility or a person, or both, accumulates in hourly costs, which is proportional to the number of data points and the number of configurations tested. In contrast to this, CFD codes can produce extremely large volumes of

data at no added expense, as well as being a very cheap method to conduct parametric studies, such as performance optimisation. As a result, it can be accredited that CFD has become an essential component in the field research as a whole; not only in the sector of improving existing research, but also in the sector of creating innovative research [59].

### Working of CFD Codes

There are three main components of numerical solution techniques namely being, the finite difference, finite element and spectral methods. Finite volume method, a special finite difference formulation, is crucial to many well established CFD codes. The numerical algorithms involve the integration of the governing equations of fluid flow over the all the control volumes of the domain, discretisation or conversion of the resulting integral equations into a system of algebraic equations and the solution of these equations by means of employing an iterative method [59].

Figure 3.1 depicts the visual representation of the solver process.



Figure A.1 Process of the Solver

CFD codes are structured around the numerical algorithms that can tackle fluid flow problems. In order to provide easy access to their solving power, all commercial CFD packages comprise of sophisticated user interfaces to input problem parameters and to examine the results. Hence, all codes contain three main elements. These are [59]:

#### ➤ PRE – PROCESSOR

The pre-processing stage entails the input of the flow problem to a CFD programme through an operator-friendly interface and the subsequent transformation of this input into a format that is suitable for solver use. The user activities at the pre-processing stage is divided into two sectors, namely being the geometry sector, which defines the geometry of the region of interest, being the computational domain; and the meshing sector, which subdivides the domain into a number of smaller, non-overlapping subdomains, being the grid generation. Additionally, this

stage also involves the requirement for the selection of the physical or chemical phenomena modelling, definition of fluid properties and the specification of appropriate boundary conditions at cells, which coincide with or touch the domain boundary [59].

#### ➤ SOLVER EXECUTION

The solver-execution stage predominantly entails the setup of the numerical model and the computation/monitoring of the solution. The setup of the numerical model includes the following [59]:

- Selection of appropriate physical models, which include turbulence, combustion, multiphase etc.
- Defining material properties, such as the fluid, solid, mixture etc.
- Defining operating conditions
- Defining boundary conditions
- Defining solver settings
- Defining initial solution
- Setting up convergence monitors

The computation of the solution includes:

- The discretised conservation equations are solved iteratively. A number of iterations are required to reach a converged solution.
- Convergence is reached when change in solution variables from one iteration to the next is negligible. Residuals provide a mechanism to assist in monitoring this trend.
- The accuracy of the converged solution is dependent upon problem setup, grid resolution, grid independence, appropriateness and accuracy of the physical model.

#### ➤ POST – PROCESSOR

The post-processing stage entails the examination of the results obtained and revision of the model based on these results. These can be further elaborated into [59]:

- Examine the results to view solution and extract useful data.
- Visualisation tools can be employed to extract the overall flow pattern, separation, shocks, shear layers etc.

- Numerical reporting tools can be employed to calculate quantitative results like forces, moments, and average heat transfer co-efficient, flux balances, surface and volume integrated quantities.
- Are physical models appropriate?
- Are boundary conditions correct?
- Is the grid adequate?
- Can grid be adapted to improve results?
- Does the boundary resolution require improvement?
- Is the computational domain sufficiently large?

Since engineering workstations are highly popular in having outstanding graphic capabilities, the leading CFD packages are now equipped with versatile data visualisation tools. These include domain geometry, grid display, vector plots, line and shaded contour plots, 2D and 3D surface plots, particle tracking, view manipulations, colour post-script output, streamlines etc. More recently, these facilities may also include animation for dynamic result display, and in addition to graphics, all codes produce reliable alphanumeric output and consist of data export facilities for further manipulation external to the codes. As in many other branches of Computer Aided Engineering (CAE), the graphics output capabilities of CFD codes have revolutionised the communication of ideas to the non-specialists [59]. A visual representation of an overview on implementing CFD based analysis to conduct investigations is presented in Figure 3.2.

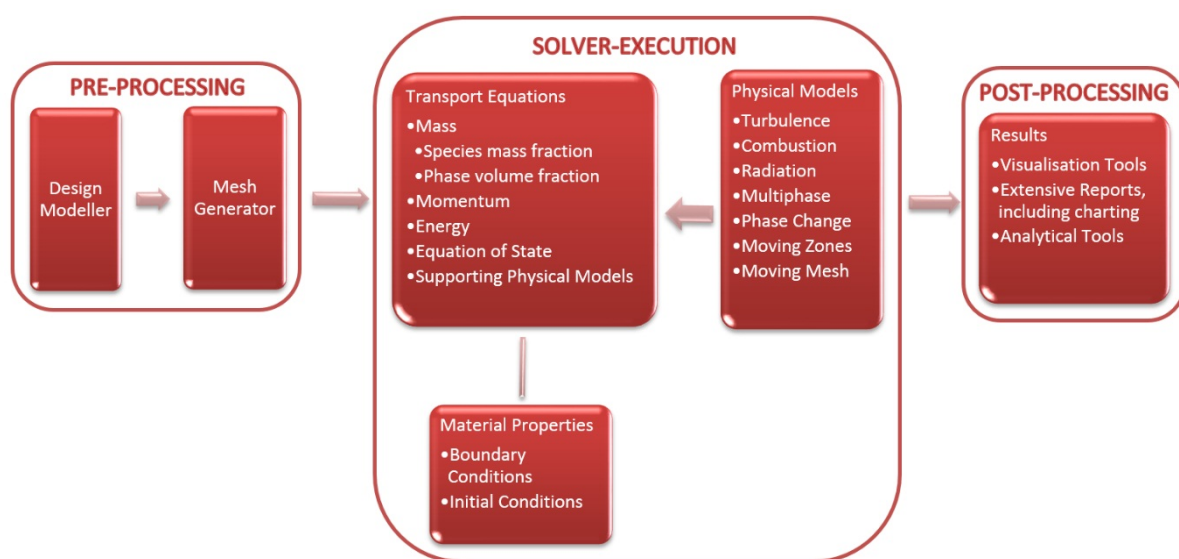


Figure A.2 CFD Overview

### Numerical Formulation of Fluid Flow

There are a range of formulations employed when simulating the flow field of a turbocharger compressor stage model. These simulations have been carried out using the CFD solver FLUENT, which is integrated into ANSYS 17. Fluent is a three-dimensional Navier-Stokes commercial code that utilises a finite-element based finite-volume method to discretize transport equations. It is a solver embedded with various equations that can be solved simultaneously, creates no limitations on time stepping, and is considered as being simple and easy to implement. This solver allows the original mesh with many elements to be converted into polyhedral mesh elements, which reduces computation time as well as the number of iterations required to achieve convergence with reasonable solutions [43].

It is important to understand a few aspects of the Navier-Stokes equations prior to continuing forward. The Navier–Stokes equations assume that the fluid being studied is a continuum, which means the matter in the body is continuously distributed and fills the entire region of space it occupies. Historically, the momentum equations were established as the Navier-Stokes equations, however at present day, this terminology has been broadened to also add the continuity and energy equations. Thus, the entire system of flow equations (Navier-Stokes) is now referred to as the continuity equation, momentum equation, and the energy equation. There are six unknown flow-field variables, density, pressure, three components of velocity in x (nominal), y (parallel), and z (orthogonal) directions, and energy, denoted respectively [60]:

$$\rho, p, u, v, w, e$$

The following governed equations are for three-dimensional, unsteady, compressible, viscous flow. The governing equation of fluid flow represents mathematical statements of the conservation laws of Physics [59, 60]:

- The mass of a fluid is conserved.
- The rate of change of momentum equals the sum of the forces on a fluid particle. (Newton's second law)
- The rate of change of energy is equal to the sum of the rate of heat addition to and the rate of work done on a fluid particle. (First law of thermodynamics)

### Conservation of Mass

The physical principle of the continuity equation states that *mass is conserved*, therefore this is also known as the conservation of mass equation. It states that [60]:

$$\begin{aligned} & \text{“Mass of the fluid flowing in the control volume – Mass of fluid out of the control volume} \\ & \quad = \text{Rate of change of mass with respect to time.”} \end{aligned}$$

$$\frac{\partial \rho}{\partial t} + \nabla \cdot (\rho V) = 0$$

*Equation A.1 Conservation of Mass*

### Conservation of Momentum

The physical principle of the momentum equation is based on Newton’s second law of motion whereby stating that the application of the net force onto the fluid particle is directly dependent on the mass and acceleration of the fluid element, denoted by [60]:

$$F = ma$$

The momentum equation is defined as:

$$\text{“Sum of all forces = Rate of change of Momentum”}$$

There are two sources of forces equating to the net force. These are body forces, which are forces that acts directly on the volumetric mass and acts at a distance, whereby is defined as [60]:

$$\text{For x-direction:} \quad \rho f_x \, dx dy dz$$

$$\text{For y-direction:} \quad \rho f_y \, dx dy dz$$

$$\text{For z-direction:} \quad \rho f_z \, dx dy dz$$

And surface forces that are applied directly on the surface and is caused by pressure distribution initiated by the external fluid surrounding the particle, as well as normal and shear stress distributions initiated by the external fluid ‘tugging’ or ‘pushing’ on the surface through

friction. These stresses are related to the time rate of change of the deformation of the fluid element [60].

Figure 3.3 depicts pressure (black) is always pushing directly into the fluid element. Shear stresses are the sliding forces on the surface. The shear stress acting on the top surface of the fluid element (green) is a tugging action, which pulls the element in a positive direction, whereas the shear stress acting on the bottom surface of the fluid element (green) is a dragging action, which pushes the element in negative direction. The shear stress (blue) acting on the front surface of the fluid element is a viscous stress that acts in the positive direction, whilst the shear stress (blue) acting on the back surface of the fluid element is a viscous stress that acts in the negative direction. The normal stress (red) acts normal to surface, which pulls the element through a viscous action acting as suction that delays the motion of the fluid element. The sum of these surface forces and body forces equates to the net force [60].

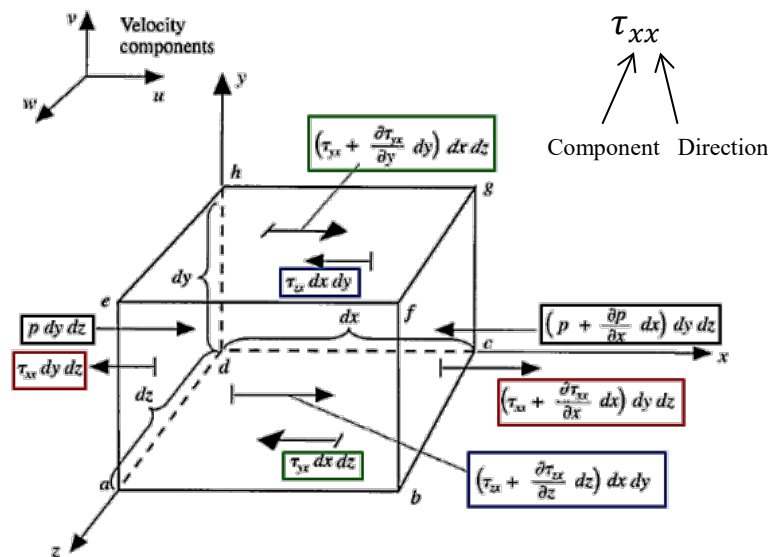


Figure A.3 Forces Acting on the Fluid Element [60]

The mass is the matter within the control volume and is defined by [60]:

$$\rho \cdot dxdydz$$

Acceleration is the increase in velocity with respect to time and is defined by:

$$\text{For x-direction:} \quad \frac{Du}{Dt}$$

$$\text{For y-direction:} \quad \frac{Dv}{Dt}$$

For z-direction:  $\frac{Dw}{Dt}$

Therefore, through implementation and simplification the momentum equations can be governed [60].

For x-direction:

$$\frac{\partial(\rho u)}{\partial t} + \nabla \cdot (\rho u V) = -\frac{\partial p}{\partial x} + \frac{\partial \tau_{xx}}{\partial x} + \frac{\partial \tau_{yx}}{\partial y} + \frac{\partial \tau_{zx}}{\partial z} + \rho f_x$$

For y-direction:

$$\frac{\partial(\rho v)}{\partial t} + \nabla \cdot (\rho v V) = -\frac{\partial p}{\partial y} + \frac{\partial \tau_{xy}}{\partial x} + \frac{\partial \tau_{yy}}{\partial y} + \frac{\partial \tau_{zy}}{\partial z} + \rho f_y$$

For z-direction:

$$\frac{\partial(\rho w)}{\partial t} + \nabla \cdot (\rho w V) = -\frac{\partial p}{\partial z} + \frac{\partial \tau_{xz}}{\partial x} + \frac{\partial \tau_{yz}}{\partial y} + \frac{\partial \tau_{zz}}{\partial z} + \rho f_z$$

Equation A.2: Conservation of Momentum

### Conservation of Energy

The physical principle of the energy equation is based on the first law of thermodynamics, which states that *energy is conserved*, therefore this is also known as the conservation of energy equation. It states that [60]:

*“The rate of change of energy inside the fluid element = Net flux of heat into the element + the rate of work done on the element due to the sum of all forces”*

Or,

$$A = B + C$$

The term ‘C’ states the rate of work done on a moving fluid element is due to the net forces (body forces + surfaces forces). This is equal to the product of the force and the velocity component in the direction of the force [60].

The term ‘B’ states the net flux of heat into the fluid element is due to volumetric heating (absorption or emission of heating), and heat transfer across the surface due to temperature gradients (thermal conductivity) [60].



The term ‘A’ states the time rate of change of energy in the fluid element. For stationary systems, the internal energy is accounted for. With regards to moving systems, internal energy and kinetic energy are both accounted for. Internal energy is the energy of each molecule or atom, summed over all molecules and atoms in the system due to random molecular motion, energy per unit mass. Kinetic energy is due to translational motion of the fluid element adding rotational and vibrational energies to the molecule, per unit mass [60].

The total energy of a molecule is the sum of its translational, rotational, vibrational and electrical energies. For both systems the energy equations can be governed as follows [60]:

$$\begin{aligned}
 & \frac{\partial}{\partial t} \left[ \rho \left( e + \frac{V^2}{2} \right) \right] + \nabla \cdot \left[ \rho \left( e + \frac{V^2}{2} \right) \mathbf{V} \right] \\
 &= \rho \dot{q} + \frac{\partial}{\partial x} \left( k \frac{\partial T}{\partial x} \right) + \frac{\partial}{\partial y} \left( k \frac{\partial T}{\partial y} \right) + \frac{\partial}{\partial z} \left( k \frac{\partial T}{\partial z} \right) - \frac{\partial (up)}{\partial x} - \frac{\partial (vp)}{\partial y} - \frac{\partial (wp)}{\partial z} + \\
 & \frac{\partial (u\tau_{xx})}{\partial x} + \frac{\partial (u\tau_{yx})}{\partial y} + \frac{\partial (u\tau_{zx})}{\partial z} + \frac{\partial (v\tau_{xy})}{\partial x} + \frac{\partial (v\tau_{yy})}{\partial y} + \frac{\partial (v\tau_{zy})}{\partial z} + \frac{\partial (w\tau_{xz})}{\partial x} + \frac{\partial (w\tau_{yz})}{\partial y} + \frac{\partial (w\tau_{zz})}{\partial z} \\
 & + \rho \mathbf{f} \cdot \mathbf{V}
 \end{aligned}$$

*Equation A.3 Conservation of Energy*

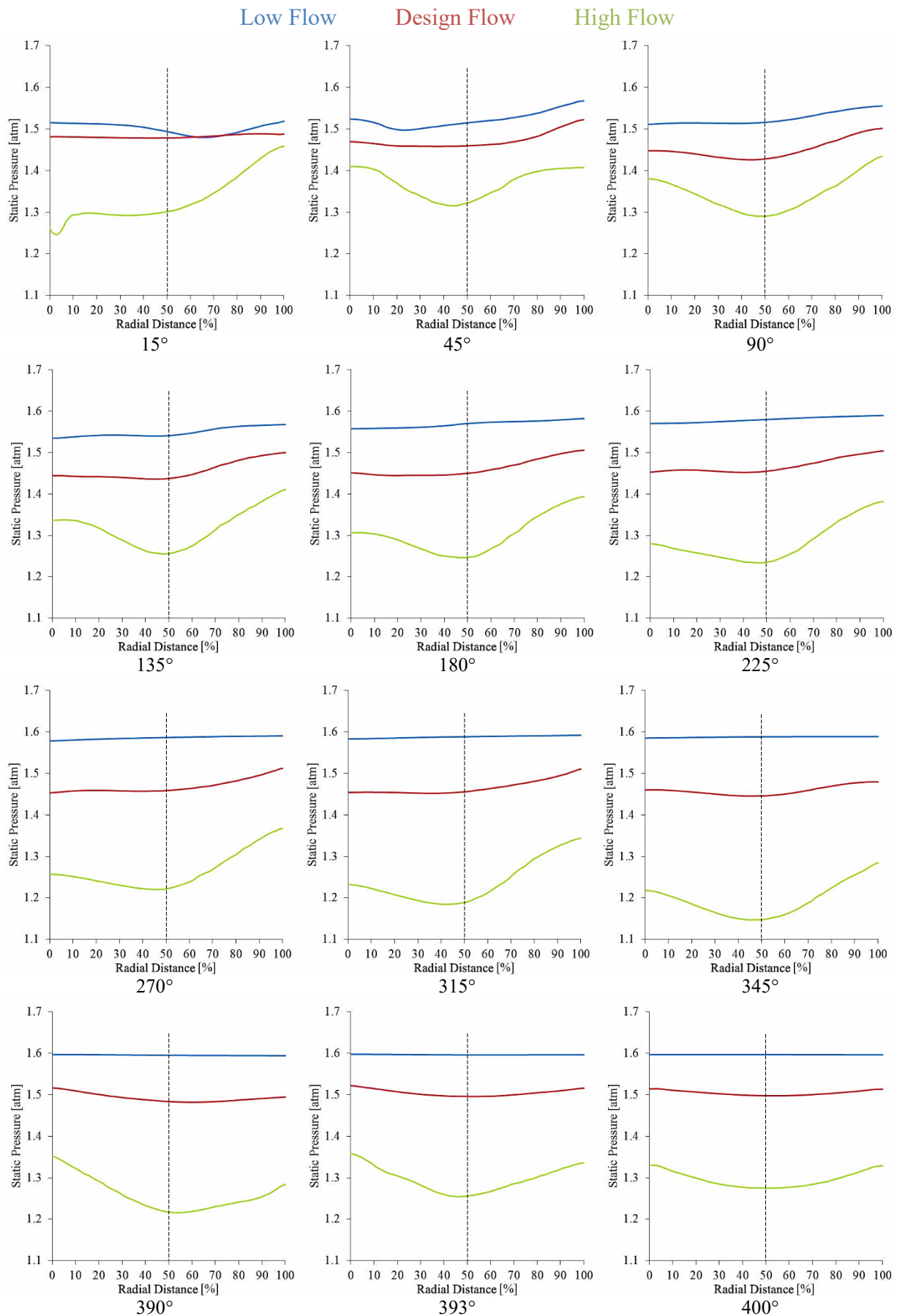
### Equation of State

The Equation of State is also known as Ideal Gas Law or ‘Perfect’ Gas Law. The equation of state closely estimates the behaviour of real gases under normal conditions when the gases are not reaching liquefaction. Gas has various properties being mass, volume, pressure and temperature, whereby this equation is applied to interrelate one variable to the other. During this calculation, it is vital to use the absolute pressures and temperatures since it is measured to absolute zero pressure [12, 28]. The equation of state is given by Equation 1.8.

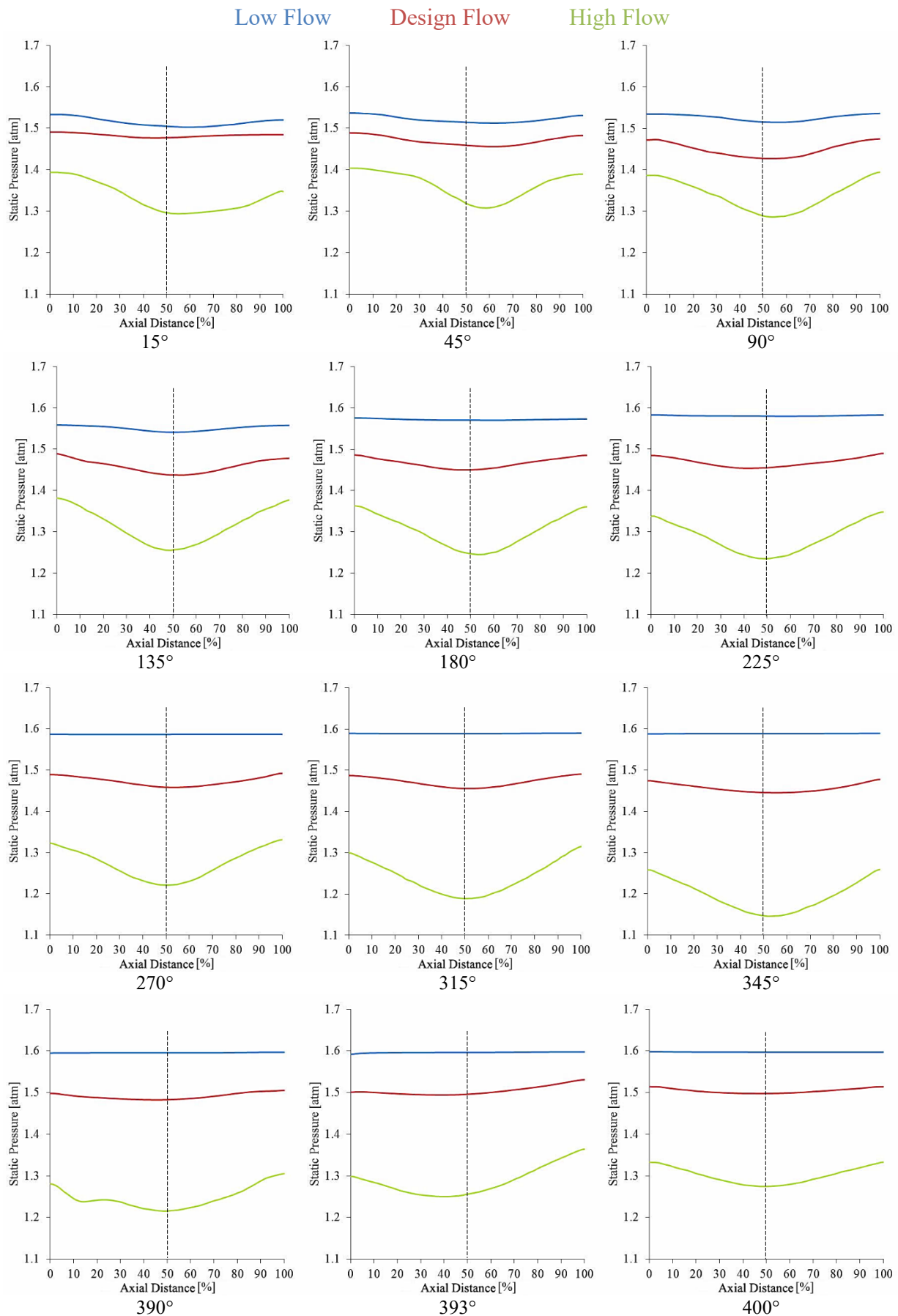
## **APPENDIX 2 Chapter 4 Flow Field Profiles along the Radial Direction and Axial Direction**

The following section depicts the variations in the flow characteristics of static pressure, velocity magnitude and static temperature at design and off-design conditions. Low flow is near the surge condition, design flow is the BEP and high flow is near the choke condition. These have been captured at low operating speed of 58.9rps/ $\sqrt{K}$  and high operating speed of 98.2rps/ $\sqrt{K}$ , along the radial and axial of each cross-sectional profile around the centrifugal compressor volute at the locations illustrated in Figure 3.9. A centreline has been displayed for each cross-section in the data set to identify the symmetry and asymmetry of the flow field variance exhibited along the radial direction of the cross-section and along the axial direction of the cross-section.

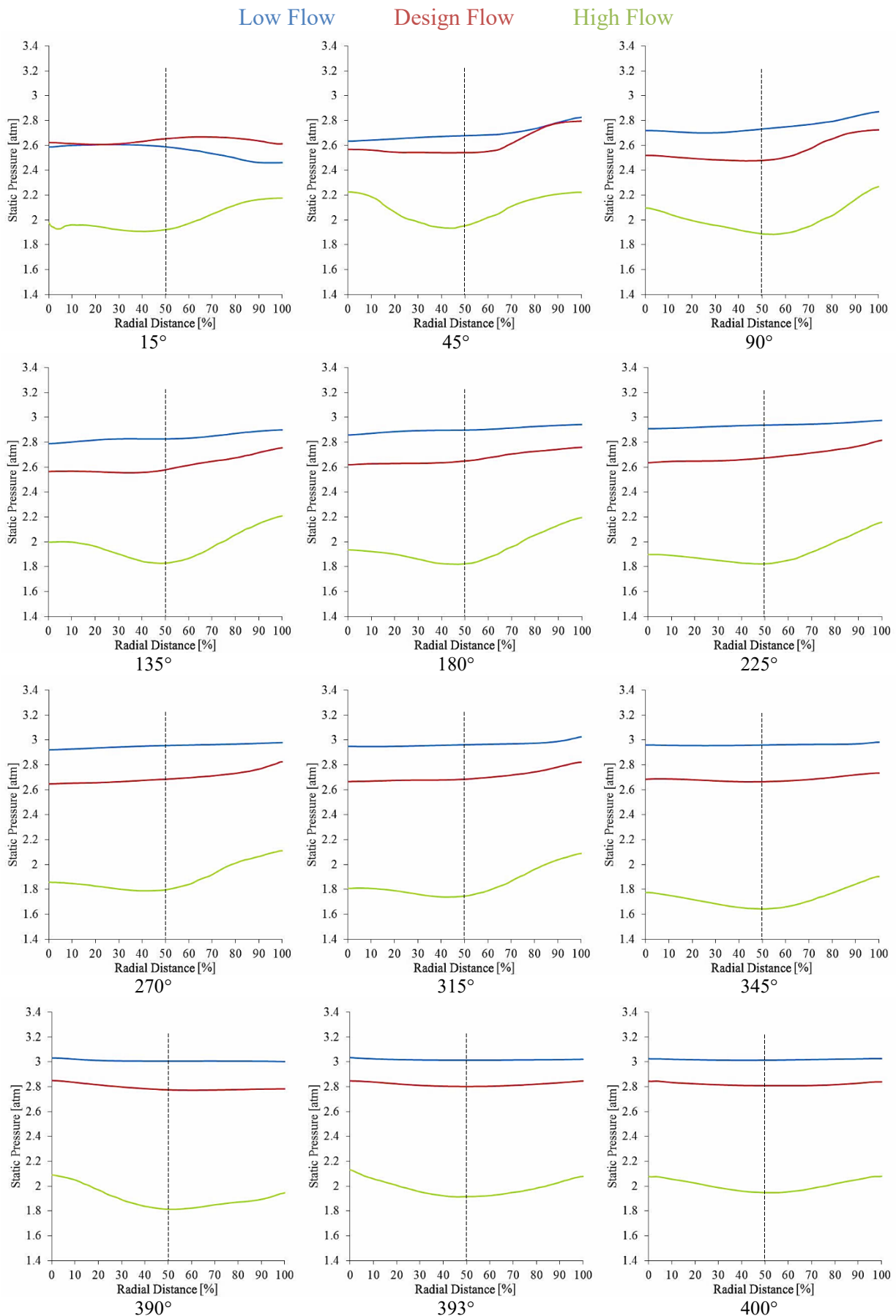
### Static Pressure along the Radial Direction at Low Operating Speed of 58.9rps/ $\sqrt{K}$



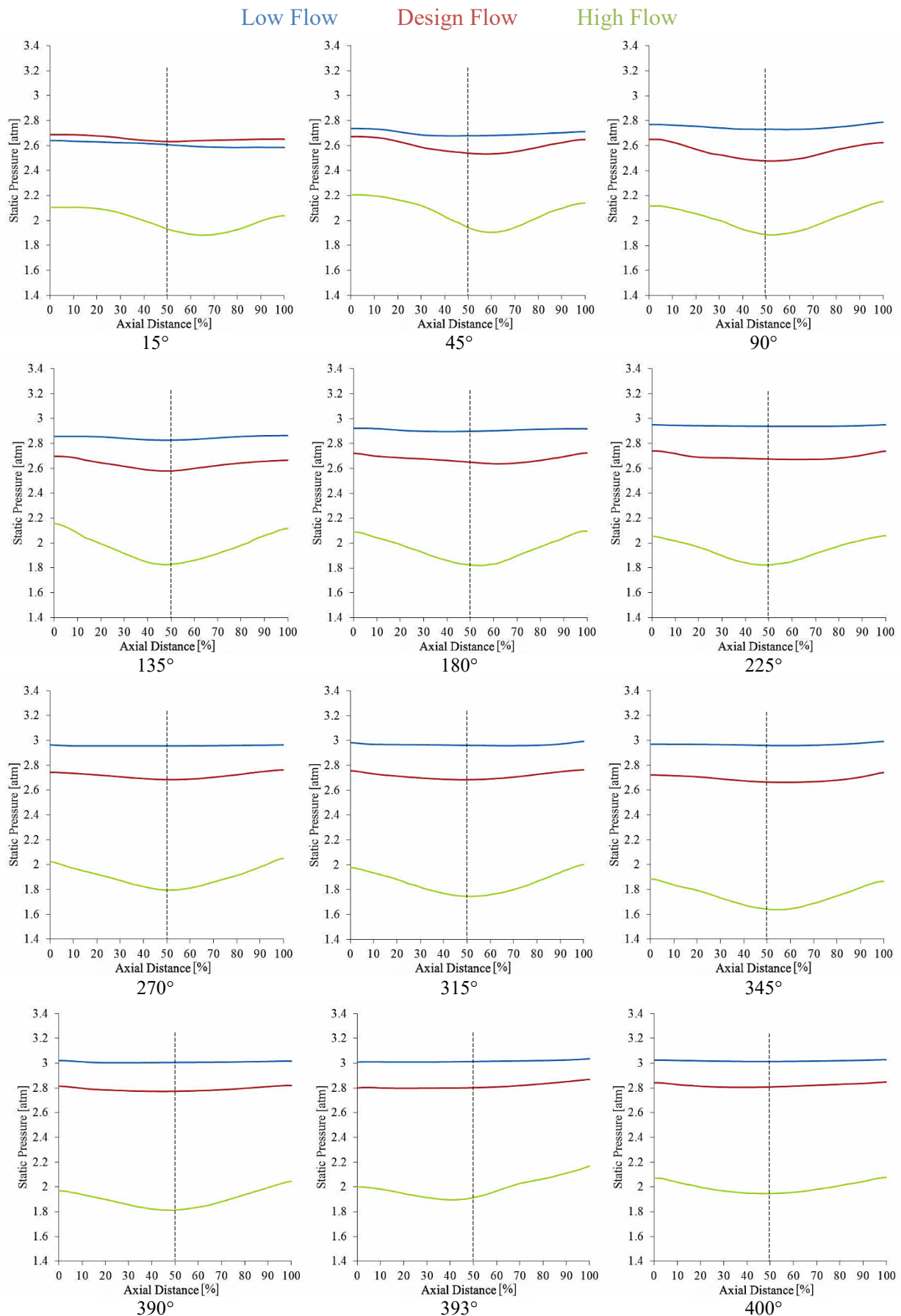
### Static Pressure along the Axial Direction at Low Operating Speed of 58.9rps/ $\sqrt{K}$



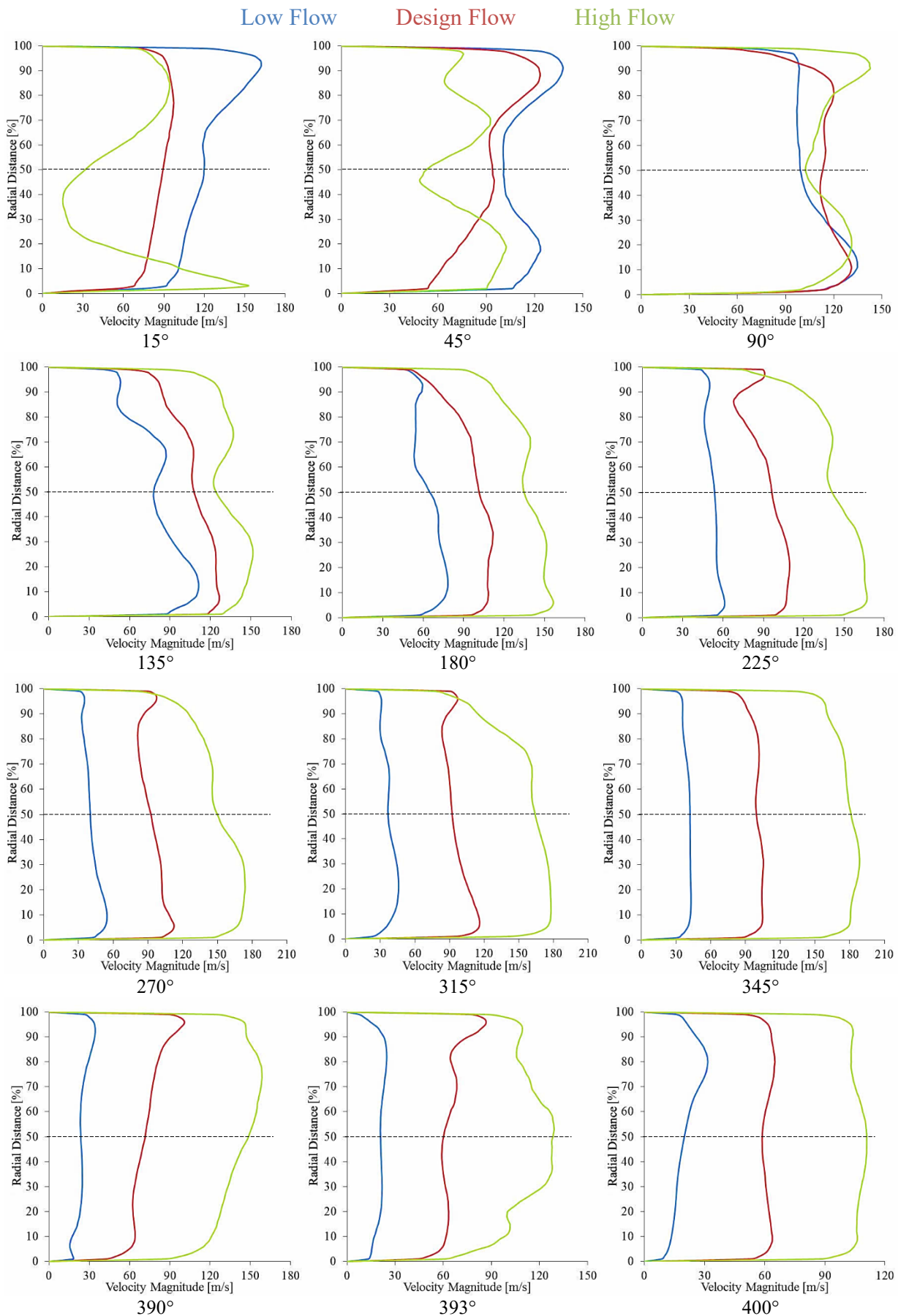
### Static Pressure along the Radial Direction at High Operating Speed of 98.2rps/ $\sqrt{K}$



### Static Pressure along the Axial Direction at High Operating Speed of 98.2rps/ $\sqrt{K}$

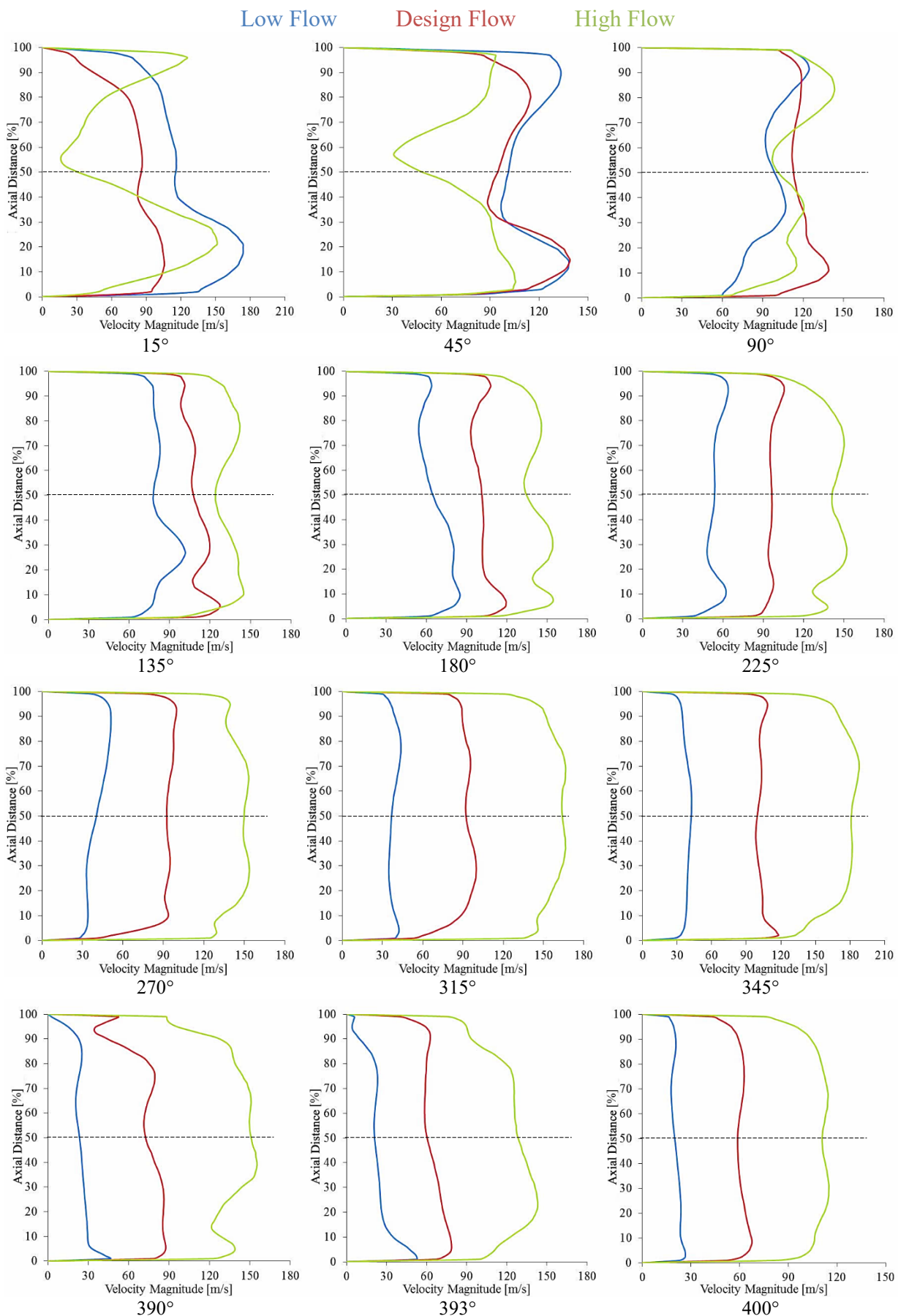


# Velocity Magnitude along the Radial Direction at Low Operating Speed of 58.9rps/ $\sqrt{K}$



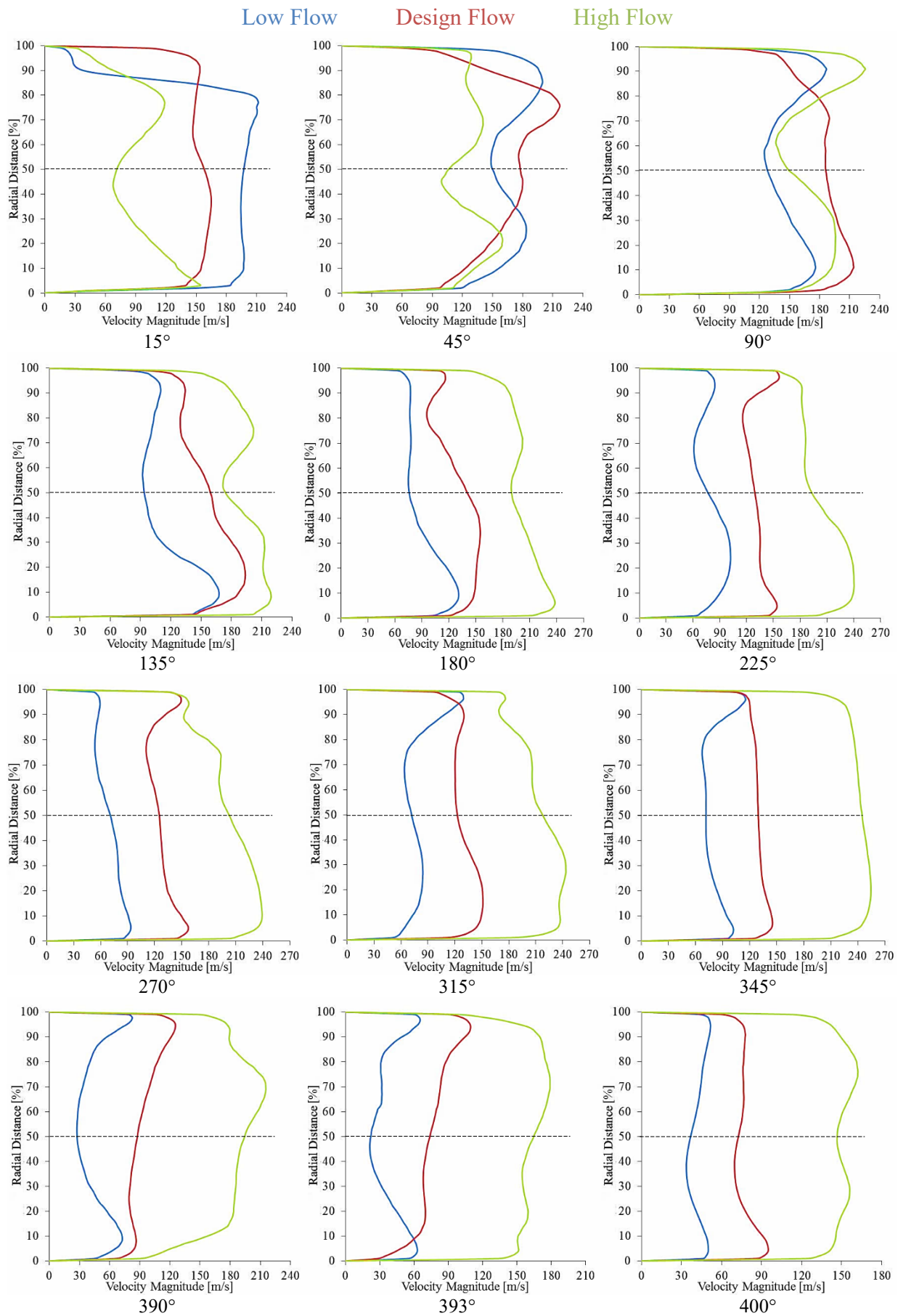


### Velocity Magnitude along the Axial Direction at Low Operating Speed of 58.9rps/ $\sqrt{K}$

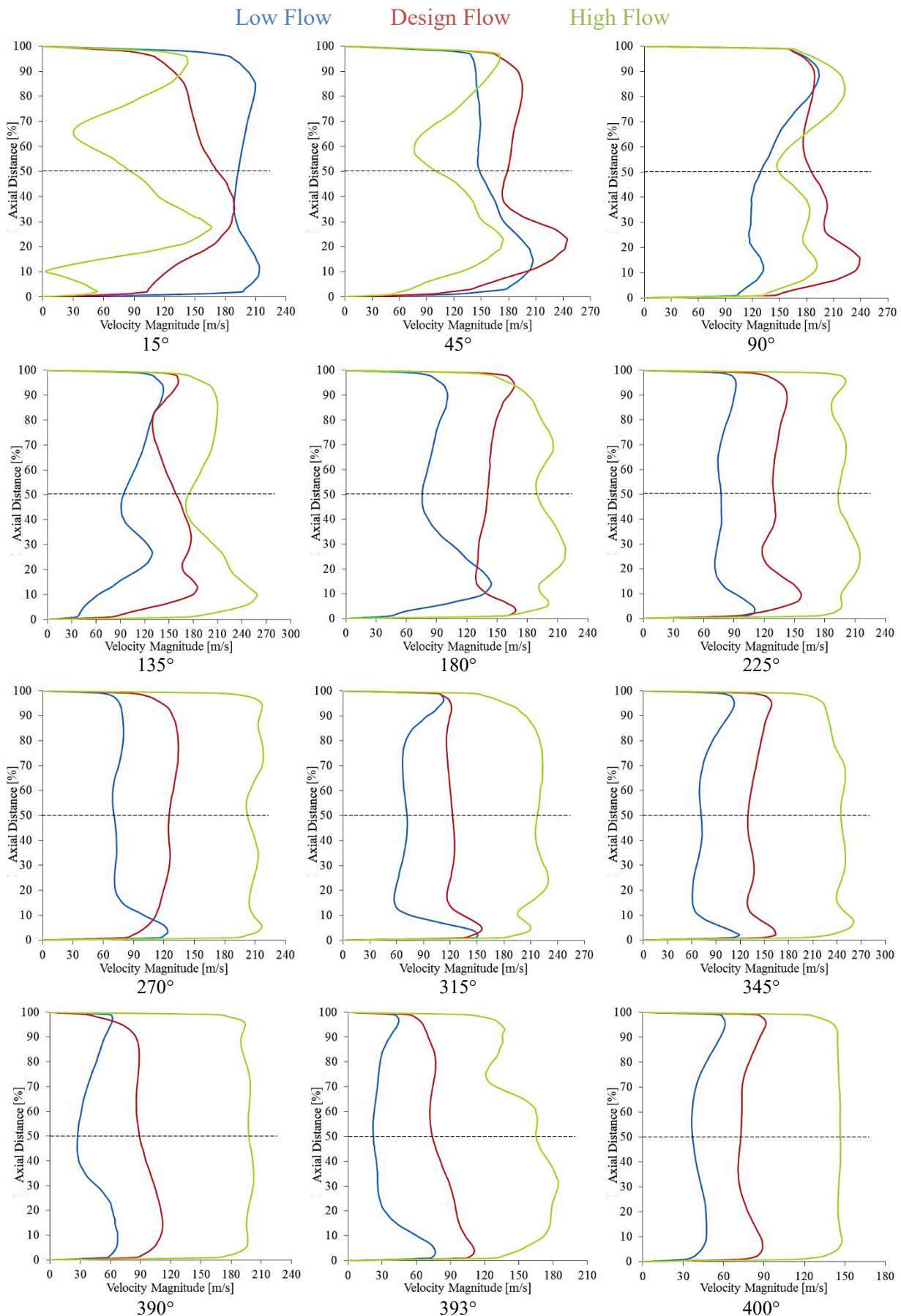




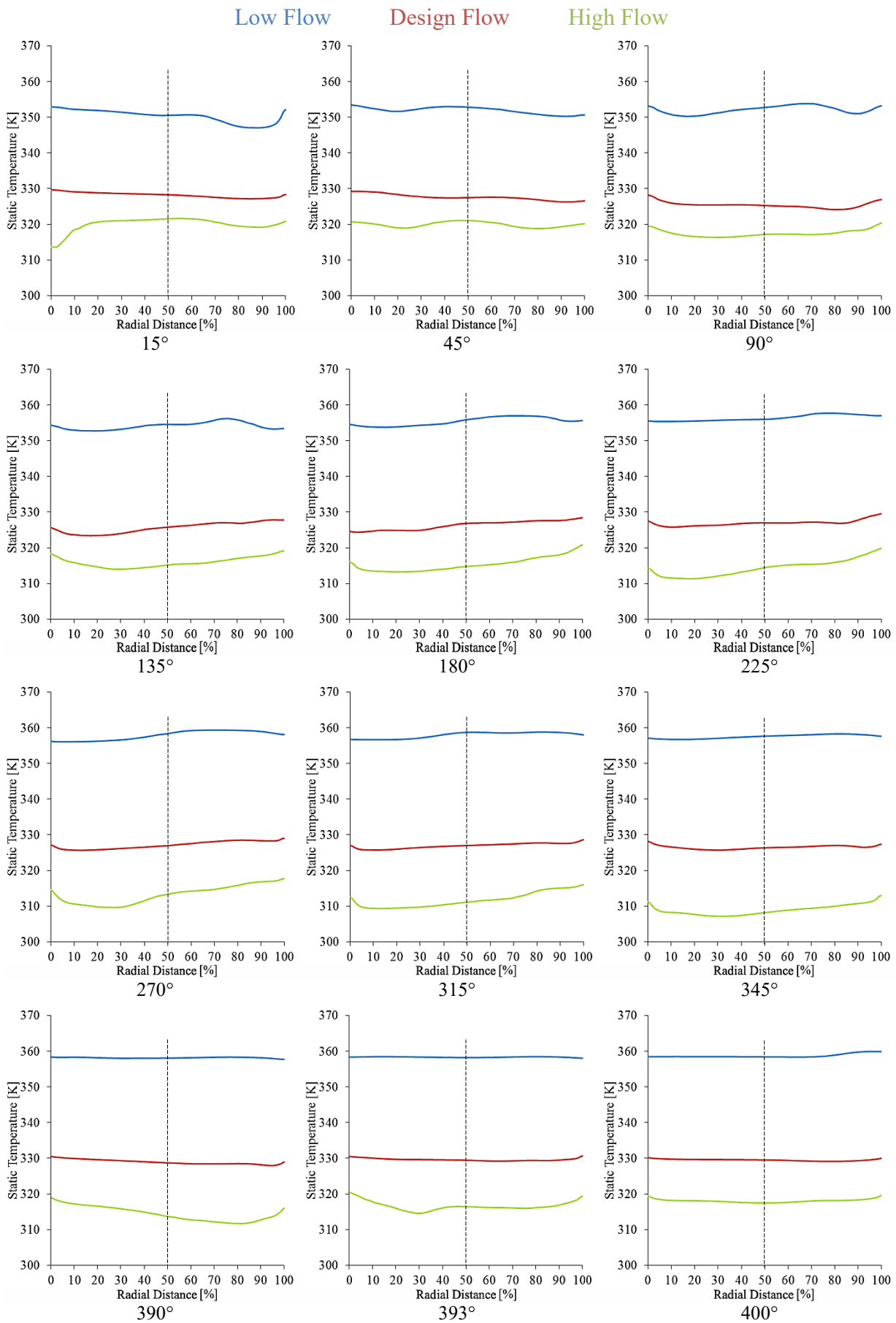
### Velocity Magnitude along the Radial Direction at High Operating Speed of 98.2rps/ $\sqrt{K}$



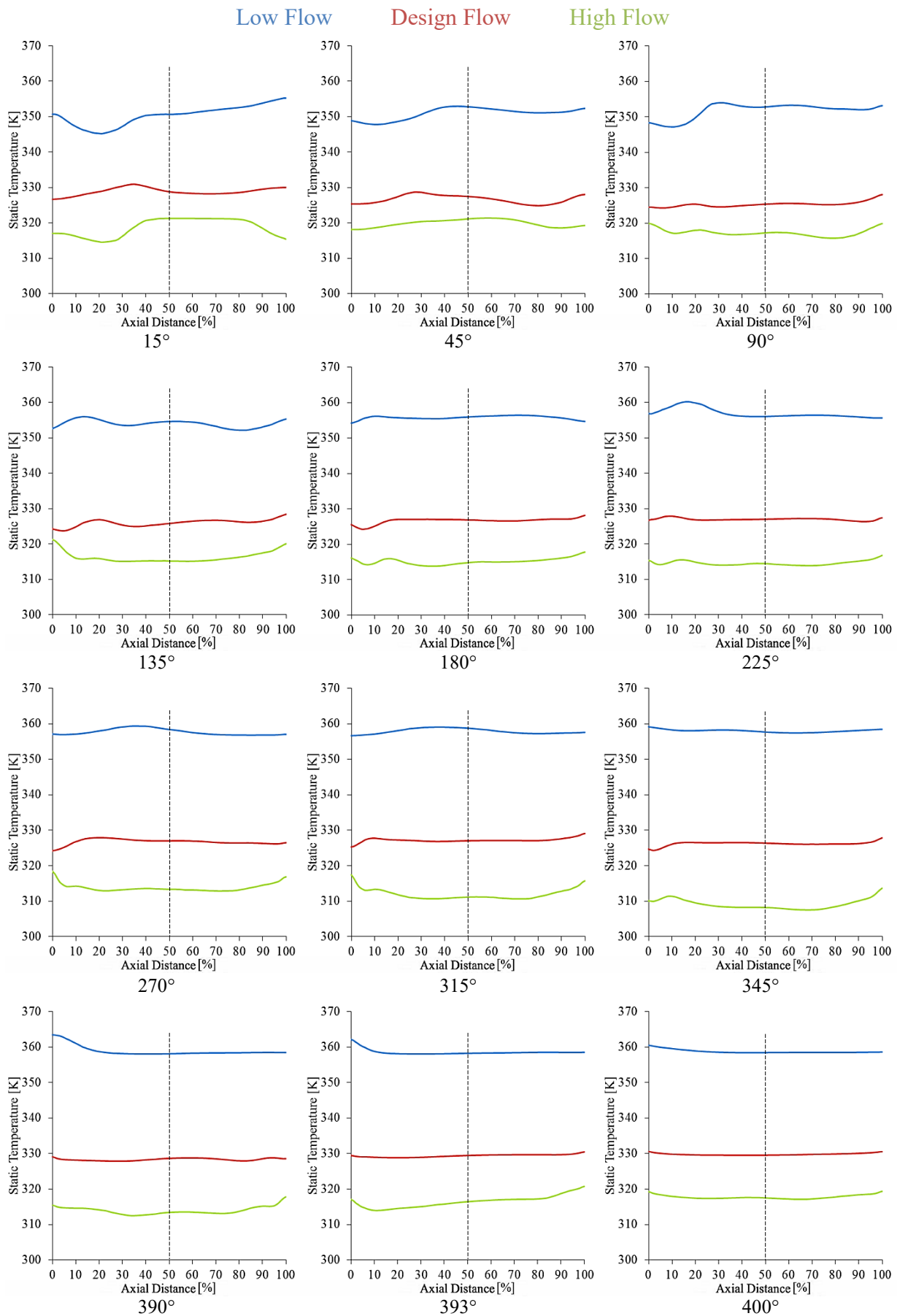
### Velocity Magnitude along the Axial Direction at High Operating Speed of 98.2rps/ $\sqrt{K}$



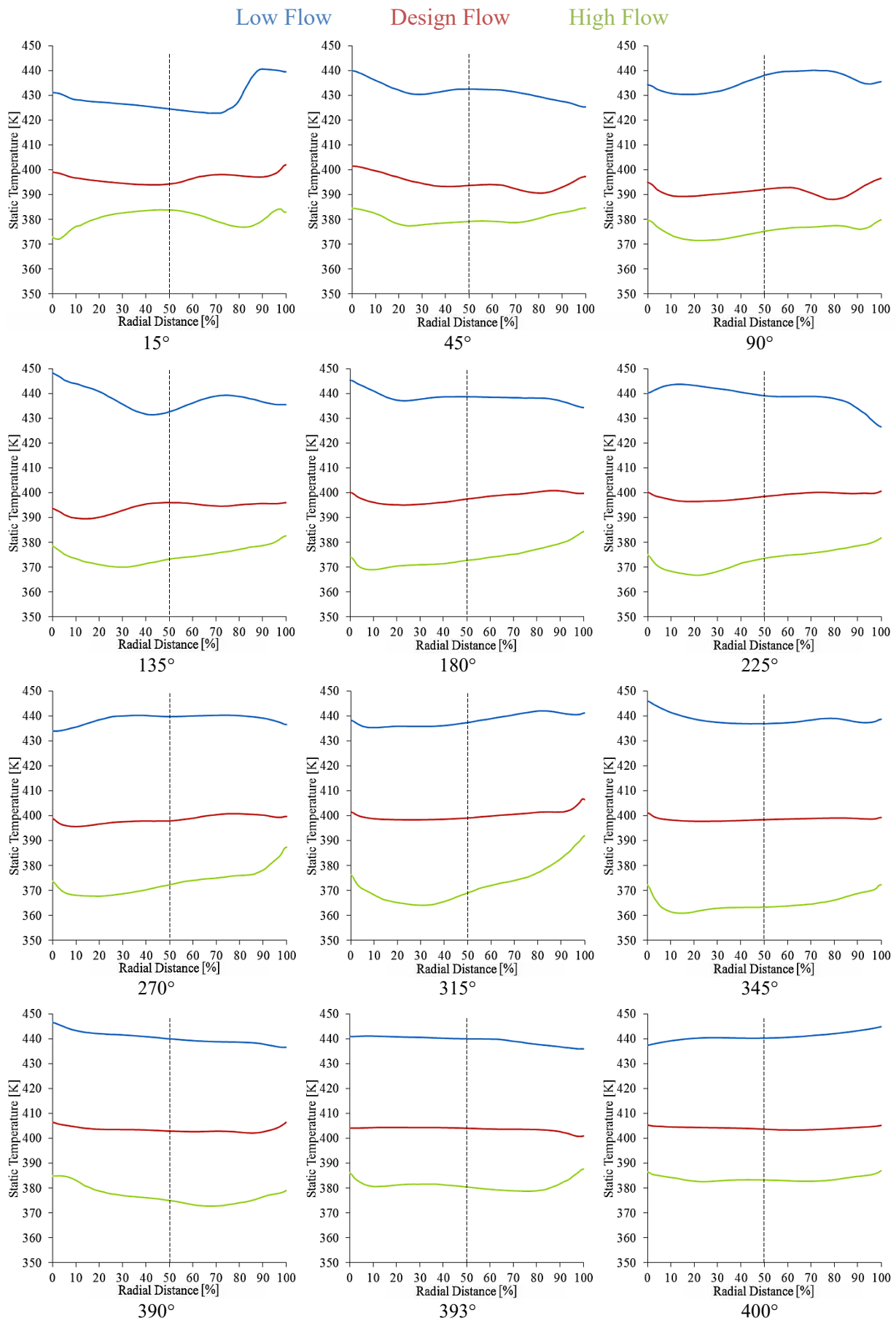
# Static Temperature along the Radial Direction at Low Operating Speed of 58.9rps/ $\sqrt{K}$



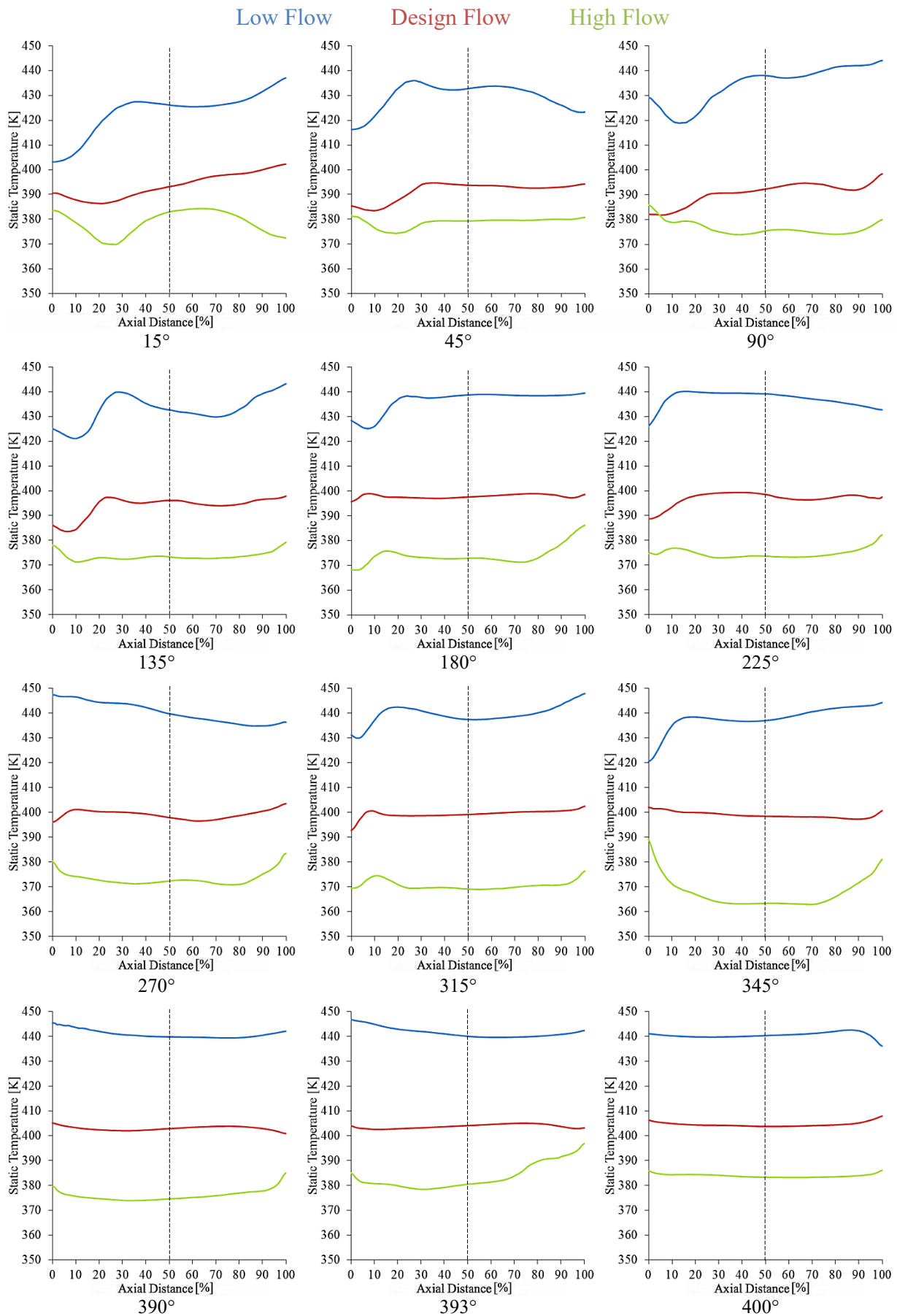
### Static Temperature along the Axial Direction at Low Operating Speed of 58.9rps/ $\sqrt{K}$



# Static Temperature along the Radial Direction at High Operating Speed of 98.2rps/ $\sqrt{K}$



# Static Temperature along the Axial Direction at High Operating Speed of 98.2rps/ $\sqrt{K}$



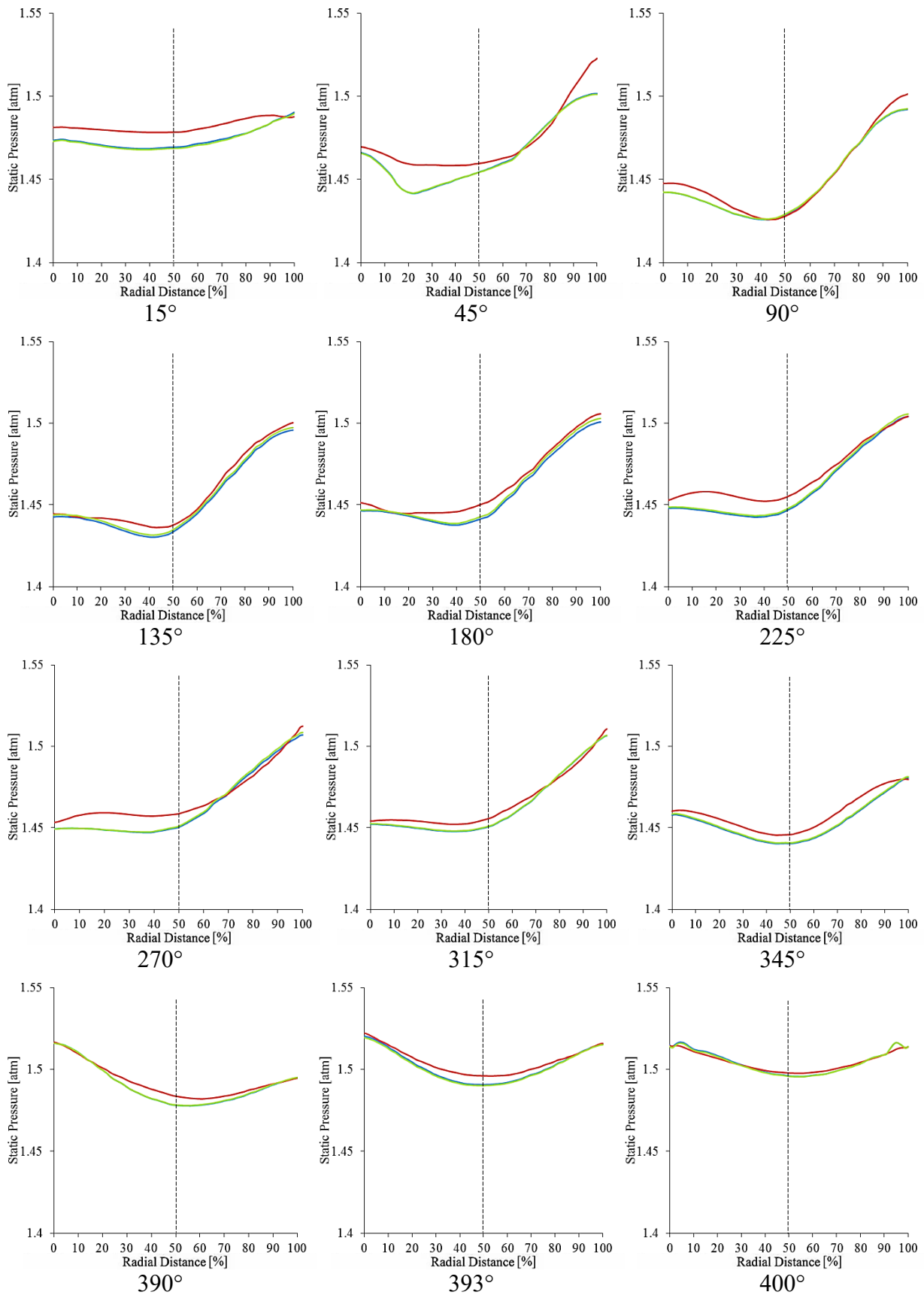
### **APPENDIX 3 Chapter 5 Flow Field Profiles along the Radial Direction and Axial Direction**

The following section depicts the variations in the flow characteristics of static pressure, velocity magnitude and static temperature at design flow conditions at two instances. The first instance is when the impeller blade is aligned with the volute tongue and the second instance is when one impeller blade has passed the volute tongue and another blade is approaching the tongue. These have been captured at low operating speed of 58.9rps/ $\sqrt{K}$  and high operating speed of 98.2rps/ $\sqrt{K}$ , along the radial and axial of each cross-sectional profile around the centrifugal compressor volute at the locations illustrated in Figure 3.9. A centreline has been displayed for each cross-section in the data set to identify the symmetry and asymmetry of the flow field variance exhibited along the radial direction of the cross-section and along the axial direction of the cross-section.



### Static Pressure along the Radial Direction at Low Operating Speed of 58.9rps/ $\sqrt{K}$

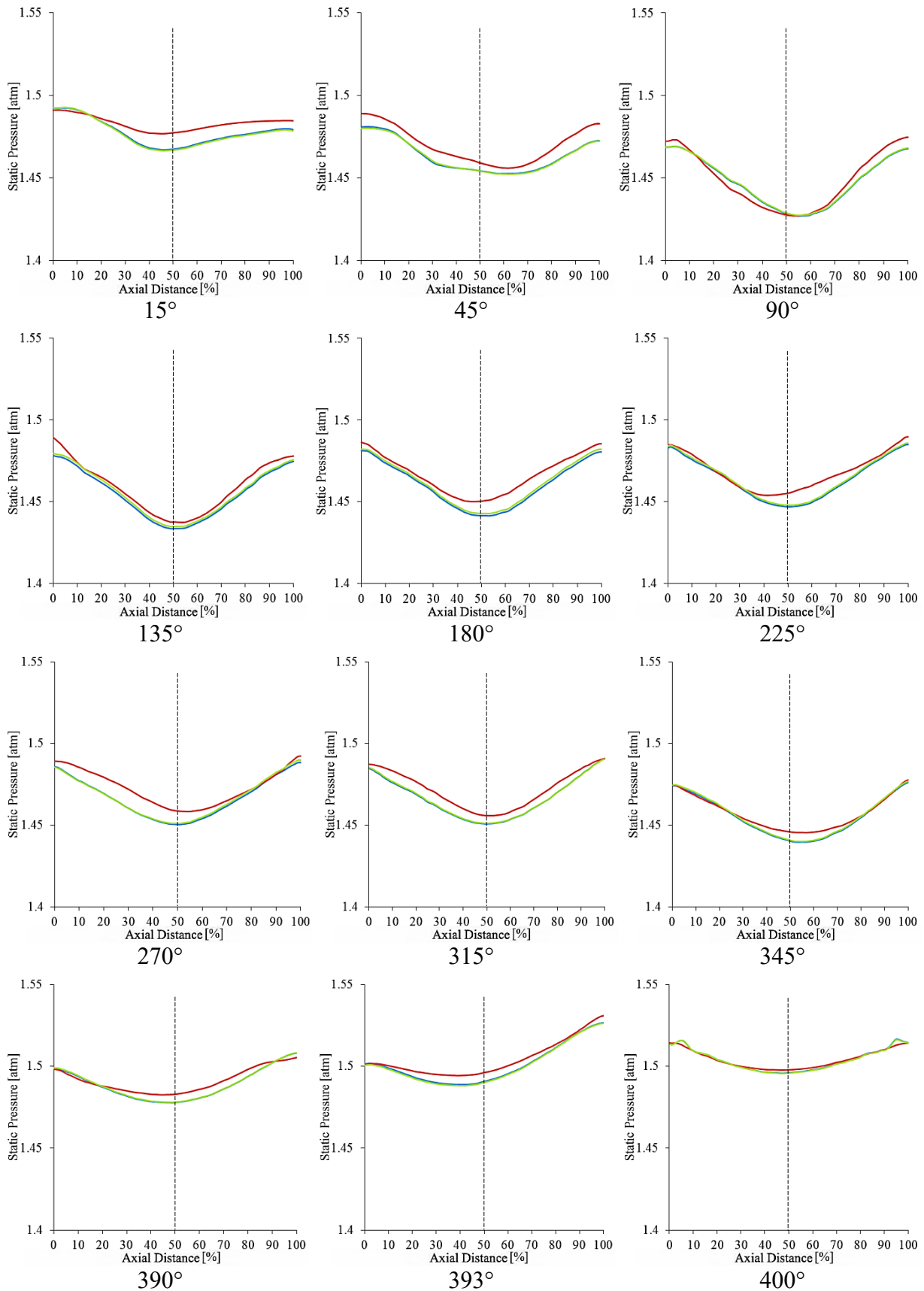
Steady      Unsteady Impeller Rotation 180°      Unsteady Impeller Rotation 225°



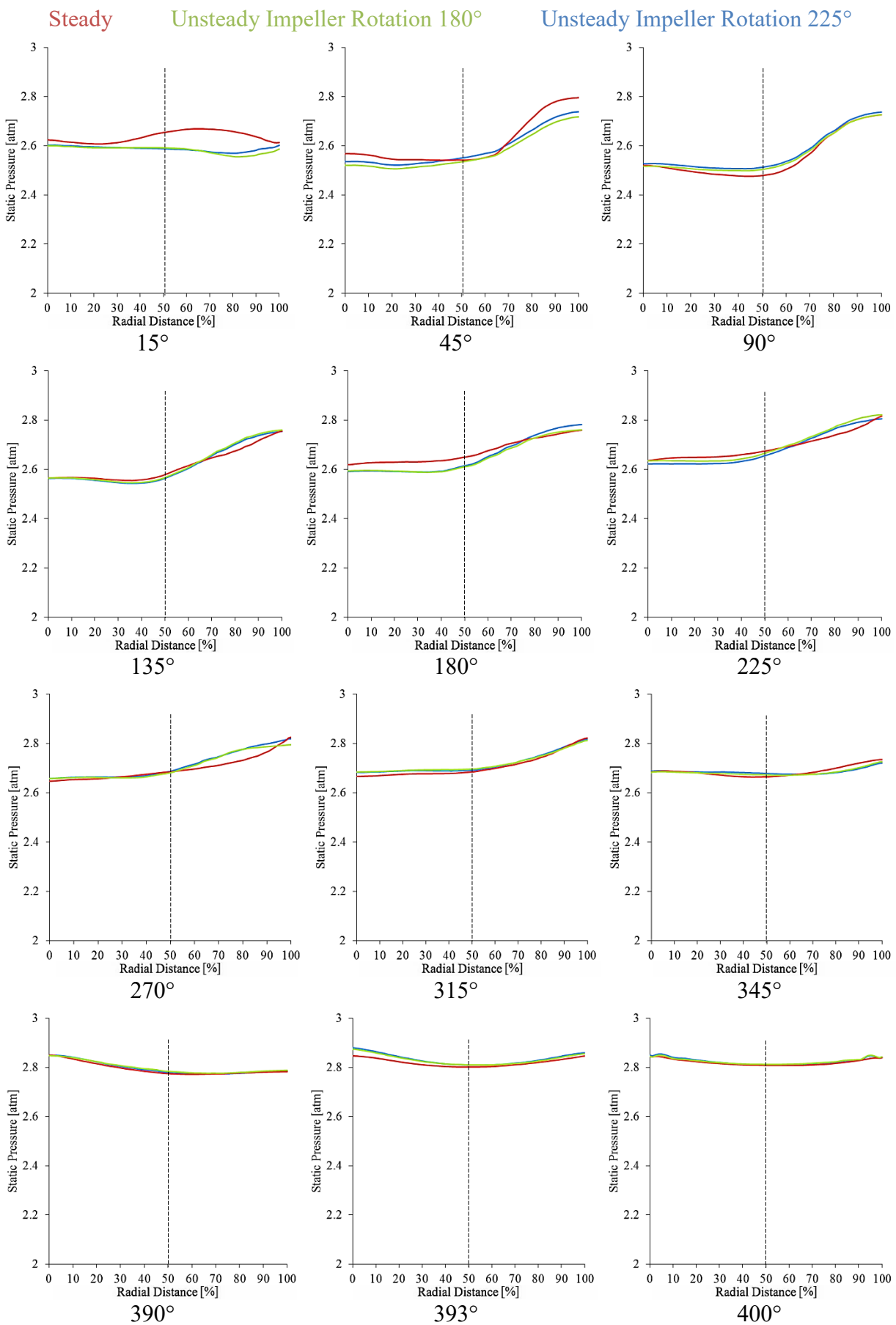


### Static Pressure along the Axial Direction at Low Operating Speed of 58.9rps/ $\sqrt{K}$

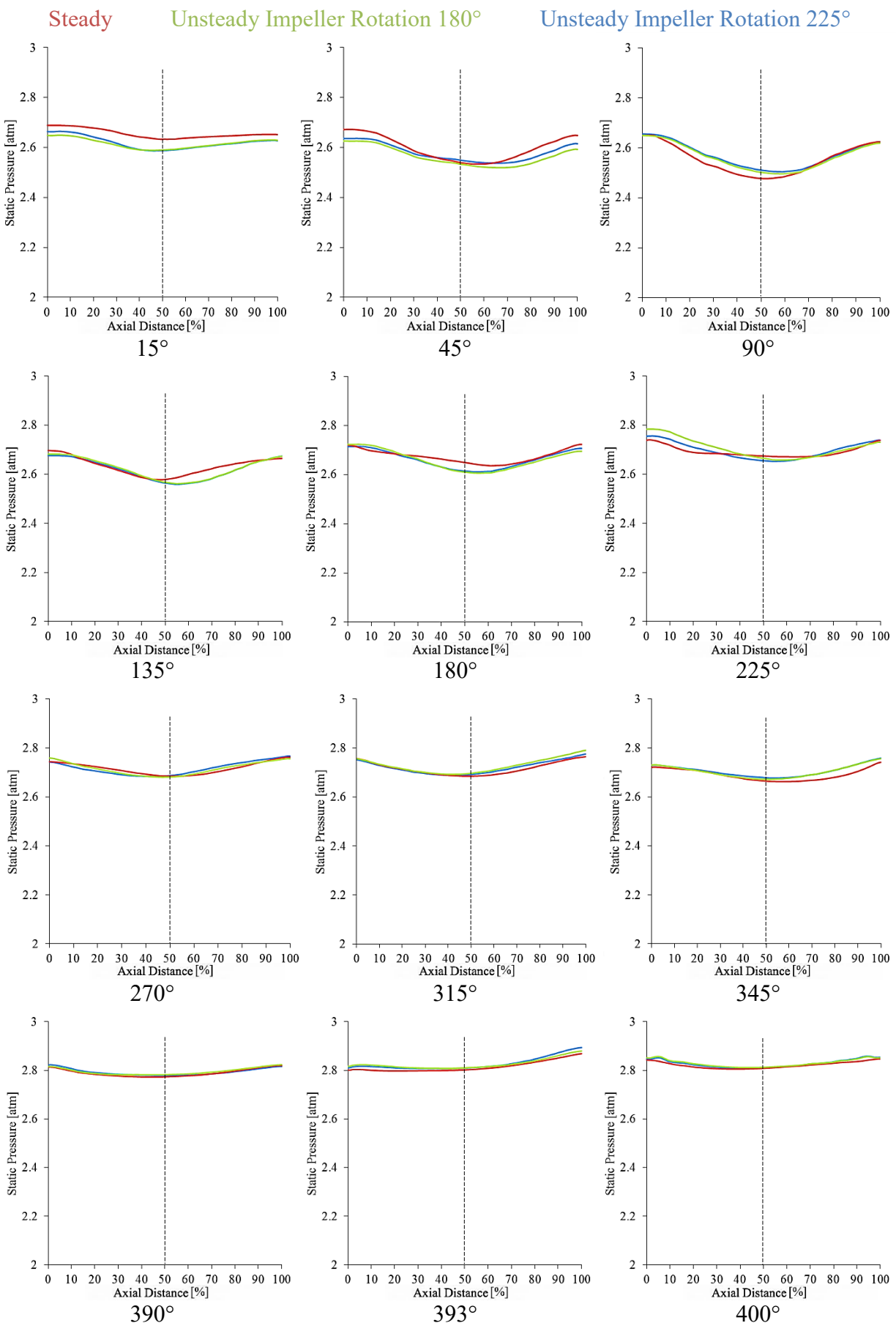
Steady      Unsteady Impeller Rotation 180°      Unsteady Impeller Rotation 225°



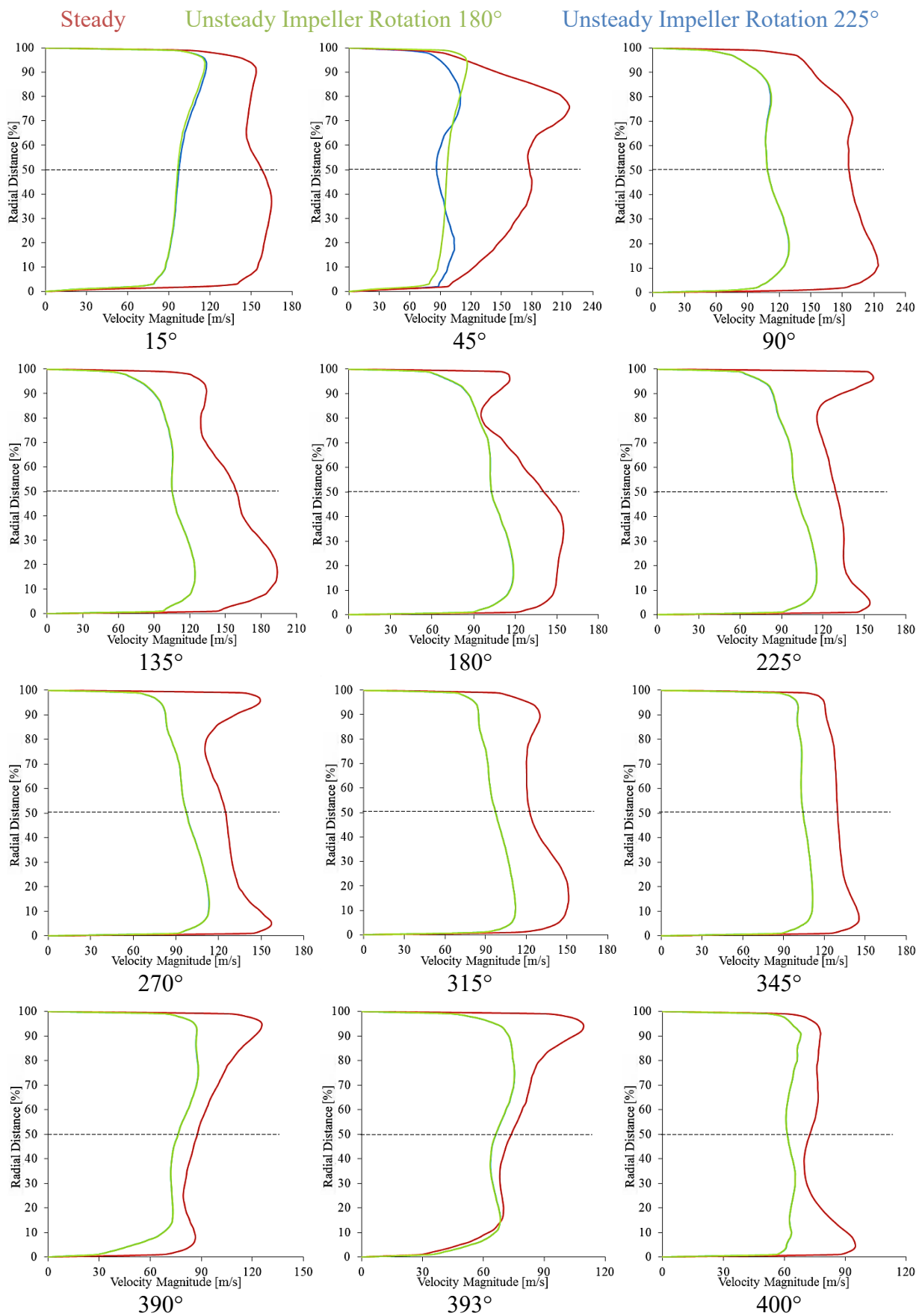
### Static Pressure along the Radial Direction at High Operating Speed of 98.2rps/ $\sqrt{K}$



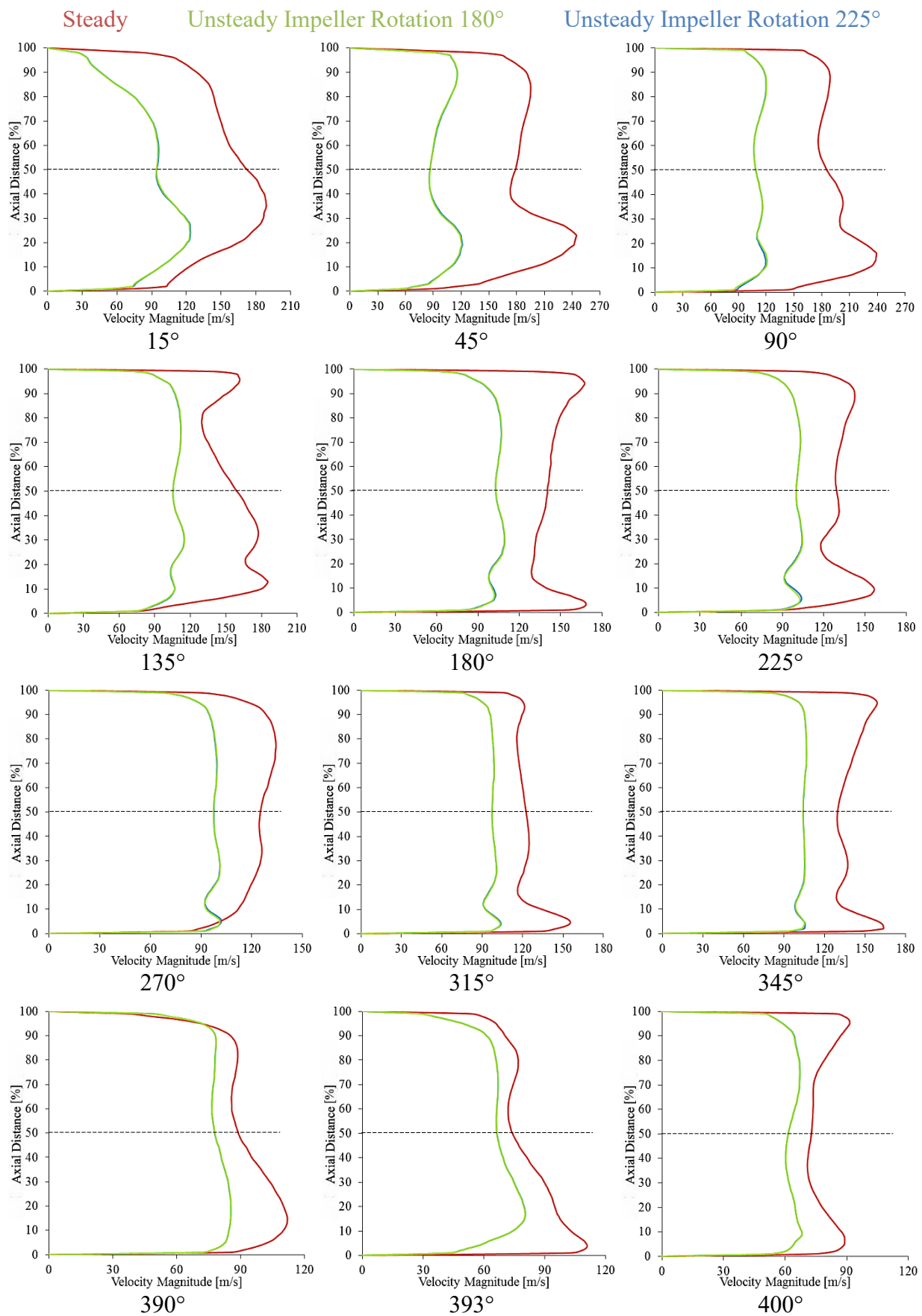
### Static Pressure along the Axial Direction at High Operating Speed of 98.2rps/ $\sqrt{K}$



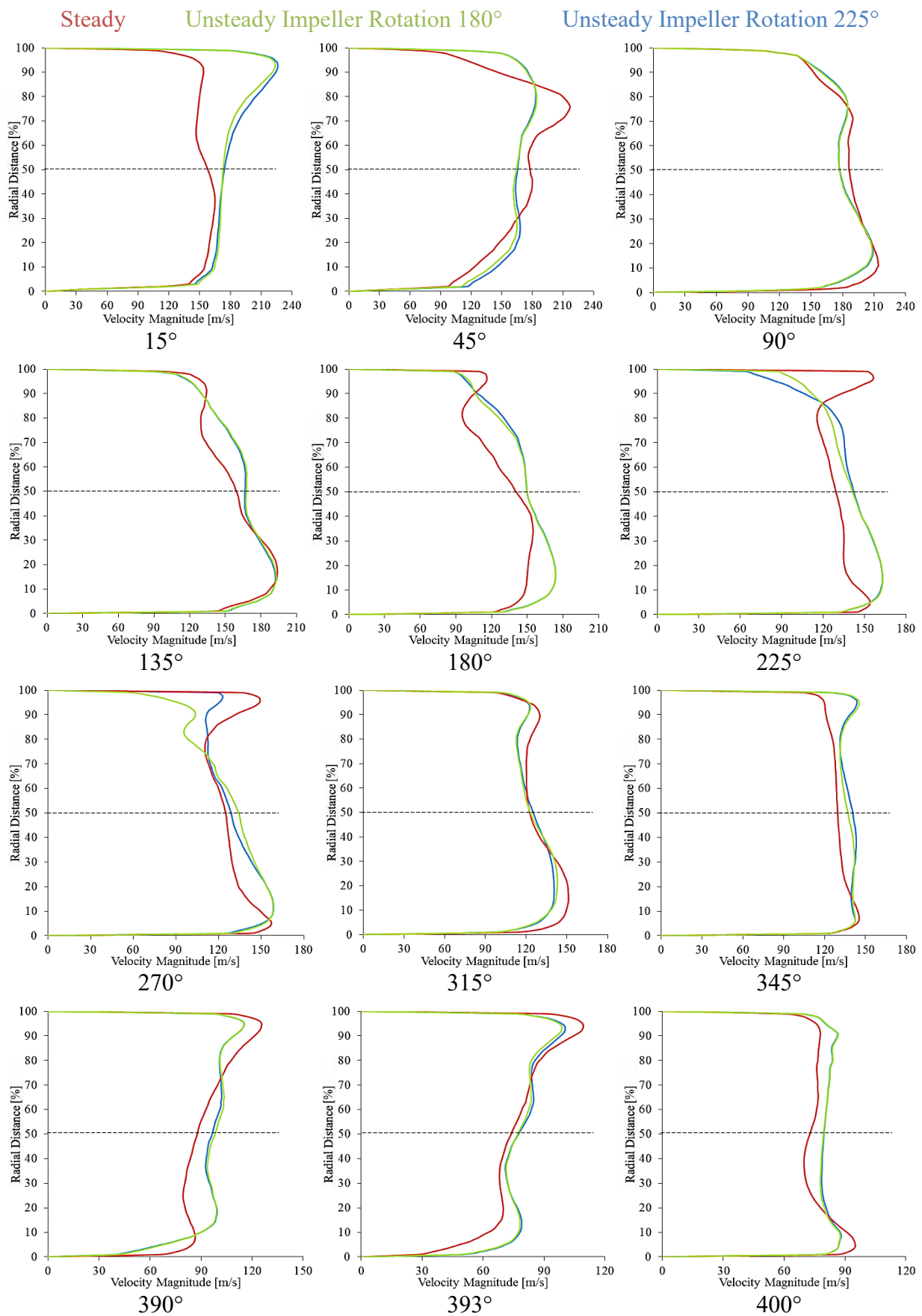
# Velocity Magnitude along the Radial Direction at Low Operating Speed of 58.9rps/ $\sqrt{K}$



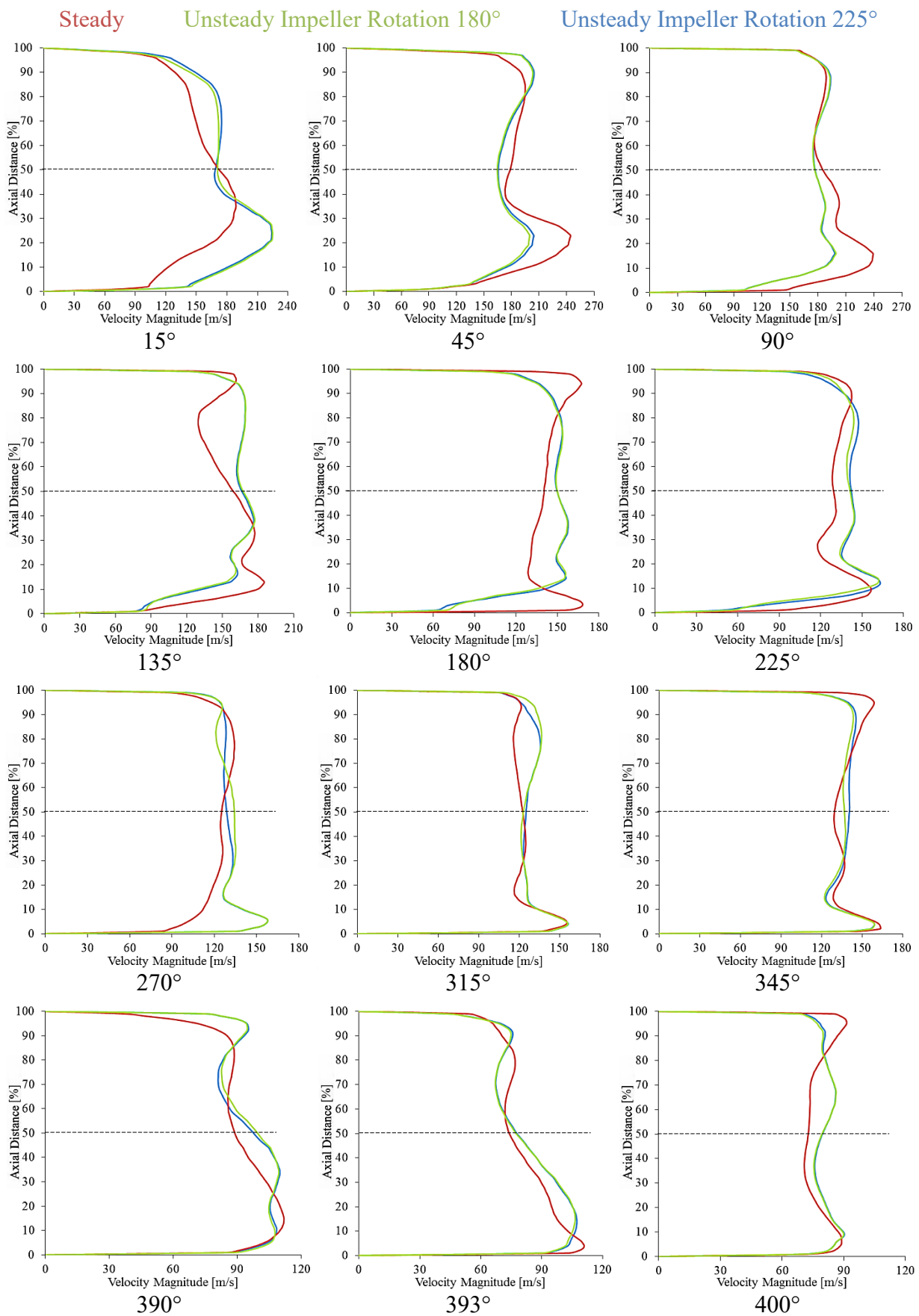
### Velocity Magnitude along the Axial Direction at Low Operating Speed of 58.9rps/ $\sqrt{K}$



# Velocity Magnitude along the Radial Direction at High Operating Speed of 98.2rps/ $\sqrt{K}$

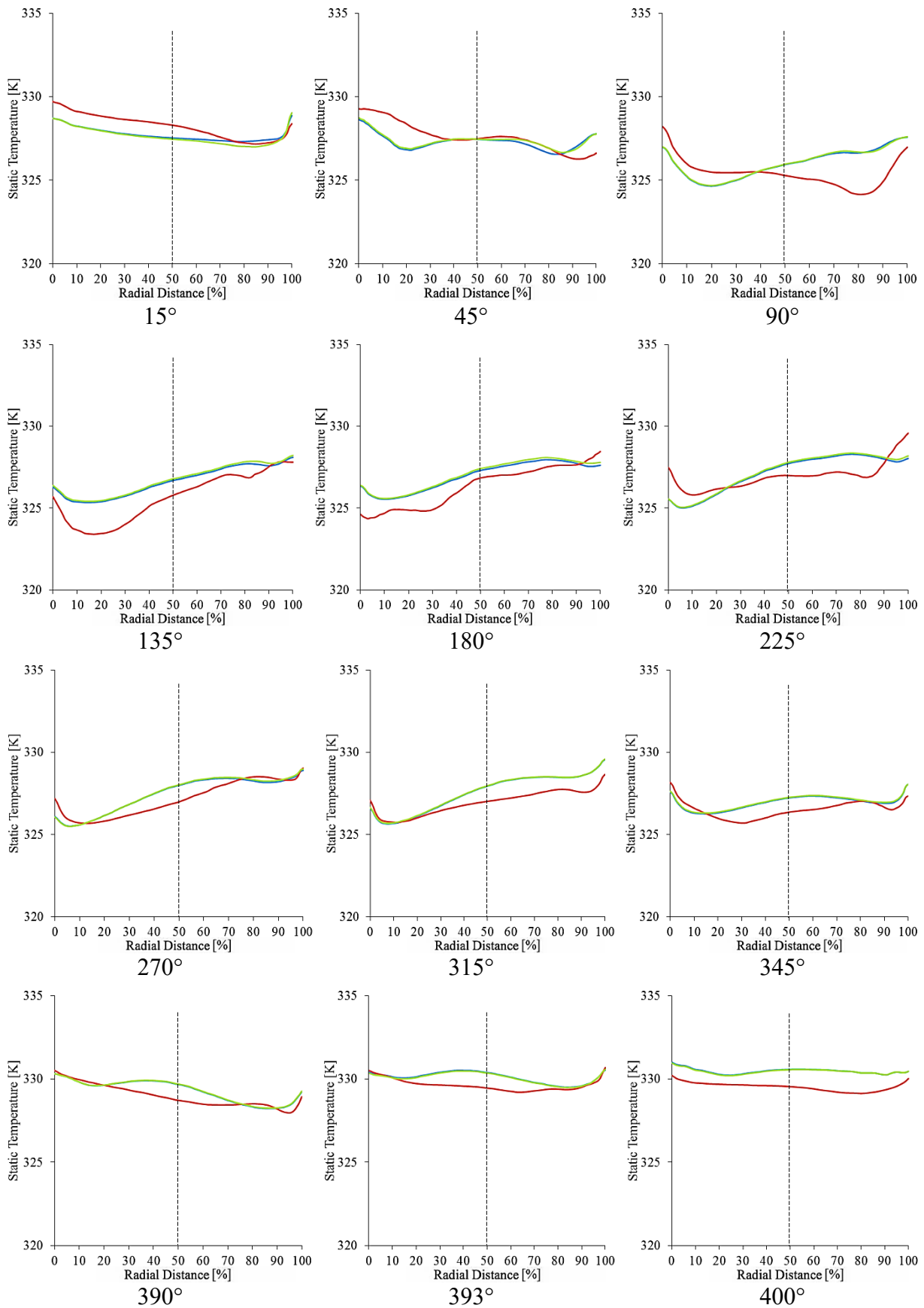


### Velocity Magnitude along the Axial Direction at High Operating Speed of 98.2rps/ $\sqrt{K}$



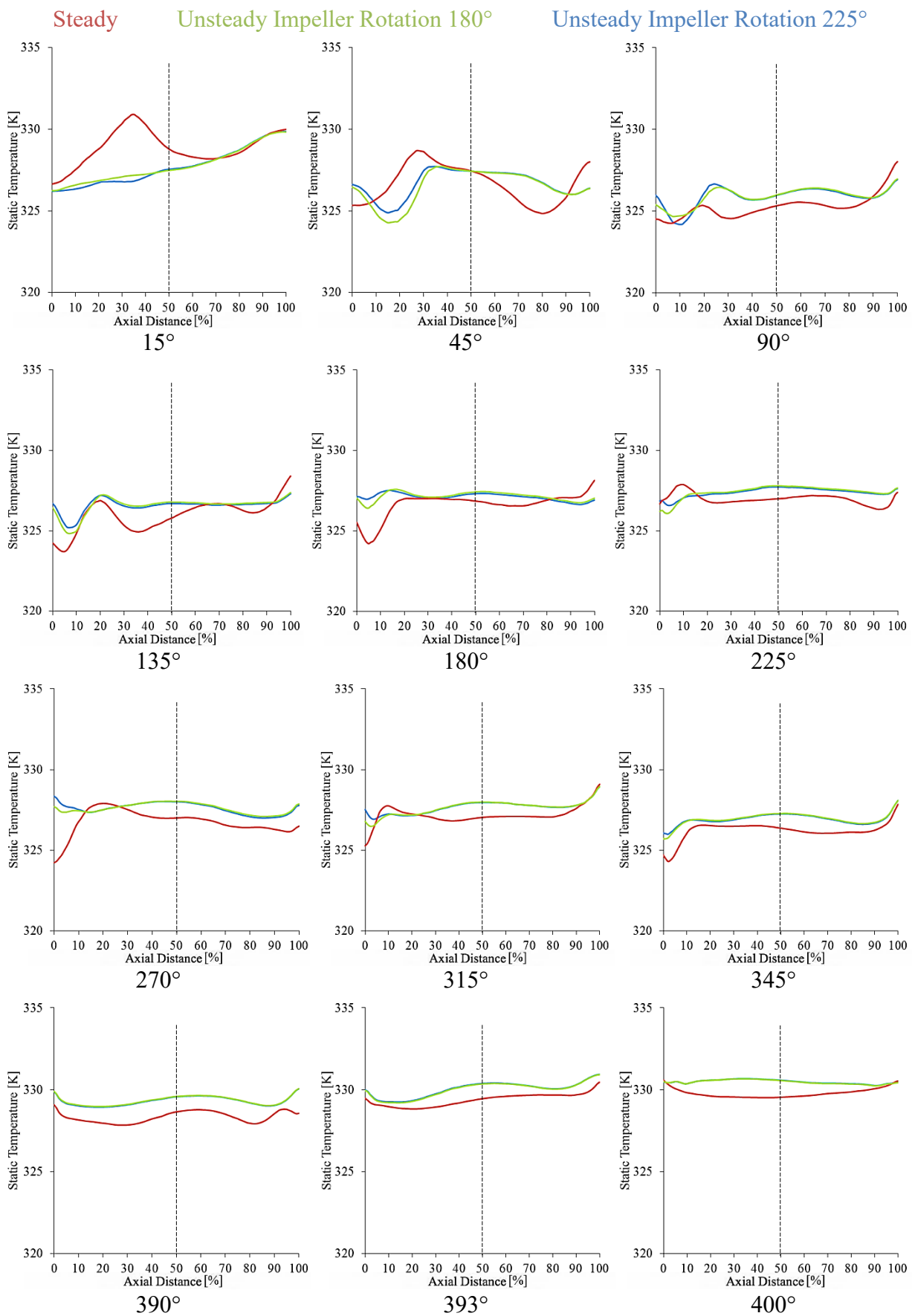
### Static Temperature along the Radial Direction at Low Operating Speed of 58.9rps/ $\sqrt{K}$

Steady      Unsteady Impeller Rotation 180°      Unsteady Impeller Rotation 225°



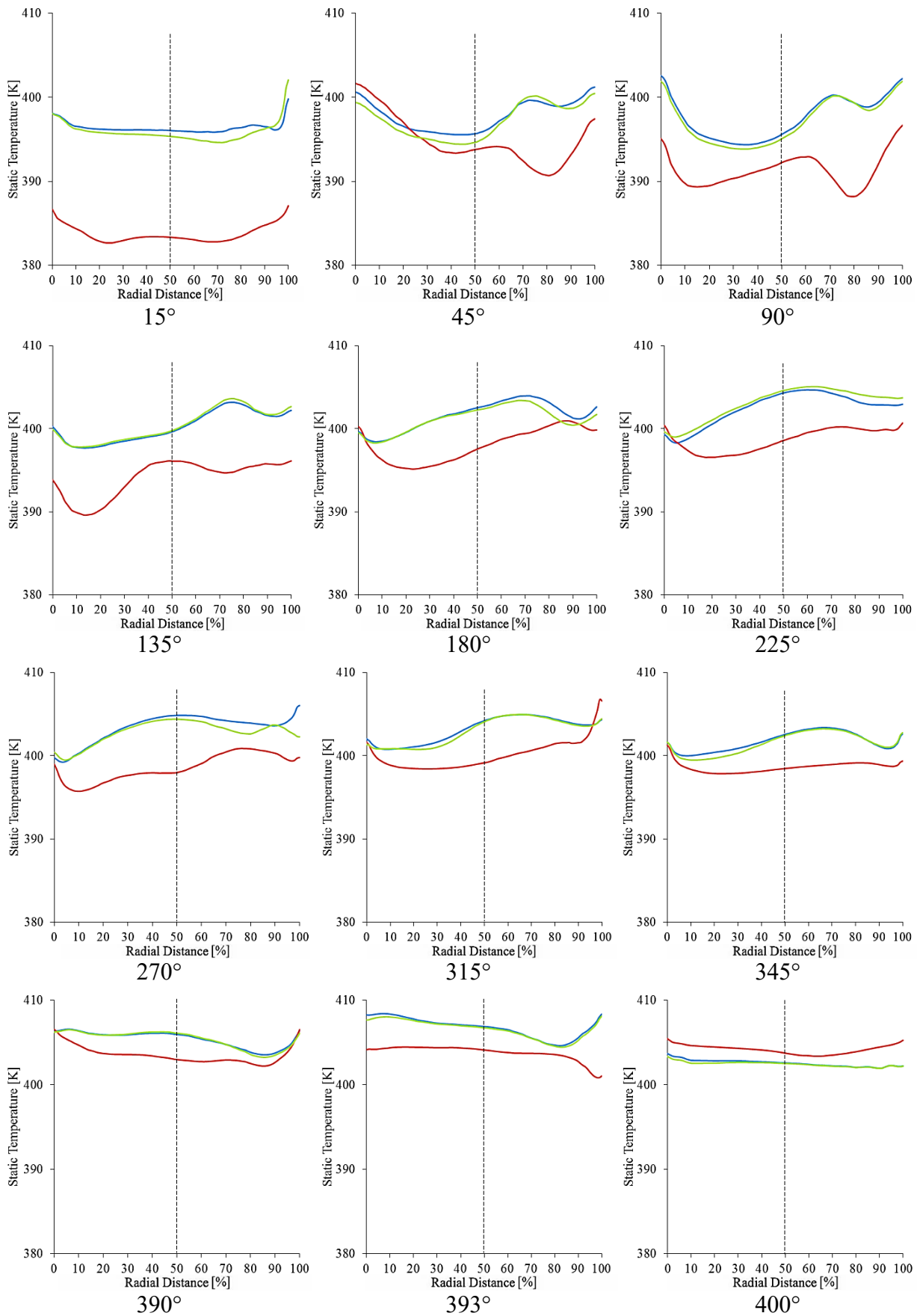


### Static Temperature along the Axial Direction at Low Operating Speed of 58.9rps/ $\sqrt{K}$



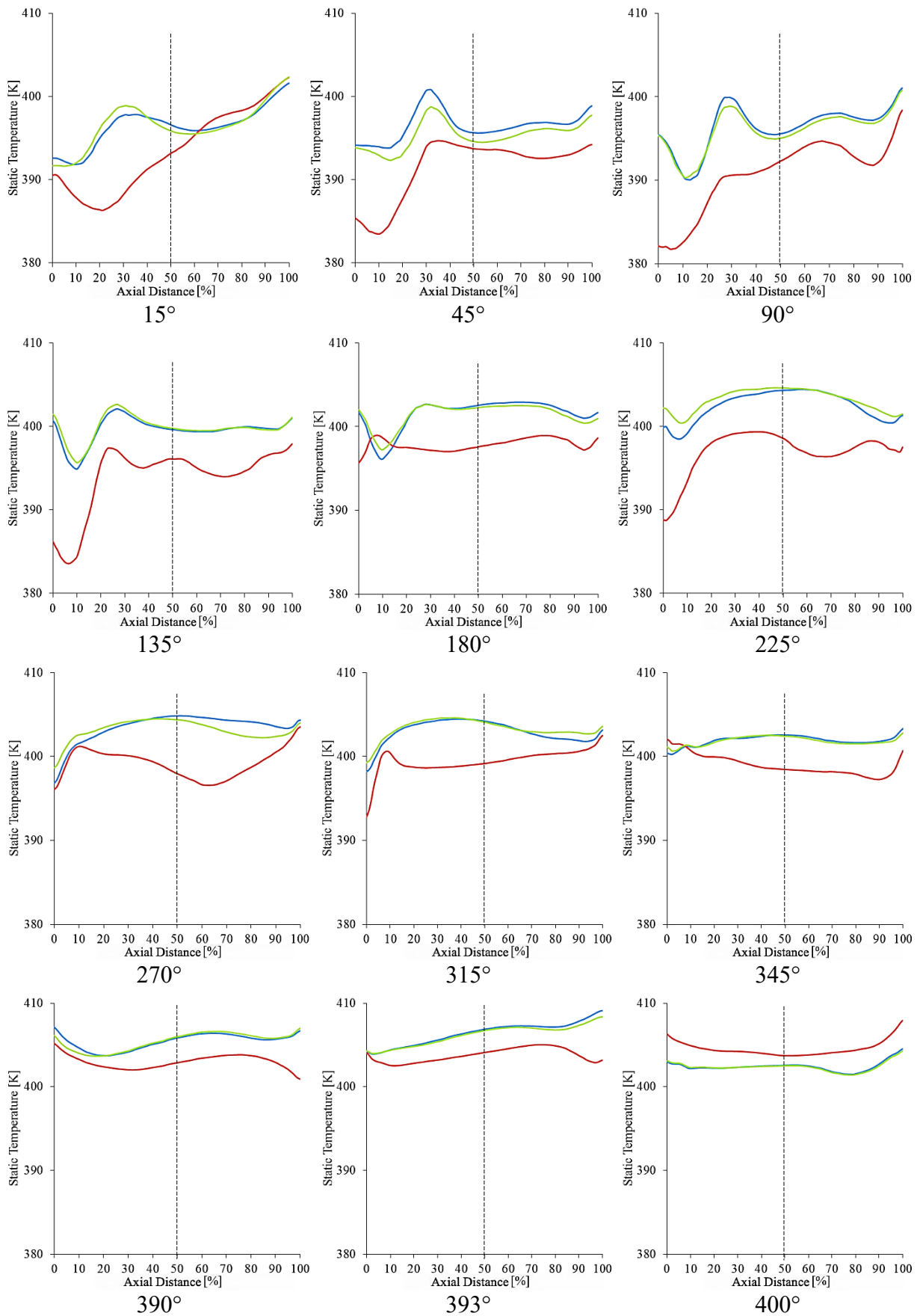
# Static Temperature along the Radial Direction at High Operating Speed of 98.2rps/ $\sqrt{K}$

Steady      Unsteady Impeller Rotation 180°      Unsteady Impeller Rotation 225°



### Static Temperature along the Axial Direction at High Operating Speed of 98.2rps/ $\sqrt{K}$

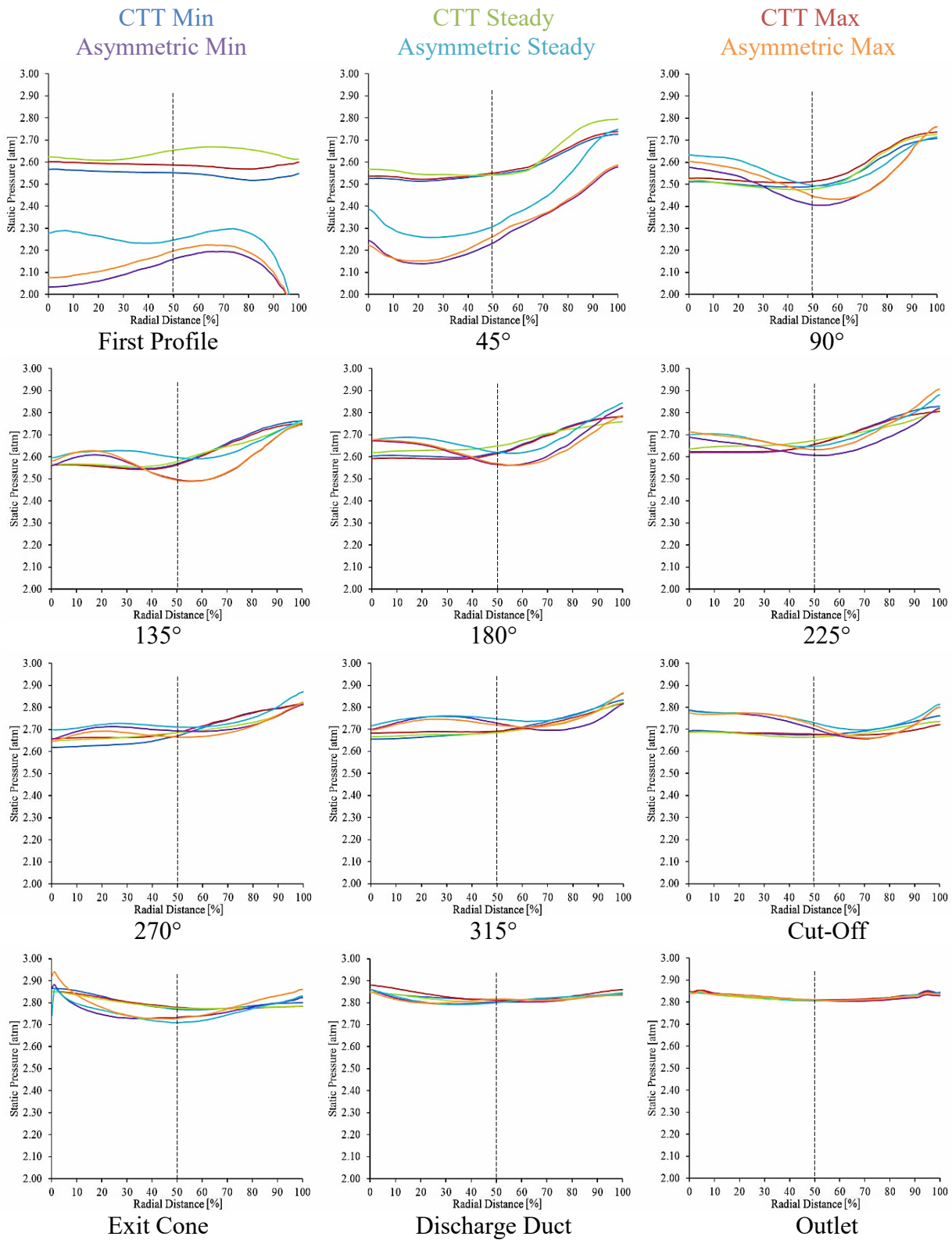
Steady      Unsteady Impeller Rotation 180°      Unsteady Impeller Rotation 225°



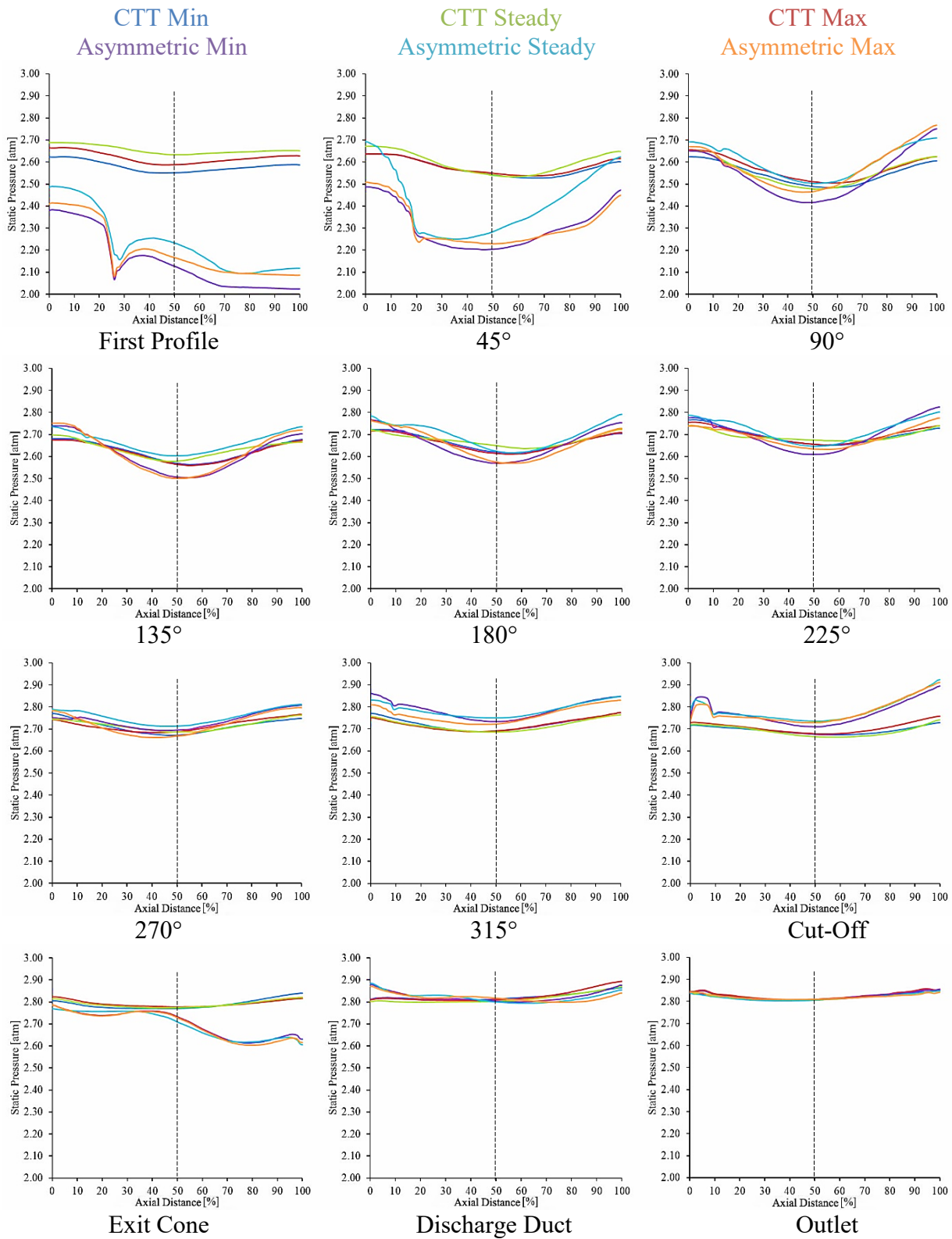
## **APPENDIX 4 Chapter 6 Flow Field Profiles along the Radial Direction and Axial Direction**

The following section depicts the variations in the flow characteristics of static pressure, velocity magnitude and static temperature at design flow conditions. These profiles depict the minimum and maximum responses for the CTT volute model and the Asymmetric volute model, which are compared against their corresponding steady responses. These have been captured at high operating speed of 98.2rps/ $\sqrt{K}$  along the radial and axial of each cross-sectional profile around the centrifugal compressor volute at the locations illustrated in Figure 3.9. A centreline has been displayed for each cross-section in the data set to identify the symmetry and asymmetry of the flow field variance exhibited along the radial direction of the cross-section and along the axial direction of the cross-section.

## Static Pressure along the Radial Direction

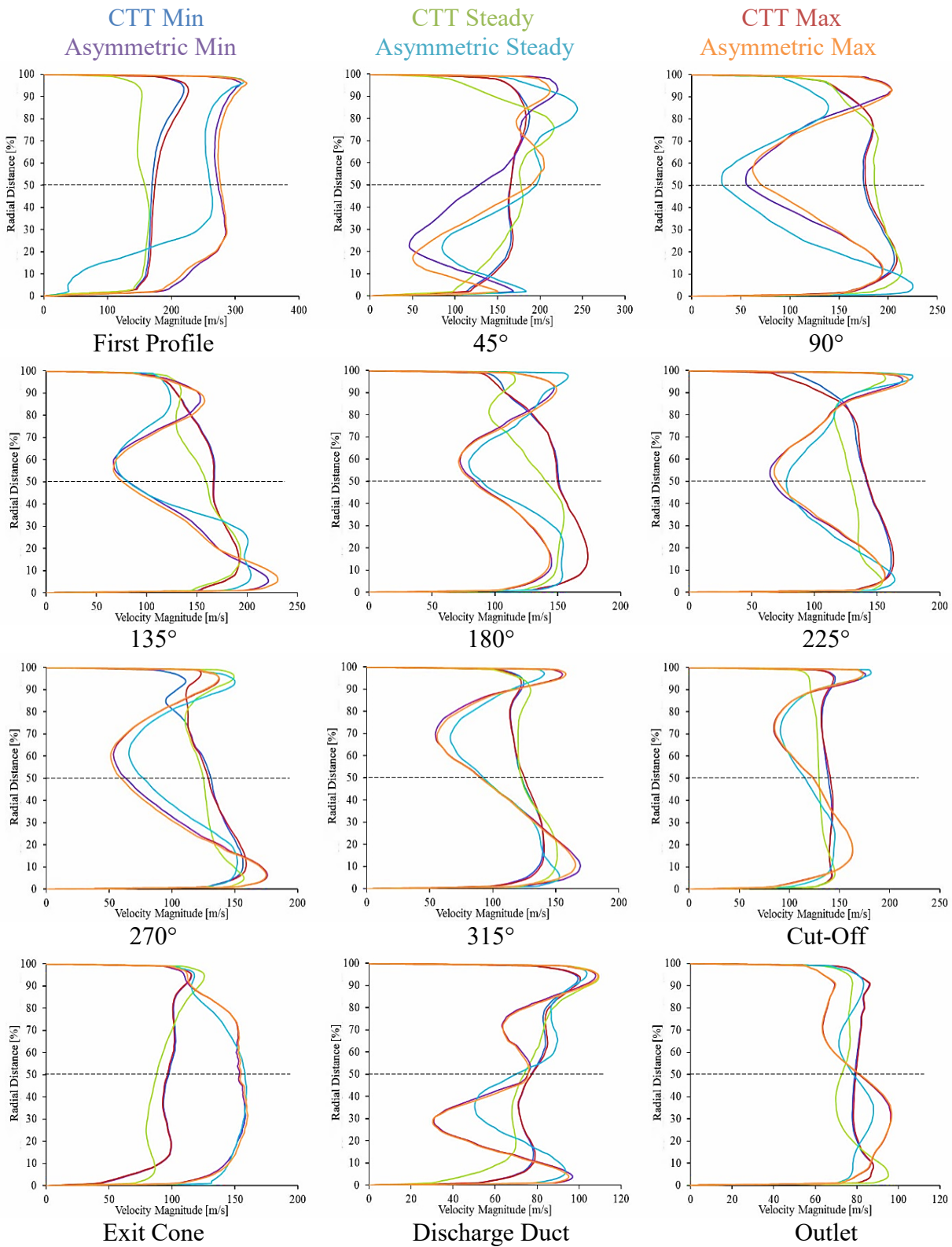


## Static Pressure along the Axial Direction

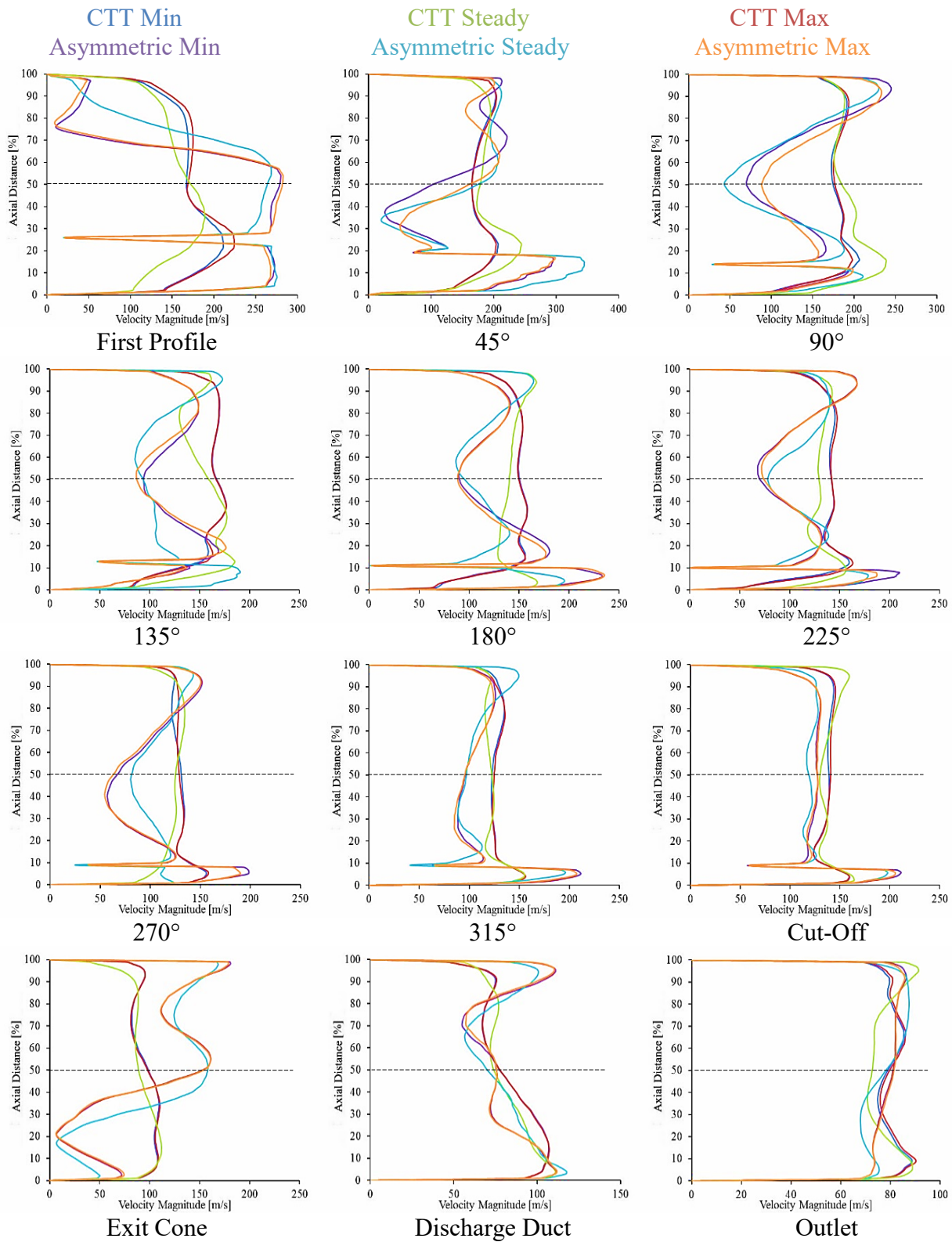




## Velocity Magnitude along the Radial Direction

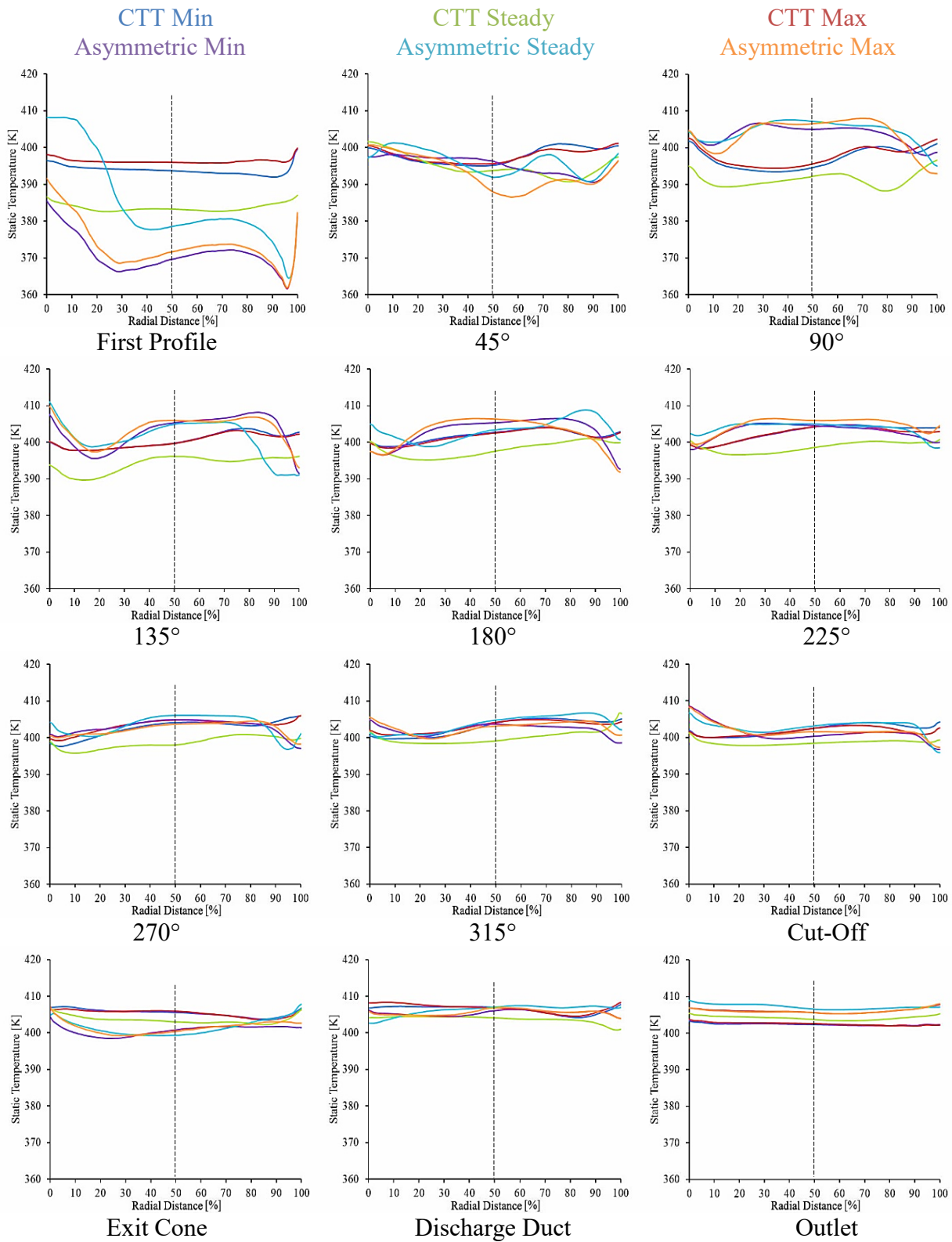


## Velocity Magnitude along the Axial Direction

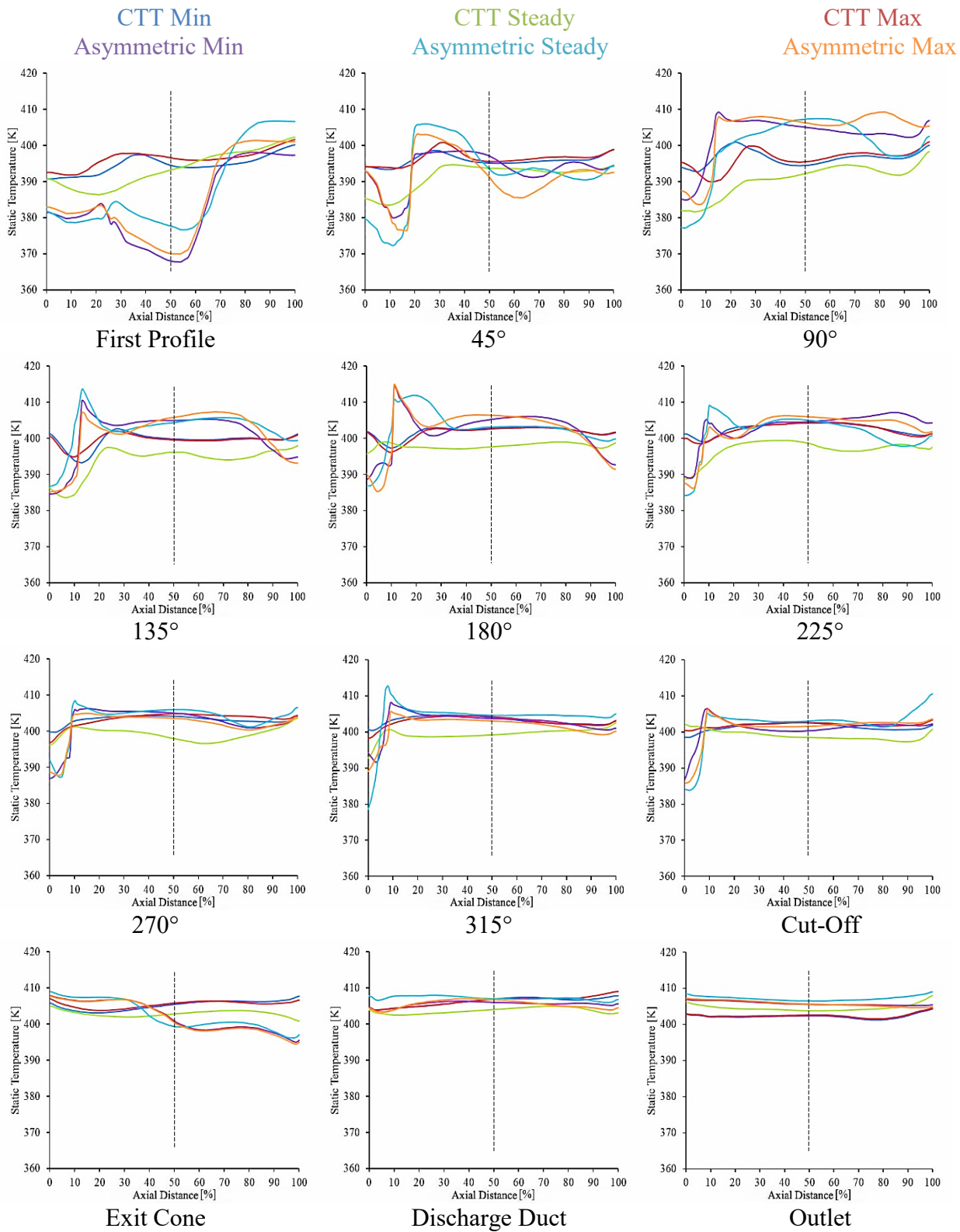




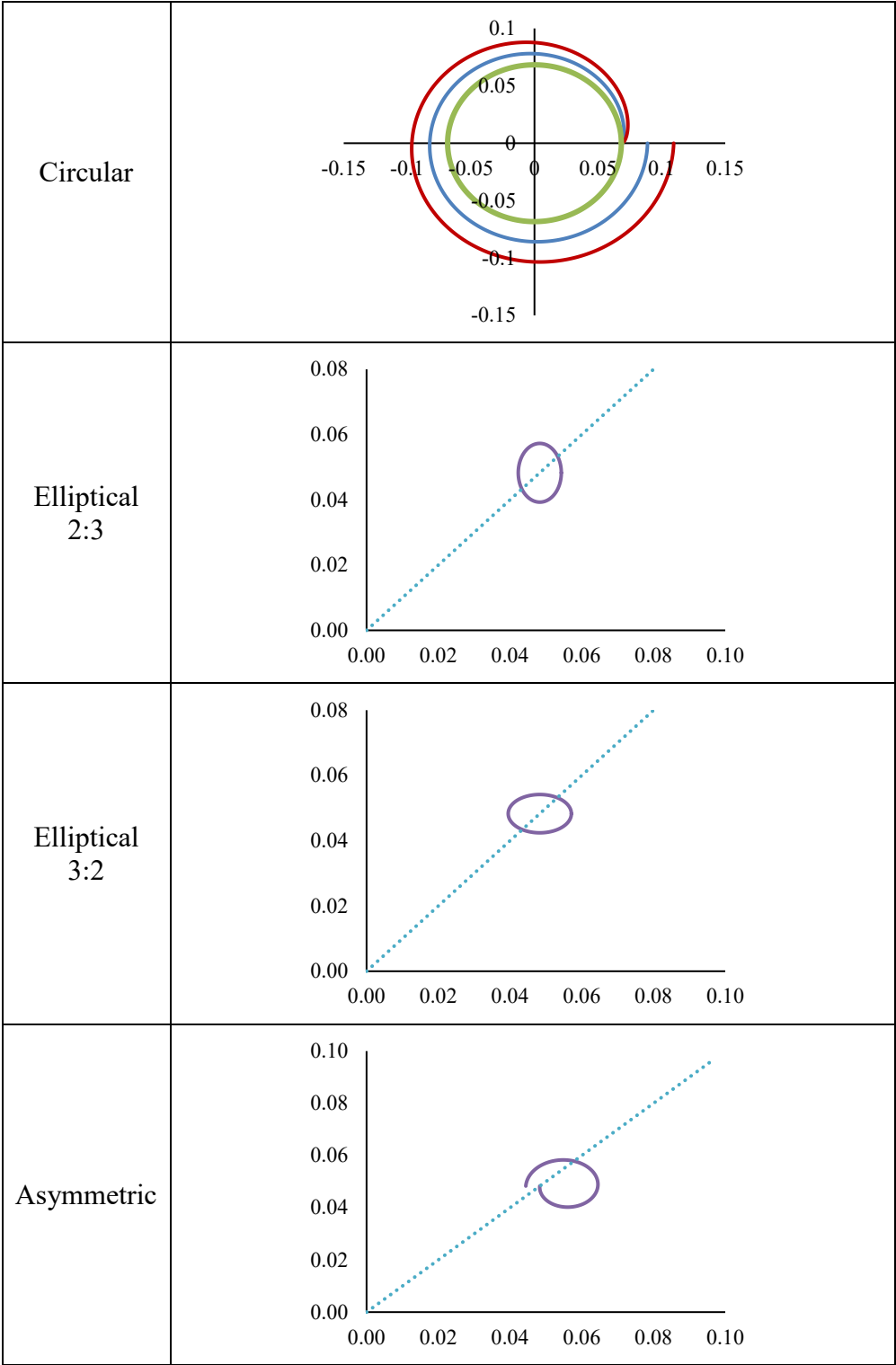
## Static Temperature along the Radial Direction



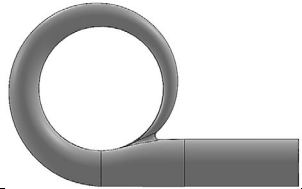


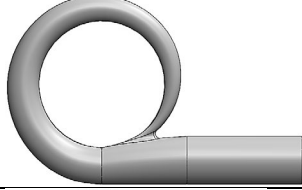





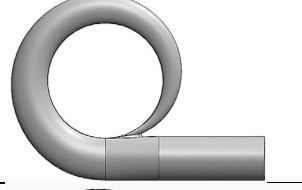


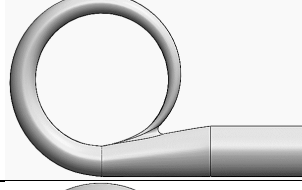











## Static Temperature along the Axial Direction



APPENDIX 5 Volute Expression Application



**APPENDIX 6 Volute Models**

Ideal Symmetric Circular			
Actual Symmetric Circular			
Ideal Symmetric Elliptical 2:3			
Actual Symmetric Elliptical 2:3			
Ideal Symmetric Elliptical 3:2			
Actual Symmetric Elliptical 3:2			
Asymmetric			
CTT			

## APPENDIX 7 Equivalent Length Calculation for Head Loss

Where length equivalent equation is given from arc length:

$$L = r\theta$$

Hence,

$$L_{eq} = \left( \frac{r_{c1} + r_{c2}}{2} \right) \cdot dl$$

And Baker's length equation is given by,

$$\frac{r_4 k}{2} \left( \frac{V}{4\pi r_4^2 C_{u4}} \theta^2 + \frac{4}{3\sqrt{k}} \sqrt{\frac{V}{2\pi^2 r_4^2 C_{u4}}} \theta^{3/2} \right)$$

$L_{eq}$	Baker's Length equation	% error
0.025382	0.024860	-2.1
0.032232	0.032263	0.1
0.060087	0.060147	0.1
0.062172	0.062199	0.0
0.063887	0.063903	0.0
0.065396	0.065407	0.0
0.066767	0.066775	0.0
0.068038	0.068044	0.0
0.022949	0.022950	0.0

Due to the negligible variance between the two equations, the standard  $L_{eq}$  had been used for simplicity, since the results are satisfactory.

## APPENDIX 8 Hydraulic Diameter Calculation for Head Loss

$$Circular = D$$

$$Elliptical = \frac{4ab(64 - 16c^2)}{(a + b)(64 - 3c^4)} \quad \text{where } c = \frac{a - b}{a + b}$$

$$Asymmetric = \frac{4A}{P}$$

**APPENDIX 9 Wall Shear Stress on Volute Scroll Sections**

Wall Shear Stress [Pa]						
$\theta^\circ$	Ideal Circular	Actual Circular	Ideal Elliptical 2:3	Actual Elliptical 2:3	Ideal Elliptical 3:2	Actual Elliptical 3:2
0 - 20	320	270	448	505	86	142
20 - 45	365	469	424	486	403	521
45 - 90	421	430	359	384	476	440
90 - 135	295	221	272	209	342	272
135 - 180	253	234	206	170	305	262
180 - 225	241	218	203	159	262	239
225 - 270	225	206	180	152	268	242
270 - 315	197	185	161	149	239	219
315 - 330	193	180	157	159	218	209

Wall Shear Stress [Pa]						
CTT	58.9rps/ $\sqrt{K}$			98.2rps/ $\sqrt{K}$		
$\theta^\circ$	High Flow Rate	Design Flow Rate	High Flow Rate	Design Flow Rate	High Flow Rate	Design Flow Rate
0 - 15	88	30	88	184	204	344
15 - 45	140	61	140	233	233	386
45 - 90	117	103	117	316	386	353
90 - 135	58	85	58	367	312	249
135 - 180	35	78	35	344	280	114
180 - 225	25	75	25	350	267	94
225 - 270	15	69	15	333	243	96
270 - 315	10	66	10	328	219	169
315 - 345	10	66	10	353	228	188
ASYMMETRIC	58.9rps/ $\sqrt{K}$			98.2rps/ $\sqrt{K}$		
$\theta^\circ$	High Flow Rate	Design Flow Rate	High Flow Rate	Design Flow Rate	High Flow Rate	Design Flow Rate
0 - 20	124	88	36	339	303	184
20 - 45	235	164	36	753	491	234
45 - 90	166	148	56	615	589	373
90 - 135	122	94	52	401	404	223
135 - 180	133	97	31	421	334	141
180 - 225	129	91	23	404	294	134
225 - 270	126	91	31	398	289	101
270 - 315	122	76	36	363	263	134
315 - 330	130	82	40	383	274	235

**APPENDIX 10 Head Loss through Volute Scroll Section**

HEAD LOSS [m]						
$\theta^\circ$	Ideal Circular	Actual Circular	Ideal Elliptical 2:3	Actual Elliptical 2:3	Ideal Elliptical 3:2	Actual Elliptical 3:2
0 - 20	162	133	229	242	44	75
20 - 45	183	227	218	234	208	264
45 - 90	265	250	234	231	307	262
90 - 135	145	100	139	100	172	126
135 - 180	106	93	90	71	130	105
180 - 225	90	78	79	60	99	86
225 - 270	77	67	65	52	93	80
270 - 315	62	56	54	48	77	67
315 - 330	19	18	17	17	22	21

HEAD LOSS [m]						
CTT	58.9rps/ $\sqrt{K}$			98.2rps/ $\sqrt{K}$		
$\theta^\circ$	High Flow Rate	Design Flow Rate	Low Flow Rate	High Flow Rate	Design Flow Rate	Low Flow Rate
0 - 15	22	7	21	35	32	59
15 - 45	62	25	61	80	66	118
45 - 90	62	52	61	131	132	127
90 - 135	26	35	25	126	87	72
135 - 180	13	28	13	104	67	28
180 - 225	9	24	8	97	57	21
225 - 270	5	21	5	86	48	19
270 - 315	3	19	3	82	41	32
315 - 345	2	12	2	59	28	23
TOTAL	203	224	199	800	560	499
ASYMMETRIC	58.9rps/ $\sqrt{K}$			98.2rps/ $\sqrt{K}$		
$\theta^\circ$	High Flow Rate	Design Flow Rate	Low Flow Rate	High Flow Rate	Design Flow Rate	Low Flow Rate
0 - 20	38	25	10	92	61	36
20 - 45	76	50	11	207	105	49
45 - 90	72	61	23	215	166	107
90 - 135	45	32	18	116	94	53
135 - 180	45	30	10	111	70	30
180 - 225	40	26	7	99	57	26
225 - 270	37	25	8	92	52	18
270 - 315	34	20	9	80	45	23
315 - 330	12	7	3	28	15	13
TOTAL	399	276	100	1040	665	356

# LIST OF PUBLICATIONS

---

Aboufares, G., Zala, K., Mishra, R. and Asim, T. (2016) 'Effects of Sand Particle Size on the Performance Characteristics of a Vertical Axis Wind Turbine'. *In: 6th International and 43rd National Conference on Fluid Mechanics and Fluid Power, December 15-17, 2016, MNNITA, Allahabad, U.P., India*

Freegah, B., Asim, T., Mishra, R. and Zala, K. (2015) 'Numerical Investigations on the Effects of Transient Heat Input and Loading Conditions on the Performance of a Single-phase Closed-loop Thermo-syphon'. *In: 42nd National Conference on Fluid Mechanics and Fluid Power, 14th - 16th December 2015, Surathkal, India*

Albarzenji, D., Pradhan, S., Mishra, R. and Zala, K. (2014) 'Effect of a swirl on void fraction profiles in multiphase flows'. *In: Proceedings of 5th International and 41st National Conference on Fluid Mechanics and Fluid Power. : Springer.*

Al-Obaidi, A., Pradhan, S., Asim, T., Mishra, R. and Zala, K. (2014) 'Numerical studies of the velocity distribution within the volute of a centrifugal pump'. *In: 27th International Congress of Condition Monitoring and Diagnostic Engineering Management, 16th - 18th September 2014, Brisbane, Australia*

Mohamed, F., Park, K., Pradhan, S., Mishra, R., Zala, K., Asim, T., Al-Obaidi, A. (2014) 'The effect of blade angles of the vertical axis wind turbine on the output performance'. *In: 27th International Congress of Condition Monitoring and Diagnostic Engineering, Brisbane, Australia*

Fleming, L., Zala, K., Ousey, K. (2014) 'Investigating the absorbency effects of LBF barrier cream', *Wounds UK, Harrogate, UK*

Asim, T., Sendanayake, I., Mishra, R., Zala, K. and Ubbi, K. (2013) 'Effects of a Moving Surface Boundary Layer Control Device (MSBC) on the Drag Reduction in Heavy Commercial Vehicles'. *In: 40th National Conference on Fluid Mechanics & Fluid Power FMFP 2013, 12-14 December 2013, NIT Hamirpur, Himachal Pradesh, India*

Asim, T., Mishra, R., Paris, A. and Zala, K. (2013) 'Optimal Design Methodology for On-shore Hydraulic Pipelines Transporting Spherical Capsules' *Procedia CIRP: TESC 2013 - 2nd International Through-life Engineering Services Conference*, 11, pp. 305-310. ISSN 2212 – 8271

Asim, T., Mishra, R., Ubbi, K. and Zala, K. (2013) 'Computational Fluid Dynamics Based Optimal Design of Vertical Axis Marine Current Turbines' *Procedia CIRP: TESC 2013 - 2nd International Through-life Engineering Services Conference*, 11, pp. 323-327. ISSN 2212 – 8271